Depth-resolved fibre photometry for Alzheimer's disease plaque pathology *in vivo*.

Nicole Byron

Feb 2024

A thesis submitted to the University of Strathclyde in accordance with the requirements for award of the degree of Doctor of Philosophy at the Strathclyde Institute of Pharmacy and Biomedical Sciences

Strathclyde Institute of Pharmacy and Biomedical Sciences, University of Strathclyde, Glasgow G4 0RE

Declaration of authenticity and author's rights

This thesis is the result of the author's original research. It has been composed by the author and has not been previously submitted for examination which has led to the award of a degree.

Signed:

Date: 11th Feb 2024

Published Work

The following papers were published during the course of this PhD:

Byron, N., Semenova, A. & Sakata, S. 2021. Mutual Interactions between Brain States and Alzheimer's Disease Pathology: A Focus on Gamma and Slow Oscillations. *Biology (Basel),* 10.

Byron, N. & Sakata, S. 2024. Fiber photometry-based investigation of brain function and dysfunction. *Neurophotonics,* 11**,** S11502.

International and national conference poster presentations

Nicole Byron, Niall McAlinden, Filippo Pisano, Jacques Ferreira, Marco Pisanello, Keith Mathieson, Massimo De Vittorio, Ferruccio Pisanello, Shuzo Sakata

Depth-resolved fibre photometry for Alzheimer's disease plaque pathology *in vivo.*

ENCODS, Jul 2022

FENS Jul 2022

ARUK, March 2023

Optogen, May 2023

Acknowledgments

While it may not be well recognised to dedicate a PhD thesis to someone, Anthony Connelly was one of a kind. He was well known as a hard-working, driven, and sociable gentleman. Amongst all memories, the major quality I have developed that I should thank my Papa Tony for, is the determination and drive that he has instilled in me since I can remember. I told him once I would do as much as I can to help cure Parkinson's disease and Papa Tony, I hope I do you proud.

Thank you to Papa Tony and the rest of my family and friends.

As well to all colleagues that trained and got me through these very challenging but rewarding years.

Table of Contents

List of Figures

List of Tables

Abbreviations

α7nAChR	Alpha-7 nicotinic acetylcholine receptor
2PM	Two-photon microscopy
5-HT	Serotonin
A	Auditory
AD	Alzheimer's disease
ADAS-Cog	Alzheimer's Disease Assessment Scale-Cognitive subscale
ADE	Amyloid degrading enzyme
AF	Autofluorescence
AGE-RAGE	Advanced glycation end-products-Receptor for AGE
AMPA	α-amino-3-hydroxy-5-methyl-4-isoxazolepropionic acid
AP	Anterior posterior
APK	Acute pharmacokinetic
APOE	Apolipoprotein E
ApoJ	Apolipoprotein J
APP	Amyloid precursor protein
AR	Adrenergic receptor
ASC	Apoptosis-associated speck-like protein containing a C-terminal caspase recruitment domain
ATP	Adenosine triphosphate
AV	Audio-visual
Aβ	Amyloid-beta
BACE	β-site amyloid precursor protein cleaving enzyme
BBB	Blood-brain-barrier
C1q	Complement component 1q
C83	83-amino-acid C-terminal APP fragment
C99	99-amino-acid C-terminal APP fragment
CCK	Cholecystokinin
CD36	Cluster of differentiation 36
CDK-5	Cyclin-dependent kinase 5
CLU	Clusterin
CNS	Central nervous system
CR1	Complement receptor 1
CT	Computed tomography
CX3CR1	CX3C motif chemokine receptor 1
dB SPL	Decibel sound pressure level
DBS	Deep brain stimulation
DMN	Default mode network
DMSO	Dimethyl sulfoxide
DNA	Deoxyribonucleic acid
DP	Depth profile
DV	Dorsoventral
E-I	Excitatory-Inhibitory
EEG	Electroencephalogram
Em	Emission
EMA	European Medicines Agency
EMG	Electromyography
Ex	Excitation
F	Female
FAD	Familial Alzheimer's disease
FDA	Food and Drug Administration
FF	Flat fibre
FITC	Fluorescein
FP	Fibre photometry

$GABA_AR$	γ-aminobutyric acid type A receptors
GECI	Genetically encoded calcium indicator
GENUS	Gamma entrainment using sensory stimulation
GEVI	Genetically encoded voltage indicator
GSK3β	Glycogen synthase kinase-3 beta
GV	Galvo voltage
GWAS	Genome-wide association studies
HC	Histology correlation
HIP	Hippocampal
I-I	Inhibitory-Inhibitory
i.p.	Intraperitoneal
i.v.	Intravenous
Iba1	Ionized calcium binding adaptor molecule 1
IL-1	Interleukin-1
IL-6	Interleukin-6
ING	Interneuron gamma
IPSP	Inhibitory postsynaptic potentials
ISF	Interstitial fluid
KI	Knock-in
KO	Knock-out
LDL	Low-density lipoprotein
LRP1	Low-density lipoprotein receptor-related protein 1
LTP	Long-term potentiation
M	Male
MAPK	Mitogen-activated protein kinase
MCI	Mild cognitive impairment
mGluR5	Group 1 metabotropic glutamate receptor
ML	Mediolateral
MMSE	Mini-Mental State Examination
Model	Modelled to day 0 autofluorescence
MRI	Magnetic resonance imaging
CSF	Cerebrospinal fluid
Mx04	Methoxy-x04
N	No
NA	Numerical aperture
NaN	Not a number
NFκB	Nuclear factor kappa B
NGSS	Normal goat serum solution
NLRP3	Nucleotide-binding domain, leucine-rich–containing family, pyrin domain–containing-3
NMDA	N-methyl-D-aspartate
Norm	Normalised to day 0
NS	No stimulation
NSAIDs	Non-steroidal anti-inflammatory drugs
NT-r	Neurotrace red
P13K-Akt	Phosphoinositide 3-kinase/protein kinase B
P2YR	Purinergic Receptor
PBS	Phosphate buffered saline
PBST	Triton X in phosphate buffered saline
PDGF-β	Platelet-derived growth factor receptor-β
PDPK	Proline-directed protein kinase
PET	Positron emission tomography
PFA	Paraformaldehyde
PFC	Prefrontal cortex
PiB	Pittsburgh Compound-B
PICALM	Phosphatidylinositol binding clathrin-assembly protein
PING	Pyramidal-interneuron gamma

PirB	Paired immunoglobulin-like receptor B
PK	Pharmacokinetic
POST	Post-subiculum
PreS	Pre-subiculum
PrP	Prion protein
PSD	Power spectral density
PSD95	Postsynaptic density 95
PSEN	Presenilin
PV	Parvalbumin
R2	R-squared
RD	Re-dose
RMS	Root-mean-squared
RMSE	Root-mean-squared-error
ROI	Region of interest
ROS	Reactive oxygen species
s.c.	Subcutaneous
SAD	Spontaneous Alzheimer's disease
sAPPα	Soluble APPα
SEM	Standard error of mean
SST	Somatostatin
SUB	Subiculum
tACS	Transcranial alternating current stimulation
tDCS	Transcranial direct current stimulation
TF	Tapered fibre
TMS	Transcranial magnetic stimulation
TNFα	Tumour necrosis factor alpha
Trem2	Triggering receptor expressed on myeloid cells 2
TS	Thioflavin-S
TYROBP	Tyrosine kinase binding protein
UK	United Kingdom
V	Visual
VISl	Lateral visual cortex
VISp	Primary visual cortex
Y	Yes

Abstract

The progression of potential Alzheimer's disease (AD) treatments to the clinic may be hindered by the pre-clinical screening approach used to access plaque-modifying effects *in vivo*. Specifically, these approaches generally lack real-time assessment across deep brain regions due to a lack of technology permitting this, leaving vital information overlooked. We investigate whether using fibre photometry with a tapered optical fibre allows *in vivo* real-time, depth-resolved monitoring of plaques in freely behaving AD mouse models. Thereby, allowing investigation of plaque modifications caused by potential AD treatments.

First, to confirm feasibility of this approach, we labelled plaques using a peripherally administered blood-brain-barrier-permeable plaque marker, Methoxy-x04, and performed fibre photometry with a conventional flat fibre across brain regions of 5xFAD mice. We confirmed significant correlation between *in vivo* photometry and post-mortem histological plaque signals, indicating that fibre photometry is a feasible approach to assess plaque pathology.

Then, we adopted tapered fibres to realise real-time, depth-resolved photometry in freely behaving 5xFAD mice. We observed a steady increase of *in vivo* fluorescence from 30-minutes after Methoxy-x04 injection, and consistently increased fluorescence when redosing Methoxy-x04 at 24-h intervals, showing greater fluorescence at regions with high plaque load.

Next, to examine the efficacy of a non-invasive treatment approach, mice were exposed to 1-hour of 40-Hz sensory stimulation while monitoring plaque pathology. Electrophysiological signals show increased 40-Hz power in cortical and hippocampal regions, in a stimulus-dependent manner. However, 40-Hz treatment resulted in no significant change in plaque pathology detected by tapered fibre photometry or histology.

Overall, for the first time, we have shown real-time, depth-resolved assessment of AD plaque pathology in freely behaving mice. While further study is required to confirm the effect of 40-Hz treatment, this novel approach can accelerate prospective treatments to the clinic and be an integral tool for investigating the multifactorial complexity of AD.

1. Introduction

The prevalence of AD is continuously increasing with limited therapeutic strategies reaching the clinic. While a major contributor to this is the complex multi-factorial pathogenesis of AD, we consider the possibility that potential treatments are not reaching clinical testing due to a lack of data collection at pre-clinical stages. For example, many possible therapies are tested in AD animal models to identify if they can beneficially modify plaque pathology, as amyloid plaques are one of the major hallmarks of AD (Alzheimer, 1907, Glenner and Wong, 1984b, Masters et al., 1985). However, the real-time effects of these therapies in deeper brain regions generally go overlooked due to the lack of technology permitting real-time, depth-resolved plaque assessment. Therefore, our major hypothesis is that establishment of a novel protocol that allows monitoring of plaques *in vivo*, in real-time, across deeper brain regions and in freely behaving mouse models will enhance understanding of the potential plaque modifying effects of new treatments, thereby supporting the progression to a clinical setting. To do so, we aimed to develop a novel approach that uses a blood-brain-barrier (BBB) permeable drug, Methoxy-x04 (Klunk et al., 2002), and a fibre photometry system. To our knowledge, this is the first laboratory-based approach allowing real-time, freely behaving plaque assessment in deep brain regions.

Therefore, throughout this chapter, I will explore the key topics of this thesis. Firstly, I will provide an overview of AD in **section 1.1**, including the disease definition **(section 1.1.1)**, risk factors of the disease **(section 1.1.1.2.1)** and some important contributors of the disease pathogenesis including molecular and neuronal pathologies **(section 1.1.2)**. This leads us into the discussion of the currently available and future treatments of AD **(section 1.2)**, emphasising that treatment options targeting neuronal aberrations to correct molecular pathologies must be considered. Lastly, an overview of the approaches currently used for monitoring plaque pathology and the animal models used is included to help readers appreciate the requirement for a novel approach **(section 1.3)**. Lastly, we will discuss the major hypotheses, aims and objectives of this project **(section 1.4)**.

1.1 Dementia & AD

Dementia is a wide-spread neurodegenerative syndrome that is associated with a progressive decline in brain functionality. This is an umbrella term for several neurodegenerative diseases, with AD being the most prominent form affecting staggering numbers of the population **(Figure 1.1A)**. With the population ageing due to developments in the clinical field, it leaves elderly-prone diseases like dementia, increasing in prevalence. As expected, this results in tremendous

socioeconomic impacts on families and health care systems around the world. Thus, it is a primary focus of clinicians and researchers to help move this field forward.

1.1.1 Disease definition

1.1.1.1 Disease discovery

Dementia occurred for many years before it was clinically recognised as a medical term in 1797 by Philippe Pinel (Yang et al., 2016). Then, in 1906, by investigating the brain sample of his patient exhibiting symptoms of short-term amnesia, memory loss, disorientation, and dysphasia, the first case of AD was identified by Alois Alzheimer (Alzheimer, 1907). He identified pathological changes in the brain within the cerebral cortex, vital for memory, language, judgement and thinking, with generation of both intra- and extra-cellular molecular pathologies and a pronounced neuroinflammatory state. However, the term 'Alzheimer's disease' came later when Emil Kraepelin, Alzheimer's collaborator, described this case in his book in 1910 (Hippius and Neundorfer, 2003, Yang et al., 2016). Throughout his life, Alzheimer published four other cases before his death in 1915 (Hippius and Neundorfer, 2003). Since then, the diagnosis and consequential prevalence of the disease has increased to devasting effects **(Figure 1.1B).**

1.1.1.2 Epidemiology

As mentioned, AD is the most common form of dementia accounting for approximately 60% of all cases (around 500,000 people in the UK) **(Figure 1.1A**) (Alzheimer's Research UK). With the prevalence of AD on the rise, it is expected that more than 1.1-million people will have dementia by 2030, increasing to more than 1.6-million by 2050 **(Figure 1.1B)** (Alzheimer's Research UK). The risk of developing AD can be exacerbated through a number of modifiable and non-modifiable risk factors.

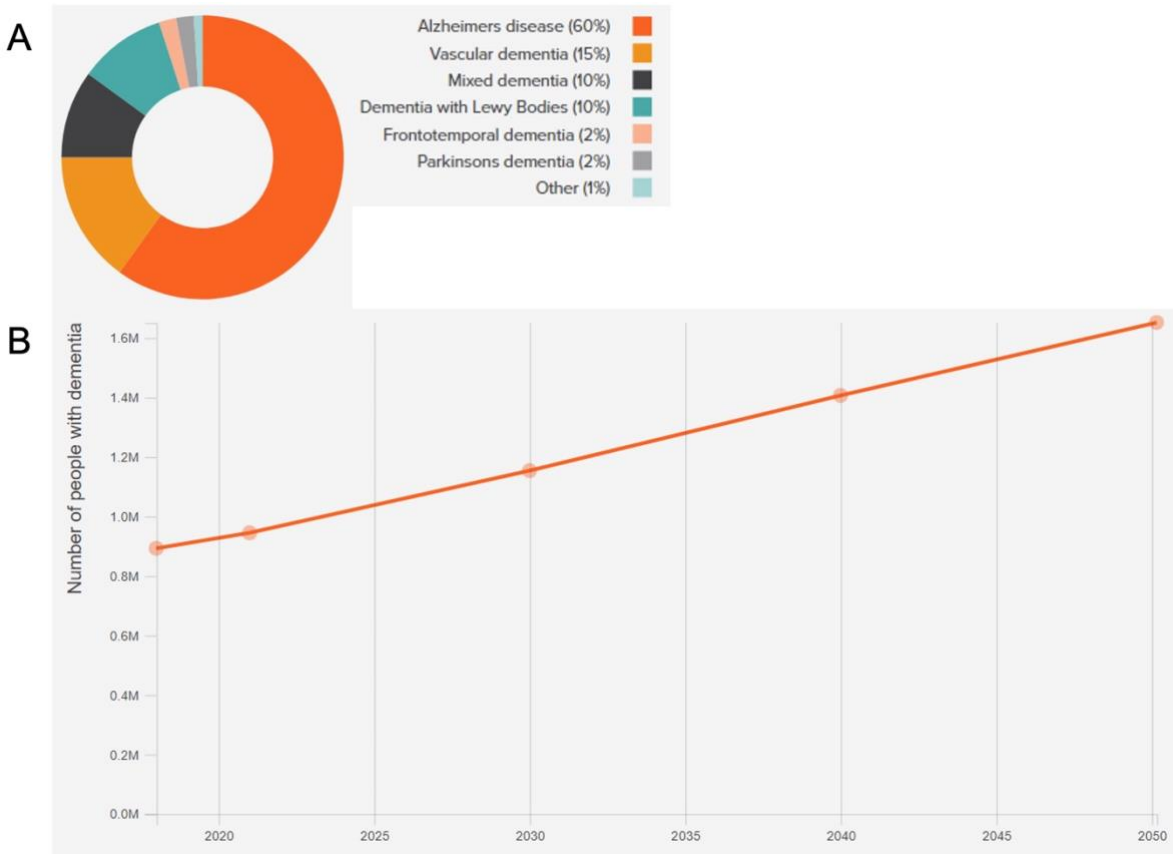

Figure 1.1. Currently available statistics for dementia and AD in the UK. (A) Pie chart of types of dementia that exist and their prevalence. (B) Projected increase in the number of people living with dementia over the next decades. Adapted from Alzheimer's Research UK, accessed 2 June 2023.

1.1.1.2.1 Risk factors of AD

There are several factors that can influence the incidence of AD (Livingston et al., 2020), which can be grouped into modifiable and non-modifiable risk factors (Jeremic et al., 2021, Reitz et al., 2011). Modifiable risk factors include diet, educational level, social interaction, comorbidities, and physical exercise. Non-modifiable risk factors include genetics, age, and sex.

1.1.1.2.1.1 Modifiable risk factors

Diets are a major modifiable risk factor, with some studies reporting that a Mediterranean diet and diets with a high intake of vitamin E and C can reduce the risk of AD (Engelhart et al., 2002, Feart et al., 2009, Masaki et al., 2000, Morris et al., 2002, Scarmeas et al., 2006a, Scarmeas et al., 2006b). This may be because of antioxidant effects which can diminish neurotoxic processes that occur throughout AD. Also, studies illustrate that those with a higher education may have a greater

cognitive reserve which may work to protect the brain from AD (Carlson et al., 2008, Fratiglioni and Wang, 2007).

Lifestyle factors and comorbidities can play a major role in the development of AD, such as diabetes, smoking, hypertension, obesity, and cardiovascular disease (Reitz et al., 2011). For example, they can alter physiological brain function through BBB dysfunction, oxidative stress, neuroinflammation and hyperinsulinemia, which can exacerbate development of molecular pathologies involved in AD (Reitz et al., 2011). For example, Type 2 diabetes increases the risk of AD by 50% (Leibson et al., 1997, Luchsinger et al., 2001, Ott et al., 1999, Reitz et al., 2011) as insulin and amyloid-β (Aβ) compete for use of the insulin degrading enzyme, which results in accumulation of Aβ within the brain (Craft, 2007). Also, there is increased formation of advanced glycosylation end products (AGEs) which increase neuronal damage upon action on their receptors (Yamagishi et al., 2005, Yan et al., 1996). With increasing obesity within the UK and US, the risk of cardiovascular disease, Type II diabetes and AD is at a high.

While physical activity has been shown to have beneficial effects on the risk of AD, by improving vascular health (Abbott et al., 2004, Colcombe and Kramer, 2003, Dishman et al., 2006), certain sports – American football, rugby, and football – can cause traumatic brain injury which increases the risk of dementia (Mackay et al., 2019, Mez et al., 2017, Russell et al., 2022, Russell et al., 2019, Stewart et al., 2023). Accordingly, several preventable health and lifestyle campaigns have been suggested.

1.1.1.2.1.2 Non-modifiable risk factors

1.1.1.2.1.2.1 Genetics

Over the years, many genetic influences on AD have been revealed, with it being considered a dichotomous disease with two genetical forms: familial AD (FAD) and sporadic AD (SAD) (Tanzi, 2012). FAD is the less dominant form within the population as it holds a highly genetic background which commonly results in early onset of AD (< 65-years old) (Tanzi, 2012). Alternatively, SAD has a late-onset (> 65-years old) and can occur due to a combination of different genetic and environmental risk factors. Interestingly, the genetic factors contributing to these disease types have strong associations with different hallmarks of AD pathology: plaques, neurofibrillary tangles and microglia (Tanzi, 2012).

1.1.1.2.1.2.1.1 FAD

FAD is a rare form characterised by mendelian inheritance, most commonly in an autosomal-dominant manner. The main genes involved are the amyloid precursor protein (APP), presenilin-1 (PSEN1) and presenilin-2 (PSEN2) (Hardy and Higgins, 1992, Hutton et al., 1998, Murphy and LeVine, 2010, Tanzi, 2012). APP is the precursor for production of Aβ peptide – the integral component of plaques – and PSEN1 and PSEN2 are subunits of the γ-secretase enzyme used for synthesis of Aβ. Therefore, mutations in these genes can contribute to abnormal regulation of the amyloidogenic pathway (see **section 1.1.2.1.1.1**).

After isolation and mapping of APP to chromosome 21 (Glenner and Wong, 1984b, Kang et al., 1987), experiments were completed to determine the genetic linkage of FAD to genetic markers on chromosome 21, in the vicinity of APP. The first pathogenetic mutation in APP for Dutch hereditary cerebral haemorrhage with amyloidosis was shown by Frangionne and colleagues after sequencing exons 16 and 17 (Levy et al., 1990). Then, by resequencing these same APP exons, Goate and colleagues in 1991, revealed the first APP mutation with a link to AD: an amino acid substitution (V717I) called the London mutation (Goate et al., 1991). Soon after, several FAD mutations were found in PSEN1 and PSEN2 (Levy-Lahad et al., 1995, Sherrington et al., 1995). APP mutations tend to be clustered in regions of the gene which result in enhanced cleavage of APP and production of long fibrillogenic forms of Aβ. Also, PSEN mutations involve a loss-of-function of γ-secretase, impairing the cleavage of APP. Ultimately this causes increased abnormal Aβ generation.

1.1.1.2.1.2.1.2 SAD

SAD, also commonly termed late-onset AD (>60 years of age), has no consistent cause of generation but several genetic and environmental risk factors that have been identified (Tanzi, 2012). Due to the complex background, it was a common problem identifying genetic risk factors contributing to SAD. However, use of genome-wide association studies (GWAS) – a genetic study where numerous single nucleotide polymorphisms can be tested for their genetic association with disease risk – has meant many risk factors continue to be discovered. Some of these include apolipoprotein E (APOE) e4, complement receptor 1 (CR1), clusterin (CLU) and phosphatidylinositol-binding clatherin assembly protein (PICALM) (Bertram and Tanzi, 2009). Alternatively, environmental factors that can simultaneously contribute to AD pathology include age, family history, co-morbidities, and lifestyle habits.

The most common and well-known risk factor of SAD is APOE ε4 (Corder et al., 1993, Musiek and Holtzman, 2015, Strittmatter et al., 1993). APOE is on chromosome 19q13, and has three major

alleles (ε2, ε3 and ε4) (Tanzi, 2012). The occurrence of these alleles depends on the different pairs of polymorphisms resulting in a switch of amino acids found at residues 112 and 158. For instance, allele ε2 will occur with amino acid combinations Cys112/Cys158, ε3 with Cys112/Arg158 and ε4 with Arg112/Arg158 (Liu et al., 2013, Tanzi, 2012). Each of these alleles have varying degrees and alternative roles of influence on AD pathology. APOE ε2 has been suggested to have protective effects against the development of AD. Whereas, APOE ε4 increases the risk of AD by 4-fold with one copy and >10-fold with two copies (Corder et al., 1993, Strittmatter et al., 1993). In any case, APOE generates apolipoprotein which is a glycoprotein consisting of 299 amino acids (Holtzman et al., 2012). It can be found throughout the central nervous system (CNS) due to production by immune cells, with release occurring due to these cells responding to foreign insults within the brain (Holtzman et al., 2012). Its homeostatic functions involve the control of lipid concentration within the CNS, by binding and transporting cholesterol and triglycerides through lymphatic and circulatory systems. Therefore, in AD, due to Aβ's nature, APOE can bind and transport it around the brain and therefore, regulate its metabolism and clearance. Thus, when altered, APOE can increase the Aβ42/40 ratio and its deposition within the brain.

While most high-risk genetic factors show an effect on the deposition of Aβ, recent evidence has shown risk factors contributing to an enhanced neuroinflammatory state, which has been reinforced due to numerous GWAS studies (Hickman et al., 2018). Interestingly, these genetic risk factors commonly involve the immune checkpoints used to gate-keep the homeostatic functions of microglia, such as triggering receptor expressed on myeloid cells 2 (Trem2) (Carmona et al., 2018, Guerreiro et al., 2013, Jiang et al., 2013, Ulrich and Holtzman, 2016). Trem2 encodes a single pass type I membrane protein which is a lipoprotein sensor that works to regulate microgliosis (Bouchon et al., 2000, Schmid et al., 2002, Ulrich and Holtzman, 2016, Ulrich et al., 2017). This protein forms a receptor-signalling complex with a tyrosine kinase binding protein (TYROBP) which works to control the phagocytic ability of microglia and the pro-inflammatory response that occurs upon activation (Guerreiro et al., 2013, Hickman et al., 2018). Many different variants of Trem2 that are associated with AD have been discovered. Specifically, a missense mutation resulting in a rare variant of Trem2 can increase the risk of neurodegeneration and AD by causing a loss of regulation over microglia-mediated functions (Ulrich and Holtzman, 2016, Yeh et al., 2017).

As discussed, GWAS has aided the discovery of numerous risk genes involved in SAD. While this can recognise genes with a high associative risk to AD development, it is important to note that many of these genes have very low degrees of risk. For example, CLU, CR1 and PICALM, discovered in 2009 by GWAS, show an allelic ratio of ~1.15 which means an increased or decreased risk of 1.15 compared to 4 or 15 for APOE (Tanzi, 2012).

1.1.1.2.1.2.2 Age

Age is the biggest risk factor for development of dementia, with the risk rising from 1 in 14 over the age of 65, to 1 in 6 over the age of 80 (Alzheimer's Research UK), as the prevalence increases exponentially between 65 and 85 years (Jeremic et al., 2021). Additionally, as life expectancy continues to rise, this increases the number of people susceptible to AD. This risk is thought to be contributed to by age-related changes in the brain which can result in atrophy, upregulation of the inflammatory profile, vascular damage, mitochondrial dysfunction, and oxidative stress (Finger et al., 2022). This in turn, can work to generate and increase the pathological state of AD including molecular pathologies and neuronal death.

1.1.1.2.1.2.3 Sex

Sex differences are also a major contributor to the risk of developing AD (Alzheimer's Research UK). This is evident worldwide, but in the UK in 2020, 65% of people with dementia were women, with ~46,000 women dying of dementia compared to ~24,000 men (Alzheimer's Research UK). While women have a higher average life expectancy than men which can contribute to age-related risk factors, biological and lifestyle factors are also involved. For instance, research has shown that hormonal changes throughout a women's life, such as menopause, can increase the risk of dementia due to the reduction of cognitive-protective hormone oestrogen (Rahman et al., 2019). Also, genetic studies have identified sex differences in neuroinflammatory pathways, synaptic function, and apoptosis (Guo et al., 2022, Lee et al., 2020). However, the reason for sex differences remains largely unclear, with this being greatly under researched. Nonetheless, some clinical studies completed using non-steroidal anti-inflammatory drugs (NSAIDs) and hormone replacement therapies in women show a reduction in the risk of developing AD (Deardorff and Grossberg, 2017, Zhang et al., 2018a, Zhou et al., 2020).

1.1.1.3 Clinical manifestations and diagnosis

AD is a proteinopathic neurodegenerative disorder characterised by a progressive decline in cognition and a change in behaviours. While the neuropathology of AD arises over 10-20 years before clinical symptoms, termed preclinical AD, diagnosis generally occurs when patients begin to present with a deterioration in higher cognitive functions such as judgement and language, personality changes and behavioural symptoms (Alzheimer's Association Report, 2023). Specifically, AD will progress in different stages starting with preclinical AD, to mild cognitive impairment (MCI), through mild, moderate, and severe stages, before a state of vegetation is reached **(Figure 1.2)** (Alzheimer's Association Report, 2023). As briefly mentioned, throughout preclinical stages, there will be no apparent cognitive deficits while exhibiting an accumulation of

neuropathology hallmarks, such as amyloid plaques, neurofibrillary tangles and resulting neuroinflammation which can activate several neurotoxic pathways that can contribute to neurodegeneration, as discussed below. As this neurodegeneration progresses, MCI may ensue, most commonly recognised through presentation of short-term memory loss, as well as apathy, depression, anxiety, irritability, sleep disturbance and agitation. The disease will continue to progress, and the cognitive deficits escalate. For example, in mild and moderate stages of AD, patients may exhibit symptoms of delusion, eating disturbance, depression, mood changes, changes in thinking, unconscious behaviour and speech, as well as trouble with new information, with patients in severe stages of AD suffering from severe memory loss, hallucination and disorientation (Alzheimer's Association Report, 2023). While the time each patient will spend in each stage of AD differs, this progress has a mean duration of ~8.5 years, meaning patients have a low life expectancy after diagnosis (Alzheimer's Association Report, 2023). Therefore, it has been widely considered that mechanistically, these neuropathological hallmarks of AD are contributing to this progressive loss of cognitive function over-time. Consequently, there is an importance of early detection, diagnosis, and intervention to help the treatment of AD.

Progression in diagnosing AD has been made over the years, as before 1980, people were diagnosed with AD if other possible causes of cognitive decline had been excluded (Reitz et al., 2011). However, now in many countries there is a strict criterion that must be met. This includes completion of neuropsychological tests, positron emission tomography (PET) and magnetic resonance imaging (MRI) scans, and symptoms relating to a loss of daily functions (Reitz et al., 2011). Unfortunately, this still leads to a lack of patients being diagnosed, with an estimated 67% diagnostic success in 2018 in Scotland (Alzheimer's Research UK), due to difficulty diagnosing in early stages, slow progression and limited public awareness of AD hallmarks. For this reason, researchers have been investigating the possibility of a screening diagnostic test available for preclinical stages **(Figure 1.2)**. For example, this would be based on either cerebrospinal fluid (CSF) (Hansson et al., 2007, Hoglund et al., 2008, Schmand et al., 2010), plasma (Lopez et al., 2008, Lui et al., 2010, van Oijen et al., 2006), PET (Engler et al., 2006, Klunk et al., 2004, Silverman et al., 2001), and MRI (Rombouts et al., 2000, Teipel et al., 2003) biomarkers so therapeutic interventions can be administered to slow or prevent the progression of this disease (Reitz et al., 2011). Current and future diagnosis approaches are most commonly centred around the identification of common hallmarks of AD pathogenesis.

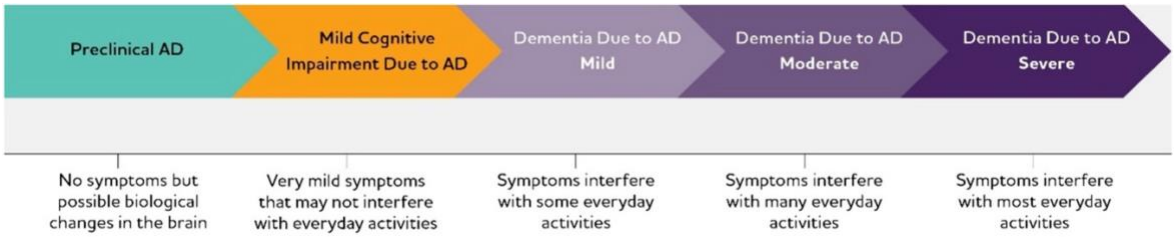

Figure 1.2. Stages of AD. The length of each stage varies per individual depending on factors such as age, genetic and sex. Adapted from Alzheimer's Association Report, 2023.

1.1.2 Disease pathogenesis

AD has a complex multi-factorial pathogenesis which has previously been explained by a single progenitor when researchers developed certain hypotheses. For example, as AD is generally manifested in brain areas with a cholinergic neuron prominence such as the hippocampus, neocortex, and amygdala (Musiek and Holtzman, 2015), Francis and colleagues developed the 'cholinergic hypothesis' which suggests that the loss of cholinergic signalling results in AD (Francis et al., 1999). However, as AD progresses to moderate and severe states it spreads throughout the brain affecting the cerebral cortex and hippocampus (Musiek and Holtzman, 2015). This is characterised by various complex molecular and cellular modifications such as a build-up of protein aggregates, like Aβ plaques. Consequently, Hardy and Higgins gave rise to the 'amyloid hypothesis', suggesting that the accumulation of Aβ plaques throughout the brain results in AD (Hardy and Higgins, 1992). However, since then, many other contributing factors have been found to be major players and these hypotheses are debated. Therefore, AD pathogenesis is largely characterised by molecular pathologies, neuroinflammation and alterations in neuronal signalling.

1.1.2.1 Molecular hallmarks

The most widely accepted hallmarks of AD are molecular pathologies which include extracellular Aβ plaques **(Figure 1.3)** and intracellular neurofibrillary tangles **(Figure 1.6)**. These were first found in 1906 by Alois Alzheimer (Alzheimer, 1907), before Kidd and Terry further characterised these pathologies using electron microscopy (Kidd, 1963, Terry, 1963). Since then, Aβ plaques and neurofibrillary tangles have dominated AD research.

As mentioned, back in the 1990s, Hardy and Higgins suggested the amyloid hypothesis: "amyloid-β protein is the causative agent in AD pathology and neurofibrillary tangles, cell loss, vascular damage and dementia follow as a direct result of this deposition" (Hardy and Higgins, 1992). They developed this hypothesis based on the findings of biochemistry, neuropathology and genetic studies which generated a compelling idea that these neuro-pathologies occur because of the

imbalance of Aβ production and clearance (Hardy and Selkoe, 2002, Hardy and Higgins, 1992, Musiek and Holtzman, 2015, Tanzi and Bertram, 2005). For many years the amyloid hypothesis was understood and believed by many (Musiek and Holtzman, 2015). While genetic data may support this hypothesis, with common FAD mutations being in Aβ-producing proteins (Hardy and Higgins, 1992, Hutton et al., 1998), there has been recent critique of the hypothesis as SAD forms are less genetically pronounced (Musiek and Holtzman, 2015). Additionally, studies on Aβ plaque and neurofibrillary tangles progression in AD brains show that Aβ pathology begins in cortical regions and spreads inwards **(Figure 1.3D)**, whereas neurofibrillary tangles show the opposite **(Figure 1.6B)**. Therefore, it is now more widely believed that Aβ is necessary, but not sufficient, to cause AD (Herrup, 2015, Musiek and Holtzman, 2015). In any case, both Aβ plaques and neurofibrillary tangles have been found to contribute to an increased neurodegenerative state due to them initiating different neurological processes that contribute to neuronal loss.

1.1.2.1.1 Aβ plaques

1.1.2.1.1.1 Aβ plaque formation

Aβ plaques are extracellular pathologies that have dominated AD research since they were first discovered by Alzheimer (Alzheimer, 1907, Glenner, 1988, Glenner and Wong, 1984a, Glenner and Wong, 1984b). They are now a common biomarker used for diagnosis in human studies, and experimental assessment in preclinical animal studies. Plaques are formed through a small molecule called Aβ, which is enzymatically cleaved from its precursor protein; APP (Glenner and Wong, 1984b). This enzyme is a glycoprotein that was first discovered and sequenced by isolating and purifying the protein from meningeal blood vessels of AD and down-syndrome patients (Glenner and Wong, 1984a, Glenner and Wong, 1984b, Hardy and Selkoe, 2002, Masters et al., 1985). It consists of a single membrane-spanning domain with a large extracellular glycosylated N-terminus and short cytoplasmic C-terminus, and ranges from 695-770 residues with the APP695 form most abundant within neurons **(Figure 1.3A)** (Chen et al., 2017, Goedert, 1987, Hardy, 1997, Kang et al., 1987, LeBlanc et al., 1991, Tanzi et al., 1987, Vannostrand, 1994).

1.1.2.1.1.1.1 Monomer

Development of pathogenic Aβ depends on the enzymatic pathway taken by APP: amyloidogenic pathway (pathogenic) or non-amyloidogenic (non-pathogenic) (Chen et al., 2017, Hampel et al., 2021, Mills and Reiner, 1999). Both pathways involve Aβ, APP and a range of proteolytic secretase enzymes that cleave APP into Aβ fragments (Chen et al., 2017, Gandy, 2005, Hampel et al., 2021, Mills and Reiner, 1999). In the non-amyloidogenic pathway, APP is cleaved by α-secretase at a

cleavage site situated within the Aβ fragment (Anderson et al., 1991, Esch et al., 1990, Wang et al., 1991) to release soluble APPα (sAPPα) from a membrane-bound 83-amino-acid C-terminal APP fragment (C83) **(Figure 1.3A)** (Chen et al., 2017, Hampel et al., 2021, Mills and Reiner, 1999, Weidemann et al., 1989). Whereas, in the amyloidogenic pathway, APP is cleaved by β-secretase at the N-terminus of the Aβ domain to release C99 (a membrane-bound fragment) and an ectodomain APPsβ (Citron et al., 1995, Paganetti et al., 1996, Seubert et al., 1993). Then, γ-secretase cleaves C99 to generate Aβ (Anderson et al., 1992, Chen et al., 2017, Hampel et al., 2021, Mills and Reiner, 1999) **(Figures 1.3A-B)**. Interestingly, the generation of Aβ is controlled through neuron activity, with action of acetylcholine on muscarinic receptors resulting in increased α-secretase activity, promoting the protective pathway (Haass et al., 1995).

Glenner and Wong first discovered the primary amino acid sequence of the Aβ peptide monomer back in 1984 (Glenner and Wong, 1984b). It was found that it can vary from 38-43 amino acids in length due to the imprecise cleavage by γ-secretase (Mills and Reiner, 1999). The most abundant fragment is Aβ40 (~80-90%), with longer fragments that have 42 amino acids (Aβ42) being less prevalent (~5-10%) (Haass et al., 1992, Seubert et al., 1992). Structural studies have shown that Aβ40 has an alpha-helix structure between residues 15 and 36, a kink at 25-27 and unstructured peptide from residues 1 to 14 (Coles et al., 1998). Whereas Aβ42 has a beta-hairpin structure at residues 31-41 which limits the flexibility of the C-terminus (Sgourakis et al., 2007). Therefore, the C-terminus is hydrophobic and promotes formation of beta-sheets (Yang and Teplow, 2008). Consequently, it is these longer forms of Aβ that are pathogenic due to their hydrophobic nature that promotes aggregation (Chen et al., 2017, Hampel et al., 2021, Mills and Reiner, 1999). This aggregation process involves progression from a monomer to a dimer, oligomer, fibril, and plaque, with many intermediate products (Chen et al., 2017, Gandy, 2005, Hampel et al., 2021) **(Figure 1.3C)**. It occurs through primary and secondary nucleation (Cohen et al., 2013, Hampel et al., 2021, Matsumura et al., 2011). Primary nucleation involves the aggregation of two or more Aβ monomers through a fibril-independent pathway. Secondary nucleation involves the aggregation of Aβ monomers on fibrils in a fibril-dependent mechanism. These pathways are not stable and will continue to undergo cycles of dissociation and reassociation at varied timescales due to changes in pH and lipid content (Brannstrom et al., 2014, Carulla et al., 2005, Cohen et al., 2013, Gruning et al., 2013, Michaels et al., 2020, Sanchez et al., 2011). However, Aβ42 is less likely to undergo dissociation due to its aggregative nature (Sanchez et al., 2011).

For many years it was thought that fibrils were the contributor to neurotoxicity seen throughout AD, but it has become clear that different stages of this aggregative cycle can provide different effects, some more toxic than others. In fact, in physiological conditions, Aβ monomers are involved in several processes such as intracellular signalling and synaptic functionality, shown to inhibit synaptic excitotoxicity (Kamenetz et al., 2003, Koo et al., 1993, Whitson et al., 1989) and some

evidence of protection against infection (Bourgade et al., 2016, Eimer et al., 2018). However, in pathological conditions where the production and clearance are unregulated, there will be aggregation of Aβ monomers into neurotoxic assemblies (Chen et al., 2017, Hampel et al., 2021).

1.1.2.1.1.1.2 Oligomer

Aβ monomers of varied length can form low-molecular weight oligomers such as dimers, trimers, tetramers and pentamers to midrange molecular weight oligomers such as hexamers, nonamers and dodecamers (Chen et al., 2017, Fandrich, 2012, Hampel et al., 2021, Huang and Liu, 2020). Therefore, Aβ oligomers are often varied in their size and confirmation (Fandrich, 2012, Huang and Liu, 2020) **(Figure 1.3C)**. While the structure of oligomers is not widely known, its insoluble form appears to have a high beta-sheet presence organised in a parallel or anti-parallel structure (Ahmed et al., 2010, Chen et al., 2017, Hampel et al., 2021, Yu et al., 2009), stabilised with hydrogen bonds (Kheterpal et al., 2003). Whereas its soluble form has no alpha-helical or beta-sheet structures (Zhang et al., 2000).

These soluble constructs can spread throughout the brain. Consequently, in high concentrations within the brain, they are now known as the most toxic form of Aβ, with the 'amyloid hypothesis' being adapted for the 'amyloid oligomer hypothesis' (Hardy and Selkoe, 2002, Huang and Liu, 2020). Specifically, it has been shown that soluble Aβ oligomers can act on various cell surface receptors – acetylcholine (Wang et al., 2000), glutamate (Abd-Elrahman et al., 2020, Haas et al., 2014, Hu et al., 2014, Um et al., 2013), β2-adrenergic (β2AR) (Wang et al., 2010), p75 neurotrophin (Kuner et al., 1998, Yaar et al., 1997) and prion (Kessels et al., 2010, Lauren et al., 2009) – which disrupt calcium signalling, ultimately causing mitochondrial dysfunction, increased oxidative stress, hyperphosphorylation of tau, synaptic dysfunction, neuronal loss, and further aggregation of Aβ (Chen et al., 2017, Hampel et al., 2021, Huang and Liu, 2020) **(Figure 1.5)**. Otherwise, oligomers in their insoluble form will progress for aggregation into fibrils.

1.1.2.1.1.1.3 Protofibril

Several intermediate products can be formed throughout this aggregation process including protofibrils which are large soluble fragments which vary in size (Fandrich, 2012, Hampel et al., 2021, Nichols et al., 2002, Walsh et al., 1997) **(Figure 1.3C)**. They are elongated compared to oligomers, but thinner and shorter than mature fibrils, containing beta-sheets (Fandrich, 2012, Nichols et al., 2002). Like other soluble Aβ aggregates, protofibrils are neurotoxic, causing inhibition of synaptic plasticity, increased neuroinflammation through accumulation within astrocytes and microglia, and neurodegeneration (Gouwens et al., 2018, Gouwens et al., 2016, Hampel et al., 2021, Hartley et al., 1999, Lasagna-Reeves and Kayed, 2011).

1.1.2.1.1.1.4 Fibril

Then, in a concentration-dependent manner, Aβ assemblies will aggregate into Aβ fibrils (Chen et al., 2017, Fandrich, 2012, Hampel et al., 2021) **(Figure 1.3C)**. Their formation involves Aβ peptides assembling into beta-sheets, arranged in a parallel nature, with hydrogen bonds for stabilisation. Then, beta-strands will be formed either parallel or anti-parallel to the elongating fibril, depending on the amino acid contacts and intermolecular interactions (Antzutkin et al., 2000, Balbach et al., 2002, Benzinger et al., 1998, Benzinger et al., 2000, Chen et al., 2017, Eanes and Glenner, 1968, Fandrich, 2012, Hampel et al., 2021, Lu et al., 2013, Paravastu et al., 2008). These are insoluble peptides which are hydrophobic, causing aggregation into plaques. Additionally, as Aβ42 has two extra residues, this creates a more hydrophobic, pathogenic form that accelerates aggregation (Chen et al., 2017).

While oligomers appear to have the most neurotoxic profile, Aβ fibrils are co-localised with disrupted neurites, regions of decreased spine density, neuronal loss, neuroinflammation and neurodegeneration (Geula et al., 1998, Hampel et al., 2021, Knowles et al., 1999, Meyer-Luehmann et al., 2008, Petkova et al., 2005).

1.1.2.1.1.1.5 Plaque

Eventually, due to their hydrophobic nature, these Aβ fibrils aggregate together to form insoluble Aβ plaques **(Figure 1.3C)**. These can exist in many forms, with the most common being diffuse and dense core plaques (DeTure and Dickson, 2019). Diffuse plaques do not have an accumulation of glial cells surrounding them. Alternatively, dense core plaques have a compact dense core of Aβ fibrils, which can be surrounded by neuritic elements, such as glial cells, synapse loss and tauopathy, termed neuritic plaques (DeTure and Dickson, 2019).

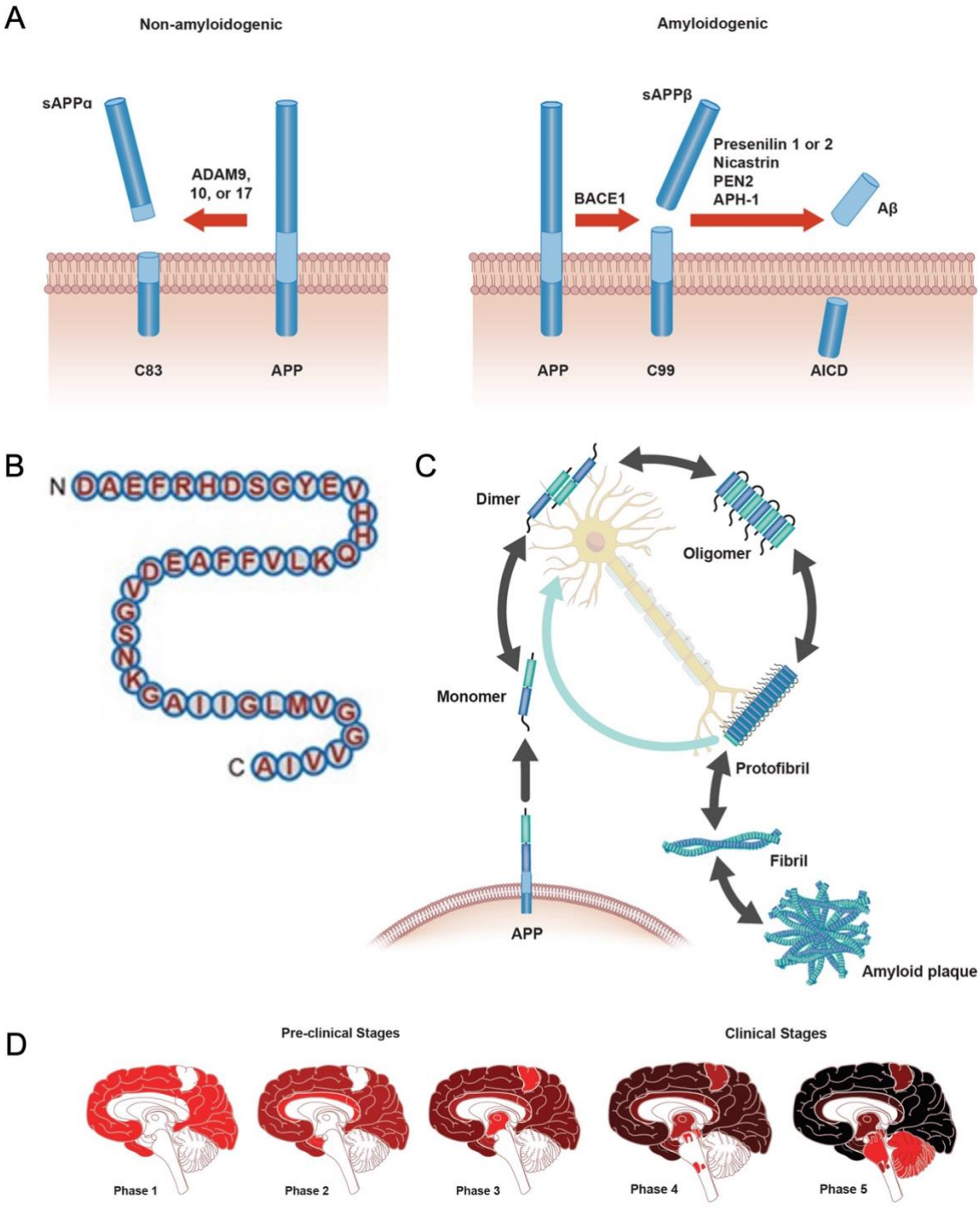

Figure 1.3. Aβ is generated through an amyloidogenic pathway, before aggregating into amyloid plaques. (A) Diagram of the non-amyloidogenic and amyloidogenic pathway for cleavage of APP. Aβ fragments are formed through the amyloidogenic pathway. (B) Primary amino acid sequence of $Aβ_{42}$. (C) Aggregation of the Aβ peptide into various structures. (D) Spread of Aβ pathology. Darker colours indicate continuous accumulation of Aβ. A, C and D are adapted from Hampel *et al.,* 2021 and B is adapted from Chen *et al.,* 2017.

1.1.2.1.1.2 Aβ homeostasis

Aβ homeostasis involves a cycle of production, aggregation, transport, degradation, and clearance. Consequently, there are several processes to regulate this which can go awry throughout the progression of AD.

1.1.2.1.1.2.1 Aβ transport

Several experiments using intracerebral injections of Aβ-rich brain extracts illustrate that the transport of Aβ pathology involves prion-like seeding, where Aβ assemblies will spread throughout the brain, promoting aggregation (Eisele et al., 2009, Kane et al., 2000, Katzmarski et al., 2020, Meyer-Luehmann et al., 2006). These Aβ seeds spread through neuronal transport passing from axonally connected brain regions (d'Errico and Meyer-Luehmann, 2020, Domert et al., 2014, Ronnback et al., 2012, Walker et al., 2002). They will be collected into intraluminal vesicles, fuse with the plasma membrane before being released into the extracellular space as exosomes (Rajendran et al., 2006, Sharples et al., 2008). Another possibility is cell-to-cell transport, which some believe due to findings of the presence of Aβ within neurons. However, to date, no groups have reported the active transport of Aβ along neurons or implicated glial cells in the spread of Aβ (d'Errico and Meyer-Luehmann, 2020). Although, due to the presence of Aβ within plasma and CSF (Mehta et al., 2000), it has been widely accepted that Aβ can spread through the vascular system. For example, Aβ is transported across the BBB through receptors for advanced glycation end-products (RAGE) (blood to brain) and low-density lipoprotein receptor-related protein 1 (LRP1) (brain to blood) receptors (Deane et al., 2009, Deane et al., 2003, Deane et al., 2004, Donahue et al., 2006, Fuentealba et al., 2010, Ma et al., 2022, Sagare et al., 2007, Selkoe, 2001, Shibata et al., 2000, Yamada et al., 2008) **(Figure 1.4)**. In addition, the APOE protein, a known risk factor of SAD, is secreted into the interstitial fluid (ISF) by glial cells, before interacting with Aβ and influencing its clearance into cells for degradation via the endocytic low-density lipoprotein (LDL) receptor family (Chen et al., 2017, Kim et al., 2009). Several other proteins – like apolipoprotein J (ApoJ) and α2-macroglobulin – and spreading mechanisms have been found to transport and spread Aβ pathology throughout the brain (Narita et al., 1997, Zlokovic et al., 2005).

1.1.2.1.1.2.2 Aβ degradation and clearance

As well as the spread throughout the brain, Aβ pathology can become pathological when there is an imbalance between metabolism and clearance. It can be cleared through several mechanisms including ISF drainage, proteolytic degradation, cell-mediated clearance, active transport, glymphatic transport regulated by sleep (Xie et al., 2013), and deposition into insoluble aggregates (Yoon and Jo, 2012) **(Figure 1.4)**. Firstly, the ISF drainage pathway involves the diffusion of Aβ

from the ISF to CSF through bulk flow before it undergoes drainage into the blood through the perivascular arterial spaces in the brain (Yoon and Jo, 2012) **(Figure 1.4)**. Secondly, it can be degraded by amyloid degrading enzymes (ADE) – neprilysin, endothelin-converting enzymes, plasmin, insulin-degrading enzyme, matrix metalloproteases 2 and 9 and cathepsin D (Backstrom et al., 1996, Chen et al., 2017, Duckworth et al., 1998, Eckman et al., 2006, Eckman et al., 2001, Edbauer et al., 2002, Farris et al., 2003, Kurochkin and Goto, 1994, Leissring et al., 2003, McDermott and Gibson, 1996, Pardossi-Piquard et al., 2005, Shirotani et al., 2001, Tucker et al., 2000, Yoon and Jo, 2012) – with remnants being trafficked out of the brain either by bulk flow or direct trafficking into peripheral circulation (Bouchon et al., 2000, Karran et al., 2011, Yoon and Jo, 2012) **(Figure 1.4)**. Secondly, microglia immune cells can contribute towards clearance by phagocytosis and astrocytes are involved in the internalisation of Aβ, through scavenger receptors, for degradation (Bard et al., 2000, Frautschy et al., 1998, Schenk et al., 1999, Wyss-Coray et al., 2003, Yoon and Jo, 2012). Thirdly, there is transport across the BBB into the blood for clearance of Aβ, controlled by LRP1 receptors (Deane et al., 2004, Donahue et al., 2006, Fuentealba et al., 2010, Sagare et al., 2007, Shibata et al., 2000, Yamada et al., 2008, Yoon and Jo, 2012) **(Figure 1.4)**. However, degradation and clearance becomes dysfunctional as the disease progresses, resulting in the accumulation within the CNS and the subsequent pathological processes that this entails (Malm et al., 2015).

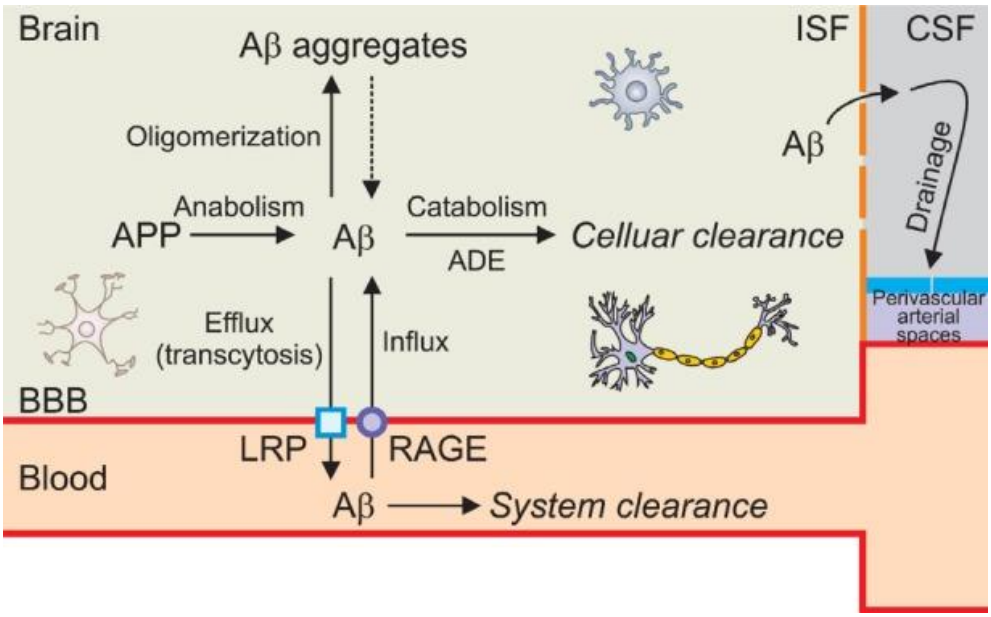

Figure 1.4. Aβ homeostasis. Diagram illustrates anabolism and catabolism approaches for Aβ. APP: amyloid precursor protein; BBB: blood-brain-barrier; LRP: lipoprotein receptor-related protein; RAGE: receptors for advanced glycation end-products; ADE: amyloid degrading enzymes; ISF: interstitial fluid; CSF: cerebrospinal fluid. Adapted from Yoon and Jo, 2012.

1.1.2.1.1.3 Aβ spread in AD

Accumulation of these Aβ pathogenic assemblies will result in the spread across the brain throughout AD progression. Interestingly, a 5-phase hierarchical spread of Aβ in AD patients was identified **(Figure 1.3D)** (Thal et al., 2002). Firstly, Aβ deposits are formed within the neocortex, before spreading to allocortical regions in phase 2 and midbrain regions including the diencephalic nuclei, striatum, and basal forebrain in phase 3 (Thal et al., 2002). In phase 4 and 5, Aβ pathology reaches the brain stem and cerebellum, respectively (Thal et al., 2002). Throughout this process, the deposition in all brain regions continues to increase, resulting in greater Aβ pathology from outward to inward brain regions (Thal et al., 2002). However, many researchers continue to believe that plaque pathology follows a spread that has no spatiotemporal pattern, with variation between individuals. This is because this study was completed on a small sample of 47 individuals, showing single time points, thereby not accounting for individual variability. Also, this trend of spread varies from that described by Braak and Braak (Braak and Braak, 1997) which again emphasises the debatable nature of Aβ pathology spread throughout AD progression.

1.1.2.1.1.4 Pathological effects of plaques

The accumulation of Aβ in the brain can induce several neurotoxic processes **(Figure 1.5)** (Chen et al., 2017, Hampel et al., 2021, Huang and Liu, 2020). It has become evident that Aβ oligomers are the most neurotoxic assemblies, as their soluble morphology allows them to bind to molecules within the extracellular space (Chen et al., 2017, Hampel et al., 2021, Huang and Liu, 2020). For example, Aβ oligomers can bind to molecular receptors which include glial cells, lipids, proteoglycans, and protein receptors such as p75 neurotrophin receptor (Kuner et al., 1998, Yaar et al., 1997), LRP1 (Deane et al., 2004, Donahue et al., 2006, Sagare et al., 2007, Shibata et al., 2000), cellular prion protein (PrP) (Kessels et al., 2010, Lauren et al., 2009), metabotropic glutamate receptors (Abd-Elrahman et al., 2020, Haas et al., 2014, Hu et al., 2014, Um et al., 2013), alpha subunit containing nicotinic acetylcholine receptor (α7nAChR) (Wang et al., 2000), N-methyl-D-asartic acid (NMDA) receptor (Texido et al., 2011), β2-AR (Wang et al., 2010), erythropoietin-producing hepatoma cell line receptor and paired immunoglobin-like receptor B (PirB) **(Figure 1.5)**. Each of these interactions can result in various alterations in physiological signalling pathways, with the consensus being that activation of these pathways can increase neurotoxicity through phosphorylation of tau, oxidative stress, neuroinflammation and neurodegeneration (Chen et al., 2017, Hampel et al., 2021, Huang and Liu, 2020).

1.1.2.1.1.4.1 Glutamate and other receptors

Aβ oligomers can interact with both α-amino-3-hydroxy-5-methyl-4-isoxazolepropionic acid (AMPA) and NMDA glutamate receptors, causing an increase in excitatory neuronal activity **(Figure 1.5)**. More specifically, Aβ binds to and activates the NMDA receptor, near the GluN2B subunits, at the neuronal surface (Costa et al., 2012, De Felice et al., 2007). It is thought that there is a concentration-dependent role in AD, with low concentrations of Aβ promoting excitatory activity and high concentrations supressing activity from synapses (Palop et al., 2007, Palop and Mucke, 2016).

With low concentrations of Aβ, excessive activation of NMDA receptors prevents the generation of new synapses and promotes neuronal death (Alberdi et al., 2010, De Felice et al., 2007, Ronicke et al., 2011, Shankar et al., 2007). Additionally, this can result in increased oxidative stress which will eventually damage molecular components such as lipids, proteins, and deoxyribonucleic acid (DNA) (Revett et al., 2013). Also, glutamate-mediated excitation can promote further Aβ accumulation via proteolysis of APP (Bordji et al., 2010, Lesne et al., 2005). In addition, these excitotoxic tendencies can be exacerbated by tauopathy through its interaction with Fyn kinase, which interacts with the postsynaptic density protein 95 (PSD95). Next, this will form a complex with the NMDA receptor, activated by Aβ, to cause excitotoxicity (De Felice et al., 2007, Ittner et al., 2010, Roberson et al., 2011, Tezuka et al., 1999, Zhang et al., 2021). These effects can also occur indirectly as Aβ can activate presynaptic acetylcholine receptors, increasing intracellular calcium concentrations and glutamate release (Palop et al., 2007, Palop and Mucke, 2016).

However, when at higher Aβ concentrations, Aβ can depress synaptic activity by supressing synaptic strength. This can be via internalisation of glutamate receptors, downregulation of voltage-gated sodium channels and loss of dendritic spines (Palop et al., 2007, Palop and Mucke, 2016). This contributes to a loss of synaptic inhibition which can promote neuronal hyperactivity in brain regions associated with learning and memory.

When bound to AMPA receptors, it can result in the reduction of AMPA receptor expression through an increase in degradation and ubiquitination (Zhang et al., 2018b). This can also be indirectly through increased tau hyperphosphorylation which diminishes AMPA signalling (Miller et al., 2014). However, Aβ oligomers can also bind to and activate metabotropic glutamate receptors, such as group 1 metabotropic glutamate receptor 5 (mGluR5), and contribute to an increase of Aβ (Kim et al., 2010), disruption of physiological calcium signalling and synaptic plasticity (Chen et al., 2017).

Additionally, Aβ oligomers can act on α7nAChR and cause endocytosis of NMDA receptors (Nagele et al., 2002, Snyder et al., 2005), increase Aβ-induced tau phosphorylation through extracellular signal-regulated kinase and Jun N-terminal kinase pathways (Wang et al., 2003) and exacerbate neurodegeneration **(Figure 1.5)**. When binding to β2ARs, this increases calcium signalling and resulting hyperactivity (Wang et al., 2013, Wang et al., 2010), while promoting tauopathy (Wang et al., 2013).

1.1.2.1.1.4.2 Tauopathy

For many years it has been debated whether Aβ has a role in exacerbating tauopathy as Aβ pathology begins several years before the development of neurofibrillary tangles. However, it has now been shown that Aβ can increase tau phosphorylation and aggregation (Zhang et al., 2021). Particularly, Aβ can bind to α2-ARs and activate glycogen synthase kinase-3 β (GSK3β) and cyclin-dependent kinase 5 (CDK-5); kinases which promote tau hyperphosphorylation (Hernandez et al., 2009, Terwel et al., 2008, Zempel et al., 2010, Zhang et al., 2020). Also, GSK3β and CDK-5 mediated activation can promote the aggregation of tau monomers into oligomers (Zhang et al., 2021). In addition, Aβ can activate caspase-3 which produces a cleaved tau protein which has high aggregation properties (Gamblin et al., 2003, Zhang et al., 2021). Additionally, through action on the cellular prion protein receptor, Aβ will activate Fyn kinase which will increase protein tyrosine kinase 2-related phosphorylation of tau, enhancing tauopathy (Chen et al., 2013a, De Mario et al., 2015, Li and Gotz, 2018, Um et al., 2012, Zhang et al., 2021).

1.1.2.1.1.4.3 Oxidative stress and mitochondrial dysfunction

When considering the effect of Aβ on oxidative stress, the interaction with various receptors can increase the production of free radicals through various pathways (Chen et al., 2017, Hampel et al., 2021, Huang and Liu, 2020, Zhang et al., 2021). For example, Aβ can bind to and activate p75 neurotrophin receptor which will activate its death domain and caspases which promote generation of reactive oxygen species (ROS) (Hashimoto et al., 2004, Perini et al., 2002). Due to their toxic nature, these ROS can damage neuronal membranes and the functionality of vital proteins, instead generating toxic products which can enhance the effect (Chen et al., 2017, Ma et al., 2022). Therefore, this puts cells under stress and results in neuronal death.

Another mechanism that results in extreme neurotoxicity and neuronal death is Aβs contribution to mitochondrial dysfunction **(Figure 1.5)**. Firstly, the precursor protein, APP, can interact with the mitochondrial membrane and block translocation, resulting in mitochondrial dysfunction (Anandatheerthavarada et al., 2003, Devi et al., 2006). Alternatively, Aβ can activate cell death pathways through activation of mitochondrial fission proteins, and/or proapoptotic factors like

alcohol dehydrogenase and cyclophilin D (Barsoum et al., 2006, Lustbader et al., 2004). The lack of adenosine triphosphate (ATP) generation and loss of mitochondrial function can cause DNA damage and neuronal death (Huang and Liu, 2020, Zhang et al., 2021).

1.1.2.1.1.4.4 Neuroinflammation

Another major contribution to AD pathology is neuroinflammation, which Aβ has been shown to exacerbate to harmful effects (Chen et al., 2017, Hampel et al., 2021, Heneka et al., 2015a, Heppner et al., 2015, Huang and Liu, 2020, Zhang et al., 2021) **(Figure 1.5)**. The contribution of neuroinflammation can be mediated through action on glial cell surfaces. For example, there are numerous receptors on the microglial membrane that can bind to Aβ resulting in a neuroinflammatory response which can contribute to neuronal death and exacerbate both plaque and tangle pathologies (Clayton et al., 2017, Heneka et al., 2015a, Heneka et al., 2015b, Hickman et al., 2018, Malm et al., 2015, McGeer and McGeer, 1995, Sarlus and Heneka, 2017). This is described in **section 1.1.2.2.1 and 1.1.2.2.2** for microglia and astrocytes, respectively.

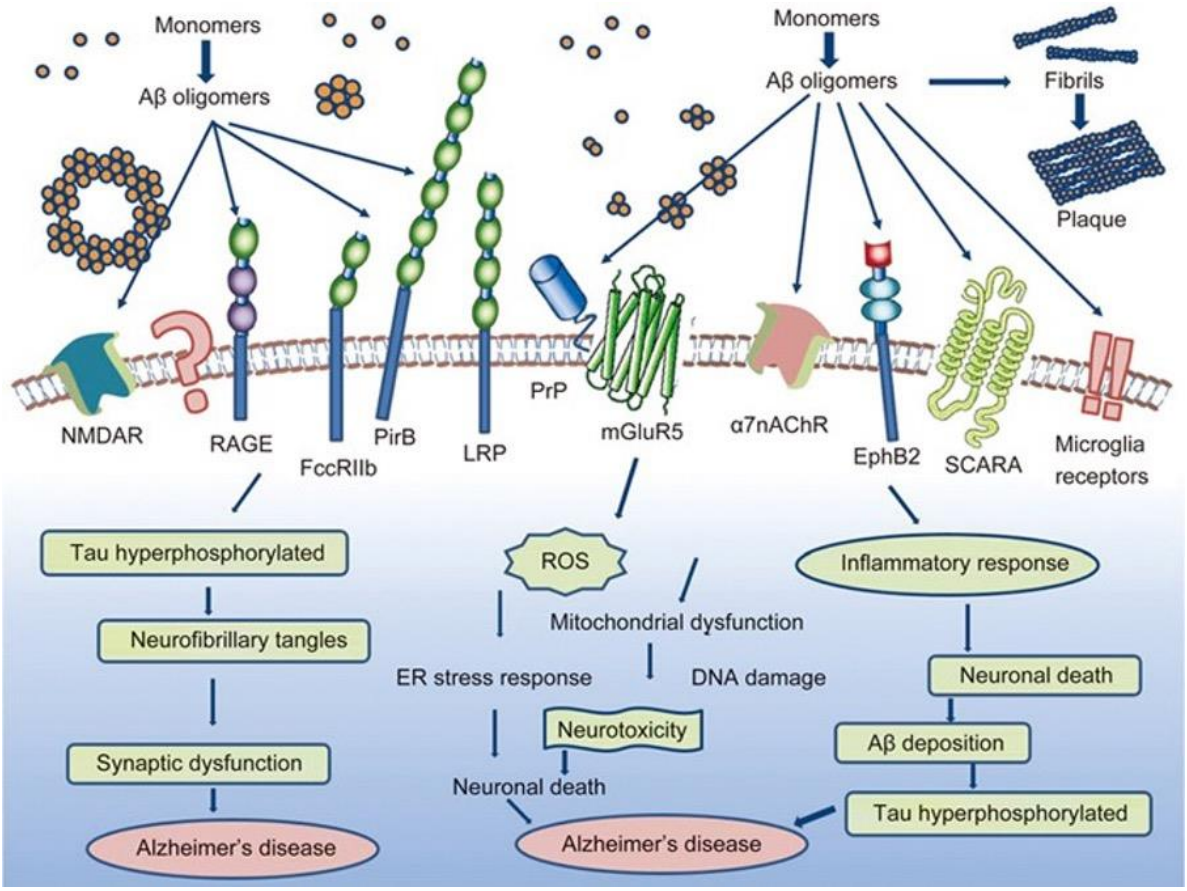

Figure 1.5. Pathological effects of Aβ. Aβ oligomers can act on various cell surface receptors and cause tau hyperphosphorylation, generation of ROS, mitochondrial dysfunction, and an enhanced inflammatory response. NMDAR: N-methyl-D-aspartic acid receptor; RAGE: receptors for advanced glycation end-products; PirB: paired immunoglobulin-like receptor B; LRP: lipoprotein receptor-related protein; PrP: prion protein; mGluR5: metabotropic glutamate receptor 5; α7nAChR: alpha subunit containing nicotinic acetylcholine receptor; EphB2: erythropoietin-producing hepatoma cell like receptor; SCARA: scavenger receptor A-1. Adapted from Chen *et al*., 2017.

Overall, Aβ plaques are a major contributor to the development and progression of AD pathogenesis, promoting several other pathologies, including neurofibrillary tangles.

1.1.2.1.2 Neurofibrillary Tangles

1.1.2.1.2.1 Neurofibrillary tangle formation

Neurofibrillary tangles are generated through hyper-phosphorylation of a microtubule stabilisation protein called tau (Ballatore et al., 2007, Buee et al., 2000) **(Figure 1.6A)**. The N-terminal of tau is a projection domain involved in interacting with other cytoskeletal elements or proteins to induce signal transduction pathways (Buee et al., 2000). The C-terminal is a microtubule binding domain,

involved in microtubule polymerisation and stabilisation, by binding to functional proteins such as kinases/phosphatases (Buee et al., 2000). Thus, tau's primary function is the induction and up-keep of tubule formation, by development of double rings around the microtubule proteins (Weingarten et al., 1975).

Under physiological conditions, tau is a highly regulated protein that's phosphorylated state is under equilibrium. Tau has several phosphorylation sites along its structure, with the longest form having 79 Serine or Threonine phosphorylation sites, which suggests that the primary source of phosphorylation is a proline directed Ser/Thr kinase (Buee et al., 2000). As mentioned, most kinases involved are a member of the proline-directed protein kinase (PDPK) family (Buee et al., 2000, Drewes et al., 1992, Vulliet et al., 1992), with tau having 14 sites for PDPK phosphorylation due to recognition of the consensus sequence: -X-(Ser/Thr)-Pro-X- (Hall et al., 1990, Vulliet et al., 1992). Examples are mitogen active protein kinase (MAPK) (Drewes et al., 1992) and GSK3 (Hanger et al., 1992). However, there are many other phosphorylation sites that are non-Ser/Thr (Buee et al., 2000). Tau proteins can also be dephosphorylated by several endogenous phosphatases (Ballatore et al., 2007, Buee et al., 2000, Garver et al., 1994). However, in AD, a downregulation of phosphatases has been noted (Matsuo et al., 1994). This can result in a kinase/phosphatase imbalance which favours kinase activity and phosphorylation of tau. When this hyper-phosphorylated state has been reached, tau loses affinity, breaks away and dissociates from the microtubules to aggregate together and form paired helical filaments which aggregate into neurofibrillary tangles (Hardy and Higgins, 1992, Kidd, 1963) **(Figure 1.6A)**.

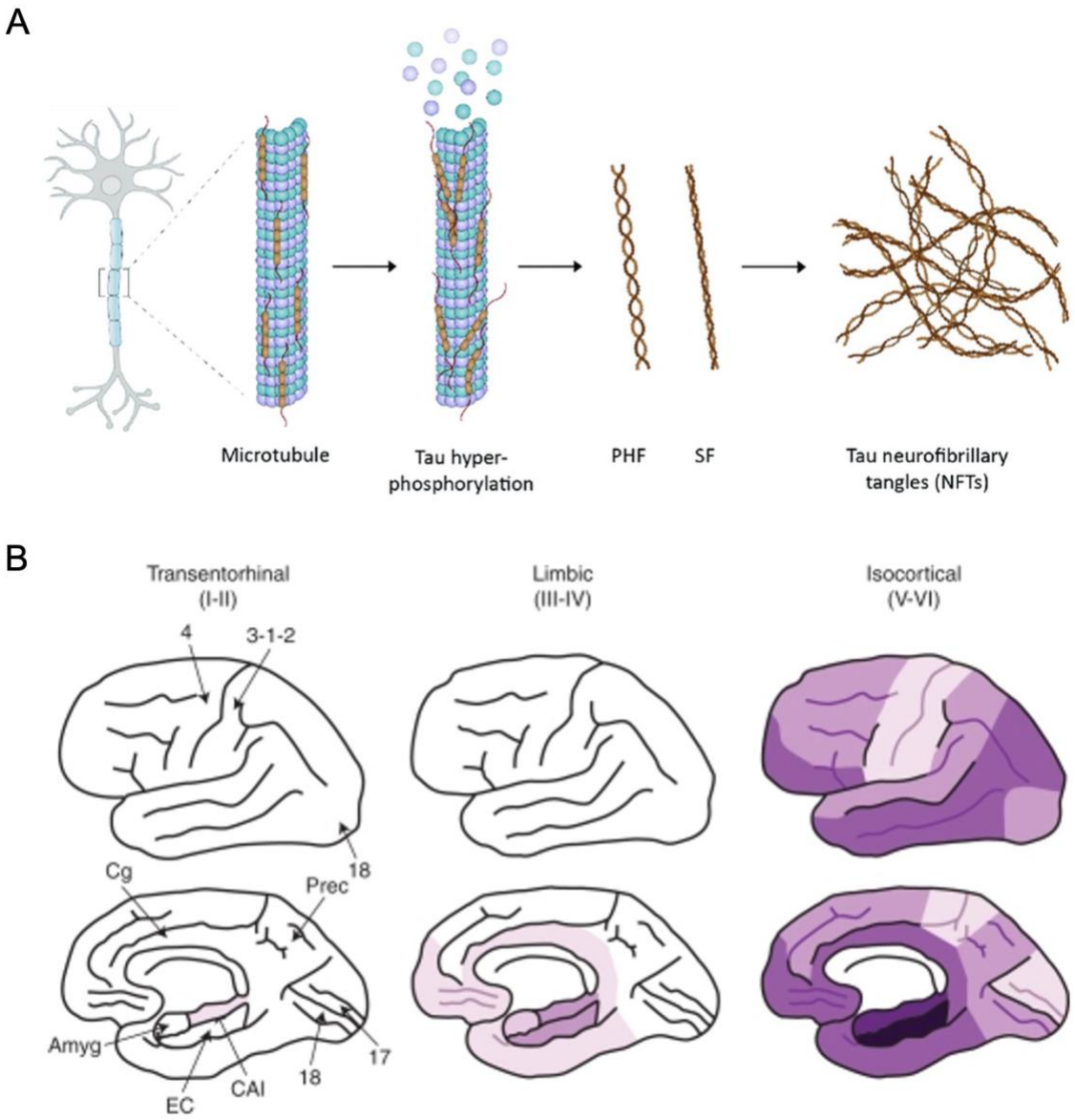

Figure 1.6. Formation of neurofibrillary tangles in AD. (A) Formation of neurofibrillary tangles. Adapted from Jie *et al*., 2021. (B) Spread of neurofibrillary tangle pathology based on Braak stages, where darker colours show greater tangle density. Amyg = Amygdala; EC = Entorhinal cortex; CA1 = Cornus ammonis 1 hippocampal subfield; Cg = Cingulate cortex; Prec = Precuneus; 4 = Primary motor cortex; 3-1-2 = Primary sensory cortex; 17 = Primary visual cortex; 18 = Associative visual cortex. Adapted from Serrano-Pozo *et al.*, 2011.

1.1.2.1.2.2 Tauopathy transport

As neurofibrillary tangles are intracellular, pathological tau can redistribute from one neuron to another, spreading tauopathy across the brain (d'Errico and Meyer-Luehmann, 2020). This trans-synaptic spreading approach is termed a prion-like model, due to similarity of mechanisms in prion diseases (Jucker and Walker, 2013, Liu et al., 2012), and involves pathological tau that works to

transform physiological tau to pathogenic (Clavaguera et al., 2009, Guo et al., 2016). This theory has been illustrated in several *in vitro* and *in vivo* studies whereby injection of tau aggregates can promote the spread of tau across cells and brain regions (Ahmed et al., 2014, Clavaguera et al., 2013, Clavaguera et al., 2009, Guo et al., 2016, Lasagna-Reeves et al., 2012). For this process, pathological tau must undergo intracellular transmission, involving the secretion and up-take from neighbouring neurons (d'Errico and Meyer-Luehmann, 2020).

This secretion can occur through 3 possible mechanisms (d'Errico and Meyer-Luehmann, 2020). First, tau will be packaged into microvesicles, internalised by exosomes, before the fusion of the vesicle with the plasma membrane (Fontaine et al., 2016, Lachenal et al., 2011, Pooler et al., 2013, Saman et al., 2012, Simon et al., 2012, Yamada et al., 2014). Secondly, in its soluble hyperphosphorylated form, tau will translocate across the plasma membrane (Plouffe et al., 2012, Pooler et al., 2012). While the direct mechanism is unclear, there can be formation of pore-like channel structures on the plasma membrane where tau secretion can occur (Lasagna-Reeves et al., 2014, Merezhko et al., 2018, Patel et al., 2015). Lastly, groups have illustrated the secretion of tau to neighbouring cells through filamentous actin-containing channels, termed nanotubes, which allow tau to be transported without secretion into the extracellular space (Abounit et al., 2016, Tardivel et al., 2016).

Once within the extracellular space, the pathogenic tau can be internalised by neighbouring neurons through different methods: receptor-mediated endocytosis, bulk-endocytosis and actin-dependent micropinocytosis (d'Errico and Meyer-Luehmann, 2020). Interestingly, tau seeding is not limited to these approaches, and in fact contributions from glial cells – astrocytes, oligodendrocytes, and microglia – have roles in tau spread (Asai et al., 2015, Maphis et al., 2015, Martini-Stoica et al., 2018, Narasimhan et al., 2017, Perea et al., 2019).

1.1.2.1.2.3 Tauopathy spread in AD

As described in **section 1.1.2.1.1.3**, the spread of Aβ pathologies throughout the AD brain has been characterised (Thal et al., 2002). However, this came years after the staging of tauopathy throughout AD as in 1991, Braak staging was implemented as it has a predictable spatiotemporal pattern **(Figure 1.6B)** (Braak et al., 2006, Braak and Braak, 1991). This was first completed using 100-µm sections from autopsy samples and allowed characterisation of six stages classified under three units: I-II, III-IV, and V-VI. Stages I-II represent identifiable tauopathy in the transentorhinal and entorhinal cortex (Braak et al., 2006, Braak and Braak, 1991). In stages III-IV, tauopathy spreads into the hippocampus, limbic allocortex and neocortex **(Figure 1.6B)**. Lastly, in stages V-VI, tauopathy spreads into secondary and primary fields **(Figure 1.6B)** (Braak et al., 2006, Braak

and Braak, 1991). Therefore, Aβ pathology and tauopathy spread through the brain in opposite directions, with tauopathy spreading inward to outward.

1.1.2.1.2.4 Pathological effects of tauopathy

Upon hyperphosphorylation of tau and formation of neurofibrillary tangles, this leaves the microtubules without sufficient stabilisation, resulting in the breakdown of microtubule structure and a disruption in axonal transport (Ballatore et al., 2007, Buee et al., 2000, Lindwall and Cole, 1984). This occurs due to large aggregates of neurofibrillary tangles causing a physical obstacle within the axons, preventing transport of vesicles and cargo. While contributing to this microtubule disengagement, aggregated neurofibrillary tangles can also sequester remaining functioning tau, resulting in a progressing loss of normal function (Ballatore et al., 2007) **(Figure 1.7)**. Therefore, the combination of loss of normal microtubule-stabilising tau and the gain of pathological hyperphosphorylated tau, have a role in exacerbating neurodegeneration in an AD brain (Ballatore et al., 2007).

Studies have also shown that phosphorylated tau can contribute to mitochondria dysfunction, further Aβ formation and disruption of calcium signalling through phosphorylation of Fyn kinase which forms a complex with PSD95, N-methyl D-aspartate receptor subtype 2B and the NMDA receptor, causing pathological effects including synaptic disruption, mitochondrial dysfunction, and neuronal death **(Figure 1.7)** (Ittner et al., 2010, Roberson et al., 2007, Tezuka et al., 1999, Zhang et al., 2021). Also, in the case of both plaques and neurofibrillary tangles, there appears to be a relationship with neuroinflammation throughout AD which exacerbates the molecular pathology within the brain (Zhang et al., 2021) **(Figure 1.7)**.

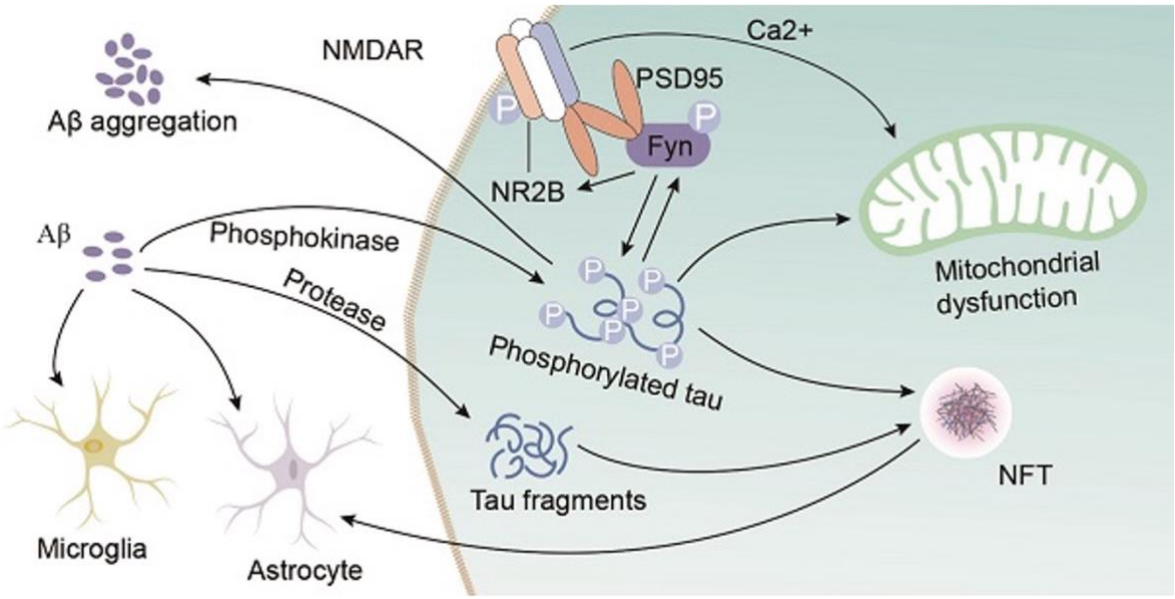

Figure 1.7. Pathological effects of neurofibrillary tangles and Aβ. Adapted from Zhang *et al.*, 2021.

1.1.2.2 Innate neuroinflammatory response

Over the years, neuroinflammation has become increasingly considered to contribute to AD pathology (Heppner et al., 2015). Despite Alzheimer identifying glial cells to be clustered around plaques, neuroinflammation remained a controversial topic due to microglia being commonly known to be protective immune cells. Now, AD is known to have crucial influence from the immune system on disease pathogenesis, with microglia and astrocytes known to interact with plaque and tangle molecular pathology.

1.1.2.2.1 Microglia

1.1.2.2.1.1 Microglia in a healthy brain

Microglia are a resident phagocyte in the CNS that shares many properties with peripheral macrophages and monocytes. As the resident phagocyte of the CNS, microglia's main role is to be protective, by scanning the brain for insults and restoring the brain back to a healthy state (Heppner et al., 2015, Hickman et al., 2018, Malm et al., 2015).

Microglia have a specific morphology and chemical state that changes depending on its response to the surrounding environment. This process is termed reactive gliosis which is induced by both chemical and morphological changes (Itagaki et al., 1989, Van Eldik et al., 2016). To simplify, there tends to be two well-established states: resting and activated. In resting state, microglia have long

processes that extend from the small cell body (Heppner et al., 2015, Hickman et al., 2018, Malm et al., 2015). These processes continuously scan the environment by extending and retracting. Upon activation, the cell body enlarges, and the processes become ramified (Malm et al., 2015, Van Eldik et al., 2016). These ramified processes now become directed towards the foreign body. This migration is thought to be dependent on ATP and activation of purinergic receptors (P2YRs) (Davalos et al., 2005, Malm et al., 2015). Upon migration to the toxic insults sensed by these processes, microglia initiate an inflammatory response (Hickman et al., 2018, Malm et al., 2015, Sarlus and Heneka, 2017). Therefore, there is increased production and release of inflammatory mediators such as cytokines, chemokines, proteases, and acute phase reactants. These work to recruit neighbouring microglia to aid in the protective response (Hickman et al., 2018, Malm et al., 2015, McGeer and McGeer, 1995, Sarlus and Heneka, 2017).

1.1.2.2.1.2 Microglia in an AD brain

Interestingly, due to the high association of microglia and plaques in the brains of AD patients, it was initially believed by Glenner in 1979, that microglia have a causative role in the generation of AD by contributing to Aβ production (Glenner, 1979, Mrak, 2012). However, with time, this theory was abandoned as evidence by Griffin and colleagues in 1989 showed microglia to primarily have an immunological function, due to high interleukin-1 (IL-1) expression (Griffin et al., 1989). However, it has now been shown that IL-1 can regulate APP synthesis, leaving the possibility for IL-1 expressing microglia to influence Aβ plaque formation (Mrak, 2012).

Microglia have several cell surface receptors, commonly termed pattern recognition receptors, that's main function is to recognise pathological insults. For example, many of these receptor complexes can recognise oligomer and fibrillar forms of Aβ: toll-like (TLR2, TLR4, TLR6 TLR9 and their co-receptor CD14), complement (CD36, CD14, CD47), scavenger (SR-A1, B2), immunoglobin, major histocompatibility class I and class II glycoproteins and leucocyte common antigens (Clayton et al., 2017, Heneka et al., 2015a, Heneka et al., 2015b, Hickman et al., 2018, Malm et al., 2015, McGeer and McGeer, 1995, Sarlus and Heneka, 2017). Upon binding, this induces an activated state, and the expression of these receptors are upregulated and inflammatory mediators like cluster of differentiation 36 (CD36), IL-1, tumour necrosis factor alpha (TNFα), and interleukin-6 (IL-6) are released. This occurs due to activation of down-stream signalling cascades which can promote NFκB-dependent transcription of genes such as those expressing markers for cytokines, ROS, phagocytosis (Malm et al., 2015). These inflammatory mediators will work to promote microglia recruitment and phagocytosis to remove pathogenic Aβ (Hickman et al., 2018, Malm et al., 2015). This is the protective function of microglia that uses its phagocytic functions to internalise and degrade Aβ for clearance from the CNS (Bard et al., 2000, Schenk et al., 1999) **(Figure 1.8)**. This extracellular degradation is aided by Aβ degrading enzymes

like neprilysin and insulin-degrading enzyme (Heneka et al., 2015a, Karran et al., 2011, Malm et al., 2015). Once degraded, clearance can be completed via a selection of pathways: phagocytosis, autophagy, and pinocytosis (Karran et al., 2011, Malm et al., 2015). Then, in cases where plaques have already been formed, to prevent further aggregation of Aβ and growth of plaques, microglia accumulate around them to form a protective barrier (Condello et al., 2015, Kayed et al., 2004).

In AD, microglia eventually reach a chronically activated state where previously beneficial functions become detrimental and can result in neuronal injury and death. This can happen through a series of direct and indirect methods (Hickman et al., 2018, Malm et al., 2015) **(Figure 1.8)**. For example, microglia can directly cause neuronal damage by undergoing respiratory burst, where in attempt to kill foreign insults it generates and stores large quantities of superoxide anions (Clayton et al., 2017, Hickman et al., 2018, McGeer and McGeer, 1995). These free radicals will migrate toward the insult upon membrane invagination during phagocytosis (McGeer and McGeer, 1995). If this primary method fails, external contact is made, meaning that surrounding healthy tissue can be affected. Additionally, several pro-inflammatory mediators released from the microglia may alter neuronal function and survival. For example, microglia can produce ROS and reactive nitrogen species, activate the nucleotide-binding domain, leucine-rich–containing family, pyrin domain–containing-3 (NLRP3) inflammasome and several cytokines that can all contribute to a self-harming effect that worsens the disease state (Hickman et al., 2018) **(Figure 1.8)**. Upon activation, the NLRP3 inflammasome will release apoptosis-associated speck-like protein containing a C-terminal caspase recruitment domain (ASC) specks, which can be released from microglia via exocytosis and can contribute to further Aβ aggregation (Venegas et al., 2017) **(Figure 1.8)**. Additionally, upon interaction with Aβ, microglia can be overwhelmed, and their phagocytic abilities can be altered. For example, there is also down-regulation of expression of Aβ-receptors and Aβ-degrading enzymes and an upregulation of β-site amyloid precursor protein cleaving enzyme (BACE) (Heneka et al., 2015a, Hickman et al., 2018, Malm et al., 2015) **(Figure 1.8)**. This will result in continued accumulation of Aβ with no functionality to slow-down AD progression and the resulting neuronal death that occurs.

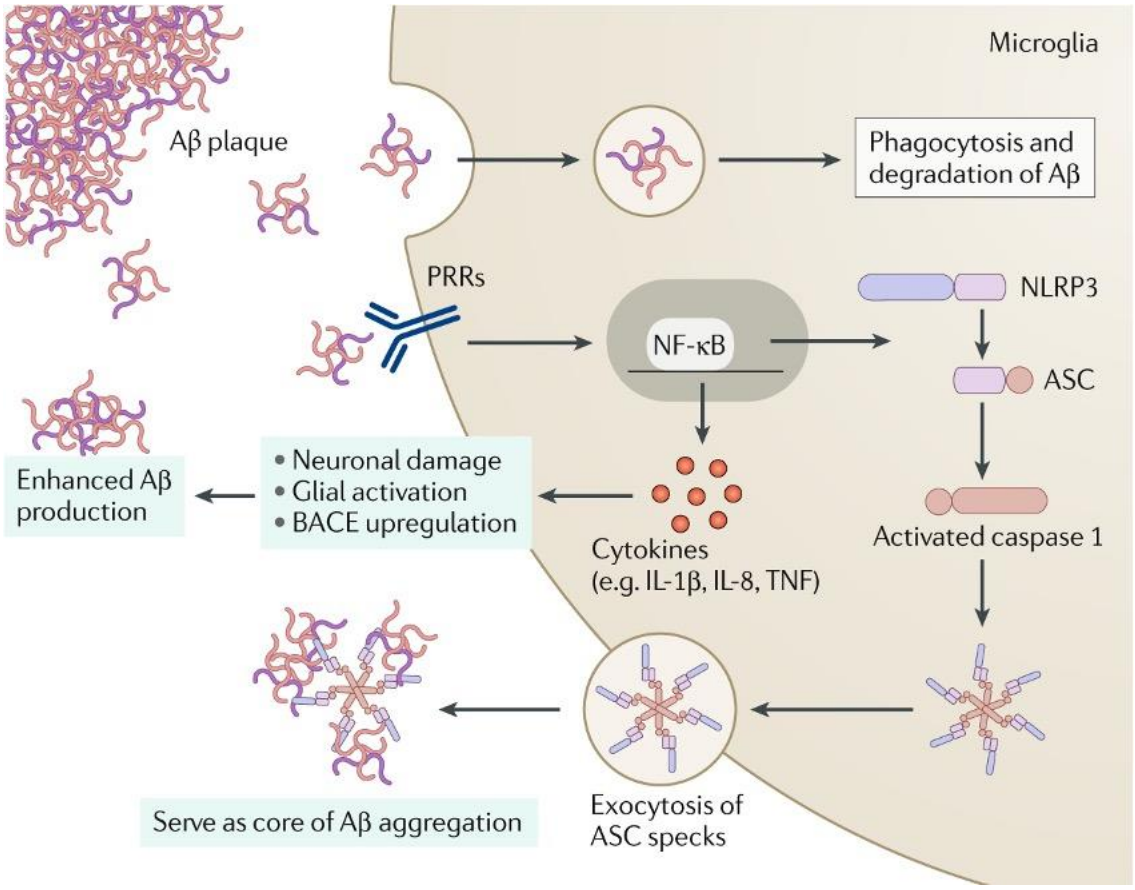

Figure 1.8. Interaction between microglia and Aβ and the resulting pathological effects. Adapted from Leng & Edison, 2021.

As well as being involved in plaque pathology, microglia can influence the spread of tauopathy in AD brains and tau can induce microglial activation (Morales et al., 2013, Wes et al., 2014). Consequently, a relationship exists between the distribution of microglia and neurofibrillary tangles (Mrak, 2012). In the initial protective phase of microglial function, microglia work to clear hyperphosphorylated tau from the brain (Bolos et al., 2016). However, when chronically activated and the phagocytising functions are awry, pro-inflammatory cytokines released from microglia can promote kinase activity and therefore, tau phosphorylation. For example, IL-1-expressing microglia have been found to increase the activity of tau kinases, particularly p38 MAPK (Li et al., 2003). This would suggest that microglia can increase the imbalance in kinase/phosphatase activity which promotes hyperphosphorylation of tau. In addition, microglia spread tau through phagocytosis and exosome secretion, contributing to disease progression (Asai et al., 2015, Wang et al., 2022).

When considering the relationships between plaques, neurofibrillary tangles and microglia, studies have found that both Aβ and microglia together can contribute to enhanced tauopathy (Felsky et al., 2019), whereas microglia and tauopathy may work together in a protective manner by promoting phagocytosis of Aβ from the brain (Chen et al., 2016). These conflicting contributions are thought to be due to the microglial TREM2-TYROBP pathway as this has been shown to

interact with both Aβ and tau, with studies indicating a large overlap of Aβ/tau-TREM2-TYROBP pathways and therefore, indicate the role of microglia as a mediator. Further studies have exemplified the role of this microglial TREM2-TYROBP network (Bolos et al., 2017, Lee et al., 2014b, Sekiya et al., 2018, Takahashi et al., 2017). In fact, contributors to this pathway, such as microglial CX3C motif chemokine receptor 1 (CX3CR1), have reduced activation throughout AD due to the loss of noradrenergic signalling acting via β2Ars and thereby contribute to neuronal death and Aβ pathology (Gonzalez-Prieto et al., 2021, Le et al., 2023). This emphasises the role of neuronal activity in both molecular and inflammatory pathogenesis.

1.1.2.2.2 Astrocytes

1.1.2.2.2.1 Astrocytes in a healthy brain

Like microglia, astrocytes are an abundant glial cell that forms a tiled organisation within the CNS. These were intensely studied by the group of Cajal who was the first to hypothesise that astrocytes can interact with neurons, other glial cells, and blood vessels (Garcia-Marin et al., 2007, Navarrete and Araque, 2014). This hypothesis was later proven by electron microscopy which illustrated interactions between astrocytic processes and neurons (Sofroniew and Vinters, 2010). Therefore, they have numerous complex functions as well as working to respond to foreign insults within the CNS (Khakh and Sofroniew, 2015, Sofroniew, 2020, Sofroniew and Vinters, 2010).

Over-time, several types of astrocytes were identified and characterised, including protoplasmic and fibrous astrocytes (Andriezen, 1893, Cajal, 1913). Protoplasmic astrocytes, most prominent in the grey matter (Raff, 1983), are star-shaped structures with protruding processes (Navarrete and Araque, 2014). These processes can interact with both neurons and blood vessels, by forming a specialised structure at the end of the process termed ‘end-feet’ (Allen and Eroglu, 2017, Khakh and Sofroniew, 2015). Whereas fibrous astrocytes, most prominent in the white matter (Raff, 1983), are elongated and are usually situated along myelinated axons, proximal to oligodendrocytes (Allen and Eroglu, 2017, Ben Haim and Rowitch, 2017). Both types of astrocytes contact blood vessels, astrocytes, and neurons through differing approaches. For example, protoplasmic astrocytes form a sheath around synapses and fibrous astrocytes interact with the nodes of Ranvier (Allen, 2014, Sofroniew and Vinters, 2010).

Astrocytes contribute to communication through gliotransmission. While astrocytes are not electrically excitable, they can increase the intracellular calcium concentrations when communicating to neurons, blood vessels or other glial cells (Charles et al., 1991, Oliveira and Araque, 2022, Volterra and Meldolesi, 2005) **(Figure 1.9)**. This enhanced calcium concentration can push for release of neurotransmitters and neuromodulators to aid communication (Angulo et

al., 2008, Bezzi et al., 1998, Bezzi et al., 2004, de Ceglia et al., 2023, Fellin et al., 2004, Jourdain et al., 2007). Upon release of neuromodulators, astrocytes can contribute to synaptic pruning by guiding migrating axons. In addition, they assist in the termination of neuronal signalling through the uptake of neurotransmitters from the synaptic cleft through transporters expressed on the astrocyte cell surface. Also, astrocytes can control blood flow through the release of mediators, such as prostaglandins and nitric oxide, that have a role in vascular dilation (Fellin and Carmignoto, 2004, Iadecola and Nedergaard, 2007, Mulligan and MacVicar, 2004, Takano et al., 2006) and are involved in direct nutrient-waste exchange for neurons based on their activity (Abbott et al., 2006, Foo et al., 2011, Simard and Nedergaard, 2004) **(Figure 1.9)**.

However, the main role of astrocytes is its immune function, where in response to a foreign body within the brain, they initiate reactive astrogliosis resulting in molecular, cellular, and functional changes (Das et al., 2020, Escartin et al., 2021, Pekny and Nilsson, 2005) **(Figure 1.9)**. Astrogliosis works to limit the area of damage, while promoting recovery of neuronal functionality by releasing inflammatory modulators such as cytokines, chemokines, growth factors and gliotransmitters (Li et al., 2019, Monterey et al., 2021) **(Figure 1.9)**. Back in 2017, Liddelow and Barres identified that in their activated form, astrocytes can adopt different inflammatory states based on the gene expression profiles: neurotoxic A1 and neuroprotective A2 (Liddelow et al., 2017). Neuroprotective A2 astrocytes protect the environment by promoting clearance, BBB repair, neuronal growth, and synaptic restoration. Whereas neurotoxic A1 astrocytes can result in neurodegeneration. Astrocytes acquire their pro-inflammatory phenotype through a microglial-astrocyte connection and paracrine signalling. Specifically, release of TNF-α, IL-1α and complement component 1q (C1q) activates the astrocytes (Liddelow et al., 2017, Sofroniew, 2020, Wu et al., 2019), through the nuclear factor kappa B (NF-kβ) signalling pathway causing an upregulation of pro-inflammatory genes (Heneka et al., 2010) **(Figure 1.9)**. However, there are several different approaches for astrocytic activation (Lawrence et al., 2023).

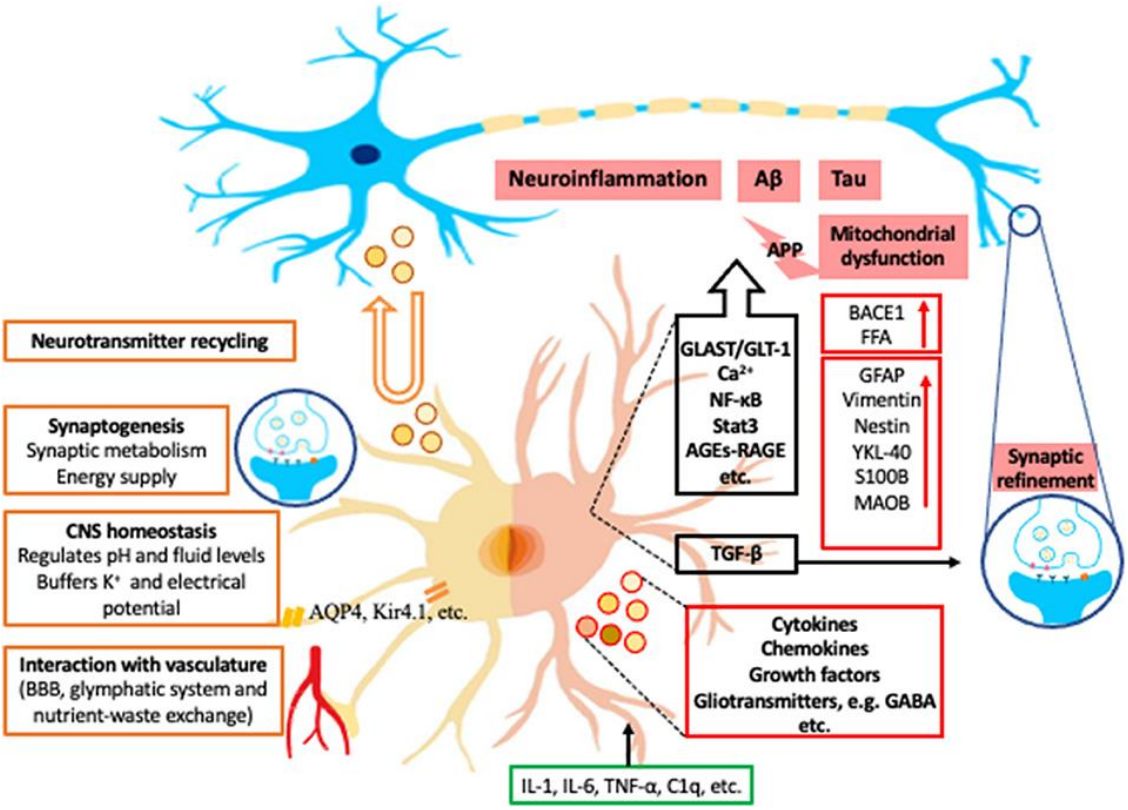

Figure 1.9. Astrocytic functions in healthy (left) and AD brain (right). Left side of astrocyte illustrates functions in a healthy brain. Right side of astrocyte illustrates a reactive astrocyte throughout AD. Orange boxes show astrocytes function in a healthy brain. Green box shows activating factors from microglia. Red boxes show the intracellular and secreted molecules. Black box shows activated signalling pathways. K+: potassium; AQP4: aquaporin-4; Kir4.1: inwardly rectifying K+ channel subunit 4.1; APP: amyloid-beta precursor protein; BACE1: β-site APP-cleaving enzyme 1; FFA: free fatty acid; GFAP: glial fibrillary acidic protein; YKL-40: chitinase-3 protein like-1; S100B: S100 calcium-binding protein B; MAOB: monoamine-oxidase-b; GLAST: glutamate aspartate transporter; GLT-1: glutamate transporter 1; Ca2+: calcium; NF-κB: nuclear factor- kappa B; Stat3: signal transducer and activator of transcription 3; AGEs: advance glycation end-products; RAGE: Receptor for advanced glycation end products; TGF-β: transforming growth factor beta; GABA: gamma-aminobutyric acid; IL: interleukin; TNF-α: tumor necrosis factor alpha; C1q: complement component 1q. Adapted from Monterey *et al.,* 2021.

1.1.2.2.2.2 Astrocytes in an AD brain

Alzheimer identified the up-regulation of astrocytes surrounding AD molecular pathology (Alzheimer, 1907), with them commonly appearing co-localised to Aβ plaques and neurofibrillary tangles (Nagele et al., 2003, Nagele et al., 2004, Olabarria et al., 2010). Like microglia, it is thought that astrocytes functionality changes throughout the progression of AD pathogenesis (Verkhratsky et al., 2010). Within early stages of the disease, atrophy of astrocytes contributes to reduced

synaptic activity, affects the control of ions and neurotransmitters, and alters metabolic support, thereby contributing to abnormalities in synaptic function **(Figure 1.9)**. However, at this stage, astrocytes remain in protective form with upregulation of genes involved in protein degradation and antioxidant defence and therefore can regulate the phagocytosis and degradation of Aβ (DeWitt et al., 1998, Liu et al., 2017, Montoliu-Gaya et al., 2017, Wyss-Coray et al., 2003, Yin et al., 2006). Whereas in late stages of the disease, there is enhanced astrogliosis through microglial activation and by the action of Aβ on astrocytic cell surface receptors (DeWitt et al., 1998) like P2Y1 (Delekate et al., 2014), nicotinic, glutamate metabotropic, and RAGEs which activates cellular signalling through AGE-RAGE, NF-kB, phosphoinositide 3-kinase/protein kinase B (P13K-Akt) pathways and result in changes in intracellular calcium concentrations (Abramov et al., 2003, Abramov et al., 2004), enhanced astrogliosis state, oxidative stress, and neuronal death (Rodriguez-Giraldo et al., 2022) **(Figure 1.9)**. Therefore, enhanced activation eventually turns astrocytes into a pathogenic enhancer, with astrocytes beginning to express BACE1 (Hartlage-Rubsamen et al., 2003, Heneka et al., 2005, Leuba et al., 2005, Rossner et al., 2001, Rossner et al., 2005) and increase APP production (Martins et al., 2001), resulting in increased production of Aβ **(Figure 1.9)**. Finally, studies have shown that astrocytic dysregulation of glutamate and GABA transport and release can accelerate AD pathogenesis (Jacob et al., 2007, Jo et al., 2014, Matos et al., 2008). This leaves astrocytes contributing to and associated with various AD pathogenic signs such as molecular pathologies, neuroinflammation, oxidative stress, hyperactivity, and excitotoxicity **(Figure 1.9)**.

Also, recent studies have shown tauopathy within astrocytes, with a correlation existing between astrocytes with tauopathy and neurodegeneration (Amro et al., 2021). In addition, there is upregulation of genes that promote the spread of tauopathy through the exosomal-dependent pathway, and through other astrocyte transport mechanisms such as astrocytic nanotubules (Amro et al., 2021) **(Figure 1.9)**. This has shown to result in irregular intracellular calcium signalling, unregulated gliotransmission, dysfunctional ATP control and disrupted synaptic activity (Piacentini et al., 2017). Therefore, astrocytes are a key player in the spread of AD pathogenesis illustrating that astrocytes loss of control of neuronal activity is detrimental.

1.1.2.3 Neuronal oscillations

Several aspects of the neuronal capabilities of the AD brain are influenced, with a well-known hallmark of AD being the reduction in acetylcholine signalling (Francis et al., 1999). However neuronal oscillations are now known to be altered throughout various brain disorders.

1.1.2.3.1 Brain oscillations

Neuronal oscillations represent fluctuations of neuronal populations across brain regions, responding to a certain cognitive or physiological state (Buzsaki and Draguhn, 2004, Buzsaki et al., 2013, Harris and Thiele, 2011). Such neuronal populations generate brain oscillations which are dominant at different frequency bands (Buzsaki and Draguhn, 2004, Buzsaki et al., 2013, Harris and Thiele, 2011). The mean frequencies are categorised based on their power spectral analysis, as the power density of the electroencephalogram (EEG) is inversely proportional to frequency within the mammalian cortex (Buzsaki and Draguhn, 2004, Freeman et al., 2000). Accordingly, using scalp EEG, the first brain oscillation was identified by Hans Berger where he found an 8-12-Hz rhythm that he classed as alpha waves (Berger, 1929). Since then, a range of brain oscillations have been identified with varied frequency bands and proposed functionality **(Figure 1.10A).** Oscillations with a smaller frequency are thought to be involved across large neuronal space, whereas higher frequency oscillations are more localised (Buzsaki and Draguhn, 2004, Csicsvari et al., 2003, Steriade, 2001). In addition, these brain states will show behavioural tendencies that will range from active to non-active (Harris and Thiele, 2011). During active states, neuronal activity is desynchronised, fluctuating at high frequencies and small amplitudes. Whereas, during non-active states, neuronal activity is synchronised, fluctuating at slow frequencies and high amplitudes. This allows several oscillatory activities to occur in parallel, across multiple temporal and spatial scales (Buzsaki and Draguhn, 2004, Buzsaki et al., 2013, Harris and Thiele, 2011).

Due to this contribution to brain-wide activity, alterations in brain oscillations have been shown in various brain disorders. Specifically, in AD, gamma oscillations can be disrupted which has prompted recent advances studying modification of them as a therapeutic strategy (Adaikkan et al., 2019, Iaccarino et al., 2016, Martorell et al., 2019). While other oscillations, such as slow oscillations, can be effected throughout AD (Byron et al., 2021), I will primarily focus on gamma oscillations.

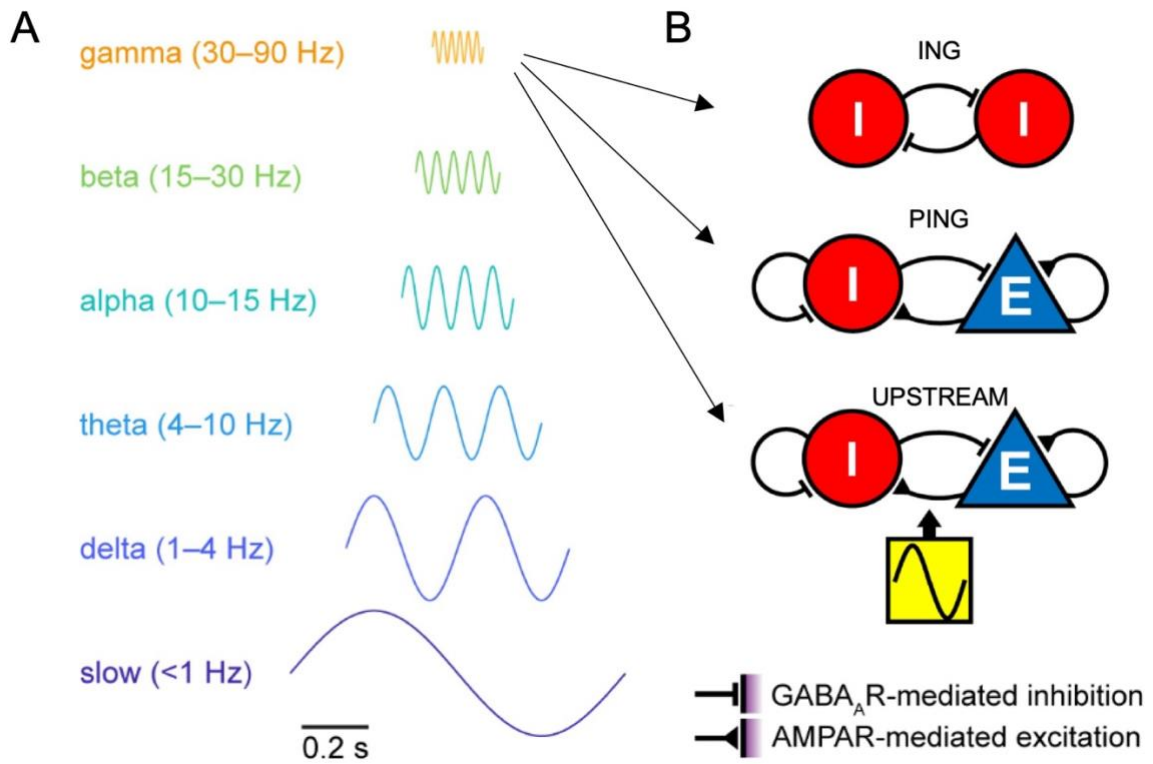

Figure 1.10. Brain oscillations. (A) Neural oscillations and their frequency bands. (B) Mechanisms of generation of gamma oscillations. *Top,* Interneuron gamma (ING) mechanism. *Middle,* Pyramidal-interneuron network gamma (PING) mechanism. *Bottom,* Inherited gamma oscillations from upstream areas. Adapted from Byron *et al.,* 2021.

1.1.2.3.1.1 Gamma oscillations

1.1.2.3.1.1.1 Background

Gamma oscillations were first identified and described in 1938 by Jasper and Andrews to be gamma waves at 35-45-Hz (Jasper, 1939). Other terms were used before gamma oscillations became the popular term after numerous papers by Freeman and colleagues (Bressler and Freeman, 1980, Freeman, 1975). They are fast, appear locally and have been shown to be involved in cognitive functions like attention (Fries, 2015, Jensen et al., 2007), memory encoding (Jensen et al., 2007, Osipova et al., 2006b), object and face recognition (Singer and Gray, 1995) and working memory (Howard et al., 2003). Additionally, they have been found to be present across many brain regions including the neocortex, entorhinal cortex (Charpak et al., 1995, Chrobak and Buzsaki, 1998, Nakazono et al., 2017), amygdala (Bauer et al., 2007), hippocampus (Buzsaki et al., 1983, Harris et al., 2003, Wang and Buzsaki, 1996), striatum (Cohen et al., 2009, Popescu et al., 2009), olfactory bulb (Beshel et al., 2007, Eeckman and Freeman, 1990), basal forebrain (Nair et al., 2018, Yague et al., 2017), and thalamus (Minlebaev et al., 2011).

It was found that gamma oscillations are most prominent in superficial cortical layers and the dentate gyrus within the cortex and hippocampus, respectively (Buffalo et al., 2011, Buzsaki et al., 1983, Chrobak and Buzsaki, 1998, Quilichini et al., 2010). While considering the commonality between these regions, the requirement of inhibitory interneurons was revealed. This was shown to involve perisomatic inhibition involving fast-spiking interneurons, first shown when recording local field potential in the hippocampus of rats (Buzsaki et al., 1983). Now it is known that the most prominent source of perisomatic inhibition is parvalbumin (PV) GABAergic neurons. However, there are other interneuron types expressing a PV, somatostatin (SST) or cholecystokinin (CCK) marker thought to be involved in generation of gamma oscillations such as chandelier cells, O-LM interneurons, basket cells and Martinotti cells (Buzsaki and Wang, 2012). In addition, while greatly unresearched, recent findings also illustrate the role of non-neuronal cells, such as glial cells, in the generation of gamma oscillations as blocking vesicle release from astrocytes prevented generation of gamma at the 30-50-Hz range in mice (Lee et al., 2014a, Makovkin et al., 2022).

1.1.2.3.1.1.2 Generation of gamma oscillations

To begin to understand the generation of gamma oscillations, many studies were completed in cortical circuits using computational models (Buzsaki and Wang, 2012, Lytton and Sejnowski, 1991, Tiesinga and Sejnowski, 2009, Traub et al., 1996b, Wang and Buzsaki, 1996, Whittington et al., 2000), brain slice experiments (Traub et al., 1996a, Whittington et al., 1995) and *in vivo* optogenetic experiments (Cardin et al., 2009, Sohal et al., 2009). The widely accepted mechanism comes from computational models which suggest three main mechanisms: the interneuron gamma (ING) mechanism, the pyramidal-interneuron gamma (PING) mechanism or inheriting gamma oscillations from upstream brain regions **(Figure 1.10B)** (Byron et al., 2021, Jefferys et al., 1996, Tiesinga and Sejnowski, 2009). These have also been explained in other papers as the inhibitory-inhibitory (I-I) and excitatory-inhibitory (E-I) models (Buzsaki and Wang, 2012). For both approaches, they involve consistent synaptic activity that enhances synaptic plasticity through long-term potentiation (LTP) and therefore, has several protective and beneficial functions which are vital for cognitive processes such as memory formation (Guan et al., 2022, Park et al., 2020). This further emphasises how the dysfunction of gamma oscillations through synaptic degeneration or dysfunction may contribute to cognitive deficits.

1.1.2.3.1.1.2.1 ING mechanism

Firstly, in the ING mechanism, otherwise known as I-I model, there is mutual inhibition between two inhibitory interneurons, through γ-aminobutyric acid type A receptor ($GABA_AR$)-mediated inhibition, resulting in strong inhibitory feedback that eventually generates gamma oscillations

(Figure 1.10B) (Buzsaki and Wang, 2012, Byron et al., 2021, Traub et al., 1996a, Wang and Buzsaki, 1996, Whittington et al., 1995). They can be generated either in a high-firing, low noise condition or irregular, noisy firing condition (Buzsaki and Wang, 2012). For the low noise condition, the inhibitory neurons will fire with sharp synchrony. Whereas, in the noisy condition, the presence of recurrent synaptic interactions will overcome this asynchronous environment, allowing the generation of synchronous gamma oscillations (Ardid et al., 2010, Brunel and Wang, 2003, Geisler et al., 2005, Wang and Buzsaki, 1996). Importantly, for both conditions, synchrony will only occur once a pool of interneurons and their partner neurons have synchronous discharges and generation of inhibitory postsynaptic potentials (IPSPs), respectively, due to $GABA_AR$ hyperpolarisation controlling the duration and resulting frequency of the oscillation (Buzsaki and Wang, 2012, Wang and Buzsaki, 1996, Whittington et al., 1995).

Studies supporting this mechanism include optogenetic experiments which show that optically activating cortical PV-positive GABAergic neurons, but not other interneuron subtypes, could generate gamma oscillations (Cardin et al., 2009, Sohal et al., 2009). In addition, *in vitro* experiments show that activating metabotropic glutamate receptors result in mutual inhibition between interneurons and generation of a gamma oscillation (Whittington et al., 1995).

1.1.2.3.1.1.2.2 PING mechanism

Secondly, the PING mechanism, otherwise known as the E-I model, involves inhibitory interneurons and excitatory pyramidal cells **(Figure 1.10B)**. It is thought that the interaction between the quick AMPAR-mediated excitation and slow $GABA_AR$-mediated feedback inhibition works to generate gamma oscillations when a strong cyclic behaviour continues (Buzsaki and Wang, 2012, Byron et al., 2021, Tiesinga and Sejnowski, 2009). For example, axon conduction and synaptic delays result in a ~5-ms phase shift between the interneuron and pyramidal spikes. These shifts determine the frequency of neuronal firing and therefore, the gamma oscillation (Buzsaki and Wang, 2012, Freeman, 1975).

Studies supporting this mechanism of gamma oscillation include both *in vitro* and *in vivo* studies (Buzsaki and Draguhn, 2004, Csicsvari et al., 2003, Hasenstaub et al., 2005, Mann et al., 2005, Tiesinga and Sejnowski, 2009). In fact, studies manipulating the connection between the interneuron and pyramidal cells by knocking down AMPARs reduces the amplitude of gamma oscillations (Fuchs et al., 2007). Additionally, the PING mechanism can work appropriately without presence of the ING mechanism, where removal of I-I connections in mice did not affect gamma power within the CA1 (Wulff et al., 2009).

1.1.2.3.1.1.2.3 Inheritance mechanism

For the final approach, the generation of gamma oscillations overcomes the normally local contribution and instead is inherited from upstream brain regions **(Figure 1.10B)** (Buzsaki and Wang, 2012, Byron et al., 2021). In this case, it is thought that phase-phase or phase-amplitude coupling can occur to result in modulation and spread of a certain rhythm (Buzsaki and Wang, 2012). For phase-phase coupling, the faster oscillation couples the several phases of a slower rhythm, resulting in phase locking (Buzsaki and Wang, 2012). For phase-amplitude coupling, the amplitude of the faster oscillation is modulated by the phase of a slower rhythm (Buzsaki and Wang, 2012). Therefore, the downstream network can respond to the rhythmic activity of upstream brain regions.

However, these three approaches are not always fully elucidated by *in vivo* experimental data, commonly resulting in an unclear conclusion on the general mechanism. For example, some brain regions known to generate gamma oscillations – basal ganglia and ventral tegmental area – are unlikely to be due to the PING as they lack these vital connections (Berke et al., 2004, Brown et al., 2002, Fujisawa and Buzsaki, 2011, Tort et al., 2008). On another note, the ING mechanism is thought to occur at least partially because of the excitatory drive within nearby pyramidal cells, thereby effecting the intensity of the mutual inhibitory tone (Buzsaki and Wang, 2012). These findings may support a mutual effect of all three mechanisms across the brain for generation of gamma oscillations. Thus, more studies must be completed to fully understand the generation and spread of gamma oscillations within the brain, healthy or diseased.

1.1.2.3.1.1.3 Gamma oscillations in AD brain

As gamma oscillations have been shown to be generated across many regions over the brain and be involved in vital cognitive processes such as attention and memory, it is not surprising that alterations in normal gamma oscillatory function have been found across several neurodegenerative diseases, one of these being AD (Mably and Colgin, 2018). Several studies have been completed to understand these alterations, in both humans with AD and AD mouse models.

1.1.2.3.1.1.3.1 Humans

In humans, several studies have illustrated the decline in LTP within the cortex, with a reported dysfunction of PV interneurons within the parietal cortex. However, human studies investigating the change of gamma oscillations using EEG or magnetoencephalography have conflicting findings, with some illustrating a reduction in gamma power within the cortex (Basar et al., 2016,

Ribary et al., 1991, Stam et al., 2002), while others show an increase in gamma power (Basar et al., 2017, Osipova et al., 2006a, Rossini et al., 2006, van Deursen et al., 2011, van Deursen et al., 2008, Wang et al., 2017). For example, an EEG study completed on 15 AD patients shows an increased gamma band power, when in resting state, listening to music or stories and under visual stimulation, compared to controls (van Deursen et al., 2008). This finding was replicated, albeit in different experimental conditions, in another 15 AD patients which showed a significantly increased 40-Hz steady state response compared to controls (van Deursen et al., 2011). Also, studies illustrate an enhanced gamma coherence in AD patients compared to controls across cortical regions (Basar et al., 2017, Rossini et al., 2006).

Some researchers believe these conflicting results may be due to experimental differences such as the assessment of gamma oscillations between varied control groups (MCI patients or healthy subjects), at different stages of AD and under different states: resting state or during sensory stimulation (Byron et al., 2021). Alternatively, a recent paper suggests that these discrepancies may be due to limitations of EEG recordings (Casula et al., 2022). Instead, they illustrate a novel approach involving the combination of EEG and transcranial magnetic stimulation (TMS), termed TMS-EEG. Here, they show a significant reduction in gamma oscillations within the frontal lobe compared to controls, as well as a greater impairment of LTP-like plasticity as seen in previous studies (Casula et al., 2022). They believe change in gamma power may be detectable with this approach, but not EEG alone.

On another note, this discrepancy may be explained by changes in gamma oscillatory activity across AD progression through compensatory mechanisms (Gaubert et al., 2019). For instance, a study completed on >300 pre-AD individuals aged 70-85 illustrated presence of an inverted U-shape relationship between Aβ depositions and gamma band power (Gaubert et al., 2019). This suggests that the gamma oscillatory power throughout AD depends on the extent of Aβ pathology. Specifically, in intermediate stages of Aβ deposition, gamma power increases, suggesting a compensatory mechanism (Gaubert et al., 2019). However, with increasing Aβ load, gamma power begins to decline, suggesting a contribution to a breakdown of neuronal circuits, with alterations in LTP and synaptic plasticity, involved in generation of gamma oscillations (Gaubert et al., 2019, Jones et al., 2016, Lim et al., 2014, Mormino et al., 2011). It is hypothesised that these alterations occur due to Aβ oligomers interfering with the PING mechanism of gamma generation (Lei et al., 2016), thereby suggesting the recovery of these abnormalities by modulating inhibitory GABAergic activity (Li and Selkoe, 2020, Manippa et al., 2022). These findings (Gaubert et al., 2019) may provide some explanation to the conflicting findings discussed above (Basar et al., 2016, Basar et al., 2017, Osipova et al., 2006a, Ribary et al., 1991, Rossini et al., 2006, Stam et al., 2002, van Deursen et al., 2011, van Deursen et al., 2008, Wang et al., 2017), but an importance in large studies with appropriate experimental parameters are required.

1.1.2.3.1.1.3.2 Mice

Table 1.1. Changes in gamma (γ) oscillations in AD mouse models. Adapted from Byron *et al.,* 2021.

Mouse Model	Age (months)	Sex	Preparation	Frequency Band (Hz)	Changes in γ Oscillations	Reference
APP-PS1	4-5	NA	Entorhinal cortical slices	20-60	Reduced γ frequency in LEC No effect in MEC	**Klein et al., 2016**
J20	4-7	M/F	in vivo cortical EEG	20-80	Reduced γ power	**Verret et al., 2013**
	7-8	M/F		30-90	Reduced γ power	**Martinez-Losa et al., 2018**
5xFAD	3	M	in vivo LFP in CA1	20-50	Reduced γ power during SWRs	**Iaccarino et al., 2016**
TgCRND8	1	NA	Hippocampal slices	θ: 3-12 low γ: 25-85 high γ: 120-250	No change in γ power Disrupted θ-γ coupling	**Goutagny et al., 2013**
	1	M	in vivo hippocampal LFP	low γ: 25-45 high γ: 60-100	Reduced γ power	**Hamm et al., 2017**
APOE4	5-8, 9-11, 13-17	F	in vivo hippocampal LFP	30-50	Reduced γ power	**Jones et al., 2020**
	4-5	F	in vivo hippocampal LFP	30-50	Reduced γ power during SWRs	**Gillespie et al., 2016**
3R tau overexpression	7	M	Hippocampal slices	50-90	Reduced γ power and peak frequency	**Richetin et al., 2020**

Despite conflicting results at the human level, a consistent interruption in gamma oscillations has been reported across various AD mouse models, including APP-PS1 (Klein et al., 2016), J20 (Martinez-Losa et al., 2018, Verret et al., 2012), 5xFAD (Iaccarino et al., 2016), CRND8 (Goutagny et al., 2013, Hamm et al., 2017), APOE4 (Gillespie et al., 2016, Jones et al., 2016) and tau models (Richetin et al., 2020) **(Table 1.1)**. Both ex-vivo slice experiments and *in vivo* electrophysiological recordings have illustrated that AD mouse models have a reduced gamma band power. In fact, some studies have shown that this decline in gamma power occurs in pre-clinical stages, before Aβ plaque deposition and cognitive decline (Etter et al., 2019, Iaccarino et al., 2016). Also, studies that have shown alterations in activity of fast-spiking inhibitory neurons involved in gamma oscillation generation, including PV-positive, SST-positive, and CCK-positive GABAergic neurons, across the hippocampus and prefrontal cortex (Fu et al., 2019, Martinez-Losa et al., 2018, Shi et al., 2020, Verret et al., 2012). This is thought to be due to these neurons being vulnerable to soluble or fibril Aβ and tauopathy (Bero et al., 2011, Fu et al., 2019, Walsh and Selkoe, 2004). However, no inverted U-shape relationship between Aβ deposition and gamma power has been identified in mouse studies despite studies investigating the change in gamma power across age. This may be due to difficulties mirroring disease progression in current animal models, which emphasises the importance for longitudinal experiments in late-onset AD mouse models for identifying if this trend is evolutionary conserved.

These effects on normal gamma oscillations have been shown to result in aberrant gamma oscillatory activity and cognitive dysfunction, thereby contributing to the AD pathogenic presentation (Goutagny et al., 2013, Mably and Colgin, 2018, Mably et al., 2017). Specifically, this degeneration in GABAergic neuron and synaptic functionality has shown to contribute to cognitive deficits and a loss of LTP within the hippocampus that is vital for long-term memory formation,

thereby reflecting the memory interruptions seen in human symptoms (Guan et al., 2022, Park et al., 2020, Verret et al., 2012). This shows that gamma oscillations are an important target for AD treatment. In fact, previous studies have illustrated that restoring PV-positive interneurons in hAPP mice had beneficial effects on gamma oscillations and cognitive function (Verret et al., 2012), that optogenetic activation of PV and SST neurons could restore gamma oscillatory functions such as theta-nested gamma oscillation-induced spike-timing dependent LTP (Park et al., 2020), and that optogenetically activating PV neurons in 5xFAD mice improved memory retrieval (Park et al., 2024). Therefore, these improvements in cognitive function, related to human spatial memory and memory retrieval deficits, illustrated that restoring gamma oscillations throughout AD has potential beneficial effects. This resulted in research groups identifying respective therapeutic strategies. However, these optogenetic routes may be complicated when transferring to the clinic resulting in several research groups investigating the possibility of inducing gamma oscillations with sensory stimulation for AD treatment (Adaikkan et al., 2019, Iaccarino et al., 2016, Martorell et al., 2019). However, a comprehensive analysis on electrophysiological biomarkers throughout AD is vital and will aid discovery of therapeutic strategies. This is vital due to the lack of beneficial therapeutics available for AD.

1.2 Treatment of AD

Pharmaceutical intervention of AD has been at a halt for years, leaving AD patients with limited treatment options **(Figure 1.11)**. Currently, there are few pharmaceutical options and instead of being preventative, they are targeted toward symptomatic therapy. This means that drugs aim to relieve symptoms to enhance the patient's quality of life, while providing some relief for the caregiver.

Currently, there are only two classes of drugs approved for treatment of AD in the UK: acetylcholinesterase inhibitors (donepezil, rivastigmine and galantamine) and NMDA antagonists (memantine) (Briggs et al., 2016, Weller and Budson, 2018). Patients are put on these drugs depending on their stage of dementia, with cholinesterase inhibitors used in mild-moderate AD and NMDA antagonists used for severe AD **(Figure 1.12)**. The main target of these drugs is cholinergic neuronal loss, based on the cholinergic hypothesis established in 1976 by Davis and Maloney (Davies and Maloney, 1976, Francis et al., 1999). However, after many years of clinical studies for anti-amyloid therapies – drugs that aim to remove Aβ from the brain in attempt to restore cognitive function – two monoclonal anti-Aβ antibodies, called aducanumab and lecanemab, were approved for use in the US for treatment after diagnosis **(Figure 1.12B)** (Sevigny et al., 2016, Sims et al., 2023, van Dyck et al., 2023). It is widely considered that the success of these drugs is limited as they are administered only throughout clinical stages of AD progression, where potentially too much neuronal damage has occurred for restoration **(Figure 1.12A)**. Consequently, many future

interventions are targeted at the pre-clinical AD for prevention and delay of AD progression **(Figure 1.12).**

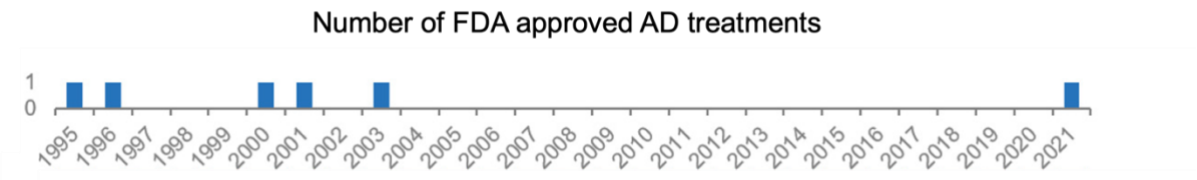

Figure 1.11. Number of FDA approved AD treatments over past decades. Adapted from Cummings *et al.,* 2021.

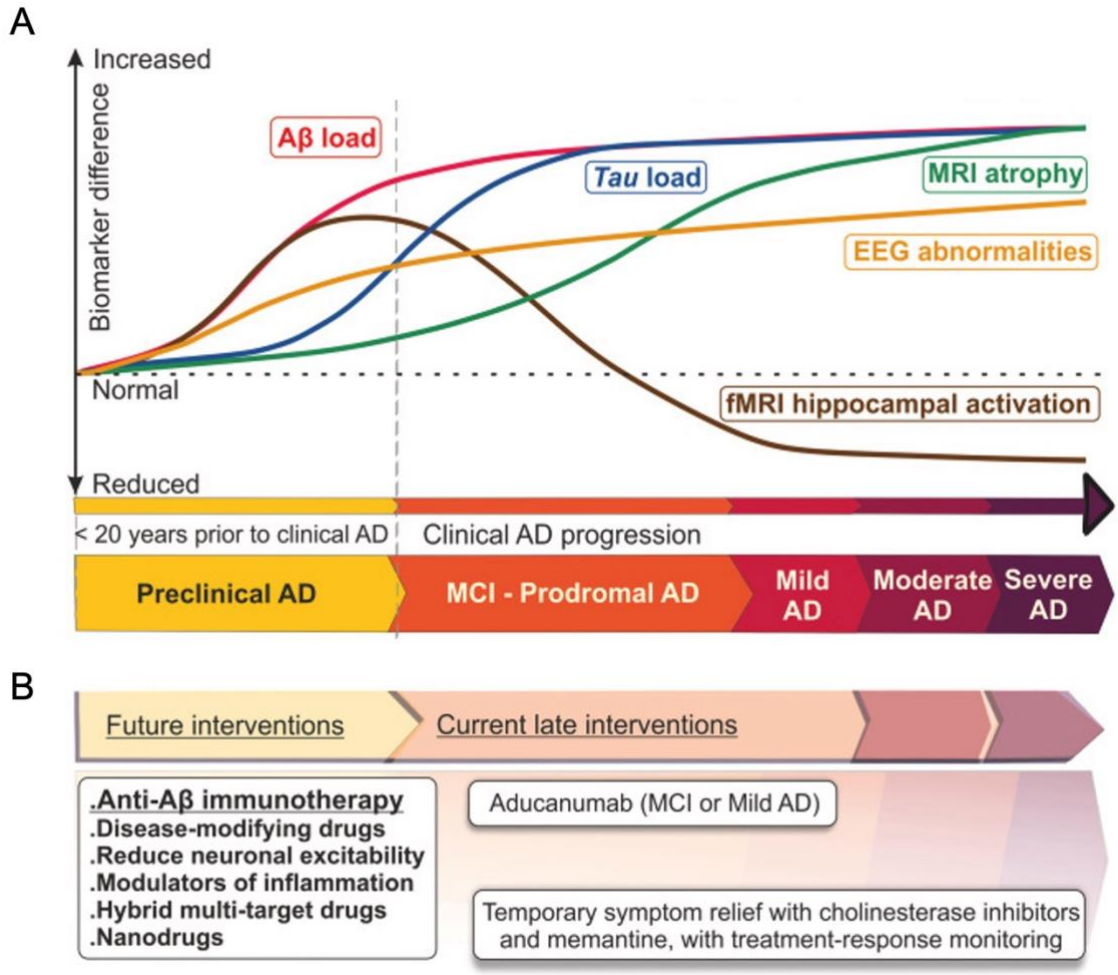

Figure 1.12. Therapies and the stage of disease they target. (A) Pathological changes with AD progression. (B) Future and current interventions at each stage of disease. Adapted from Jeremic *et al.,* 2021.

1.2.1 Traditional treatments

1.2.1.1 Acetylcholinesterase inhibitors

Acetylcholinesterase inhibitors work to promote acetylcholine signalling by increasing the extracellular acetylcholine levels for action on receptors (Briggs et al., 2016, Chu, 2012, Mendiola-Precoma et al., 2016). Acetylcholinesterase is an enzyme involved in the chemical breakdown of acetylcholine. Thus, by chemically binding to this enzyme, it prevents interaction with acetylcholine and its resulting degradation. This causes a build-up of acetylcholine within the extracellular fluid that can act on the receptors and promote cholinergic signalling.

The first generation of acetylcholinesterase inhibitors, which included tacrine, was stopped due to an undesirable side effect of liver toxicity (Chu, 2012). However, the second generation included donepezil, rivastigmine and galantamine which are still in use today. Several clinical studies have shown these drugs to have therapeutic benefit by delaying disease progression. For example, it was shown that they can significantly delay cognitive decline and the onset of behavioural symptoms by 6-12-months, with assessment using the Alzheimer's Disease Assessment Scale-Cognitive subscale (ADAS-Cog) score showing improvements of 3-4-points (Chu, 2012, Hampel et al., 2018). Also, findings show donepezil to increase cerebral blood flow, reduce cortical thinning, reduce hippocampal and basal forebrain atrophy, and maintain current cognition and behavioural aspects (Hampel et al., 2018). Interestingly, despite these three drugs having differing chemical structure, most studies suggest there is no substantial differences in the therapeutic benefit. However, a short-term (12-week) study shows donepezil to have slight improvements over galantamine (Chu, 2012, Hampel et al., 2018). Side effects from these therapeutics are generally mild but have been shown to be dose-related which may become an issue as patients can show treatment-resistance. For example, only 60% of AD patients show a therapeutic response to these drugs, which leaves a large percentage of patients with no therapeutic relief (Chu, 2012).

1.2.1.2 NMDA receptor antagonist

Memantine is an NMDA receptor antagonist. NMDA receptors are highly distributed in pyramidal cells within the cortex and hippocampus and are activated by glutamate to cause LTP involved in learning and memory (Chu, 2012). Throughout AD there can be excessive NMDA receptor activation where glutamate can cause excitotoxic stress. Memantine works by non-competitively binding to the active side of the NMDA receptor and blocking glutamate (Chu, 2012). By doing so, this prevents over-activation of the receptor and reduces the occurrence of glutamate-induced excitotoxicity. Interestingly, it is also thought to reduce hyper-phosphorylation of tau by down-regulating the activity of tau kinase, GSK-3β. Clinical trials show this to be an effective method of

treatment, with significant improvements in cognition and behaviour in moderate-severe patients only. While these improvements are significant, they are small which is why they are commonly combined with acetylcholinesterase inhibitors for severe patients.

1.2.2 New treatments

Over several decades the main focus for new treatments has been targeting molecular pathologies to rectify circuit dysfunctions, such as abnormal neuronal oscillations and hyperactivity **(Figure 1.13)**. However, little effort has been put into targeting the disease from the opposite approach; attempting to rectify circuit dysfunctions to reduce molecular, synaptic, and cellular pathologies and resulting cognitive decline **(Figure 1.13)**. This is because it is known that molecular pathology alters synaptic activity, but recent findings have shown that modulating synaptic activity can also alter levels of Aβ (Bero et al., 2011, Cirrito et al., 2005, Rodriguez et al., 2020, Yamamoto et al., 2015, Yuan and Grutzendler, 2016). This forms a hypothesis that targeting neuronal aberrations may help ameliorate molecular and cellular pathologies within AD.

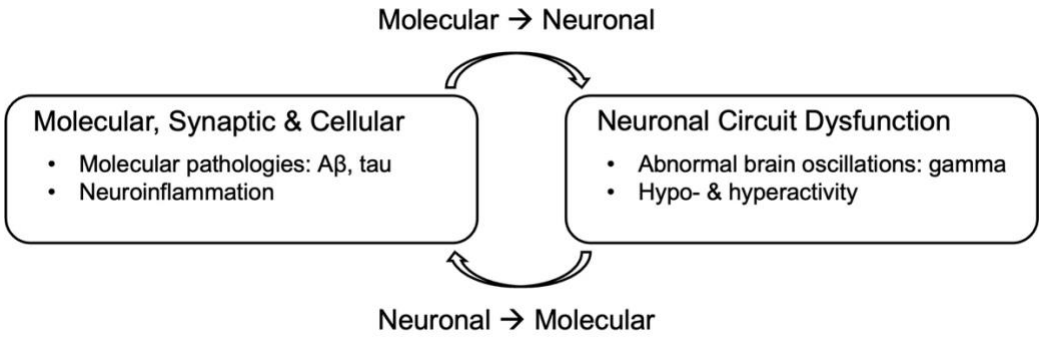

Figure 1.13. Potential directions of treatments for AD.

1.2.2.1 Molecular to Neuronal

The prominent focus of researchers has and currently remains the treatment of molecular, synaptic, and cellular abnormalities in the hope that they will resolve neuronal circuit dysfunction and cognitive decline. This has been across several scales, with the biggest drive surrounding production of anti-amyloid therapies targeting the AD hallmark, Aβ plaques **(Figure 1.14)**. Therefore, in this section, I will explain the progress in development of anti-amyloid therapies **(section 1.2.2.1.1)** and other targets **(section 1.2.2.1.2)**.

1.2.2.1.1 Anti-amyloid therapies

In 2021, excitement came to the field when the US Food and Drug Administration (FDA) approved a new drug for AD treatment on their accelerated approval pathway, under the condition that a 9-year post-approval trial is completed. This means they have concluded that it may provide some meaningful therapeutic benefit, making it the first approved therapy that treats the underlying biology of AD. Aducanumab is a monoclonal antibody that works to sequester Aβ fibrils from the brain (Budd Haeberlein et al., 2022, Schneider, 2020, Sevigny et al., 2016) **(Figure 1.14)**. It is administered intravenously (i.v.) via a 45–60-minute infusion every 4-weeks, at hospital.

However, this approval was controversial resulting in three members of the FDA advisory committee resigning (Mahase, 2021) and rejection of approval from the European Medicines Agency (EMA). This is because only one subset of participants showed a slight cognitive benefit, with severe adverse effects such as oedema and microhaemorrhages being evident in some participants (Budd Haeberlein et al., 2022). Additionally, since this study was completed in those living with early AD, there is no efficacy or safety data regarding treatment initiation at other disease stages. Therefore, due to the unclear link between the reduction in Aβ from the brain and the benefits to an AD patient's life, the conflicting data, lacking evidence surrounding drug safety and overall, inability to show any strong data for the effectiveness of the drug, the EMA have currently rejected approval of aducanumab.

Nonetheless, there are many other anti-amyloid therapies currently undergoing clinical trials with another being approved by the FDA early 2023. Lecanemab is another monoclonal antibody that works to clear Aβ from the brain and has undergone testing in a clinical study with ~1800 participants that have early-stage AD (Swanson et al., 2021, van Dyck et al., 2023). Treatment involves an i.v. infusion of either lecanemab or placebo every two weeks for the duration of the trial. In Phase III, lecanemab has shown decreased Aβ within the brain and a 0.45-point improvement in cognitive score after 18-months of treatment – close to the clinical improvement range of 0.5-2 points (van Dyck et al., 2023). However, it is important to note that some adverse effects are seen in ~20% of participants such as brain oedema or bleeding, but this was less than 3% within the treatment group compared to 40% within phase III for aducanumab (Budd Haeberlein et al., 2022, van Dyck et al., 2023).

However, there are several different therapeutic opportunities when it comes to tackling the formation and aggregation of Aβ and several therapies have been developed and are undergoing testing at different stages, with some reaching phase II and III **(Figure 1.14)**. This includes drugs which are targeting the amyloidogenic pathway directly, such as β-secretase inhibitors, α-

secretase activators, and γ-secretase inhibitors/modulators. Alternatively, therapeutics can target different stages of the aggregation pathway, working as anti-aggregation agents **(Figure 1.14)**.

Despite numerous therapeutic agents being tested, the majority have not been approved. This may be due to the loss of action of β- and γ-secretase causing loss of the physiological, neuroprotective functions of Aβ monomers. In addition, these studies are mostly completed at clinical AD stages where existing pathology may be irreversible, illustrating the desirability for a pre-clinical treatment. Lastly, there are many other neuropathic factors in AD so reducing Aβ pathology may not be sufficient, illustrating the attractiveness of combination treatment when such therapeutics are available.

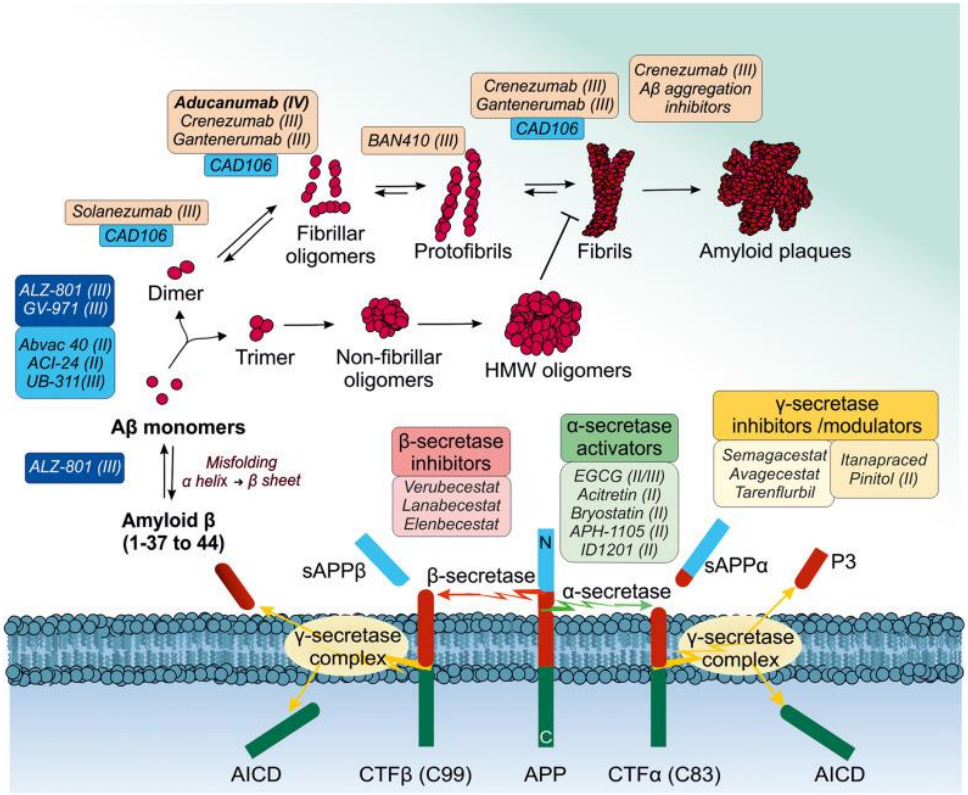

Figure 1.14. Current drugs undergoing testing in clinical trials targeted at Aβ. Adapted from Jeremic *et al.,* 2021.

1.2.2.1.2 Other targets

As expected, there has been investigation into the therapeutics that target tauopathy, including immunotherapy (Selkoe, 2021). Also, senolytic therapy has proved beneficial, with an ongoing clinical trial (Gonzales et al., 2023).

Alternatively, there are other therapeutics that have been considered and are commonly prescribed to AD patients. For example, oxidative stress can contribute to AD pathology and therefore, antioxidants – vitamin supplementation – have been heavily considered as a therapeutic strategy. Specifically, administration of selegiline and alpha-tocopherol (vitamin E) show slight therapeutic benefits in moderate-severe patients (Chu, 2012). Additionally, once AD progresses, behavioural and psychotic problems can occur. Thus, antipsychotics are often prescribed. The double-edged sword with this type of treatment is that it can often result in severe extrapyramidal impairment and sedation, where falls and a highly sedated state can be challenging for caregivers (Chu, 2012).

1.2.2.2 Neuromodulation

With the molecular to neuronal route proving challenging, with limited success over several decades, researchers began to consider the treatment of circuit dysfunctions, with the idea that this would resolve molecular, synaptic, and cellular abnormalities and cognitive decline **(Figure 1.13)**. This involved an approach called “neuromodulation” (Krames, 2018). Neuromodulation involves the manipulation of neuronal activity to promote or reinstate normal neuronal functionality and its use has been tested and implemented in several brain disorders (Krames, 2018). In terms of AD, reinstating normal neuronal health in attempt to improve cognitive function has been tested in several clinical trials (Chang et al., 2018, Polania et al., 2018). More recently, targeting gamma oscillations with neuromodulation appeared to be a desirable approach (Adaikkan et al., 2019, Bobola et al., 2020, Cimenser et al., 2021, Da et al., 2024, He et al., 2021, Iaccarino et al., 2016, Martorell et al., 2019). Therefore, this approach was investigated using invasive approaches, with promising results prompting researchers to find a suitable way to transfer this treatment to the clinic.

1.2.2.2.1 Targeting neuronal activity

Neuromodulation has been a therapeutic approach that has been approved for other neurodegenerative diseases, such as Parkinson’s disease, but not AD, despite numerous pre-clinical and clinical trials over several decades (Chang et al., 2018, Polania et al., 2018, Sanches et al., 2020). The consensus was that there is a correlation between neuronal and synaptic health and cognitive abilities, and therefore by restoring neuronal health, cognitive decline may be halted. Therefore, several invasive and non-invasive approaches have been tested for their capabilities in enhancing neuronal activity and reducing cognitive decline (Chang et al., 2018, Polania et al., 2018, Sanches et al., 2020).

1.2.2.2.1.1 Invasive

Deep brain stimulation (DBS), where electrodes are chronically implanted into the human brain for delivery of electronic pulses, was first tested for AD in 1984, but no improvements in cognition was evident (Turnbull et al., 1985). However, in 2020, a clinical trial using DBS in the fornix/hypothalamus reached phase II (Lozano et al., 2016) after reductions in cognitive decline and increased hippocampal volume were found in phase I (Hamani et al., 2008, Laxton et al., 2010, Sankar et al., 2015). Yet, in phase II, they found that patients aged <65 years cognition worsened, while those aged >65 years had slight improvements, which resulted in termination of the trial (Lozano et al., 2016). In addition, vagus nerve stimulation involved implantation of electrodes into the vagus nerve with electronical stimulation (Chang et al., 2018). This has shown some improvement in cognitive abilities as rated by the cognitive score tests, Mini-Mental State Examination (MMSE) and ADAS-Cog (Sjogren et al., 2002). However, none of these approaches have been approved and this invasive approach is not desirable as it may introduce other complications.

1.2.2.2.1.2 Non-invasive

Merton and Morton first illustrated an approach for non-invasive brain stimulation, involving no opening of the skull, where electrical currents supplied over the human scalp resulted in activation of cortical regions (Merton and Morton, 1980). While this original approach did not remain due to side effects, it resulted in the development of other transcranial brain stimulation methods like TMS, transcranial direct current stimulation (tDCS) and transcranial alternating current stimulation (tACS) (Chang et al., 2018, Polania et al., 2018, Sanches et al., 2020). TMS is an approach developed by Anthony Barker in the mid-80s that works by delivering a rapidly alternating current through a coiled wire which is placed above the human scalp (Barker et al., 1985). Altering the stimulation pattern of TMS, alters the effects on neuronal activity (Chang et al., 2018, Sanches et al., 2020). This was tested for its effects on cognition by many groups (Sanches et al., 2020), with Zhao and colleagues showing that 30 sessions of 20-Hz for 6-weeks provided an improvement in cognitive scores (Zhao et al., 2017). Alternatively, tDCS works by delivering current through electrodes which are placed on the scalp surface, with the electrical current passing through and penetrating the skull (Chang et al., 2018, Nitsche and Paulus, 2000, Nitsche et al., 2005, Radman et al., 2009, Rahman et al., 2013, Sanches et al., 2020). This can modulate the neuronal activity by altering the membrane polarisation and potentials through anodal and cathodal electrodes. This anodal electrode shifts the resting potential towards its firing potential, while cathodal stimulation hyperpolarises surrounding neurons (Chang et al., 2018, Nitsche and Paulus, 2000, Nitsche et al., 2005, Radman et al., 2009, Rahman et al., 2013, Sanches et al., 2020). This approach has shown an improvement in cognitive tests after treatment for 10 days in AD patients (Khedr et al., 2014).

Also, tACS works by delivering an oscillating current at a certain frequency, working to entrain and synchronise brain networks (Kanai et al., 2008, Marshall et al., 2006, Reinhart and Nguyen, 2019, Sanches et al., 2020). While studies completed on healthy subjects show capabilities of improving specific cognitive functions, studies in AD patients are limited (Antonenko et al., 2016, Chang et al., 2018). Again, as with invasive approaches, no non-invasive approaches have been approved for use for treatment of AD despite some studies showing promising effects on cognition.

Overall, it remains largely unclear how such approaches can exhibit their effects on cognition, but it is suggested that this prolonged and enhanced neuronal activity will promote synaptic plasticity through LTP and long-term depression (Polania et al., 2018). However, by looking at all studies, there is variabilities across findings, which may partly be due to trials using a diverse range of stimulation parameters, treatment groups, small sample sizes and differing reporting methods which can increase the variability and hinder the accurate estimation of the treatment efficacy (Button et al., 2013, Open Science Collaboration, 2015, Polania et al., 2018). Therefore, to overcome such limitations, a specific set of guidelines for testing must be implemented and followed (Polania et al., 2018), with perhaps a specific neuronal target, such as gamma oscillations (Buzsaki and Draguhn, 2004, Buzsaki and Wang, 2012, Byron et al., 2021).

1.2.2.2.2 Targeting gamma oscillations

As described above, alterations in gamma oscillations occurs throughout AD. Thereby, researchers considered the possibility of using neuromodulation to restore gamma oscillatory function, with potential therapeutic benefits for AD pathology (Adaikkan et al., 2019, Iaccarino et al., 2016, Martorell et al., 2019, Park et al., 2021, Yao et al., 2020). Accordingly, invasive, and non-invasive approaches for enhancing gamma oscillations and the subsequent effects on AD pathology were tested **(Table 1.2)**.

Table 1.2. Modulation of AD phenotypes from invasive and non-invasive neuromodulation. Adapted from Byron *et al.,* 2021.

	Induction Method	Protocol	Duration	Model	Sex	Age (months)	Modulated AD Phenotype	Reference
Invasive	Optogenetic	1 ms pulses, 40 Hz, CA1	1 h	5xFAD::PV-Cre, AAV5-EF1α-DIO-ChR2-eYFP	M	3	Reduced Aβ; Neuroinflammation	Iaccarino et al., 2016
		12 ms pulses, 40 Hz, Medial Septum	10 min	PVJ20, AAVdj-EF1α-DIO-ChETA-eYFP	M/F	NA	Improved spatial memory	Etter et al., 2019
		40 Hz, Basal Forebrain	1 h/d for 3 days	5xFAD::PV-Cre::Ai32	M/F	4-6	Increased Aβ	Wilson et al., 2020
Non-Invasive	Visual	12.5 ms on, 12.5 ms off, 40 Hz flicker, Visual Cortex	1 h/day for 7 days	5xFAD	M	6	Reduced Aβ	Iaccarino et al., 2016
				APP/PS1	M/F	5	Reduced Aβ	
				TauP301S	M	4	Reduced tau phosphorylation	
		40 Hz flicker, Visual Cortex	1 h/day for 30 days	APP/PS1	F	8	Reduced Aβ; Reduced tau phosphorylation; Increased sleep regulation	Yao et al., 2020
		12.5 ms on, 12.5 ms off, 40 Hz, Visual Cortex	1 h/day for 22 days	TauP301S	M	7.5-8	Reduced neuronal damage; Reduced neuroinflammation; Reduced tau phosphorylation; Improved spatial memory	Adaikkan et al., 2019
			1 h/day for 6 weeks	CK-p25	M/F	6-9	Reduced neuronal damage; Reduced neuroinflammation; Improved spatial memory	
		12.5 ms on, 12.5 ms off, 10 s on, 10 s off, 40 Hz flicker, Visual Cortex	1 h/day for 7 days	5xFAD	M/F	7	No change in Aβ or neuroinflammation	Soula et al., 2023
	Auditory	1 ms 10 kHz tones, 40 Hz, 60 dB, Auditory Cortex, CA1, Medial Prefrontal Cortex	1 h/day for 7 days	5xFAD	NA	6	Reduced Aβ; Neuroinflammation; Improved memory	Martorell et al., 2019
				APP/PS1		6-9	Reduced Aβ; Neuroinflammation	
				TauP301S		2	Reduced tau phosphorylation	
	Combined Auditory and Visual	10 s on (rotation of auditory or visual stimulation), 10 s off, Auditory Cortex, CA1, Medial Prefrontal Cortex	1 h/day for 7 days	5xFAD		6	Reduced Aβ; Neuroinflammation	
	Visual and Exercise	40 Hz light flicker and 30-50 min exercise	Daily, 6 days a week for 12 weeks	3xTg	M	12-15	Reduced Aβ; Reduced tau phosphorylation; Reduced neuronal damage; Improved spatial memory	Park et al., 2020
	Transcranial Focused Ultrasound	400 μs pulses, 5 s on 5 s off, 40 Hz, Hippocampus	1 h/day for 5 days	5xFAD	M	6	Increased microglia/Aβ Co-localisation	Bobola et al., 2020

1.2.2.2.2.1 Invasive

Interestingly, within a landmark study, Iaccarino and colleagues illustrated that invasively stimulating fast-spiking PV-interneurons at 40-Hz in the CA1, using optogenetics, resulted in electrophysiological and molecular alterations **(Table 1.2)** (Iaccarino et al., 2016). Increases in LFP gamma power at 40-Hz was evident, with reductions in Aβ (by ~50%) and increased microglial activation in the hippocampus (Iaccarino et al., 2016). The proposed mechanism of action was that the enhanced microglial phagocytic phenotype would increase clearance of Aβ from the brain (Iaccarino et al., 2016). Later, another group found that optogenetic activation of the medial septum

at 40-Hz improved spatial memory **(Table 1.2)** (Etter et al., 2019). However, Wilson and colleagues optogenetically activated PV+ neurons within the basal forebrain in the attempt to entrain gamma oscillations indirectly through projection of basal forebrain PV neurons to cortical GABAergic neurons **(Table 1.2)** (Wilson et al., 2020). However, this resulted in an increased Aβ plaque pathology across brain regions, which suggests the effect on molecular and cellular pathology is specific to the gamma oscillation induction mechanism (Wilson et al., 2020). As optogenetic stimulation is currently not transferable to human studies, non-invasive approaches to stimulate neurons at 40-Hz were investigated **(Table 1.2)** (Adaikkan et al., 2019, Iaccarino et al., 2016, Martorell et al., 2019, Soula et al., 2023).

1.2.2.2.2.2 Non-invasive

To modify gamma oscillations, several non-invasive approaches were suggested and studied such as tACS, sensory stimulus, temporal interference, and ultrasound stimulation (Adaikkan and Tsai, 2020). For example, previous human studies have shown success in modulating gamma activity using tACS (Benussi et al., 2021, He et al., 2021, Sprugnoli et al., 2021). Also, a study by Bobola and colleagues illustrate that transcranial focused ultrasound at 40-Hz, targeting the hippocampus, for 1-h per day for 5-days, caused an increase in microglia and co-localisation of microglia and Aβ, suggesting an enhanced protective microglial state **(Table 1.2)** (Bobola et al., 2020). However, sensory stimulation has recently been illustrated to have beneficial effects for treating AD (Adaikkan et al., 2019, Iaccarino et al., 2016, Martorell et al., 2019, Park et al., 2021, Soula et al., 2023, Yao et al., 2020).

*1.2.2.2.2.2.1 **G**amma **EN**trainment **U**sing **S**ensory stimulus (GENUS)*

Several decades ago, an approach for non-invasive sensory stimulation using a light flicker was implemented at 40-Hz in cats, where they illustrated that neurons were entrained in the visual cortex (Rager and Singer, 1998), which was then replicated in awake human subjects (Herrmann, 2001, Jones et al., 2019, Pastor et al., 2003). After studies exemplified the benefits of restoring gamma oscillatory activity in AD mouse models through improvements in both spatial memory and memory retrieval, this justified targeting gamma oscillations for identifying a potential AD treatment (Park et al., 2024, Park et al., 2020, Verret et al., 2012). This led to further studies using visual and auditory stimulation in humans and mice where they see evoked gamma oscillations not only in sensory cortices, but spread across forebrain regions or CA1 and prefrontal cortex (PFC) (Lustenberger et al., 2018, Martorell et al., 2019, Pastor et al., 2002). Since then, animal studies have shown success of using non-invasive sensory stimulus to entrain gamma oscillations and reduce AD pathology, in a method they call GENUS (Adaikkan et al., 2019, Iaccarino et al., 2016,

Martorell et al., 2019, Park et al., 2021, Soula et al., 2023, Yao et al., 2020) **(Table 1.2)**, with several human studies now being completed.

1.2.2.2.2.2.1.1 *In vivo* studies

Excitingly, using GENUS, provisional data in rodents shows a reduced Aβ load, tau phosphorylation, upregulation of cytoprotective proteins, reduced DNA damage, reduced neuronal and synaptic loss and improved cognitive function across various AD mouse models (5xFAD, APP/PS1, P301S, CK-p25) (Adaikkan et al., 2019, Iaccarino et al., 2016, Martorell et al., 2019, Park et al., 2021, Soula et al., 2023, Yao et al., 2020) **(Table 1.2)**.

This began when a pioneering study completed by Iaccarino and colleagues illustrated that non-invasive visual light flicker stimulation could reduce Aβ levels within the visual cortex and hippocampus by 50% and resulted in an enhanced phagocytic microglia phenotype in 5xFAD mice, with a reduction of phosphorylated tau in TauP301S mice (Iaccarino et al., 2016). Interestingly, with acute stimulation (1-h), the reduced soluble Aβ levels began to recover within 12-24-hours (Iaccarino et al., 2016). Consequently, studies implemented a chronic stimulation protocol for 1-h daily for 7 days, where the protective effects reducing Aβ production was enhanced, reducing plaque load and area in the visual cortex but not somatosensory cortex or hippocampal regions **(Table 1.2)** (Iaccarino et al., 2016). Beyond this, Adaikkan and colleagues adopted this approach and reported an improved cognition in AD mouse models **(Table 1.2)** (Adaikkan et al., 2019). Overall, these effects were specific to 40-Hz, but it remained to be determined if alterations in pathology can be seen within the hippocampus (Adaikkan et al., 2019, Iaccarino et al., 2016).

While visual stimulation resulted in changes within the visual cortex, an approach that could be spread across several sensory areas and potentially having an effect beyond these regions was desirable. Therefore, Tsai and colleagues investigated the effect of auditory stimulus alone and in combination with visual stimulation (audio-visual) **(Table 1.2)** (Martorell et al., 2019). For auditory stimulation alone, they show entrainment of gamma in the auditory cortex and hippocampus, a reduced Aβ load in the auditory cortex and hippocampus, improvement in behavioural tasks testing contextual and spatial memory, an increase in the vascular association with Aβ, vascular dilation that reduces tau phosphorylation and seeding and upregulation of the microglial and astrocytic response (Martorell et al., 2019). Then, for the first time, they illustrated that audio-visual stimulation at 40-Hz could entrain the firing rate in the CA1 and medial PFC, demonstrating the spread beyond sensory cortices (Martorell et al., 2019). Additionally, audio-visual stimulus resulted in the generation of an activated clustering phenotype of microglia across the auditory cortex, hippocampus, and prefrontal cortex (Martorell et al., 2019). This was able to reduce the Aβ load within the medial PFC, while auditory or visual stimulation alone could not.

Also, other groups have illustrated the beneficial effects of GENUS on the circadian circuit and learning and memory (Yao et al., 2020). Furthermore, Tsai and collaborators have now also illustrated that sensory tactile stimulation, through vibrations of the cage, can increase neuronal activity and reduce tauopathy and neuronal loss in P301S and CK-p25 mice (Suk et al., 2023).

However, more recently, a study has reported that both acute and chronic visual stimulation does not cause the same reduction in Aβ pathology or enhanced phagocytic microglial phenotype across ages and genotypes of animal models **(Table 1.2)** (Soula et al., 2023). This may arise due to the heterogeneity of Aβ pathology across mice which would make histology or ELISA an unreliable measure of the end-point effects of GENUS (Soula et al., 2023). Also, differences in sample preparation from original studies may result in some variability (Iaccarino et al., 2016, Martorell et al., 2019, Soula et al., 2023). Overall, this emphasises the need for GENUS to undergo further testing to determine the real-time effects on AD pathology. Despite this, several human studies were initiated.

1.2.2.2.2.2.1.2 Human studies

The first trial was completed by Ismail and colleagues in 2018, where 10-days of 40-Hz light for 2-h per day was completed in 6 patients (either AD or MCI) but reported no significant decrease of Aβ across tested brain regions (Ismail et al., 2018). Consequently, for future studies the duration of treatment was increased. Following studies were completed by Tsai and colleagues using combined audio-visual stimulation for 1-h/day at 40-Hz for either 4 or 8-weeks on 10 patients that had MCI (He et al., 2021). They found that neuronal activity was entrained at 40-Hz during stimulation sessions with improved functional connectivity in the default mode network (DMN) after 8-weeks but no significant changes in Aβ pathology, tauopathy or immune profiles (He et al., 2021). Next, an investigation of the effects of audio-visual stimulation in patients with mild to moderate AD, using 1-h stimulation per day for 6-months with eyes closed was completed (Cimenser et al., 2021). This illustrated an improved circadian rhythmicity and cognition appeared to remain stable throughout the trial, while control groups seen a decline in cognitive scores (Cimenser et al., 2021). Another study show that 3-months audio-visual stimulation entrained gamma oscillations across multiple brain regions, including cortical and deeper regions such as the hippocampus and amygdala, resulting in a decreased ventricular enlargement, improved circadian rhythmicity, improved functional connectivity of the DMN, reduced hippocampal atrophy and improvements in face-name association delayed recall tests (Chan et al., 2022, Da et al., 2024). While no significant changes were noted in the cognitive score tests, improvements in the behavioural tests are known to be a sensitive marker for amyloid-related memory impairments (Chan et al., 2022, Da et al.,

2024). Also, there are many other preliminary studies using GENUS being completed showing promising findings (Boasso, 2021, Hempel, 2021, McNett et al., 2023, Suk, 2020, Williams, 2021).

Overall, some studies do not find any significant differences in cognitive score after months of treatment (Chan et al., 2021a, He et al., 2021), whereas others show a maintenance or slight improvement (Cimenser et al., 2021). Also, no studies have reported alterations in molecular and cellular pathologies (Chan et al., 2022, Cimenser et al., 2021, Da et al., 2024, He et al., 2021). However, a large clinical trial testing sensory stimulation therapy for 1-h audio-visual treatment per day for up to 1-year, in several hundred mild-to-moderate AD patients is now underway (Cognito Therapeutics Inc, 2023). Another positive note is that studies have shown a strong adherence to treatment with rare and mild adverse side effects after completion of 1-hour of daily treatment of sensory stimulus in mild AD patients for several months (Chan et al., 2021a, Cimenser et al., 2021, He et al., 2021). Some side effects noted were worsening of hearing loss, mild dizziness, and headaches, but it is unconfirmed if this is due the light flicker.

1.2.2.2.2.2.1.3 Mechanism of action

Since the landmark study, work has been completed to determine the mechanism of action of GENUS (Garza et al., 2020, Prichard et al., 2023) **(Figure 1.15)**. As evidenced by the upregulated morphological, gene and protein expression of microglia following GENUS, this implies an important role for glial cells (Garza et al., 2020, Iaccarino et al., 2016, Martorell et al., 2019). As glial cells may be involved in the generation of gamma oscillations, researchers have generated possible ways GENUS can recruit glial cells to entrain gamma oscillations (Adaikkan and Tsai, 2020, Guan et al., 2022). First, glial cells could use their ion buffering functions to regulate the ionic flow across cortical layers (Adaikkan et al., 2019, Adaikkan and Tsai, 2020, Martorell et al., 2019), working to entrain gamma, or are involved in a secondary-mediated response through the action on noradrenaline pathways (Adaikkan and Tsai, 2020, Liu et al., 2019). Secondly, due to the role of GABAergic receptor signalling in gamma oscillation generation, it was suggested that GABAergic neurons were involved in this effect, where administration of a GABA antagonist in fact attenuated the neuronal and microglial effects (Iaccarino et al., 2016).

However, the main consensus is that GENUS promotes an enhanced uptake of Aβ and reduced tau phosphorylation through the upregulated phagocytic microglia phenotype (Adaikkan et al., 2019, Iaccarino et al., 2016, Martorell et al., 2019) **(Figure 1.15)**. Studies revealed that 40-Hz GENUS treatment can introduce a neuroinflammatory profile by increasing expression of cytokines through the NF-kB and MAPK pathways (Garza et al., 2020). For example, this study illustrates an increased phosphorylation of cascade proteins after several minutes of 40-Hz flicker, resulting in stimulation of the NF-κB pathway in the mouse visual cortex, enhanced MAPK pathway signalling

after 15-minutes and a resulting increased expression of cytokines that are involved in microglial recruitment, neurotrophic properties, and synaptic plasticity (Garza et al., 2020). This suggests that microglia are activated, cluster around the plaques and promote phagocytosis and clearance of them from the brain (Garza et al., 2020, Martorell et al., 2019). In addition, the vascular-dilation response illustrates that there will be a promotion of clearance of Aβ through amyloid transvascular transport (Adaikkan and Tsai, 2020, Martorell et al., 2019). This had been shown in human studies where gamma stimulation resulted in vascular dilation and cerebral blood perfusion (Chan et al., 2021b, Sprugnoli et al., 2021) **(Figure 1.15)**. Consequently, reduction of Aβ plaques and neurofibrillary tangles would contribute to a better neuronal health in terms of synaptic function, neuronal firing, anatomical structure, and vascular health (Adaikkan and Tsai, 2020, Guan et al., 2022, Manippa et al., 2022). Restoring such mechanisms can then work to improve cognitive function **(Figure 1.15)**.

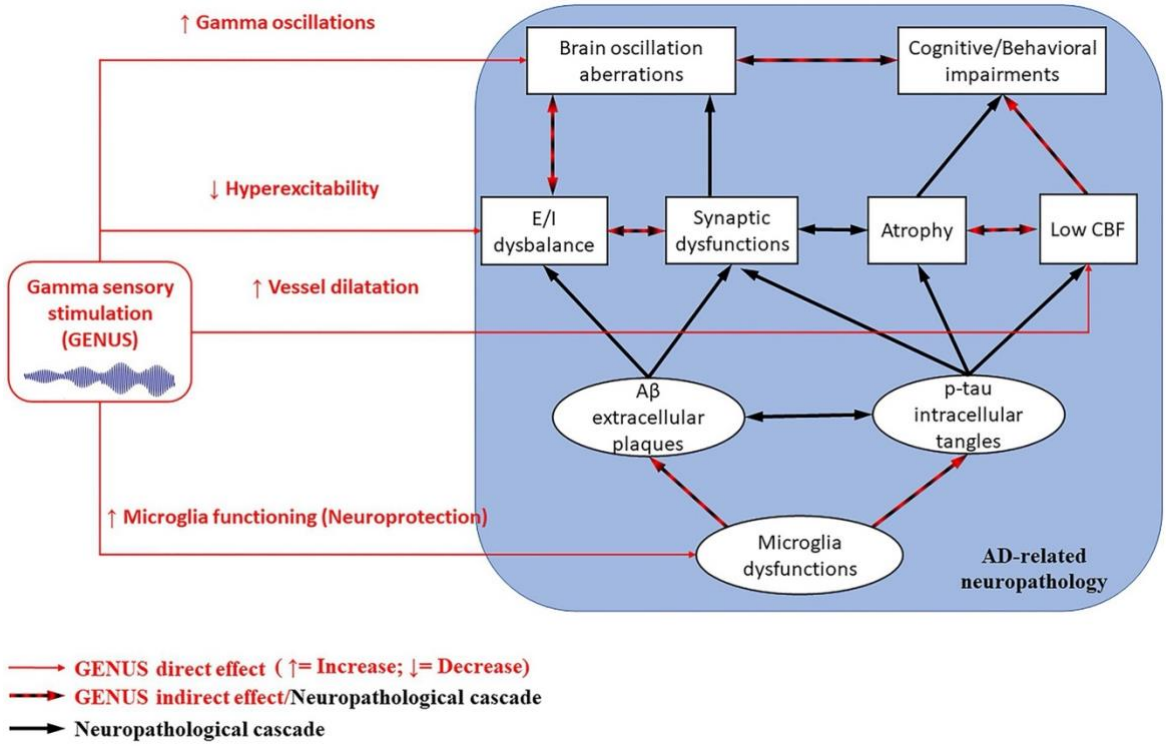

Figure 1.15. Potential mechanism of action of GENUS. Red lines show a direct effect. Red dashed and black line show an indirect effect with neuropathological cascade. Black line show effect of a neuropathological cascade. Adapted from Manippa *et al.,* 2022.

Overall, GENUS has been shown to have some beneficial effects at modulating AD pathology across several cells and brain regions, but further investigation must be completed to fully understand and clarify the mechanisms of action.

1.2.2.2.2.2.1.4 Pros and cons

Due to such promising findings, neuromodulation of gamma oscillations through this non-invasive sensory stimulation has gained a lot of attention. Benefits of this approach include its simple, low cost and easy implementation (Attokaren et al., 2023). As AD is a financial burden for both patients and countries, this would be an attractive approach. In fact, some of the pioneering authors have worked to establish a flexible, user-friendly device for GENUS treatment which is undergoing clinical testing (Abbott et al., 2006, Attokaren et al., 2023, Chan et al., 2021a, Cimenser et al., 2021, Da et al., 2024, He et al., 2021). Additionally, tissue damage seen with other neuromodulation approaches will not occur. Limitations with this approach are the lack of cell-type specificity seen with optogenetic stimulation. Also, the effects across disease stage, sex-differences and if beneficial effects are evolutionally conserved remain unclear. In addition, brain-wide effects, the complete mechanism of action, side effects, and why conflicting findings may occur is not fully elucidated. Also, it remains unclear if AD patients do exhibit a decline in gamma power throughout disease progression. Lastly, the mechanisms of the stimulation and the effect of enhanced microglial activation has not been studied, specifically over long-term periods (McDermott et al., 2018).

It is due to these conflicting results and variation in trial parameters that a greater pool of knowledge surrounding optimal GENUS parameters is required. For this, further animal studies must be completed to reach a confident conclusion on how GENUS can affect AD pathology (Carstensen, 2023). However, a main challenge in collecting this information is that real-time assessment of AD pathology in deep brain regions in a laboratory setting is limited. This means a full understanding of the potential beneficial or detrimental effects of such interventions remain unknown. However, if implementable, manipulating such neuronal oscillations appears to be a promising therapeutic strategy in the treatment of neurodegenerative disease like AD.

1.3 Assessment of plaque pathology

Appropriate methods to monitor plaque pathology in animal models are vital for monitoring success of treatments and to establish new interventions. Over the years there has been a focus on improving plaque detection methods for rodent use. These include but are not limited to, structural and functional imaging (Chen et al., 2018, Dong et al., 2010, Yang, 2021, Klunk et al., 2004, Silverman et al., 2001, Small et al., 2008, Sundaram et al., 2014, Zhang et al., 2004), post-mortem histological assessment and probes which can bind to and label Aβ, *in vivo* (Chen et al., 2018, Dong et al., 2010, Yang, 2021, Klunk et al., 2002, Klunk et al., 2004, Skovronsky et al., 2000, Sundaram et al., 2014). Most have been tested in a laboratory setting using AD mouse models, and here we will begin by discussing the pros and cons of these techniques **(section 1.3.2)**,

followed by an explanation of our proposed approach that we believe will allow real-time plaque assessment, *in vivo* **(section 1.3.2.5)**. However, another major factor for assessing the state of plaque pathology and the changes throughout the progression is the choice of AD mouse model. Therefore, we will begin by explaining the possible options, while explaining pros and cons with each model **(section 1.3.1)**.

1.3.1 AD mouse models

While the choice of an animal model can be conflicting, mouse models are powerful for research to understand pathogenic mechanisms of diseases and identify and test therapeutic options. For this, it is important to choose an animal model that is suitable for the type of experiment being completed. Over the years, several types of AD animal model have been used, including rodents (Hock and Lamb, 2001, McKean et al., 2021, Sanchez-Varo et al., 2022, Sasaguri et al., 2017, Spires and Hyman, 2005, Watamura et al., 2022a, Yokoyama et al., 2022), non-human primates (Bons et al., 1994, Braidy et al., 2015, Chambers et al., 2010, Giannakopoulos et al., 1997, Heuer et al., 2012, Perez et al., 2013, Perez et al., 2016, Picq et al., 2012, Rosen et al., 2008, Walker et al., 1987, Walker et al., 1990), dogs (Schmidt et al., 2015, Schutt et al., 2016, Smolek et al., 2016), drosophila (Fernandez-Funez et al., 2015), zebrafish (Paquet et al., 2009) and C. Elegans (Alexander et al., 2014). However, the most frequently used is mouse models as mice have a short- lifespan, rapid reproduction, and are easily maintained within a lab environment. As wildtype mice don't develop AD pathology with age, genetic engineering has generated mouse models that harbour common AD genetic mutations, promoting the generation of AD pathology (Hock and Lamb, 2001, McKean et al., 2021, Sanchez-Varo et al., 2022, Sasaguri et al., 2017, Spires and Hyman, 2005, Watamura et al., 2022a, Yokoyama et al., 2022).

However, by considering the clinical manifestations of human patients described in **section 1.1.1.3**, it is important to understand the translational relevance of the phenotype mouse models exhibit. Particularly, as discussed below, mouse models of AD often illustrate a build-up of amyloid plaque pathology in early stages of their life, reflecting the preclinical AD stages within AD patients. Commonly, as mice age and the pathological hallmarks have progressed, cognitive impairments generally become pronounced, often shown through deficits in memory tasks such as spatial learning and recognition memory. However, these findings are not always consistent, with some studies showing a decline in memory deficits before pathological hallmarks, or not at all. For example, mouse models can show cognitive deficits before or at the same time as amyloid deposition, which illustrates one of the limitations of genetically engineering disease.

Thus, the main focus in the generation of AD mouse models became ensuring formation of molecular pathology, such as the deposition of Aβ. Therefore, advances in genetic manipulation

techniques aided the development of AD models which include APP-based models **(Table 1.3)**, seeding models and knock-out/in lines. However, there has been a focus on generation of mouse models harbouring over-expression of tau such as 3xTgAD (Oddo et al., 2003), Tau P301S (Yoshiyama et al., 2007) and rTg4510 mice (Santacruz et al., 2005). Additionally, some researchers have been driving the generation of late-onset AD mouse models for better representation of the disease progression (Oblak et al., 2020). Accordingly, mice used can either be heterozygous or homozygous, meaning that they will express either one or two of the mutated alleles, respectively, with homozygous mouse models thought to exert a greater genetic dosage of the mutations causing an enhanced phenotype. Therefore, this is another vital parameter when choosing the AD mouse model used.

1.3.1.1 APP-based models

Table 1.3. Summary of some APP-based AD mouse models and their phenotype. Adapted from Yokoyama *et al.,* 2022.

Model mouse	Gene (Mutation)	Promoter	Aβ pathology	Tau pathology	Neuronal loss	Cognitive impairment
PDAPP	*APP* (V717F)	PDGF-β promoter	+ (6 mo~)	-	-	+ (3 mo~)
Tg2576	*APP* (KM670/671NL)	hamster prion promoter	+ (11 mo~)	-	-	+ (6 mo~)
APP23	*APP* (KM670/671NL)	Thy1 promoter	+ (6 mo~)	-	+ (12 mo~)	+ (3 mo~)
J20	*APP* (KM670/671NL, V717F)	PDGF-β promoter	+ (8 mo~)	-	+ (3 mo~)	+ (4 mo~)
TgCRND8	*APP* (KM670/671NL, V717F)	hamster prion promoter	+ (3 mo~)	-	+ (6 mo~)	+ (3 mo~)
PS2APP	*APP* (KM670/671NL) *PSEN2* (N141I)	APP: Thy1.2 promoter *PSEN2*: mouse prion promoter	+ (9 mo~)	-	unknown	+ (8 mo~)
APPswe/PSEN1dE9 (APP/PS1)	*APP* (KM670/671NL) *PSEN1* (delta9)	mouse prion promoter	+ (6 mo~)	-	+ (8 mo~)	+ (12 mo~)
Tg-ArcSwe	*APP* (KM670/671NL, E693G)	Thy1 promoter	+ (5 mo~)	-	-	+ (4 mo~)
5xFAD	*APP* (KM670/671NL, I716V, V717I) *PSEN1* (M146L, L286V)	Thy1 promoter	+ (2 mo~)	-	+ (6 mo~)	+ (4 mo~)
A7	*APP* (KM670/671NL, T714I)	Thy1.2 promoter	+ (9 mo~)	unknown	unknown	unknown
NL-G-F	humanized Aβ sequence (KM670/671NL, I716F, E693G)	Endogenous promoter (knock-in model)	+ (2 mo~)	-	-	+ (6 mo~)

The first generation of amyloidogenic mice were established in the 1990s after advances in genetical engineering and identification of prominent FAD mutations (Games et al., 1995). These were transgenic mice, formed through transgenesis, harbouring FAD mutations, driven by various promoters: platelet-derived growth factor-β (PDGF-β), PrP and Thy-1. These mutations worked to result in the overexpression of APP, causing an increase in Aβ production, aggregation and resulting cognitive decline **(Table 1.3)** (Chishti et al., 2001, Games et al., 1995, Hsiao et al., 1996, Mucke et al., 2000, Sturchler-Pierrat et al., 1997). However, they failed to generate tauopathy and

neurodegeneration, so researchers investigated the potential of monogenic models containing mutations in PSEN1/2 as an alternative (De Strooper et al., 1998). However, these models failed to result in Aβ deposition, clarifying that APP is essential for Aβ deposition in mice (De Strooper et al., 1998). Finally, this led to the generation of double transgenic mice, that co-express mutations in both APP and PSEN1/2, to result in a more comprehensive AD phenotype. Studies have shown that co-expression of FAD mutations can have additive effects when generating the AD phenotype, causing enhanced Aβ42 formation (Borchelt et al., 1997, Borchelt et al., 1996, Casas et al., 2004, Citron et al., 1997, Holcomb et al., 1998, Oakley et al., 2006, Radde et al., 2006, Schmitz et al., 2004). This resulted in the generation of the most commonly used mouse models: APP/PS1 (Radde et al., 2006) and 5xFAD (Oakley et al., 2006, Oblak et al., 2021). These have aggressive pathogenesis and presence of neurodegeneration compared to single APP-based models, but still don't contain tauopathy, leaving a major pathway of AD pathology unaccounted for **(Table 1.3)**. There have been several attempts to replicate a tauopathy AD phenotype (Bolmont et al., 2007, Lewis et al., 2001), with Oddo and colleagues generating a triple transgenic mouse model, 3xTg-AD, which overexpress APP (Swedish mutation) and TauP301I transgenes on a PSEN1 (M146V) knock-in background, resulting in formation of Aβ deposits, tauopathy, gliosis, synaptic damage, and memory deficits (Oddo et al., 2003). However, a major limitation of this is that the mutation used to affect the tau protein is based on the MAPT gene, where currently no known mutations are known to cause AD.

APP-based models are the most widely used approach, but they do have limitations. For example, the level of APP expression is not authentic, and while it leads to the generation of the AD phenotype, it will result in off target effects due to the enhanced production of APP and APP fragments (Chang and Suh, 2005, Chiba et al., 2014, Gunawardena and Goldstein, 2001, Nhan et al., 2015). For example, several APP-related fragments have roles in several neuronal functions like spatial memory, calcium homeostasis and transcription (Chang and Suh, 2005, Kerridge et al., 2015, Nicolas and Hassan, 2014) and therefore, overexpression can potentially result in memory impairments that is not easily distinguished from the AD phenotype, which may explain the cognitive decline seen before Aβ pathology in some mouse models (Hsiao et al., 1996, Mucke et al., 2000). Additionally, while the pathogenesis for cases of FAD and SAD are similar, use of these models which are based on FAD mutations leads to a bias for FAD pathogenesis. However, there are now research groups working on identifying appropriate risk genes from GWAS studies to generate a new group of AD mouse models that have a phenotype that better represents SAD.

1.3.1.1.1 Examples

1.3.1.1.1.1 PDAPP Mice

The first generation of AD mouse models with an accumulation of Aβ pathology throughout the brain was PDAPP mice, back in 1995 **(Table 1.3)** (Games et al., 1995). These were generated by genetically expressing the human APP gene that contained the Indiana mutation (V717F), driven by the PDGF-β promoter. Post-mortem studies found that Aβ deposition began from 6-months within the cerebral cortex, generating both dense and diffuse plaque pathology by 8-months in the entorhinal cortex, cingulate cortex, and hippocampus, and progressed with enhanced gliosis, with age (Games et al., 1995). In addition, at 8-months, synaptic disorders are developed, showing a reduction in synaptic and dendritic densities within the hippocampus (Games et al., 1995). These pathological processes can be linked with the preclinical stage of AD which illustrates a progressive accumulation of neuropathological proteins and their resulting neurotoxic effects. However, by 18-months, the Aβ load was greater than end-stage human AD, with no signs of tauopathy or neurodegeneration. In addition, memory tests showed that a cognitive decline was evident before the generation of plaques, at 3-months, continuing to decline with age (Dodart et al., 1999, Hartman et al., 2005). This can conflict with the temporal progression of human symptoms, where cognitive decline occurs only after a large duration of molecular pathology. While this illustrates strong molecular, inflammatory, synaptic, and cognitive pathology resonating with AD, the late generation of plaques is a challenge when completing short-term laboratory studies.

1.3.1.1.1.2 Tg2576 Mice

A widely used AD mouse model is Tg2576, which contains mutations in human APP (Swedish mutation: KM670/671NL) under the hamster prion promoter **(Table 1.3)** (Hsiao et al., 1996). Plaque pathology and gliosis occurs from 10-months and progresses with age (Frautschy et al., 1998, Hsiao et al., 1996). Memory function, such as spatial alternation and reference learning show impairments at 10-months (Hsiao et al., 1996), despite no neuronal loss being detected (Irizarry et al., 1997).

1.3.1.1.1.3 J20 Mice

Another commonly used mouse model, J20, overexpress human APP as a result of two FAD mutations expressed under the PDGF-β promoter (Swedish: KM670/671NL and Indiana: V717F) **(Table 1.3)** (Mucke et al., 2000). Post-mortem analysis shows formation of diffuse Aβ plaques from 5-6-months, with high hippocampal Aβ load from 8-10-months (Mucke et al., 2000). Accordingly, an enhanced neuroinflammatory profile with increased gliosis is seen within the hippocampus from

6-9-months, with progressive neuronal loss from 3-months (Wright et al., 2013). Again, cognitive deficits appear before these pathological features, with spatial deficits 4-months (Cheng et al., 2007, Wright et al., 2013).

1.3.1.1.1.4 APP/PS1 Mice

APP/PS1 are one of the most commonly used mouse models that is based off the co-injection of two vectors that contain the APP Swedish mutation (KM670/671NL) and the PSEN1 gene without exon 9 (dE9) **(Table 1.3)** (Radde et al., 2006). Fibrillar and neuritic plaques accumulate from 6-months and continue to spread across cortical and hippocampal regions with age (Radde et al., 2006), in parallel with gliosis (Kamphuis et al., 2012). Importantly, this animal model shows an increase in molecular pathologies associated with behavioural impairments, with declines in working and spatial memory occurring from 5-6-months and continuing with age up to 15-months (Radde et al., 2006, Serneels et al., 2009).

1.3.1.1.1.5 5xFAD Mice

Previous studies suggested that incorporating several FAD mutations that increase Aβ production would work in an additive manner when creating the AD phenotype (Borchelt et al., 1997, Borchelt et al., 1996, Casas et al., 2004, Citron et al., 1997, Holcomb et al., 1998, Radde et al., 2006, Schmitz et al., 2004). Therefore, to create an AD mouse model with an aggressive phenotype, researchers developed 5xFAD mice which are co-transgenic with a total of five FAD mutations that are expressed in APP (Swedish: K670N/M671L; Florida: I716V; London: V717I) and PSEN1 (M146L and L286V) **(Table 1.3)** (Oakley et al., 2006, Oblak et al., 2021). This was completed by site-directed mutagenesis of the FAD mutations into APP and PS1 complementary DNA, before subcloning them onto the Thy-1 promoter (Oakley et al., 2006). Once created, these transgenes were microinjected into the pronuclei of single cell embryos, where the Thy-1 promoter would drive the expression within the brain.

Studies found that 5xFAD mice have rapid formation of Aβ depositions, aggregating into fibrillar and neuritic plaques from 2-months and increasing in an age-dependent manner (Oakley et al., 2006, Oblak et al., 2021). With this, gliosis rapidly increases. For both Aβ deposits and gliosis, accumulation begins within deeper cortical layers and the subiculum (SUB) before spreading to superficial cortical layers, hippocampus, thalamic regions, brainstem, and olfactory bulb, but not cerebellum (Oakley et al., 2006, Oblak et al., 2021). Studies found that synaptic degeneration occurs from 4-months, with neuronal loss occurring across multiple brain regions from around 6-months, occurring in areas with large Aβ accumulation (Eimer and Vassar, 2013, Oakley et al.,

2006). Interestingly, at 6-months there was a reduction in the number of cholinergic neurons in the basal forebrain (Devi and Ohno, 2010), and 30% less PV+ inhibitory interneurons at 12-months (Flanigan et al., 2014). They found that this particularly large loss of pyramidal neurons in cortical layer 5, was associated with formation of intraneuronal Aβ which aggregated with a similar spatial pattern (Crowe and Ellis-Davies, 2013). Memory impairments have been shown from 6-months for spatial and associative memory (Flanigan et al., 2014, O'Leary et al., 2020, O'Leary et al., 2018, Xiao et al., 2015), with some deficits seen as early as 4-5-months (Devi and Ohno, 2010, Oakley et al., 2006). Additionally, it has been shown that 5xFAD mice show a tendency of hyperactivity which may make them an undesirable choice when analysing cognitive behaviour (Oblak et al., 2021). It is important to note that despite this aggressive phenotype, 5xFAD mice fail to exhibit signs of tauopathy (Oakley et al., 2006). However, various phospho-tau epitopes remain to be tested. In addition, studies show sex-specific differences in the pathogenesis of 5xFAD mice, with females showing a more aggressive phenotype (O'Leary et al., 2018, Oakley et al., 2006, Oblak et al., 2021). For example, while Aβ pathology in males appears to plateau around ~10-months, females continue to progress up to 14-months (Bhattacharya et al., 2014), with previous studies investigating transcriptome analysis of sex-differences in 5xFAD mouse models.

Therefore, 5xFAD mice are a desirable choice due to their rapid and aggressive phenotype, showing plaque pathology from 2-months and neurodegeneration across various cell types and brain regions (Devi and Ohno, 2010, Eimer and Vassar, 2013, Flanigan et al., 2014, Oakley et al., 2006, Oblak et al., 2021). In addition, they show neuronal loss in inhibitory interneurons and pyramidal cells which are likely to be involved in generation of gamma oscillations (Flanigan et al., 2014), perhaps contributing to another aspect of AD pathology. Plus, the 5xFAD mouse model is appropriate for the study of sex-differences (O'Leary et al., 2018, Oakley et al., 2006, Oblak et al., 2021). Therefore, this animal model can provide a greater insight into AD pathology than others, even though there are no human cases of AD that have been shown to have multiple FAD mutations.

1.3.1.2 Knock-in (KI) models

In attempt to overcome limitations of APP overexpression artifacts, a second generation of mouse models were formed (Sasaguri et al., 2017, Watamura et al., 2022a). This was an APP KI approach which worked to result in the same overproduction of Aβ, without causing the overexpression of APP. For this, single APP-KI mouse models contained humanised Aβ – created by changing three amino acids that are different between mouse and humans (G676R, F681Y, H684R) – which contained FAD mutations in APP (Swedish and Beyreuthr/Iberian) (Saito et al., 2014). This APPNL-F animal model showed increased Aβ generation, with limited changes in APP expression, while allowing formation of Aβ deposits across brain regions and gliosis from 6-months (Saito et

al., 2014). In addition, studies noted changes in synaptic health (Saito et al., 2014), with cognitive decline seen at 18-months (Masuda et al., 2016, Saito et al., 2014). To generate more aggressive forms, other mutations have been introduced (Cheng et al., 2007, Flood et al., 2002, Li et al., 2014). While this approach overcomes the drawbacks of overexpression of APP, these mouse models still do not present with tauopathy and may represent 'preclinical AD' (Sasaguri et al., 2017). Also, other researchers have worked on the generation of knock-out (KO)/KI lines as a model of late-onset AD: hAβ-KI, tau-KI and APOE4-KI (IU/JAX/UCI MODEL-AD Consortium, 2023). While these mouse models are hypothesised to better reflect the human symptoms of AD along with the delayed progression of cognitive symptoms, these approaches are not well established compared to some APP-based models.

Then, other mouse models were developed as the location of the APP Swedish mutation can affect the processing of APP which will interfere with the testing of new therapeutics that target cleavage of APP, such as β-secretase inhibitors. Therefore, these have the same phenotype as previous generations, without the overexpression of APP and the Swedish mutation. For example, Sato and colleagues generated APPNL-F/PSENP117L mice (Sato et al., 2021). Also, researchers created a line of single APP-KI mice using the Artic and Beyreuther/Iberian mutations, generating the APPG-F model which reported Aβ pathology, gliosis, and synaptic damage, with no overexpression of C-terminal fragment-β (Watamura et al., 2022b).

Overall, due to all mouse models having different mutations, promoters, and background strains, standardisation and interpretation across studies is a challenge. Therefore, in the future, it is vital for a standardised way of choosing a mouse model and analysing and comparing findings across studies to be formed.

1.3.1.3 AD mouse model for this project – 5xFAD

However, when it came to deciding an appropriate mouse model for this project, many considerations were made. As the main goal is to identify and track Aβ pathology, deciding on an animal model that has an aggressive Aβ load was essential for system establishment. Additionally, as we were not investigating the detailed pathological contributions of Aβ, we do not require the native expression pattern that would be preserved with KI models. In addition, we do not require the presence of tauopathy. Therefore, it was clear that an APP-based model would be applicable, and use of a KI/KO model would not be required. Also, we wish to identify strong Aβ plaque signals as quick as possible to help establish a robust system. This clarifies the need for APP-based models that show rapid formation of plaques. Consequently, 5xFAD mice are the best choice for this project as compared to other APP-based mouse models, this genotype exhibits a much faster and enhanced aggregation of Aβ pathology which will allow detection by an appropriate monitoring

approach (Oakley et al., 2006, Oblak et al., 2021). Lastly, we considered whether to use either heterozygous or homozygous 5xFAD mice. Despite detailed characterisation showing the aggressive phenotype of heterozygous 5xFAD mice (Oakley et al., 2006, Oblak et al., 2021), another group detail the enhanced phenotype with homozygous 5xFAD mice, specifically behavioural deficits, perhaps due to the enhanced molecular pathology (Richard et al., 2015). As we are not testing any behavioural parameters and heterozygous have an already aggressive phenotype without the risk of added physiological abnormalities that may occur in homozygous models, we opted for use of heterozygous 5xFAD mice.

1.3.2 Monitoring approaches

There are several existing methods used for monitoring plaque pathology in AD mouse models. Here, I will describe and critically analyse their use **(Table 1.4)**. Lastly, I will explain the gap for a real-time, *in vivo*, depth-resolved monitoring approach in freely behaving conditions, by introducing the novel method established throughout this project.

Table 1.4. Strengths and limitations of different approaches to monitor plaque pathology in AD mouse models.

Method	Temporal Resolution	Spatial Resolution	Penetration depth	Invasiveness	Strengths	Limitations
Histology	Low	High		Low	Easy Economical Reliable	Single read-out Labour-intenstive Sections damaged/lost Lack of 3D distribution
Microdialysis	Low (h)	Low		Medium	Repeat measure	Tissue inflammation Depletion surrounding probe Low temporal resolution
Multiphoton imaging	Medium (s)	Very high (~1 µm)	2PM: ~500 µm 3PM: ~1300 µm	High	Longitudinal measurements Minimal bleaching Good image resolution	Commonly requires head-fixation & anaesthesia Thinning of skull increases inflammation Low depth penetration
CT	Medium (s)	High (1 mm)		Low	Low cost High availability 3D analysis	Low image resolution Low temporal resolution
MRI	Medium (s)	High (3-6 mm)		Low	High resolution Moderate cost Probes are stable Longitudinal monitoring 3D analysis	Low image resolution Low temporal resolution
PET	Medium (s)	High (5 mm)		Low	Available probes Longitudinal monitoring 3D analysis	Expensive Low availability Probes unstable Varied results across models
Fibre photometry	High (ms)	Low		Medium	Simple Low cost Freely behaving measurements Scalable & reconfigurable Multi-region imaging	Tissue inflammation Low spatial resolution

1.3.2.1 Histological assessment

The most common method for plaque assessment in animal models is post-mortem histological analysis **(Table 1.4)**. This involves the removal and fixation of brain tissue before staining with a plaque antibody or stain. This can be combined with various types of microscopies (e.g., epifluorescence, confocal and light-sheet) to allow for imaging of plaque-stained brain sections. While this provides an easy, economical, and reliable read-out of plaque pathology, limitations exist. Firstly, this is a single read-out, meaning that there is no way to monitor the progression up to and after the stage of assessment. Additionally, the processing protocol is labour-intensive and time-consuming, can cause sections to become damaged or deformed, and commonly limits the ability to provide an explanation of the 3D plaque distribution. As these limitations exist, much effort has been put into improving other techniques.

1.3.2.2 Microdialysis

An *in vivo* approach that allows repeat measures of plaque pathology over several days is microdialysis **(Table 1.4)**. This is a method commonly used for sampling of neurotransmitters, neuropeptides, hormones, and more recently Aβ within the brain ISF (Cirrito et al., 2003, Yuede et al., 2016). As soluble Aβ is released by neurons into the brain ISF, the ISF concentration provides a measure of Aβ metabolism and degradation. This technique involves chronic implantation of a microdialysis probe that is composed of a tubular dialysis membrane, lacking Aβ. When perfused it allows transport of ISF Aβ across this semi-permeable membrane for sample analysis, using a range of analytical techniques (Cirrito et al., 2003). Therefore, this provides a precise measure of Aβ over several time points. However, the microdialysis probe will result in tissue injury, meaning that long-term implantations will result in neuroinflammation surrounding the probe. Due to the correlations seen with microglia and plaque pathology in AD, this may influence the plaque measurement. Additionally, due to depletion surrounding the probe after sample collection, the level of Aβ within this area is artificially changed. This results in a low temporal resolution with sample collection every 2-hours (Cirrito et al., 2003), preventing a real-time measurement.

In attempt to improve the temporal resolution, the same group developed a microimmunoelectrode coated in Aβ antibodies for rapid detection of changes in ISF Aβ (every 60-seconds over several hours) (Yuede et al., 2016). This used amperometry – an electrochemical technique that quantifies oxidation of the tyrosine residue at position 10 on human Aβ. Here, the measure of current is directly proportional to the number of tyrosine residues, and hence Aβ present. While they were able to detect oxidation of Aβ with 60-second resolution and limited damage to the brain tissue

due to the 5-μm electrode diameter, a loss in sensitivity of the microimmunoelectrode was found after 2-hours use *in vivo* (Yuede et al., 2016). Additionally, it is only able to detect human Aβ, limiting studies to mouse models that produce the human form of Aβ. Therefore, while this technique shows promise, there is still room for improvement in terms of long-term, real-time plaque measure with a strong temporal resolution.

1.3.2.3 Structural and functional imaging

1.3.2.3.1 Multiphoton imaging

Due to the nature of the brain, with several biomolecules causing light scattering in tissues which can alter the collection of signals, access to monitor plaques within the brain can be difficult. This can result in invasive protocols that involve a BBB-permeable plaque marker, cranial windows, and multiphoton microscopy **(Table 1.4)**. While this is an invasive approach, multiphoton imaging has a high resolution (~1-μm) which allows for focused images of plaque lesions (Delatour et al., 2010, Dong et al., 2010). Then, by using vascular landmarks, the same plaques can be tracked over repeat measurements. For example, several longitudinal studies can be completed over weeks and months which monitor the effects of treatments on plaque pathology (Hefendehl et al., 2011). Additionally, repeat measurements can continue without excessive photobleaching or tissue damage due to the pulsed laser excitation multiphoton microscopy uses (Dong et al., 2010). However, this invasive process usually requires animals to be head-fixed or anaesthetised which can alter the morphology of plaques (Dong et al., 2009, Eckenhoff et al., 2004, Jiang and Jiang, 2015, Liang et al., 2020, Xie et al., 2008, Xie et al., 2006, Xu et al., 2011). Also, while the cranial window allows for repeat measurements, the thinning of the skull can have effects on glial activation and neuronal death. As neuroinflammation has been shown to influence plaque pathology (Heppner et al., 2015), this may influence the plaque read-out. Another limitation could be the slow scanning acquisition that generally exists with multiphoton imaging. However, studies have worked to successfully reduce this (Botcherby et al., 2012). Lastly, multiphoton microscopy cannot penetrate deeper than cortical layers, meaning there are many vital regions involved in AD pathology not being monitored. To surpass the challenges of deeper imaging, endoscopes can be used but this can result in substantial damage that can hinder normal brain function. Alternatively, structural imaging can be implemented which can allow 3D scans of plaque pathology (Delatour et al., 2010, Silverman et al., 2001, Small et al., 2008, Zhang et al., 2004).

1.3.2.3.2 Computerized tomography (CT) and MRI scans

Structural imaging includes CT and MRI and has been used to monitor plaque pathology in clinical and laboratory settings (Delatour et al., 2010, Dudeffant et al., 2017, Small et al., 2008, Zhang et al., 2004) **(Table 1.4)**. CT can identify lesions as it has a high resolution (~1-mm) and due to its low cost and high availability, it is commonly used. Additionally, MRI has been successfully established in anaesthetised AD animal models. Identification of plaques using this method can be enhanced through peripheral administration of amyloid-binding probes. Therefore, there are several benefits of MRI: high spatial resolution, moderate cost, use of probes that can be stored long-term and avoidance of danger from radiation. Additionally, this set-up can allow repeat measures over an animal's lifetime. When comparing with histology, MRI allows 3D analysis of the brain, providing information on plaque pathology free of deformation and time-consuming factors. However, when comparing to both histology and multiphoton microscopy, image resolution is lower with the inability to obtain any cellular information due to the limited availability of imaging contrasts. This means some plaques may go undetected, making the detection sensitivity lower than other methods.

1.3.2.3.3 PET scans

An exciting moment in the field was the development of PET and AD-related tracers as this tackled both resolution and repeat measures (Delatour et al., 2010, Klunk et al., 2004, Silverman et al., 2001, Small et al., 2008, Sundaram et al., 2014) **(Table 1.4)**. Since the first discovery, many plaque tracers have been developed to monitor the concentration of these deposits *in vivo*. Additionally, tracers are now available and being tested for microglia, tau, and several neurotransmitters (dopamine, choline, and serotonin (5-HT)). The most established plaque tracer is Pittsburgh Compound-B (PiB) which was synthesised from its derivative, Thioflavin-T (Klunk et al., 2004). This involves the rodent receiving an i.v. injection of a radioactive tracer that in the brain undergoes biochemical changes. While PET scans are expected to lead clinical diagnosis in humans over the next decades, the expensive nature remains a severe limitation when it comes to setting up for use in rodents. Scanners and tracers are high in cost and PET tracers have low availability, meaning this is not an accessible way to monitor plaques in a laboratory setting. This is exaggerated by the tracer's short half-life and storage complications. Other disadvantages include the varied results seen across animal models of AD (Delatour et al., 2010). While in human studies, plaque measurements seem consistent and reliable, PiB binding to plaques has been found to be reduced in rhesus macaques, chimpanzees, and squirrel monkeys despite their high plaque load, or show no change between mouse models and controls (Delatour et al., 2010).

1.3.2.3.4 3-dimensional whole brain scans

Recently, a research group had some success in implementing an optical molecular-imaging approach that permitted 3D mapping of Aβ across the whole mouse brain, with a resolution of 150-µm (Ni et al., 2022). This involved i.v. injection of an infrared Aβ tracer, a laser with wavelength tunability, allowing excitation of the whole brain at various wavelengths, while collecting signals with a custom-made spherical matrix array transducer that had ultrasound detection. While this granted repeat measures over one month, experiments were completed in a lightly anaesthetised, head-fixed condition which can alter normal plaque activity (Dong et al., 2009, Eckenhoff et al., 2004, Jiang and Jiang, 2015, Liang et al., 2020, Xie et al., 2008, Xie et al., 2006, Xu et al., 2011).

1.3.2.4 Amyloid probes

Following on from PET and amyloid-binding tracers, many Aβ markers that can pass the BBB have been generated (Chen et al., 2018, Dong et al., 2010, Yang, 2021, Klunk et al., 2002, Klunk et al., 2004, Skovronsky et al., 2000, Sundaram et al., 2014). One group proved that both ingestion and intravascular injection of curcumin can stain plaques in the retina for retinal imaging (Koronyo-Hamaoui et al., 2011). Additionally, another group took inspiration from Methoxy-x04 (Klunk et al., 2002), discussed in **section 1.3.2.5.1**, by modifying existing Aβ-plaque markers to create a BBB permeable marker with high affinity for Aβ. In this case, they modified Thioflavin-T by the addition of benzothiazoles to create what they term benzothiazole amyloid binding agents (Klunk et al., 2004). They found that these molecules were able to bind to Aβ fibrils with nanomolar affinity to allow PET imaging. Another is a radioligand probe called [(trans,trans)-1-bromo-2,5-bis-(3-hydroxycarbonyl-4-hydroxy)styrylbenzene] (BSB) which when injected via intrahippocampal or intravascular injections in anaesthetised mice show strong affinity to Aβ peptides post-mortem (Skovronsky et al., 2000). Interestingly, another way to combat *in vivo* plaque monitoring is by using AkaLumine, a new substrate for luciferase which is sequestered by Aβ to release AkaLumine. This will create bioluminescence which can be used as an indirect measure of plaque load (Yang, 2021). This group were able to show successful detection of plaques and deep tissue penetration. This method will provide a good signal to noise ratio and may be a strong alternative to other BBB permeable dyes currently on the market. Another large focus has been the development of near-infrared probes for detection of plaques *in vivo*. For example, CRANAD-3 is a dye that has longer excitation/emission spectra, facilitating imaging in deeper cortical layers, without major influence of autofluorescence (AF), as well as providing staining of plaques (Chen et al., 2018). Previous molecules have shown strong fluorescence properties but are designed for use with macroscopic near-infrared fluorescence imaging, meaning spatial resolution is limited (Chen et al., 2018). Overall, development of a BBB permeable dyes is beneficial for repeat, *in vivo*

measurements. Using a dye that has strong affinity for Aβ and can be administered to animal models peripherally will allow for establishment of procedures that can monitor plaques in real-time.

1.3.2.5 Our hypothesised method for real-time plaque assessment

Overall, these current approaches have been well-established in monitoring plaque pathology *in vivo*. For example, post-mortem approaches like histology and ELISA can provide reliable outputs but are limited to a single measure. This illustrates the benefit of structural and functional imaging, but these have low spatial resolution. This is overcome with multi-photon microscopy, while also providing the functionality of real-time monitoring. However, this is limited to only several micrometres below the brain surface, thereby preventing monitoring across multiple brain regions. Also, due to the microscope weight, this is usually in a head-fixed condition, under light anaesthesia. Therefore, there is currently no well-established method that allows real-time plaque monitoring across multiple brain regions, in a freely behaving condition. Accordingly, when using these approaches to monitor disease progression under a novel therapeutic, vital information on potential plaque modifications go overlooked.

On that note, we suggest that combination of a BBB permeable dye, Methoxy-x04 (Klunk et al., 2002), and fibre photometry (Adelsberger et al., 2005, Simpson et al., 2023), will allow real-time plaque assessment in deep brain regions of freely behaving mice. Methoxy-x04 was produced with the aim of developing a new amyloid-binding marker that has a small molecular weight and lipophilic nature that allows it to pass the BBB and mark Aβ plaques (Klunk et al., 2002). Use of this has been confirmed both *in vitro* and *in vivo*, with histological staining and 2-photon imaging, respectively (Condello et al., 2011, Crowe and Ellis-Davies, 2013, Hefendehl et al., 2016, Hefendehl et al., 2011, Jung et al., 2015, Klunk et al., 2002, Liu et al., 2010, Meyer-Luehmann et al., 2008). Specifically, signals have been shown using 2-photon imaging after peripheral (intraperitoneal (i.p.) and i.v.) administration but has been restricted to cortical surfaces (Condello et al., 2011, Crowe and Ellis-Davies, 2013, Hefendehl et al., 2011, Klunk et al., 2002, Liu et al., 2010, Meyer-Luehmann et al., 2008). While the Methoxy-x04-stained plaques have been monitored in cortical regions, it is vital to have information on plaque pathology in deeper brain regions. To allow this, a different optical technique which can provide access to deep brain regions is required.

Consequently, we combine the use of Methoxy-x04 with fibre photometry (Adelsberger et al., 2005, Byron and Sakata, 2024, Simpson et al., 2023). Fibre photometry is an optical method which involves implanting an optic fibre into the brain of an animal model and illuminating and collecting emitted fluorescence. This technique can tackle many hurdles that occur with previously discussed

methods: real-time measurement with rapid temporal resolution, access to deeper brain regions, compatibility with awake and freely behaving animals and feasible set-up in a lab with opportunities for scaling-up (Byron and Sakata, 2024, Simpson et al., 2023). While these benefits come at a cost of lower spatial resolution and a risk of neuroinflammation around the fibre implant, combination of fibre photometry with Methoxy-x04 gives an opportunity to monitor plaque pathology in multiple brain regions (Pisanello et al., 2017, Pisanello et al., 2014, Pisano et al., 2019), surpassing the cortical regions, in awake and freely behaving mice. There is also opportunity to reduce the risk of neuroinflammation around the fibre implant with less invasive tapered fibres (TFs) (Pisanello et al., 2017, Pisanello et al., 2014, Pisano et al., 2019). Additionally, this can be used as a closed-loop system to monitor any benefits and adjust protocols to enhance beneficial disease-modifying effects. Therefore, if we can successfully implement this procedure, it will provide more knowledge about how plaque pathology responds to potential intervention strategies.

1.3.2.5.1 Methoxy-x04

Over many years, research groups have worked to develop plaque indicators that can be applied *in vivo*. For this, they must pass specific protocol including peripheral administration, BBB-permeability, and selectivity. The group of Klunk found success, generating several markers, with the most attractive option called Methoxy-x04 (Klunk et al., 2002). In their landmark study they illustrate the capabilities for both *in vitro* and *in vivo* use, proving its BBB-permeability and peripheral administration (Klunk et al., 2002). Therefore, in this section, I will discuss the development of Methoxy-x04 **(section 1.3.2.5.1.1)**, its use *in vitro* and *in vivo* **(section 1.3.2.5.1.2)** and its pros and cons **(section 1.3.2.5.1.3)**.

1.3.2.5.1.1 Development

For many years, a plaque marker known as Congo Red was used (Howie and Brewer, 2009). Structural experiments discovered that its binding site was beta-sheet structures existing on Aβ fibrils and protofibrils (Carter and Chou, 1998, Klunk et al., 1994, Klunk et al., 1989, Maezawa et al., 2008, Wu et al., 2007). More specifically, Congo Reds prominent binding pattern was parallel to the fibrils, but anti-parallel to the beta sheets (Klunk et al., 1994, Klunk et al., 1989), requiring a minimum of 5 Aβ monomers (Klunk et al., 1994), while occasionally binding in the opposite orientation (Carter and Chou, 1998, Reinke and Gestwicki, 2011). Then, hydrogen bonds form between positively charged amino acid residues on beta-sheets and negatively charged sulfonate groups on Congo Red (Carter and Chou, 1998, Klunk et al., 1994, Klunk et al., 1989). Congo Red was vital for understanding more about Aβ structure, but the selectivity was poor, and their

hydrophilic charge – due to presence of nitrogen double bonds and sulfonic acid groups – meant it was incapable of passing the BBB (Maezawa et al., 2008).

Therefore, Congo Red was used to generate a plaque marker suitable for *in vivo* use by reducing the molecular weight and increasing the lipophilicity. This generated Chyrsamine-G, Methoxy-x34, and Methoxy-x04 **(Figure 1.16A)** (Klunk et al., 2002, Klunk et al., 1995, Styren et al., 2000). Firstly, acidic naphthalenesulfonic acid groups were removed and replaced with less acidic and more lipophilic salicylic groups, resulting in the formation of Chrysamine-G (Klunk et al., 1995). This dye was less acidic with a lipophilicity 100x greater than Congo Red (Klunk et al., 1995). However, it had poor optical properties. Then, by completing the same acidic group changes, as well as replacement of nitrogen double bonds with carbon double bonds, Methoxy-x34 was developed (Styren et al., 2000). This reduced the molecular weight, improved the fluorescent properties, but reduced lipophilic properties, which limited entry into the brain (Styren et al., 2000). Finally, Klunk and colleagues removed carboxylic groups, leaving only the weakly acidic phenols which generated Methoxy-x04 (Klunk et al., 2002). This reduced the molecular weight, improved the lipophilicity and was shown to label fibrillar Aβ, but not any deposit that doesn't contain beta-pleated sheets (Klunk et al., 2002). In fact, based on binding studies, it was found that these analogues remained with the same binding sites (Crystal et al., 2003). A consideration was how this binding site may affect the growth of plaques, with it thought that binding should not affect the fibril growth, but when this binding site becomes saturated, markers may start to bind at the face of the growing fibril, eventually disrupting monomer aggregation and elongation (Reinke and Gestwicki, 2011).

1.3.2.5.1.2 Previous use

Due to the limitations with other monitoring approaches, as discussed in **section 1.3.2,** research groups began to investigate use of Methoxy-x04 as a plaque marker in combination with multiphoton imaging. Firstly, in the landmark study, Klunk and colleagues determined its BBB-permeability properties and ability to be administered peripherally by testing the properties after both i.p. and i.v. injection (Klunk et al., 2002). Using two-photon microscopy (2PM), they identified a strong fluorescence staining of an Aβ plaque, 1-h after i.v. injection in an anaesthetised AD mouse model, with comparable staining as the conventional Thioflavin-S (TS) dye, applied topically to the brain surface **(Figure 1.16B)** (Klunk et al., 2002). In addition, they illustrate that 24-h after i.p. injection, strong plaque signals can be detected using 2PM (Klunk et al., 2002). This prompted the use of Methoxy-x04 across several *in vitro* and *in vivo* studies (Condello et al., 2011, Crowe and Ellis-Davies, 2013, Hefendehl et al., 2016, Hefendehl et al., 2011, Jung et al., 2015, Klunk et al., 2002, Liu et al., 2010, Meyer-Luehmann et al., 2008), illustrating the capabilities of Methoxy-x04 and 2PM for longitudinal monitoring of plaque pathology (Condello et al., 2011,

Hefendehl et al., 2011, Meyer-Luehmann et al., 2008). While studies show that re-dosing Methoxy-x04 across several weeks to monitor the progression of plaque growth is feasible **(Figure 1.16C)** (Condello et al., 2011, Hefendehl et al., 2011, Meyer-Luehmann et al., 2008), other studies illustrate that Methoxy-x04 was able to remain stably bound to plaques for at least 90-days, showing no change in fluorescence intensity or size, suggesting that once bound, Methoxy-x04 does not dissociate, clear, or lose fluorescence (Liu et al., 2010, Meyer-Luehmann et al., 2008).

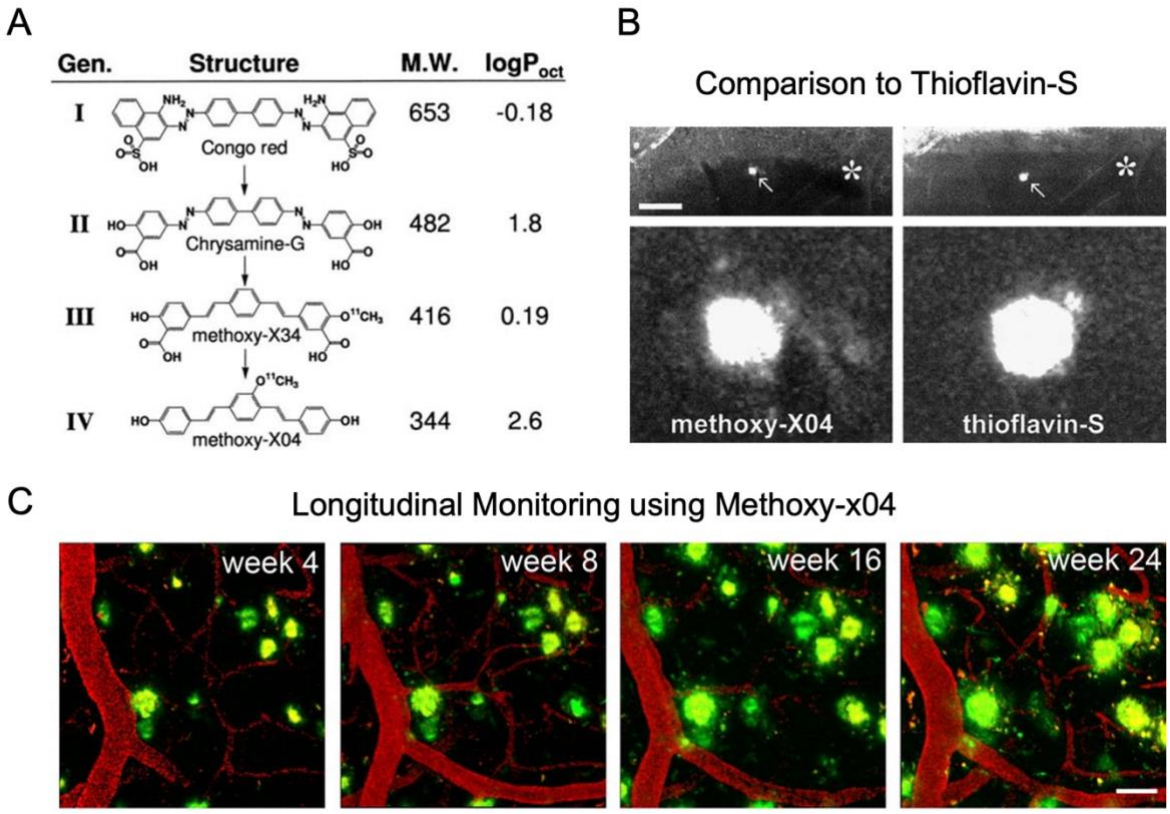

Figure 1.16. Methoxy-x04 structure and confirmation *in vivo*. (A) Generation of Methoxy-x04 from its derivatives. (B) Example of Methoxy-x04 staining following 1-h after i.v. injection in an anaesthetised 7-month-old PS1/APP transgenic mouse (left) and topical administration of TS (right). (C) Longitudinal *in vivo* imaging of the same region of interest, staining plaques with Methoxy-x04 (green) and blood vessels stained with Texan red dextran (red). A and B are adapted from Klunk *et al.,* 2002. C is adapted from Hefendehl *et al.,* 2011.

1.3.2.5.1.3 Pros and cons

Across various studies, Methoxy-x04 has proved to be a desirable option for *in vivo* plaque detection. It shows good BBB permeability (Klunk et al., 2002), it can be administered by both i.p. and i.v. routes, it remains stably bound for several months (Meyer-Luehmann et al., 2008) and it

is comparable to previous, well-established plaque markers such as TS (Klunk et al., 2002). As well as this, it is one of the only available plaque markers that is feasible for use *in vivo*.

However, the excitation/emission spectra overlaps with various other optical sensors, which limits possibilities for future all-optical experiments. Additionally, its spectra are susceptible to tissue AF. For example, low wavelengths within the brain can result in high scattering and absorption from biological tissue. On another note, Methoxy-x04 binds specifically to beta-sheets, rather than Aβ, which means that there can be some off-target fluorescence. However, as the 5xFAD mouse model used throughout this study does not show tauopathy (Oakley et al., 2006, Oblak et al., 2021), this may not be a major consideration. Additionally, there is a lack of knowledge surrounding the binding and bleaching characteristics of Methoxy-x04 which can make understanding of longitudinal re-dosing paradigms challenging. For example, while studies have suggested that derivatives of Congo Red, such as Methoxy-x04, should have similar binding sites (Crystal et al., 2003), it remains unclear if the binding of Methoxy-x04 is reversible, changes conformation upon photobleaching or what its potential clearance mechanisms from the brain may be. Despite Klunk and colleagues investigating the clearance of radioactive Methoxy-x04 from non-plaque brains (Klunk et al., 2002), little is understood about the relationship between the binding of Methoxy-x04 to the amyloid fibrils and how its binding properties reflect the fluorescent signal. Considering these limitations, Methoxy-x04 remains the optimal plaque marker available for *in vivo* optical imaging.

1.3.2.5.2 Fibre photometry

To detect changes of Methoxy-x04 within the brain, an optical approach that will allow for collection of fluorescent signals from deep brain regions is required. Fibre photometry is an optical method that collects fluorescence signals using an implantable optic fibre (Byron and Sakata, 2024, Simpson et al., 2023) **(Table 1.4)**. Commonly used for monitoring real-time, neuronal population activity in freely behaving animals, we suggest scaling up this approach for molecular pathologies, such as Aβ plaques.

1.3.2.5.2.1 Background

Despite fibre photometry being used for other fields, it was not translated for use in neuroscience until 2005 (Adelsberger et al., 2005). Here, Adelsberger stained the neocortex through multi-cell bolus loading of the fluorescent calcium indicator, Oregon green 488 BAPTA-1, to identify spontaneous calcium transients of neurons (Adelsberger et al., 2005). Despite this ground-breaking implementation, its use did not begin to spike until the mid-2010s, where it has now became widely adopted for use in characterising neuronal activity **(Figure 1.17).** This was greatly attributed to the rapid development of novel genetically encoded calcium sensors. For example,

both genetically encoded calcium indicators (GECIs) and genetically encoded voltage indicators (GEVIs) can be genetically expressed in mouse models, allowing monitoring of calcium activity due to the fluorescence emitted from these indicators. In addition, fibre photometry has been implemented in use for optogenetic experiments and to monitor calcium signals from glial cells. Despite this massive growth in applications, to our knowledge, fibre photometry has not been applied for assessment of molecular pathologies, such as Aβ plaques.

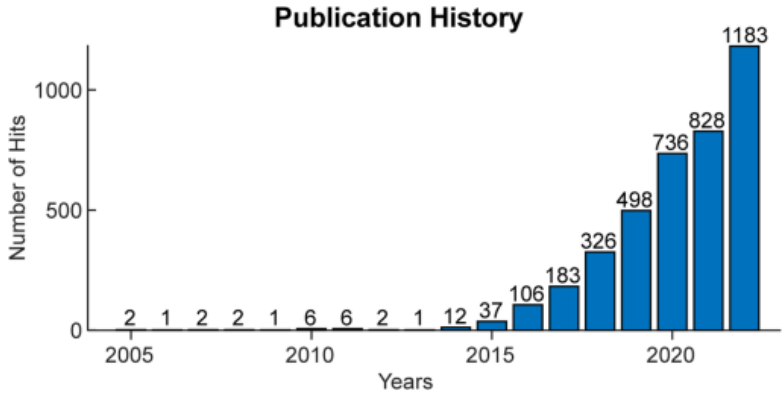

Figure 1.17. Publication hits for fibre photometry. Total number of hits from PubMed, Web of Science, and Google Scholar when searching either “fiber photometry” or “fibre photometry” across all available years. Adapted from Byron & Sakata, 2024

1.3.2.5.2.2 Principles of fibre photometry

Across all applications, the general principle of fibre photometry remains the same **(Figure 1.18A)** (Byron and Sakata, 2024, Simpson et al., 2023). Using an optical implant **(Figure 1.18B)** and fluorescent indicator **(Figure 1.18C)**, light at an excitation wavelength specific to the indicator will pass through the implant to the brain tissue. Accordingly, the fluorescent indicator will become excited and give off fluorescence which passes back through the implant and emission light is collected by a photodetector. For each experimental protocol, each system will be modified appropriately, for appropriate excitation LED/Lasers, emission filters and other optical elements. However, a large benefit of fibre photometry is the simple, low-cost, reconfigurability and scalability of its system (Byron and Sakata, 2024, Simpson et al., 2023).

1.3.2.5.2.2.1 Implant

As shown in **Figure 1.18B**, different optical implants can be chosen. The most common and well-established option is the flat cleaved fibre (FF), which is flat across the implantable surface over a chosen diameter, most commonly either 200 or 400-μm **(Figure 1.18B)**. This is commercially

available and easily custom-made, with them being relatively low cost and providing reliable light output. However, their flat surface can introduce difficulties with implantation, resulting in a dimpling effect due to a conflicting force from the fibre and brain tissue. With this and the thick diameter, this can result in substantial tissue damage and resulting neuroinflammation and cell death. Lastly, light can only propagate from this flat cleaved region of the FF, which reduces spatial resolution and leaves only one depth monitored. Some studies have been completed in attempt to characterise the spatial properties of such light profiles (Cui et al., 2013, Gonzalez et al., 2016, Kupferschmidt et al., 2017, Natsubori et al., 2017, Pisanello et al., 2019, Tecuapetla et al., 2014), but overall, it is lacking.

Therefore, a focus into increasing the depth of tissue being monitored arose, with the group of Massimo De Vittorio developing state-of-the-art TFs that are mechanically pulled to extend the optic fibre, allowing light propagation and light collection across 1.8-mm (Pisanello et al., 2017, Pisanello et al., 2014, Pisano et al., 2019) **(Figure 1.18B)**. This created a sharp fibre tip reaching only several nanometres in diameter (Pisanello et al., 2014). Therefore, this approach overcomes limitations in implantation, invasiveness, neuroinflammation and spatial resolution (Byron and Sakata, 2024, Simpson et al., 2023). First evidence of *in vivo* detection was by identifying changes in dopamine transients within the striatum, while freely behaving mice were performing a behavioural task (Pisano et al., 2019). To do so, they characterised the light profiles from the TFs, and emphasised the capability of engineering the light propagation from the TF (Pisano et al., 2019). Overall, for real-time, depth-resolved measurements, TFs are the optimal choice. However, for use *in vivo*, further characterisation would be required.

1.3.2.5.2.2.2 Indicator

To complete fibre photometry, an appropriate fluorescent indicator must be used (Byron and Sakata, 2024, Simpson et al., 2023). Over recent years, a wide range of fluorescent indicators for fibre photometry have been developed, with the most used being a group of GECIs called GCaMPs **(Figure 1.18C)** (Abdelfattah et al., 2022, Wu et al., 2022b). The first GCaMP was developed by Nakai and colleagues in 2001, where they reported the use of this calcium sensor in HEK-293 cells (Nakai et al., 2001). Since then, this family of sensors has continued to grow with use *in vivo*, development of red sensors and sensors with a greater sensitivity and varied kinetics **(Figure 1.18C)** (Akerboom et al., 2012, Chen et al., 2013b, Dana et al., 2016, Dana et al., 2019, Tallini et al., 2006, Tian et al., 2009, Zhang et al., 2023). This has allowed investigation into many aspects of neuroscience, including population neuronal activity in healthy and diseased brains (Abdelfattah et al., 2022). While these are the most widely used due to their superior brightness and signal-to-noise ratio, there are GEVIs (Abdelfattah et al., 2022), as well as indicators for a wide range of other neuronal components such as dopamine, 5-HT, nicotine, noradrenaline, acetylcholine, ATP

etc. (Abdelfattah et al., 2022, Berg et al., 2009, Jing et al., 2020, Jing et al., 2018, Kagiampaki et al., 2023, Lobas et al., 2019, Marvin et al., 2019, Patriarchi et al., 2018, Patriarchi et al., 2020, Shivange et al., 2019, Sun et al., 2018, Tantama et al., 2013, Unger et al., 2020). However, an indicator for molecular pathologies is lacking and instead involve peripheral administration and the requirement of BBB-permeability.

The main considerations when choosing an indicator is biocompatibility, a high signal to noise ratio, photostability, an appropriate excitation/emission spectra and kinetics (Wu et al., 2022b). Another major consideration is how the indicator will be expressed, with common options being transgenesis, viral gene delivery, in utero electroporation and multicell bolus loading (Luo et al., 2008, Luo et al., 2018, Simpson et al., 2023). Each of these options comes with their own strengths and limitations and therefore, it is important to consider the optimal approach for a given experiment (Luo et al., 2008, Luo et al., 2018). Firstly, transgenesis involves the generation of animal models that will genetically express the fluorescent indicator in an appropriate cell line (Luo et al., 2008, Luo et al., 2018). Other possibilities are through KI or KO models to allow expression of a transgene in a specific cell or under a certain condition (Luo et al., 2008, Luo et al., 2018). A benefit of this approach is that there is brain-wide expression of the indicator that appears to remain stable over several generations. However, this approach has shown to have variations of expression across the brain, which may interfere with region- or pathway-specific experiments. In order to achieve such direct expression in a region and cell-specific manner, many researchers opt for a viral gene delivery approach as this can provide specificity to the location, cellular subtype (including neurons and glial cells (Lee et al., 2008, Okada et al., 2022)), cellular localisation, and synaptic direction (Luo et al., 2008, Luo et al., 2018). This approach involves virally packing the fluorescent indicator with a cell-specific promoter and virally injecting into the desired brain region. After several weeks of incubation, this provides adequate viral expression.

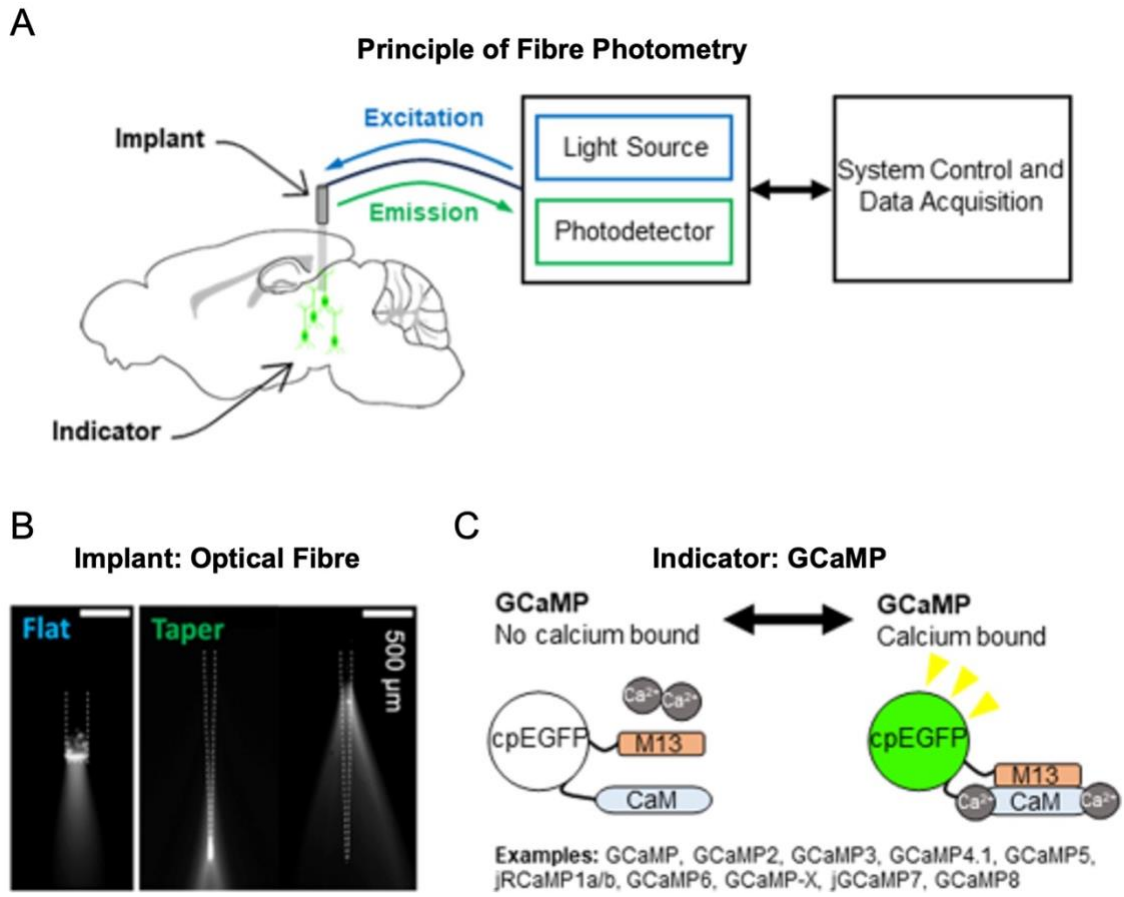

Figure 1.18. General principle of fibre photometry. (A) General set-up of fibre photometry. Used set-ups will contain other optical elements. (B) Example of light profile of a flat (left) and tapered (right) fibre that can be implanted into the mouse brain. (C) Example of the function of GCaMP indicators commonly used for fibre photometry measurements. Adapted from Byron and Sakata (2024).

1.3.2.5.2.3 Pros and cons

Fibre photometry can provide cell-type and region-specific monitoring, across deep brain regions, in real-time due to quick system control (Byron and Sakata, 2024, Simpson et al., 2023). Additionally, due to the optic implant being lightweight, fibre photometry recordings can be completed in a freely behaving condition. It has rapid temporal resolution, on a millisecond scale, but does lack spatial resolution **(Table 1.4)**. However, with implementation of TFs, this helps boost the depth-resolution of fibre photometry, allowing multi-site recordings (Pisanello et al., 2017, Pisanello et al., 2014, Pisano et al., 2019). While some neuroinflammation can be expected due to the implantation of a foreign object into the brain, this should be to a lower extent, as shown by a reduced microglia and astrocyte aggregation around TF implants compared to FF implants (Pisanello et al., 2017) **(Table 1.4)**. Lastly, compared to all other approaches, this is a reasonably low-cost option that can be set-up in a laboratory environment, scalable and easily reconfigured.

1.3.2.5.3 Considerations for implementing this approach

When developing a novel approach, it is vital to consider contributing factors that may limit the design for completing recordings and analysis. We believe we must consider the possibility of AF, movement artefacts in freely behaving recordings, light propagation from the TFs and analysis approaches.

1.3.2.5.3.1 AF

A major influence may be the contribution of AF, which can originate from two sources: brain tissue or fibre photometry system (Bianco et al., 2021, Byron and Sakata, 2024, Formozov et al., 2023, Schlegel et al., 2018, Simpson et al., 2023). For example, the excitation/emission spectra of Methoxy-x04 are short which has previously been shown to increase the light scattering and absorption within the brain (Jun et al., 2017). In addition, there are several brain depositions that can contribute to AF that exist at this wavelength. An example is lipofuscin which is an ageing-pigment that form depositions of incomplete lysosomal degradation as a result of damaged mitochondria (Gray and Woulfe, 2005). They have been shown to emit strong AF, particularly at lower wavelengths with a peak around 650-nm, but with a broad emission bandwidth of 200-nm, thereby overlapping with all detection channels and Methoxy-x04 spectra (Eichhoff et al., 2008, Kwan et al., 2009). Also, throughout recordings this tissue AF can decrease overtime due to photobleaching (Byron and Sakata, 2024, Simpson et al., 2023). Accordingly, implementing approaches to account for such noise is essential. A well-established approach of doing so would be estimating the time-course of photobleaching by fitting a curve to the signal and correcting accordingly (Simpson et al., 2023).

Alternatively, AF can also occur from the fibre photometry system, specifically the optic fibres and patch cable (Bianco et al., 2021, Byron and Sakata, 2024, Formozov et al., 2023, Schlegel et al., 2018, Simpson et al., 2023). As light passes through the patch cable, light is internally reflected due to differences in the optic fibre glass and polymer reflective index. Therefore, some of the light's energy will be released into the patch cable cladding at each reflection. Within this polymer cladding, an unknown component can transform this energy and generate fluorescence, which has been shown to vary in intensity and can recover over-time. While this may not influence experiments where rapid temporal resolution is desired as a $\Delta F/F$ can be calculated, monitoring fluorescence over longer times can be problematic and will require a high signal-to-noise ratio and baseline adjustment (Byron and Sakata, 2024, Simpson et al., 2023). Currently, there is no solid solution to this difficulty, but low-AF patch cables are available, and leaving the light source on for several hours to bleach the internal AF before each recording is essential (Byron and Sakata,

2024, Simpson et al., 2023). In addition, studies have illustrated that TFs provide a greater AF that FFs, which must be considered (Bianco et al., 2021). Accordingly, to account for both tissue and system AF, we implemented an analytical approach described in **sections 1.3.2.5.3.4 and 4.2.1.5.2.**

1.3.2.5.3.2 Movement artefacts

While completing freely behaving recordings, moving artifacts can be introduced that can interfere with signal collection (Byron and Sakata, 2024, Simpson et al., 2023). This arises due to displacement between the brain tissue and optic fibre and movements of the patch cable. This artifact is usually corrected using signals from an isosbestic channel that shows signals independent of the indicator (Byron and Sakata, 2024, Kim et al., 2016, Patel et al., 2020, Simpson et al., 2023). However, as the temporal resolution and sampling interval required for tracking plaque pathology will be low, this will reduce the influence of moving artefacts.

1.3.2.5.3.3 TF light propagation

While FFs have a consistent light profile, TFs now propagate light along 2-mm, and this can vary in strength (Pisano et al., 2019). For example, the light output of the TF starts to decline as it reaches further away from the TF tip. This would mean that signals collected would not be representative of the pathological state, as regions will not be excited at consistent levels. The previous group illustrate how light can be engineered to modify the light propagation along the TF. Accordingly, in this study we adopted two light protocols for equalising light power or power density along the TF (Pisano et al., 2019). This will overcome limitations surrounding the light output from the TF, while providing evidence for the optimal approach for collecting TF signals.

1.3.2.5.3.4 Analytical approaches

In addition, as recordings will be completed across several days and across several mice, an appropriate analytic approach is required. Therefore, there may be variation in Methoxy-x04 concentration, age of mice, plaque load, light excitation, and level of AF. The most common and well-established approach for accounting for such variations would be normalising the data by converting signals into units of ΔF/F (the change in fluorescence divided by the baseline) (Simpson et al., 2023). While this is appropriate for multi-photon microscopy, use for fibre photometry may be challenging due to the presence of AF which may alter the baseline signal (Simpson et al., 2023). Accordingly, for this approach we considered a baseline signal to be a recording where no Methoxy-x04 was present. Then, we created two possible analytical approaches to characterise the optimal way to assess TF signals. The first was to calculate the ΔF/F from the baseline signal.

The second was to account for the changes in AF throughout each recording based of the baseline recording. This would involve fitting a model to baseline data which would represent the AF contributions from brain tissue and the fibre photometry system, for removal from each recording.

1.4 Hypotheses and Specific Aims

Overall, as AD is a wide-spread disorder that continues to have limited available therapies, it is important that an appropriate method for monitoring the success of possible treatment options is available. Due to the vital role of plaque pathology in AD pathogenesis, this is an appropriate molecular target to track the progression of AD. However, as described above, existing methods for *in vivo* plaque assessment come with limitations including real-time feedback and deep brain access, limiting the collection of information.

Thus, real-time assessment of AD pathology, *in vivo*, would be advantageous. This may accelerate the development of AD interventions by providing real-time feedback of any beneficial disease-modifying effects. The real-time capabilities are important because it allows us to track the optimal treatment duration for potential therapies, as well as allowing longitudinal feedback across varied durations of time. Therefore, in this study we hypothesise that combination of the BBB-permeable drug, Methoxy-x04 (Klunk et al., 2002), and fibre photometry (Byron and Sakata, 2024, Simpson et al., 2023) will develop a novel approach for real-time assessment of AD pathology in deep brain regions, *in vivo*. Accordingly, this study was divided into 3 sub-projects with appropriate hypotheses and aims **(Figure 1.19A)**:

1. Firstly, in **Chapter 3**, we hypothesise that combination of Methoxy-x04 and conventional FF photometry will allow detection of plaques, *in vivo*. To this end, we aimed to confirm that this novel approach of Methoxy-x04 and fibre photometry is feasible to monitor plaque pathology by identifying if there is a positive correlation between photometry and histology plaque signals.
2. Secondly, in **Chapter 4**, we hypothesise that TF photometry will allow *in vivo*, real-time, depth-resolved plaque detection. Thus, we aim to establish a novel protocol for real-time, *in vivo* plaque assessment across depth by determining optimal light protocols and analytical approaches when using TFs.
3. Thirdly, in **Chapter 5**, we hypothesise that our novel approach will allow monitoring of plaque modifications caused by GENUS. Accordingly, we aimed to expose mice to GENUS and monitor changes in AD pathology by determining the effects on neuronal activity and plaque pathology in AD mouse models.

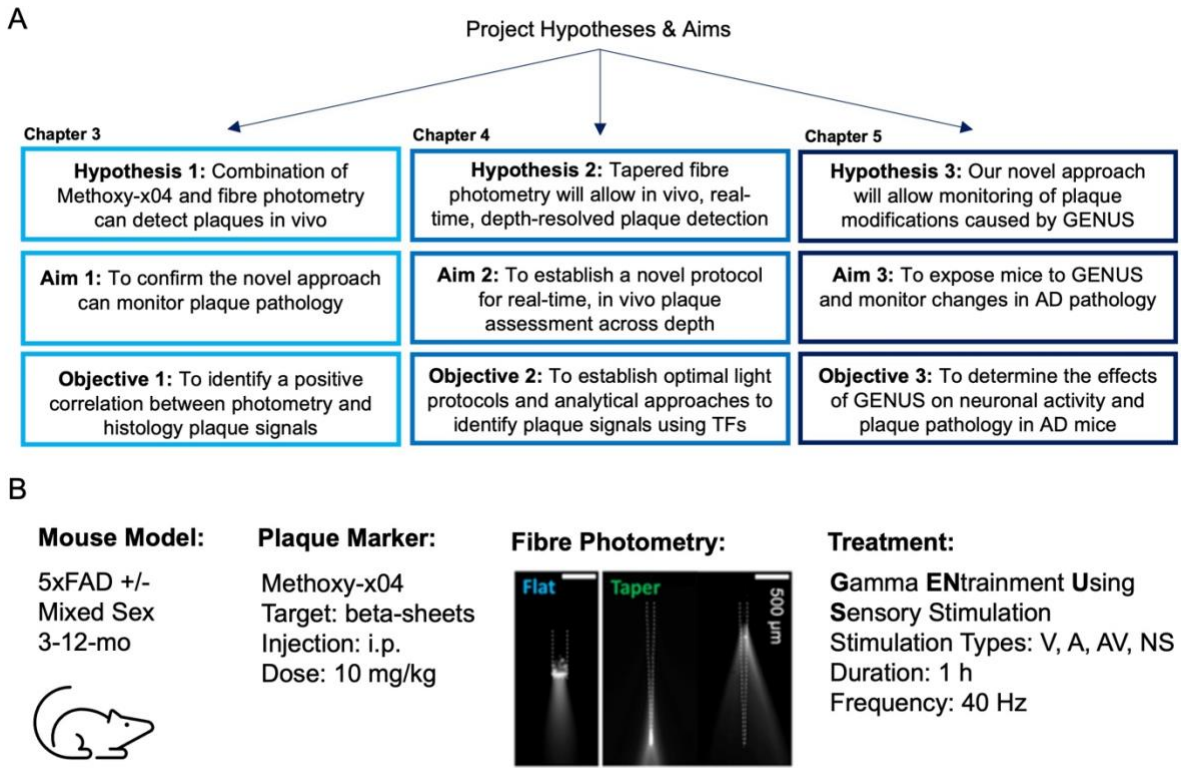

Figure 1.19. Hypotheses, aims and objectives of the project and the tools used. (A) Project hypotheses & aims. (B) Main tools used throughout the project. V: visual; A: auditory; AV: audio-visual; NS: no stimulation.

To this end, we will establish a fibre photometry system that can detect fluorescence from Methoxy-x04-stained plaques in 5xFAD mice. Once established, we will use this novel approach to monitor changes in plaque pathology when mice undergo GENUS treatment.

The justification of mouse model, plaque marker, fibre photometry and treatment have been thoroughly described in **section 1.3.1.3, 1.3.2.5.1, 1.3.2.5.2 and 1.2.2.2.2.2.1**, respectively **(Figure 1.19B)**. In summary, 5xFAD mouse models are used due to their rapid and aggressive Aβ pathogenic phenotype which will aid the establishment of this novel protocol (Oakley et al., 2006, Oblak et al., 2021). In addition, they have been well characterised which will aid understanding of our findings. Next, Methoxy-x04 was chosen as the fluorescent indicator as it has previously had success when peripherally administered to pass the BBB and stain Aβ (Condello et al., 2011, Crowe and Ellis-Davies, 2013, Hefendehl et al., 2016, Hefendehl et al., 2011, Jung et al., 2015, Klunk et al., 2002, Liu et al., 2010, Meyer-Luehmann et al., 2008). In addition, there are minimal alternatives in amyloid-binding dyes that pass the BBB for *in vivo* work. Then, fibre photometry was chosen as this provides this approach with a real-time, depth-resolved capability, as well as permitting multi-site recordings in freely behaving animals (Byron and Sakata, 2024, Simpson et al., 2023). This overcomes limitations with temporal resolution, invasiveness, inflammation, and

depth-resolution seen with alternative optical approaches. Lastly, mice will undergo GENUS treatment as it is a novel approach working to combat the circuit dysfunctions that exist throughout AD (Adaikkan et al., 2019, Iaccarino et al., 2016, Martorell et al., 2019, Soula et al., 2023). In addition, it is an attractive, non-invasive treatment approach that has recently shown conflicting findings which need investigated.

Additionally, we had a variation of target implant sites. For depth profile experiments, we targeted brain regions that would have a variation of plaque dense and plaque sparse regions from the brain surface to deeper regions because we wanted to illustrate the ability of our novel approach to monitor changes in fluorescence signals based on the plaque load. Accordingly, we investigated sites that would pass the medial septum, thalamus, and subiculum as these are largely populated with plaques in 5xFAD mice. After, our main target was the subiculum due to this being an area in the 5xFAD mouse brain that is densely populated with plaques, allowing us to identify the strongest signal possible. Also, with use of TFs, this would span through the subiculum and visual cortex, allowing us to monitor changes in the related sensory cortex when investigating the effects of GENUS.

Overall, by establishing this protocol we expect to show for the first time, a novel approach involving the combination of Methoxy-x04 and fibre photometry, that allows *in vivo*, real-time, depth-resolved assessment of plaque pathology in freely behaving AD mouse models. Accordingly, we expect to allow monitoring of plaque pathology when exposed to GENUS in real-time.

2. Methodology Overview

Due to the wide range of methods throughout this project, this chapter provides an overview of all methodology before directing the reader to appropriate sections within each subsequent chapter for a detailed description of appropriate methodology. First, it will provide a description of methodology that is used across all chapters. This includes an overview of the BBB-permeable plaque marker, Methoxy-x04 (**section 2.1.1**), a description of the animals used (**section 2.1.2**), and the analytical approach used to align histological images to the Allen brain atlas (**section 2.1.3**) **(Figure 2.1)**. Secondly, this chapter will provide a roadmap of the appropriate methodology for each chapter, directing the reader to the relevant section **(Figure 2.1)**.

For reference, **Chapter 3** shows confirmation of the novel approach to monitor plaque pathology FF photometry (**section 2.2**). **Chapter 4** shows real-time, depth-resolved plaque detection (**section 2.3**). **Chapter 5** shows monitoring of plaque pathology in response to GENUS (**section 2.4**) **(Figure 2.1).**

Figures created for this thesis were created using Adobe Illustrator, BioRender and Microsoft PowerPoint.

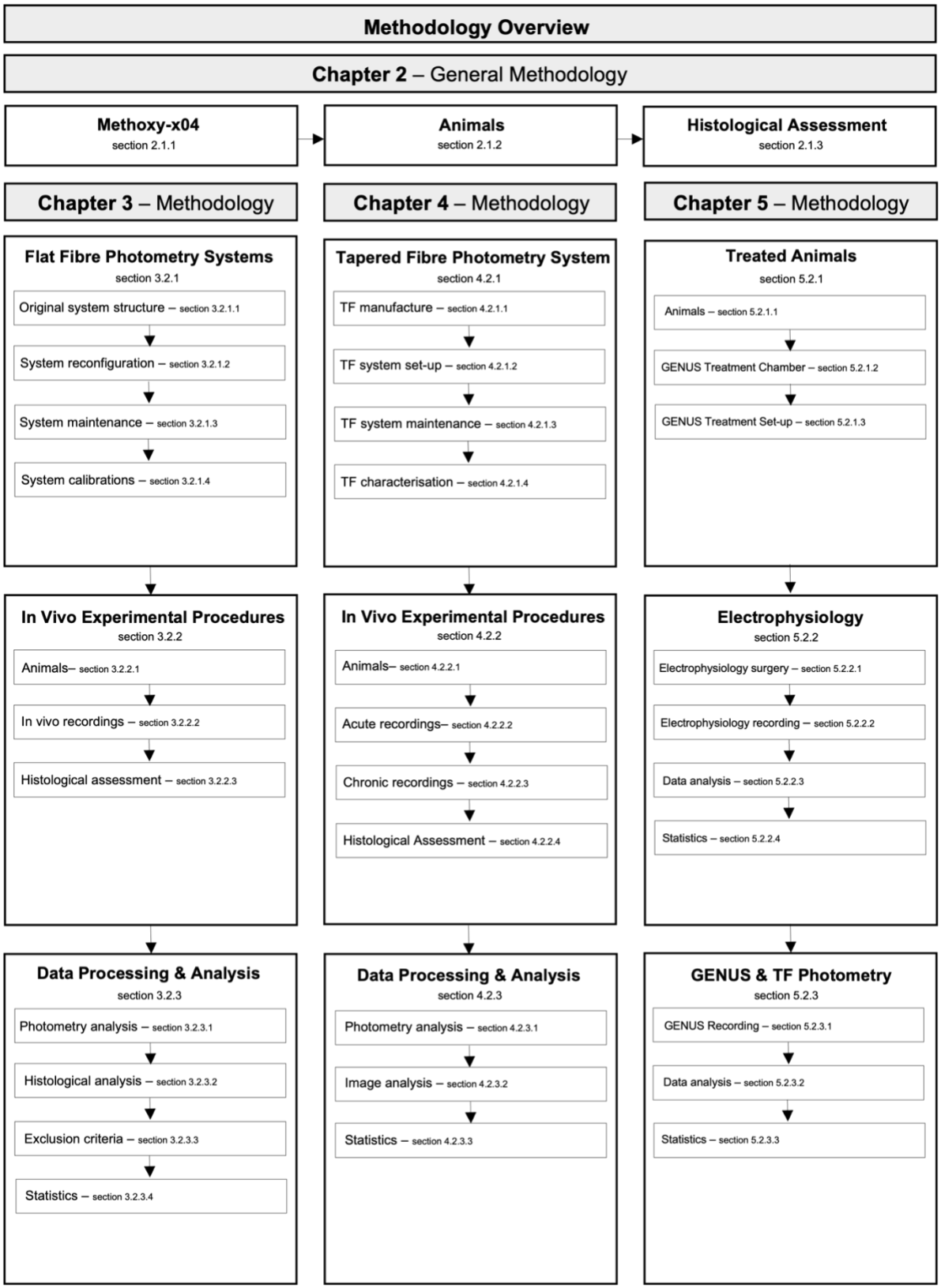

Figure 2.1. Roadmap of all methodology sections throughout this thesis. Chapter 2 includes general methodology used for all sub-projects. **Chapter 3, 4** and **5** have their own methodology section.

2.1 General Methodology

2.1.1 Methoxy-x04

2.1.1.1 Properties of Methoxy-x04

Methoxy-x04 is a BBB-permeable plaque marker, that has been successfully implemented *in vitro* and *in vivo* (Condello et al., 2011, Hefendehl et al., 2016, Hefendehl et al., 2011, Jung et al., 2015). Methoxy-x04 (1,4-bis(4'-hydroxystyryl)-2-methoxybenzene) has a molecular weight of 344, a pK_a of 10.82 + 0.07 and a $logP_{oct}$ of 2.6, thereby promoting BBB-permeability and a good binding affinity for beta-sheets (K_i = 26.8-nM) **(Figure 2.2)**. Methoxy-x04s peak excitation is ~380-nm, and peak emission is ~450-nm.

Step	Chemical	MW	$logP_{oct}$
1	Congo Red	653	-0.18
2	Chrysamine-G	482	1.8
3	Methoxy-X34	416	0.19
4	**Methoxy-X04**	**344**	**2.6**

Figure 2.2. Chemical properties of Methoxy-x04 and its derivatives.

2.1.1.2 Methoxy-x04 Concentrations

A stock solution of Methoxy-x04 (4920, Tocris) was made by diluting Methoxy-x04 to 5-mg/ml using a sterile solution of 10% dimethyl sulfoxide (DMSO)/45% propylene glycol/45% phosphate buffered saline (PBS). To ensure Methoxy-x04 was diluted in this solution, it was gently heated on a magnetic stirrer (US152, Stuart) for several days. After, this was aliquoted and stored at -20°C. For *in vitro* measurements, a range of Methoxy-x04 concentrations were used (0.005, 0.01, 0.05, 0.1, and 0.5-mM). All solutions of Methoxy-x04 were made by diluting in 10% DMSO/45% propylene glycol/45% PBS. For *in vivo* recordings, a dose of 10-mg/kg was administered with a drug concentration of 5 mg/ml in 10% DMSO/45% propylene glycol/45% PBS via i.p. injection, as this was the most commonly used combination, as seen in the landmark study (Klunk et al., 2002). When administered, the desired volume was topped up to 0.3-ml with sterile saline to facilitate injection.

2.1.2 Animals

Experiments were performed in accordance with the UK Animals (Scientific Procedures) Act of 1986 Home Office regulations and approved by the Home Office (PP068894). Mice were housed with sex-matched littermates on a 12-hour/12-hour light/dark cycle, with access to food and water ad libitum. If a same-sex littermate was unavailable, mice were housed alone or with a BALB/c mouse. All experiments were performed during the light period.

Male and female 5xFAD+/- (AD+) and 5xFAD-/- (AD-) (on a >F10 C57BL/6 background) congenic mouse models (JAX006554, The Jackson Laboratory) (Oakley et al., 2006, Oblak et al., 2021) at ages 3-12 months, depending on experimental protocol, were used throughout this study. To ensure the genetic background, mice were ear-tagged, and tissue was genotyped using real-time polymerase chain reaction (by Transnetyx). A total of 83 mice were used throughout the whole project, with exact sample numbers for each experiment shown in **Figure 2.3** and discussed within the methodology section of each chapter **(Figure 2.1)**. Randomisation and exclusion protocols are discussed in each chapter **(Figure 2.1)**. 7 mixed genotype mice were used for training and optimisation of experimental procedures. This includes cadavers and retired breeders that were used for gaining experience completing terminal and recovery surgical procedures.

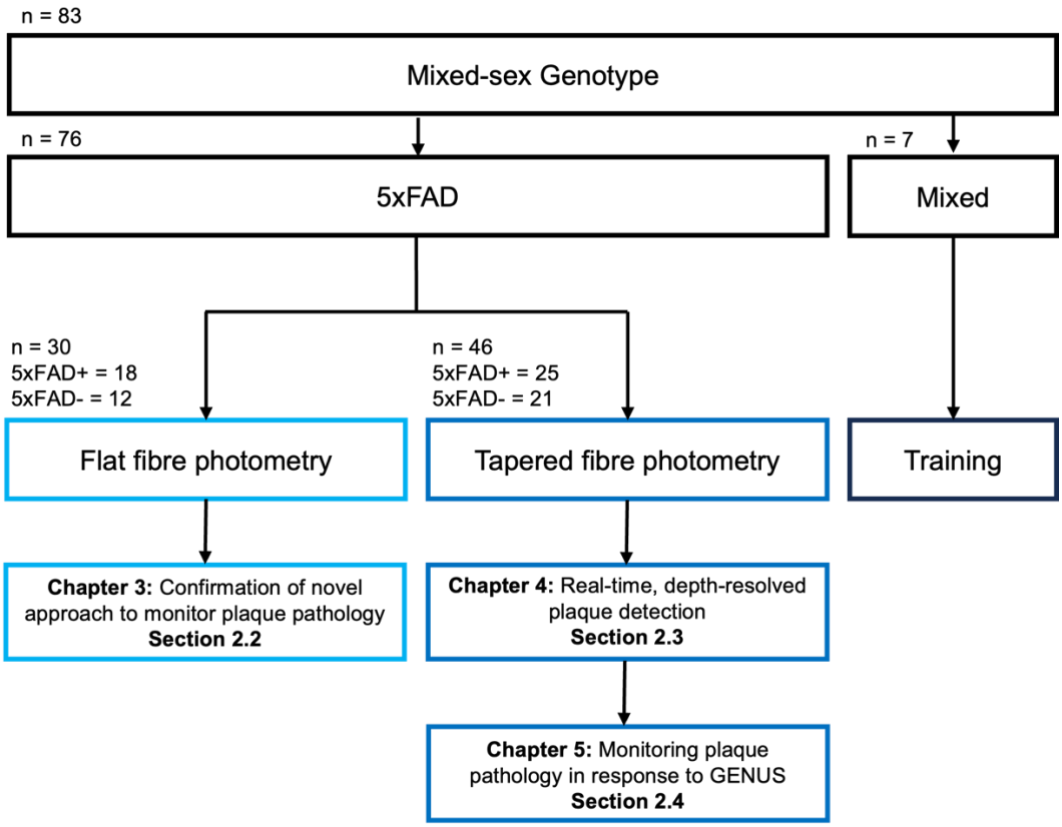

Figure 2.3. Flow chart illustrating the genotype and number of animals used throughout the whole project and the chapters these were used for. The sample numbers for each type of experiment are shown with the number of each genotype used. For training, mice of mixed genotype were used and are grouped together for simplicity. The chapter each group of mice were used for is shown.

2.1.3 Histological Assessment

All histological images were aligned to the mouse Allen Mouse Brain Common Coordinate Framework. For this, images underwent a post-processing pipeline that involved image stitching, alignment to the Allen brain atlas, automated plaque detection, manual fibre track detection and photometry Vs histology correlative assessment **(Figure 2.4A)**. This was allowed due to custom MATLAB code and a MATLAB-based software called AMaSiNe (Song et al., 2020). An in-depth discussion of this can be found here: https://github.com/vsnnlab/AMSiNe. AMaSiNe was chosen after comparing with other tools such as SHARP-Track (Shamash et al., 2018), as it was an automated approach for aligning histological images which had a built-in tool for automatic plaque detection. Therefore, this removes bias from manual alignment and plaque detection that exists with other approaches.

This protocol was mainly consistent for the FF and TF experiments, excluding the fibre track detection and photometry Vs histology correlation assessment. Thus, these specific protocols for

FF or TF experiments will be described in **Chapter 3, section 3.2.3.2** or **Chapter 4, section 4.2.3.2**, respectively **(Figure 2.1)**.

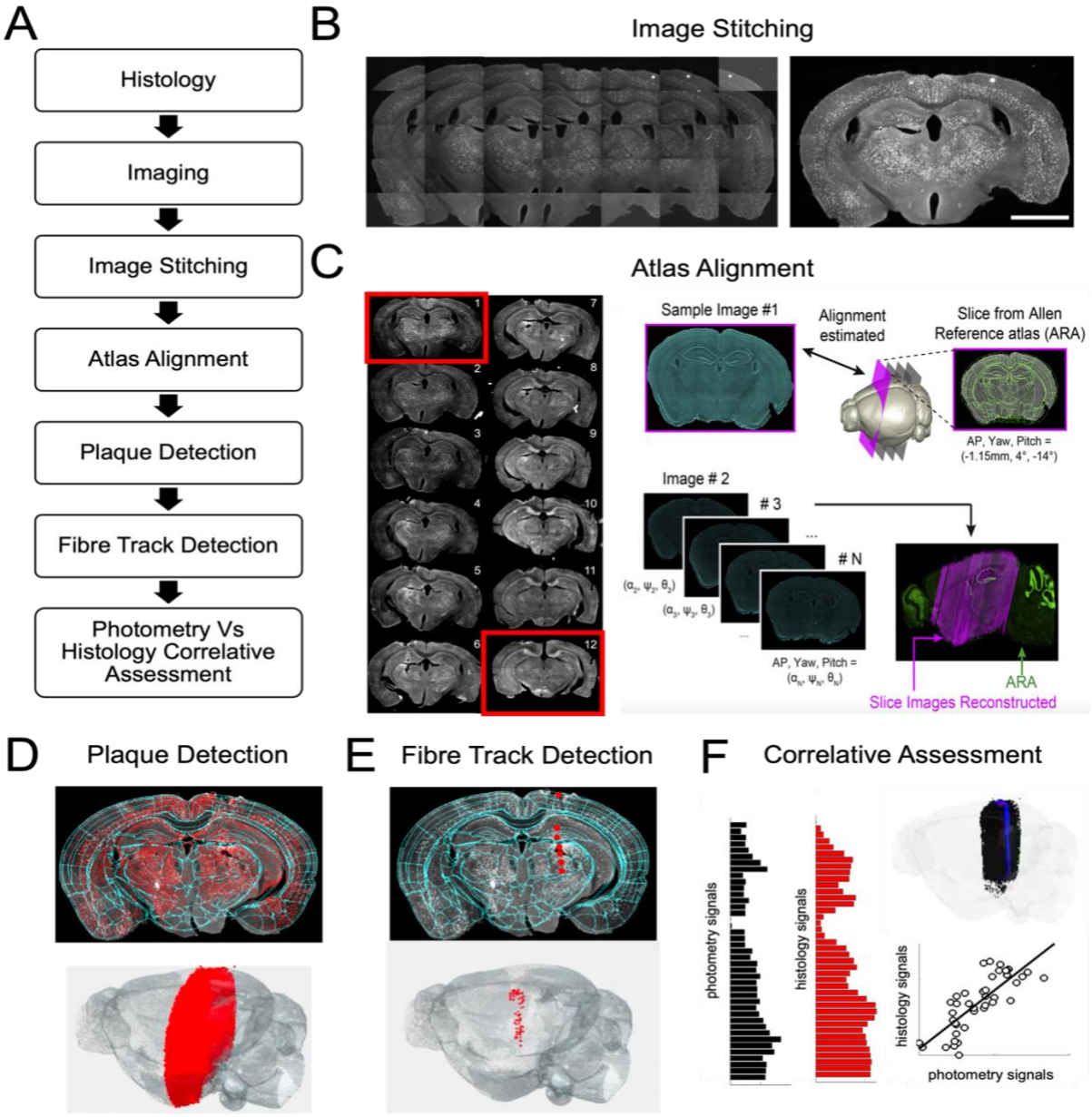

Figure 2.4. Process for histological quantification of Methoxy-x04 stained plaques along the fibre implant site. (A) Flow chart of the image analysis process. (B) Image stitching of all original images (*left*) to the final stitched image (*right*). Scale bar: 2-mm. (C) The first and final stitched image (*shown with red border*) are anchor images used for atlas alignment. Anchor images are used to determine several alignment parameters before all image slices are reconstructed onto the atlas. Figure adapted from Song *et al*., 2020. (D) *Top*, Automated plaque detection on an aligned brain slice. *Bottom,* Detected plaques on all aligned brain slices, visualised on a whole brain. (E, F) Examples are taken from a FF experiment. Please note that this varied for TF photometry. (E) *Top*, Manual fibre track detection on an aligned brain slice. *Bottom,* Detected fibre

track on all aligned brain slices, visualised on a whole brain. (F) Approach for photometry Vs histology correlative assessment. Plaques within 200-µm of the manually annotated fibre track (*red*), on the contralateral hemisphere are quantified. All plaques are shown as black dots. Quantified plaques are shown within a blue circle. Histology and photometry signals from the brain surface to 4000-µm are compared, as shown in bar graphs (*left*), before correlative assessment (*bottom*).

2.1.3.1 Stitching

Post-processing was completed through a custom MATLAB code that allowed automated image stitching. 1920x1200-pixel images went through a compression process by re-sizing the images to 960x600-pixels. This was completed either before or after stitching, depending on stitching accuracy. By going through each image, landmark features were detected (MATLAB function: detect SURF features) before finding any matching features between adjacent images (MATLAB function: extract Features). Once found, the shift of each feature from one image to the next is calculated and used to stitch all images together **(Figure 2.4B)**. Lastly, all images underwent transfer to 8-bit, contrast adjustment and application of their pseudo-colour using Fiji ImageJ (version 2.0.0-rc-69/1.52s).

2.1.3.2 Atlas Alignment

After brain sections from an implant site have been appropriately stitched and contrast adjusted using Fiji ImageJ (version 2.0.0-rc-69/1.52s), AMaSiNe is used to align each section to the Allen brain atlas **(Figure 2.4C)**. This involves numerous stages: parameter setting, pre-processing, angle searching and image warping.

For alignment, pre-processed images were binarized so that only the brain slice remains. Then, anchor images – the first and last imaged section – are selected and the sampling interval between each section (section thickness) is used **(Figure 2.4C)**. The software runs through numerous computational processes to identify the positions of the anchor images on the Allen brain atlas, subsequently allowing identification of the non-anchor images by determining equal distances between the two anchor images.

2.1.3.3 Plaque Detection

AMaSiNe was used to label plaques on each hemisphere throughout the aligned histological brain images **(Figure 2.4D)**. AMaSiNe acquires the anterior-posterior (AP), medio-lateral (ML) and dorso-ventral (DV) coordinates of each plaque, which is reconstructed using the alignment

information previously acquired as described in **section 2.1.3.2**, to assign each plaque to the appropriate brain region. Using said coordinates, each plaque is then assigned to an appropriate hemisphere, with ML coordinates >0 being the left hemisphere and those <=0 being the right hemisphere. This provides a list of all brain regions, with a list of coordinates for each identified plaque within each brain region, for each hemisphere **(Figure 2.4D)**. Only plaques with a radius between 11-20-µm, with a fluorescent threshold compared to the background fluorescence >0.07 were quantified. These parameters were chosen as they provided optimal plaque detection with minimal false positives or negatives. However, these values were occasionally adjusted per implant site, to allow for optimal plaque detection. This was visually examined by the experimenter.

2.1.3.4 Fibre track detection

Following plaque quantification, the fibre track on the aligned sections was manually labelled using an AmaSiNe built-in graphical user face **(Figure 2.4E)**. This allows manual annotation on each aligned image, where the fibre track was marked. Using the aligned images, the AP, ML and DV coordinates of the manually labelled fibre track are identified. The exact labelling approach varies for FF and TF experiments so see **Chapter 3, section 3.2.3.2.1** or **Chapter 4, section 4.2.3.2.1**, respectively **(Figure 2.1)**.

2.1.3.5 Photometry Vs histology correlative assessment

Lastly, in attempt to mirror the plaque signals collected from photometry experiments, plaques that fall within a certain radius of the fibre track coordinates were quantified **(Figure 2.4F)**. From here we can determine the quantified plaques at increasing depths along the fibre and compare to photometry data **(Figure 2.4F)**. For FF or TF-relevant protocols, please refer to **Chapter 3, section 3.2.3.2.2** or **Chapter 4, section 4.2.3.2.2**, respectively **(Figure 2.1)**.

2.2 Chapter 3 Methodology

Chapter 3 illustrates the proof-of-concept study completed to determine if the proposed novel approach was a feasible method for monitoring plaque pathology. This involved experiments under terminal anaesthetic using a FF photometry system, before taking histological images for analysis. Appropriate methodology is described in detail in **Chapter 3** and a roadmap is shown in **Figure 2.5.**

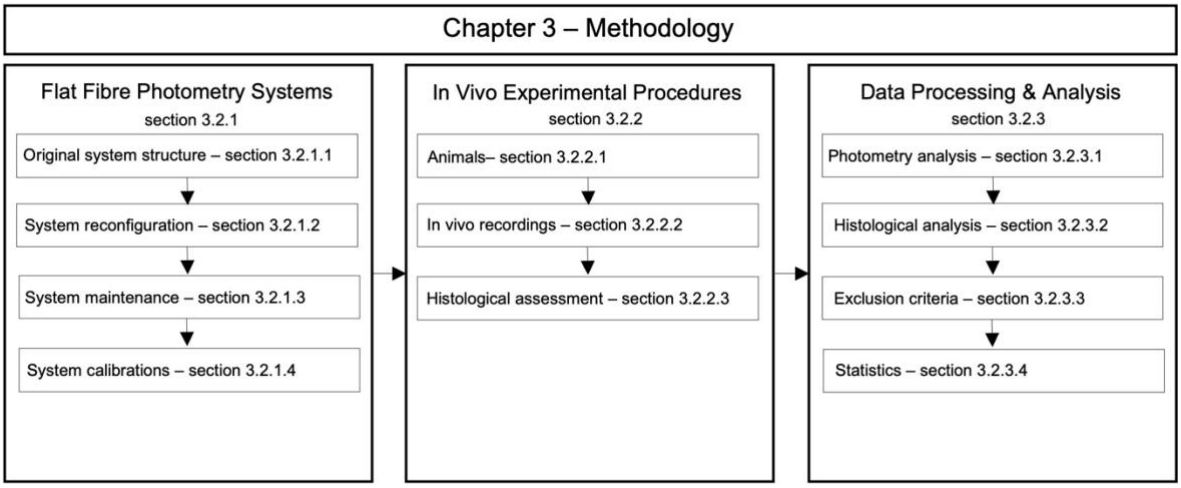

Figure 2.5. Roadmap of chapter 3 methodology. Protocols regarding the FF photometry system are explained within **section 3.2.1**. *In vivo* experimental procedures completed using the FF photometry system are described in **section 3.2.2**. Data processing and analysis is explained in **section 3.2.3**.

2.2.1 FF photometry systems

Initial experiments for a proof-of-concept study used FF photometry which is described in detail in the methodology section within **Chapter 3, section 3.2.1.** This section describes the original system structure **(section 3.2.1.1)**, system reconfiguration **(section 3.2.1.2)**, system maintenance **(section 3.2.1.3)** and system calibrations **(section 3.2.1.4) (Figure 2.5)**.

2.2.2 *In vivo* experiments

Mice underwent terminal anaesthetic, and several craniotomies were completed for a FF photometry recording. After, histological plaque pathology was quantified to confirm success of this novel approach. These experiments are described in detail in **Chapter 3, section 3.2.2.** This section describes the animals used **(section 3.2.2.1)**, *in vivo* recordings **(section 3.2.2.2)** and histological assessment **(section 3.2.2.3) (Figure 2.5)**.

2.2.3 Data processing & analysis

Approaches for processing and analysing photometry and histology data for chapter 3 experiments are described in **Chapter 3, section 3.2.3.** This describes photometry analysis **(section 3.2.3.1)**, histological analysis **(section 3.2.3.2)**, exclusion criteria **(section 3.2.3.3)** and statistical analysis **(section 3.2.3.4) (Figure 2.5).**

2.3 Chapter 4 Methodology

Chapter 4 illustrates real-time, depth-resolved capabilities of this novel approach by completing recordings on freely behaving mice. This was possible with use of TF photometry. Appropriate methodology is described in detail in **Chapter 4** and a roadmap is shown in **Figure 2.6.**

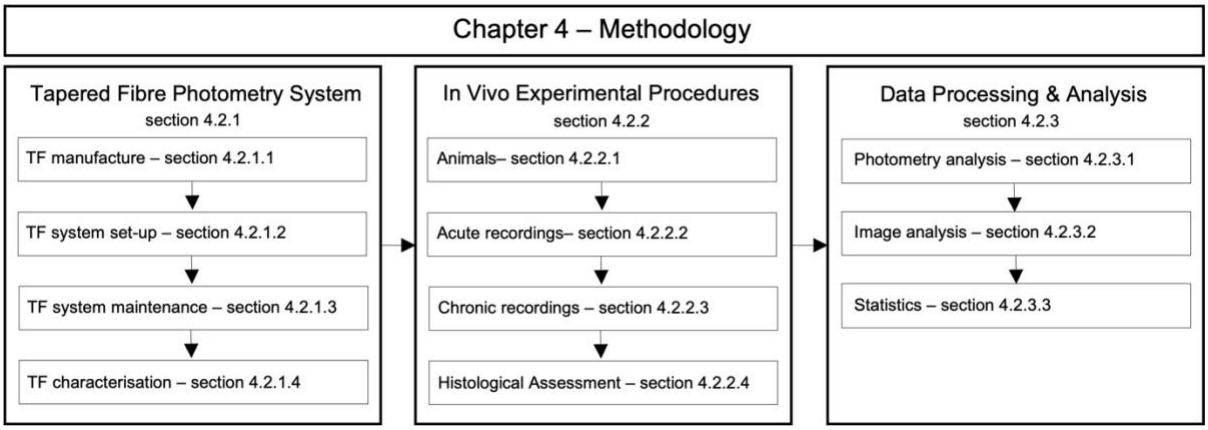

Figure 2.6. Roadmap of chapter 4 methodology. Protocols regarding the TF system are explained within **section 4.2.1**. *In vivo* experimental procedures completed using the TF system are described in **section 4.2.2**. Data processing and analysis for TF data is explained in **section 4.2.3**.

2.3.1 TF system

Once this novel method was proved feasible for monitoring plaques, long-term chronic recordings in awake, freely behaving mice were completed to investigate the possibility of detecting small changes in plaque pathology. These experiments were completed using TF photometry, which is described in detail in **Chapter 4, section 4.2.1.** This section describes TF manufacture **(section 4.2.1.1)**, TF system set-up **(section 4.2.1.2)**, TF system maintenance **(section 4.2.1.3)** and TF characterisation **(section 4.2.1.4) (Figure 2.6).**

2.3.2 *In vivo* experiments

In vivo recordings were completed using the TF photometry system to detect plaques in a real-time, depth-resolved manner in freely behaving mice. Appropriate procedures are explained in detail in **Chapter 4, section 4.2.2.** This includes a description of animals used **(section 4.2.2.1)**, acute recordings **(section 4.2.2.2)**, chronic recordings **(section 4.2.2.3)** and histological assessment **(section 4.2.2.4) (Figure 2.6).**

2.3.3 Data processing & analysis

Approaches for processing and analysing photometry and histology data for **Chapter 4** experiments are described in **Chapter 4, section 4.2.3.** This describes photometry analysis **(section 4.2.3.1)**, histological analysis **(section 4.2.3.2)** and statistical analysis **(section 4.2.3.3) (Figure 2.6).**

2.4 Chapter 5 Methodology

Chapter 5 illustrates the capability of this novel approach to monitor plaque pathology while mice undergo a potential AD treatment. The chosen treatment was GENUS; a non-invasive sensory stimulus approach, previously been shown to reduce plaque pathology. Appropriate methodology is described in detail in **Chapter 5** and a roadmap for **Chapter 5** methodology is shown in **Figure 2.7.**

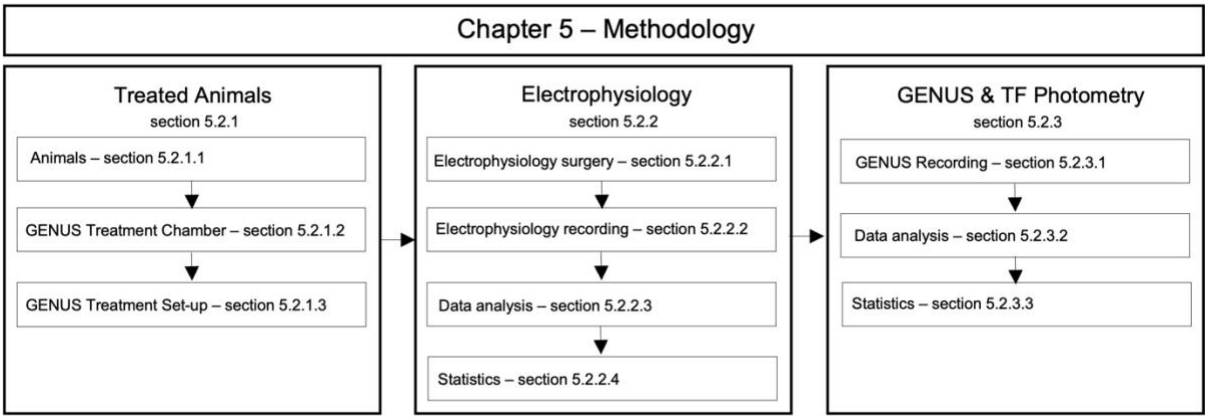

Figure 2.7. Roadmap of chapter 5 methodology. Animal information is covered in **section 5.2.1**. Electrophysiology procedures are described in **section 5.2.2**. GENUS & TF photometry procedures are described in **section 5.2.3**.

2.4.1 Treated Animals

Mice were used either for electrophysiology or GENUS & TF photometry experiments. For both, they were placed in a GENUS treatment chamber. These details are described in detail in **Chapter 5, section 5.2.1.** Animals used are described in **section 5.2.1.1** and the treatment chamber and set-up are described in **section 5.2.1.2 and section 5.2.1.3**, respectively **(Figure 2.7).**

2.4.2 Electrophysiology

As the potential AD intervention aimed to modify plaque pathology by increasing gamma power in the brain, we completed electrophysiology recordings while mice were exposed to GENUS treatment. These experiments are described in **Chapter 5, section 5.2.2.** This includes a description of the electrophysiology surgery **(section 5.2.2.1)**, recording **(section 5.2.2.2)**, data analysis **(section 5.2.2.3)** and statistics **(section 5.2.2.4) (Figure 2.7)**.

2.4.3 GENUS & TF Photometry

Plaque pathology was monitored using our TF photometry system while mice underwent GENUS treatment. These procedures are described in **Chapter 5, section 5.2.3.** This includes a description of the recording **(section 5.2.3.1)**, data analysis **(section 5.2.3.2)** and statistics **(section 5.2.3.3) (Figure 2.7).**

3. Real-time, *in vivo* plaque assessment at depth

3.1 Introduction

3.1.1 Background

As discussed in **Chapter 1**, plaques are a major hallmark of AD pathology, receiving much attention due to the 'amyloid hypothesis' suggesting its involvement in the progression of AD pathogenesis (Chen et al., 2017, Francis et al., 1999, Hampel et al., 2021). This resulted in detection and targeting of plaques being investigated for potential diagnosis and treatment possibilities. For example, recently FDA-approved amyloid sequestering antibody drugs, such as aducanumab (Budd Haeberlein et al., 2022, Schneider, 2020, Sevigny et al., 2016) and lecanemab (Swanson et al., 2021, van Dyck et al., 2023), target and bind to plaques for clearance from the CNS .

For such clinical studies to occur, many preclinical animal laboratory studies are completed using new treatments to screen for potential beneficial effects. To do so, the effect of the treatment on modifying plaque pathology is monitored. Approaches commonly used to do so include histology, PET scan, microdialysis (Cirrito et al., 2003, Yuede et al., 2016), and multiphoton imaging (Hefendehl et al., 2011, Klunk et al., 2002, Meyer-Luehmann et al., 2008). As previously mentioned, existing approaches have a variety of limitations that involve access to deeper brain regions, real-time feedback, and longitudinal recording in freely behaving conditions. Therefore, it can be considered that vital information regarding the effects of the tested interventions may be missed, resulting in a loss of information that could prove beneficial for the field. Consequently, we suggest that there is a requirement for a novel approach for plaque assessment that allows real-time, *in vivo* plaque assessment at depth.

3.1.2 Hypotheses and aims

Therefore, we hypothesise that combination of Methoxy-x04 and fibre photometry will allow detection of plaques, *in vivo*. To test this hypothesis, we aimed to confirm this novel approach is feasible to monitor plaque pathology. For this, we determined if there is a positive correlation between photometry and histology plaque signals. Histology signals were chosen as a comparison as this is a well-established method of plaque quantification.

3.1.3 Overview

Within this chapter, I will begin by describing the process taken to establish a successful novel approach for real-time assessment. This includes a description of the original FF photometry set-up, required system modifications and experimental procedures completed **(section 3.2).** Then, we show the inability to achieve strong Methoxy-x04 plaque signals *in vivo* with the original FF photometry system in **section 3.3.1**. Next, we illustrate that with appropriate system modifications, Methoxy-x04 plaque signals are detected **(section 3.3.2)** and the FF photometry signals are positively correlated with histological signals, a well-established method for plaque assessment **(section 3.3.3)**. However, we were unable to acquire real-time Methoxy-x04 signals using FFs **(section 3.3.4)**. Finally, we provide an overview of our findings and discuss their implications and potential limitations **(section 3.4)**. In all, we believe this illustrates the first use of fibre photometry to monitor plaque pathology, allowing collection of plaque signals at depth.

3.2 Methods

This section provides a description of the methodology used for confirmation of this novel approach **(Figure 3.2.1)**. Firstly, an overview of the fibre photometry system used for FF experiments is described, with an overview of the appropriate maintenance and calibration protocols **(section 3.2.1)**. Next, we introduce *in vivo* protocols with an overview of the animals used for these experiments, followed by a description *in vivo* recordings and histological assessment **(section 3.2.2)**. Lastly, data processing and analysis for photometry and histology is included, as well as the appropriate exclusion criteria and statistical analysis completed **(section 3.2.3)**. All protocols completed across various sub-projects, such as Methoxy-x04 properties, animals and histological processing are discussed in **Chapter 2** in **sections 2.1.1, 2.1.2 and 2.1.3**, respectively.

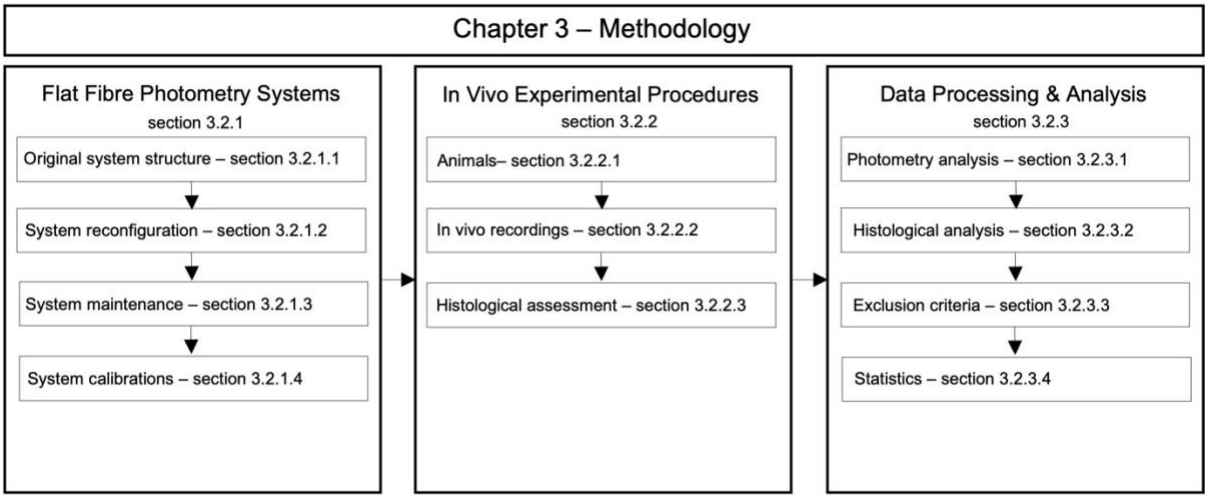

Figure 3.2.1. Roadmap of chapter 3 methodology. Protocols regarding the FF photometry system are explained within **section 3.2.1**. *In vivo* experimental procedures completed using the FF photometry system are described in **section 3.2.2**. Data processing and analysis is explained in **section 3.2.3**.

3.2.1 FF photometry systems

The FF photometry system was previously built and characterized by Dr Niall McAlinden and Dr Amisha Patel (Patel et al., 2020) **(Figure 3.2.2)**. The original FF photometry set-up excited Methoxy-x04 with 405-nm light, a control measure at 470-nm light, with emission light collected at 525-nm **(Figure 3.2.3A)**. Experiments showed that Methoxy-x04 was detected *in vitro*, but not *in vivo*, resulting in a reconfigured system being used: excitation at 405-nm, with collection of emitted light at 440 and 550-nm **(Figures 3.2.3B & Figure 3.2.4)**.

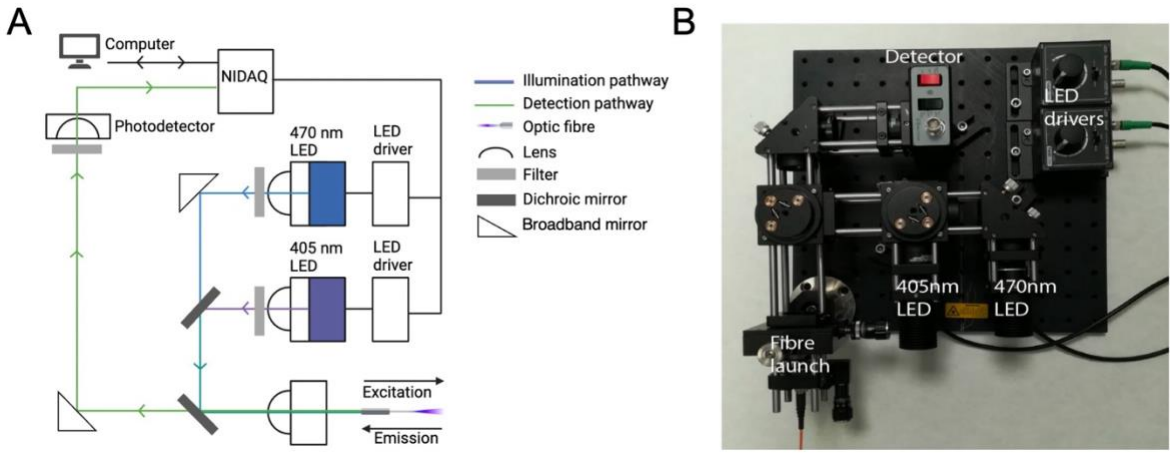

Figure 3.2.2. Original FF photometry system set-up. (A) Schematic of the system configuration. Created with BioRender.com. (B) Image of the system. Adapted from Patel *et al*., 2020 (Patel et al., 2020).

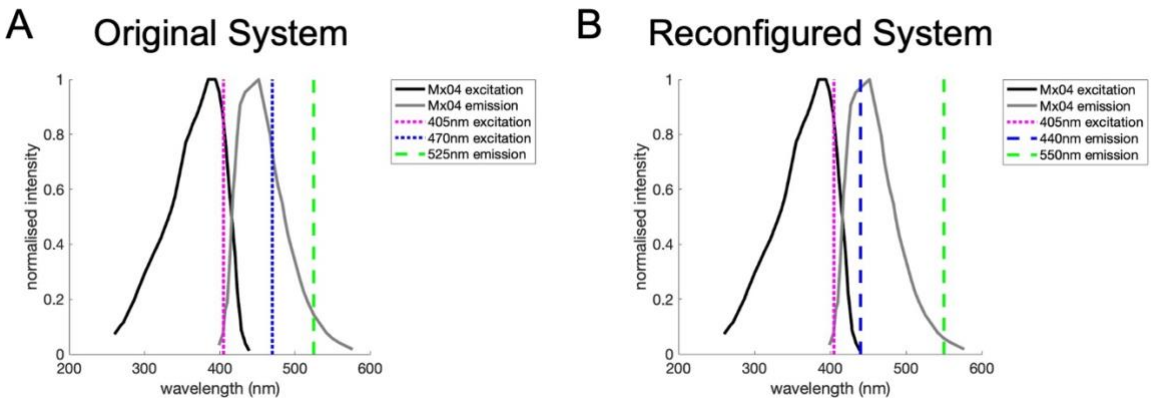

Figure 3.2.3. Methoxy-x04 spectra with optical system parameters for the original and reconfigured system. Excitation/emission spectrum of Methoxy-x04 with wavelengths used for excitation and emission in the original system (*A*) and reconfigured system (*B*) shown. Thin dashed lines represent LED excitation. Thick dashed lines represent emission filters. Wavelengths are colour coded.

3.2.1.1 Original System Structure

The FF photometry system consists of two light pathways: illumination and detection **(Figure 3.2.2)**. The illumination pathway has 2 LEDs – 405 (M405L3, Thorlabs) and 470-nm (M470L3, Thorlabs) – controlled by two LED drivers (LEDD1B, Thorlabs), that project light through the system. Light from each LED was collimated using an aspheric lens (f = 20-mm, numerical aperture (NA) = 0.54) (AL2520M-A, Thorlabs) before being filtered using bandpass filters (FB405-10 and FB470-10, Thorlabs). 405 and 470-nm light paths merge onto a 425-nm long-pass dichroic mirror to combine both beams (DMLP425R, Thorlabs). Then, after reflecting off a 498-nm long-pass dichroic mirror (MD498, Thorlabs), light was directed towards the fibre launch system (KT110/M, Thorlabs) where appropriate light-path alignment and an aspheric lens (f = 20-mm, NA = 0.54) (AL2520M-A, Thorlabs) coupled the light into a low AF multimode patch cable (MAF3L1, Thorlabs). This cable was connected to an implantable FF (CFM52L10, Thorlabs), via a mating sleeve (ADAF1-5, Thorlabs). Finally, light output from the FF tip allows excitation of fluorophores **(Figure 3.2.2)**.

The detection pathway collects light from the FF and delivers it to a photodetector (NewFocus 2151, Newport) for measurement. After travelling back along the cable to the fibre launch system, light is collimated by the same aspheric lens used in the illumination pathway. Light passes through the 498-nm long-pass dichroic mirror (MD498, Thorlabs) and is directed toward the photodetector using a broadband mirror (BB1-E02, Thorlabs), before passing through a 525-nm emission filter (MF525-39-GFP, Thorlabs) to exclude excitation light. Finally, light is focused onto the

photodetector using an aspheric lens **(Figure 3.2.2)**. Signals collected at the photodetector were then digitized to analogue signals using a NIDAQ device (NI USB-6211, National Instruments).

The system components were controlled by the NIDAQ device and custom LABVIEW code (written by Dr Shuzo Sakata). All components are mounted to an optical breadboard using cage rods, post holders and optical mounts to create a stable structure for all optical elements (ER2-P4, ER2.5-P4, ER1-P4, UPH50/M and TRM0/M-P5, Thorlabs). All filters, aspheric lenses and mirrors were stabilised in filter holders (C4W, B4C/M and FFM1, Thorlabs), lens tubes (SM103-P5, Thorlabs), cage plates (CP08/M, Thorlabs) and mirror mounts (KCB1C/M, Thorlabs) **(Figure 3.2.2B)**. All components – patch cable, FF, and mating sleeve – had a 2.5-mm setting for ferrules. The patch cable and FF parameters chosen were 400-µm, 0.50˚ low AF patch cable (MAF3L1, Thorlabs) and a 200-µm, 0.50˚ FF (CFM52L10, Thorlabs). An in-depth description of the construction of this system is provided by Patel and colleagues (Patel et al., 2020).

3.2.1.2 System Reconfiguration

A system reconfiguration involved 405-nm excitation and emission collection at 440 and 550-nm **(Figure 3.2.4A)**. This should provide a strong Methoxy-x04 signal at 440-nm, while tissue AF can be detected at 550-nm **(Figure 3.2.3B)**. This system reconfiguration was designed by Dr Niall McAlinden and Nicole Byron and was completed by Nicole Byron.

Before system reconfiguration occurred, the light output was measured, and system calibration was completed for reference. Firstly, 425-nm and 498-nm long-pass dichroic mirrors were swapped to modify the system for one LED excitation path only **(Figure 3.2.4B)**. Secondly, two detection pathways were established by replacement of the 525-nm emission filter (MF525-39 – GFP, Thorlabs) with a 440 or 550-nm emission filter (FB440-10 and FB550-10, Thorlabs) held in a drop-in filter holder (DCP1, Thorlabs) **(Figure 3.2.4C)**. For this, the detector, lens tube and lens were removed to allow removal of the 525-nm filter. Then, the detector, lens tube and lens were replaced, and the new filters were attached to the cage mount before the lens using the drop-in filter holder. Once these amendments were made, the system was realigned by small alterations of the mirrors (**Figure 3.2.4C**) to enhance light output and intensity of fluorescence recorded on the photodetector. Only once the system was providing light outputs and fluorescent read-outs as before, the system reconfiguration was complete.

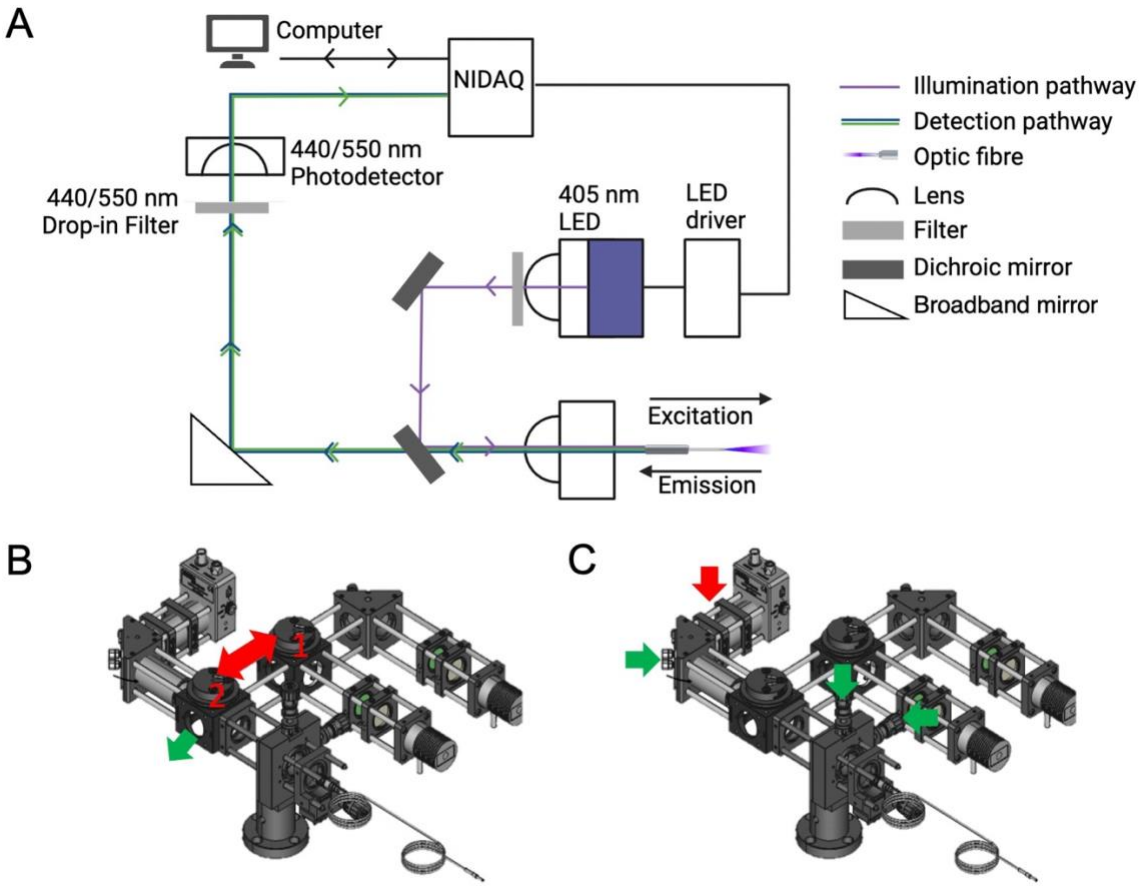

Figure 3.2.4. Reconfigured FF photometry system set-up. (A) Schematic of the system configuration. Created with BioRender.com. (B) Schematic showing the system changes completed throughout step 1 of this reconfiguration, involving swapping dichroic mirrors. Red arrows show the swap of mirrors and points used for realignment. The green arrow shows the light flow desired after the mirror swap. (C) Schematic showing the system changes completed throughout step 2 of this reconfiguration, involving changing the detection pathway. Red arrows show region of changes. Green arrows show regions used for realignment. Adapted from Patel *et al*., 2020 (Patel et al., 2020).

3.2.1.3 System Maintenance

The FF photometry system was regularly monitored to ensure light output from the FF and fluorescent output was consistent. This involved several procedures: measuring light output from the patch cable and FF tip, photobleaching of the patch cable and system calibrations with Methoxy-x04 (4920, Tocris) **(Figure 3.2.5)**. Firstly, to ensure the light path was appropriately aligned and remained constant, the light output at the end of the patch cable (MAF3L1, Thorlabs) and FF tip (CFM52L10, Thorlabs) was consistently measured with a light sensor (PM100A and

S120C, Thorlabs). This allowed calculation of the coupling efficiency of the system with the FF as follows:

$$\text{coupling efficiency (\%)} = \frac{P_P}{P_o}\ x\ 100,$$

where P_p and P_o represent the light output at the end of patch cable (MAF3L1, Thorlabs) and FF (CFM52L10, Thorlabs), respectively. If misaligned, this would be measured while altering the angle of the mirrors **(Figure 3.2.4C**) until light output was optimal. Secondly, *in vitro* calibrations with Methoxy-x04 (4920, Tocris) were completed to ensure the fluorescent output remained consistent. This experimental procedure is described in **section 3.2.1.4.1**. Thirdly, as patch cable AF can interfere with signal collection, photobleaching of the patch cable (MAF3L1, Thorlabs) was completed by leaving the LED (M405L3 and M470L3, Thorlabs) on continuously at full power to cause a decay of AF within the fibre and cladding. This involved an initial bleaching session lasting >8-hours, followed by a 1-hour top-up before each use. Fluorescence was measured at the photodetector (NewFocus 2151, Newport) at a sampling frequency of 1000-Hz, controlled by the NIDAQ device (NI USB-6211, National Instruments) and custom LABVIEW code. All measurements were completed in the dark.

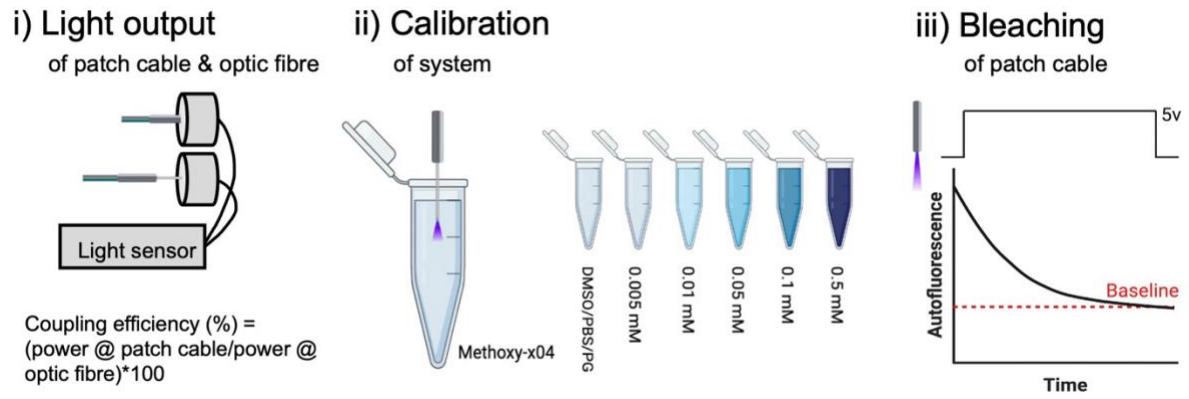

Figure 3.2.5. Fibre photometry system maintenance experiments. Schematic showing the experimental set-up for system maintenance experiments completed. Created with BioRender.com.

3.2.1.4 System calibrations

After all system calibrations, the FF (CFM52L10, Thorlabs) was submerged in enzyme remover (Superdrug) for several minutes, followed by several minutes in distilled water and finished by a few dips in propranol for sterilisation. All measurements were completed in dark conditions.

3.2.1.4.1 System Calibration

The system was characterised with a range of Methoxy-x04 concentrations (0.005, 0.01, 0.05, 0.01 and 0.1-mM) (4920, Tocris). A FF (CFM52L10, Thorlabs) was submerged into each concentration – from lowest to highest – and underwent an illumination protocol. This illumination protocol was 10-ms ON, 5-ms OFF (10 repetitions) separated by a 10-ms baseline, across several powers. This protocol ran through the LED(s) (M405L3 and M470L3, Thorlabs), collecting data at the photodetector(s) (NewFocus 2151, Newport) at 5000-Hz, controlled by the NIDAQ device (NI USB-6211, National Instruments) and custom LABVIEW code.

3.2.1.4.2 System Sensitivity

System sensitivity was established by determining the lowest Methoxy-x04 (4920, Tocris) concentration the system can detect. A FF (CFM52L10, Thorlabs) was submerged into a solution of 10% DMSO/45% propylene glycol/45% PBS. After 10 or 30-minutes of baseline recording, Methoxy-x04 (0.01-mM) was added every 2-minutes to increase the concentration in 5-nM steps until 300-nM or 100-nM, for the original and reconfigured system respectively. To aid diffusion, the solution is in a 24-well plate with a magnetic bar, situated on a stirrer (US152, Stuart). The illumination protocol was reduced to prevent photobleaching: 10-ms ON, 5-ms OFF (5 repetitions) separated by a 5-ms baseline, across several powers, with a sampling interval of 5-s. In parallel, fluorescence was collected at the detector (NewFocus 2151, Newport) at 5000-Hz, controlled by the NIDAQ device (NI USB-6211, National Instruments) and custom LABVIEW code.

3.2.2 *In vivo* experimental procedures

3.2.2.1 Animals

Table 3.2.1. Animals used for all FF photometry experiments. The final column represents the type of FF photometry experiment that was completed. DP: depth profile. APK: acute pharmacokinetic.

System used	Mouse ID	Genotype	Sex	Age (mo)	Exp type
Original	FAD1	5xFAD+	M	8.55	DP
	FAD2	5xFAD+	F	6.48	DP
	FAD3	5xFAD+	M	6.21	DP
	FAD4	5xFAD-	F	6.51	DP
	FAD5	5xFAD+	M	5.56	DP
	FAD6	5xFAD-	M	5.59	DP
Reconfigured	FAD7	5xFAD+	M	8.12	APK
	FAD8	5xFAD+	M	8.75	APK
	FAD9	5xFAD+	F	8.78	APK
	FAD11	5xFAD+	F	8.45	DP
	FAD12	5xFAD-	F	8.48	DP
	FAD13	5xFAD+	M	8.52	DP
	FAD15	5xFAD+	F	7.73	APK
	FAD16	5xFAD-	F	7.99	DP
	FAD18	5xFAD+	F	8.38	APK
	FAD19	5xFAD+	M	5.46	APK
	FAD20	5xFAD+	M	8.42	DP
	FAD21	5xFAD-	M	8.45	DP
	FAD22	5xFAD+	M	6.84	DP
	FAD23	5xFAD-	M	6.87	DP
	FAD41	5xFAD+	M	7.63	DP
	FAD42	5xFAD+	M	6.87	DP
	FAD46	5xFAD-	F	8.94	DP
	FAD47	5xFAD+	F	6.87	DP
	FAD48	5xFAD-	F	6.90	DP
	FAD49	5xFAD-	M	6.97	DP
	FAD50	5xFAD+	M	7.13	DP
	FAD53	5xFAD-	F	8.42	DP
	FAD54	5xFAD-	M	7.10	DP
	FAD55	5xFAD-	M	7.13	DP

Detailed animal information was described in **Chapter 2, section 2.1.2**. For FF photometry experiments, 6-9-month-old male and female 5xFAD+ and 5xFAD- mice were used **(Table 3.2.1)** (JAX006554, The Jackson Laboratory). A total of 30 mice were used for all FF photometry experiments **(Figure 3.2.6).** A total of 24 mice were used for all depth profile experiments, with 6 being used with the original FF photometry system and 18 being used for protocol confirmation

with the reconfigured FF photometry system. Six mice were used for acute pharmacokinetic experiments. Both depth profile and acute pharmacokinetic experiments involved surgery and FF photometry recordings under terminal anaesthetic before brain tissue was recovered for post-mortem analysis.

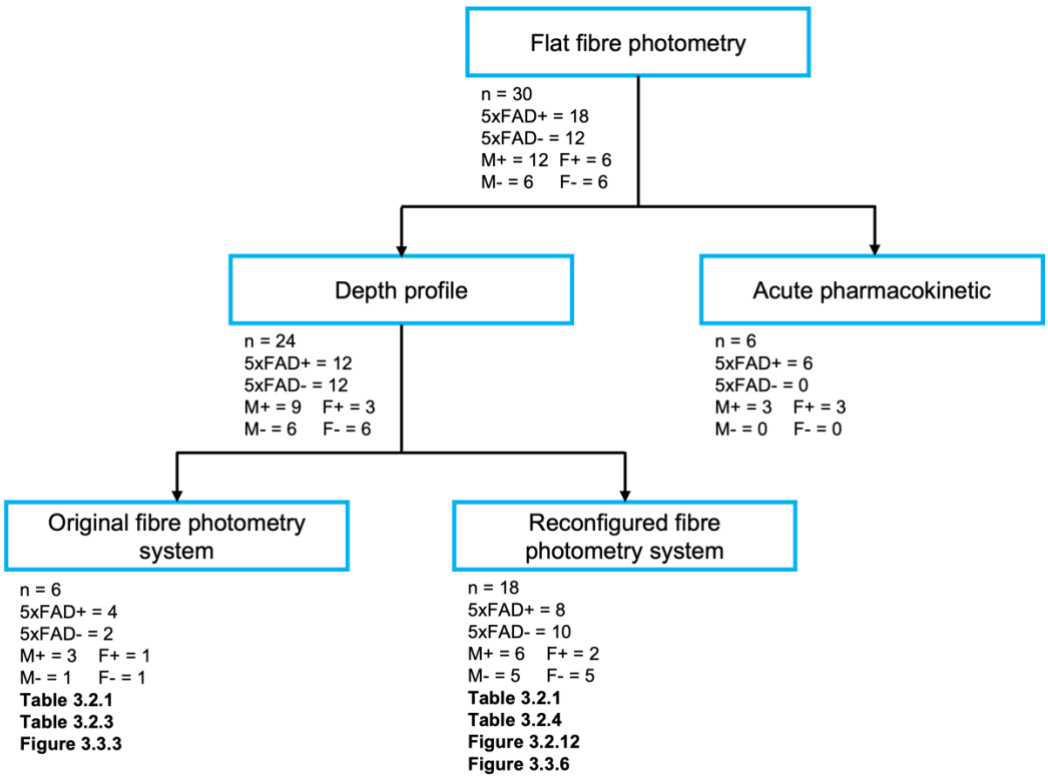

Figure 3.2.6. Flow chart illustrating the genotype and number of animals used for all FF photometry experiments. The sample numbers for each type of experiment are shown with the number of each genotype and sex used. Not all mice included here made it through the exclusion criteria. Tables and figures refer the reader to further animal breakdown.

3.2.2.2 In vivo recordings

Before any *in vivo* measurement, the FF would be submerged in propranol for sterilisation. After all *in vivo* measurements, the FF was cleaned by being submerged in enzyme remover (049008, Superdrug) for several hours, followed by several minutes in distilled water and finished by a few dips in propranol for sterilisation. All *in vivo* measurements were completed in dark conditions.

3.2.2.2.1 Terminal anaesthesia and craniotomies

For all FF photometry experiments, 5xFAD+ and 5xFAD- littermates underwent terminal anaesthesia and craniotomies **(Figure 3.2.7)**. On the day of recording, mice underwent terminal

anaesthetic (20% urethane). Before surgery, 60% of the urethane dose (1.5 g/kg) was given through a series of 4-injections spaced 15-minutes apart. Post-surgery the remainder of the urethane dose was administered, if required. Throughout surgery, the anaesthetic plane was enhanced by placing the mouse in an anaesthetic chamber where isoflurane (Covetrus) was maintained between 5% and 0.8 L/min air flow until the mouse is fully immobile, before being reduced to 3% and 0.8 L/min air flow. Once under, the head was shaved, and the mouse was placed on an incisor breather for administration of isoflurane (Covetrus) and oxygen via a nose cone. Anaesthetic (isoflurane) was maintained between 1.5% and 1% and 0.8 L/min air flow. Eyes were protected by application of eye gel (Lacri-lube, Hylonight or Viscotears, Bausch&Lomb) and the mouse was maintained at 37°C by being placed on a heat mat (ATC 100, World Precision Instruments), under a surgical light (KL 1500, Lambda Photometrics) **(Figure 3.2.7)**. Breathing and pinch reflexes were monitored throughout the surgery and levels of anaesthetic were adjusted accordingly.

The mouse was stabilized by ear-bars attached to a stereotaxic frame (KOPF Instruments). Then, the surgical area was cleaned using cotton buds (Johnson's) with ethanol (70%) and betadine (Alkaloid). Using a scalpel (847-7584, RS Components), an incision along the midline was made that was expanded with surgical scissors to create a 2-mm wide circle around the midline, exposing bregma and lambda. To remove the periosteal membrane, hydrogen peroxide (3%) was applied to the skull surface and debris was removed with a cotton bud (Johnson's) and scissors. Next, skull alignment between bregma and lambda was set between 0-50-μm, before marking the craniotomy sites, under a stereomicroscope (SZ51, Olympus) using a glass pipette (504949, World Precision Instruments) made with a pipette puller (PC-10, Narishige), held by the stereotaxic frame manipulator (KOPF Instruments). For depth profile experiments completed on the original system configuration, there were two craniotomy sites for Site 1 (AP: +0.30-mm, ML: 0.25-mm), and Site 2 (AP: -3.27-mm, ML: 1.75-mm). For depth profile experiments completed on the reconfigured system craniotomy sites were modified for Site 1 (AP: +0.49-mm, ML: 0.25-mm), Site 2 (AP: -1.79-mm, ML: 1.50-mm), and Site 3 (AP: -3.30-mm, AP: 2.80-mm) **(Figure 3.2.9B)**. For acute pharmacokinetic experiments, a craniotomy was completed above the SUB: (AP: -3.80-mm, ML: 3.30-mm, DV: 2.50-mm) **(Figure 3.2.10B)**. These craniotomies were completed using a surgical drill (Volvere Vmas drill, NSK) and a duratomy was performed using craniotomy scissors to aid insertion of FFs. Lastly, to protect brain tissue, KwikSil (World Precision Instruments) was applied over the craniotomy sites and removed before recordings.

For depth profile and acute pharmacokinetic experiments completed using the original system configuration, recordings were completed while the mouse remained on the stereotaxic frame (KOPF Instruments) used for craniotomies **(Figure 3.2.7)** with a low maintenance of isoflurane (Covetrus), if required. Whereas, for depth profile experiments completed on the reconfigured

system, the mouse was taken off anaesthetic (isoflurane), removed from the stereotaxic frame (KOPF Instruments) and placed in its home-cage for transfer to another recording set-up **(Figure 3.2.8)**. Here, the mouse was placed on a heat mat maintained at 37˚C (Harvard apparatus), stabilized by ear-bars attached to a stereotaxic frame (Thorlabs and Narishige), under a surgical light (PL2000, Photonic) before skull alignment between bregma and lambda was set to 0-50 μm using a glass pipette (504949, World Precision Instruments).

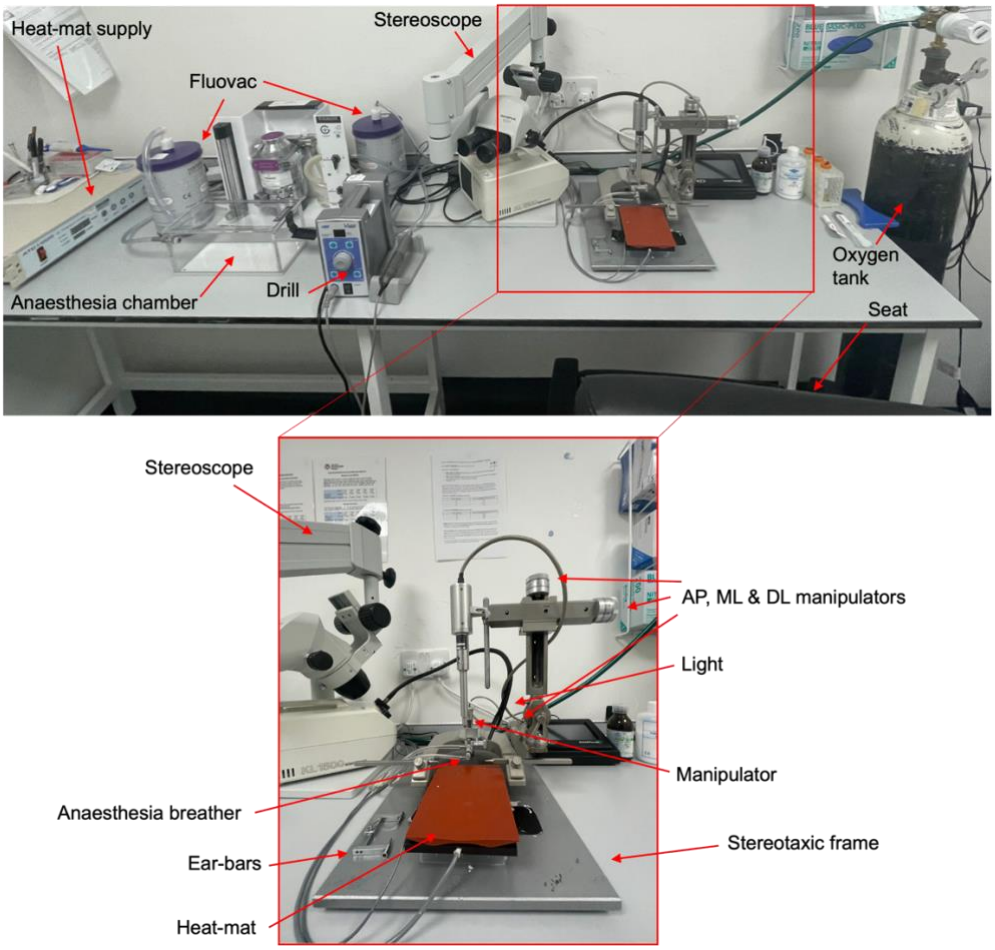

Figure 3.2.7. Set-up for the craniotomy surgery.

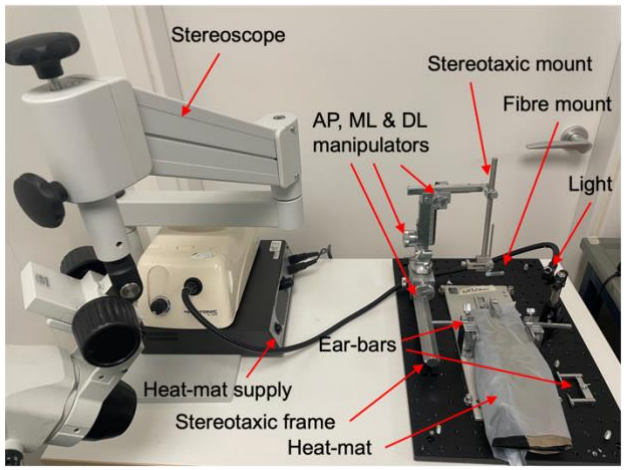

Figure 3.2.8. Recording rig set-up.

3.2.2.2.2 Depth profile recordings

Depth profile recordings were completed as a proof-of-concept investigation to illustrate that we could acquire photometry signals that are well correlated with histological quantification across the DV axis of the Methoxy-x04 stained brain. 24-hours before recording, mice were injected (i.p.) with 10-mg/kg of Methoxy-x04 (5-mg/ml) **(Figure 3.2.9A)** (4920, Tocris). This was completed 24-hours before as this was consistent with previous studies and the landmark Methoxy-x04 paper (Klunk et al., 2002). After craniotomies under terminal anaesthesia were completed, mice underwent a recording protocol for depth profile experiments.

A 10-mm long FF (200-μm core diameter, 0.50˚ NA) (CFM52L10, Thorlabs) was used. Using the stereotaxic frame (Thorlabs and Narishige), the fibre was positioned directly above the target site **(Figure 3.2.9B)** before lowering to the brain surface. A measurement was taken at 0-μm before beginning to lower the fibre in 100-μm steps, with recordings occurring at each depth **(Figure 3.2.9A)**. The final depth was 4000-μm, before slowly removing the FF from the brain. This was completed for all craniotomy sites. Once the recording was complete, the mouse was removed from the stereotaxic frame (Thorlabs and Narishige) and placed in home cage (on a heat mat), before removal of brain tissue **(**see **section 3.2.2.3.1)**.

This illumination protocol was 10-ms ON, 5-ms OFF (10 repetitions) separated by a 10-ms baseline, for several powers. For the original system, powers ranged from 0.1 to 5-V. For the reconfigured system, powers ranged from 0.1 to 1-mW/mm^2. The voltage required for each desired irradiance was calculated by creating a linear regression model using the light output from the FF, measured using the light sensor (PM100A and S120C, Thorlabs) as described in **section 3.2.1.3**. This protocol ran through both LEDs (M405L3 and M470L3, Thorlabs), depending on the system configuration, collecting data at the photodetector (NewFocus 2151, Newport) at 5000-Hz,

controlled by the NIDAQ device (NI USB-6211, National Instruments) and custom LABVIEW code. For depth profile measurements completed on the reconfigured system, the 440 and 550-nm filter (FB440-10 and FB550-10, Thorlabs) was manually swapped, using the drop-in filter holders (DCP1, Thorlabs), between each illumination protocol to get a measurement at each wavelength, at each depth. Digitised data was stored for off-line analysis. A custom MATLAB code was used to extract signals and detect events from the data files as described in **section 3.2.3.1**.

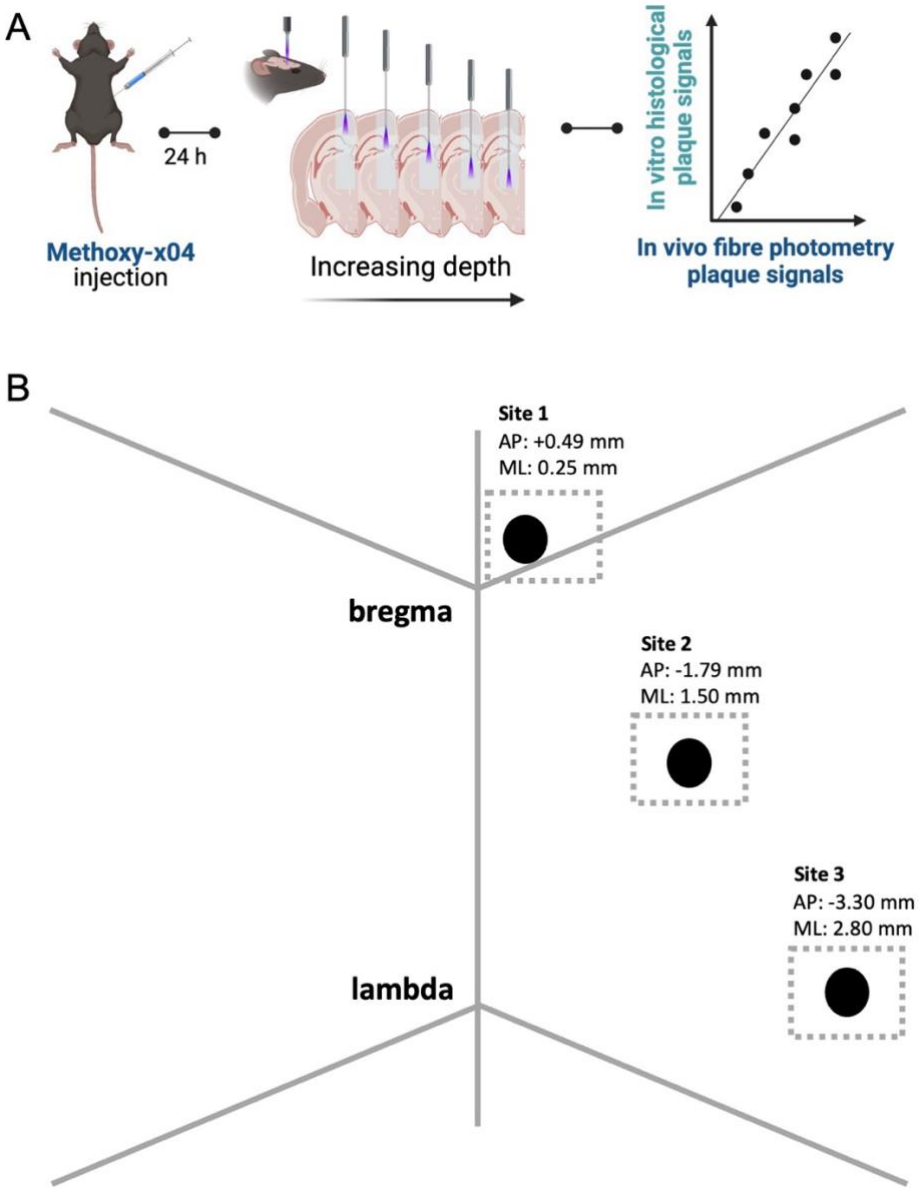

Figure 3.2.9. Experimental design for depth profile measurements. (A) Schematic showing the experimental set-up. Created with BioRender.com. (B) Craniotomy (grey) and target implantation site (black) coordinates, for Site 1 (top), Site 2 (middle) and Site 3 (bottom), used in depth profile measurements with the reconfigured system. Diagram not to scale.

3.2.2.2.3 Acute pharmacokinetic recording

An acute pharmacokinetic recording was completed to identify if we could monitor small changes in Methoxy-x04 concentration over-time on a single day, replicating what we could potentially see once administering a plaque-modifying therapeutic, while also gaining information about the rate of entry of Methoxy-x04 to the brain. A 10-mm long FF (200 μm core diameter, 0.50˚ NA) (CFM52L10, Thorlabs) was used. Using the stereotaxic frame (KOPF Instruments), the fibre (CFM52L10, Thorlabs) was positioned directly above the target site **(Figure 3.2.10B)** before lowering to the brain surface. Depth profile measurements, as described in **section 3.2.2.3.2**, were completed to determine if the target site was reached by detecting an increase in fluorescence indicative of a plaque dense region. Once the target was reached, the recording began. The recording protocol involved a 30-minute baseline recording before injection (i.p.) of 10-mg/kg of Methoxy-x04 (5-mg/ml) (4920, Tocris). Then, the pharmacokinetic profile of Methoxy-x04 was recorded for as long as the mouse remained stable under urethane **(Figure 3.2.10A)**. Once the recording was complete, the mouse was taken off anaesthetic (isoflurane), removed from the stereotaxic frame (KOPF Instruments), and placed in home cage (on a heat mat), before removal of brain tissue **(**see **section 3.2.2.3.1)**.

This illumination protocol was 10-ms ON, 5-ms OFF (5 repetitions) separated by a 5-ms baseline, with a 30-second sampling interval. This protocol ran through several irradiances of the 405-nm LED (M405L3, Thorlabs), collecting data at the photodetector (NewFocus 2151, Newport) at 5000-Hz, controlled by the NIDAQ device (NI USB-6211, National Instruments) and custom LABVIEW code. Specifically, powers ranged from 1 to 5-V or from 0.1 to 1-mW/mm^2. As it was completed on the reconfigured system, the acute pharmacokinetic recording was measured with the 440-nm filter only (FB440-10, Thorlabs). Digitised data was stored for off-line analysis. A custom MATLAB code was used to extract signals and detect events from the data files as described in **section 3.2.3.1**.

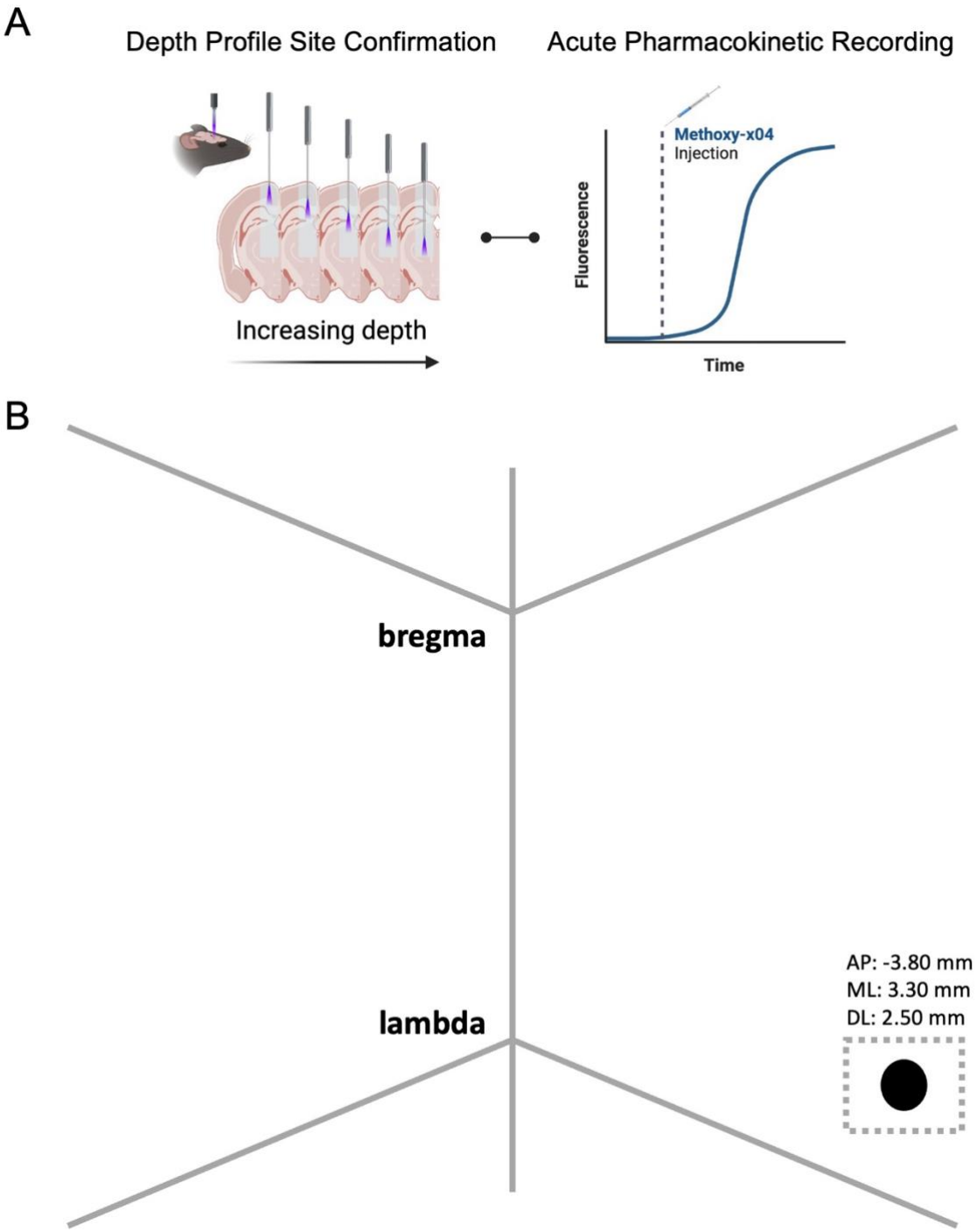

Figure 3.2.10. Experimental design for acute pharmacokinetic experiments. (A) Schematic showing the experimental set-up. Mice underwent terminal anaesthetic before implanting a FF at increasing depths in the brain to detect the target site. Pharmacokinetic recordings were completed, with Methoxy-x04 (10-mg/kg) being injected i.p. after a 30-minute baseline. Lastly, histological sections were used to assess the implant site. Created with BioRender.com. (B) Craniotomy (grey) and target implantation site (black) coordinates, for the SUB. Diagram not to scale.

3.2.2.3 Histological assessment

3.2.2.3.1 Tissue Removal

Immediately after *in vivo* recordings, mice were injected (i.p.) with lidocaine (2%)/naropin (7.5-mg/ml solution, Aspen) and pentobarbital (200-mg/ml solution, Vetoquinol) before transcardial infusion with PBS (0.1-M) (20-mL) and then immediately after, 4% paraformaldehyde (PFA) (20-mL). Brain tissue was removed and post-fixated in 4% PFA (10-mL) overnight at 4°C. Next, fixed brain tissue was submerged in 30% sucrose/0.1-M PBS for several days. Once sunk, processed brain tissue was sectioned into 100-μm slices using a microtome (SM2010R, Leica). Dry ice allowed OCT (OCT Embedding Matrix, CellPath) to attach the brain tissue onto the microtome stage for sectioning. Each section was immediately placed into a 24-well plate filled with PBS + 0.02% sodium azide and stored at 4°C until histological processing.

3.2.2.3.2 Histology

Table 3.2.2. Histological protocol for FF experiments. Headings show the target of the stain with colours representing the colour channel it was imaged in.

	Stain used for each channel		
Experiment Type	**Plaque**	**Plaque**	**Nissl**
Depth Profile – Original System	Methoxy-x04	Thioflavin-S	Neurotrace-Red
Depth Profile – Reconfigured System	Methoxy-x04		
Acute Pharmacokinetic	Methoxy-x04	Thioflavin-S	Neurotrace-Red

As all mice will have been injected with Methoxy-x04 within the recording protocols, all their histological sections will contain Methoxy-x04 plaque signals. For depth profile measurements completed on the original system configuration and acute pharmacokinetic measurements, free-floating sections were also stained with plaque-marker, TS (T1892, Sigma-Aldrich), and nissl marker, Neurotrace-red (NT-r) (Fisher), for analysis of the plaque pathology and fibre track, respectively **(Table 3.2.2)**. Free-floating sections containing the fibre implant targets and 500-μm adjacent sections were stained. These sections were floating within a 24-well plate for washing (3 x 10-minutes in PBST (0.3% Triton X in PBS)) before a 15-minute incubation at room temperature in TS (0.01%, plaque marker; T1892, Sigma-Aldrich) and NT-r (0.1%, nissl marker; Fisher) on an orbital shaker (Mini Orbital Shaker SSM1, Stuart) (dark conditions). After, sections were washed (3 x 5-minutes in PBS) before rinsing in Gelatin solution (0.5%) and mounting onto glass slides.

Whereas, for brain tissue from depth profile experiments completed on the reconfigured system, free-floating sections underwent washing (3 x 5-minutes in PBS) before rinsing in Gelatin solution (0.5%) and mounting onto glass slides **(Table 3.2.2)**. Slides air-dried overnight before being sealed with cover slips using fluoromount solution (Invitrogen, ThermoFisher Scientific Fluoromount G). These staining protocols were different because at first, we wanted to confirm the Methoxy-x04 labelling with a back-up plaque stain and use a Nissl stain to help identify brain architecture. However, we found that this was not necessary and therefore, continued with Methoxy-x04 only.

3.2.2.3.3 Imaging

All images were taken using an upright Nikon Eclipse E600 epifluorescent microscope (TheMicroscopeCompany, UK) and an ORCA-spark Digital CMOS camera (C11440-36U, Hamamatsu). For acute pharmacokinetic and depth profile experiments using the original system configuration, 960x600 pixel images were taken using Strathclyde electrophysiology software (WinFluor 3.7.3) with an exposure time of 1000-ms, at 4x magnification. All other images were taken using a custom LABVIEW code. These were 1920x1200-pixel images taken with an exposure time of 500-ms, at 4x magnification.

Brain regions implanted with the FF were identified. Once identified, the whole brain section was imaged for post-mortem analysis. It is vital to image any sections that include part of the fibre track and some sections anterior and posterior to the implant site for analysis.

3.2.3 Data processing and analysis

3.2.3.1 Photometry analysis

3.2.3.1.1 Pre-processing

Digitised data was stored for off-line analysis by a custom MATLAB code. Firstly, data was offset to allow the minimal signal in LED OFF periods to be 0 by adding the mean of the signals from the first 5-ms of each channel. Then, events were detected by extracting signals greater than 0.05-V in the LED sync channels, as this illustrated LED ON periods. From this, event times are extracted and used to extract data from the photodetector channel(s) for signal processing. Then, data from the signal channel(s) is extracted from time sample 3-ms to 9-ms for each repetition, for all detected events. A median, mean, and standard error of mean (SEM) is calculated from these repetitions, providing the final output for each event. An event is classed as a time where the LED is turned on, at a single irradiance of one wavelength.

3.2.3.1.2 Data processing

3.2.3.1.2.1 *In vitro* experiments

For system calibration measurements **(section 3.2.1.4.1)** as shown in **Figures 3.3.1B and 3.3.4B**, the mean and SEM of fluorescence at each concentration and irradiance was determined across experimental repetitions and compared.

For system sensitivity measurements **(section 3.2.1.4.2)** as shown in **Figures 3.3.1C and 3.3.4C**, the median fluorescent signal across time, at one concentration was calculated. This allowed determination of the mean sensitivity threshold; the lowest concentration of Methoxy-x04 where an increase in fluorescence was seen.

3.2.3.1.2.2 *In vivo* experiments

Initially, to determine if the system was detecting Methoxy-x04-stained plaques from depth profile experiments **(section 3.2.2.2.2)**, exemplar and summary data was analysed. For the original system, data excited at both 405 and 470-nm (Excitation) was used. For the reconfigured system, data collected at both 440 and 550-nm (Emission) was used. For both the original and reconfigured system, only the highest illumination power was used: 5-V and 1-mW/mm^2 respectively. For exemplar data, as shown in **Figures 3.3.3D-E and 3.3.6D-F**, the change in fluorescence was calculated by baseline normalisation that involves scaling the mean raw fluorescence to the mean raw fluorescence from 0-500-µm, using the formula:

$$dF = \frac{F - mean(F_{D0-500})}{mean(F_{D0-500})}$$

where dF is the change in fluorescence, F is the raw fluorescence at each depth and $F_{D0\text{-}500}$ is the raw fluorescence from 0-500-µm. This was completed to identify changes from the baseline signal at the brain surface. For summary analysis, as shown in **Figures 3.3.6G-I**, the mean and SEM of the scaled fluorescence (as above) was calculated across recordings. Additionally, to acquire a smoothed profile, the moving median over 500-µm was calculated.

For FF photometry and histology correlation analysis **(section 3.2.3.2.2)**, as shown in **Figure 3.3.7**, only data collected at 440-nm and excited at 1-mW/mm^2 was used. Then, then change in fluorescence was calculated by minimum-based normalisation that involves scaling the mean raw fluorescence at each depth to the minimum raw fluorescence across depths, using the formula:

$$dF = \frac{F - F_{min}}{F_{min}}$$

where dF is the change in fluorescence, F is the raw fluorescence at each depth and F_{min} is the minimum fluorescence across all measured depths. This was completed for good interpretation of values from 0-1 and to aid identification of small changes in fluorescence change. Then, the scaled depth profile was compared to the histological depth profile using a correlative assessment described in **section 3.2.3.2.2**.

For acute pharmacokinetic analysis **(section 3.2.2.2.3)** as shown in **Figure 3.3.9**, only data collected at 440 nm and excited at 5-V was used. The z-scored fluorescence change was calculated overtime, using the formula:

$$dF = \frac{F - mean(F_0)}{std(F_0)}$$

where dF is the z-scored fluorescence, F is the raw fluorescence at each time point and F_0 is the baseline fluorescence across the 30-minute baseline recording before injection. This was chosen to determine if fluorescence values were increased compared to baseline. Then, the mean z-scored fluorescence signal was determined across 5-minute time-bins.

3.2.3.2 Histological Analysis

Protocols for histological assessment including image stitching, atlas alignment and plaque detection are described in detail in **section 2.1.3**. After plaque detection, there was manual fibre track detection and photometry vs histology correlative assessment to allow direct comparison of the photometry data to quantified histological plaques.

3.2.3.2.1 Fibre track detection

Following plaque quantification, the fibre track on the aligned sections was manually labelled using an AMaSiNe built-in graphical user face **(Figure 3.2.11A)**. This allows manual annotation on each aligned image, where the fibre track was marked from the brain surface to fibre tip. Using the aligned images, the AP, ML and DV coordinates of the manually labelled track were identified. However, in order to acquire coordinates for a single fibre track across sections, with coordinates sampled at the sampling resolution of the FF photometry measurements, further analysis was required. Thus, two major parameters are determined: the depth alignment scaling factor and the sampling depths. To determine the depth alignment scaling factor, the estimated length of the fibre track, as determined by the manual labelling on histological sections, was divided by the actual length, as determined by depth reached during the *in vivo* experiment (4000-µm). The sampling depths were determined by calculating equal intervals of the recording resolution (100-µm) multiplied by the scaling factor, from the most dorsal to the most ventral annotated coordinate**.** Next, using the AP, ML, DV coordinates and sampling depths, the coordinates for the full fibre

track are estimated using a two-step regression model. Lastly, using the list of all brain regions, provided by the Allen Institute, the coordinates allow identification of brain regions the fibre track passes.

3.2.3.2.2 Photometry vs histology correlative assessment

Plaques that fall within a 200-µm radius of the fibre track coordinates, on the contralateral hemisphere, were quantified **(Figure 3.2.11B)**. Setting the contralateral hemisphere is vital to avoid tissue damage from the implant interfering with accurate quantification, thereby taking the assumption that plaque pathology is consistent across hemispheres. Also, 200-µm was chosen based off previous studies that have estimated that the light cone for FFs is less than several hundred micrometres (Pisanello et al., 2019).

To determine if the histological quantification of Methoxy-x04 stained plaques was correlated to photometry data, Pearson's correlation coefficient was used. Photometry data normalised as described in **section 3.2.3.1.2**, was used. Histological data was the quantified plaque pathology along the fibre track. In 5xFAD- mice, where noise was quantified as a plaque, signals were removed manually by setting the value to 0. In cases where no plaque pathology was quantified, addition of MATLAB-generated random noise in values <0.00001 was added to histological quantification. Next, the correlation between photometry and histological signals was determined using Pearson's correlation coefficient. For summary analysis, the mean and SEM of correlation coefficients was calculated for each recording site and across all sites.

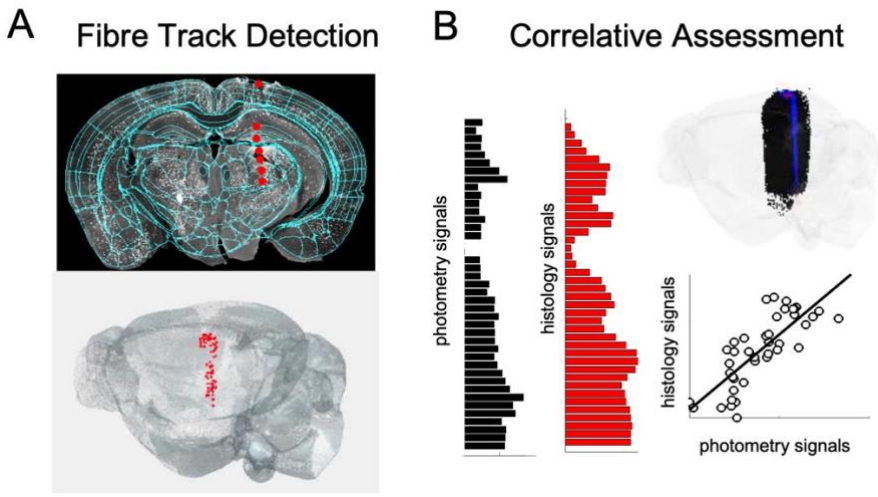

Figure 3.2.11. Process for histological quantification of Methoxy-x04 stained plaques along the fibre implant site. (A) *Top*, Manual fibre track detection on an aligned brain slice. *Bottom,* Detected fibre track on all aligned brain slices, visualised on a whole brain. (B) Approach for photometry Vs histology correlative assessment. Plaques within 200-µm of the manually annotated

fibre track (*red*), on the contralateral hemisphere are quantified. All plaques are shown as black dots. Quantified plaques are shown within a blue circle. Histology and photometry signals from the brain surface to 4000-µm are compared, as shown in bar graphs (*left*), before correlative assessment (*bottom*).

3.2.3.3 Exclusion criteria

Table 3.2.3. Animal experimental details for depth profile experiments completed on the original FF photometry system.

Site	Mouse ID	Genotype	Sex	Age (mo)
1	FAD3	5xFAD+	M	6.21
	FAD4	5xFAD-	F	6.51
	FAD5	5xFAD+	M	5.56
	FAD6	5xFAD-	M	5.59
2	FAD1	5xFAD+	M	8.55
	FAD2	5xFAD+	F	6.48
	FAD3	5xFAD+	M	6.21
	FAD4	5xFAD-	F	6.51
	FAD5	5xFAD+	M	5.56
	FAD6	5xFAD-	M	5.59

Table 3.2.4. Animal experimental details for depth profile experiments completed on the reconfigured FF photometry system. Clarification on data that was used for FP or HC analysis is included. FP is for fibre photometry data. HC is for histology correlation data. Y is for yes. N is for no.

Site	Mouse ID	Genotype	Sex	Age (mo)	FP	HC
1	FAD41	5xFAD+	M	7.63	Y	N
	FAD42	5xFAD+	M	6.87	Y	Y
	FAD47	5xFAD+	F	6.87	Y	N
	FAD48	5xFAD-	F	6.90	Y	N
	FAD49	5xFAD-	M	6.97	Y	Y
	FAD50	5xFAD+	M	7.13	Y	Y
	FAD53	5xFAD-	F	8.42	Y	Y
	FAD54	5xFAD-	M	7.10	Y	N
2	FAD41	5xFAD+	M	7.63	Y	Y
	FAD42	5xFAD+	M	6.87	Y	Y
	FAD47	5xFAD+	F	6.87	Y	Y
	FAD48	5xFAD-	F	6.90	Y	Y
	FAD49	5xFAD-	M	6.97	Y	N
	FAD50	5xFAD+	M	7.13	Y	Y
	FAD54	5xFAD-	M	7.10	Y	Y
	FAD55	5xFAD-	M	7.13	Y	Y
3	FAD13	5xFAD+	M	8.52	Y	Y
	FAD16	5xFAD-	F	7.99	Y	Y
	FAD20	5xFAD+	M	8.42	Y	Y
	FAD21	5xFAD-	M	8.45	Y	Y
	FAD42	5xFAD+	M	6.87	Y	Y
	FAD47	5xFAD+	F	6.87	Y	Y
	FAD48	5xFAD-	F	6.90	Y	N
	FAD49	5xFAD-	M	6.97	Y	Y
	FAD50	5xFAD+	M	7.13	Y	Y
	FAD53	5xFAD-	F	8.42	Y	Y
	FAD55	5xFAD-	M	7.13	Y	Y

For original FF photometry system depth profile experiments, all data was used as histological correlation analysis was not completed **(Table 3.2.3)**. For depth profile experiments completed on the reconfigured FF photometry system, recordings used for FF photometry comparisons and histology correlation analysis are shown in **Table 3.2.4**.

Table 3.2.5. Excluded recordings and reasons for exclusion. FP is for fibre photometry data. HC is for histology correlation data. Urethane means the mouse was unstable under urethane anaesthetic and died before the recording was complete. Set-up faults included fibre breakage or other equipment failures.

Site	Mouse ID	Genotype	Sex	Age (mo)	Stage of Exclusion	Reason
	FAD12	5xFAD-	F	8.48	Before both	Urethane
	FAD22	5xFAD+	M	6.84	Before both	Set-up faults
	FAD46	5xFAD-	F	8.94	Before both	Urethane
1	FAD55	5xFAD-	M	7.13	FP	Urethane
	FAD41	5xFAD+	M	7.63	HC	Estimated track depth & image quality
	FAD47	5xFAD+	F	6.87	HC	Image quality
	FAD48	5xFAD-	F	6.90	HC	Estimated track depth
	FAD54	5xFAD-	M	7.10	HC	Image quality
2	FAD53	5xFAD-	F	8.42	FP	Set-up faults
	FAD49	5xFAD-	M	6.97	HC	Estimated track depth
3	FAD11	5xFAD+	F	8.45	FP	Urethane
	FAD41	5xFAD+	M	7.63	FP	Urethane
	FAD23	5xFAD-	M	6.87	FP	Set-up faults
	FAD54	5xFAD-	M	7.10	FP	Urethane
	FAD48	5xFAD-	F	6.90	HC	Image quality

For depth profile experiments on the reconfigured photometry system, only data that passed the exclusion criteria was used. FF photometry recordings were only used if the target depth of 4000-µm was reached. For histology correlation analysis, data was excluded on two grounds: estimated track depth and image quality. By plotting the estimated track depth, calculated from the histological track detection described in **section 3.2.3.2.1**, any that were greater or lower than a standard deviation of 1.5 away from the group mean estimated track depth were excluded. Aligned images after histological image alignment were scored by an experimenter on various aspects of alignment and image quality from 0-5 (5 being perfect). These included the quality of alignment of images to the Allen brain atlas, the quality of images (damaged or missing), if the full fibre track was shown across images and if the fibre track was warped due to the alignment process. Then, the mean image quality score was calculated and recordings that had a score that was 1.5 standard deviations lower than the mean were excluded. **Table 3.2.5** shows recordings that were excluded with reasons, with total sample numbers at each stage shown in **Figure 3.2.12**.

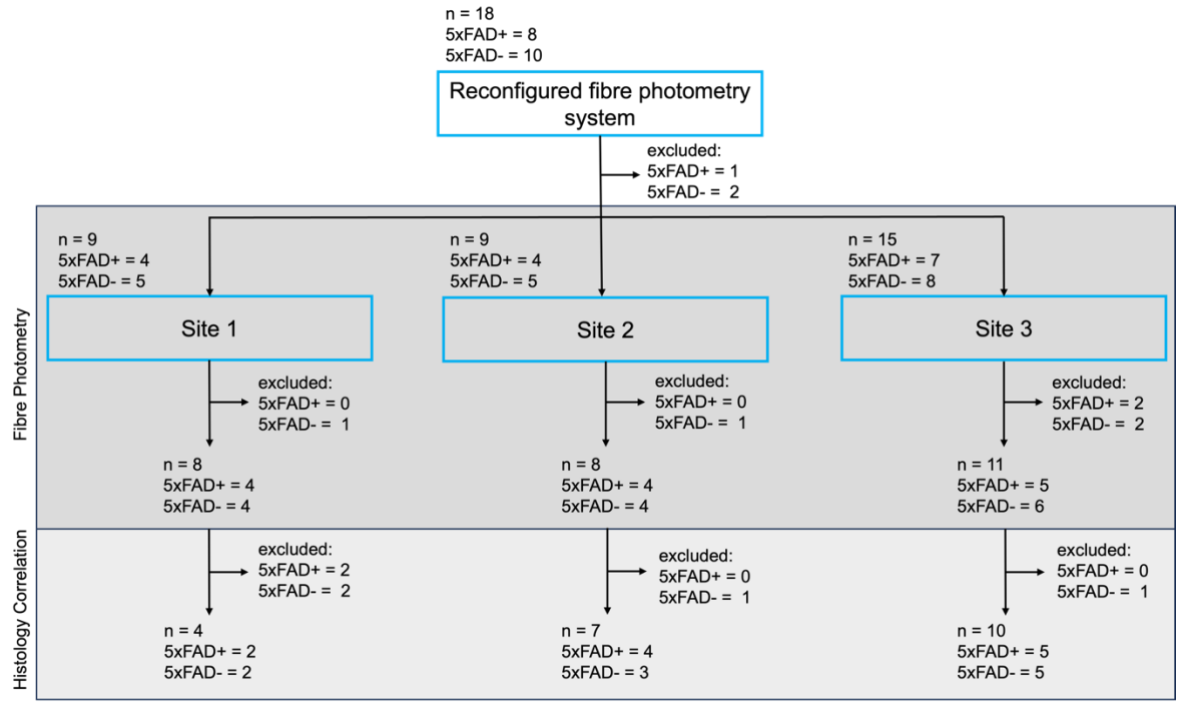

Figure 3.2.12. Sample number for each recording site for FF photometry and histology correlation analysis of depth profile experiments using the reconfigured FF photometry system. For detailed information on age and sex of animals used go to **Figure 3.3.5**. While this shows the sample number for animals used, each animal may have several recordings per site.

3.2.3.4 Statistics

All statistical analysis was completed on MATLAB. To compare summary depth profiles for 5xFAD+ and 5xFAD- groups, a two-way ANOVA was completed comparing genotypes and depths, with post-hoc multi-comparison tests. For correlative analysis, Pearson's correlation coefficient was completed, determining the r- and p-value. Summary correlation coefficients were compared using two-sample t-tests. Data is shown as mean ± SEM. Significance was set as $\alpha = 0.05$. $p < 0.001$ (****), $p < 0.005$ (***), $p < 0.01$ (**), $p < 0.05$ (*), ns not significant.

3.3 Results

We worked to illustrate that this novel approach was a feasible way to monitor plaque pathology across depth, *in vivo*. Therefore, we completed FF photometry recordings in 5xFAD+ and 5xFAD- mice, injected with Methoxy-x04, under terminal anaesthetic and monitored the fluorescence at increasing depths for comparison to histological plaque load. First, we illustrate that the original system set-up did not provide strong *in vivo* signals, despite *in vitro* calibration studies suggesting good sensitivity **(section 3.3.1).** Accordingly, a system reconfiguration was completed and provided a boost of *in vitro* and *in vivo* signals, allowing detection of plaque signals across depth,

in vivo **(section 3.3.2)**. To determine the feasibility, we assess the correlation between these photometry signals and histological plaque load **(section 3.3.3)**. Finally, as the system appeared to be feasible for plaque assessment, we attempted to monitor the acute pharmacokinetic profile of Methoxy-x04 in 5xFAD mice, under terminal anaesthetic **(section 3.3.4)**.

3.3.1 Original sub-optimal FF photometry system set-up does not detect strong Methoxy-x04 signals *in vivo*, despite *in vitro* calibrations showing promising system sensitivity

To confirm our novel approach for real-time monitoring of plaque pathology, using Methoxy-x04 and fibre photometry, we wanted to illustrate the ability to extract Methoxy-x04 signals from photometry that were consistent with what would be seen in a well-established method, such as histological assessment. For this, we require an optical system that can detect Methoxy-x04 signals *in vivo*. Thus, we work to establish a FF photometry system that can excite and collect emitted light from Methoxy-x04 stained plaques. To do so, we begin by completing *in vitro* measurements using concentrations of Methoxy-x04 to determine a suitable excitation and emission FF photometry set-up. Once an appropriate system calibration was complete, *in vivo* measurements of plaque pathology were done. Therefore, this section describes data from characterisation of and initial *in vivo* experiments using the original FF photometry system.

3.3.1.1 In vitro experiments show reasonable Methoxy-x04 system sensitivity

Several *in vitro* measurements were completed to determine if the system set-up was appropriate for Methoxy-x04 detection. With future experiments requiring strong sensitivity to track changes in plaque load, a system that can detect small changes in fluorescent output is vital. Thus, we started by determining if this original FF photometry set-up can provide positive signals. Additionally, we wanted to determine if Methoxy-x04 fluorescence is insensitive to 470-nm excitation so this wavelength could be used as a control measure.

A FF was placed in Eppendorf's with increasing concentration of Methoxy-x04 and the fluorescent output was measured using an illumination protocol that ran through several irradiances and two wavelengths **(Figure 3.3.1A)**. Data shows that 405-nm excitation provides an amplified fluorescence output with increasing concentration and irradiance **(Figure 3.3.1B).** Whereas fluorescence output remains at the baseline when excited with 470-nm.

Next, system sensitivity to Methoxy-x04 was determined by increasing the concentration of Methoxy-x04 in 5-nM steps **(Figure 3.3.1A). Figure 3.3.1C** shows that at 50-nM, there is an increase in fluorescence output at all irradiances, that continues to increase with increasing concentration.

Overall, we have found that the current system set-up is appropriate for Methoxy-x04 *in vitro* detection. It was shown that 405-nm excitation provided strong Methoxy-x04 signals, with the system detecting a rise in fluorescence output at as low as 50-nM of Methoxy-x04. Therefore, this system was taken forward for *in vivo* measurements.

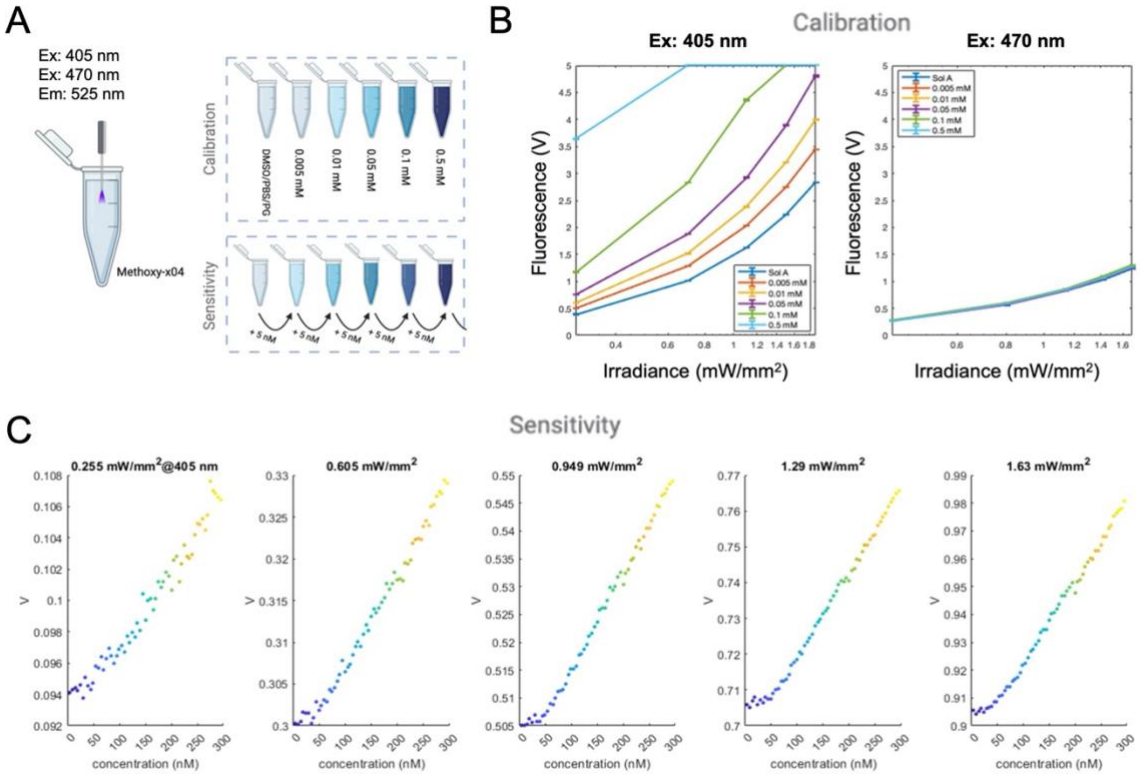

Figure 3.3.1. Original FF photometry system set-up shows Methoxy-x04 detection at 405-nm, with a minimum Methoxy-x04 detection at 50-nM. (A) Schematic illustrating two experimental set-ups to determine the system sensitivity for Methoxy-x04. Calibration experiments tested the fluorescent output when Methoxy-x04 was excited (Ex) at 405-nm and 470-nm, and emission (Em) collected at 525-nm, using a range of Methoxy-x04 concentrations. These wavelengths represent the dual-excitation original photometry system. Sensitivity experiments determined the lowest concentration of Methoxy-x04 the system can detect by monitoring the fluorescent output at increasing concentrations of Methoxy-x04, in 5-nM steps. Created with BioRender.com. (B) Fluorescent output from calibration studies at 405-nm (left) and 470-nm (right) excitation. (C) Fluorescent output from sensitivity studies at increasing

concentrations, across increasing irradiances. Colours from blue to yellow represent increasing concentration.

3.3.1.2 In vivo experiments show difficulty achieving Methoxy-x04 signals

After *in vitro* system calibration suggested that the original system set-up was appropriate *for in vivo* measurement, we completed *in vivo* depth profile measurements for confirmation of this novel approach. Here, we wanted to determine if photometry signals excited at 405-nm were stronger in 5xFAD+ mice and illustrated a fluorescent profile that was comparable to plaque load in histological assessment.

This involved injection of Methoxy-x04 (10-mg/kg) 24-hours before completing a terminal depth profile procedure where the FF was implanted into different implant sites in 5xFAD+ or 5xFAD- mice brain **(Figures 3.3.2 and 3.3.3)**. Site 1 and site 2 were chosen due to the variation in signal intensity across the 4000-µm, ranging from plaque-sparse to plaque-dense regions **(Figure 3.3.3B)**. For example, site 1 should enter the medial septum and site 2 should pass the SUB which are dense with plaque pathology. In attempt to confirm the success of this protocol, histological sections from these implant sites were prepared to show the Methoxy-x04 signals surrounding the implant site, where a comparable signal profile should be seen.

3.3.1.2.1 Datasets and mice

In total, 6 mixed-sex mice were used for depth profile experiments completed using the original FF photometry system **(Figure 3.3.2A)**. These mice either underwent monitoring at site 2 or both site 1 and 2 **(Figure 3.3.2A).** Mice were aged between 5.5 and 8.5 months old **(Figure 3.3.2B)**.

Due to the quick assessment that the original system confirmation was not suitable to achieve strong Methoxy-x04 signals **(Figure 3.3.3)**, experiments were stopped before using more animals.

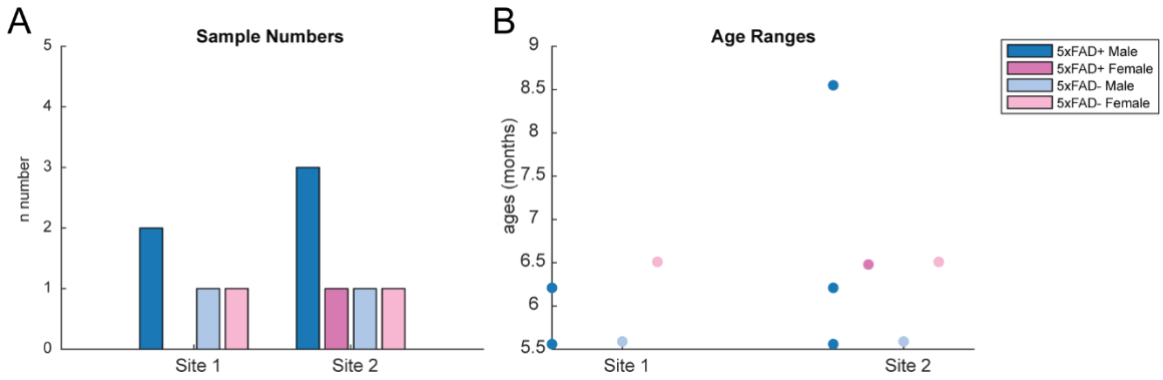

Figure 3.3.2. Sex, age, and genotype information for animals used for depth profile recordings at site 1 or 2 using the original FF photometry system. (A) Sample numbers for each site across sex and genotype. (B) Age of animals for each site across sex and genotype.

3.3.1.2.2 Depth profile experiments show lack of Methoxy-x04 detection, *in vivo*

Figures 3.3.3A-C shows the experimental design where the fibre was lowered into a mouse either at site 1 or site 2, that had been injected with Methoxy-x04 24-hours before. Depth profiles at 405-nm showed a slight increase in fluorescence at regions of high plaque load in 5xFAD+ recordings **(Figures 3.3.3D-E).** For example, at site 1 in the 5xFAD+ mouse, there was a slight increase in fluorescence from ~2000-3000-µm, which corresponds to a region of plaques as shown in the histological images **(Figure 3.3.3D).** Additionally, there is an increase in fluorescence at ~1000-1500-µm in the 5xFAD+ mouse at site 2, with histological images showing a region of high plaque load **(Figure 3.3.3E).** However, similar profiles were seen for 5xFAD- recordings, where no plaques were seen **(Figures 3.3.3D-E)**. Additionally, fluorescence increases at similar depths at 470-nm, which is out of the excitation range of Methoxy-04. This suggests that the signal to noise ratio for Methoxy-x04 signals may not be strong enough when using the original FF photometry system, with anatomical structures and AF within the brain potentially being responsible for these fluorescent profiles.

Overall, due to the lack of strongly convincing Methoxy-x04 plaque detection, the original system set-up was deemed not optimal for *in vivo* measurements. While *in vitro* experiments suggested that the sensitivity was appropriate, it became clear that brain AF would be an important factor to consider when completing *in vivo* measures. Thus, a system reconfiguration was required.

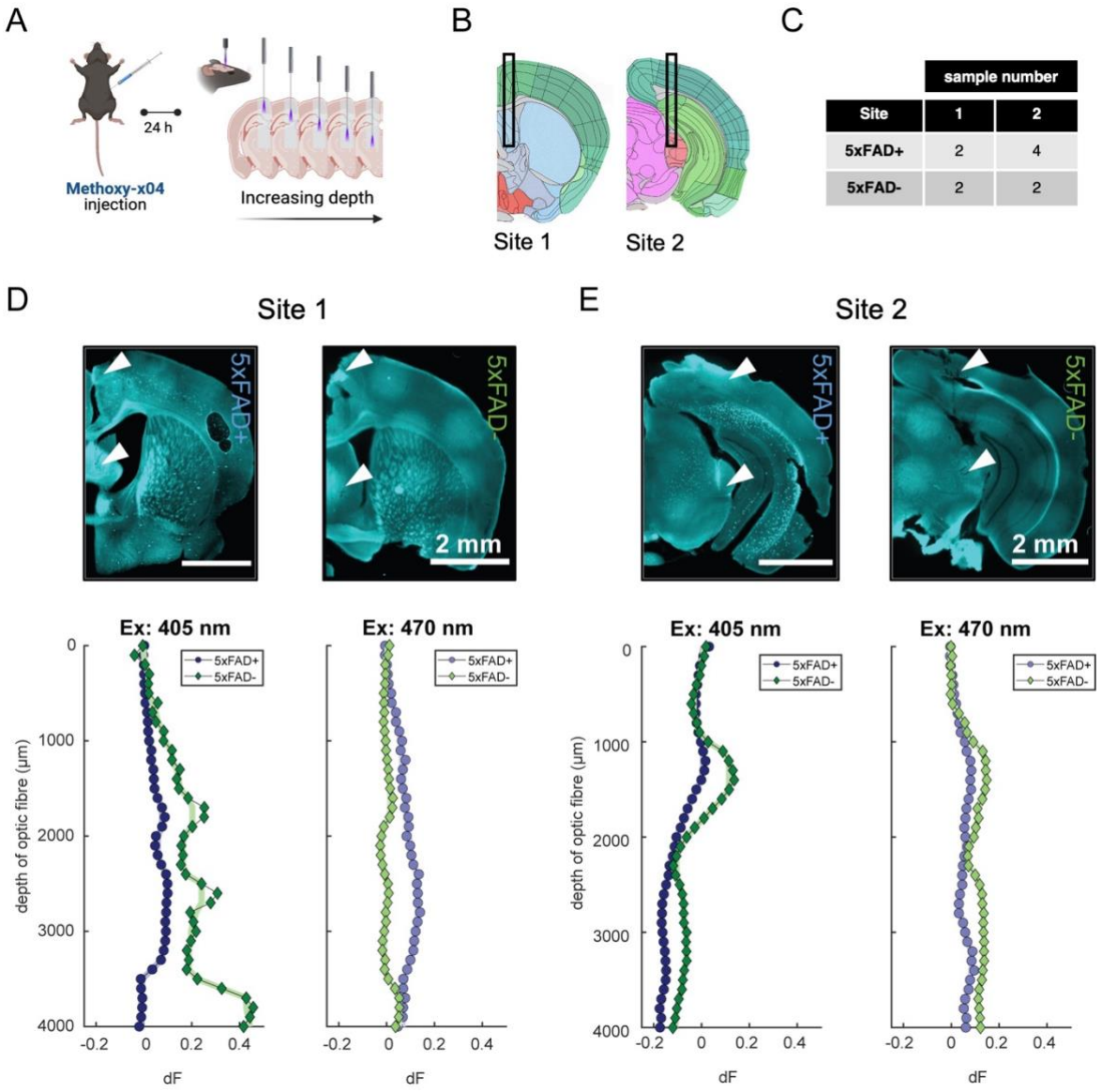

Figure 3.3.3. Depth profile experiments with the original system show lack of Methoxy-x04 signals. (A) Schematic of experimental set-up. Methoxy-x04 is injected 24-hours before terminal depth profile procedure. Created with BioRender.com. (B) Brain atlas showing the implant site for site 1 (left) and site 2 (right) from the Allen Mouse Brain Atlas, mouse.brain-map.org. (C) Number of depth profiles recorded from each implant site in 5xFAD+ or 5xFAD- mice. (D, E) *Top,* Histological images of the implant site for site 1 (D) and site 2 (E). White arrows show the track. Scale: 2-mm. *Bottom,* Normalised depth profile from 0 to 4000-µm in 5xFAD+ (blue) and 5xFAD- (green) mice, at excitation (Ex) wavelengths of 405-nm and 470-nm. Normalised values were calculated using a baseline normalisation approach detecting the change in fluorescence from the mean signal from 0-500-µm. Pale coloured line shows the filtered moving median fluorescence across 500-µm.

3.3.2 System reconfiguration allows strong Methoxy-x04 detection

After *in vivo* experiments with the original system set-up illustrated that a system reconfiguration was required, emission filters were changed in attempt to boost system sensitivity. An emission filter to collect strong Methoxy-x04 signals was chosen, and another to collect brain AF. To confirm this, *in vitro* experiments were repeated **(Figure 3.3.4)**, followed by *in vivo* depth profile experiments **(Figure 3.3.6 & 3.3.7)**.

3.3.2.1 In vitro experiments show improved Methoxy-x04 detection using the reconfigured system set-up

Several *in vitro* measurements were completed to determine if the reconfigured system set-up was better for Methoxy-x04 detection. We wanted to see if there was an improvement in system sensitivity, with limited Methoxy-x04 signals at 550-nm.

A FF was placed in Eppendorf's with increasing concentration of Methoxy-x04 and the fluorescent output was measured using an illumination protocol that ran through several irradiances **(Figure 3.3.4A)**. As with the original system set-up, data shows that there is an increasing fluorescence output with increasing concentration and irradiance at 440-nm **(Figure 3.3.4B).** Whereas fluorescence output remains at baseline when collected at 550-nm. However, there is a noticeable decrease in fluorescent output compared to the original set-up. This can be explained by a reduction in unspecific wavelengths being collected, decreasing the baseline fluorescence.

Next, the reconfigured systems sensitivity to Methoxy-x04 was determined by increasing the concentration of Methoxy-x04 in 5-nM steps **(Figure 3.3.4A). Figure 3.3.4C** shows that at 5-nM, there is an increase in fluorescence output at all irradiances, continuing to increase with increasing concentration. This illustrates that the reconfigured system has greater sensitivity, able to detect Methoxy-x04 signals in the 5-nM range, without being greatly influenced by the bleaching of system AF.

Overall, calibration and sensitivity experiments on the reconfigured system have shown great improvements in system sensitivity, showing a boost from 50-nM to 5-nM. This came in combination with a reduction of baseline fluorescence noise of the system. Therefore, we believe the system reconfiguration will provide the boost in signal intensity, with a reduction in AF, that is required for *in vivo* measurements.

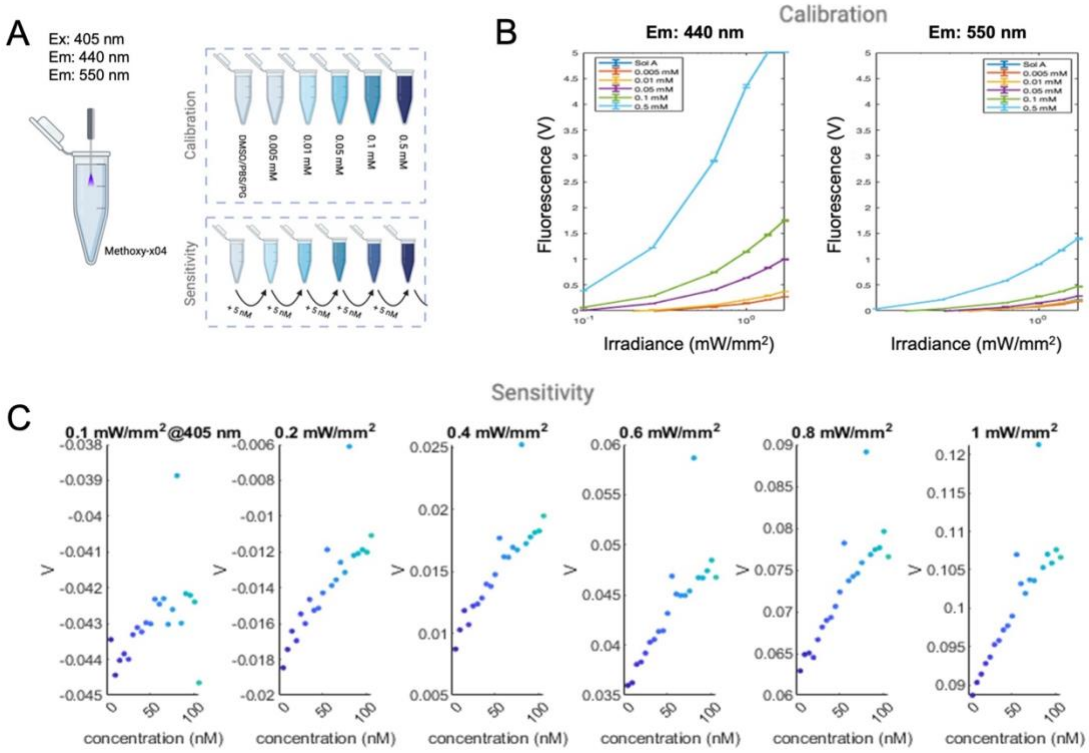

Figure 3.3.4. Reconfigured FF photometry system set-up shows Methoxy-x04 detection at 440-nm, with a minimum Methoxy-x04 detection at 5-nM. (A) Schematic illustrating two experimental set-ups to determine the system sensitivity for Methoxy-x04. Calibration experiments tested the fluorescent output when Methoxy-x04 was excited (Ex) with 405-nm and emission (Em) collected at 440-nm and 550-nm, using a range of Methoxy-x04 concentrations. These wavelengths represent the new dual-detection reconfigured photometry system. Sensitivity experiments determined the lowest concentration of Methoxy-x04 the system can detect by monitoring the fluorescent output at increasing concentrations of Methoxy-x04, in 5-nM steps. Sensitivity experiments completed on the reconfigured system went up to 100 nM as experiments on the original system show that this range was acceptable to identify the system sensitivity. Created with BioRender.com. (B) Fluorescent output from calibration studies at 440-nm (left) and 550-nm (right) emission. (C) Fluorescent output from sensitivity studies at increasing concentrations, across increasing irradiances. Colours from dark to light blue represent increasing concentration.

3.3.2.2 In vivo experiments show detection of Methoxy-x04 signals using the reconfigured system set-up

3.3.2.2.1 Datasets and mice

Following appropriate exclusion criteria, **Figures 3.3.5A&C** shows the number of mice used across each site, genotype, and sex for FF photometry recordings **(Figure 3.3.5A)** and histology correlation analysis **(Figure 3.3.5C)**. Mice were used either for site 3 only recordings or site 1, 2 and 3 recordings. Mice were mixed sex, but according to availability there was a higher proportion of 5xFAD+ male mice used over 5xFAD+ female mice (**Figures 3.3.5A&C)**. For 5xFAD- mice, the male and female split was more proportionate (**Figures 3.3.5A&C)**. Sex differences were not considered for the following analysis due to small sample numbers for some groups.

For both FF photometry recordings **(Figure 3.3.5B)** and histology correlation analysis **(Figure 3.3.5D)** the age of mice ranged from 6.8-8.6 months. 5xFAD+ mice at this age have a high plaque load across several brain regions.

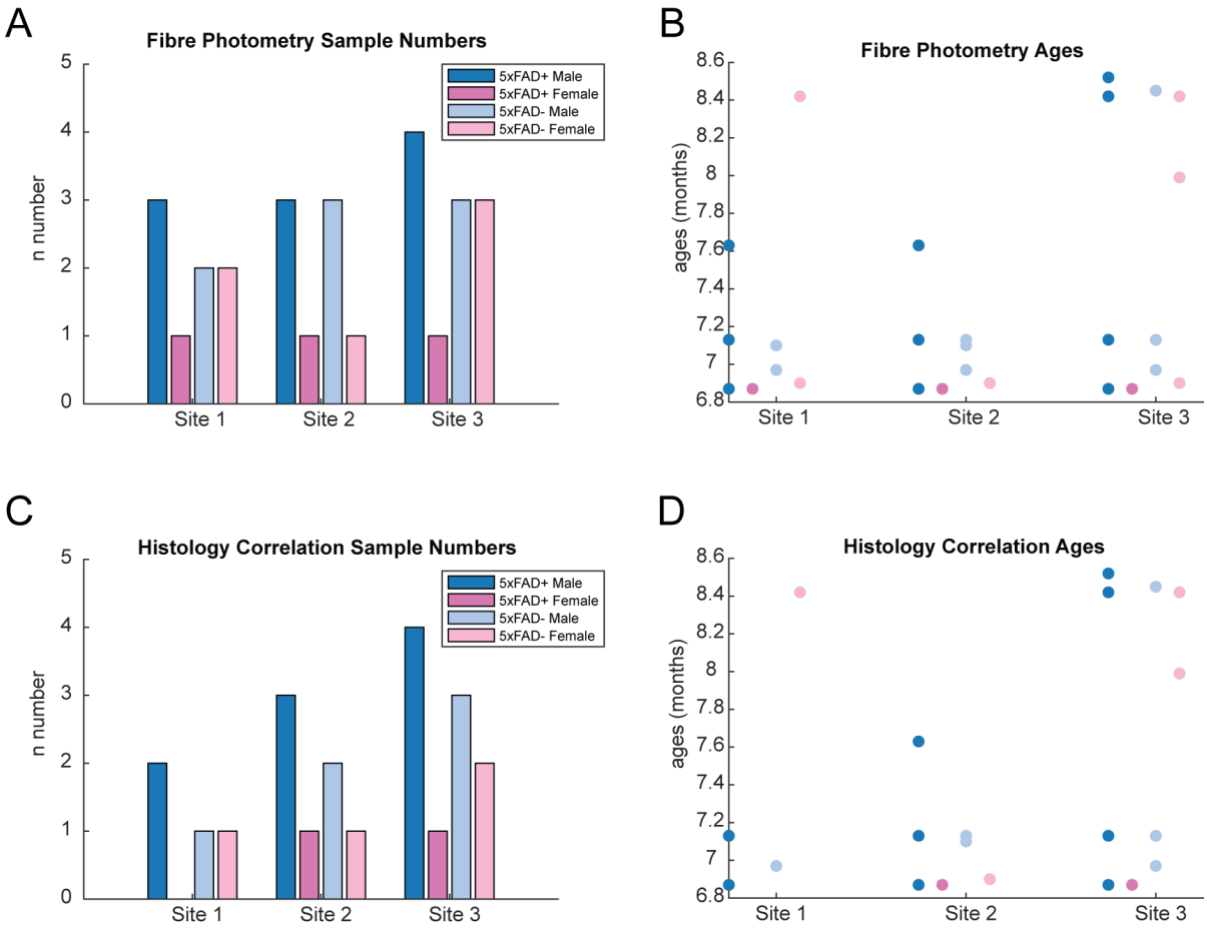

Figure 3.3.5. Sex, age, and genotype information for animals used for depth profile recordings at site 1, 2 or 3 using the reconfigured FF photometry system. (A, C) Sample numbers for each site across sex and genotype for fibre photometry (A) and histology correlation (C) analysis. (B, D) Age of animals for each site across sex and genotype for fibre photometry (B) and histology correlation (D) analysis. Colour coding is the same as in A and C.

3.3.2.2.2 Depth profile experiments show Methoxy-x04-stained plaque signals *in vivo*

Following recharacterization of the optimised FF photometry system, we repeated *in vivo* depth profile measurements for confirmation of this novel approach. Again, we wanted to ensure that photometry signals at 440-nm were stronger in 5xFAD+ mice, showing a fluorescent profile comparable to histological images. 24-hours after injection of Methoxy-x04 (10-mg/kg) a terminal depth profile procedure where the FF was implanted into three different implant sites in 5xFAD+ or 5xFAD- mice brain was completed. Then, post-mortem histological images were prepared to show the Methoxy-x04 signals surrounding the implant site **(Figures 3.3.6A-C)**. Again, sites 1, 2 and 3 were chosen due to the variation in signal intensity across the 4000-µm. For example, site

1 should enter the medial septum, site 2 will pass hippocampal and thalamic regions and site 3 should pass the SUB which is dense with plaque pathology.

Firstly, exemplar depth profiles are shown comparing fluorescence depth profiles for 5xFAD+ mice and 5xFAD- mice, at both 440-nm and 550-nm **(Figures 3.3.6D-F)**. At site 1, a rise in fluorescence is not as evident in 5xFAD+ mice, with little change between profiles at 440-nm and 550-nm **(Figure 3.3.6D)**. We believe that due to the anatomical structure of this brain region, where the fibre likely passes through the ventricle to re-enter at regions of the medial septum, the fibre has not reached its target and instead may be pressed against the tissue surface which would increase AF recorded. This hypothesis was further exemplified when the fibre tracks rarely appeared to reach 4000-µm on histological images at this site.

However, at both site 2 and 3 there is greater fluorescence change in 5xFAD+ mice, compared to 5xFAD- mice, at 440-nm that appears to reflect the plaque load seen in histological images. Specifically, at site 2 at 440-nm, in the 5xFAD+ mice, there is a sharp rise in photometry fluorescence at ~800-1400-µm which is comparable to a dense plaque region at the cortex/hippocampal border seen in histological images **(Figure 3.3.6E)**. Additionally, when entering the thalamic regions at ~2000-µm onwards, there is a steady rise in photometry fluorescence that is mirrored by an increasing plaque load in histological images **(Figure 3.3.6E)**. In the 5xFAD+ mice at site 3, at 440-nm, there is a rise in fluorescence between 600-1700-µm where it is passing the highly plaque dense SUB, seen in histological images **(Figure 3.3.6F)**. Also, for both site 2 and 3, a similar but less pronounced profile is seen at 550-nm. However, across site 1, 2 and 3, the fluorescent profile for 5xFAD- mice have no increases in fluorescence and remains flat at both 440-nm and 550-nm **(Figures 3.3.6D-F)**.

Again, summary plots show potentially unrepresentative profiles for site 1 as there was no pronounced increase in fluorescence in 5xFAD+ mice compared to 5xFAD- mice across depth. This was illustrated by no significant differences in fluorescence at 440-nm and 550-nm across depth ($F(40) = 0.7147$, $p = 0.8991$, and $F(40) = 0.9830$, $p = 0.5057$, respectively, two-way ANOVA) **(Figure 3.3.6G)**. However, a significantly increased fluorescence was found for 5xFAD- mice compared to 5xFAD+ mice ($F(1) = 15.3810$, $p = 0.0001$, two-way ANOVA) at 440-nm, which was not seen at 550-nm ($F(1) = 0.0290$, $p = 0.8649$, two-way ANOVA). Despite this, no significant differences were found with post-hoc multi-comparison tests ($p > 0.47$ for all).

Site 2 maintains the varied increased fluorescence intensity across depth in 5xFAD+ mice, showing increased fluorescence at hippocampal and thalamic regions compared to 5xFAD- mice **(Figure 3.3.6H)**. Therefore, at 440-nm and 550-nm, significant increases in fluorescence were found in 5xFAD+ mice compared to 5xFAD- mice ($F(1) = 22.1547$, $p < 0.0001$ and $F(1) = 42.9148$,

$p < 0.0001$, respectively, two-way ANOVA) and across depth ($F(40) = 2.3382$, $p < 0.0001$ and $F(40) = 4.6437$, $p < 0.0001$, respectively, two-way ANOVA).

Site 3 shows a higher fluorescence at varied intensities across depth for 5xFAD+ mice, compared to 5xFAD- mice at 440-nm, and to a lesser extend 550-nm **(Figure 3.3.6l)**. This is shown by significant differences between 5xFAD+ and 5xFAD- mice at 440-nm and 550-nm ($F(1) = 79.1328$, $p < 0.0001$ and $F(1) = 84.4641$, $p < 0.0001$, respectively, two-way ANOVA), but not across depth ($F(40) = 0.7554$, $p = 0.8630$ and $F(40) = 0.9697$, $p = 0.5260$, respectively, two-way ANOVA). This occurs because 550-nm is towards the tail end of the Methoxy-x04 emission spectra and now is collecting small plaque signals.

Overall, it appears that the system reconfiguration has increased Methoxy-x04 sensitivity and reduced AF collection enough to allow collection of Methoxy-x04 plaque signals from site 2 and 3, with trouble collecting consistent signals from site 1 due to the risk of hitting the ventricle. Thus, for the first time, depending on the site of implantation we show a detected change in fluorescence with depth, that appears reflective of plaque pathology, using FF photometry. This is seen despite the pooling of all data, which includes small variations in mouse age and therefore, plaque pathology, as well as implant sites that can account for the variation in fluorescence levels across recordings.

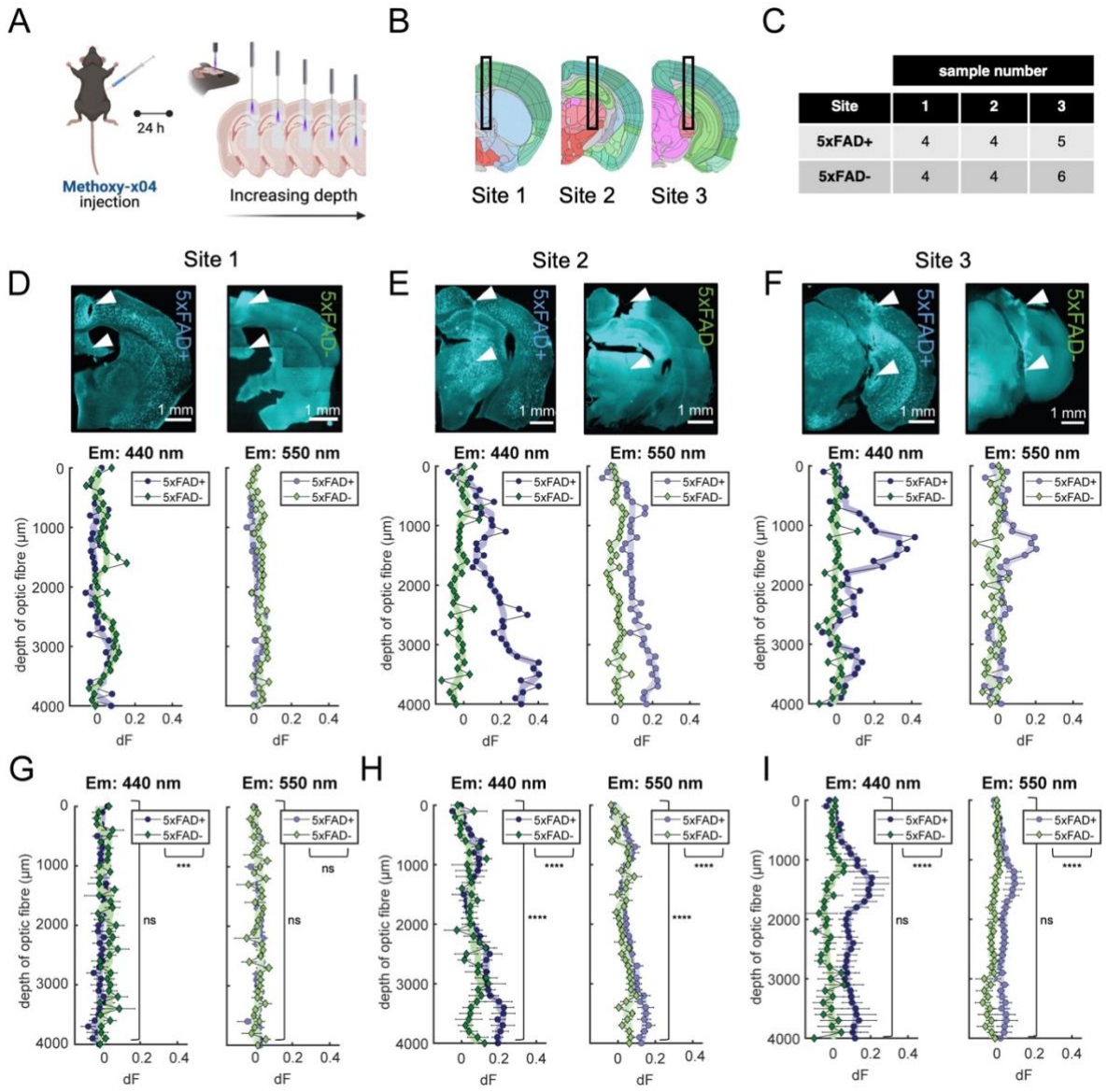

Figure 3.3.6. Depth profile experiments with the reconfigured system show positive Methoxy-x04 signals. (A) Schematic of experimental set-up. Methoxy-x04 is injected 24-hours before terminal depth profile procedure. Created with BioRender.com. (B) Brain atlas showing the implant site for site 1 (left), site 2 (middle) and site 3 (right) from the Allen Mouse Brain Atlas, mouse.brain-map.org. (C) Number of mice where FF photometry analysis was completed from each implant site in 5xFAD+ or 5xFAD- mice. Occasionally, some mice had more than one analysis completed for one site. (D, E, F) *Top,* Histological images of the implant site for site 1 (D), site 2 (E) and site 3 (F). White arrows show the track. Scale: 1-mm. *Bottom,* Normalised depth profile from 0 to 4000-µm in 5xFAD+ (blue) and 5xFAD- (green) mice with emission (Em) collection at 440-nm and 550-nm. (G, H, I) Summary normalised depth profile from 0 to 4000-µm in 5xFAD+ (blue) and 5xFAD- (green) mice with emission collection at 440-nm and 550-nm at site 1 (G), site 2 (H) and site 3 (I). Normalised values were calculated using a baseline normalisation approach detecting the change in fluorescence from the mean signal from 0-500-µm. Pale coloured line shows the filtered moving median fluorescence across 500-µm. Mean ±

SEM. A two-way ANOVA with post-hoc multi-comparison tests were completed comparing the example and summary normalised fluorescence of 5xFAD+ and 5xFAD- mice across depth at each emission and implant site. Annotations illustrate the significance across depth and genotype. P-values: $p < 0.001$ (****), $p < 0.005$ (***), $p < 0.01$ (**), $p < 0.05$ (*), not significant (ns). Site 1 and 2: n = 4 recordings in 4 5xFAD+ and 5xFAD- mice. Site 3: n = 7 recordings in 5 5xFAD+ mice and n = 8 recordings in 6 5xFAD- mice.

3.3.3 Photometry and histological Methoxy-x04 signals are positively correlated in 5xFAD+ mice models, across multiple implant sites

Since we show the reconfigured FF photometry system detected *in vivo* Methoxy-x04 plaque signals that appeared reflective of histological images, we wanted to directly compare *in vivo* photometry plaque signals to quantified histological plaque load as this is a well-established method for assessing plaque pathology. Therefore, we complete correlation analysis of photometry and histological signals for confirmation of this novel approach **(Figure 3.3.7A)**. This involved aligning histological images showing the fibre track to the Allen brain atlas for sites 1, 2 and 3 **(Figure 3.3.7B)**, manually marking the fibre track, and quantifying the plaques within 200-µm. Thus, creating a histological depth profile for comparison with the photometry depth profile. From there, it was determined if there was correlation between photometry and histological signals. If positively correlated, it would suggest that this novel approach is comparable to well-established histological quantification for plaque detection. The sample number of mice that had histology correlation analysis is shown in **Figure 3.3.7C.**

Figures 3.3.7D-L shows the photometry and histological depth profiles and correlative comparison. A positive correlation between photometry and histological Methoxy-x04 signals is shown across all 5xFAD+ implant sites, where photometry signals are nicely aligned with the quantified plaque pathology values **(Figures 3.3.7 D, G, J)**. However, when comparing 5xFAD- photometry and histological signals, across all brain regions there is no histological plaque detection and thus, the low photometry signal is not correlated with histological signals in 5xFAD- mice models **(Figures 3.3.7 E, H, K)**.

Therefore, when comparing the summary correlation coefficient for 5xFAD+ and 5xFAD- mice at each site, there was a significantly higher correlation coefficient in 5xFAD+ mouse models for site 2 ($p = 0.0009$, two-sample t-test) **(Figure 3.3.7I)** and site 3 ($p = 0.0017$, two-sample t-test) **(Figure 3.3.7L)**, but not at site 1 ($p = 0.5283$, two-sample t-test) **(Figure 3.3.7F)** likely due to the errors discussed above. For example, in some recordings at site 1 we can acquire good correlation between photometry and histological signals, while in other recordings we do not. The reason for this is because when the FF passes directly through the medial septum to reach the target depth

we can achieve our desired profile. However, others have been slightly off target and have passed through the ventricle where it cannot re-enter the brain tissue due to the flat-cleaved fibre. Also, we note that for site 2 and 3 we do not have a perfect positive correlation, with some recordings at site 3 showing particularly weak positive correlation. We suggest this is due to the requirement of quantifying plaque pathology on the contralateral hemisphere, potentially losing hemisphere specific trends in plaque load.

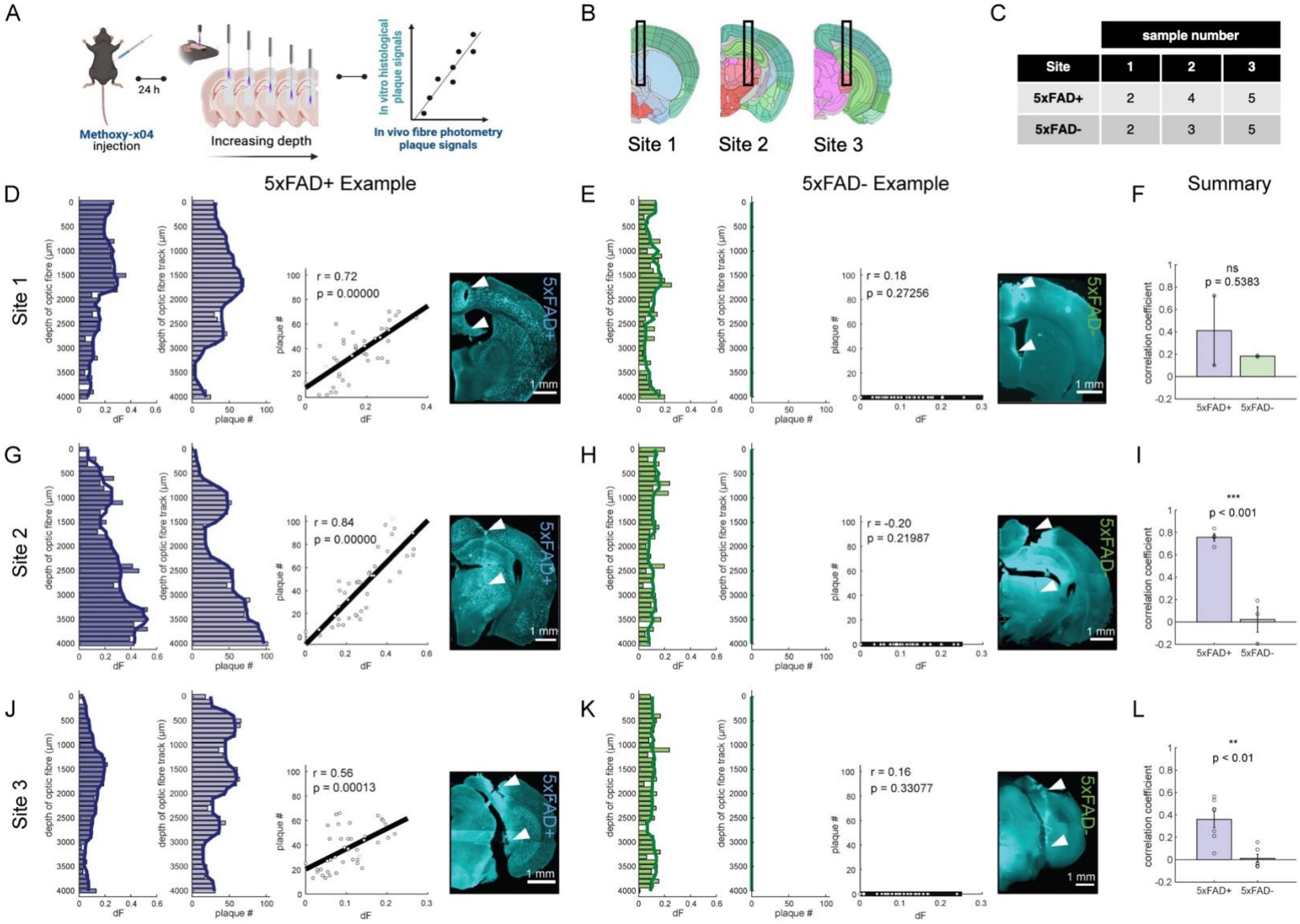
A
24 h
Methoxy-x04 injection
Increasing depth
In vitro histological plaque signals
In vivo fibre photometry plaque signals
B
Site 1
Site 2
Site 3
C
sample number
Site | 1 | 2 | 3
5xFAD+ | 2 | 4 | 5
5xFAD- | 2 | 3 | 5
D
5xFAD+ Example
Site 1
r = 0.72
p = 0.00000
E
5xFAD- Example
r = 0.18
p = 0.27256
F
Summary
ns
p = 0.5383
G
Site 2
r = 0.84
p = 0.00000
H
r = -0.20
p = 0.21987
I
***
p < 0.001
J
Site 3
r = 0.56
p = 0.00013
K
r = 0.16
p = 0.33077
L
**
p < 0.01
depth of optic fibre (µm)
depth of optic fibre track (µm)
plaque #
dF
correlation coefficient
5xFAD+
5xFAD-
1 mm

Figure 3.3.7. Photometry and histological Methoxy-x04 signals are positively correlated in 5xFAD+ mouse models. (A) Schematic of experimental set-up. Methoxy-x04 is injected 24-hours before terminal depth profile procedure. After, mice brains undergo histological processing to quantify plaques surrounding the fibre track. Created with BioRender.com. (B) Brain atlas showing the implant site for site 1 (left), site 2 (middle) and site 3 (right) from the Allen Mouse Brain Atlas, mouse.brain-map.org. (C) Number of mice where histological correlation analysis was completed from each implant site in 5xFAD+ or 5xFAD- mice. Occasionally, some mice had more than one analysis completed for one site. (D, G, J) Depth profile of photometry (dark blue) and histological (light blue) Methoxy-x04 signals, correlative analysis, and histological image of the fibre track across site 1 (D), site 2 (G) and site 3 (J) in 5xFAD+ mice. (E, H, K) Depth profile of photometry (dark green) and histological (light green) Methoxy-x04 signals, correlative analysis, and histological image of the fibre track across site 1 (E), site 2 (H) and site 3 (K) in 5xFAD- mice. Photometry signals were normalised using a minimum-based normalisation approach detecting the change in fluorescence from the minimum signal. Dark lines represent the filtered moving median fluorescence across 500-µm. Pearson's correlation coefficient is calculated with r- and p-values shown. White arrows on histological image illustrate the fibre track. Scale: 1-mm. (F, I, L) Summary mean Pearson's correlation coefficient for 5xFAD+ and 5xFAD- mice across all implants at site 1 (F), site 2 (I) and site 3 (L). Mean ± SEM. Two-sample t-tests were completed comparing the mean correlation coefficient of 5xFAD+ and 5xFAD- mice at each site. P-values: $p < 0.001$ (****), $p < 0.005$ (***), $p < 0.01$ (**), $p < 0.05$ (*), not significant (ns). Site 1: n = 2 recordings in 2 5xFAD+ and 5xFAD- mice. Site 2: 4 or 3 recordings in 4 or 3 5xFAD+ and 5xFAD- mice, respectively. Site 3: 7 recordings in 5 5xFAD+ mice and 6 recordings in 5 5xFAD- mice.

Overall, the positive correlation between photometry and histological Methoxy-x04 signals suggests that this novel approach is a feasible method to monitor plaque pathology, depending on the brain region implanted with the FF. More specifically, it illustrates that by implanting the FF into a brain of a mouse previously injected with Methoxy-x04, you can achieve a reliable measure of plaque pathology, that is comparable to histological quantification across various brain regions, with care required in regions like site 1 where passing of ventricles may contribute to inaccurate depth resolution. Additionally, we show that certain brain regions show a stronger positive correlation than others, potentially due to our post-mortem assessment approach requiring quantification from the contralateral hemisphere.

3.3.4 Difficulties exist acquiring real-time Methoxy-x04 signals using FFs

The main goal of developing this novel approach is to monitor plaque load in response to pharmaceutical or non-pharmaceutical interventions. Therefore, it is vital that the protocol and photometry system is appropriate for long-term monitoring. The first step in determining if this was true was completing an acute experiment to determine the pharmacokinetic profile of Methoxy-x04 **(Figure 3.3.8)**. While confirming if the system was sensitive enough to illustrate small changes in fluorescence when the Methoxy-04 is entering the brain, it will also illustrate the time-profile of Methoxy-x04.

Mice underwent a terminal procedure, where a FF was implanted into the SUB before a photometry recording. There was a 30-minute baseline recording, before injection of 10-mg/kg Methoxy-x04 i.p. Then, the change in fluorescence was tracked over several hours to determine if there was an increase due to Methoxy-x04 **(Figure 3.3.8A)**.

Results show that no rise in fluorescence was identified after injection of Methoxy-04 **(Figure 3.3.8B)**. Instead, the fluorescence continued to decline, as seen within the 30-minute baseline recording. However, the histological image shows that the fibre was not implanted into a plaque dense region; rather slightly off-target **(Figure 3.3.8C),** which was consistent for all other acute pharmacokinetic recordings that were completed where no real-time signal was detected **(Figure 3.3.8C)**. This is seen here as unlike depth profile experiments where we were manipulating the DV coordinate with each measure, here we track the same brain region across time meaning that we are limited to a single DV coordinate. With FFs cone of light collecting signals from a region of only several hundred micrometres, there is a greater likelihood that small errors in depth can result in a missed target.

Overall, the inability to achieve a reliable, consistent, and strong increase in fluorescence following Methoxy-x04 injection suggests that a change in experimental protocol may be desired. Specifically, the nature of FF's ability to damage tissue and have a limited volume of tissue illuminated means collecting these signals will be challenging.

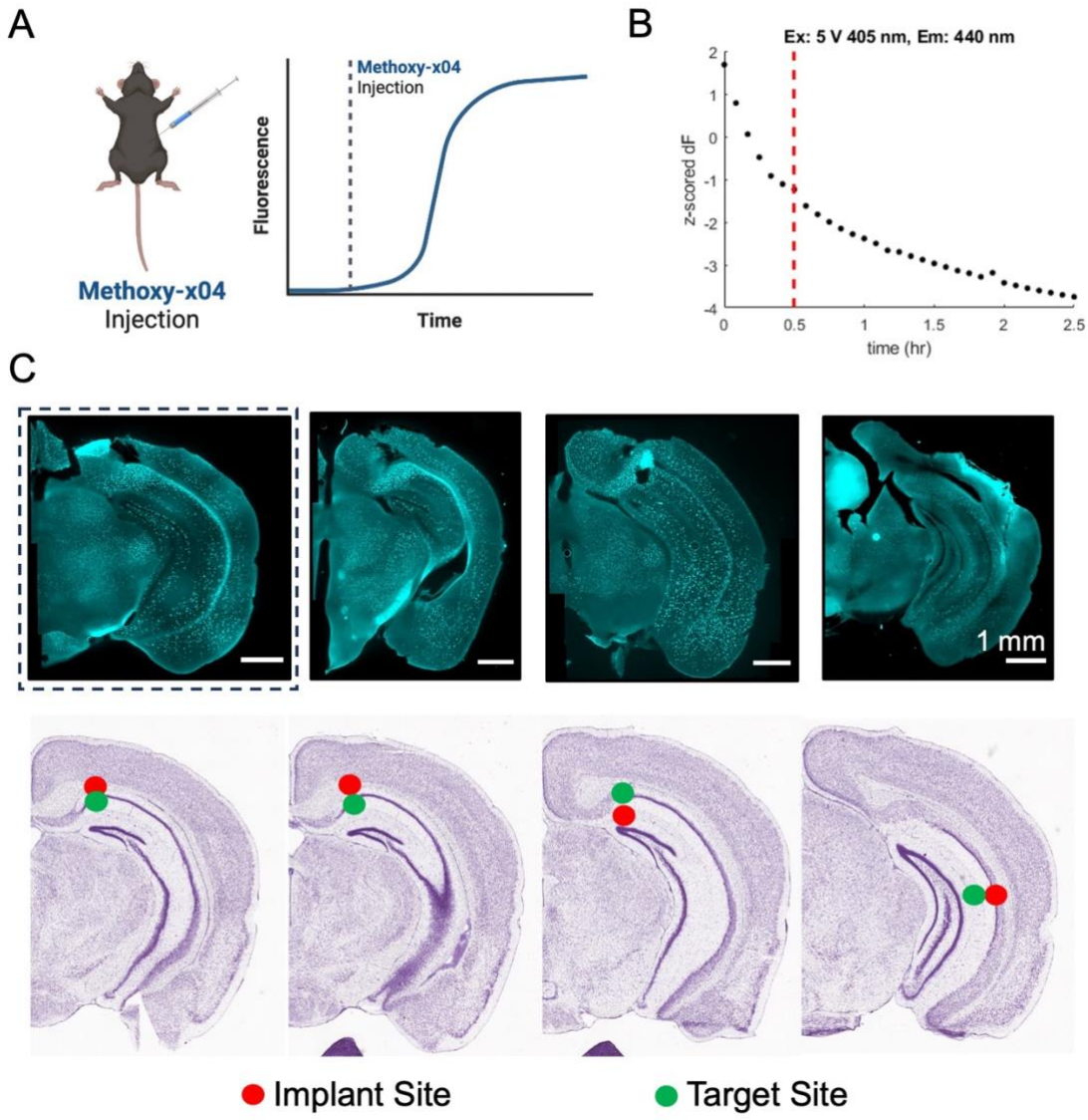

Figure 3.3.8. Difficulties acquiring appropriate depth of FFs for monitoring the acute pharmacokinetic profile of Methoxy-x04. (A) Schematic of experimental paradigm. Methoxy-x04 is injected (i.p.) after 30-minutes baseline recording and the fluorescence is monitored for several hours. Data on graph is hypothesised. Created with BioRender.com. (B) Example image of the fluorescent change following Methoxy-x04 injection at 30-minutes, when excited (Ex) with 5-V 405-nm light with emitted (Em) light collected at 440-nm. Red dashed line shows the time of Methoxy-x04 injection. Data was z-scored against the 30-minute baseline. Data is from the image with the black dashed line surrounding it. (C) Histological images showing the fibre track and atlas images showing the implant (red) and target site (green). Atlas images are from the Allen Mouse Brain Atlas, mouse.brain-map.org. Histology scale: 1-mm.

3.4 Discussion

3.4.1 Discussion of findings

3.4.1.1 Main findings

While plaques have been a constant hallmark of AD, methods for *in vivo* analysis remain limited and challenging. This means that real-time assessment of plaque pathology *in vivo* remains underexplored, leaving any beneficial effects from possible interventions potentially undetected. With the importance of this in mind, we aimed to establish a novel method for monitoring plaque pathology in real-time, using a combination of a BBB-permeable drug, Methoxy-x04 (Klunk et al., 2002), and fibre photometry (Byron and Sakata, 2024, Simpson et al., 2023). To show the success of this proposed protocol, we designed a FF photometry system that monitors Methoxy-x04 fluorescence and recorded Methoxy-x04-stained plaques *in vivo*. Initial results showed that the system configuration can detect Methoxy-x04 fluorescence *in vitro*: 405 nm excitation provided strong Methoxy-x04 signals, with the system showing sensitivity in the nanomolar range **(Figure 3.3.1)**. However, *in vivo* depth profile experiments showed that brain AF seems to interfere with Methoxy-x04 signals **(Figure 3.3.3)**. Therefore, a system reconfiguration was completed in attempt to improve system sensitivity and Methoxy-x04 detection. Following this, results show the reconfigured system to have increased sensitivity, allowing detection of Methoxy-x04 signals *in vivo* and therefore, confirmation of our novel approach (**Figures 3.3.4 & 3.3.6**). The approach was further confirmed through histological correlation analysis **(Figures 3.3.7)**. However, attempts to monitor the pharmacokinetics of Methoxy-x04, *in vivo*, proved challenging **(Figure 3.3.8).** Therefore, a protocol improvement to increase the volume of tissue being recorded is desired.

3.4.1.2 Original system configuration was not appropriate for in vivo measurement

We wished to establish a system that was able to detect Methoxy-x04 with high sensitivity. Data showed that the existing configuration was suitable for Methoxy-x04 detection, with 405-nm of light successfully exciting Methoxy-x04 fluorophores, whilst 470-nm of light did not produce Methoxy-x04 signals, consistent with previous 2PM studies (Condello et al., 2011, Hefendehl et al., 2011, Klunk et al., 2002, Meyer-Luehmann et al., 2008) **(Figure 3.3.1B)**. This occurs due to the general principle of fluorescence, where excitation within a range of wavelengths specific to the fluorophore causes an energy shift, where energy is emitted as light (Morrison, 2008). It is important that the excitation and emission parameters of the fluorophore are met by the system as it will promote the

intensity of fluorescence emitted (Wu et al., 2022b). However, the original system was set-up to collect signals at a sub-optimal setting of 525-nm.

Consequently, *in vivo* measurements showed comparable profiles across both genotypes of mice and wavelengths of light **(Figure 3.3.3)**. This suggested that no Methoxy-x04 was being detected and perhaps AF could be deteriorating pure signal collection. This is consistent with several papers that illustrate the influence of AF in fibre photometry for collecting a strong *in vivo* signal (Bianco et al., 2021, Formozov et al., 2023, Schlegel et al., 2018, Simpson et al., 2023). Particularly, biomolecules within the brain have varying excitation/emission spectra's which make it difficult to obtain a signal that is not disrupted by AF. Most biomolecules responsible for AF emit in blue and green wavelengths, such as lipofuscin, making our need to excite at 405-nm for Methoxy-x04 result in high risk of AF (Eichhoff et al., 2008, Gray and Woulfe, 2005, Kwan et al., 2009). As Methoxy-x04 has a blue-shifted emission spectra, it is possible that anatomical structures and biomolecule AF have masked Methoxy-x04 signals **(Figure 3.3.3)**. This theory can be backed as plaques are successfully stained when analysing histological sections post-surgery. Therefore, we determined that a FF photometry system modification is required.

3.4.1.3 Reconfigured system configuration was appropriate for in vivo measurement

Therefore, a FF photometry system modification to boost Methoxy-x04 detection was completed. This involved generating a dual-detection pathway for collection at 440-nm and 550-nm for Methoxy-x04 and AF, respectively. As expected, changing the emission filters to match Methoxy-x04s emission spectra provided a boost in system sensitivity **(Figure 3.3.4)**, suggesting stronger signal collection, consistent with the principles of fluorescence and Methoxy-x04s spectra (Chen et al., 2018, Morrison, 2008).

When comparing the fluorescent profile of 5xFAD+ and 5xFAD- mouse models, we show a significant rise in fluorescence in 5xFAD+ mice at 440-nm **(Figure 3.3.6)**. However, this was also noted at 550-nm in some cases, which must be due to 550-nm being towards the tail of Methoxy-x04s emission spectra as shown by Chen and colleagues (Chen et al., 2018). Therefore, we cannot use 550-nm as a Methoxy-x04-devoid control. Additionally, depth profiles were not as expected for the majority of site 1 experiments, which we believe must be due to the anatomical structure at this implant site. Difficulties with the FF re-entering the brain tissue after the ventricle may result in large increases in tissue AF and prevent adequate recording of plaque pathology and accurate depth resolution. However, for all sites combined, site 2 and 3, fluorescence profiles are greater in 5xFAD+ mouse models, with a positive correlation between photometry and histological plaque signals **(Figures 3.3.7)**. This suggests that our novel approach for monitoring plaque pathology

provides a fluorescence read-out that is comparable with histology – a well-established method for plaque assessment – albeit depending on the brain region implanted. Therefore, for the first time, we show detection of plaque pathology using FF photometry.

3.4.1.4 Monitoring plaque pathology over-time proves challenging

After confirmation of the novel approach to be a feasible method to monitor plaque pathology, we wanted to begin characterising the system and Methoxy-x04 for chronic recordings. To do so, we investigated the pharmacokinetic profile of Methoxy-x04 over several hours to determine if the system was sensitive enough to detect small changes in fluorescence over-time. Results showed a decline in fluorescence after injection **(Figure 3.3.8)**, which was replicated across experiments, suggesting that Methoxy-x04 signals have not been detected. In fact, as a decline in fluorescence was seen pre- and post-Methoxy-x04 injection, this suggests that there may be bleaching of either or both the FF photometry system and brain tissue fluorescence, commonly noted within FF photometry recordings (Byron and Sakata, 2024, Simpson et al., 2023). This would not have been seen in depth profile experiments as we do not repeat sample, reducing the bleaching of tissue. This can be indicative of the light power being too high, causing bleaching at a rate greater than Methoxy-x04 signal increase, or due to the fibre being off-target, missing collection of Methoxy-x04 signals and instead bleaching surrounding AF. Accordingly, histological analysis suggested reaching the target area for plaque monitoring was challenging, with FFs resulting in large tissue damage, consistent with other implant studies (Benveniste and Diemer, 1987, Jaquins-Gerstl and Michael, 2009, Kahan et al., 2021, Kozai et al., 2015, Kozai et al., 2012, Sych et al., 2019, Woodroofe et al., 1991). Therefore, we suggest that use of FFs may be limiting the collection of plaque signals over-time due to limiting the recording to one site, unlike depth profile experiments where we continuously manipulated the depth of the fibre. This would not be suitable for our end-goal experiments where freely behaving, longitudinal experiments are desired. We believe having the possibility to increase the volume of tissue being illuminated will enhance the success of this novel approach.

3.4.2 Limitations

While we confirmed that this approach is feasible for monitoring plaque pathology, there are several limitations with the equipment and analysis that should be noted.

3.4.2.1 System limitations

Firstly, all experiments were completed with mice under terminal anaesthetic. While this was unavoidable for this confirmation protocol, it has been shown across various studies that

anaesthesia can affect plaque pathology (Dong et al., 2009, Eckenhoff et al., 2004, Jiang and Jiang, 2015, Liang et al., 2020, Xie et al., 2008, Xie et al., 2006, Xu et al., 2011). However, as the mouse remained under anaesthesia while the brain was removed for histological analysis, plaques should remain in the same anaesthetic state for both photometry and histological measurement. Additionally, studies suggest that urethane is a good candidate for recordings under anaesthesia as it has minimal effect on altering the neuronal state compared to other anaesthetics (Shumkova et al., 2021).

Secondly, while FFs are a conventional, well-established approach for fibre photometry recordings within the brain, it has several limitations that can affect data collection. When inserting the FF into the brain, it is common to get some resistance from the tissue, interfering with the desired implantation. This can result in large tissue damage which will interfere with collection of an accurate plaque measurement, while also contributing to tissue inflammation (Benveniste and Diemer, 1987, Jaquins-Gerstl and Michael, 2009, Kahan et al., 2021, Kozai et al., 2015, Kozai et al., 2012, Sych et al., 2019, Woodroofe et al., 1991). Additionally, the inability to smoothly pass through brain tissue can affect accurate depth resolution being achieved. While we troubleshooted this by completing a durotomy to ease insertion, this was not perfect. Another limitation with conventional FFs is that you have only a limited volume of tissue that will be illuminated, limiting the region of collection (Cui et al., 2013, Gonzalez et al., 2016, Kupferschmidt et al., 2017, Natsubori et al., 2017, Pisanello et al., 2019, Tecuapetla et al., 2014), and increasing the risk of missing the target region. Introducing newly developed TFs from Pisanello and colleagues will allow all limitations to be minimised (Pisanello et al., 2017, Pisanello et al., 2014, Pisano et al., 2019).

3.4.2.2 Analysis limitations

To confirm that this approach is feasible, we aimed to correlate photometry signals with histological quantification along the fibre track. Due to tissue damage along the track site, we opted to quantify on the contralateral hemisphere. For this, we hypothesised that plaque pathology is consistent across hemispheres. However, we now know that cross-hemisphere plaque pathology can have some variations, shown by a detailed 3D analysis completed by the group of Buzsaki (Soula et al., 2023). Therefore, we must consider that some plaque quantifications are not a full representative of the photometry measure, which may contribute to some R-value outliers.

Additionally, throughout histological processing, it is common for some sections to be lost or damaged. This prevents histological quantification and thus, correlation assessment. Additionally, when aligning to the Allen brain atlas, either of these limitations can contribute to inaccurate alignment or warping of the histological section. In more detail, the alignment software will stretch

the section to fit the appropriate atlas section. Thereby, the wrong plaques and brain region can be quantified, interfering with accurate plaque quantification. This hereby illustrates the importance of our novel approach being a feasible route for monitoring plaque pathology.

3.4.3 Future work

To achieve real-time feedback, in freely behaving mice, we believe we will need to optimise this approach. As discussed, for collection of Methoxy-x04 signals over-time, FFs have some limitations. Over recent years, a new TF has been introduced by the labs of De Vittorio and Pisanello (Pisanello et al., 2017, Pisanello et al., 2014, Pisano et al., 2019). These are optic fibres that have been mechanically pulled at the tip, resulting in a long sharp active region. Additionally, there is increased functionality of illumination, having the ability to release and collect light over 1.8-mm. While allowing to record from 1.8-mm of brain tissue at the same time, it reduces the risk of missing your target and tissue inflammation. We hypothesise that designing and implementing a TF system will allow depth-resolved monitoring of plaque pathology, in freely behaving mouse models. We believe this enhancement will move the project forward in the desired direction.

3.4.4 Conclusions

Overall, for the first time, we illustrate that our novel approach combining Methoxy-x04 and fibre photometry for monitoring plaque pathology is feasible, thereby allowing monitoring of plaque pathology across depth, depending on the brain region implanted. However, to acquire real-time plaque monitoring we need to overcome implantation difficulties that occur when using FFs and we believe that by implementing the use of TFs, we can achieve in vivo real-time, depth-resolved plaque monitoring in freely behaving conditions.

4. Depth-resolved optical interrogation of plaque pathology, in real-time, in freely behaving mice

4.1 Introduction

4.1.1 Background

As previously discussed in **Chapter 1**, real-time feedback in deep regions of the mouse brain often go missed when monitoring plaque pathology in response to therapeutics. As deeper brain regions, such as the hippocampus, are vital for memory formation and processing, it would be beneficial to investigate the effects in these brain regions when investigating a memory disorder such as AD. With confirmation that a combined approach of Methoxy-x04 and fibre photometry is a feasible method for monitoring plaques, it is desirable to modify this approach to allow for long-term monitoring of plaque pathology across depth. Implanting optic fibres allows access to deep brain regions. However, it has no depth resolution, only illuminating at one depth. TFs are a less invasive optic fibre that allows depth resolution by having an illumination and collection pattern over 1.8-mm (Pisanello et al., 2017, Pisano et al., 2019). By implanting these, we can monitor 1.8-mm of brain tissue at one time, over-time. However, as they are newly established several aspects of their use for monitoring real-time fluorescent biological signals remain to be investigated.

4.1.2 Aims and hypotheses

Over this chapter, we had two major hypotheses. First, we hypothesised that use of TFs will allow real-time, depth-resolved plaque assessment over-time. Secondly, we hypothesised that manipulating the light propagation along the TF and testing different analytical approaches will realise a stronger, reliable Methoxy-x04 signal. To test these hypotheses, we aimed to design and implement protocols that allow TFs to dissect plaque pathology across depth. Then, using these protocols to determine if this approach can detect changes in Methoxy-x04 signals in a depth and time-resolved manner.

4.1.3 Overview

Within this chapter, I will begin by describing the methodology of the system establishment and experiments completed to attain the following results **(section 4.2)**. Then, I will show the pharmacokinetic profile of Methoxy-x04 and the subsequent re-dosing protocol, shown with a variation of light protocols and analytical approaches **(section 4.3.3)**. After, we attempt to correlate

TF photometry plaque signals with histologically quantified plaque signals **(section 4.3.4)**. Lastly, we discuss the implication of these findings, as well as limitations and potential future studies **(section 4.4)**.

4.2 Methods

This section provides a detailed description of the TF photometry-specific methodology used throughout this project **(Figure 4.2.1)**. Firstly, a description of the fibre photometry system used for TF experiments is provided, with an overview of system design and maintenance procedures explained in multiple sub-sections within **section 4.2.1.** Next, all *in vivo* experimental procedures completed with the TF system are introduced, including animals used **(section 4.2.2.1)**, recording protocols **(sections 4.2.2.2 and 4.2.2.3)** and histological assessment **(section 4.2.2.4)**. Lastly, data processing and analytical approaches are described in **section 4.2.3**. All protocols completed across various sub-projects, such as Methoxy-x04 properties, animals and image data analysis are discussed in **Chapter 2** in **sections 2.1.1, 2.1.2 and 2.1.3.**

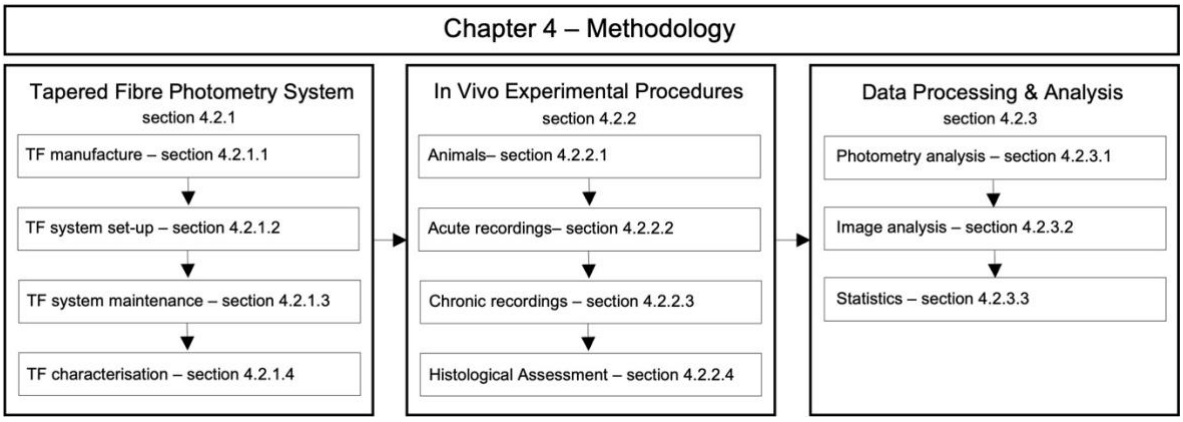

Figure 4.2.1. Roadmap of chapter 4 methodology. Protocols regarding the TF system are explained within **section 4.2.1**. *In vivo* experimental procedures completed using the TF system are described in **section 4.2.2**. Data processing and analysis for TF data is explained in **section 4.2.3.**

4.2.1 TF photometry system

FFs are well-established and allow for interrogation of several biological signals within the brain. However, FFs can result in significant tissue damage, and have a small spatial resolution. Recent developments have resulted in the manufacture of TFs which have a greater region of collection and are less invasive (Pisanello et al., 2017, Pisano et al., 2019). Therefore, we wanted to implement this approach for monitoring plaque pathology, in real-time. Therefore, a TF photometry system was designed and manufactured by Dr Niall McAllinden and collaborators at Istituto Italiano

di Tecnologia and OptogeniX S.r.l. Once set-up, the system underwent various maintenance protocols and calibration experiments before *in vivo* use.

4.2.1.1 TF manufacture

Multimode TFs were designed and created by the group of Massimo De Vittorio and are now commercially sold (OptogeniX). Custom TFs (200-µm core, 0.39˚ NA) with a 1.8-mm active region – where light can be released and collected – and 5-mm total length were used. These are developed through a heat and pull process which involves melting of the fibre core and cladding and pulling of the optic fibre to a sharp tip **(Figure 4.2.2)**. This leaves a TF with a core of 200-µm that tapers gradually to reach ~500-nm, with a small taper angle that determines the active region. Details on the manufacture process have been described before (Pisanello et al., 2017). This design provides several benefits over FFs **(Figure 4.2.2).**

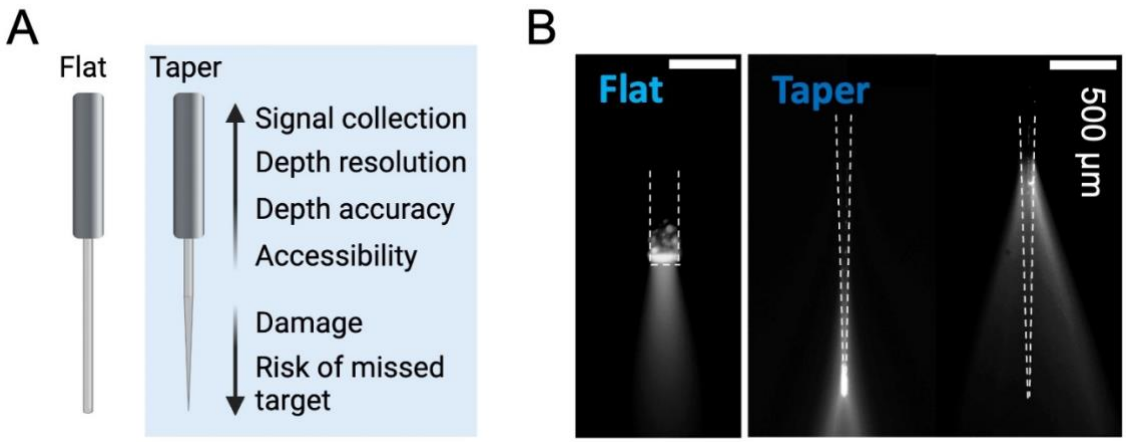

Figure 4.2.2. Benefits of TFs. (A) Schematic illustrating the differences in structure of the TF, with a list of benefits. Created with BioRender.com. (B) Images of the light profile in fluorescein solution when using a flat (left) or tapered (right) fibre. For the TF, at 0V galvo voltage the light has minimal internal reflection and will propagate out of the tip of the TF (left). At 5V galvo voltage, the light has greater internal reflection within the TF and propagates at the top of the tapered shaft. Scale: 500-µm.

4.2.1.2 TF photometry system set-up

The TF photometry system has a similar set-up to the FF photometry system, with the main differences including the use of a laser rather than LED, introduction of a galvo mirror (see **section 4.2.1.2.1**) and three separate detection pathways rather than two (405, 440 and 550-nm). A laser is required for this system to provide a coherent light beam and fast initialisation times. A galvo

mirror is required to modulate the angle light enters the TF to control where it is propagated from the TF (see **section 4.2.1.2.1** for a detailed description).

The TF photometry system has three light pathways: illumination (405-nm), illumination detection (405-nm) and signal detection (440 and 550-nm) **(Figures 4.2.3-4)**. Throughout the project, the original laser (MDL-III-405-50-mW, CI90055, CNI lasers) deteriorated, and a new laser (Cobolt 06-01 Series, Hubner Photonics), based on a heat-sink (HS-03, Hubner Photonics) was implemented. When this occurred laser light was reflected of a glass slide and focussed onto a new photodetector (PDA25K-EC, Thorlabs) to monitor laser stability **(Figures 4.2.3A-B)**. The laser light passes through a neutral density filter (optical density: 0.4, Thorlabs), held by a mount (LMR 1/M, Thorlabs), and through a combination of mirrors (DMSP490R, Thorlabs). Then, light passed an aspheric lens (AC254-050-A-ML) (50-mm focal length doublet, 25.4-mm diameter) which focused light onto a galvo mirror (GVS001, Thorlabs) (see **section 4.2.1.2.1**). Light output was then collimated from the galvo mirror using an aspheric lens (AC254-050-A-ML, Thorlabs) (50-mm focal length doublet, 25.4-mm diameter). Now, light passes through a 425-nm short-pass dichroic mirror and was directed towards the fibre launch system, where appropriate light-path alignment and an aspheric lens (AC254-030-A-ML, Thorlabs) (30-mm focal length doublet, 25.4-mm diameter) coupled the light into a custom-made multimode patch cable (length: 0.7-m, fibre core: 200-µm, NA: 0.39˚) (custom or FT200EMT-CUSTOM, Thorlabs). This cable was connected to an implantable TF (OptogeniX) via a mating sleeve (ADAL1-5, Thorlabs). Now, light output from the TF allows excitation of fluorophores.

The signal detection pathway collects light from the TF and passes it back to the fibre launch system for delivery to the photodetectors (NewFocus 2151, Newport) for measurement **(Figures 4.2.3-4)**. After travelling back along the patch cable (custom or FT200EMT-CUSTOM, Thorlabs), the light beam is collimated by the same aspheric lens used in the illumination pathway. Light is reflected off the 425-nm short-pass dichroic mirror (DMSP425T, Thorlabs) and is directed toward the appropriate photodetector using a 525-nm short-pass dichroic mirror (Thorlabs). Light below 525-nm passes, before reaching a 440-nm emission filter (FB440-10, Thorlabs), where remaining light is focussed onto the photodetector by an aspheric lens (AC254-030-A-ML, Thorlabs) (30-mm focal length doublet, 25.4-mm diameter) for measurement. Light above 525-nm reflects, before passing a 550-nm emission filter (FB550-10, Thorlabs), where remaining light is focussed onto the photodetector by an aspheric lens (AC254-030-A-ML, Thorlabs) (30-mm focal length doublet, 25.4-mm diameter) for measurement. Signals collected at the photodetector were then digitized to analogue signals using a NIDAQ device (NI USB-6343, National Instruments).

The system components were controlled by the NIDAQ device and custom LABVIEW code (written by Dr Shuzo Sakata, Dr Niall McAlinden and Nicole Byron). The whole system is enclosed in a

safety box (XE25C7/M, Thorlabs) **(Figure 4.2.4A)**, only removed if total system realignment or redesign was required, with optical components secured by mirror mounts (KM100 and CF088/3, Thorlabs), filter mounts (FFM1, Thorlabs), lens mount (CXY1, Thorlabs), lens tube end caps (SM1CP2, Thorlabs) and cage cubes and plates (C4W, CP12 and CMI-DCH/M Thorlabs) **(Figure 4.2.4B)**. All components – patch cable (custom or FT200EMT-CUSTOM, Thorlabs), TF (OptogeniX), and mating sleeve (ADAL1-5, Thorlabs) – had a 1.25-mm setting for ferrules. The patch cable and TF core diameter and NA was 200-µm and 0.39˚, respectively.

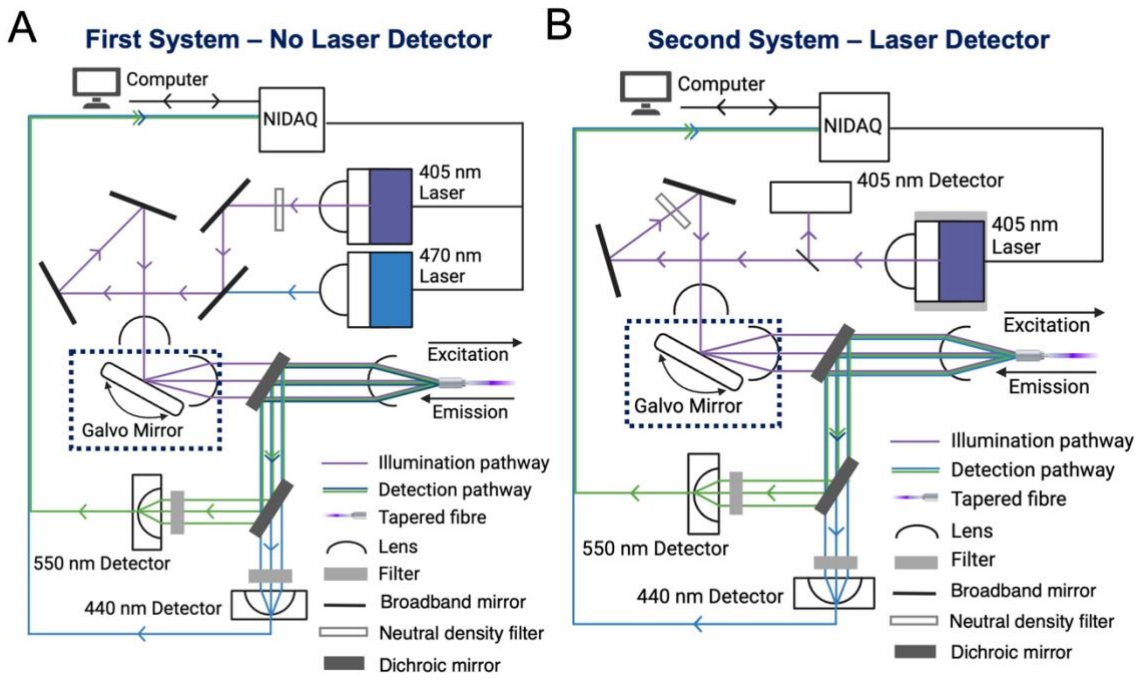

Figure 4.2.3. Diagram of the TF set-up. (A) First system set-up where there was a dual-laser pathway, with no photodetector to monitor laser stability. (B) Second system set-up where the single-laser was placed on a heat-sink and light was reflected and monitored by a photodetector to monitor laser stability. Insets represent the galvo mirror which is described in detail in **section 4.2.1.2.1**. Created with BioRender.com.

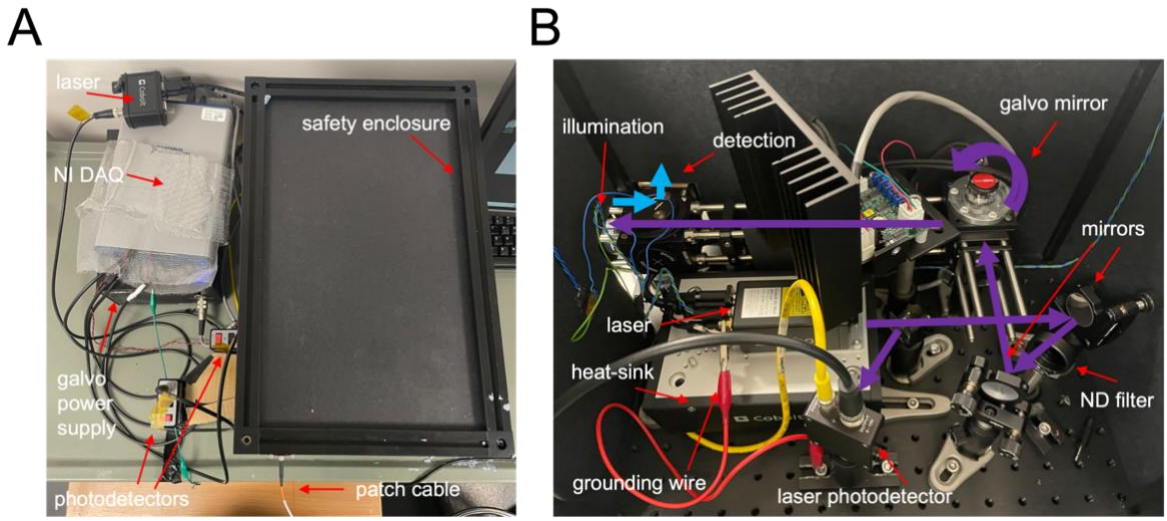

Figure 4.2.4. Images of the TF photometry system. (A) TF system with the safety enclosure closed. Light from inside the safety enclosure is coupled into the external patch cable. Detection photodetectors are outside of the safety enclosure. All power supplies and the NIDAQ are outside of the safety enclosure. (B) Inside the safety enclosure. Purple arrows illustrate the illumination light path which travels to the patch cable outside of the safety enclosure. Blue arrows illustrate the detection light path which travels to the photodetectors outside of the safety enclosure.

4.2.1.2.1 Galvo Mirror

To achieve depth-resolution, different light patterns must be propagated from the TF. Therefore, light propagation into the TF must be finely controlled. The way to do so involves the use of an electronically controlled motorised optical mirror – galvo mirror (GVS001, Thorlabs) **(Figure 4.2.5)**. The system used is a single axis motorised system consisting of a motor and mirror assembly, an optical mount, an electronic driver card and a heat sink. The motorised component is termed a galvanometer and will rotate the motor when current is applied. When aligned within an optical system, light beams will deflect off the mirror over the angular range of the galvanometer. We control this motorised component by supplying different input voltages, through the power supply (GPS011, Thorlabs). Application of the input voltage moves the mirror at an angle, resulting in the laser beam shifting from the centre of the mirror. Therefore, higher input voltages will move the mirror at the greater angle, resulting in a greater deflection of laser light **(Figure 4.2.5)**.

The angle of reflected light will alter the angle light will couple into the TF. This light will internally reflect within the TF, resulting in differing angles of light propagation along the fibre shaft **(Figure 4.2.5i)**. For example, when voltage is low, internal reflectance will be minimal resulting in light propagating out regions at the TF tip. Whereas higher input voltages result in greater angular reflections, greater internal reflectance, and light propagation out higher regions along the TF shaft.

As this occurs, the light profile from the TF will form uniform rings of laser light that can be seen by pointing the TF towards white paper **(Figure 4.2.5ii)**.

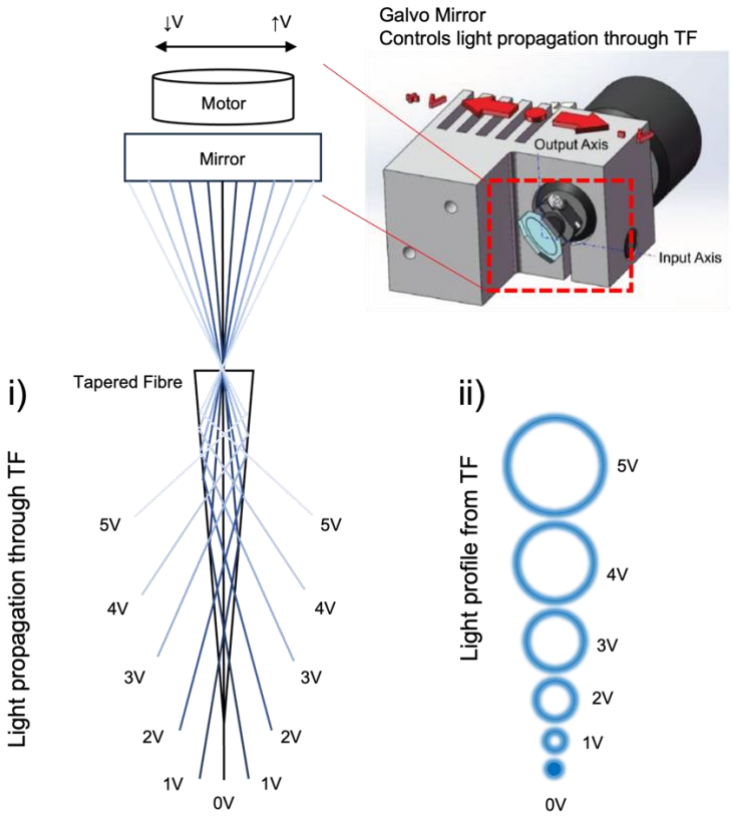

Figure 4.2.5. Functionality of the galvo mirror for controlling light propagation through the TF. *Top right,* Diagram of the galvo mirror with the electrical motor, adapted from the Thorlabs manual (GVS001). The electrical motor is driven at varying voltages to move in different directions. Inset shows the corresponding equipment in a diagram. *Top left,* Diagram illustrating the light propagation through the TF using the galvo mirror. When the motor is driven at 0-V, the mirror remains in original condition allowing light propagation straight through the fibre, with light propagating from the fibre tip. When the motor is driven at increasing voltages, the mirror changes its angle, altering the angle the light enters the TF. Therefore, light will reflect within the TF and propagate at increasing depths away from the fibre tip. Therefore, a depth-resolved light propagation along a TF can be achieved. This shows the i) light propagation through the TF and the ii) resulting light profile from the TF when shown against white paper.

4.2.1.3 System maintenance

Before each recording, the system must undergo regular maintenance to ensure that it is functioning appropriately and to ensure consistency. To do so, several parameters were consistently monitored, and a variation of protocols were undertaken.

4.2.1.3.1 Alignment

Light must be appropriately aligned onto the laser detection photodetector, the fibre launch system, and the signal photodetectors. Before each recording, a regular alignment check was completed **(Figure 4.2.6)**. This involved measuring the light output at the end of the patch cable (custom or FT200EMT-CUSTOM, Thorlabs), at increasing galvo voltage (GV), when the laser was at 1-V, using a light sensor (PM100A and S120C, Thorlabs). Additionally, appearance of appropriate galvo rings was checked. These should increase in size with GV, while maintaining a uniform light distribution **(Figure 4.2.6A)**.

If the light output was not consistent or galvo rings were disrupted, 5 steps of increasing complication would be completed **(Figure 4.2.6B)**. Firstly, all NIDAQ connections (NI USB-6343, National Instruments) and battery levels were checked. Secondly, laser stability was checked using the photodetector (PDA25K-EC, Thorlabs). Consistent laser intensity at 1-V was ~2.4-V on the photodetector. Thirdly, patch cable ferrules were cleaned using propanol (FCS3, Thorlabs) and lint-free tissues (LFW90, Thorlabs). Next, manual alignment of the fibre launch system using screws to change the x-, y- and z- axis was completed to modify the output of the laser into the patch cable, optimising light power across each GV. The final and most severe step was a full system clean and re-alignment. This involved removing the safety enclosure (XE25C7/M, Thorlabs) and completing a deep clean of optical components and modifying component angles until the beam path was optimal. Throughout all steps, the user would be wearing laser safety goggles (LG3B, Thorlabs), room lights were on, and the room would be off access to non-laser users.

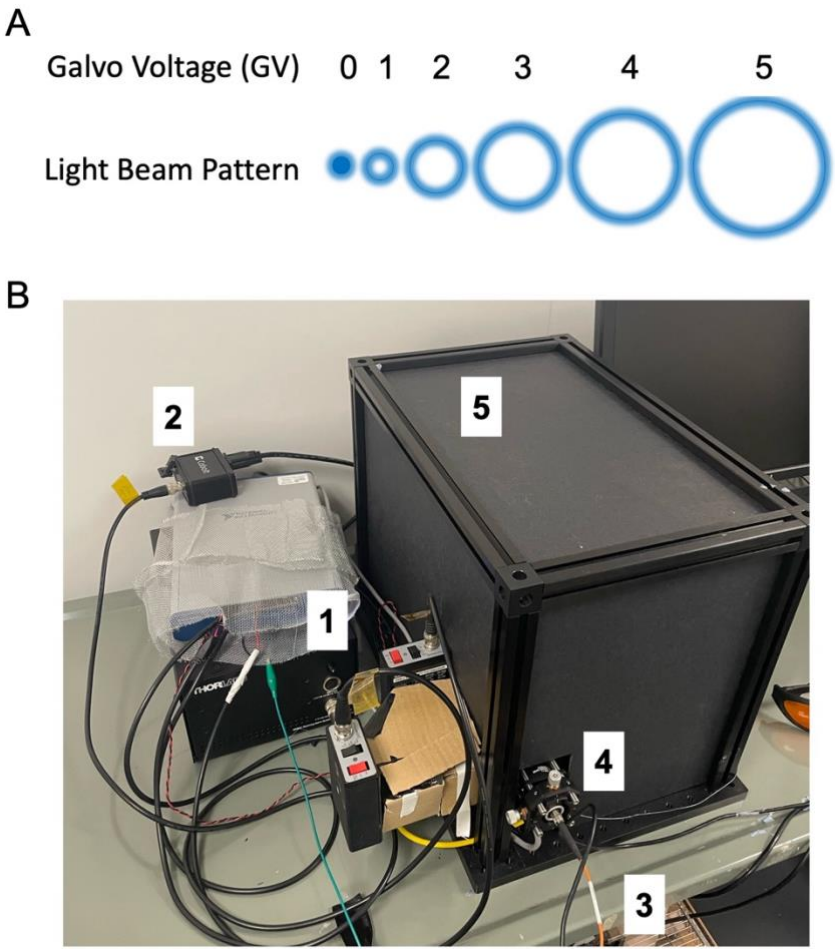

Figure 4.2.6. TF system alignment protocols. (A) Ring structure expected from the end of the patch cable when pointed at white paper, across galvo voltages (GVs), when the system was appropriately aligned. (B) Image of the TF photometry system with numbers corresponding to the different steps of realignment. (1) NIDAQ connections and battery levels; (2) Laser stability; (3) Patch cable maintenance; (4) External alignment; (5) Internal alignment and system clean.

4.2.1.3.2 Light power

Firstly, before and throughout recordings, the fluorescence measured at the 405-nm detector (PDA25K-EC, Thorlabs) was monitored to determine if the laser was supplying a consistent power at the same driving voltage.

Secondly, light output at the end of the patch cable was measured before each recording, using a light sensor (PM100A and S120C, Thorlabs). If major variations in power and alignment were seen, several steps were taken to repair this **(section 4.2.1.3.1)**. However, if small day-to-day variations occurred, we completed a re-calibration of the system. This involved measuring the light power at the end of the patch cable, using the light sensor (PM100A and S120C, Thorlabs), across several laser voltages (from 0.6-0.7-V, consistent with the voltage level used for *in vivo* recordings) and

across several GVs (0-4-V). Accordingly, the laser was driven at the first voltage and the GV was increased when the measurement was taken. Once the final GV measurement had been taken, the laser was driven at the next voltage and the GV was reset. This was repeated across all laser voltages. We monitored this by controlling the NIDAQ (NI USB-6343, National Instruments) using a custom LABVIEW code, which calculated a linear regression model for each GV, using the light power measurements. From here, we acquired a y-intercept and slope for each GV. These parameters were used for all TF photometry measurements as a reflection of the laser power state and used to determine the driving voltages required to achieve the desired light power for recordings **(**see **section 4.2.1.4.3)**.

4.2.1.3.3 Bleaching

Bleaching of the system involved stabilising the patch cable ferrule using a cannula holder (FCM13/M, Thorlabs) and helping hand. Next, the laser (MDL-III-405-50-mW, CI90055, CNI lasers or Cobolt 06-01 Series, Hubner Photonics) was left on continuously at full power. This involved an initial bleaching session lasting >8-hours. After this, a bleaching protocol was followed before each recording.

Over time, this protocol progressed. Firstly, full power of the 405-nm laser, at 0-V galvo (GVS001, Thorlabs) was applied for 30- or 60-minutes. Accordingly, the laser and galvo are continuously driven at the chosen voltages. Secondly, full power of the 405-nm laser, sweeping across all GVs was applied for 30-minutes. Accordingly, after 10-seconds baseline, the laser was continuously driven at the chosen voltage: either 4-V or 1-V depending on laser used **(Figure 4.2.3)**. In parallel, the light is swept along all GVs using the galvo mirror driven at -1-V to 5-V at 1-Hz. Thirdly, light was swept across all GVs until a bleach threshold had been reached. Accordingly, once the 440-nm photodetector fluorescence is less than a chosen voltage, the laser and GVs will return to 0-V. The bleach threshold was determined by calculating the moving median of recorded 440-nm fluorescence over-time. When fluorescence at 440-nm reached a plateau, this value would be taken as the bleaching threshold. This value changed occasionally depending on laser strength and system alignment. Across all protocols, fluorescence was continuously recorded across all implemented photodetectors (405, 440 and 550-nm) at 1000-Hz, with analogue signals being digitised for analysis. The system was controlled by the NIDAQ (NI USB-6343, National Instruments) using a custom LABVIEW code.

4.2.1.3.4 AF recovery

First, the TF (OptogeniX) was attached to the patch cable ferrule via a mating sleeve (ADAL1-5, Thorlabs) and stabilised using a cannula holder (FCM13/M, Thorlabs) and a helping hand. Then,

AF of the system was tested by running a dual bleaching and AF recovery experiment involving a 30-minutes bleaching protocol before a 12-h AF recovery experiment. As above, the bleaching protocol was 10-seconds baseline, followed by continuously driving the laser (MDL-III-405-50-mW, CI90055, CNI lasers) at the chosen voltage for 30-minutes. In parallel, the light is swept along the TF using the galvo mirror (GVS001, Thorlabs) driven at -1-V to 5-V at 1-Hz. Immediately after this 30-minute bleaching session, the AF recovery was tested. This began with a 30-second sampling interval before running through the illumination protocol. This was 405-nm laser excitation for 10-ms ON, 5-ms OFF, for the chosen power: 140-µW as this was the highest *in vivo* experiment light power used. In parallel, the light is swept along the TF using the galvo mirror driven at -1-V to 4.5-V over the 10-ms laser ON period, remaining at 0-V during the 5-ms OFF period. This was completed only once. Once complete, this whole protocol was repeated after the sampling interval: 30 seconds. Throughout the whole protocol the emission at 440 and 550-nm was collected at 5000-Hz. Signals were not collected at 405-nm as these recordings were completed before the system change. The system was controlled by the NIDAQ (NI USB-6343, National Instruments) using a custom LABVIEW code.

4.2.1.4 Fibre characterisation and illumination

Before use of any TF (OptogeniX), they had to be fully characterised. This involved determining their coupling efficiency and establishing two light protocols that modify the light profile across the active region of the TF **(Figure 4.2.7A)**.

4.2.1.4.1 Coupling efficiency

Each fibre would be tested to determine its coupling efficiency; the percentage of light from the system being coupled with the TF. Light at the end of the patch cable (custom or FT200EMT-CUSTOM, Thorlabs) while a TF (OptogeniX) was and was not attached, via a mating sleeve (ADAL1-5, Thorlabs), was measured across several powers and GVs (GVS001, Thorlabs), as described in **section 4.2.1.3.2**. From this, the coupling efficiency was calculated across all GVs using the following calculation:

$$\text{coupling efficiency (\%)} = P_p/P_{TF} \times 100,$$

where P_p and P_{TF} represent the light output at the end of patch cable and TF, respectively. If the coupling efficiency was less than 40%, the TF was not used. These values were used for all recordings to determine the driving voltages required to achieve the desired light power for recordings (see **section 4.2.1.4.3**).

4.2.1.4.2 Light protocols

To modify the light profile along the TF, *in vitro* and image-based light protocols were implemented. As described in **section 1.3.2.5.3.3**, the light profile will vary across the active region of each TF due to alignment limits. This commonly presents as a decline in light output with increasing GVs. Consequently, for an equal measure along the TF for comparable depth-resolution, protocols must be implemented to modulate the light power along the TF. Firstly, we equalise the light power along the TF **(Figure 4.2.7B)**. Secondly, we equalise the power density along the TF **(Figure 4.2.7C)**. For comparison, all recordings were also completed with the original light protocol where light was not modulated, and the TFs natural propagation pattern was used.

4.2.1.4.2.1 In vitro

An *in vitro* light protocol was established to equalise light power along the TF **(Figure 4.2.7B)**. To do so, a TF was placed in uniform Methoxy-x04 concentration and underwent an illumination protocol. Fluorescence at each depth was used to calculate the required power for uniform fluorescence measurements.

A TF (OptogeniX), connected to the TF photometry system via a mating sleeve (ADAL1-5, Thorlabs), was placed into a uniform concentration of 0.1 mM Methoxy-x04 (prepared as described in **section 2.1.1.2**) (4920, Tocris) and underwent an illumination protocol. This was 405-nm laser (MDL-III-405-50-mW, CI90055, CNI lasers or Cobolt 06-01 Series, Hubner Photonics) excitation for 10-ms ON, 5-ms OFF, for each power: 60 and 80-µW. In parallel, the light is swept along the TF using the galvo mirror (GVS001, Thorlabs) driven at -1-V to 5-V over the 10-ms laser ON period, remaining at 0-V during the 5-ms OFF. These processes were repeated 5 times separated by a 5-ms baseline. Throughout the whole illumination protocol, signals were collected at the implemented photodetectors (405, 440 and 550-nm) (PDA25K-EC, Thorlabs and NewFocus 2151, Newport) at 5000-Hz, controlled by the NIDAQ (NI USB-6343, National Instruments) using a custom LABVIEW code. Online analysis was completed using a custom MATLAB code to calculate a galvo-power ratio. Here, the mean signal was transformed to a relative required power using the formula shown in **Figure 4.2.7B**. The desired GVs (-1 to 4.5-V with a 0.1-V resolution) were matched with the subsequent relative required power and saved within a .mat file for use in future recordings.

4.2.1.4.2.2 Image

An image-based light protocol was established to equalise the power density – light power per unit volume of brain tissue – along the TF **(Figure 4.2.7C)**. This was completed as the light distribution

varies along the TF, with higher GVs having a cone of light that can cover larger volumes of tissue. However, as light power decreases at these GVs, the power density is not equalised along the depth measured.

A TF (OptogeniX), connected to the TF photometry system via a mating sleeve (ADAL1-5, Thorlabs), was lowered into a cuvette filled with a uniform concentration of fluorescein (FITC) (0.1-M) and underwent an illumination protocol **(Figure 4.2.7C)**. This illumination protocol involved continuous 405-nm excitation at a chosen voltage: optimal range was usually ~1.8-V on the old laser and between 0.635 and 0.654-V on the new laser (MDL-III-405-50-mW, CI90055, CNI lasers or Cobolt 06-01 Series, Hubner Photonics). In parallel, light was swept along the TF from 4.5-V galvo to -4.5-V galvo (GVS001, Thorlabs) at a resolution of 0.1-V. Throughout this, images of the light profile were captured at an interval of 0.5-seconds to visualise the FITC fluorescence surrounding the TF. Images of the TF within the cuvette were taken before illumination, in light conditions, to visualise the tapered structure for analysis. Additionally, images of a scale bar calibration slide showing 1 mm was taken at the same magnification to allow calculation of the scale. This equipment was controlled by the NIDAQ (NI USB-6343, National Instruments) using a custom LABVIEW code. For analysis, scale information was determined by measuring the pixel to micrometre ratio using the scale bar image. After converting images (to .jpg) and creating a video of the emission profile by combining image frames, the active region of the TF was labelled and visually inspected. Next, pixel intensities along the line marking the active region were calculated across adjacent frames. Using this, power densities were calculated by determining the power across a defined area around the active region of the TF, using calculations and custom codes depending on the taper angle, provided by our collaborators. Then, the power density ratio and relative required power per GV was calculated to determine a galvo-power ratio, using the formula shown in **Figure 4.2.7C**. The desired GVs (-1 to 4.5-V with a 0.1-V resolution) were matched with the subsequent relative required power and saved within a .mat file for use in future recordings.

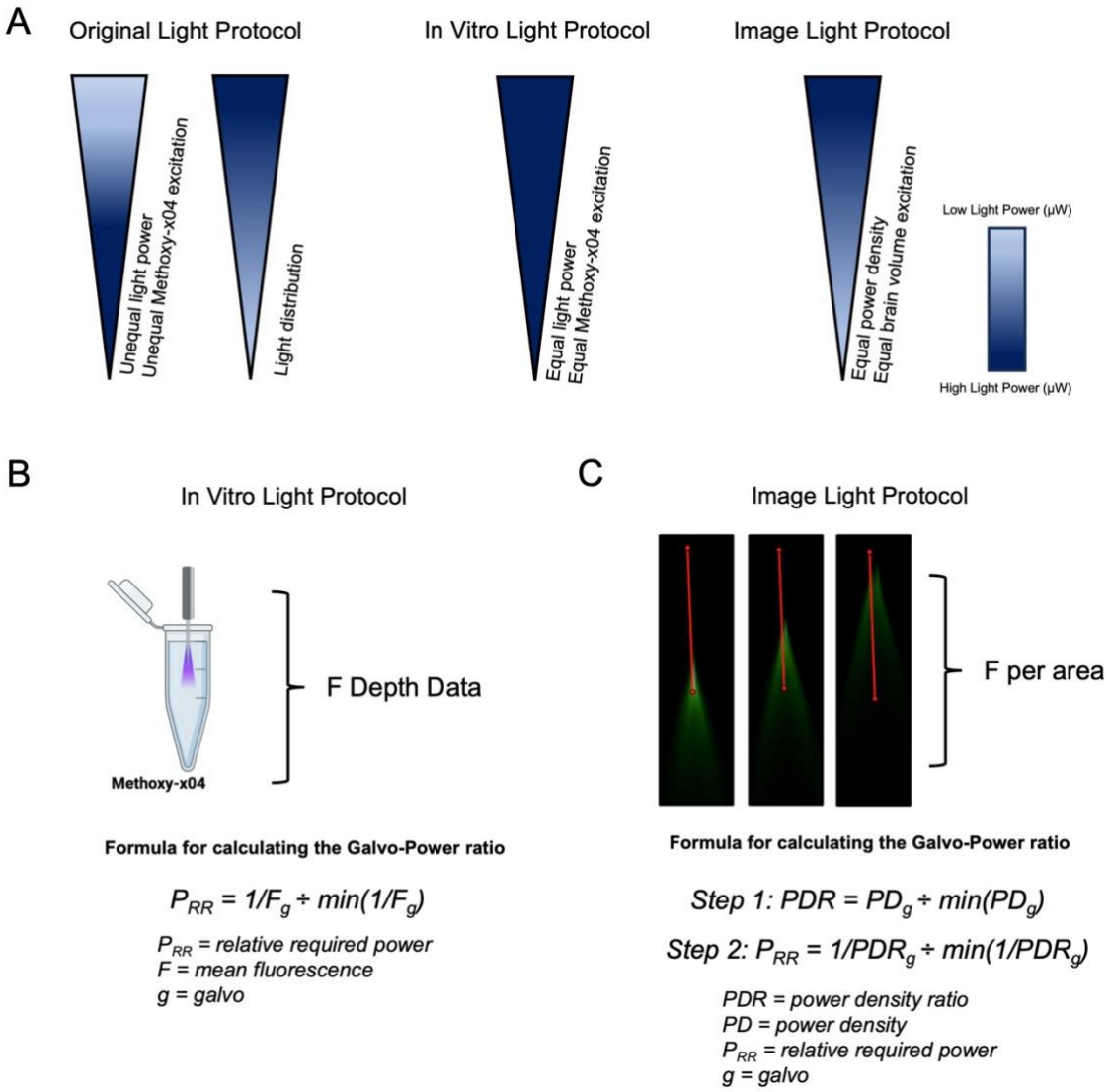

Figure 4.2.7. Rationale and protocol to establish different light protocols. (A) Schematic of the rationale of desired outcomes from light protocols. The original light protocol has unequal light power along the TF. The distribution of light is also greater at the base of the TF. The *in vitro* light protocol aimed to achieve equal light power along the TF for equal Methoxy-x04 excitation. The image light protocol aimed to achieve equal power density along the TF for equal brain volume excitation. Scale shows the range of light power. (B) Protocol for establishing an *in vitro* light protocol. (C) Protocol for establishing an image light protocol.

4.2.1.4.3 Calibration

Lastly, the TF underwent calibration protocols to illustrate the success of its characterisation. The TF (OptogeniX) was lowered into a Methoxy-x04 concentration (0.1-mM) (4920, Tocris) and underwent an illumination protocol. The illumination protocol involved excitation at 405-nm, across various power intensities (20, 40, 60, 80, 100, 120 and 140-μW), for original, *in vitro*, and image-

based light protocols. Parameters determined for a GV of 3-V were used as a reference for slope, intercept and coupling efficiency, acquired as described in **section 4.2.1.3.2**, due to them consistently providing the most accurate power estimations.

Laser voltages for the original light protocol were calculated using a calculation as shown in **Figure 4.2.8.** Original light protocol involves no modulation of power across GVs, meaning the same voltage will be applied across all GVs. Laser voltages for *in vitro* and image light protocols for each GV were calculated using previously determined Galvo-Power ratios (as described in **section 4.2.1.4.2**) and a custom MATLAB and LABVIEW code. For this, the Galvo-Power ratio is resampled to reflect the galvo sampling rate used for *in vivo* recordings (50 measures from -1 to 4.5-V; resolution of 0.1-V). Then, for each desired power, the required power is calculated using the ratio as shown in **Figure 4.2.9.**

Using the calculated voltages for each desired power and light protocol (original, *in vitro* and image), the illumination protocol began with the first light protocol (*in vitro*). This was excitation of the 405-nm laser (MDL-III-405-50-mW, CI90055, CNI lasers or Cobolt 06-01 Series, Hubner Photonics) for 10-ms ON, 5-ms OFF, for each power. In parallel, the light is swept along the TF using the galvo mirror (GVS001, Thorlabs) driven at -1 V to 4.5-V over the 10-ms laser ON period, remaining at 0-V during the 5-ms OFF. These processes were repeated 5 times separated by a 5-ms baseline. After the last 5-ms baseline, the illumination protocol restarted for the second light protocol (image). After the last 5-ms baseline in this iteration, the illumination protocol restarted for the third light protocol (original). Throughout the whole protocol, fluorescence was recorded at implemented photodetectors (405, 440 and 550-nm) (PDA25K-EC, Thorlabs and NewFocus 2151, Newport) at 5000-Hz. Additionally, sync channels of the 405-nm laser and galvo mirror were monitored for post-processing. This equipment was controlled by the NIDAQ (NI USB-6343, National Instruments) using a custom LABVIEW code. This LABVIEW VI generated a .dat file for each photometry measure.

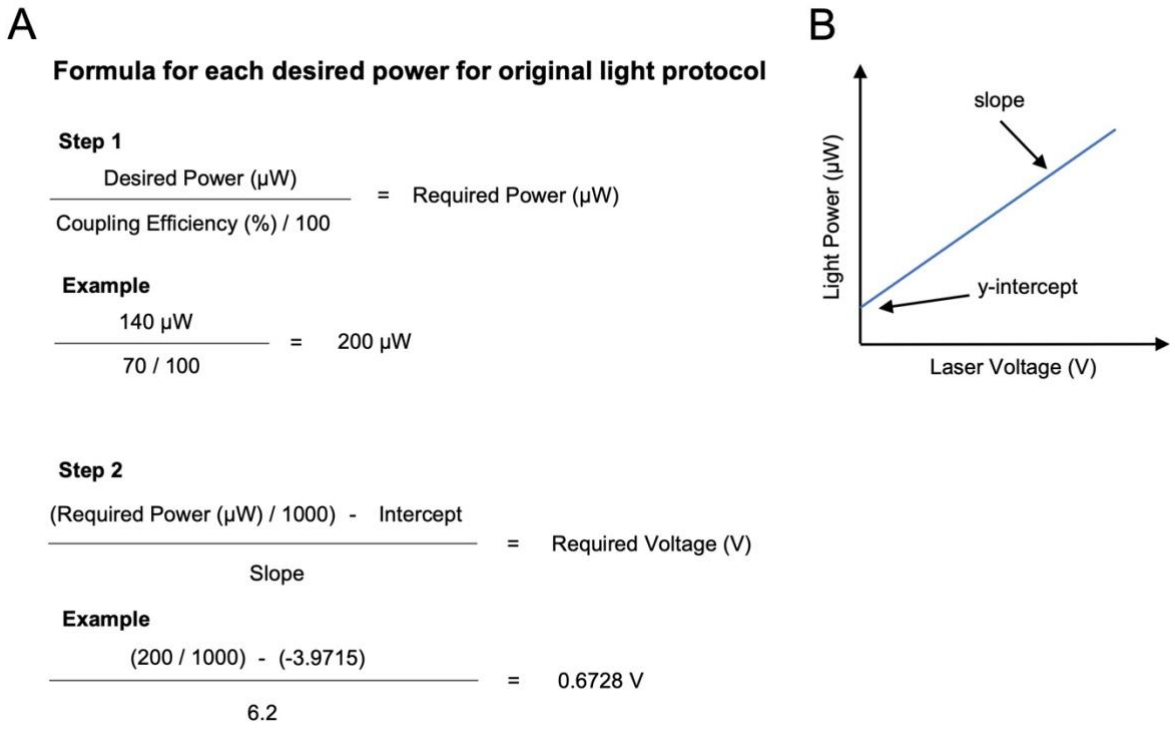

Figure 4.2.8. Calculating the required voltages for the original light protocol. (A) Formula for each desired power for the original light protocol. The required voltage will be supplied for all GVs. This is calculated automatically using custom MATLAB and LABVIEW code. The coupling efficiency, intercept and slope are determined as described in **section 4.2.1.3.2**. (B) Schematic illustrating how the y-intercept and slope is determined. The light power is measured at increasing laser voltages as described in **section 4.2.1.3.2**.

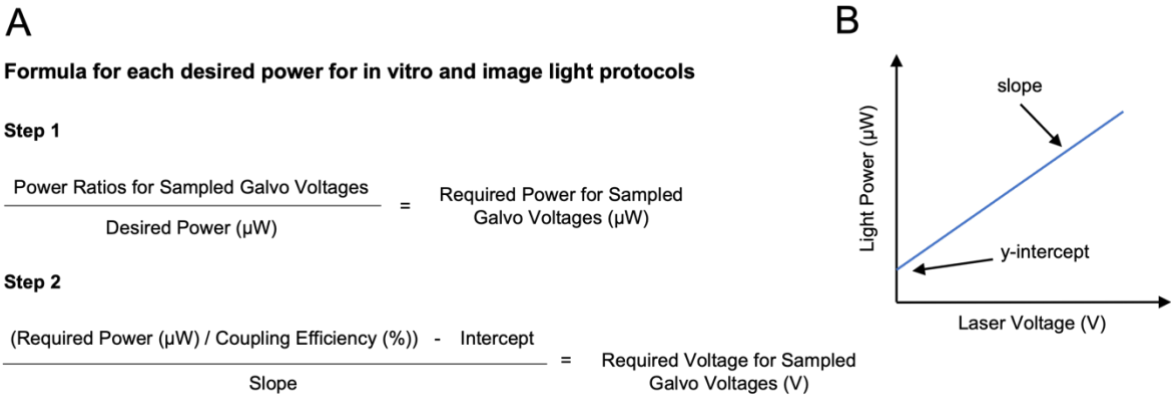

Figure 4.2.9. Calculating the required voltage for *in vitro* and image light protocols. (A) Formula for each desired power for *in vitro* and image light protocols. The required voltage will be varied across sampled GVs for each desired power and light protocol. This is calculated automatically using custom MATLAB and LABVIEW code. The galvo-power ratios are determined as described in **section 4.2.1.4.2**. The coupling efficiency, intercept and slope are

determined as described in **section 4.2.1.3.2**. (B) Schematic illustrating how the y-intercept and slope is determined. The light power is measured at increasing laser voltages as described in **section 4.2.1.3.2**.

4.2.2 *In vivo* experimental procedures

Before any *in vivo* measurement, the TF would be characterised as described above and submerged in propranol a few times for sterilisation. All *in vivo* measurements were completed in dark conditions.

4.2.2.1 Animals

Detailed animal information can be found in **Chapter 2, section 2.1.2**. For TF experiments, male and female 5xFAD+ (Alzheimer's positive) and 5xFAD- (Alzheimer's negative, C57BL/6 littermates) mice were used (JAX006554, The Jackson Laboratory). A total of 46 mice were used for all TF photometry experiments **(Figure 4.2.10 & Table 4.2.1)**. 14 of these were used for acute experiments, including 4 for depth profile experiments and 10 for acute pharmacokinetic. 27 mice were used for chronic experiments **(Table 4.2.1)**. Out of all 27 chronically implanted mice, 25 were used for pharmacokinetic experiments, and out of these 25, 14 mice were used for re-dose experiments and 12 were used for GENUS treatment experiments **(detailed information provided in Chapter 5) (Table 4.2.1)**. 5 mice were used for other purposes, where brain samples were taken for use for an additional project with collaborators **(Table 4.2.1)**.

All acute experiments were completed under terminal anaesthetic before immediate removal of brain tissue for post-mortem analysis. Both chronic pharmacokinetic and re-dose experiments involved surgery and freely behaving TF photometry recordings within a chamber before brain tissue was recovered for post-mortem analysis.

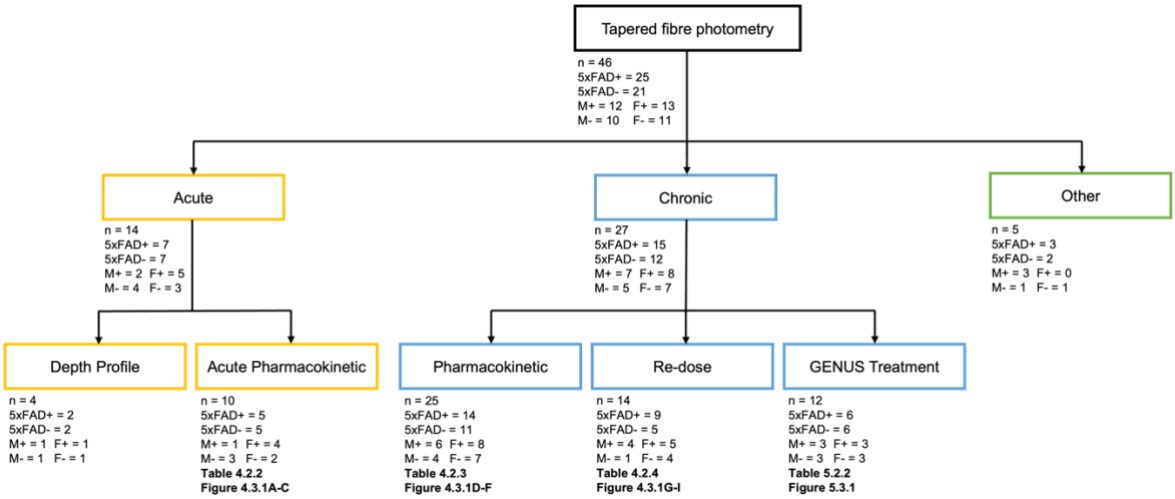

Figure 4.2.10. Flow chart illustrating the number of animals used per recording. Yellow represents acute experiments; blue represents chronic experiments and green represents other use. Sex sample numbers are shown. Figure and table numbers show summary plots of animals. M+, 5xFAD+ male. F+, 5xFAD+ female. M-, 5xFAD- male. F-, 5xFAD- female.

Table 4.2.1. Fate of all animals used for TF photometry experiments. DP, depth profile. APK, acute pharmacokinetic. PK, pharmacokinetic. RD, re-dose. GENUS, gamma entrainment using sensory stimulus. Yellow represents acute experiments; blue represents chronic experiments and green represents other use. Reason if none describes why no recordings were completed on the mouse. Age at time of experiment can be found in the specific experimental parameters table: **Table 4.2.2 (APK), Table 4.2.3 (PK), Table 4.2.4 (RD) and Table 5.2.2 (GENUS)**.

Animals	Genotype	Sex	DP	APK	PK	RD	GENUS	Other	Reason if none
FAD25	+	M							
FAD26	-	M							
FAD27	-	F							
FAD28	+	F							Urethane
FAD29	+	F							Urethane
FAD30	+	F							
FAD31	+	F							
FAD32	-	F							
FAD33	-	M							
FAD34	-	M							
FAD35	+	M							
FAD36	-	F							
FAD37	+	F							
FAD38	+	F							
FAD39	-	M							
FAD40	-	F							
FAD43	-	M							
FAD44	+	M							Implanting issue
FAD45	+	F							
FAD51	+	M							
FAD52	-	F							
FAD56	-	M							Fibre fell out
FAD57	+	M							
FAD58	+	F							
FAD59	-	F							
FAD60	-	F							
FAD61	-	M							
FAD62	+	M							
FAD63	+	F							
FAD64	-	F							
FAD65	+	F							
FAD66	-	M							
FAD67	+	M							
FAD68	+	F							
FAD69	-	F							
FAD70	-	F							
FAD71	+	F							
FAD72	+	M							
FAD73	-	M							
FAD74	+	F							
FAD75	+	M							
FAD_IIT_1	+	M							
FAD_IIT_2	+	M							
FAD_IIT_3	-	M							
FAD_IIT_4	-	F							
FAD_IIT_5	+	M							

4.2.2.2 Acute recordings

Before any *in vivo* measurement, the TF would be submerged in propanol a few times for sterilisation. After all *in vivo* measurements, the TF went through a cleaning protocol that involved being submerged in enzyme remover (Superdrug) for several hours, followed by several minutes in distilled water and finished by a few dips in propanol for sterilisation. All *in vivo* measurements were completed in dark conditions.

4.2.2.2.1 Terminal anaesthesia and craniotomies

For all acute TF photometry experiments, 5xFAD+ and 5xFAD- littermates underwent terminal anaesthesia and craniotomies as described in **section 3.2.2.2.1**. For acute pharmacokinetic experiments, a craniotomy was completed above the SUB: (AP: -3.80 mm, ML: 3.30 mm, DV: 2.50 mm) **(Figure 4.2.11)**. This craniotomy site was chosen as, if implanted correctly, should be submerged within a largely plaque-dense region to minimise error.

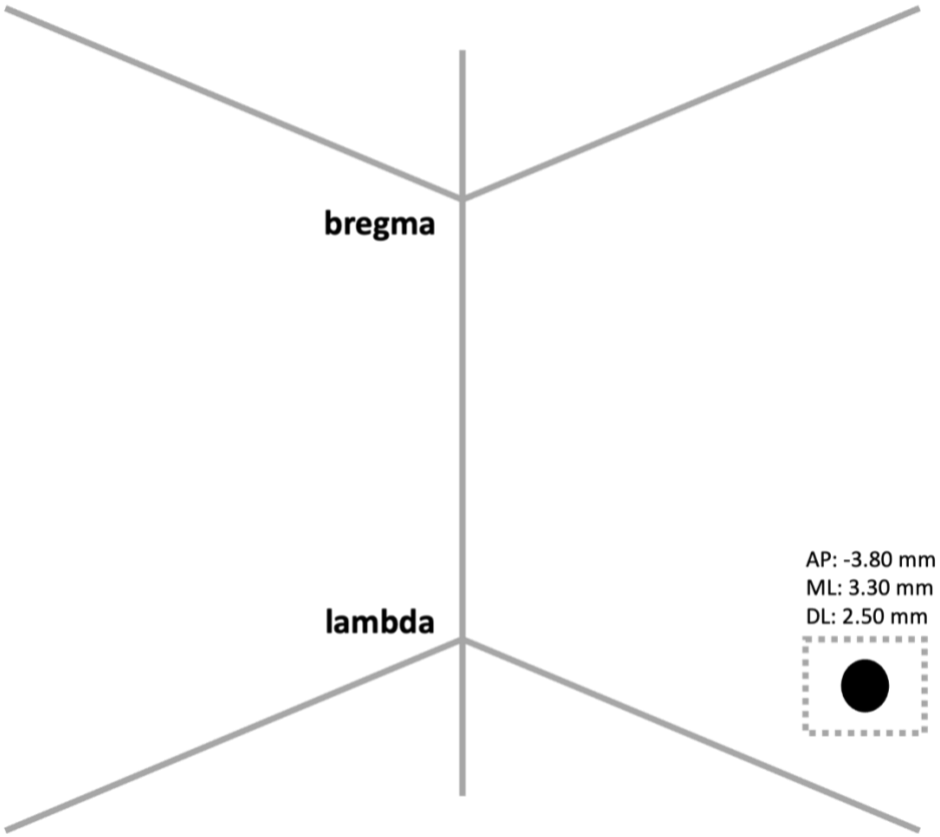

Figure 4.2.11. Implant site for TF acute pharmacokinetic experiments. Craniotomy (grey) and target implantation site (black) coordinates, for the SUB. Diagram not to scale.

4.2.2.2.2 Acute pharmacokinetic recording

Table 4.2.2. Summary of acute pharmacokinetic recording parameters. Age is the age at time of recordings. Laser type represents the first or second laser used. Laser stability shows presence of the photodector monitoring laser signals. Bleaching protocol was 'unknown' if the exact parameters used for bleaching (GV and duration) is unclear, due to the exact parameters being unnoted. Reasons for exclusion are explained.

Animals	Genotype	Sex	Age (mo)	Power (µW)	Repetitions	Sampling interval (s)	Bleaching protocol	Laser type	Laser stability	Excluded	Reason for exclusion
FAD25	+	M	7.73	5, 10, 15, 20, 25, 30	5	5	None	1	N	N	n/a
FAD26	-	M	7.76	5, 25, 50, 75, 100, 150, 200, 250	5	5	None	1	N	N	n/a
FAD27	-	F	7.96	5, 10, 20, 40, 60, 80, 100, 150	5	10	None	1	N	N	n/a
FAD28	+	F	7.99							Y	Urethane
FAD29	+	F	8.25							Y	Urethane
FAD30	+	F	7.50	5, 10, 20, 40, 60, 80, 100, 150	5	10	@ 4V Galvo & Laser	1	N	N	n/a
FAD31	+	F	6.31	5, 10, 20, 30, 40, 50, 60	5	10	unknown	1	N	N	n/a
FAD32	-	F	6.48	5, 10, 20, 30, 40, 50, 60	5	10	@ 4V Galvo & Laser	1	N	N	n/a
FAD33	-	M	6.67	5, 10, 20, 30, 40, 50, 60	5	10	unknown	1	N	N	n/a
FAD34	-	M	6.94	5, 10, 20, 30, 40, 50, 60	5	10	unknown	1	N	N	n/a

Acute pharmacokinetic measurements were mainly completed as described in **section 3.2.2.2.3**, with some varied parameters **(Table 4.2.2)**. The mouse was transferred to the recording stereotaxic frame (KOPF Instruments) as described in **section 3.2.2.2.1**. A 5-mm long TF (1.8-mm active region, 200-µm core diameter, 0.39˚ NA) (OptogeniX) was used. Using a stereotaxic frame (KOPF Instruments) and a cannula holder (FCM13/M, Thorlabs), the fibre was positioned directly above the target site before lowering to the target depth.

After completing the appropriate recording preparation such as TF characterisation **(section 4.2.1.4)** and TF system maintenance **(section 4.2.1.3)**, recordings were completed **(Figure 4.2.12A)**. This recording started with the length of the chosen sampling interval **(Table 4.2.2) (Figure 4.2.12B)**. Then, the excitation of the 405-nm laser (MDL-III-405-50-mW, CI90055, CNI lasers) was activated. This was for 10-ms ON, 5-ms OFF, for each power. Powers were as shown in **Table 4.2.2**. Appropriate laser voltages were determined as described in **section 4.2.1.4.3** and shown in **Figure 4.2.8**. For acute pharmacokinetic recordings, only the original light protocol was used. In parallel, the light is swept along the TF using the galvo mirror (GVS001, Thorlabs) driven at -1-V to 4.5-V over the 10-ms laser ON period, remaining at 0-V during the 5-ms OFF. These processes were repeated 5 times separated by a 5-ms baseline. Once complete, this whole protocol was repeated after the chosen sampling interval; as shown in **Table 4.2.2**. Throughout the whole protocol the emission at 440 and 550-nm was collected at 5000-Hz. Signals were not collected at 405-nm as these recordings were completed before the system change. Additionally, sync channels of the 405-nm laser and galvo mirror were monitored for post-processing. This equipment was controlled by the NIDAQ (NI USB-6343, National Instruments) using a custom

LABVIEW code. This LABVIEW VI generated a .dat file for each photometry measure and a .txt file containing the time of each measure.

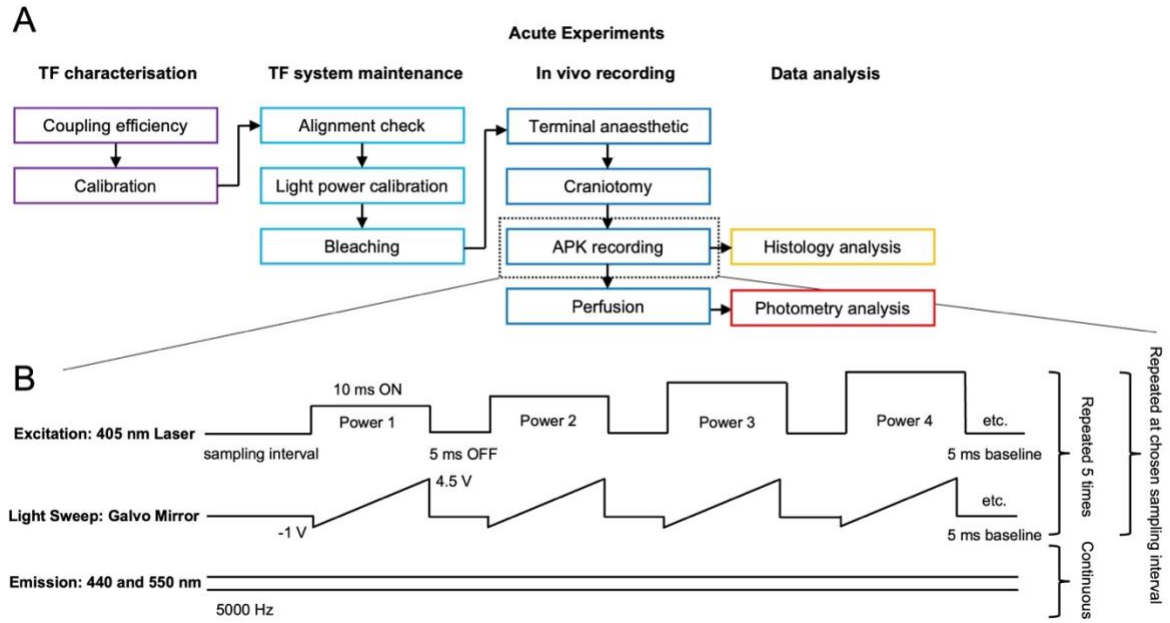

Figure 4.2.12. Experimental protocol for acute experiments. (A) Flow chart of the experimental procedures. (B) Optical protocol for acute experiments. Excitation was completed with a 405-nm laser. The laser went through several powers for 10-ms ON, 5-ms OFF, repeated 5 times separated with a 5-ms baseline. In parallel, the light is swept along the TF using the galvo mirror from -1-V to 4.5-V over the 10-ms laser ON period, remaining at 0-V during the 5-ms OFF, repeated 5 times. This laser excitation and light sweep was repeated at a chosen sampling interval. Throughout this, emission at 440 and 550-nm is continuously measured at 5000-Hz. Appropriate parameters are shown in **Table 4.2.2**.

4.2.2.3 Chronic recordings

4.2.2.3.1 Fibre implant head-cap surgery

5xFAD+ and 5xFAD- littermates underwent fibre implant head-cap surgery from 3-7 months **(Figures 4.2.13 & 4.2.14)**. If possible, mice housed together underwent surgery on the same day. For two days before surgery mice were placed in a large cage and accustomed to baby food (Cow and Gate).

On the day of recording, various preparation was completed. Anaesthetic's, fluovac (Harvard apparatus) and analgesics were prepared. Both the surgical environment and equipment were aseptically prepared using an autoclave (Tuttnauer). The TF (OptogeniX) being implanted was mounted in the stereotaxic holder (FCM13/M, Thorlabs) and was appropriately sterilised using propanol.

Once completed, mice were placed in an anaesthetic chamber where isoflurane (Covetrus) was maintained at 5% and 0.8 L/min air flow until the mouse is fully immobile, before being reduced to 3% and 0.8 L/min air flow. Once under, the head was shaved, and the mouse was placed on an incisor breather for administration of isoflurane and oxygen via a nose cone. Anaesthetic (isoflurane) (Covetrus) was maintained between 1.5% and 1% and 0.8 L/min air flow. Eyes were protected by application of eye gel (Lacri-lube, Hylonight or Viscotears, Bausch&Lomb) and the mouse was maintained at 37°C by being placed on a heat mat (ATC 100, World Precision Instruments), under a surgical light (KL 1500, Photometrics). Breathing and pinch reflexes were monitored throughout the surgery and levels of anaesthetic were adjusted accordingly. Once on the anaesthetic breather, the surgical area and the rump was cleaned using cotton buds (Johnson's) with ethanol (70%). Next, Naroprin (local anaesthetic, 8-mg/kg; 7.5-mg/ml solution, Aspen) was administered subcutaneously (s.c.) to the surgical area. Vetergesic (analgesic, 0.1-mg/kg, 0.01% diluted in injecting saline; 0.3-mg/ml solution, Ceva), Rimadyl (non-steroidal anti-inflammatory drug, 20-mg/kg, 0.01% diluted in injecting saline; 50-mg/ml solution, Zoetis) and 0.3-ml of saline (FKE1323, Baxter) was administered (s.c.) to the rump. Then, the mouse was stabilized by ear-bars attached to a stereotaxic frame (Model 963, KOPF Instruments) **(Figure 4.2.13)**.

Now, I prepared myself aseptically and wore sterile gloves (Gammex latex gloves, Ansell). Once prepared, betadine (Alkaloid) was applied to the skull using a cotton bud (Johnson's). Next, using a scalpel (847-7584, RS Components), an incision along the midline was made that was expanded with surgical scissors to create a 2-mm wide circle around the midline, exposing bregma and lambda. To remove the periosteal membrane, hydrogen peroxide (3%) was applied to the skull surface and debris was removed with a cotton bud and scissors. Next, skull alignment between bregma and lambda was set between 0-50-μm, before marking the fibre implant site, under a stereomicroscope (SZ51, Olympus), using a glass pipette (504949, World Precision Instruments) made with a pipette puller (PC-10, Narishige), secured with the stereotaxic frame (Model 963, KOPF Instruments). Fibre implant sites were optimised overtime. These included a target of the SUB and were either site 1 (AP: -3.50-mm, ML: 2.25-mm, DV: 2.50-mm), site 2 (AP: -3.50-mm, ML: 2.25-mm, DV: 2.00-mm), and site 3 (AP: -3.60-mm, ML: 2.80-mm, DV: 2.00-mm) **(Figures 4.2.14B-C)**. Next, using surgical callipers, sites of skull screws were marked (AP: +1.50-mm, ML: 1:00-mm (both hemispheres); AP: -1.00-mm, ML: 4.00-mm (right hemisphere); AP: -3.00-mm, ML: 4.00-mm (left hemisphere); AP: -2.00-mm (from lambda), ML: 2.00-mm (left hemisphere) **(Figure 4.2.14A)**. These burr holes were completed using a surgical drill (Volvere Vmas drill, NSK) and a duratomy was performed over the fibre implant site, using craniotomy scissors, to aid insertion of TFs. Next, skull screws (418-7123, RS Components) were inserted into each site. Then, the stereotaxic holder and cannula holder (FCM13/M, Thorlabs) with the TF (OptogeniX) was mounted

onto the stereotaxic frame. The fibre was slowly lowered to the brain surface, before slowly descending to the target depth. Once reached, a small volume of Kwik Kast (KWIK-CAST, World Precision Instruments) was applied to cover the remaining exposed brain tissue surrounding the TF, using a toothpick. Now, various layers of superglue (918-6872, RS-Pro) and dental cement (Simplex rapid liquid and powder mixed, Kemdent) were applied to regions surrounding the TF. Once secure, the stereotaxic mount was removed from the TF, allowing dental cement to be generously applied across the skull and skin edges. Lastly, a small straw was cemented to the back of the headcap for head-fixation and a protective cap (CAPL, Thorlabs) was placed onto the TF ferrule.

Once dental cement was dry, the mouse was removed from anaesthesia, eye gel was removed from eyes using a KimWipe (122-3088, RS Components) and the mouse was returned to home cage, placed on a heat-mat. The mouse was left on the heat-mat to recover for a couple of hours, until behaving normally. On the day after surgery, Rimadyl (non-steroidal anti-inflammatory drug, 20-mg/kg, 0.01% diluted in injecting saline) was administered. Before, immediately after and for several days following surgery, weight, behaviour, and appearance was closely monitored. If anything was concerning, appropriate precautions were taken.

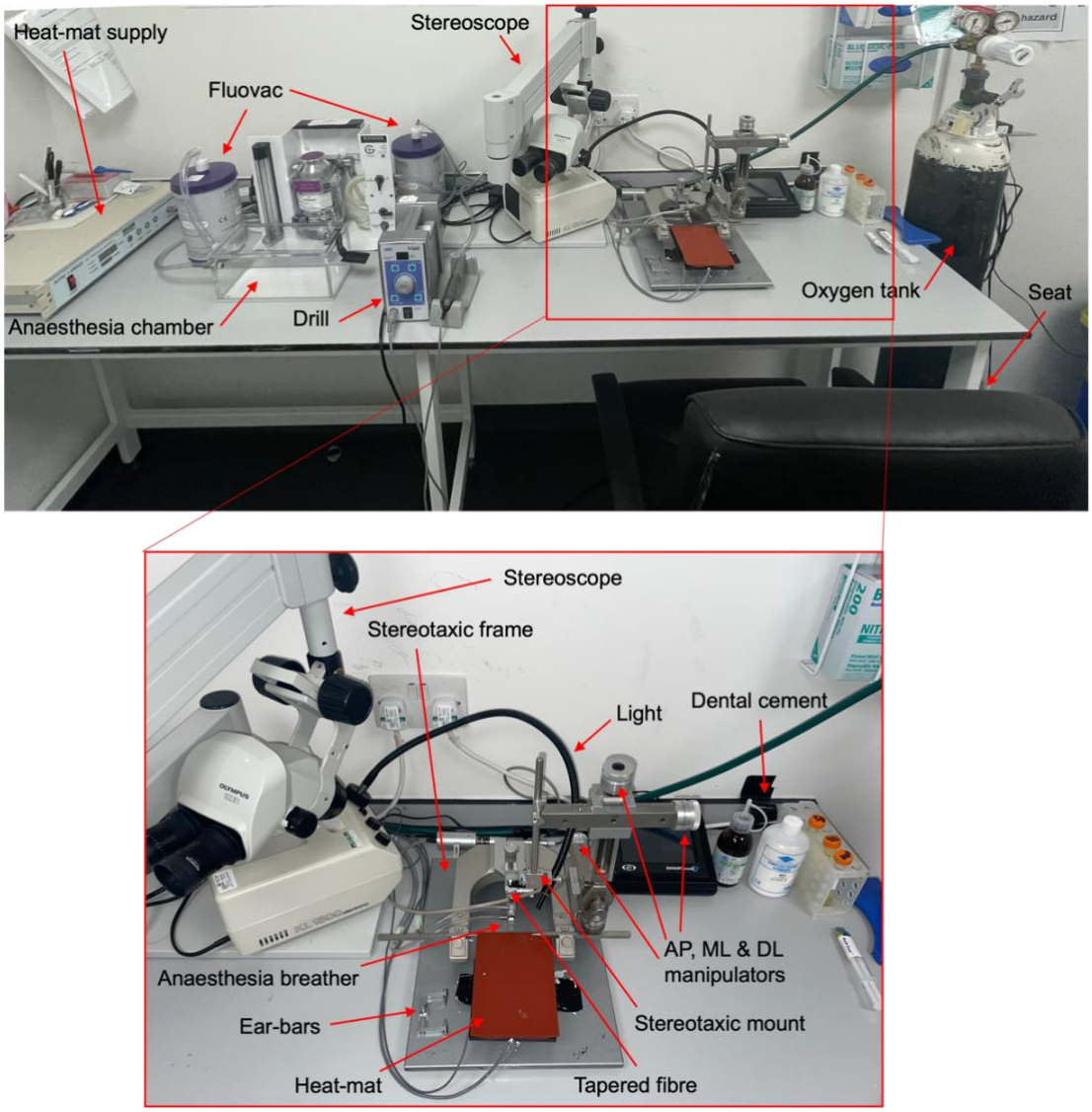

Figure 4.2.13. Image of the chronic surgery set-up.

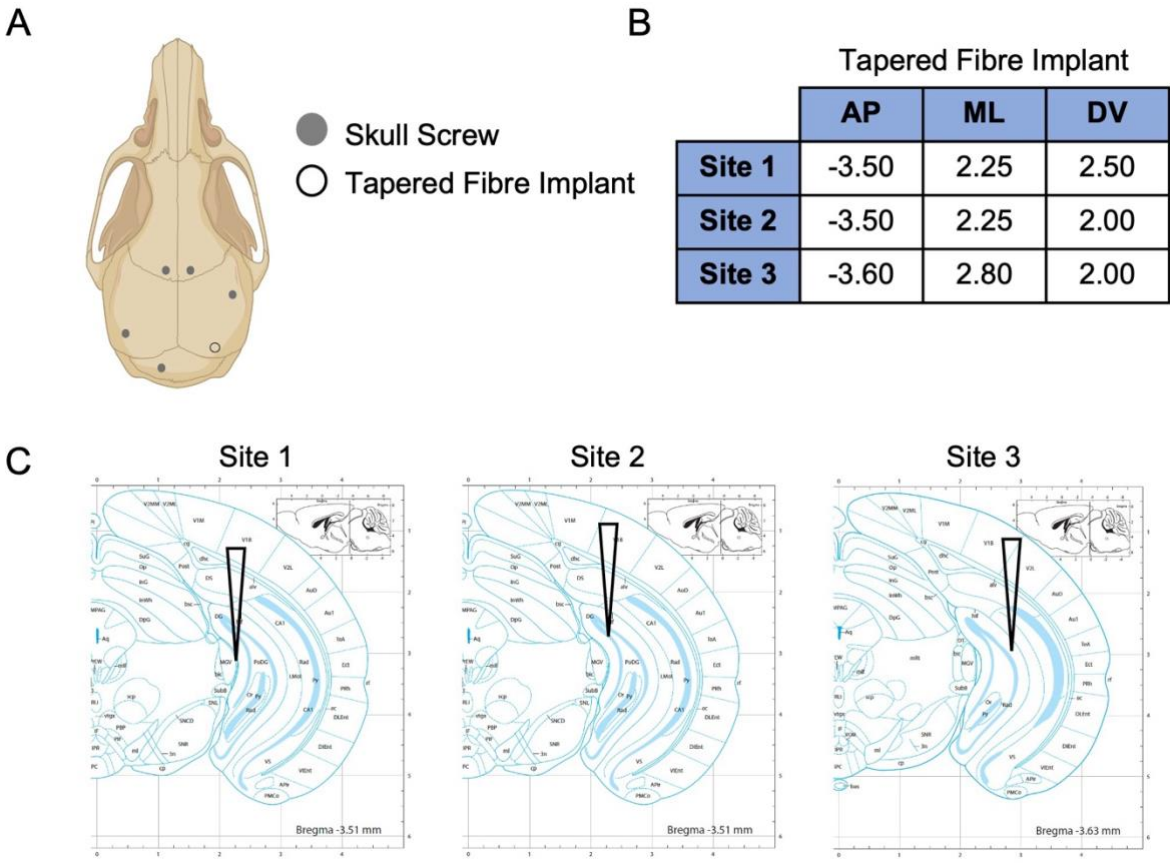

Figure 4.2.14. Implants for the head-cap surgery. (A) Schematic showing implants of the skull screws and TF. Created with BioRender.com. (B) Exact coordinates for the TF implant across different sites (in mm). Coordinates are from bregma. (C) Brain atlas sections labelled with the target TF implant. TF not to exact scale. Images from the Allen Mouse Brain Atlas, mouse.brain-map.org.

4.2.2.3.2 Pharmacokinetic

Table 4.2.3. Summary of pharmacokinetic recording parameters. Age is the age on day 0 of the recordings. Target site represents the TF implant coordinates site (**Figure 4.2.14).** Rec shows the recording number. Bleaching protocol progressed over-time, with 3.5-V occassionally being used due to the deterioration in laser power at high outputs. Laser type represents the first or second laser used. Laser stability shows presence of the photodector monitoring laser signals. Reasons recordings were excluded for 4-day summary analysis are shown as explained in **section 4.2.3.1.4**.

Animals	Genotype	Sex	Age (mo)	Target Site	Rec	Power (µW)	Reps	Sampling interval (s)	Bleaching protocol	Laser type	Laser stability	Excluded	Reason for exclusion
FAD37	+	F	4.93	1	1	10, 20, 40, 60, 80, 100, 120, 140	3	30	@ 4V Galvo for 1h	1	N	Y	Investigative time samples
			5.69		2	10, 20, 40, 60, 80, 100, 120, 140	3	30	@ 4V Galvo for 1h	1	N	Y	Investigative time samples
			6.02		3	10, 20, 40, 60, 80, 100, 120, 140	3	30	@ 4V Galvo for 1h	1	N	Y	Inaccurate power calculation
			7.33		4	10, 20, 40, 60, 80, 100, 120, 140	3	30	@ 4V Galvo for 1h	1	N	Y	Inaccurate power calculation
			7.50		5	10, 20, 40, 60, 80, 100, 120, 140	3	30	@ 4V Galvo for 1h	1	N	Y	Inaccurate power calculation
FAD40	-	F	4.80	1	1	10, 20, 40, 60, 80, 100, 120, 140	3	30	@ 4V Galvo for 1h	1	N	Y	Investigative time samples
			5.69		2	10, 20, 40, 60, 80, 100, 120, 140	3	30	@ 4V Galvo for 1h	1	N	Y	Investigative time samples
			6.15		3	10, 20, 40, 60, 80, 100, 120, 140	3	30	@ 4V Galvo for 1h	1	N	Y	Inaccurate power calculation
			7.07		4	10, 20, 40, 60, 80, 100, 120, 140	3	30	@ 4V Galvo for 1h	1	N	Y	Inaccurate power calculation
			7.33		5	10, 20, 40, 60, 80, 100, 120, 140	3	30	@ 4V Galvo for 1h	1	N	Y	Inaccurate power calculation
FAD43	-	M	5.49	1	1	10, 20, 40, 60, 80, 100, 120, 140	3	30	@ 4V Galvo for 1h	1	N	Y	Inaccurate power calculation
			6.15		2	10, 20, 40, 60, 80, 100, 120, 140	3	30	@ 4V Galvo for 0.5h	1	N	Y	Inaccurate power calculation
			7.10		3	80, 100, 120, 140	3	60	@ 3.5V Galvo for 0.5h	1	N	Y	Inaccurate power calculation
			8.02		4	80, 100, 120, 140	3	60	none	1	N	Y	Laser dying
			10.52		5	80, 100, 120, 140	3	60	Baseline	2	Y	Y	Fibre fell out on day 2
FAD45	+	F	5.69	1	1	10, 20, 40, 60, 80, 100, 120, 140	3	30	@ 4V Galvo for 1h	1	N	Y	Inaccurate power calculation
			6.35		2	10, 20, 40, 60, 80, 100, 120, 140	3	30	@ 4V Galvo for 0.5h	1	N	Y	Inaccurate power calculation
			7.00		3	80, 100, 120, 140	3	60	@ 3.5V Galvo for 0.5h	1	N	N	n/a
			7.33		4	80, 100, 120, 140	3	60	@ 3.5V Galvo for 0.5h	1	N	N	n/a
			7.99		5	80, 100, 120, 140	3	60	None	1	N	Y	Laser dying
			10.52		6	80, 100, 120, 140	3	60	All galvos for 1h	2	Y	N	n/a
FAD51	+	M	6.97	2	1	80, 100, 120, 140	3	60	None	1	N	Y	Mouse needed further habituation
			7.66		2	80, 100, 120, 140	3	60	None	1	N	Y	Laser dying
			9.47		3	80, 100, 120, 140	3	60	All galvos for 0.5h	2	Y	N	n/a
			9.93		4	80, 100, 120, 140	3	60	Threshold	2	Y	N	n/a
FAD52	-	F	7.46	2	1	80, 100, 120, 140	3	60	None	1	N	Y	Laser dying
			9.44		2	80, 100, 120, 140	3	60	Threshold	2	Y	N	n/a
FAD57	+	M	8.48	2	1	80, 100, 120, 140	3	60	Threshold	2	Y	N	n/a
			8.98		2	60, 80, 100, 120	3	90	Threshold	2	Y	N	n/a
FAD58	+	F	11.70	2	1	60, 80, 100, 120	3	300	Threshold	2	Y	N	n/a
FAD59	-	F	8.98	2	1	60, 80, 100, 120	3	90	Threshold	2	Y	N	n/a
FAD60	-	F	4.18	2	1	60, 80, 100, 120	3	300	Threshold	2	Y	N	n/a
FAD61	-	M	4.18	2	1	60, 80, 100, 120	3	300	Threshold	2	Y	N	n/a
FAD62	+	M	3.91	2	1	60, 80, 100, 120	3	300	Threshold	2	Y	Y	Inaccurate power calculation
			4.34		2	60, 80, 100, 120	3	300	Threshold	2	Y	N	n/a
FAD63	+	F	3.91	2	1	60, 80, 100, 120	3	300	Threshold	2	Y	Y	Inaccurate power calculation
			4.34		2	60, 80, 100, 120	3	300	Threshold	2	Y	N	n/a
FAD64	-	F	4.11	3	1	80, 100, 120, 140	5	300	Threshold	2	Y	N	n/a
FAD65	+	F	4.11	3	1	80, 100, 120, 140	5	300	Threshold	2	Y	N	n/a
FAD66	-	M	4.44	3	1	80, 100, 120, 140	5	300	Threshold	2	Y	N	n/a
FAD67	+	M	4.44	3	1	80, 100, 120, 140	5	300	Threshold	2	Y	N	n/a
FAD68	+	F	8.65	3	1	80, 100, 120, 140	5	300	Threshold	2	Y	N	n/a
FAD69	-	F	8.88	3	1	80, 100, 120, 140	5	300	Threshold	2	Y	N	n/a
FAD70	-	F	3.72	3	1	80, 100, 120, 140	5	300	Threshold	2	Y	N	n/a
			5.03		2	80, 100, 120, 140	5	300	Threshold	2	Y	N	n/a
FAD71	+	F	3.78	3	1	80, 100, 120, 140	5	300	Threshold	2	Y	N	n/a
			5.06		2	80, 100, 120, 140	5	300	Threshold	2	Y	N	n/a
FAD72	+	M	5.29	3	1	80, 100, 120, 140	5	300	Threshold	2	Y	N	n/a
FAD73	-	M	5.33	3	1	80, 100, 120, 140	5	300	Threshold	2	Y	N	n/a
FAD74	+	F	7.04	3	1	80, 100, 120, 140	5	300	Threshold	2	Y	Y	Inaccurate power calculation
			7.69		2	80, 100, 120, 140	5	300	Threshold	2	Y	N	n/a
FAD75	+	M	7.10	3	1	80, 100, 120, 140	5	300	Threshold	2	Y	N	n/a
			7.69		2	80, 100, 120, 140	5	300	Threshold	2	Y	N	n/a

Before each recording, the appropriate alignment and bleaching maintenance protocols were completed. Additionally, the chamber was cleaned with disinfectant and 70% ethanol. All recordings were completed in dark conditions, with only a red bulbed light.

Using the cannula holder (FCM13/M, Thorlabs), helping hand and haemostat, the mating sleeve (ADAL1-5, Thorlabs) was attached to the patch cable ferrule. Mice were head-fixed using the straw on their head-cap, for removal of the protective cap (CAPL, Thorlabs) and attachment of the patch cable to the implanted TF (OptogeniX) **(Figure 4.2.15A)**. Occasionally, mice were not head-fixed, and the patch cable was attached while the mouse was scruffed. Then, mice were placed within a rectangular recording chamber (46.5 x 21.5-cm) with a white paper sheet stuck to it, that contained bedding, sunflower seeds, and chow (**Figure 4.2.15B)**. Once the recording was complete, the mouse was scruffed and head-fixed, to remove the patch cable and attach the protective cap (CAPL, Thorlabs), before being returned to their home-cage.

Investigation of the pharmacokinetic profile of Methoxy-x04 occurred over several days. **Figure 4.2.15C** illustrates the recording protocol, where day 0 provides a baseline measurement with no Methoxy-x04, for 5-hours. On day 1, after a 30-minute baseline measurement, 10-mg/kg (5-mg/ml) of Methoxy-x04 (4920, Tocris) is administered (i.p.) and the change in fluorescence is monitored for a further 4.5-hours. On days 2 and 3, the fluorescence is monitored for 2-hours.

After completing the appropriate recording preparation such as TF characterisation **(section 4.2.1.4)** and TF system maintenance **(section 4.3.1.3) (Figure 4.2.16A)**, the illumination protocol shown in **Figure 4.2.16B** was completed. Recordings began with the length of the chosen sampling interval **(Table 4.2.3)** before running through the illumination protocol for the first light protocol (*in vitro*). Here, the excitation of the 405-nm laser (MDL-III-405-50-mW, CI90055, CNI lasers or Cobolt 06-01 Series, Hubner Photonics) was activated across each power: as shown in **Table 4.2.3**. This was for 10-ms ON, 5-ms OFF, for each power. Appropriate laser voltages were determined as described in **section 4.2.1.4.3** and shown in **Figures 4.2.8** and **4.2.9**. In parallel, the light is swept along the TF using the galvo mirror (GVS001, Thorlabs) driven at -1-V to 4.5-V over the 10-ms laser ON period, remaining at 0-V during the 5-ms OFF. This protocol was repeated a chosen number of times **(Table 4.2.3)** separated by a 5-ms baseline. After the last 5-ms baseline, the illumination protocol restarted for the second light protocol (image). After the last 5-ms baseline in this iteration, the illumination protocol restarted for the third light protocol (original). Once complete, this whole process was repeated after the chosen sampling interval **(Table 4.2.3)**. Throughout the whole process the emission at 440 and 550-nm was collected at 5000-Hz. For some recordings, emission was also collected at 405-nm at 5000-Hz **(Table 4.2.3)**. Additionally, sync channels of the 405-nm laser and galvo mirror were monitored for post-processing. All

procedures were controlled by a LABVIEW programme through a NIDAQ (USB-6343, National Instruments). This LABVIEW VI generated a .dat file for each photometry measure and a .txt file containing the time of each measure.

4.2.2.3.3 Re-dose

Table 4.2.4. Summary of re-dose recording parameters. Age is the age on day 0 of the recordings. Target site represents the TF implant coordinates site (**Figure 4.2.14).** Rec shows the recording number. Laser type represents the first or second laser used. Laser stability shows presence of the photodector monitoring laser signals. Reasons recordings were excluded for 4-day summary analysis are shown, as explained in **section 4.2.3.1.4**.

Animals	Genotype	Sex	Age (mo)	Target Site	Rec	Power (µW)	Reps	Sampling interval (s)	Bleaching protocol	Laser type	Laser stability	Excluded	Reason for exclusion
FAD43	-	M	10.09	1	1	80, 100, 120, 140	3	60	Threshold	2	Y	N	n/a
			10.26		2	80, 100, 120, 140	3	60	Threshold	2	Y	N	n/a
FAD45	+	F	10.09	1	1	80, 100, 120, 140	3	60	Threshold	2	Y	N	n/a
			10.26		2	80, 100, 120, 140	3	60	Threshold	2	Y	N	n/a
FAD51	+	M	8.84	2	1	80, 100, 120, 140	3	60	Threshold	2	Y	N	n/a
			9.01		2	80, 100, 120, 140	3	60	Threshold	2	Y	N	n/a
FAD52	-	F	8.98	2	1	80, 100, 120, 140	3	60	Threshold	2	Y	N	n/a
FAD57	+	M	11.47	2	1	60, 80, 100, 120	3	300	Threshold	2	Y	Y	Incomplete recording
FAD58	+	F	11.47	2	1	60, 80, 100, 120	3	300	Threshold	2	Y	Y	Incomplete recording
FAD59	-	F	10.59	2	1	60, 80, 100, 120	3	300	Threshold	2	Y	N	n/a
FAD60	-	F	5.46	2	1	60, 80, 100, 120	3	300	Threshold	2	Y	Y	Incomplete recording
			5.46		2	60, 80, 100, 120	3	300	Threshold	2	Y	N	n/a
FAD62	+	M	5.46	2	1	60, 80, 100, 120	3	300	Threshold	2	Y	N	n/a
			5.69		2	60, 80, 100, 120	3	300	Threshold	2	Y	N	n/a
FAD63	+	F	5.46	2	1	60, 80, 100, 120	3	300	Threshold	2	Y	N	n/a
			5.69		2	60, 80, 100, 120	3	300	Threshold	2	Y	N	n/a
FAD68	+	F	8.92	3	1	80, 100, 120, 140	5	300	Threshold	2	Y	N	n/a
FAD69	-	F	8.68	3	1	80, 100, 120, 140	5	300	Threshold	2	Y	N	n/a
FAD74	+	F	8.61	3	1	80, 100, 120, 140	5	300	Threshold	2	Y	N	n/a
FAD75	+	M	8.61	3	1	80, 100, 120, 140	5	300	Threshold	2	Y	N	n/a

The experiment was set-up as described in **section 4.2.2.3.2**. Investigation of the Methoxy-x04 re-dose protocol occurred over several days. **Figure 4.2.15D** illustrates the recording protocol, where day 0 provides a baseline measurement with no Methoxy-x04, for 2-hours. Immediately after this recording, 10-mg/kg (5-mg/ml) of Methoxy-x04 (4920, Tocris) was administered (i.p.). Then, fluorescence was monitored 24-hours later for 2-hours, with an injection of 10-mg/kg (5-mg/ml) of Methoxy-x04 (4920, Tocris) (i.p.) immediately after. After, this was repeated for two more days. Variation in recording parameters can be found in **Table 4.2.4.**

The illumination protocol was as described in **section 4.2.2.3.3** and shown in **Figure 4.2.16B**, with differences in recording parameters shown in **Table 4.2.4**.

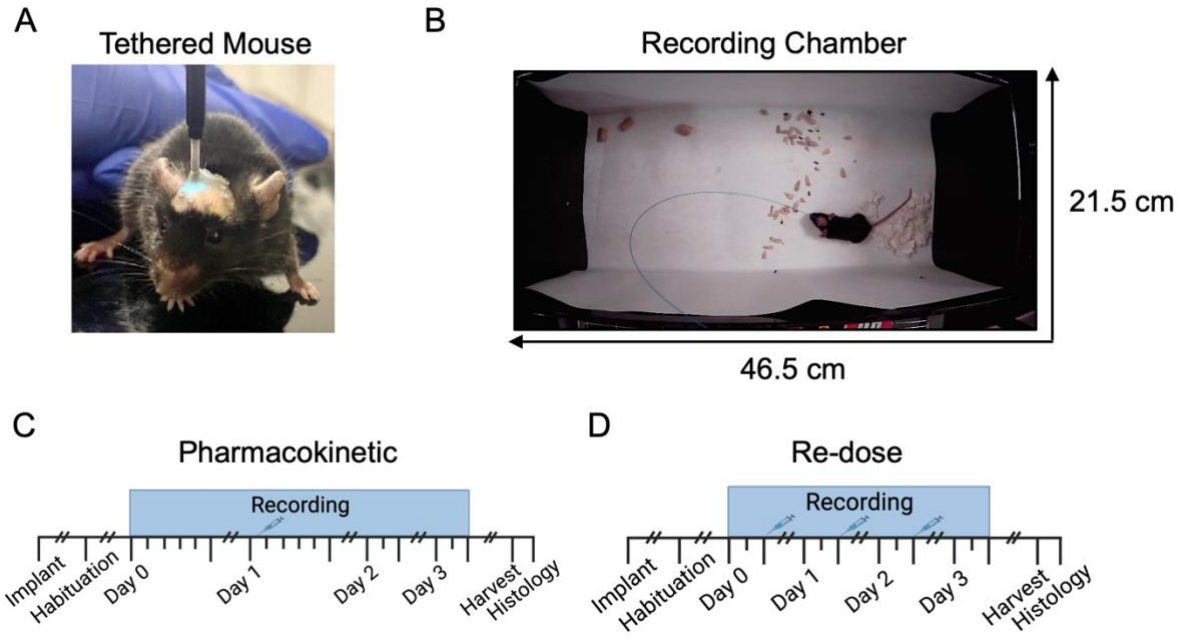

Figure 4.2.15. Experimental paradigm for chronic TF experiments. (A) Image of tethered mouse. (B) Recording chamber. (C) Recording schedule for pharmacokinetic recordings. Methoxy-x04 was injected on day 1 after 30-minutes. (D) Recording schedule for re-dose recordings. Methoxy-x04 was injected at the end of the recording on day 0, 1 and 2. Created with BioRender.com.

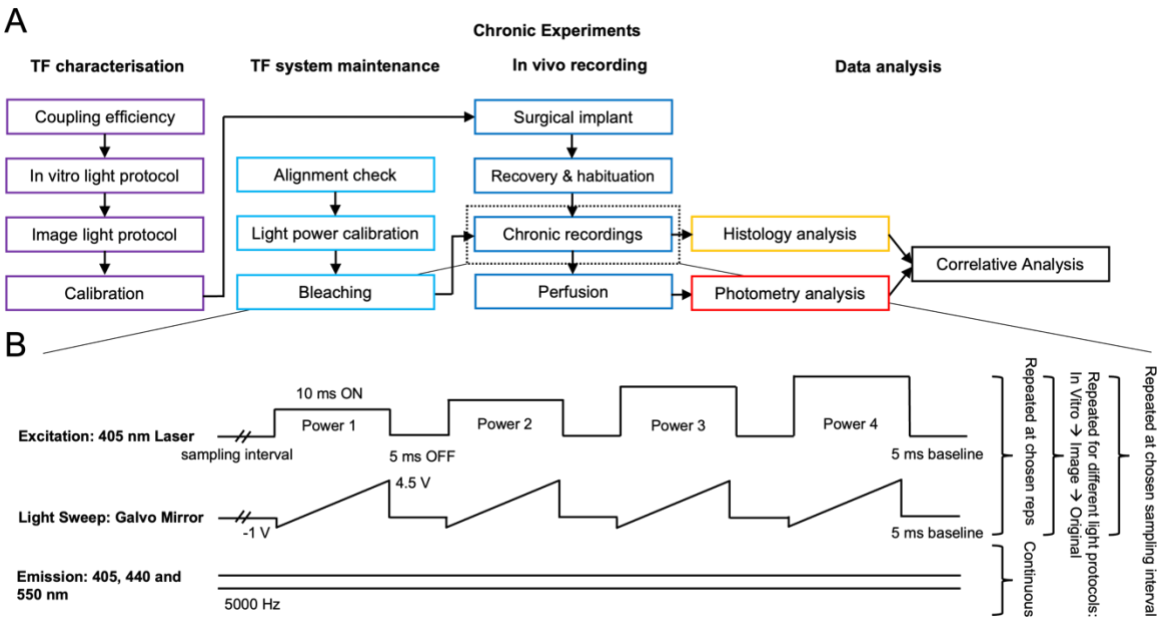

Figure 4.2.16. Experimental protocol for chronic experiments. (A) Flow chart of the experimental procedures. (B) Optical protocol for chronic experiments. Excitation was completed with a 405-nm laser. The laser went through several powers for 10-ms ON, 5-ms OFF, repeated a chosen number of times separated with a 5-ms baseline. In parallel, the light is swept along the TF using the galvo mirror from -1-V to 4.5-V over the 10-ms laser ON period, remaining at 0-V during the 5-ms OFF, repeated a chosen number of times. This is completed for 3 light protocols in the following order: *in vitro*, image and original. This laser excitation and light sweep was repeated at a chosen sampling interval. Throughout this, emission at 405, 440 and 550-nm is continuously measured at 5000-Hz. Appropriate parameters are shown for chronic pharmacokinetic and re-dose experiments in **Table 4.2.3** and **Table 4.2.4**, respectively.

4.2.2.4 Histological Assessment

4.2.2.4.1 Tissue Removal

After all *in vivo* recordings had been completed, mice were humanly culled by anaesthetic overdose and perfusion. Mice were injected (i.p.) with lidocaine (2%)/naropin (7.5-mg/ml solution, Aspen) and pentobarbital (200-mg/ml solution, Vetoquinol) before transcardial infusion with PBS (0.1-M) and 4% PFA. Brain tissue was removed and post-fixated in 4% PFA overnight at 4°C. Next, fixed brain tissue was submerged in 30% sucrose/0.1-M PBS for several days. Once sunk, processed brain tissue was sectioned into 50-µm slices using a microtome (SM2010R, Leica). Dry ice allowed OCT (OCT Embedding Matrix, CellPath) to attach the brain tissue onto the microtome stage for sectioning. Each section was immediately placed into a 24-well plate filled with PBS + 0.02% sodium azide and stored at 4°C until histological processing.

4.2.2.4.2 Histology

Table 4.2.5. Histological staining channels. Colour channels for each stain for chronic TF experiments.

	Stain used for each channel		
Experiment Type	**Plaque**	**Plaque**	**Microglia**
Acute Pharmacokinetic	Methoxy-x04		
Chronic tapered fibre implants	Methoxy-x04	Thioflavin-S	Iba-1

For chronic fibre implant experiments, free-floating sections were histochemically stained with plaque-marker, TS, and microglial marker, Ionized calcium binding adaptor molecule 1 (Iba1), for analysis of plaque pathology and fibre track, respectively **(Table 4.2.5)**. As mice were injected with Methoxy-x04 throughout recording paradigms before perfusion, sections were also monitored for Methoxy-x04 (plaque) staining. Free-floating sections containing the fibre implant targets and 500-μm adjacent sections were stained. First, these sections were floating within a 24-well plate for washing before a 1-hour blocking incubation (10% normal goat serum solution (NGSS) (G9023; Sigma-Aldrich) in PBST). After, sections were incubated with the Iba1 primary antibody overnight at 4˚C (1:1000 diluted in 3% NGSS in PBST; ab178846; Abcam). The next day, sections were washed before undergoing a 2-hour secondary antibody incubation with the Alexa Fluor 594 anti-rabbit IgG secondary antibody solution (1:1000 diluted in 3% NGSS in PBST; A-11005, ThermoFisher) (dark conditions). Next, sections were washed before a 15-minute incubation at room temperature in TS (0.01% in PBS, T1892, Sigma-Aldrich) (dark conditions). After, sections were washed before rinsing in Gelatin solution (0.5%) and mounting onto glass slides. Whereas, for brain tissue from acute pharmacokinetic experiments, free-floating sections underwent washing before rinsing in Gelatin solution (0.5%) and mounting onto glass slides **(Table 4.2.5)**. Slides air-dried overnight before being sealed with cover slips using fluoromount solution (Invitrogen, ThermoFisher Scientific Fluoromount G).

Washes throughout this experiment involved incubating the sections in the 24-well plates for 3 x 5-minutes in PBS (0.1-M), on the orbital shaker (Mini Orbital Shaker SSM1; Stuart); this shaker was used for all incubations, apart from primary antibody.

4.2.2.4.3 Imaging and Assessment

All images were taken using an upright Nikon Eclipse E600 epifluorescent microscope (TheMicroscopeCompany, UK) and an ORCA-spark Digital CMOS camera (C11440-36U, Hamamatsu). 1920x1200-pixel images were taken using a custom LABVIEW code, with an exposure time of 700-ms, at 4x magnification. Images were taken in three wavelength channels for detection of blue (Methoxy-x04), green (TS), and red (Iba1) signals **(Table 4.2.5)**.

Brain regions implanted with the TF were identified. Once identified, the whole brain section was imaged for post-mortem analysis. It is vital to image any sections that include part of the fibre track and some sections anterior and posterior to the implant site for analysis.

4.2.3 Data processing and analysis

4.2.3.1 Photometry analysis

4.2.3.1.1 Pre-processing

Digitised data and recorded time points were stored for off-line analysis by a custom MATLAB code. Once the .dat file was open, data across all recorded channels were adjusted with addition of their channel baseline. Next, events were detected by extracting sync pulses greater than 0.5-V (for acute pharmacokinetic and laser 2) or 1-V (for laser 1), to identify laser ON periods. An event was classed as when the laser is on, at a single power. From this, event times were extracted and used with the number of sweep points across the TF – calculated by determining the frequency of sweeps per second – to extract data from the galvo and photodetector channels for signal processing. For this, a complimentary empty 10 data points are added to each pulse due to initialisation delays of the galvo mirror. Data was stored in a matrix for final processing.

Occasionally computer lagging resulted in incomplete data acquisition, identifiable by an abnormal file size. Therefore, files that were 5% of the standard deviation away from the median file size, were removed and time indexes were stored. If any files were removed, the index of the excluded file was used to interpolate data at relevant time points. Interpolated data was entered into the final matrix. Occasionally the connection between the system and mouse was disrupted. This was detected by determining if signal was less than 95% of the global median signal. If detected, data was interpolated at the relevant time point and entered into the final matrix. The final matrix, power, galvo, and times information were saved into a mat file for further analysis.

For chronic recordings, completed over several days, a custom MATLAB code ran through each day to create these output mat files. Then, raw data across all days was combined into one mat file.

4.2.3.1.2 Data processing

To establish an optimal method for analysing TF data, several approaches were tested. This included conventional raw fluorescent signals – with matrixes extracted as described in **section 4.2.3.1.1**. Also, by using these raw signals, data was either normalised to (Norm) or modelled against (Model) day 0 signals **(Figure 4.2.17)**. Norm was chosen to show the change in signal intensity from when no Methoxy-x04 was present. Model was chosen as AF was a contributor that reduced the signal to noise ratio. Therefore, removing this component will potentially leave a purer Methoxy-x04 signal.

For Norm, raw data mat files from each day of the recording are used **(Figure 4.2.17B)**. First, using day 0 data, the moving median fluorescence over 50-minutes was calculated across all time points at each GV, power, emission, and light protocol **(Figure 4.2.17Bi)**. Next, the median fluorescence across all time points is determined (F0) and is saved in a mat file **(Figure 4.2.17Bii)**. Next, by running through each mat file across days, the moving median fluorescence over 50-minutes of the data across all time points at each GV, power, emission, and light protocol is determined. Then, the data is normalised using F0 to calculate the relative change of fluorescence with the following equation:

$$RC(g,e,p|l) = \frac{(F - F0)}{F0}$$

where RC is relative change, g is galvo trial, e is emission, p is power, l is light protocol, F is fluorescence and F0 is day 0 baseline fluorescence. Here, relative change depends on galvo trial, emission, and power conditionally on light protocol. Then, data matrices across all days were combined into one mat file.

For Model, raw data mat files from each day of the recording are used. First, day 0 data is used to generate a model reflective of the AF of the TF, patch cable and brain tissue which could be removed to realise Methoxy-x04 signals **(Figure 4.2.17C)**. To increase the number of k-folds within the model, to mitigate overfitting for parameter estimation, fluorescence and time data were subsampled, creating two-folds. Each data set was assigned to be either test or train for each fold. A linear polynomial curve was fitted to the subsequent train data at each GV, emission, power, and light protocol. Then, the two folds were combined by calculating the mean model coefficients. Additionally, the goodness of fit was examined using train models and test data, allowing

calculation of the r-squared (R2), adjusted r-squared and root mean squared error (RMSE) **(Figure 4.2.17Cii)**.

The final model was used to extract modelled AF across each day of the recording **(Figure 4.2.17Ci)**. By running through each mat file of raw data across days, the appropriate model coefficients, data, and times for each GV, power, emission, and light protocol are extracted. Then, the predicted AF component is calculated by the following equation:

$AFp = (a \times t) + b$,

where AF is autofluorescence, p is predicted, t is time and a and b are the model coefficients. Once calculated, the data and time for each GV, power, emission, and light protocol are extracted and the predicted autofluorescence is removed as shown in the following equation:

$Fm = F - AFp$,

where F is fluorescence, m is modelled and Afp is predicted autofluorescence **(Figure 4.2.17Ciii)**. Then, matrices across all days were combined into one mat file.

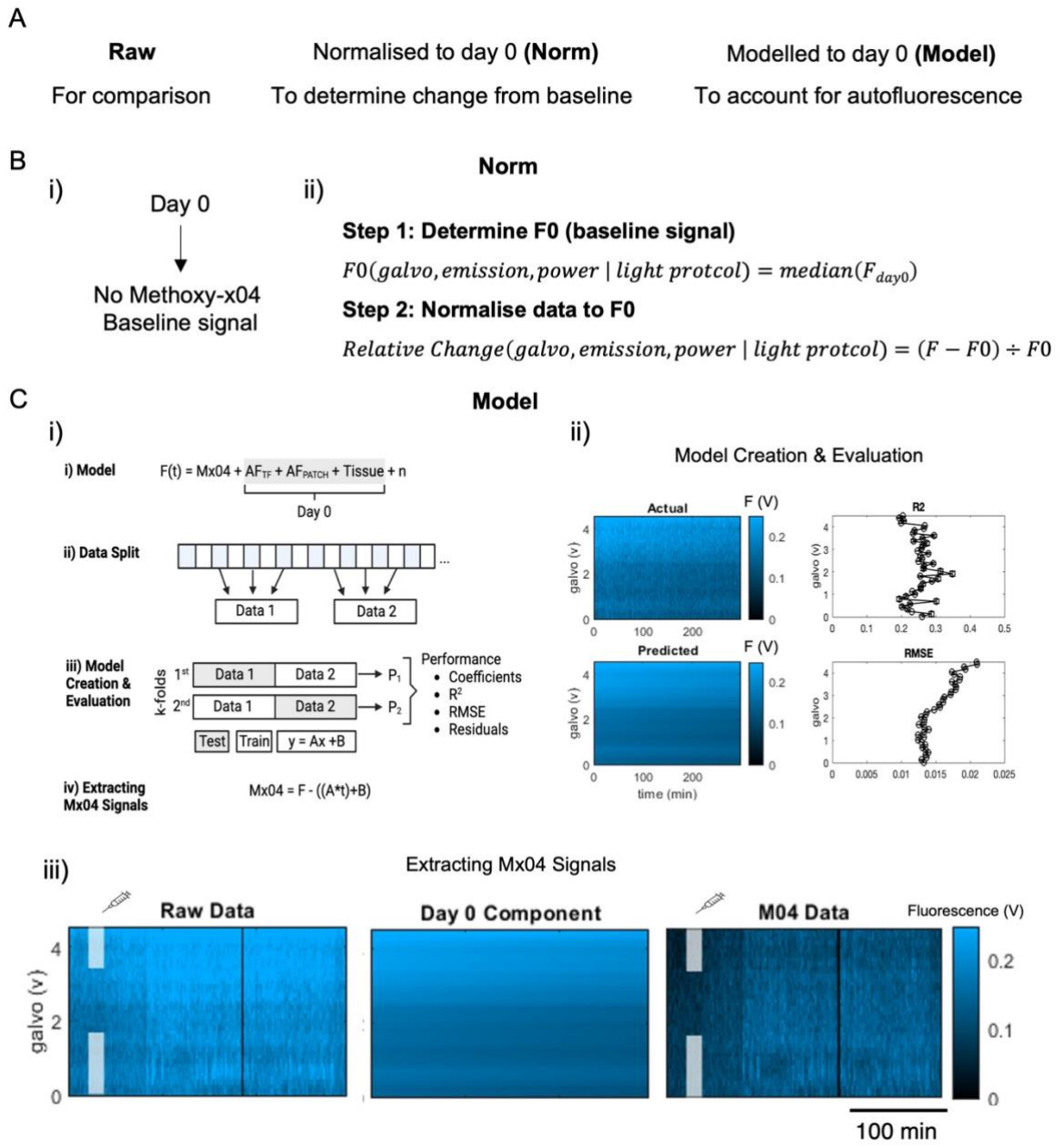

Figure 4.2.17. Analytical approaches for chronic TF recordings. (A) The three analytical approaches used were raw, normalised to day 0 (Norm) and modelled to day 0 (Model). (B) Norm involved using day 0 as the baseline signal as there was no Methoxy-x04 present (i), before calculating the normalised fluorescence (ii). (C) (i) Schematic illustrating the steps of establishing a model that predicts the AF component of TF recordings. Using the day 0 recording, data undergoes a 2-fold model creation to estimate the AF in the TF, patch cable and brain tissue as a function of time. This can be subtracted from signals to realise a pure Methoxy-x04 signal. (ii) Example of the model creation and evaluation. *Left,* Fluorescence (F) across time and depth for actual data and data predicted using the model. *Right,* Goodness of fit parameters. (iii) Example of extracting Methoxy-x04 signals using the model using day 1 pharmacokinetic data. After subtraction of the estimated day 0 component, Methoxy-x04 signals are left.

4.2.3.1.3 Data analysis

4.2.3.1.3.1 Acute and system characterisation analysis

For acute pharmacokinetic and AF recovery recordings, described in **sections 4.2.2.2.2 and 4.2.1.3.4**, respectively and shown in **Figure 4.3.2**, data at 120-µW and 440-nm was used, with galvo measures below 0-V removed. 120-µW was used as this was the highest power used, providing strong Methoxy-x04 signals, across all recordings. 440-nm was used as this was the Methoxy-x04 sensitive detection channel. Example recordings were chosen to show the fluorescence profile across several hours. Plots show the median raw fluorescence. To identify the galvo-dependent fluorescent changes, baseline fluorescence was determined by taking an average of data points acquired at 30-minutes across each chosen GV (0, 1, 2, 3 and 4-V). The change in fluorescence was determined by subtracting this from the fluorescence at 210-minutes across each chosen GV.

To show changes in the light output from the end of the patch cable and TF, as described in **section 4.2.1.3.2** and shown in **Figure 4.3.2**, the light output readings for the example recordings were taken and plotted across increasing GV. Dashed lines were applied to illustrate the power if it was equalised across all GVs.

4.2.3.1.3.2 Chronic analysis

For all chronic recordings, as described in **section 4.2.2.3** and shown in **Figures 4.3.4-18**, data at 120-µW at 440-nm was used, with galvo measures below 0-V removed. 120-µW was used as this was the highest power used, providing strong Methoxy-x04 signals, across all recordings. 440-nm was used as this was the Methoxy-x04 sensitive detection channel. Galvo measures below 0-V were removed because they will reflect the measures above 0-V. Example recordings are chosen to show the fluorescence profile across days. For this, heatmaps of each day for raw, Norm and Model data were used where the colour range was determined by calculating the minimum and maximum fluorescence across all data points across each day in the recording for the specific analytical approach.

For summary analysis, data was extracted at chosen time points of interest. For pharmacokinetic recordings, time points of 0 and 60-minutes were taken across days 0, 2 and 3, with time points of 0, 30, 60, 90, 120, 150, 180 and 210-minutes taken on day 1. For re-dose recordings, time points of 0 and 60-minutes were taken across days 0, 1, 2 and 3. If data was missing at a time-point for a recording, data was not a number (NaN). Data was extracted at chosen GVs: 0, 1, 2, 3 and 4-V.

Data was presented in boxplots to illustrate the distribution across recordings. Traces of the profile for each recording were presented on the same plots. 5xFAD+ and 5xFAD- data was shown in galvo-related shades of blue and green respectively, with darker colours representing lower GVs.

4.2.3.1.4 Exclusion criteria

For final analysis, chronic TF data must pass the exclusion criteria. Here, if the power was not calculated appropriately or the appropriate bleaching protocol was not followed, the full recording was excluded. Also, for recordings where the first laser showed some deterioration throughout were excluded. Lastly, to avoid exclusion, the recording must include day 0 and day 1 data at a minimum. Reasons for exclusions for chronic pharmacokinetic and re-dose experiments are shown in **Table 4.2.3 and Table 4.2.4**, respectively.

4.2.3.2 Image Analysis

Image analysis was consistent with previously described methods in **Chapter 2, section 2.1.3**, bar detection of the fibre track and correlative assessment.

4.2.3.2.1 Fibre track detection

To identify the TF track, there was various manual steps **(Figure 4.2.18A)**. Firstly, the fibre track and TF tip was identified using Iba1 signals on histological images **(Figure 4.2.18B)**. From the TF tip, 1.62-mm (the estimated active region of the TF) was measured to identify the full TF active region. The full active region of the TF is 1.8-mm, representing up to 5-V galvo, but as we only record up to 4.5-V galvo throughout *in vivo* experiments, we scaled the active region of the TF appropriately. Then, the fibre track on the Methoxy-x04-stained aligned sections was manually labelled using an AmaSiNe built-in graphical user face **(Figure 4.2.18C)**. This allows manual annotation on each aligned image, along the TF active region. Using the aligned images, the AP, ML and DV coordinates of the manually labelled TF track are identified.

While this provided scattered coordinates across sections, in order to estimate the fibre track coordinates across sections and at a sampling interval that mirrored the TF photometry experiments, further analysis was required. First, two major parameters are determined: the depth alignment scaling factor and the sampling depths. To determine the depth alignment scaling factor, the estimated length of the TF active region, as determined by the manual labelling on histological sections, was divided by the actual length (1.62-mm) **(Figure 4.2.18D)**. To determine the sampling depths, equal sampling intervals at the TF resolution (the distance between each measure) was calculated **(Figure 4.2.18E)**. The TF resolution was the length of the active region divided by the

number of measures minus 1, multiplied by the scaling factor. The sampling depths were determined by calculating equal sampling intervals of the TF resolution from the most dorsal to the most ventral annotated coordinate **(Figure 4.2.18E).** Then, using the AP, ML, DV coordinates and sampling depths, the coordinates for the full fibre track are estimated using a two-step regression model. Lastly, using the list of all brain regions, provided from the Allen Institute, the coordinates allow identification of brain regions the fibre track passes.

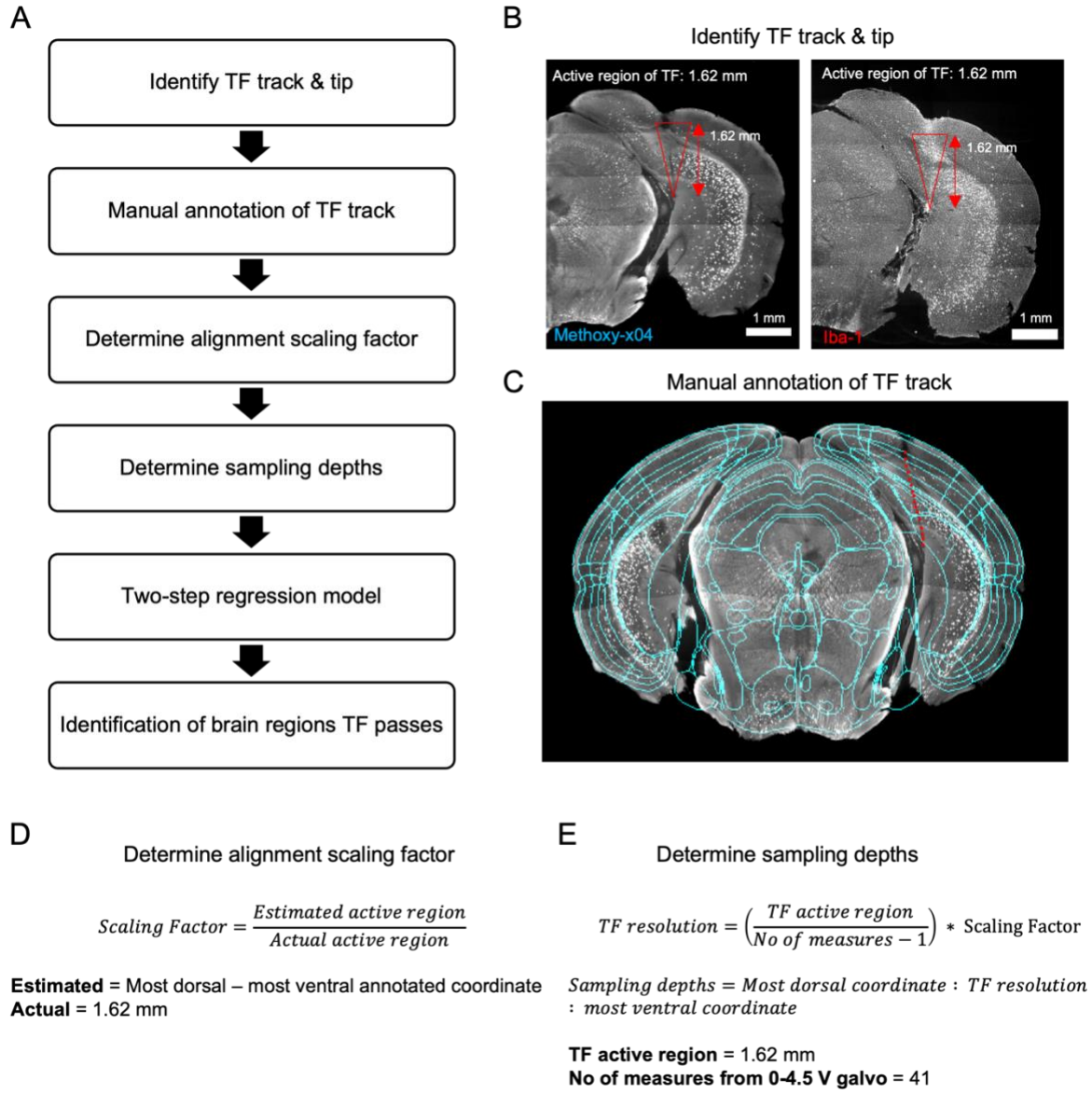

Figure 4.2.18. Process for TF fibre track detection. (A) Steps of fibre track detection. (B) Identify TF track and tip using histological images showing Methoxy-x04 (left) and Iba1 (right) signals. Iba1 signals allow identification of the TF track due to accumulation of microglia. By using the scale, 1.62-mm was marked from the TF tip, representing the active region of the TF from 0-4.5-V galvo, as this is what was used for *in vivo* experiments. Scale: 1-mm. (C) Manual annotation of the TF track on aligned histological images. Red dots show the annotated TF active region. Blue shows

the aligned atlas to the respective histological section. (D) Calculation to determine the alignment scaling factor. The estimated active region of the TF was determined by subtracting the most ventral coordinate, from the most dorsal. This accounts for differences in depth from *in vivo* to histology. (E) Calculation to determine the sampling depths. TF resolution was calculated by dividing the TF active region by the number of measures. The number of measures was as used for *in vivo* experiments, with 41 measures from 0-4.5-V galvo. Sampling depths were calculated from the most dorsal coordinate to the most ventral coordinate at TF resolution intervals.

4.2.3.2.2 Photometry Vs histology correlative assessment

Table 4.2.6. Summary of histological correlation analysis parameters. Reasons mice were excluded are explained. Exclusion criteria is described in **sections 4.2.3.1.4 and 4.2.3.2.3**.

Animals	Genotype	Target coordinates	PK recording	Time from PK Day 0 to perfusion (days)	Excluded	Reason for exclusion
FAD37	+	1	5	2		Recording error
FAD40	-	1	5	0		Recording error, estimated track depth & image quality
FAD43	-	1	4	77		Recording error
FAD45	+	1	6	3		Recording error & estimated track depth
FAD51	+	2	4	3		
FAD52	-	2	2	3		Estimated track depth
FAD57	+	2	2	86		
FAD58	+	2	1	3		
FAD59	-	2	1	86		
FAD60	-	2	1	54		
FAD61	-	2	1	55		
FAD62	+	2	2	50		
FAD63	+	2	2	49		
FAD64	-	3	1	19		
FAD65	+	3	1	28		
FAD66	-	3	1	9		Estimated track depth & image quality
FAD67	+	3	1	25		
FAD68	+	3	1	12		Image quality
FAD69	-	3	1	3		
FAD70	-	3	2	21		
FAD71	+	3	2	22		
FAD72	+	3	1	15		
FAD73	-	3	1	14		
FAD74	+	3	2	31		
FAD75	+	3	2	30		

Lastly, in attempt to mirror the plaque signals collected from photometry experiments, plaques that fall within a 200-µm radius of the fibre track coordinates, on the same implant site on the contralateral hemisphere, were quantified. Setting the contralateral hemisphere is vital to avoid tissue damage from the implant interfering with accurate quantification. This approach assumes

plaque pathology is consistent across hemispheres. Again, the TF track resolution was determined for each galvo measure. From here we can determine the quantified plaques at increasing depths along the fibre and compare to photometry data.

To determine if the histological quantification of Methoxy-x04 stained plaques was correlated to photometry data, photometry data from the last pharmacokinetic recording was used **(Table 4.2.3** and **Table 4.3.6)**. Here, data at 120-µW and 440-nm on day 1 of the recording was used. The median signal for raw, Norm and model data between 120- and 180-minutes was calculated, omitting NaN values where data was missing. Histological data was the quantified plaque pathology along the fibre track. In 5xFAD- mice, where noise was quantified as a plaque, signals were removed manually by setting the value to 0. In cases where no plaque pathology was quantified, addition of MATLAB-generated random noise in values <0.00001 was added to histological quantification. Next, the correlation between photometry and histological signals was determined using Pearson's correlation coefficient. For summary analysis, the mean and SEM of correlation coefficients were calculated for each recording site and across all sites. Lastly, the correlation coefficients for 5xFAD+ mice were compared across analytical approaches to determine the optimal approach.

4.2.3.2.3 Exclusion Criteria

For TF histology correlation analysis, only data that passed the exclusion criteria was used. Fibre photometry recordings were only used if they were not previously excluded, as explained in **section 4.2.3.1.4.** For histology data, it was excluded on two grounds: estimated track depth and image quality. By plotting the estimated track depth, calculated from the histological track detection described in **section 4.2.3.2.1**, any that were greater or lower than a standard deviation of 1.5 away from the group mean were excluded. Aligned images after histological image alignment were scored by an experimenter on various aspects of alignment and image quality from 0-5 (5 being perfect). These included the quality of alignment of images to the Allen brain atlas, the quality of images (damaged or missing), if the full fibre track was shown across images and if the fibre track was warped due to the alignment process. Then, the mean image quality score was calculated and recordings that had a score that was 1.5 standard deviations lower than the mean were excluded. **Table 4.2.6** shows recordings that were excluded with reasons. Detailed reasons for exclusion of photometry recordings are shown in **Table 4.2.3.**

4.2.3.3 Statistics

All statistical analysis was completed on MATLAB. Significance was set as $\alpha = 0.05$, with p-values coded as follows: $p < 0.001$ (****), $p < 0.005$ (***), $p < 0.01$ (**), $p < 0.05$ (*), ns not significant.

One-sample Kolmogorov–Smirnov tests were completed to check the normality of data. Pharmacokinetic and re-dose experiments distribution was shown using boxplots and were statistically tested using the non-parametric Kruskal-Wallis test. If $p < 0.05$, post-hoc multi-comparisons with Bonferroni corrections were completed. For correlative analysis, Pearson's correlation coefficient calculated the r- and p-value. Summary correlation data was shown as mean ± SEM, and two-sample t-tests were completed on appropriate data sets.

4.3 Results

Here, we aim to use state-of-the-art TF photometry to realise *in vivo*, depth-resolved, real-time plaque monitoring in the freely behaving condition. First, we began with acute recordings under terminal conditions to try monitor real-time plaque signals, following injection of Methoxy-x04. After this, we use knowledge gained to optimise procedures for freely behaving recordings and completed pharmacokinetic and re-dose recordings to identify optimal light protocols and analytical approaches for TF recordings, while examining the properties of Methoxy-x04 over-time. Finally, we determine if TF photometry measures are positively correlated to histological quantification, as seen with FF photometry.

4.3.1 Datasets and mice

Figure 4.3.1 shows animal information for TF experiments following exclusions (described in **sections 4.2.2.2.2, 4.2.2.3.2, 4.2.2.3.3 and 4.2.3.2.2**, respectively). More 5xFAD- mice were used for acute pharmacokinetic recordings than 5xFAD+ mice as we were trying to determine the cause of AF **(Figures 4.3.1A&C)**. Mice used for acute pharmacokinetic recordings were aged between 6-8-months **(Figure 4.3.1B)**.

Most chronic pharmacokinetic recordings were completed at TF implant site 2 and 3 **(Figure 4.3.1D)** where the tip of the TF should be within the SUB up to the superficial layers of the visual cortex. Pharmacokinetic recordings were completed on a large age range of mice from 3-12-months **(Figure 4.3.1E).** Re-dose experiments were completed on mixed-sex, -genotype, and -implant sites **(Figure 4.3.1D)**, with an age range from 5-11-months **(Figure 4.3.1H).** The total number of recordings for both 5xFAD+ and 5xFAD- mice were higher than the total number of mice for both pharmacokinetic and re-dose experiments as some mice were recorded from several times **(Figure 4.3.1F & Figure 4.3.1I).**

Following exclusion analysis, 18 mice were used for histology correlation analysis: 11 5xFAD+ and 7 5xFAD- **(Figure 4.3.1L)**. These were varied across implant site, sex, and age **(Figure 4.3.1J-K)**.

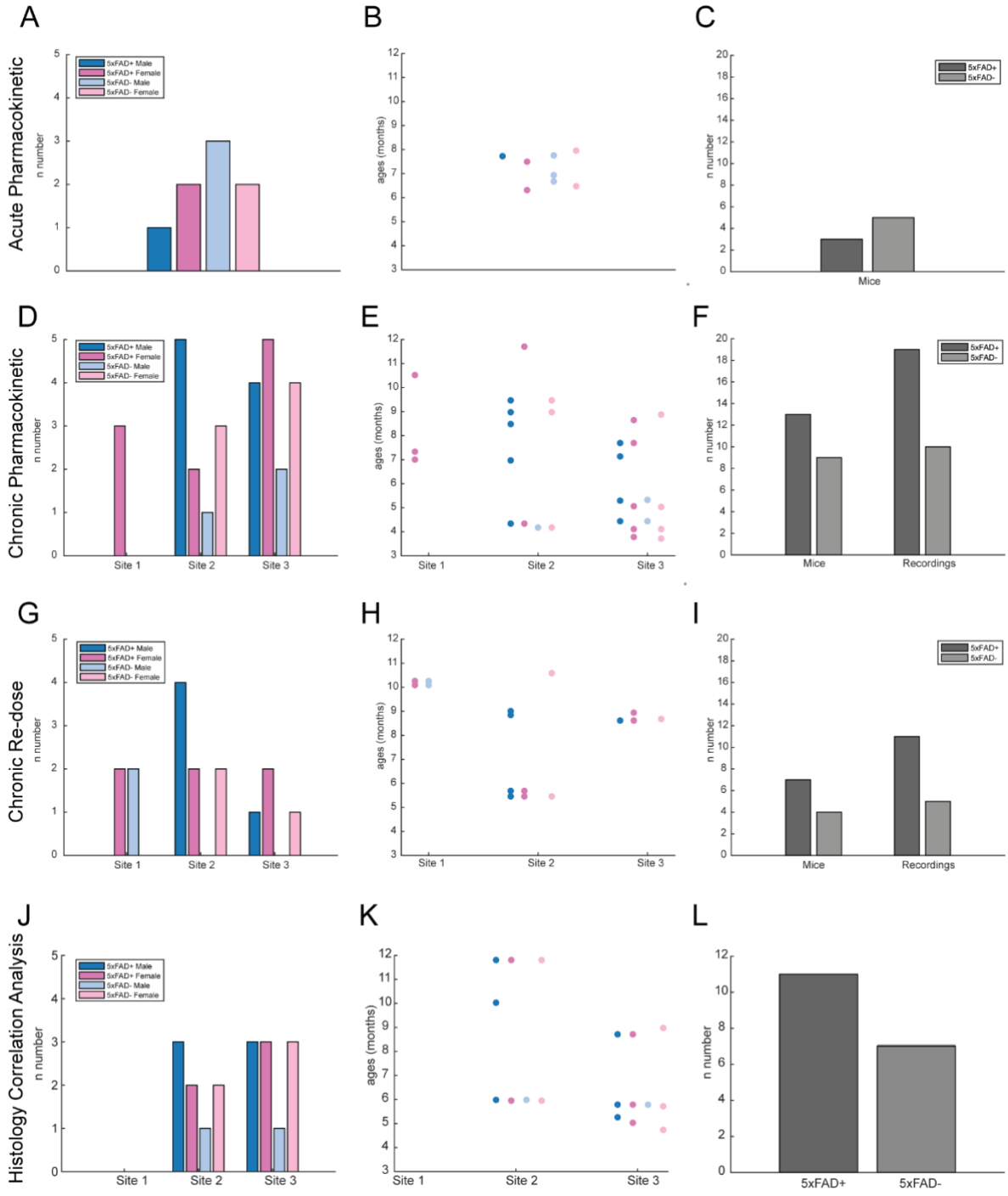

Figure 4.3.1. Sex, age, and genotype information for recordings completed and animals used for acute and chronic TF experiments. Number of recordings and age of animals at each recording across sex and genotype for acute pharmacokinetic (A,B), chronic pharmacokinetic (D,E), chronic re-dose (G,H) and histology correlation analysis (J,K). Total sample number for mice or recordings for acute pharmacokinetic (C), chronic pharmacokinetic (D), chronic re-dose (I) and histology correlation analysis (L). Some mice were recorded from

several times. Histology correlation age is at time of perfusion. Each site number shows the TF implant coordinate site **(Figure 4.2.14)**.

4.3.2 AF and TF light properties are important considerations for *in vivo* recordings

To validate the detection of real-time, depth-resolved Methoxy-x04 signals and enhance understanding of the *in vivo* signals attainable using TFs, we conducted acute pharmacokinetic experiments **(Figure 4.3.2A)**. Subsequently, we recognized that AF and characteristics of TF light propagation may influence signal collection. To investigate this, we also conducted *in vitro* AF characterisations **(Figures 4.3.2A&D)**.

In vivo recordings involved the administration of Methoxy-x04 (10-mg/kg) after 0.5-hours of baseline recording, under terminal anaesthesia **(Figure 4.3.2A)**. Preliminary observations in a 5xFAD+ mouse model revealed a gradual increase in fluorescence post-Methoxy-x04 injection, across all depths of the TF at varying intensities **(Figure 4.3.2B)**. Specifically, there was a more pronounced change in fluorescence at 3 and 4-V galvo. While this implied Methoxy-x04 signals may be detected, replicating experiments in a 5xFAD- mouse model, where no plaque pathology occurs, showed a similar fluorescence profile post-Methoxy-x04 injection **(Figure 4.3.2C)**. This suggests something other than Methoxy-x04 may be contributing to this signal, such as AF. For example, AF of the photometry system can regenerate over-time, potentially influencing all recordings.

To confirm this and gain further insight into what influence TF photometry may have on chronic experiments, we assessed the AF recovery following a bleaching protocol **(Figure 4.3.2A)**. This was done without the use of animals, where a TF attached to the system was stabilised in the air. Also, this protocol was designed to mirror the methodology used in acute pharmacokinetic experiments. **Figure 4.3.2D** illustrates that AF began to rise within 30-minutes from the end of the bleaching process, coinciding with the injection time in *in vivo* experiments. Additionally, this increased fluorescence was greater at higher GVs.

Also, we examined the light output of the patch cable with and without the TF attached on the day of both 5xFAD+ and 5xFAD- acute pharmacokinetic recordings. This was done without the use of animals, where a TF attached to the system was stabilised in the air. It was shown that for the patch cable and TFs used for both 5xFAD+ and 5xFAD- recordings, a reduction in light output was noted with increasing GV **(Figure 4.3.2E)**. This suggests that as light passes to higher regions on the TF, the coupling of light from the system begins to decrease due to alignment limits.

Consequently, light power along the TF will be varied, meaning that brain tissue would not be recorded at uniform light intensity across depth.

In summary, while an increase in fluorescence was seen across both genotypes, it appears to be influenced by the recovery of AF and light power. In all, there is a clear necessity for additional protocols for TF *in vivo* recordings to ensure consistent excitation, signal collection, and extraction of true Methoxy-x04 signals.

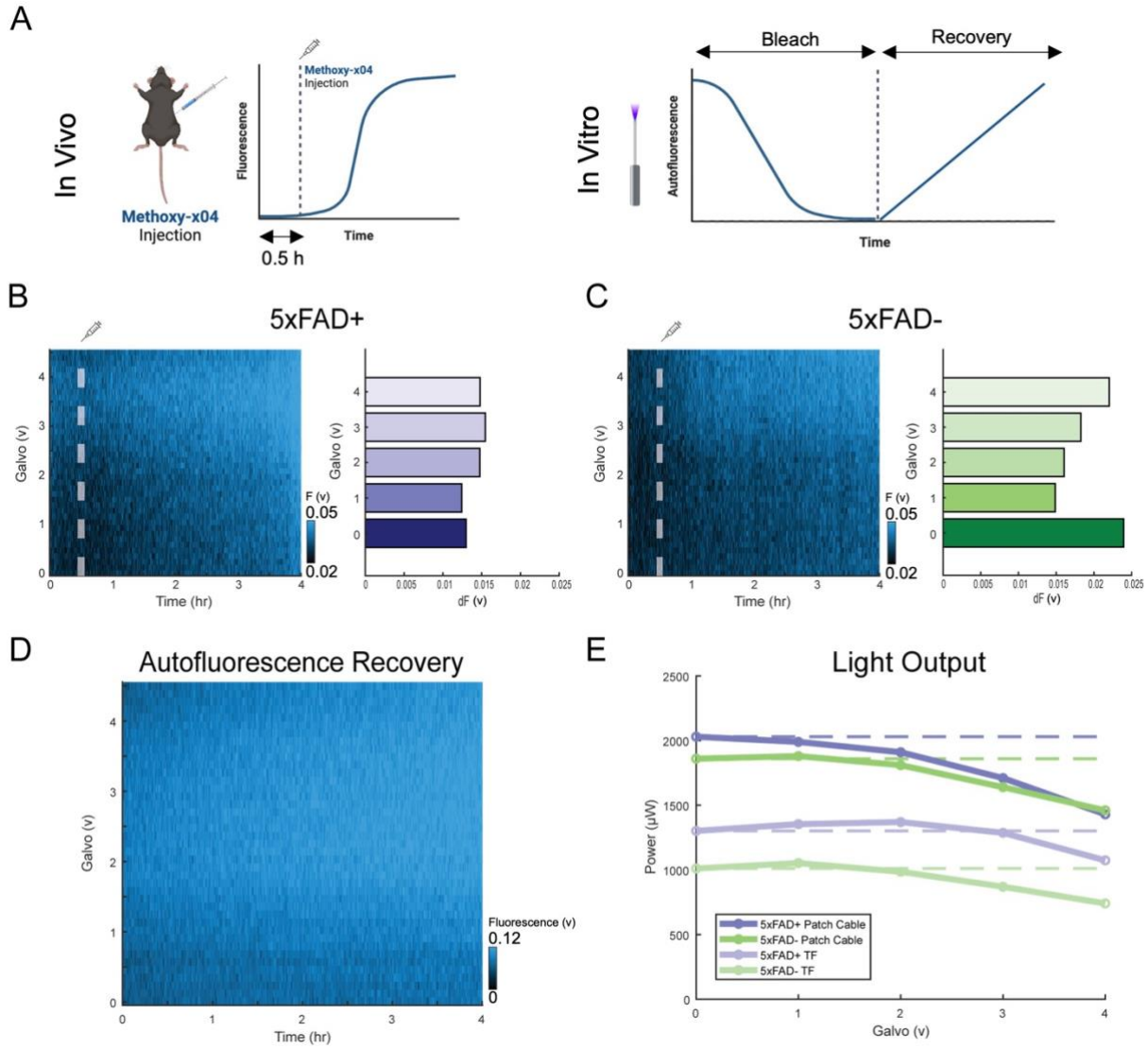

Figure 4.3.2. Acute pharmacokinetic recordings may be influenced by AF and ununiform light propagation from TFs. (A) Schematic illustrating the *in vivo* and *in vitro* procedures completed. For *in vivo* acute pharmacokinetic experiments, fluorescence was recorded from a TF implanted in a 5xFAD+ or 5xFAD- mouse, with Methoxy-x04 (10-mg/kg) being injected after a 0.5-h baseline. *In vitro* AF characterisation involved bleaching the system while the TF was not implanted, before monitoring AF recovery. Characterisation suggested the bleaching process was exponential, whereas the recovery was near-linear. (B, C) *Left,* Fluorescence across depth (GV),

over time in 5xFAD+ (B) and 5xFAD- (C) mice. White dashed line illustrates the injection time. Colour map shows the fluorescence (F) range. *Right,* Change of fluorescence at 3.5-h compared to 0.5-h. (D) AF recovery across depth, over time. Colour map shows the AF range. (E) Light output at increasing GVs on the day of the 5xFAD+ (B) and 5xFAD- (C) recording. Dashed lines show the power at 0-V galvo.

4.3.3 Real-time, depth-resolved Methoxy-x04 signals intensified with adopted light protocols and analytical approaches

For chronic recordings, a TF was chronically implanted in the brain. The target was to have the tip of the TF hitting the plaque-dense SUB, with the shaft reaching up through the visual cortex layers. Three implant coordinates were used with adjustments made to improve targeting **(Figure 4.2.14).**

After all appropriate recordings were completed, brains were taken for post-mortem histological assessment. **Figure 4.3.3** shows Methoxy-x04 stained brain sections illustrating the fibre track for all 5xFAD+ and 5xFAD- mice. Across several mice, the implant was slightly medial and posterior of the target, with only ~50% of implants reaching the post-subiculum (POST), with none hitting the SUB **(Figure 4.3.3C)**. However, most implants passed visual cortical regions. All site 3 implants appear to have some of the TF passing a plaque dense hippocampal region in 5xFAD+ mice **(Figure 4.3.3A)**, with 5xFAD- implants occurring in similar regions **(Figure 4.3.3B).** While site 1 and 2 do not necessarily pass a region as plaque dense as site 3 implants, they do have surrounding plaque pathology that is greater at deeper regions of the TF. Overall, many recordings appear to have hit the approximate target for chronic recordings.

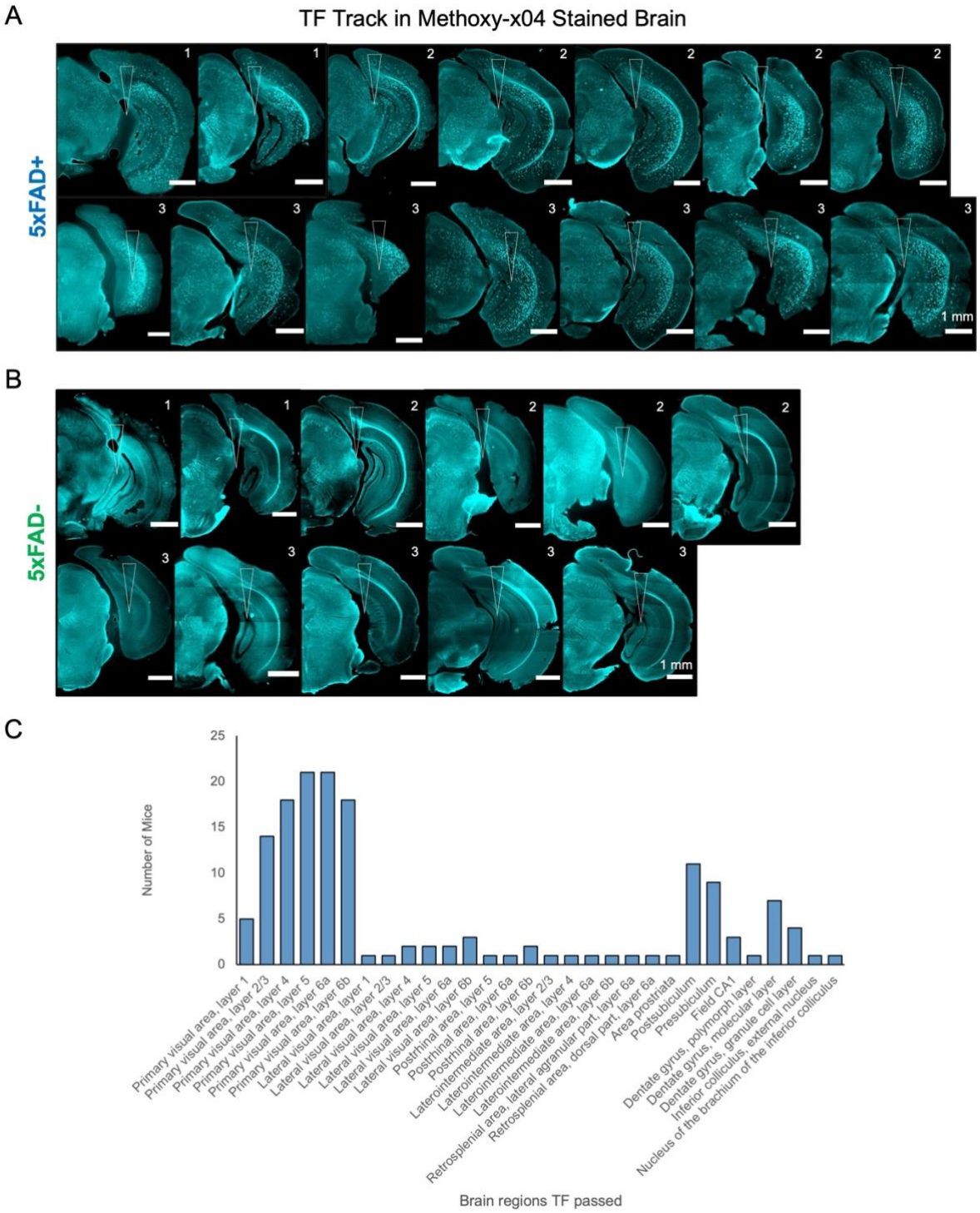

Figure 4.3.3. Histological analysis of the location of TF implants. (A, B) Methoxy-x04-stained histological coronal sections from 5xFAD+ (A) and 5xFAD- (B) mice. White triangles show the location of the fibre track. Numbers on the top right indicate the type of implant coordinates **(Figure 4.2.14)**. Scale: 1-mm. (C) Quantification of brain regions the implants passed according to histological brain atlas alignment data, described in **section 4.2.3.2.1**.

4.3.3.1 Methoxy-x04 was detected within 30-minutes of injection across depth, in 5xFAD+ mice

Discovering that light propagation from the TF provides varied signal intensities resulted in the implementation of light protocols that manipulate the light power along the TF. These protocols were termed original (no modifications), *in vitro* (equalised light power) and image (equalised power density). Also, to account for AF, data was normalised to the baseline signal (Norm) or extracted from modelled AF (Model) and compared to raw data. As well as this, additional protocols were implemented to minimise AF such as a shorter patch cable and rigorous photobleaching before each recording, as discussed in **section 4.2.1.3.3**.

Using these light protocols and analytical approaches, *in vivo* pharmacokinetic recordings were completed to determine if *in vivo* Methoxy-x04 signals can be detected in freely behaving animals, across depth and what combination of light protocol and analytical approach provides optimal signals. Mice chronically implanted with a TF underwent a 5-hour baseline recording (Day 0). On day 1, Methoxy-x04 (10-mg/kg) was injected at 0.5-h **(Figure 4.3.4A)**. In 5xFAD+ mice, a steady rise in fluorescence was expected, with stronger signal intensities at deeper regions where plaque pathology is dense **(Figure 4.3.3)**. Whereas in 5xFAD- mice, no change was expected.

Figure 4.3.4 shows the pharmacokinetic profile in 5xFAD+ mice for the original light protocol. Here, the declining fluorescence over day 0 is seen for raw and Norm data **(Figure 4.3.4B)**. On day 1 we see a rise in fluorescence following Methoxy-x04 injection within 30-60-minutes, with Norm data illustrating a quicker incline, followed by a decline over days 2 and 3 **(Figure 4.3.4B)**. Notably, original light protocol has no clear alterations of signal intensity across GVs, with signals reasonably constant across depth **(Figure 4.3.4B).**

Summary raw data show no trends of increased fluorescence post-injection across all GVs, with no significant differences overtime (0-V, $H(13) = 6.1698$, $p = 0.9398$; 1-V, $H(13) = 4.315$, $p = 0.9874$; 2-V, $H(13) = 2.146$, $p = 0.9997$; 3-V, $H(13) = 2.445$, $p = 0.9993$; 4-V, $H(13) = 3.1210$, $p = 0.9975$, Kruskal-Wallis test) **(Figure 4.3.4C)**.

Additionally, while individual traces illustrate many recordings having an increase in fluorescence post-injection, summary Norm plots do not show a pronounced increase on day 1 across GVs, despite small trends seen at 0-2-V galvo **(Figure 4.3.4D)**. Statistical tests show significance for Norm data at 4-V ($H(13) = 25.2268$, $p = 0.0215$, Kruskal-Wallis test), but not others (0-V, $H(13) = 11.4546$, $p = 0.5728$; 1-V, $H(13) = 12.4758$, $p = 0.4891$; 2-V, $H(13) = 14.2600$, $p = 0.3558$; 3-V, $H(13) = 20.2660$, $p = 0.0888$, Kruskal-Wallis test), with post-hoc tests showing no significant differences between groups **(Table 4.3.1)**.

Also, summary model data show significance at 1-V (H(13) = 22.3747, p = 0.0498, Kruskal-Wallis test), 2-V (H(13) = 22.8073, p = 0.0440, Kruskal-Wallis test), 3-V (H(13) = 26.9004, p = 0.0128, Kruskal-Wallis test) and 4-V (H(13) = 22.9134, p = 0.0427, Kruskal-Wallis test) but not 0-V (H(13) = 17.9431, p = 0.1597, Kruskal-Wallis test) **(Figure 4.3.4E)**. However, post-hoc tests show no significant differences between groups **(Table 4.3.1)**.

Therefore, without modulating the light propagation from the TF, depth resolution and a prominent increase post-injection remains to be fully elucidated. Therefore, alternatives were explored.

Table 4.3.1. Statistical summary for 5xFAD+ pharmacokinetic experiments completed with the original light protocol. Kruskal-Wallis tests were completed across time points for each GV, supplying a group comparison significance. If the Kruskal-Wallis test provided a p-value <0.05, post-hoc tests with Bonferroni correction were completed. Day 0 time points are compared with all other time points. Comparisons not shown in the table were non-significant. D0, D1, D2 and D3 represents day 0, 1, 2 and 3, respectively. **** p < 0.001, *** p < 0.005, ** p < 0.01, * p < 0.05, ns not significant.

		Original														
		Raw					Norm					Model				
		Galvo (V)														
Group 1	Group 2	0	1	2	3	4	0	1	2	3	4	0	1	2	3	4
Group Comparison		ns	ns	ns	ns	ns	ns	ns	ns	ns	*	ns	*	*	*	*
D0, 0-min	D0, 60-min										1		1	1	1	1
	D1, 0-min										1		1	1	1	1
	D1, 30-min										1		1	1	1	1
	D1, 60-min										1		1	1	1	1
	D1, 90-min										1		1	1	1	1
	D1, 120-min										1		1	1	1	1
	D1, 180-min										1		1	1	1	1
	D1, 210-min										1		1	1	1	1
	D1, 240-min										1		1	1	1	1
	D2, 0-min										1		1	1	1	1
	D2, 60-min										1		1	1	1	1
	D3, 0-min										0.267		1	1	1	1
	D3, 60-min										0.932		1	1	1	1
D0, 60-min	D1, 0-min										1		1	1	1	1
	D1, 30-min										1		1	1	1	1
	D1, 60-min										1		1	1	1	1
	D1, 90-min										1		1	1	1	1
	D1, 120-min										1		1	1	1	1
	D1, 180-min										1		1	1	1	1
	D1, 210-min										1		1	1	1	1
	D1, 240-min										1		1	1	1	1
	D2, 0-min										1		1	1	1	1
	D2, 60-min										1		1	1	1	1
	D3, 0-min										0.057		1	1	1	1
	D3, 60-min										0.238		1	1	1	1

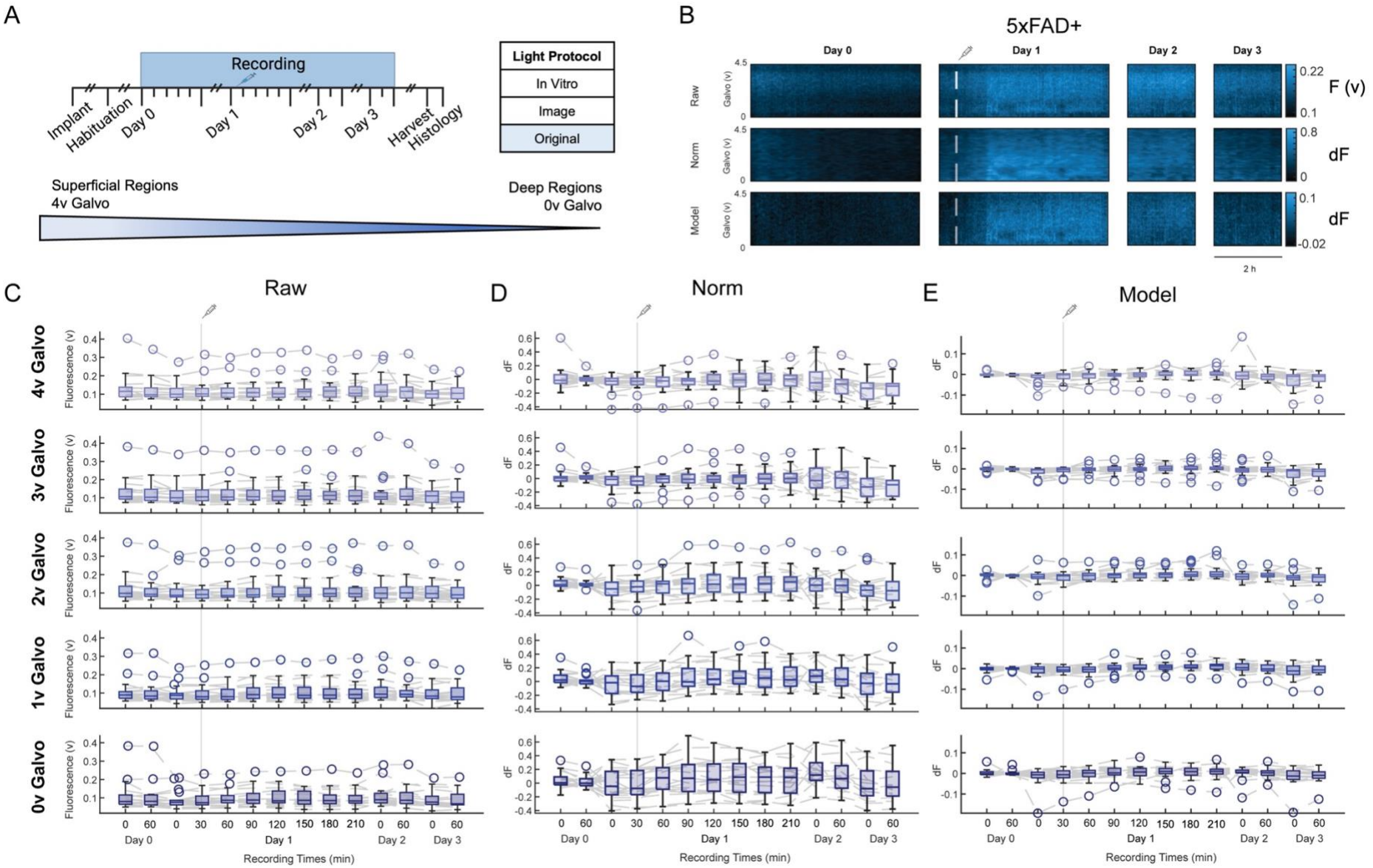
A
Recording
Implant
Habituation
Day 0
Day 1
Day 2
Day 3
Harvest
Histology
Light Protocol
In Vitro
Image
Original
Superficial Regions
4v Galvo
Deep Regions
0v Galvo
B
5xFAD+
Day 0
Day 1
Day 2
Day 3
Raw
Norm
Model
Galvo (v)
F (v)
dF
2 h
C
Raw
D
Norm
E
Model
4v Galvo
3v Galvo
2v Galvo
1v Galvo
0v Galvo
Fluorescence (v)
dF
Recording Times (min)

Figure 4.3.4. Pharmacokinetic profile of Methoxy-x04 in a 5xFAD+ mouse using the original light protocol, analysed with different approaches. (A) *Top left*, Recording paradigm. Methoxy-x04 was injected at 0.5-h on day 1 of the 4-day recording schedule. Each dash on the recording days represents 1-h. *Top right,* Table highlighting the light protocol: original. *Bottom,* Schematic of the TF showing that higher GVs represent superficial regions, whereas lower GVs represent deeper brain regions. Colour coding is consistent with the colour coding of the summary plots. (B) Example heatmaps of the fluorescence across depth and time, over the 4-day pharmacokinetic recording in a 5xFAD+ mouse. Each vertical row represents a different data analytical approach: raw, normalised to day 0 (Norm) and modelled to day 0 (Model). White dashed line represents the time of Methoxy-x04 injection. Colour map represents the fluorescence range. Scale: 2-h. Example plots come from FAD45, pharmacokinetic recording 6. (C, D, E) Summary plots of the pharmacokinetic profile of Methoxy-x04 across time and depth, for raw (C), Norm (D) and Model (E) data. Plot colours get darker as the recording region on the TF gets deeper. Grey line illustrates the time of Methoxy-x04 injection. Data was statistically compared using a Kruskal-Wallis test, followed by multi-comparison tests with Bonferroni correction if $p < 0.05$. n = 19 recordings in 13 5xFAD+ mice.

Then, the *in vitro*-based light protocol was explored, as this involved equal light power along the TF which should provide a more reliable excitatory profile of Methoxy-x04 across depth. **Figure 4.3.5** shows the pharmacokinetic profile of Methoxy-x04 for 5xFAD+ mice with the *in vitro*-based light protocol. Example plots show that raw data on day 0 has a greater fluorescence at higher GV, which declines across the 5-hour recording **(Figure 4.3.5B)**. On day 1, a rise in fluorescence occurs from ~60-minutes across the full depth of the TF. However, while Norm data has a fluorescence decline across day 0, the rise in fluorescence post-injection is clear within 30-minutes showing variations of signal strength across GV **(Figure 4.3.5B)**. This depth-resolved rise within 30-minutes was consistent with Model data, however the decline across day 0 was not seen **(Figure 4.3.5B)**. Across all analytical approaches, but more notably seen with Norm data, on day 2, fluorescence is maintained in a depth-resolved manner **(Figure 4.3.5B)**. However, throughout days 2 and 3, fluorescence begins to decline back to a pre-injection level.

Summary plots for AF-contaminated raw data did not show any significant changes over time across GVs (0-V galvo, $H(13) = 4.9171$, $p = 0.9770$; 1-V galvo, $H(13) = 4.3745$, $p = 0.9865$; 2-V galvo, $H(13) = 3.1108$, $p = 0.9975$; 3-V galvo, $H(13) = 2.8165$, $p = 0.9985$; 4-V galvo, $H(13) = 3.5289$, $p = 0.9952$, Kruskal-Wallis test) **(Figure 4.3.5C) (Table 4.3.2)**.

However, Norm data show some variations across depth, with a trend of increasing fluorescence on day 1 from 30-minutes across all GV, with a more pronounced change in median fluorescence across time seen at 0 and 1-V galvo (median fluorescence at 0-V galvo: -0.049-V, 0.048-V, 0.065-

V, 0.071-V, 0.089-V, 0.115-V and 0.108-V, at 30, 60, 90, 120, 150, 180 and 210-minutes, respectively) compared to 4-V galvo (median fluorescence at 4-V galvo: -0.0507-V, -0.008-V, -0.007-V, -0.019-V, -0.036-V, -0.006-V and -0.017-V, at 30, 60, 90, 120, 150, 180 and 210-minutes, respectively) **(Figure 4.3.5D)**. However, statistical significance was only seen across time at 3-V ($H(13) = 25.2481$, $p = 0.0214$, Kruskal-Wallis test) and 4-V galvo ($H(13 = 27.1491$, $p = 0.0119$, Kruskal-Wallis test), and not at 0-V ($H(13) = 13.9795$, $p = 0.3753$, Kruskal-Wallis test), 1-V ($H(13) = 13.4799$, $p = 0.4115$, Kruskal-Wallis test) and 2-V ($H(13) = 14.7816$, $p = 0.3212$, Kruskal-Wallis test). Post-hoc statistical tests illustrate that there is a statistically significant difference between 60-minutes on day 0 and both time points on day 3 at 4-V galvo ($p = 0.028$ and $p = 0.021$, respectively, post-hoc Bonferroni tests) **(Table 4.3.2)**. This is representative of the decline in fluorescence seen across all GV on days 2 and 3 (median fluorescence: 0-V galvo, 0.163-V to -0.040-V; 1-V galvo, 0.074-V to -0.019-V; 2-V galvo, -0.001-V to -0.078-V; 3-V galvo, -0.039-V to -0.092-V; 4-V galvo, -0.056-V to -0.099-V for day 2 0-minutes and day 3 60-minutes, respectively) **(Figure 4.3.5D)**.

Whereas in Model data, an increase in fluorescence on day 1 was seen across all GV, with an increase occurring within the first 30-minutes post-injection **(Figure 4.3.5E).** However, the median change in fluorescence was within a very small range and remained more pronounced at 0-V galvo (median fluorescence at 0-V galvo: -0.012-V, -0.005-V, 0.001-V, 0.007-V, 0.007-V, 0.016-V and 0.014-V, at 30, 60, 90, 120, 150, 180 and 210-minutes, respectively) compared to 4-V galvo (median fluorescence at 4-V galvo: -0.009-V, -0.002-V, -0.002-V, 0-V, 0.002-V, 0-V and 0.003-V, at 30, 60, 90, 120, 150, 180 and 210-minutes, respectively). Additionally, a decline in fluorescence over days 2 and 3 are seen (median fluorescence: 0-V galvo, 0.014-V to 0-V; 1-V galvo, 0.002-V to -0.006-V; 2-V galvo, -0.005-V to –0.008-V; 3-V galvo, -0.007-V to -0.012-V; 4-V galvo, -0.007-V to -0.011-V for day 2 0-minutes and day 3 60-minutes, respectively) **(Figure 4.3.5E).** Despite these trends, statistical tests show no significant difference across depth (0-V galvo, $H(13) = 19.4220$, $p = 0.1106$; 1-V galvo, $H(13) = 21.1609$, $p = 0.0698$; 2-V galvo, $H(13) = 20.3020$, $p = 0.0879$; 3-V galvo, $H(13) = 21.6422$, $p = 0.0612$; 4-V galvo, $H(13) = 22.1106$, $p = 0.0537$, Kruskal-Wallis test) **(Table 4.3.2)**.

Table 4.3.2. Statistical summary for 5xFAD+ pharmacokinetic experiments completed with the *in vitro* light protocol. Kruskal-Wallis tests were completed across time points for each GV, supplying a group comparison significance. If the Kruskal-Wallis test provided a p-value <0.05, post-hoc tests with Bonferroni correction were completed. Day 0 time points are compared with all other time points. Comparisons not shown in the table were non-significant. D0, D1, D2 and D3 represents day 0, 1, 2 and 3, respectively. Arrows indicate the direction of change. **** p < 0.001, *** p < 0.005, ** p < 0.01, * p < 0.05, ns not significant.

		In Vitro														
		Raw					Norm					Model				
		Galvo (V)														
Group 1	Group 2	0	1	2	3	4	0	1	2	3	4	0	1	2	3	4
Group Comparison		ns	ns	ns	ns	ns	ns	ns	ns	*	*	ns	ns	ns	ns	ns
D0, 0-min	D0, 60-min									1	1					
	D1, 0-min									1	1					
	D1, 30-min									1	1					
	D1, 60-min									1	1					
	D1, 90-min									1	1					
	D1, 120-min									1	1					
	D1, 180-min									1	1					
	D1, 210-min									1	1					
	D1, 240-min									1	1					
	D2, 0-min									1	1					
	D2, 60-min									1	1					
	D3, 0-min									0.462	0.859					
	D3, 60-min									0.220	0.678					
D0, 60-min	D1, 0-min									1	0.810					
	D1, 30-min									1	0.589					
	D1, 60-min									1	1					
	D1, 90-min									1	1					
	D1, 120-min									1	1					
	D1, 180-min									1	1					
	D1, 210-min									1	1					
	D1, 240-min									1	1					
	D2, 0-min									1	1					
	D2, 60-min									1	0.735					
	D3, 0-min									0.185	0.028 ↓					
	D3, 60-min									0.085	0.021 ↓					

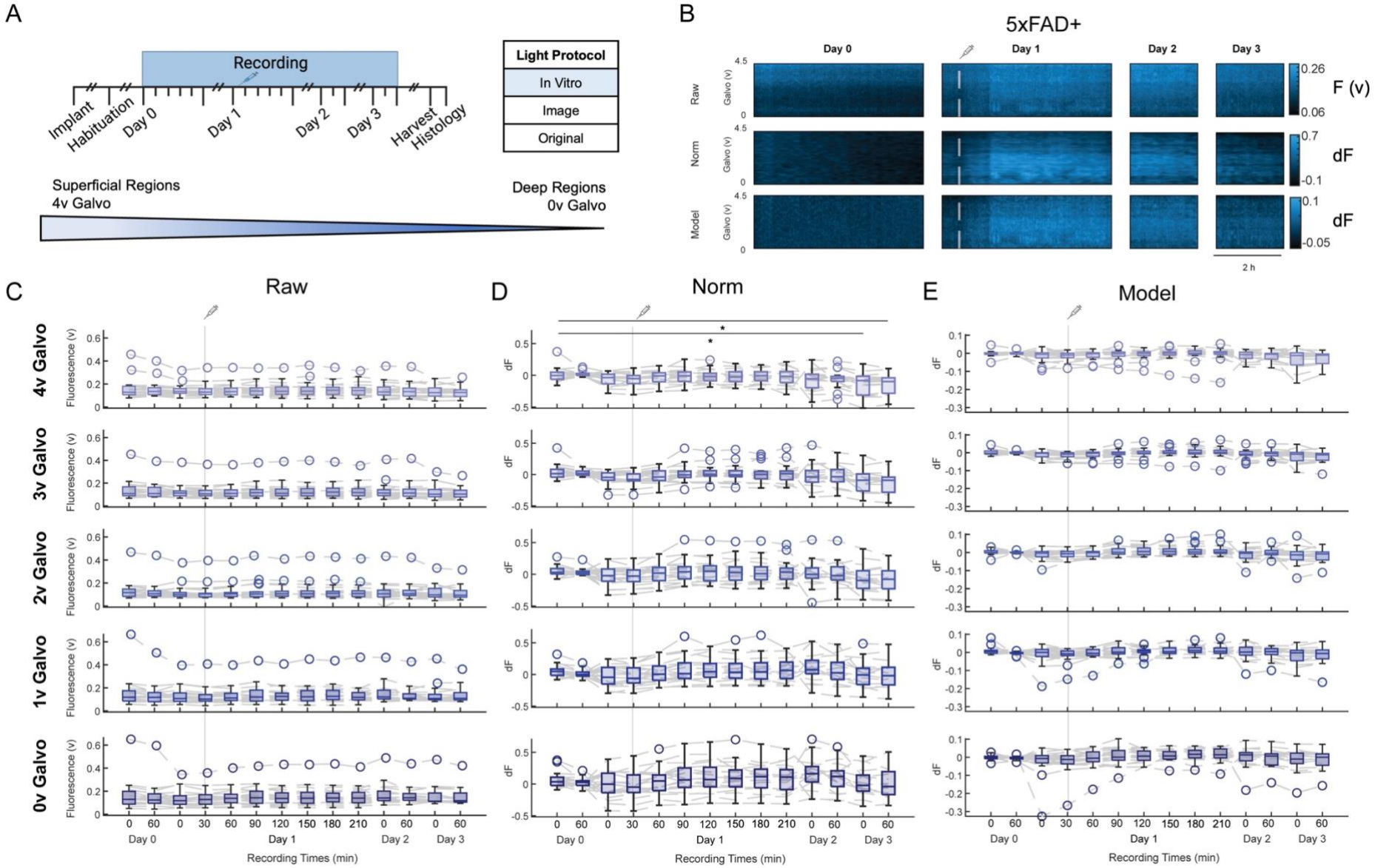
A
Recording
Implant
Habituation
Day 0
Day 1
Day 2
Day 3
Harvest
Histology
Light Protocol
In Vitro
Image
Original
Superficial Regions
4v Galvo
Deep Regions
0v Galvo
B
5xFAD+
Day 0
Day 1
Day 2
Day 3
Raw
Norm
Model
Galvo (v)
F (v)
dF
2 h
C
Raw
D
Norm
E
Model
4v Galvo
3v Galvo
2v Galvo
1v Galvo
0v Galvo
Fluorescence (v)
dF
Recording Times (min)

Figure 4.3.5. Pharmacokinetic profile of Methoxy-x04 in a 5xFAD+ mouse using an *in vitro*-based light protocol, analysed with different approaches. (A) *Top left*, Recording paradigm. Methoxy-x04 was injected at 0.5-h on day 1 of the 4-day recording schedule. Each dash on the recording days represents 1-h. *Top right,* Table highlighting the light protocol: *in vitro*. *Bottom,* Schematic of the TF showing that higher GVs represent superficial regions, whereas GVs voltages represent deeper brain regions. Colour coding is consistent with the colour coding of the summary plots. (B) Example heatmaps of the fluorescence across depth and time, over the 4-day pharmacokinetic recording in a 5xFAD+ mouse. Each vertical row represents a different data analytical approach: raw, normalised to day 0 (Norm) and modelled to day 0 (Model). White dashed line represents the time of Methoxy-x04 injection. Colour map represents the fluorescence range. Scale: 2-h. Example plots come from FAD45, pharmacokinetic recording 6. (C, D, E) Summary plots of the pharmacokinetic profile of Methoxy-x04 across time and depth, for raw (C), Norm (D), and Model (E) data. Plot colours get darker as the recording region on the TF gets deeper. Grey line illustrates the time of Methoxy-x04 injection. Data was statistically compared using a Kruskal-Wallis test, followed by multi-comparison tests with Bonferroni correction if $p < 0.05$, with p-values shown: $p < 0.001$ (****), $p < 0.005$ (***), $p < 0.01$ (**), $p < 0.05$ (*), ns not significant. n = 19 recordings in 13 5xFAD+ mice.

Next, the in image-based light protocol was explored, as this involved equal power density along the TF which should provide an equal excitation of brain volume across depth. **Figure 4.3.6** shows the pharmacokinetic profile of Methoxy-x04 collected using the image-based light protocol. Example plots show a saturated fluorescent signal on day 0 **(Figure 4.3.6B)**. Therefore, no change in fluorescence intensity is noted after Methoxy-x04 injection from raw data. However, Norm and Model data continue to show a rise in fluorescence within ~30-60-minutes, with increased change in fluorescence at lower GVs **(Figure 4.3.6B)**. However, unlike data collected using the *in vitro* light protocol **(Figure 4.3.6)**, a decline in fluorescence is not evident on day 2 and 3 **(Figure 4.3.6B)**.

Summary raw data illustrate little change in fluorescence from baseline, with no significant changes detected over time (0-V galvo, $H(13) = 6.2299$, $p = 0.9374$; 1-V galvo, $H(13) = 3.1184$, $p = 0.9975$; 2-V galvo, $H(13) = 1.7013$, $p = 0.999$; 3-V galvo, $H(13) = 2.2068$, $p = 0.9996$; 4-V galvo, $H(13) = 3.3249$, $p = 0.9965$, Kruskal-Wallis test) **(Figure 4.3.6C) (Table 4.3.3)**.

Norm data demonstrates a trend of increased fluorescence across depths. However, comparing medians show minimal change across time **(Figure 4.3.6D).** Nonetheless, a decline in fluorescence was evident across days 2 and 3. Overall, Norm data have significant differences at 3-V ($H(13) = 23.1471$, $p= 0.0399$, Kruskal-Wallis test) and 4-V ($H(13) = 24.2791$, $p=0.0287$, Kruskal-Wallis test) but not at 0-V ($H(13) = 20.8804$, $p = 0.0753$, Kruskal-Wallis test), 1-V ($H(13) =$

15.0689, p = 0.3031, Kruskal-Wallis test) and 3-V (H(13) = 14.6242, p = 0.3314, Kruskal-Wallis test). Post-hoc tests found a significant decrease in fluorescence between 60-minutes on day 0 and day 3 at 4-V galvo **(Table 4.3.3)**.

Model data show trends for increased fluorescence across all GVs, with a stronger tendency from 0-2-V. Additionally, fluorescence appears to begin to decline from day 2, reaching pre-injection levels by day 3 **(Figure 4.3.6E)**. While Model data show significant differences across time at 0-V galvo (H(13) = 27.4096, p = 0.0109), but not at others (1-V galvo, H(13) = 14.0384, p = 0.3711; 2-V galvo, H(13) = 18.6726, p = 0.1336; 3-V galvo, H(13) = 18.7071, p = 0.1325; 4-V galvo, H(13) = 18.3807, p = 0.1436, Kruskal-Wallis test), post-hoc tests found no significant differences between groups at 0-V galvo **(Table 4.3.3) (Figure 4.3.6E).**

Table 4.3.3. Statistical summary for 5xFAD+ pharmacokinetic experiments completed with the image light protocol. Kruskal-Wallis tests were completed across time points for each GV, supplying a group comparison significance. If the Kruskal-Wallis test provided a p-value <0.05, post-hoc tests with Bonferroni correction were completed. Day 0 time points are compared with all other time points. Comparisons not shown in the table were non-significant. D0, D1, D2 and D3 represents day 0, 1, 2 and 3, respectively. Arrows indicate the direction of change. **** $p < 0.001$, *** $p < 0.005$, ** $p < 0.01$, * $p < 0.05$, ns not significant.

		Image														
		Raw					Norm					Model				
		Galvo (V)														
Group 1	Group 2	0	1	2	3	4	0	1	2	3	4	0	1	2	3	4
Group Comparison		ns	ns	ns	ns	ns	ns	ns	ns	*	*	*	ns	ns	ns	ns
D0, 0-min	D0, 60-min									1	1	1				
	D1, 0-min									1	1	1				
	D1, 30-min									1	1	1				
	D1, 60-min									1	1	1				
	D1, 90-min									1	1	1				
	D1, 120-min									1	1	1				
	D1, 180-min									1	1	1				
	D1, 210-min									1	1	1				
	D1, 240-min									1	1	1				
	D2, 0-min									1	1	1				
	D2, 60-min									1	1	1				
	D3, 0-min									0.182	0.789	1				
	D3, 60-min									0.178	0.330	1				
D0, 60-min	D1, 0-min									0.930	0.753	1				
	D1, 30-min									1	1	0.832				
	D1, 60-min									1	1	1				
	D1, 90-min									1	1	1				
	D1, 120-min									1	1	1				
	D1, 180-min									1	1	1				
	D1, 210-min									1	1	1				
	D1, 240-min									1	1	1				
	D2, 0-min									1	1	1				
	D2, 60-min									1	1	1				
	D3, 0-min									0.128	0.054	1				
	D3, 60-min									0.125	0.020 ↓	1				

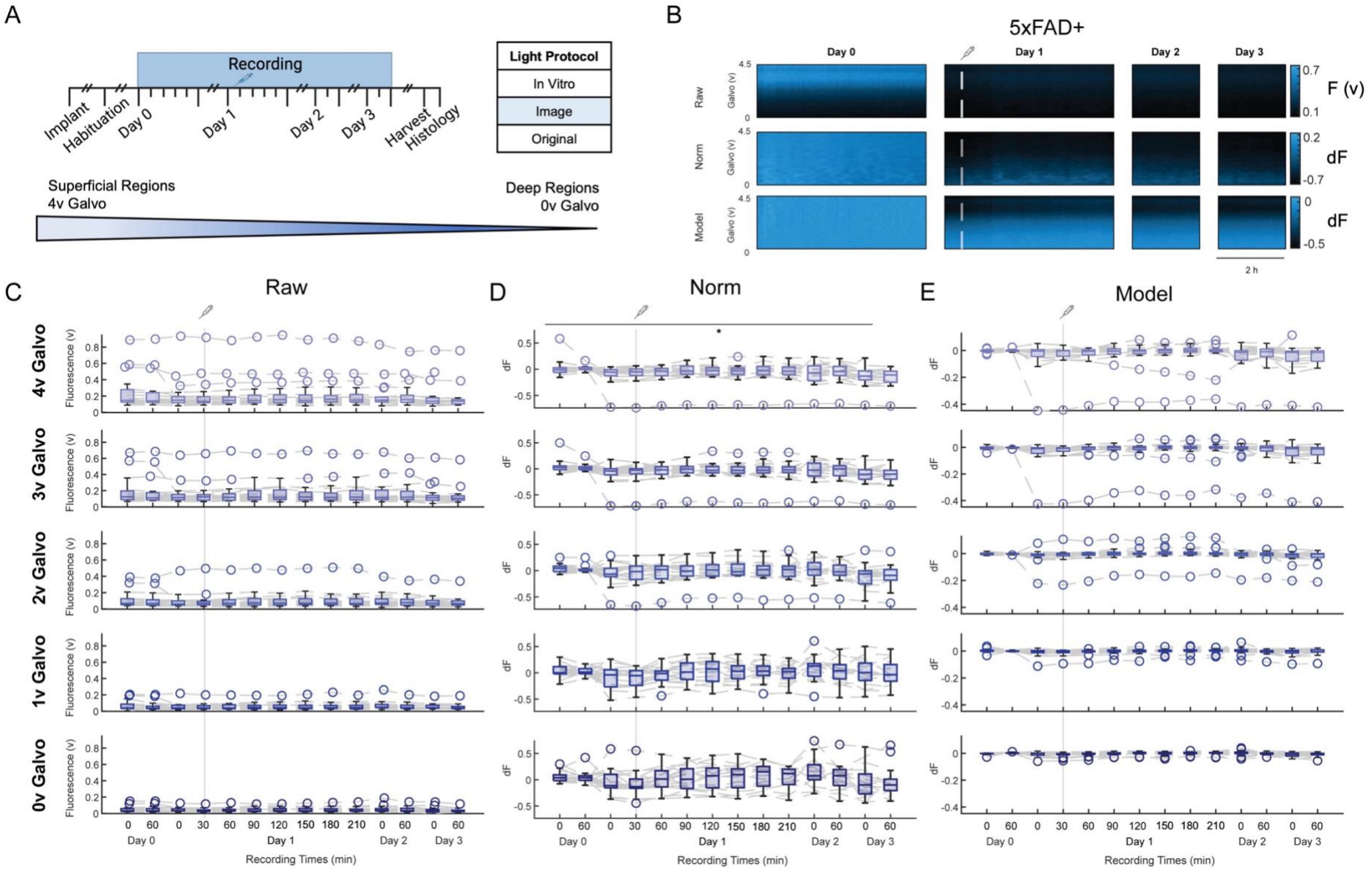
A
Recording
Implant
Habituation
Day 0
Day 1
Day 2
Day 3
Harvest
Histology
Light Protocol
In Vitro
Image
Original
Superficial Regions
4v Galvo
Deep Regions
0v Galvo
B
5xFAD+
Day 0
Day 1
Day 2
Day 3
Raw
Norm
Model
Galvo (v)
F (v)
dF
2 h
C
Raw
D
Norm
E
Model
4v Galvo
3v Galvo
2v Galvo
1v Galvo
0v Galvo
Fluorescence (v)
dF
Recording Times (min)

Figure 4.3.6. Pharmacokinetic profile of Methoxy-x04 in a 5xFAD+ mouse using an image-based light protocol, analysed with different approaches. (A) *Top left*, Recording paradigm. Methoxy-x04 was injected at 0.5-h on day 1 of the 4-day recording schedule. Each dash on the recording days represents 1-h. *Top right,* Table highlighting the light protocol: image. *Bottom,* Schematic of the TF showing that higher GVs represent superficial regions, whereas lower GVs represent deeper brain regions. Colour coding is consistent with the colour coding of the summary plots. (B) Example heatmaps of the fluorescence across depth and time, over the 4-day pharmacokinetic recording in a 5xFAD+ mouse. Each vertical row represents a different data analytical approach: raw, normalised to day 0 (Norm) and modelled to day 0 (Model). White dashed line represents the time of Methoxy-x04 injection. Colour map represents the fluorescence range. Scale: 2-h. Example plots come from FAD45, pharmacokinetic recording 6. (C, D, E) Summary plots of the pharmacokinetic profile of Methoxy-x04 across time and depth, for raw (C), Norm (D), and Model (E) data. Plot colours get darker as the recording region on the TF gets deeper. Grey line illustrates the time of Methoxy-x04 injection. Data was statistically compared using a Kruskal-Wallis test, followed by multi-comparison tests with Bonferroni correction if $p < 0.05$, with p-values shown: $p < 0.001$ (****), $p < 0.005$ (***), $p < 0.01$ (**), $p < 0.05$ (*), ns not significant. n = 19 recordings in 13 5xFAD+ mice.

Table 4.3.4. Statistical summary for 5xFAD+ pharmacokinetic experiments. Kruskal-Wallis tests were completed across time points for each GV, supplying a group comparison significance. If the Kruskal-Wallis test provided a p-value <0.05, post-hoc tests with Bonferroni correction were completed. Day 0 time points are compared with all other time points. Comparisons not shown in the table were non-significant. D0, D1, D2 and D3 represents day 0, 1, 2 and 3, respectively. Arrows indicate the direction of change. **** p < 0.001, *** p < 0.005, ** p < 0.01, * p < 0.05, ns not significant.

			In Vitro					Image					Original				
			Galvo (V)														
	Group 1	Group 2	0	1	2	3	4	0	1	2	3	4	0	1	2	3	4
Raw	Group Comparison		ns	ns	ns	ns	ns	ns	ns	ns	ns	ns	ns	ns	ns	ns	ns
Norm	Group Comparison		ns	ns	ns	*	*	ns	ns	ns	*	*	ns	ns	ns	ns	*
	D0, 0-min	All				ns	ns				ns	ns					ns
	D0, 0-min	D1, 30-min				ns	ns				ns	ns					ns
		D1, 60-min				ns	ns				ns	ns					ns
		D1, 90-min				ns	ns				ns	ns					ns
		D1, 120-min				ns	ns				ns	ns					ns
		D1, 180-min				ns	ns				ns	ns					ns
		D1, 210-min				ns	ns				ns	ns					ns
		D1, 240-min				ns	ns				ns	ns					ns
		D2, 0-min				ns	ns				ns	ns					ns
		D2, 60-min				ns	ns				ns	ns					ns
		D3, 0-min				ns	*↓				ns	ns					ns
		D3, 60-min				ns	*↓				ns	*↓					ns
Model	Group Comparison		ns	ns	ns	ns	ns	*	ns	ns	ns	ns	ns	*	*	*	*
	D0, 0-min	All						ns						ns	ns	ns	ns
	D0, 60-min	All						ns						ns	ns	ns	ns

Overall, this novel approach provides evidence for TF photometry allowing real-time, depth-resolved plaque detection in freely behaving mice illustrated by a slight increase in fluorescence across GVs, in a depth-resolved manner. Firstly, the original light protocol and raw data had poor performance at extracting pure Methoxy-x04 signals across depth. Alternatively, a combination of the *in vitro* light protocol and Norm analytical approach appeared to provide the greatest and fastest signal increase with depth-resolved capabilities. Model data show trends of increasing fluorescence across day 1, but the fluorescence range is low. Additionally, this approach was able to detect Methoxy-x04 within the brain at ~30-minutes when using the Norm and *in vitro* approaches, with the fluorescence continuing to increase over several hours, before declining on following days. This trend was seen in the other protocols but at a slower and less pronounced profile. Despite this, no significant increases across time were noted **(Table 4.3.4)**. In all, this data suggests this may be a potential approach for monitoring plaque pathology in real-time, across depth, in freely behaving mice, illustrating trends of increased fluorescence following Methoxy-x04 injection to 5xFAD+ mice only. However, this finding may be improved by aligning all TF recordings to enhance the depth-resolved fluorescent increases."

4.3.3.2 Methoxy-x04 was not detected across depth, in 5xFAD- mice

While this novel approach has shown increases in fluorescence post-injection in a depth-resolved manner in 5xFAD+ mice, it is vital to confirm this change is from increases in Methoxy-x04 concentration, rather than other contributing factors such as AF. Therefore, pharmacokinetic recordings were completed in 5xFAD- mice **(Figure 4.3.7A)**.

Figure 4.3.7 shows the pharmacokinetic profile of Methoxy-x04 for 5xFAD- mice for the original light protocol. Example plots show no change in fluorescence across days, or analytical approaches **(Figure 4.3.7B)**. Summary data shows no changes in fluorescence across days with no significant differences found with raw data (0-V, $H(13) = 3.5105$, $p = 0.9954$; 1-V, $H(13) = 2.8441$, $p = 0.9984$; 2-V, $H(13) = 2.2329$, $p = 0.9995$; 3-V, $H(13) = 1.4018$, $p = 0.9999$; 4-V, $H(13) = 1.2432$, $p = 0.9999$, Kruskal-Wallis test) **(Figure 4.3.7C)**, Norm data (0-V, $H(13) = 10.1611$, $p = 0.6807$; 1-V, $H(13) = 9.5677$, $p = 0.7288$; 2-V, $H(13) = 12.2664$, $p = 0.5059$; 3-V, $H(13) = 5.3217$, $p = 0.9674$; 4-V, $H(13) = 5.0705$, $p = 0.9736$, Kruskal-Wallis test) **(Figure 4.3.7D)** or Model data (0-V, $H(13) = 10.4995$, $p = 0.6527$; 1-V, $H(13) = 7.6951$, $p = 0.8629$; 2-V, $H(13) = 11.1870$, $p = 0.5952$; 3-V, $H(13) = 5.0333$, $p = 0.9745$; 4-V, $H(13) = 4.6047$, $p = 0.9829$, Kruskal-Wallis test) **(Figure 4.3.7E)**.

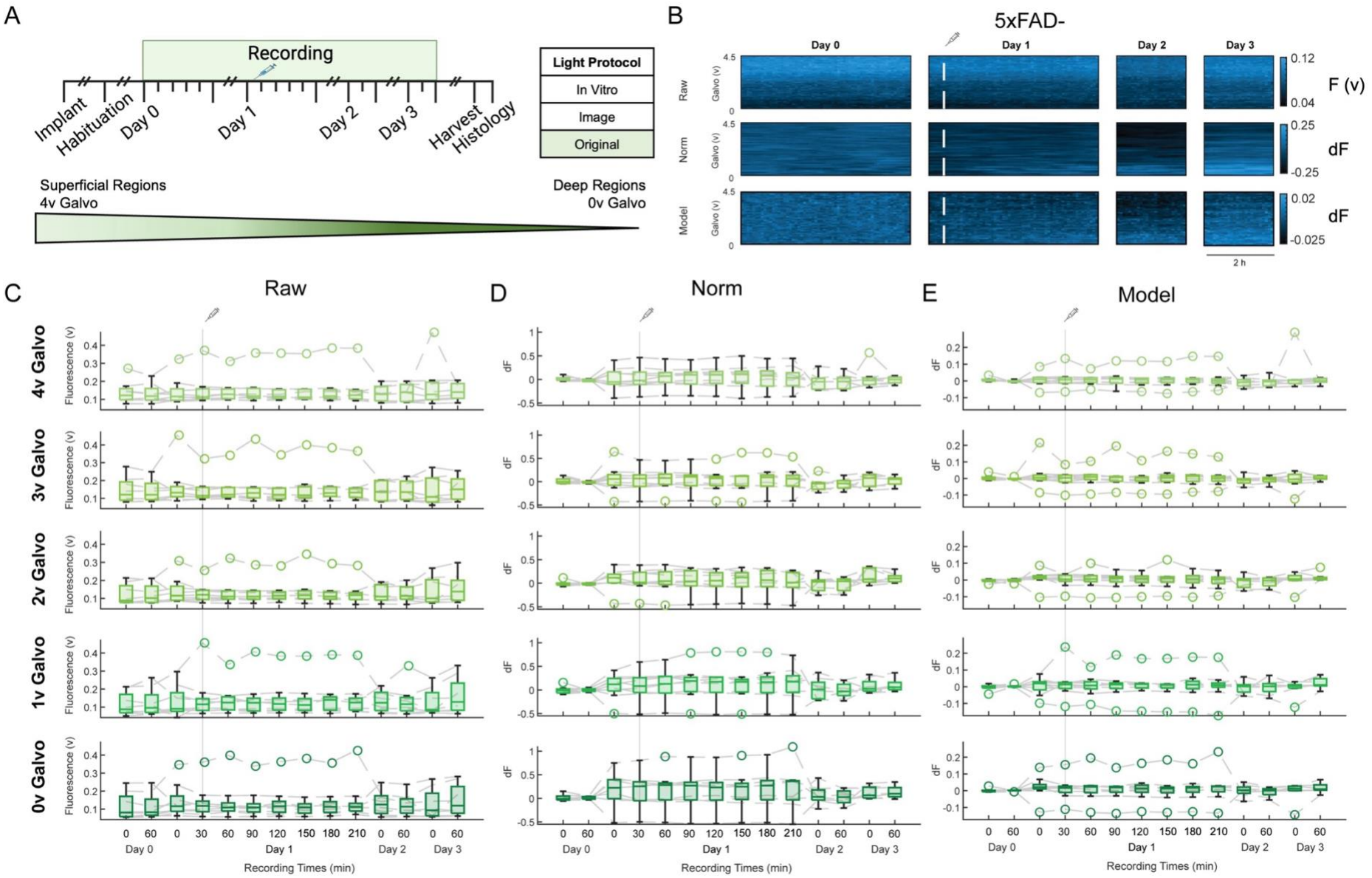
A
Recording
Implant
Habituation
Day 0
Day 1
Day 2
Day 3
Harvest
Histology
Light Protocol
In Vitro
Image
Original
Superficial Regions
4v Galvo
Deep Regions
0v Galvo
B
5xFAD-
Day 0
Day 1
Day 2
Day 3
Raw
Norm
Model
Galvo (v)
F (v)
dF
2 h
C
Raw
D
Norm
E
Model
4v Galvo
3v Galvo
2v Galvo
1v Galvo
0v Galvo
Fluorescence (v)
dF
Recording Times (min)

Figure 4.3.7. Pharmacokinetic profile of Methoxy-x04 in a 5xFAD- mouse using the original light protocol, analysed with different approaches. (A) *Top left*, Recording paradigm. Methoxy-x04 was injected at 0.5-h on day 1 of the 4-day recording schedule. Each dash on the recording days represents 1-h. *Top right,* Table highlighting the light protocol: original. *Bottom,* Schematic of the TF showing that higher GVs represent superficial regions, whereas lower GVs represent deeper brain regions. Colour coding is consistent with the colour coding of the summary plots. (B) Example heatmaps of the fluorescence across depth and time, over the 4-day pharmacokinetic recording in a 5xFAD- mouse. Each vertical row represents a different data analytical approach: raw, normalised to day 0 (Norm) and modelled to day 0 (Model). White dashed line represents the time of Methoxy-x04 injection. Colour map represents the fluorescence range. Scale: 2-h. Example plots come from FAD64, pharmacokinetic recording 1. (C, D, E) Summary plots of the pharmacokinetic profile of Methoxy-x04 across time and depth, for raw (C), Norm (D) and Model (E) data. Plot colours get darker as the recording region on the TF gets deeper. Grey line illustrates the time of Methoxy-x04 injection. Data was statistically compared using a Kruskal-Wallis test, followed by multi-comparison tests with Bonferroni correction if $p < 0.05$. n = 9 recordings in 8 5xFAD- mice.

Figure 4.3.8 shows the pharmacokinetic profile for 5xFAD- mice with an *in vitro*-based light protocol. Across all data analytical approaches, no change in fluorescence is seen across the recording paradigm, with no response following the injection of Methoxy-x04 **(Figure 4.3.8B)**. Additionally, the declining fluorescence previously seen on day 0 **(Figure 4.3.5)** is no longer seen, suggesting bleaching of plaque AF could occur **(Figure 4.3.8B)**.

Summary data shows that while there may have been slight variations of fluorescence in some recordings across different days, most likely contributed to by system alterations, there was consistently no change in fluorescence on day 1 following injection, with no decline in fluorescence seen in following days **(Figures 4.3.8C-E)**. Statistical tests show no significant differences over time for raw data (0-V, $H(13) = 3.6606$, $p = 0.9943$; 1-V, $H(13) = 2.9883$, $p = 0.9980$; 2-V, $H(13) = 1.7462$, $p = 0.9999$; 3-V, $H(13) = 1.7789$, $p = 0.9999$; 4-V, $H(13) = 2.9530$, $p = 0.9981$, Kruskal-Wallis test) **(Figure 4.3.8C)**, Norm data (0-V, $H(13) = 10.2375$, $p = 0.6744$; 1-V, $H(13) = 9.8207$, $p = 0.7085$; 2-V, $H(13) = 6.1786$, $p = 0.9394$; 3-V, $H(13) = 5.5847$, $p = 0.9600$; 4-V, $H(13) = 5.0300$, $p = 0.9745$, Kruskal-Wallis test) **(Figure 4.3.8D)** and Model data (0-V, $p = 0.993$; 1-V, $p = 0.994$; 2-V, 0.991; 3-V, $p = 0.971$; 4-V, $p = 0.873$, Kruskal-Wallis test) **(Figure 4.3.8E)**.

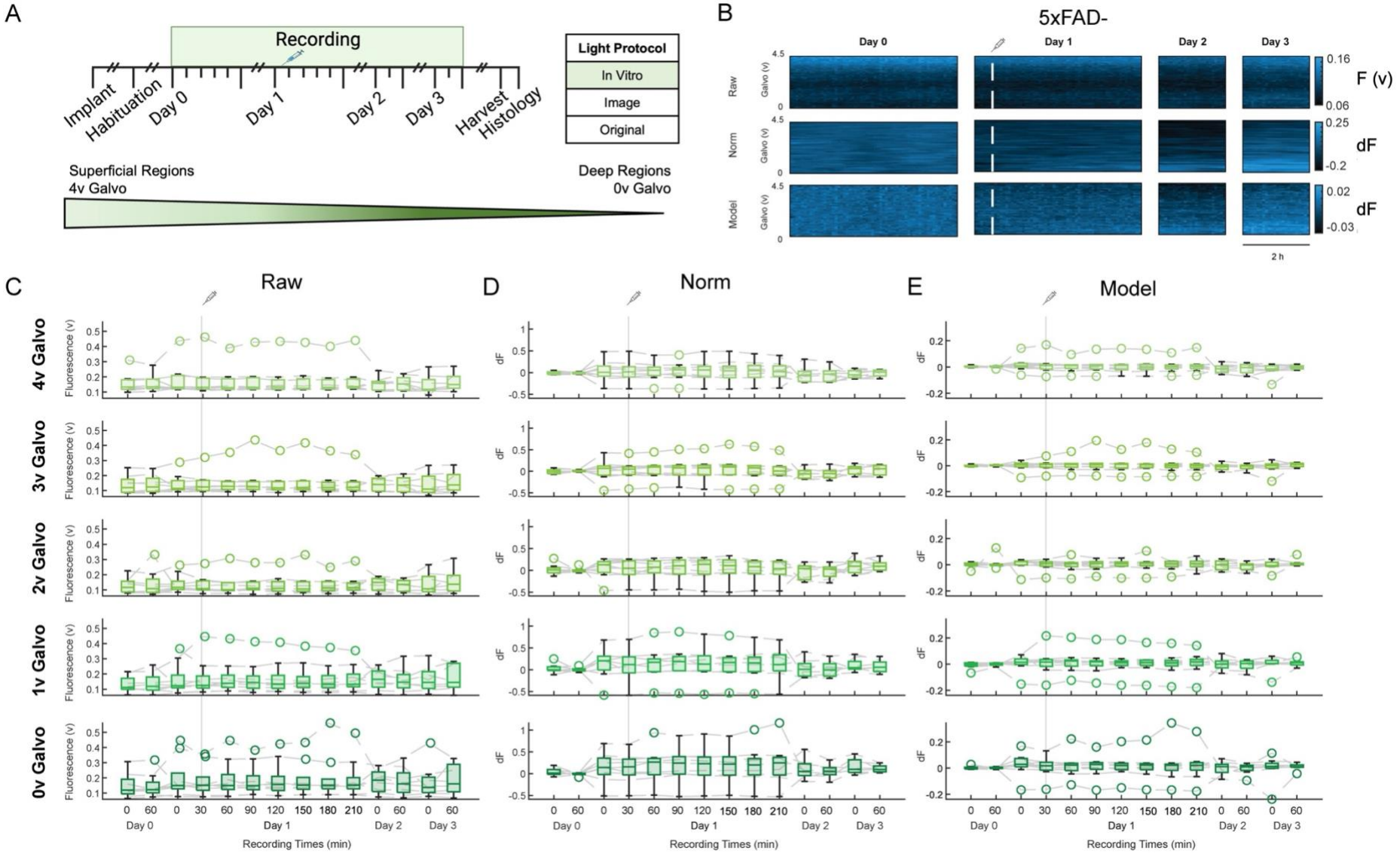
A
Recording
Implant
Habituation
Day 0
Day 1
Day 2
Day 3
Harvest
Histology
Light Protocol
In Vitro
Image
Original
Superficial Regions
4v Galvo
Deep Regions
0v Galvo
B
5xFAD-
Day 0
Day 1
Day 2
Day 3
Raw
Norm
Model
Galvo (v)
F (v)
dF
2 h
C
Raw
D
Norm
E
Model
4v Galvo
3v Galvo
2v Galvo
1v Galvo
0v Galvo
Fluorescence (v)
dF
Recording Times (min)

Figure 4.3.8. Pharmacokinetic profile of Methoxy-x04 in a 5xFAD- mouse using an *in vitro*-based light protocol, analysed with different approaches. (A) *Top left*, Recording paradigm. Methoxy-x04 was injected at 0.5-h on day 1 of the 4-day recording schedule. Each dash on the recording days represents 1-h. *Top right,* Table highlighting the light protocol: *in vitro*. *Bottom,* Schematic of the TF showing that higher GVs represent superficial regions, whereas lower GVs represent deeper brain regions. Colour coding is consistent with the colour coding of the summary plots. (B) Example heatmaps of the fluorescence across depth and time, over the 4-day pharmacokinetic recording in a 5xFAD- mouse. Each vertical row represents a different data analytical approach: raw, normalised to day 0 (Norm) and modelled to day 0 (Model). White dashed line represents the time of Methoxy-x04 injection. Colour map represents the fluorescence range. Scale: 2-h. Example plots come from FAD64, pharmacokinetic recording 1. (C, D, E) Summary plots of the pharmacokinetic profile of Methoxy-x04 across time and depth, for raw (C), Norm (D), and Model (E) data. Plot colours get darker as the recording region on the TF gets deeper. Grey line illustrates the time of Methoxy-x04 injection. Data was statistically compared using a Kruskal-Wallis test, followed by multi-comparison tests with Bonferroni correction if $p < 0.05$. n = 9 recordings in 8 5xFAD- mice.

Figure 4.3.9 shows the pharmacokinetic profile of Methoxy-x04 for 5xFAD- mice for image-based light protocols. Again, example plots show no change in fluorescence across days, or analytical approaches **(Figure 4.3.9B)**. Summary data shows no changes in fluorescence across days with no significant differences found with raw data (0-V, $H(13) = 2.0361$, $p = 0.9997$; 1-V, $H(13) = 2.6694$, $p = 0.9989$; 2-V, $H(13) = 1.5901$, $p = 0.9999$; 3-V, $H(13) = 1.1117$, $p = 1$; 4-V, $H(13) = 0.7666$, $p = 1$, Kruskal-Wallis test) **(Figure 4.3.9C)**, Norm data (0-V, $H(13) = 8.5970$, $p = 0.8027$; 1-V, $H(13) = 13.0535$, $p = 0.4437$; 2-V, $H(13) = 8.4276$, $p = 0.8147$; 3-V, $H(13) = 8.9922$, $p = 0.7735$; 4-V, $H(13) = 3.7958$, $p = 0.9932$, Kruskal-Wallis test) **(Figure 4.3.9D)** or Model data (0-V, $H(13) = 8.0389$, $p = 0.8411$; 1-V, $H(13) = 5.8506$, $p = 0.9514$; 2-V, $H(13) = 3.6277$, $p = 0.9945$; 3-V, $H(13) = 2.7944$, $p = 0.9986$; 4-V, $H(13) = 2.4562$, $p = 0.9993$, Kruskal-Wallis test) **(Figure 4.3.9E)**.

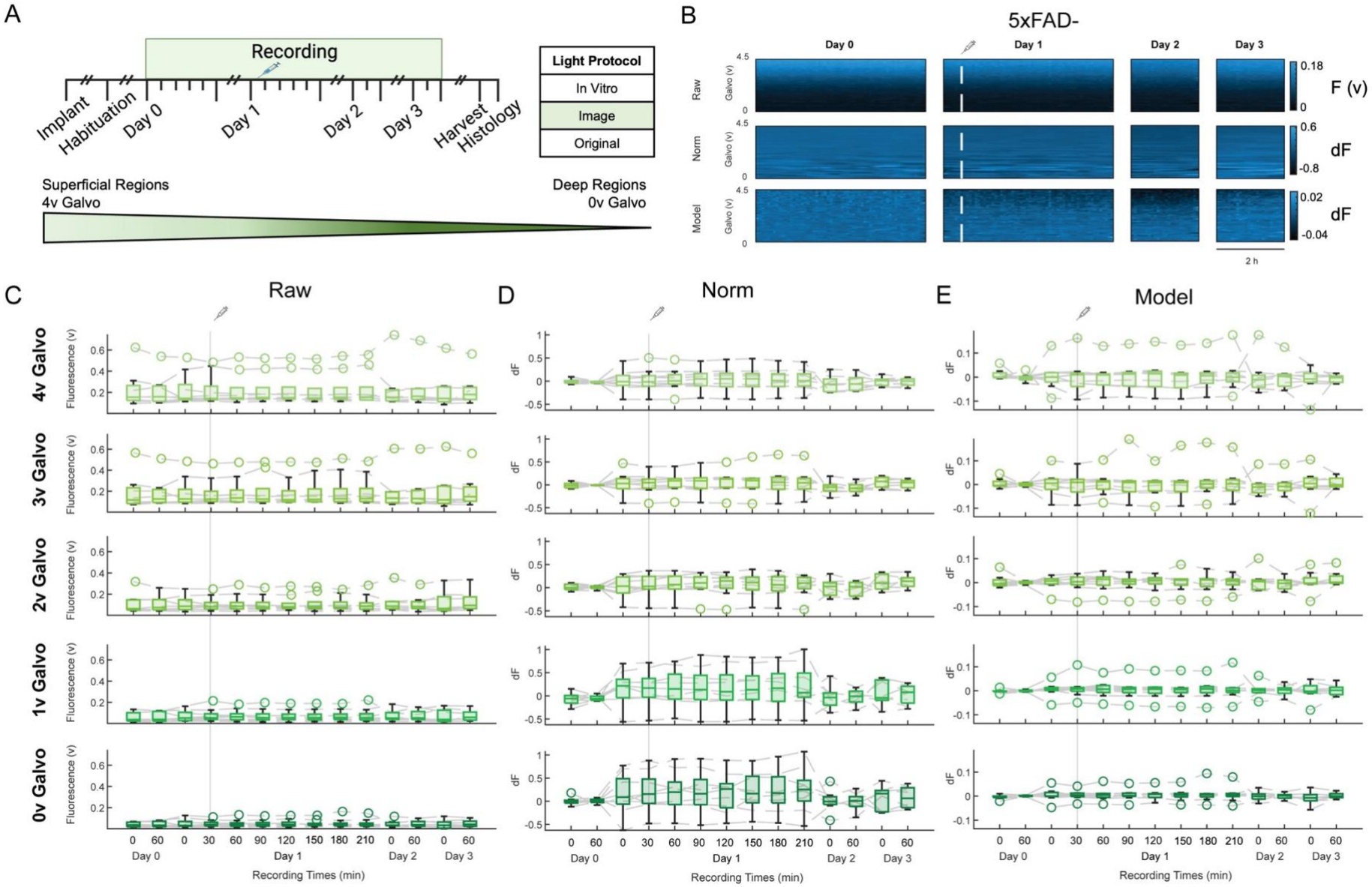
A
Recording
Implant
Habituation
Day 0
Day 1
Day 2
Day 3
Harvest
Histology
Light Protocol
In Vitro
Image
Original
Superficial Regions
4v Galvo
Deep Regions
0v Galvo
B
5xFAD-
Day 0
Day 1
Day 2
Day 3
Raw
Norm
Model
Galvo (v)
F (v)
dF
2 h
C
Raw
D
Norm
E
Model
4v Galvo
3v Galvo
2v Galvo
1v Galvo
0v Galvo
Fluorescence (v)
dF
Recording Times (min)

Figure 4.3.9. Pharmacokinetic profile of Methoxy-x04 in a 5xFAD- mouse using an image-based light protocol, analysed with different approaches. (A) *Top left*, Recording paradigm. Methoxy-x04 was injected at 0.5-h on day 1 of the 4-day recording schedule. Each dash on the recording days represents 1-h. *Top right,* Table highlighting the light protocol: image. *Bottom,* Schematic of the TF showing that higher GVs represent superficial regions, whereas lower GVs represent deeper brain regions. Colour coding is consistent with the colour coding of the summary plots. (B) Example heatmaps of the fluorescence across depth and time, over the 4-day pharmacokinetic recording in a 5xFAD- mouse. Each vertical row represents a different data analytical approach: raw, normalised to day 0 (Norm) and modelled to day 0 (Model). White dashed line represents the time of Methoxy-x04 injection. Colour map represents the fluorescence range. Scale: 2-h. Example plots come from FAD64, pharmacokinetic recording 1. (C, D, E) Summary plots of the pharmacokinetic profile of Methoxy-x04 across time and depth, for raw (C), Norm (D), and Model (E) data. Plot colours get darker as the recording region on the TF gets deeper. Grey line illustrates the time of Methoxy-x04 injection. Data was statistically compared using a Kruskal-Wallis test, followed by multi-comparison tests with Bonferroni correction if $p < 0.05$. $n = 9$ recordings in 8 5xFAD- mice.

These findings illustrate that when no plaque pathology is present within the mouse brain, injecting Methoxy-x04 will not result in an increase in fluorescence. Thereby, this suggests that the small signal changes detected in deeper brain regions in 5xFAD+ mice may be due to Methoxy-x04 binding to plaques. Therefore, this provides evidence towards the confirmation that this approach can detect plaque signals across depth, in freely behaving mice, that would be solidified with an analytical approach that aligns fibre implants to acquire potentially stronger depth-resolved fluorescent signals.

4.3.3.3 Re-dosing Methoxy-x04 each day allows increased levels of fluorescence over several days in 5xFAD+ mice

Pharmacokinetic recordings illustrated that Methoxy-x04 was detected in 5xFAD+ mice but not 5xFAD- mice, showing that we can detect real-time, depth-resolved plaque signals. Additionally, findings pointed towards a combined approach of *in vitro* light protocol and Norm data analysis for optimal signal detection. Now, we wished to determine what re-dose strategy would allow for a consistent and stable fluorescence over days, while continuing to determine the optimal light protocol and analytical approach. Therefore, mice chronically implanted with a TF underwent a 4-day recording protocol which consisted of a 2-hour baseline, followed by injection of Methoxy-x04, repeated each day **(Figure 4.3.10A)**. Previous studies re-dose Methoxy-x04 24-hours before each imaging session (Crowe and Ellis-Davies, 2013, Hefendehl et al., 2011); therefore, we expect to see a consistent level of fluorescence that remains stable for the recording duration.

As with pharmacokinetic recordings, we firstly determined if an increase in fluorescence was detected following Methoxy-x04 re-dosing, using the original light protocol in 5xFAD+ mice **(Figure 4.3.10)**. Example heat plots show that the signal intensity greatly increases on days 1, 2 and 3 compared to day 0, across depths for all analytical approaches **(Figure 4.3.10B)**. For Norm data, a depth-resolved signal can be seen with a greater signal intensity at deeper regions, whereas raw data shows similar signal intensity across depth **(Figure 4.2.10B)**. Additionally, some fluctuations in fluorescence are illustrated across days, while fluorescence remains relatively stable across each 2-hour recording.

Raw summary data has modest signal change following injection, with no statistical differences across all GVs (0-V, $H(7) = 6.3875$, $p = 0.4953$; 1-V, $H(7) = 7.5889$, $p = 0.3702$; 2-V, $H(7) = 7.008$, $p = 0.4281$; 3-V, $H(7) = 2.4209$, $p = 0.9329$; 4-V, $H(7) = 2.1835$, $p = 0.9490$, Kruskal-Wallis test) **(Figure 4.3.10C) (Table 4.3.5)**.

However, Norm data shows a trend for increased fluorescence on days 1, 2 and 3 compared to day 0, which is shown to be more prominent at 0-2-V galvo, emphasised with significant differences shown at 0-V ($H(7) = 23.5304$, $p = 0.0014$, Kruskal-Wallis test), 1-V ($H(7) = 30.2374$, $p = 0.0001$, Kruskal-Wallis test) and 2-V ($H(7) = 22.1545$, $p = 0.0024$, Kruskal-Wallis test) but not 3-V ($H(7) = 12.2962$, $p = 0.0940$, Kruskal-Wallis test) and 4-V ($H(7) = 7.7684$, $p = 0.3535$, Kruskal-Wallis test) **(Figure 4.3.10D)**. Post-hoc tests show significant increases from day 0 **(Table 4.3.5)**.

Additionally, Model data has increased fluorescence in a depth resolved manner, showing statistical significance at 1-V ($H(7) = 21.0699$, $p = 0.0037$, Kruskal-Wallis test) and 2-V ($H(7) = 22.5141$, $p = 0.0021$, Kruskal-Wallis test) but not others (0-V galvo, $H(7) = 12.4282$, $p = 0.0873$; 3-

V galvo, H(7) = 13.2274, p = 0.0668; 4-V galvo, H(7) = 10.1227, p = 0.1817, Kruskal-Wallis test) **(Figure 4.3.10E)**. Post-hoc tests show significant increases from day 0 **(Table 4.3.5)**.

Table 4.3.5. Statistical summary for 5xFAD+ re-dose experiments completed with the original light protocol. Kruskal-Wallis tests were completed across time points for each GV, supplying a group comparison significance. If the Kruskal-Wallis test provided a p-value <0.05, post-hoc tests with Bonferroni correction were completed. Day 0 time points are compared with all other time points. D0, D1, D2 and D3 represents day 0, 1, 2 and 3, respectively. Arrows indicate the direction of change. **** p < 0.001, *** p < 0.005, ** p < 0.01, * p < 0.05, ns not significant.

		Original														
		Raw					Norm					Model				
		Galvo (V)														
Group 1	Group 2	0	1	2	3	4	0	1	2	3	4	0	1	2	3	4
Group Comparison		ns	ns	ns	ns	ns	***	***	***	ns	ns	ns	***	***	ns	ns
D0, 0-min	D0, 60-min						1	1	1				1	1		
	D1, 0-min						0.217	0.105	0.052				1	0.020 ↑		
	D1, 60-min						0.080	0.249	0.205				0.426	0.230		
	D2, 0-min						0.051	0.017 ↑	0.043 ↑				0.047 ↑	0.011 ↑		
	D2, 60-min						0.410	0.137	0.268				0.327	0.306		
	D3, 0-min						0.038 ↑	0.012 ↑	0.141				0.250	0.088		
	D3, 60-min						1	0.184	0.074				0.175	0.133		
D0, 60-min	D1, 0-min						0.415	0.085	0.345				1	0.404		
	D1, 60-min						0.163	0.205	1				0.654	1		
	D2, 0-min						0.104	0.013 ↑	0.270				0.078	0.223		
	D2, 60-min						0.728	0.112	1				0.498	1		
	D3, 0-min						0.076	0.010 ↑	0.698				0.380	1		
	D3, 60-min						1	0.153	0.406				0.271	1		
D1, 0-min	D1, 60-min						1	1	1				1	1		
	D2, 0-min						1	1	1				1	1		
	D2, 60-min						1	1	1				1	1		
	D3, 0-min						1	1	1				1	1		
	D3, 60-min						1	1	1				1	1		
D1, 60-min	D2, 0-min						1	1	1				1	1		
	D2, 60-min						1	1	1				1	1		
	D3, 0-min						1	1	1				1	1		
	D3, 60-min						1	1	1				1	1		
D2, 0-min	D2, 60-min						1	1	1				1	1		
	D3, 0-min						1	1	1				1	1		
	D3, 60-min						1	1	1				1	1		
D2, 60-min	D3, 0-min						1	1	1				1	1		
	D3, 60-min						1	1	1				1	1		
D3, 0-min	D3, 60-min						1	1	1				1	1		

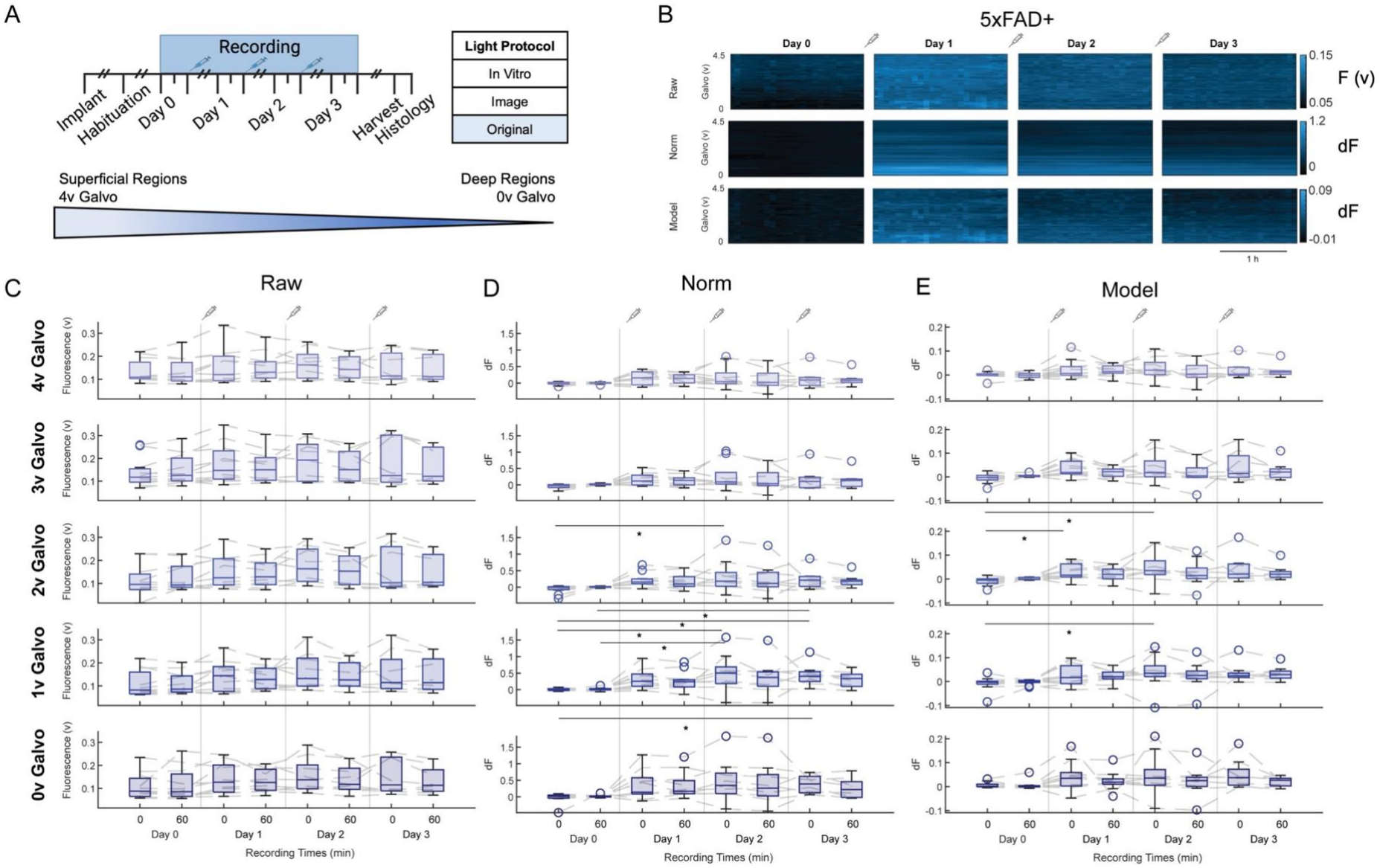
A
Recording
Implant
Habituation
Day 0
Day 1
Day 2
Day 3
Harvest
Histology
Light Protocol
In Vitro
Image
Original
Superficial Regions
4v Galvo
Deep Regions
0v Galvo
B
5xFAD+
Day 0
Day 1
Day 2
Day 3
Raw
Norm
Model
Galvo (v)
F (v)
dF
1 h
C
Raw
D
Norm
E
Model
4v Galvo
3v Galvo
2v Galvo
1v Galvo
0v Galvo
Fluorescence (v)
dF
Recording Times (min)

Figure 4.3.10. Fluorescence profile while re-dosing Methoxy-x04 in a 5xFAD+ mouse using the original light protocol, analysed with different approaches. (A) *Top left*, Recording paradigm. Methoxy-x04 was injected at the end of recording on days 0, 1 and 2 and recorded for 2-h across days 0, 1, 2 and 3. Each dash on the recording days represents 1-h. *Top right,* Table highlighting the light protocol: original. *Bottom,* Schematic of the TF showing that higher GVs represent superficial regions, whereas lower GVs represent deeper brain regions. Colour coding is consistent with the colour coding of the summary plots. (B) Example heatmaps of the fluorescence across depth and time, over the 4-day re-dose recording in a 5xFAD+ mouse. Each vertical row represents a different data analytical approach: raw, normalised to day 0 (Norm) and modelled to day 0 (Model). Syringes represent the time of Methoxy-x04 injection. Colour map represents the fluorescence range. Scale: 1-h. Example plots come from FAD68. (C, D, E) Summary plots of the re-dose profile of Methoxy-x04 across time and depth, for raw (C), Norm (D) and Model (E) data. Plot colours get darker as the recording region on the TF gets deeper. Grey line illustrates the time of Methoxy-x04 injection. Data was statistically compared using a Kruskal-Wallis test, followed by multi-comparison tests with Bonferroni correction if $p < 0.05$, with p-values shown: $p < 0.001$ (****), $p < 0.005$ (***), $p < 0.01$ (**), $p < 0.05$ (*), ns not significant. $n = 11$ recordings in 7 5xFAD+ mice.

Figure 4.3.11 shows the re-dose fluorescence profile in a 5xFAD+ mouse model using the *in vitro*-based light protocol. Example heat maps show that the signal intensity greatly increases on days 1, 2 and 3 compared to day 0, across depths, for all analytical approaches **(Figure 4.3.11B)**. For all approaches, a depth-resolved signal intensity can be seen with a greater signal intensity at deeper regions **(Figure 4.3.11B)**. Additionally, fluorescence remains stable across each 2-hour recording.

Summary raw data shows a slight increased median fluorescence on day 1-3 compared to day 0, specifically at 1-3-V galvo **(Figure 4.3.11C)**. This fluorescence remains relatively stable throughout each recording. However, statistical tests show no significant difference overtime (0-V, $H(7) = 4.5510$, $p = 0.7146$; 1-V, $H(7) = 7.9223$, $p = 0.3395$; 2-V, $H(7) = 2.7765$, $p = 0.9049$; 3-V, $H(7) = 2.9293$, $p = 0.8915$; 4-V, $H(7) = 3.4837$, $p = 0.8370$, Kruskal-Wallis test) **(Table 4.3.6)**.

Whereas summary Norm data shows a large increase in median fluorescence from day 1, with a prominent increase at 0 and 1-V galvo, with smaller trends towards superficial layers **(Figure 4.3.11D).** At 0 and 1-V galvo there are some small variations in median across days, with a trend for a slight decrease in fluorescence at 60-minutes compared to 0-minutes on days 1-3 (median fluorescence at 0-V galvo: day 1, 0.217-V and 0.266-V; day 2, 0.563-V and 0.445-V; day 3, 0.439-V and 0.354-V for 0- and 60-minutes, respectively, compared to 0-V at day 0, 60-minutes) (median fluorescence at 1-V galvo: day 1, 0.176-V and 0.249-V; day 2, 0.493-V and 0.337-V; day 3, 0.427-

V and 0.2814-V for 0- and 60-minutes, respectively, compared to -0.005-V at day 0, 60-minutes) **(Figure 4.3.11D)**. Norm data shows significant difference across all GVs (0-V, H(7) = 27.9370, p = 0.0002; 1-V, H(7) = 28.1533, p = 0.0002; 2-V, H(7) = 15.9786, p = 0.0253; 3-V, H(7) = 15.7525, p = 0.0275, Kruskal-Wallis test), bar 4-V (H(7) = 12.5443, p = 0.0840, Kruskal-Wallis test) **(Figure 4.3.11D)**. Post-hoc tests show significant increases from day 0 to day 1, 2 and 3 **(Table 4.3.6)**.

Accordingly, Model data illustrates an increase in fluorescence on day 1-3 compared to day 0 across all GVs with a greater increase from 0-2-V galvo **(Figure 4.3.11E)**. Statistical tests show significant differences for modelled data overtime at 0-V (H(7) = 20.9744, p = 0.0038, Kruskal-Wallis test), 1-V (H(7) = 23.8552, p = 0.0012, Kruskal-Wallis test), 3-V (H(7) = 14.7661, p = 0.0391, Kruskal-Wallis test), but not 2-V (H(7) = 11.2491, p = 0.1281, Kruskal-Wallis test) and 4-V (H(7) = 11.4546, p = 0.1200, Kruskal-Wallis test) **(Figure 4.3.11E)**. At 0-V and 3-V no significant differences between groups are found **(Table 4.3.6)**. At 1-V galvo, significant increases from day 0 were found **(Table 4.3.6)**.

Table 4.3.6. Statistical summary for 5xFAD+ re-dose experiments completed with the *in vitro* light protocol. Kruskal-Wallis tests were completed across time points for each GV, supplying a group comparison significance. If the Kruskal-Wallis test provided a p-value <0.05, post-hoc tests with Bonferroni correction were completed. D0, D1, D2 and D3 represents day 0, 1, 2 and 3, respectively. Arrows indicate the direction of change. **** $p < 0.001$, *** $p < 0.005$, ** $p < 0.01$, * $p < 0.05$, ns not significant.

		In Vitro														
		Raw					Norm					Model				
		Galvo (V)														
Group 1	Group 2	0	1	2	3	4	0	1	2	3	4	0	1	2	3	4
Group Comparison		ns	ns	ns	ns	ns	****	****	*	*	ns	***	***	ns	*	ns
D0, 0-min	D0, 60-min						1	1	1	1		1	1		1	
	D1, 0-min						0.704	0.482	0.578	0.092		0.472	1		0.394	
	D1, 60-min						0.415	0.855	1	0.135		0.336	1		0.448	
	D2, 0-min						0.111	0.096	1	0.306		0.137	0.174		1	
	D2, 60-min						0.232	0.449	1	1		0.162	0.518		1	
	D3, 0-min						0.106	0.089	1	1		0.100	0.121		1	
	D3, 60-min						0.577	1	1	1		0.608	0.375		1	
D0, 60-min	D1, 0-min						0.085	0.036 ↑	0.053	0.516		0.687	0.654		0.205	
	D1, 60-min						0.044 ↑	0.080	0.687	0.712		0.497	0.271		0.236	
	D2, 0-min						0.010 ↑	0.006 ↑	0.238	1		0.206	0.030 ↑		0.633	
	D2, 60-min						0.025 ↑	0.038 ↑	0.595	1		0.243	0.108		1	
	D3, 0-min						0.010 ↑	0.006 ↑	0.376	1		0.151	0.021 ↑		1	
	D3, 60-min						0.081	0.125	0.488	1		0.849	0.078		1	
D1, 0-min	D1, 60-min						1	1	1	1		1	1		1	
	D2, 0-min						1	1	1	1		1	1		1	
	D2, 60-min						1	1	1	1		1	1		1	
	D3, 0-min						1	1	1	1		1	1		1	
	D3, 60-min						1	1	1	1		1	1		1	
D1, 60-min	D2, 0-min						1	1	1	1		1	1		1	
	D2, 60-min						1	1	1	1		1	1		1	
	D3, 0-min						1	1	1	1		1	1		1	
	D3, 60-min						1	1	1	1		1	1		1	
D2, 0-min	D2, 60-min						1	1	1	1		1	1		1	
	D3, 0-min						1	1	1	1		1	1		1	
	D3, 60-min						1	1	1	1		1	1		1	
D2, 60-min	D3, 0-min						1	1	1	1		1	1		1	
	D3, 60-min						1	1	1	1		1	1		1	
D3, 0-min	D3, 60-min						1	1	1	1		1	1		1	

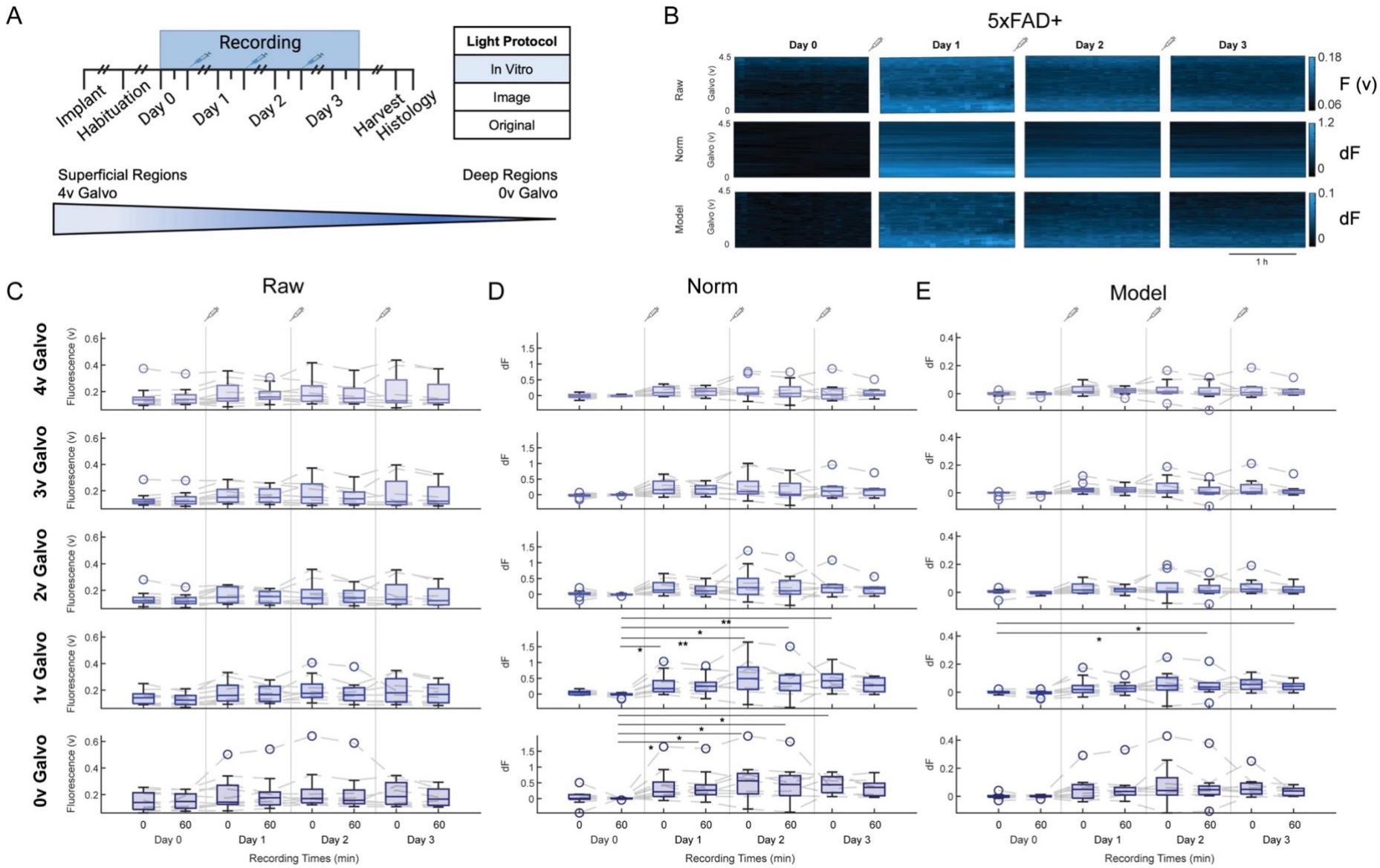
A
Recording
Implant
Habituation
Day 0
Day 1
Day 2
Day 3
Harvest
Histology
Light Protocol
In Vitro
Image
Original
Superficial Regions
4v Galvo
Deep Regions
0v Galvo
B
5xFAD+
Day 0
Day 1
Day 2
Day 3
Raw
Norm
Model
Galvo (v)
F (v)
dF
1 h
C
Raw
D
Norm
E
Model
4v Galvo
3v Galvo
2v Galvo
1v Galvo
0v Galvo
Fluorescence (v)
dF
Recording Times (min)

Figure 4.3.11. Fluorescence profile while re-dosing Methoxy-x04 in a 5xFAD+ mouse using an *in vitro*-based light protocol, analysed with different approaches. (A) *Top left*, Recording paradigm. Methoxy-x04 was injected at the end of recording on days 0, 1 and 2 and recorded for 2-h across days 0, 1, 2 and 3. Each dash on the recording days represents 1-h. *Top right,* Table highlighting the light protocol: *in vitro*. *Bottom,* Schematic of the TF showing that higher GVs represent superficial regions, whereas lower GVs represent deeper brain regions. Colour coding is consistent with the colour coding of the summary plots. (B) Example heatmaps of the fluorescence across depth and time, over the 4-day re-dose recording in a 5xFAD+ mouse. Each vertical row represents a different data analytical approach: raw, normalised to day 0 (Norm) and modelled to day 0 (Model). Syringes represent the time of Methoxy-x04 injection. Colour map represents the fluorescence range. Scale: 1-h. Example plots come from FAD68. (C, D, E) Summary plots of the re-dose profile of Methoxy-x04 across time and depth, for raw (C), Norm (D), and Model (E) data. Plot colours get darker as the recording region on the TF gets deeper. Grey line illustrates the time of Methoxy-x04 injection. Data was statistically compared using a Kruskal-Wallis test, followed by multi-comparison tests with Bonferroni correction if $p < 0.05$, with p-values shown: $p < 0.001$ (****), $p < 0.005$ (***), $p < 0.01$ (**), $p < 0.05$ (*), ns not significant. $n = 11$ recordings in 7 5xFAD+ mice.

Figure 4.3.12 shows the re-dose fluorescence profile in a 5xFAD+ mouse model for the image-based light protocol. Example heat plots show that the signal intensity greatly increases on days 1, 2 and 3 compared to day 0, for all analytical approaches. However, fluorescence is stronger in Norm and Model plots, with fluorescence depth-resolution clear only for Norm data **(Figure 4.3.12B).** While there are some differences in fluorescence levels across days, fluorescence appears stable throughout each recording **(Figure 4.3.12B)**.

Summary raw data illustrates no change in fluorescence following injection, across all days, with statistical tests finding no significant differences in fluorescence overtime (0-V, $H(7) = 4.8426$, 0.6792, $p = 0.6792$; 1-V, $H(7) = 4.0065$, $p = 0.7790$; 2-V, $H(7) = 1.1437$, $p = 0.9922$; 3-V, $H(7) = 1.6255$, $p = 0.9776$; 4-V, $H(7) = 2.0458$, $p = 0.9573$, Kruskal-Wallis test) **(Figure 4.3.12C) (Table 4.3.7)**.

Whereas summary Norm data shows a large increase in median fluorescence from day 1, with increases across all GVs **(Figure 4.3.12D).** There are some small variations in median across days, with a trend for decreased fluorescence at 60-minutes compared to 0-minutes on days 1-3 (median fluorescence at 0-V galvo: day 1, 0.407-V and 0.195-V; day 2, 0.139-V and 0.239-V; day 3, 0.583-V and 0.357-V for 0- and 60-minutes, respectively, compared to 0.02-V at day 0, 60-minutes) (median fluorescence at 1-V galvo: day 1, 0.466-V and 0.230-V; day 2, 0.471-V and 0.140-V; day 3, 0.394-V and 0.320-V for 0- and 60-minutes, respectively, compared to 0.003-V at

day 0, 60-minutes) **(Figure 4.3.12D)**. Norm data shows significant difference at 0-V ($H(7) = 22.1886$, $p = 0.0024$) and 1-V ($H(7) = 23.5160$, $p = 0.0014$, Kruskal-Wallis test), but not others (2-V, $H(7) = 12.4819$, $p = 0.0858$; 3-V, $H(7) = 8.6541$, $p = 0.2785$; 4-V, $H(7) = 11.2290$, $p = 0.1289$, Kruskal-Wallis test) **(Figure 4.3.12D)**. Post-hoc tests show significant increases from day 0 and to 1, 2 and 3 **(Table 4.3.7)**.

Despite summary Model data showing stable fluorescence across recordings and days, little change in fluorescence from baseline following Methoxy-x04 injection across days is recorded **(Figure 4.3.12E).** However, statistical tests on modelled data shows significant difference across time at 1-V ($H(7) = 15.2699$, $p = 0.0327$, Kruskal-Wallis test), but not others (0-V, $H(7) = 13.5611$, $p = 0.0596$; 2-V, $H(7) = 11.2804$, $p = 0.1268$; 3-V, $H(7) = 12.3789$, $p = 0.0888$; 4-V, $H(7) = 11.9138$, $p = 0.1034$, Kruskal-Wallis test) **(Figure 4.3.12E)**. However, post-hoc tests found no statistical significance between groups **(Table 4.3.7)**.

Table 4.3.7. Statistical summary for 5xFAD+ re-dose experiments completed with the image light protocol. Kruskal-Wallis tests were completed across time points for each GV, supplying a group comparison significance. If the Kruskal-Wallis test provided a p-value <0.05, post-hoc tests with Bonferroni correction were completed. D0, D1, D2 and D3 represents day 0, 1, 2 and 3, respectively. Arrows indicate the direction of change. **** $p < 0.001$, *** $p < 0.005$, ** $p < 0.01$, * $p < 0.05$, ns not significant.

		Image														
		Raw					Norm					Model				
		Galvo (V)														
Group 1	Group 2	0	1	2	3	4	0	1	2	3	4	0	1	2	3	4
Group Comparison		ns	ns	ns	ns	ns	***	***	ns	ns	ns	ns	*	ns	ns	ns
D0, 0-min	D0, 60-min						1	1					1			
	D1, 0-min						0.014 ↑	0.033 ↑					1			
	D1, 60-min						0.016 ↑	0.243					1			
	D2, 0-min						0.131	0.110					1			
	D2, 60-min						0.269	0.442					1			
	D3, 0-min						0.016 ↑	0.038 ↑					0.995			
	D3, 60-min						0.140	0.311					1			
D0, 60-min	D1, 0-min						0.853	0.096					0.670			
	D1, 60-min						0.916	0.593					1			
	D2, 0-min						1	0.277					0.276			
	D2, 60-min						1	0.975					0.947			
	D3, 0-min						0.708	0.101					0.062			
	D3, 60-min						1	0.692					0.124			
D1, 0-min	D1, 60-min						1	1					1			
	D2, 0-min						1	1					1			
	D2, 60-min						1	1					1			
	D3, 0-min						1	1					1			
	D3, 60-min						1	1					1			
D1, 60-min	D2, 0-min						1	1					1			
	D2, 60-min						1	1					1			
	D3, 0-min						1	1					1			
	D3, 60-min						1	1					1			
D2, 0-min	D2, 60-min						1	1					1			
	D3, 0-min						1	1					1			
	D3, 60-min						1	1					1			
D2, 60-min	D3, 0-min						1	1					1			
	D3, 60-min						1	1					1			
D3, 0-min	D3, 60-min						1	1					1			

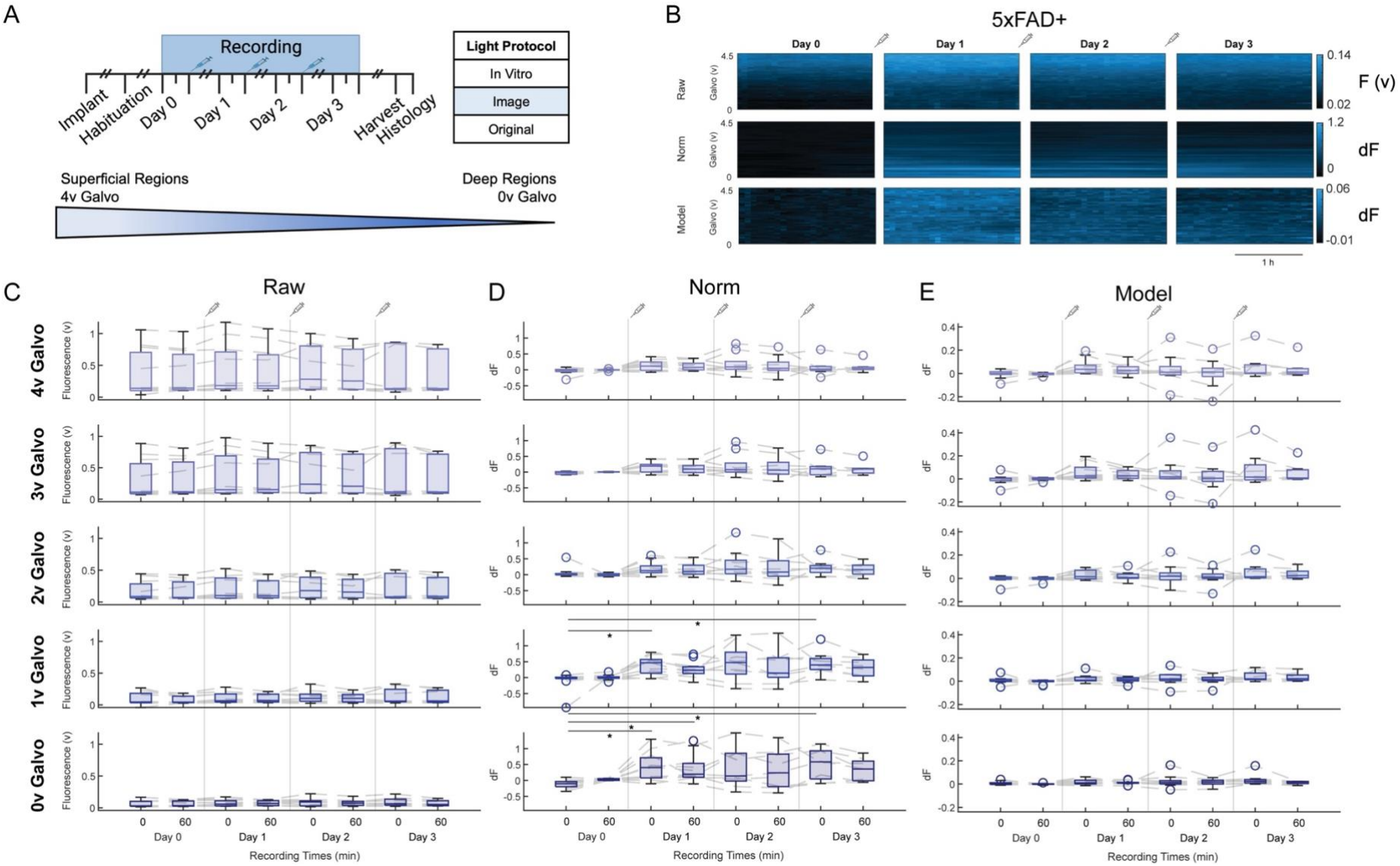
A
Recording
Implant
Habituation
Day 0
Day 1
Day 2
Day 3
Harvest
Histology
Light Protocol
In Vitro
Image
Original
Superficial Regions
4v Galvo
Deep Regions
0v Galvo
B
5xFAD+
Day 0
Day 1
Day 2
Day 3
Raw
Norm
Model
Galvo (v)
F (v)
dF
1 h
C
Raw
D
Norm
E
Model
4v Galvo
3v Galvo
2v Galvo
1v Galvo
0v Galvo
Fluorescence (v)
dF
Recording Times (min)

Figure 4.3.12. Fluorescence profile while re-dosing Methoxy-x04 in a 5xFAD+ mouse using an image-based light protocol, analysed with different approaches. (A) *Top left*, Recording paradigm. Methoxy-x04 was injected at the end of recording on days 0, 1 and 2 and recorded for 2-h across days 0, 1, 2 and 3. Each dash on the recording days represents 1-h. *Top right,* Table highlighting the light protocol: image. *Bottom,* Schematic of the TF showing that higher GVs represent superficial regions, whereas lower GVs represent deeper brain regions. Colour coding is consistent with the colour coding of the summary plots. (B) Example heatmaps of the fluorescence across depth and time, over the 4-day re-dose recording in a 5xFAD+ mouse. Each vertical row represents a different data analytical approach: raw, normalised to day 0 (Norm) and modelled to day 0 (Model). Syringes represent the time of Methoxy-x04 injection. Colour map represents the fluorescence range. Scale: 1-h. Example plots come from FAD68. (C, D, E) Summary plots of the re-dose profile of Methoxy-x04 across time and depth, for raw (C), Norm (D), and Model (E) data. Plot colours get darker as the recording region on the TF gets deeper. Grey line illustrates the time of Methoxy-x04 injection. Data was statistically compared using a Kruskal-Wallis test, followed by multi-comparison tests with Bonferroni correction if $p < 0.05$, with p-values shown: $p < 0.001$ (****), $p < 0.005$ (***), $p < 0.01$ (**), $p < 0.05$ (*), ns not significant. n = 11 recordings in 7 5xFAD+ mice.

Table 4.3.8. Statistical summary for 5xFAD+ re-dose experiments. Kruskal-Wallis tests were completed across time points for each GV, supplying a group comparison significance. If the Kruskal-Wallis test provided a p-value <0.05, post-hoc tests with Bonferroni correction were completed. Day 0 time points are compared with all other time points. D0, D1, D2 and D3 represents day 0, 1, 2 and 3, respectively. Arrows indicate the direction of change. **** p < 0.001, *** p < 0.005, ** p < 0.01, * p < 0.05, ns not significant.

			In Vitro					Image					Original				
			Galvo (V)														
	Group 1	Group 2	0	1	2	3	4	0	1	2	3	4	0	1	2	3	4
Raw	Group Comparison		ns	ns	ns	ns	ns	ns	ns	ns	ns	ns	ns	ns	ns	ns	ns
Norm	Group Comparison		****	****	*	*	ns	***	***	ns	ns	ns	***	***	***	ns	ns
	D0, 0-min	D0, 60-min	ns	ns	ns	ns		ns	ns				ns	ns	ns		
		D1, 0-min	ns	ns	ns	ns		* ↑	* ↑				ns	ns	ns		
		D1, 60-min	ns	ns	ns	ns		* ↑	ns				ns	ns	ns		
		D2, 0-min	ns	ns	ns	ns		ns	ns				ns	*	*		
		D2, 60-min	ns	ns	ns	ns		ns	ns				ns	ns	ns		
		D3, 0-min	ns	ns	ns	ns		* ↑	* ↑				*	*	ns		
		D3, 60-min	ns	ns	ns	ns		ns	ns				ns	ns	ns		
	D0, 60-min	D1, 0-min	ns	* ↑	ns	ns		ns	ns				ns	ns	ns		
		D1, 60-min	* ↑	ns	ns	ns		ns	ns				ns	ns	ns		
		D2, 0-min	* ↑	** ↑	ns	ns		ns	ns				ns	*	ns		
		D2, 60-min	* ↑	* ↑	ns	ns		ns	ns				ns	ns	ns		
		D3, 0-min	* ↑	** ↑	ns	ns		ns	ns				ns	*	ns		
		D3, 60-min	ns	ns	ns	ns		ns	ns				ns	ns	ns		
Model	Group Comparison		***	***	ns	*	ns	ns	*	ns	ns	ns	ns	***	***	ns	ns
	D0, 0-min	D0, 60-min	ns	ns		ns			ns					ns	ns		
		D1, 0-min	ns	ns		ns			ns					ns	* ↑		
		D1, 60-min	ns	ns		ns			ns					ns	ns		
		D2, 0-min	ns	ns		ns			ns					* ↑	* ↑		
		D2, 60-min	ns	* ↑		ns			ns					ns	ns		
		D3, 0-min	ns	ns		ns			ns					ns	ns		
		D3, 60-min	ns	* ↑		ns			ns					ns	ns		
	D0, 60-min	D1, 0-min	ns	ns		ns			ns					ns	ns		
		D1, 60-min	ns	ns		ns			ns					ns	ns		
		D2, 0-min	ns	ns		ns			ns					ns	ns		
		D2, 60-min	ns	ns		ns			ns					ns	ns		
		D3, 0-min	ns	ns		ns			ns					ns	ns		
		D3, 60-min	ns	ns		ns			ns					ns	ns		

Overall, we were able to detect an increase in fluorescence in 5xFAD+ mice that was maintained over several days following repeat dose of Methoxy-x04 at 24-hour intervals. Again, the combination of *in vitro* light protocol and Norm analytical approach appears to provide optimal signal detection, with significant increases in fluorescence detected across days 1-3 compared to day 0 at 0-V and 1-V galvo **(Table 4.3.8)**. This depth resolution was maintained with Norm data across *in vitro*, image and original light protocols. However, while we note an increased fluorescence across days compared to baseline with no Methoxy-x04, we must consider other

possibilities that could be contributing to the small declines in fluorescence across days, such as the long-term binding and bleaching characteristics of Methoxy-x04.

4.3.3.4 Re-dosing Methoxy-x04 each day does not increase fluorescence over several days in 5xFAD- mice

Now it is vital to confirm this change in fluorescence is occurring due to changes in Methoxy-x04 concentration. Therefore, re-dose recordings were completed in 5xFAD- mice **(Figure 4.3.13A)**.

Figure 4.3.13 shows the re-dose fluorescence profile in a 5xFAD- mouse model for the original light protocol. Example heat plots show no change following any Methoxy-x04 injection, across all three analytical approaches **(Figure 4.3.13B)**.

Individual recording traces illustrate a stable fluorescence across days, with no increases following each injection **(Figures 4.3.13C-E).** Summary statistics show no significant difference over time for raw data (0-V, $H(7) = 1.1971$, $p = 0.9910$; 1-V, $H(7) = 0.6234$, $p = 0.9989$; 2-V, $H(7) = 1.0390$, $p = 0.9942$; 3-V, $H(7) = 2.0020$, $p = 0.9597$; 4-V, $H(7) = 1.7298$, $p = 0.9733$, Kruskal-Wallis test) **(Figure 4.3.13C)**, Norm data (0-V, $H(7) = 5.5083$, $p = 0.5982$; 1-V, $H(7) = 7.7502$, $p = 0.3551$; 2-V, $H(7) = 3.3249$, $p = 0.8534$; 3-V, $H(7) = 3.9512$, $p = 0.7854$; 4-V, $H(7) = 6.9571$, $p = 0.4334$, Kruskal-Wallis test) **(Figure 4.3.13D)** or Model data (0-V galvo, $H(7) = 6.9278$, $p = 0.4364$; 1-V galvo, $H(7) = 2.3239$, $p = 0.9398$; 2-V galvo, $H(7) = 3.2634$, $p = 0.8596$; 3-V galvo, $H(7) = 4.1941$, $p = 0.7572$; 4-V galvo, $H(7) = 6.8254$, $p = 0.4473$, Kruskal-Wallis test) **(Figure 4.3.13E)**.

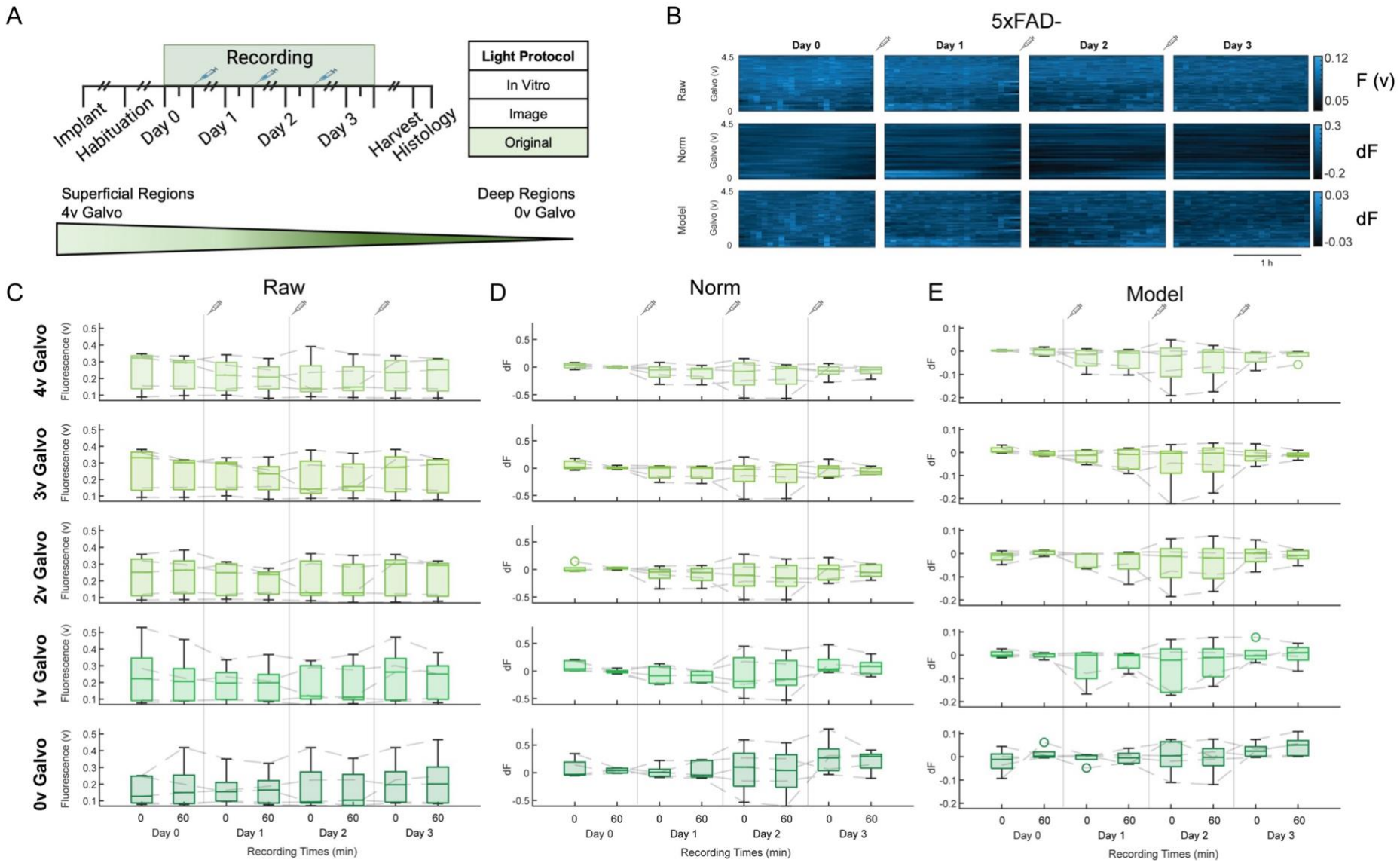
A
Recording
Implant
Habituation
Day 0
Day 1
Day 2
Day 3
Harvest
Histology
Light Protocol
In Vitro
Image
Original
Superficial Regions
4v Galvo
Deep Regions
0v Galvo
B
5xFAD-
Day 0
Day 1
Day 2
Day 3
Raw
Norm
Model
Galvo (v)
F (v)
dF
1 h
C
Raw
D
Norm
E
Model
4v Galvo
3v Galvo
2v Galvo
1v Galvo
0v Galvo
Fluorescence (v)
dF
Recording Times (min)

Figure 4.3.13. Fluorescence profile while re-dosing Methoxy-x04 in a 5xFAD- mouse using the original light protocol, analysed with different approaches. (A) *Top left*, Recording paradigm. Methoxy-x04 was injected at the end of recording on days 0, 1 and 2 and recorded for 2-h across days 0, 1, 2 and 3. Each dash on the recording days represents 1-h. *Top right,* Table highlighting the light protocol: original. *Bottom,* Schematic of the TF showing that higher GVs represent superficial regions, whereas lower GVs represent deeper brain regions. Colour coding is consistent with the colour coding of the summary plots. (B) Example heatmaps of the fluorescence across depth and time, over the 4-day re-dose recording in a 5xFAD- mouse. Each vertical row represents a different data analytical approach: raw, normalised to day 0 (Norm) and modelled to day 0 (Model). Syringes represent the time of Methoxy-x04 injection. Colour map represents the fluorescence range. Scale: 1-h. Example plots come from FAD69. (C, D, E) Summary plots of the re-dose profile of Methoxy-x04 across time and depth, for raw (C), Norm (D) and Model (E) data. Plot colours get darker as the recording region on the TF gets deeper. Grey line illustrates the time of Methoxy-x04 injection. Data was statistically compared using a Kruskal-Wallis test, followed by multi-comparison tests with Bonferroni correction if $p < 0.05$. $n = 5$ recordings in 4 5xFAD- mice.

Figure 4.3.14 shows the re-dose fluorescence profile in a 5xFAD- mouse model for the *in vitro*-based light protocol. Example heat plots show that the signal intensity remains largely consistent across days, with no change following any Methoxy-x04 injection, across all three analytical approaches **(Figure 4.3.14B)**.

Across all three analytical approaches, individual recording traces illustrate a trend of no change of fluorescence across days, and across depth **(Figures 4.3.14C-E)**. Statistical tests show no significant difference over time for raw (0-V, $H(7) = 1.7971$, $p = 0.9702$; 1-V, $H(7) = 1.3668$, $p = 0.9866$; 2-V, $H(7) = 1.7824$, $p = 0.9709$; 3-V, $H(7) = 1.6712$, $p = 0.9758$; 4-V, $H(7) = 1.3990$, $p = 0.9856$, Kruskal-Wallis test) **(Figure 4.3.14C)**, Norm (0-V, $H(7) = 6.0439$, $p = 0.5346$; 1-V, $H(7) = 5.0868$, $p = 0.6494$; 2-V, $H(7) = 3.4068$, $p = 0.8450$; 3-V, $H(7) = 6.6380$, $p = 0.4675$; 4-V, $H(7) = 11.3502$, $p = 0.1241$, Kruskal-Wallis test) **(Figure 4.3.14D)** and Model data (0-V, $H(7) = 9.5590$, $p = 0.2150$; 1-V, $H(7) = 3.2429$, $p = 0.8617$; 2-V, $H(7) = 3.4420$, $p = 0.8413$; 3-V, $H(7) = 8.4702$, $p = 0.2930$; 4-V, $H(7) = 11.4878$, $p = 0.1187$, Kruskal-Wallis test) **(Figure 4.3.14E)**.

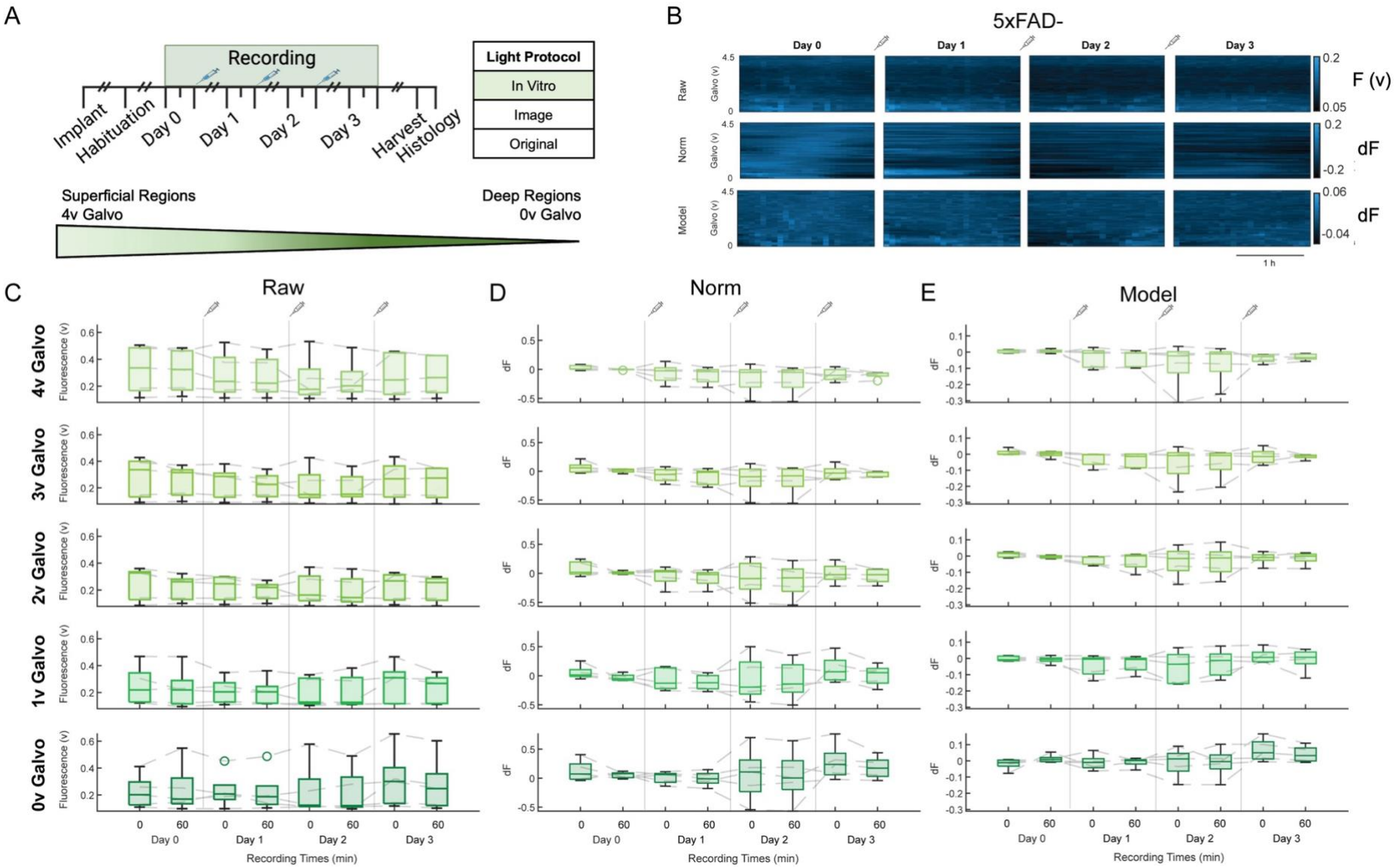
A
Recording
Implant
Habituation
Day 0
Day 1
Day 2
Day 3
Harvest
Histology
Light Protocol
In Vitro
Image
Original
Superficial Regions
4v Galvo
Deep Regions
0v Galvo
B
5xFAD-
Day 0
Day 1
Day 2
Day 3
Raw
Norm
Model
Galvo (v)
F (v)
dF
1 h
C
Raw
D
Norm
E
Model
4v Galvo
3v Galvo
2v Galvo
1v Galvo
0v Galvo
Fluorescence (v)
dF
Recording Times (min)

Figure 4.3.14. Fluorescence profile while re-dosing Methoxy-x04 in a 5xFAD- mouse using an *in vitro*-based light protocol, analysed with different approaches. (A) *Top left*, Recording paradigm. Methoxy-x04 was injected at the end of recording on days 0, 1 and 2 and recorded for 2-h across days 0, 1, 2 and 3. Each dash on the recording days represents 1-h. *Top right,* Table highlighting the light protocol: *in vitro*. *Bottom,* Schematic of the TF showing that higher GVs represent superficial regions, whereas lower GVs represent deeper brain regions. Colour coding is consistent with the colour coding of the summary plots. (B) Example heatmaps of the fluorescence across depth and time, over the 4-day re-dose recording in a 5xFAD- mouse. Each vertical row represents a different data analytical approach: raw, normalised to day 0 (Norm) and modelled to day 0 (Model). Syringes represent the time of Methoxy-x04 injection. Colour map represents the fluorescence range. Scale: 1-h. Example plots come from FAD69. (C, D, E) Summary plots of the re-dose profile of Methoxy-x04 across time and depth, for raw (C), Norm (D), and Model (E) data. Plot colours get darker as the recording region on the TF gets deeper. Grey line illustrates the time of Methoxy-x04 injection. Data was statistically compared using a Kruskal-Wallis test, followed by multi-comparison tests with Bonferroni correction if $p < 0.05$. $n = 5$ recordings in 4 5xFAD- mice.

Figure 4.3.15 shows the re-dose fluorescence profile in a 5xFAD- mouse model for the image-based light protocol. Example heat plots show that the signal intensity remains largely consistent across days, with no change following any Methoxy-x04 injection, across all three analytical approaches **(Figure 4.3.15B)**.

Summary data show no increase in fluorescence across time, GVs and analytical approaches **(Figures 4.3.15C-E).** In fact, there is a slight decreasing trend of fluorescence at higher GVs, seen in both Norm and Model data **(Figure 4.3.15D & Figure 4.3.15E)**. Statistical tests show no significant difference in raw data over time (0-V, $H(7) = 1.7971$, $p = 0.9702$; 1-V, $H(7) = 2.8654$, $p = 0.8972$; 2-V, $H(7) = 0.84$, $p = 0.9970$; 3-V, $H(7) = 0.6615$, $p = 0.9986$; 4-V, $H(7) = 1.4634$, $p = 0.9835$, Kruskal-Wallis test) **(Figure 4.3.15C) (Table 4.3.9)**. However, Norm data shows significance at 1-V ($H(7) = 15.2693$, $p = 0.0327$, Kruskal-Wallis test) and 4-V ($H(7) = 19.0683$, $p = 0.0080$, Kruskal-Wallis test), but not others (0-V, $H(7) = 11.5990$, $p = 0.1145$; 2-V, $H(7) = 5.8566$, $p = 0.5566$; 3-V, $H(7) = 9.6937$, $p = 0.2066$, Kruskal-Wallis test) **(Figure 4.3.15D)**. Post-hoc tests on Norm data show no statistical differences between groups at 1-V galvo **(Table 4.3.9)**. At 4-V galvo, significant decreases from day 0 to day 3 are reported **(Table 4.3.9)**. Also, Model data shows significance at 4-V ($H(7) = 18.4712$, $p = 0.0100$) but not others (0-V, $H(7) = 5.7190$, $p = 0.5729$; 1-V, $H(7) = 11.2361$, $p = 0.1286$; 2-V, $H(7) = 10.039$, $p = 0.1864$; 3-V, $H(7) = 6.3834$, $p = 0.4958$, Kruskal-Wallis test) **(Figure 4.3.15E)**. At 4-V galvo, significant decreases from day 0 to day 3 are reported **(Table 4.3.9)**.

Table 4.3.9. Statistical summary for 5xFAD- re-dose experiments, with the image light protocol. Kruskal-Wallis tests were completed across time points for each GV, supplying a group comparison significance. If the Kruskal-Wallis test provided a p-value <0.05, post-hoc tests with Bonferroni correction were completed. D0, D1, D2 and D3 represents day 0, 1, 2 and 3, respectively. Arrows indicate the direction of change. **** $p < 0.001$, *** $p < 0.005$, ** $p < 0.01$, * $p < 0.05$, ns not significant.

		Image														
		Raw					Norm					Model				
		Galvo (V)														
Group 1	Group 2	0	1	2	3	4	0	1	2	3	4	0	1	2	3	4
Group Comparison		ns	ns	ns	ns	ns	ns	*	ns	ns	**	ns	ns	ns	ns	*
D0, 0-min	D0, 60-min							0.853			1					1
	D1, 0-min							0.743			0.602					0.191
	D1, 60-min							1			0.106					0.082
	D2, 0-min							1			0.069					0.063
	D2, 60-min							1			0.176					0.333
	D3, 0-min							1			0.069					0.048 ↓
	D3, 60-min							1			0.043 ↓					0.176
D0, 60-min	D1, 0-min							1			1					1
	D1, 60-min							1			1					1
	D2, 0-min							1			0.976					0.976
	D2, 60-min							1			1					1
	D3, 0-min							1			0.976					0.797
	D3, 60-min							1			0.693					1
D1, 0-min	D1, 60-min							1			1					1
	D2, 0-min							1			1					1
	D2, 60-min							1			1					1
	D3, 0-min							0.176			1					1
	D3, 60-min							1			1					1
D1, 60-min	D2, 0-min							1			1					1
	D2, 60-min							1			1					1
	D3, 0-min							0.149			1					1
	D3, 60-min							1			1					1
D2, 0-min	D2, 60-min							1			1					1
	D3, 0-min							0.285			1					1
	D3, 60-min							1			1					1
D2, 60-min	D3, 0-min							1			1					1
	D3, 60-min							1			1					1
D3, 0-min	D3, 60-min							1			1					1

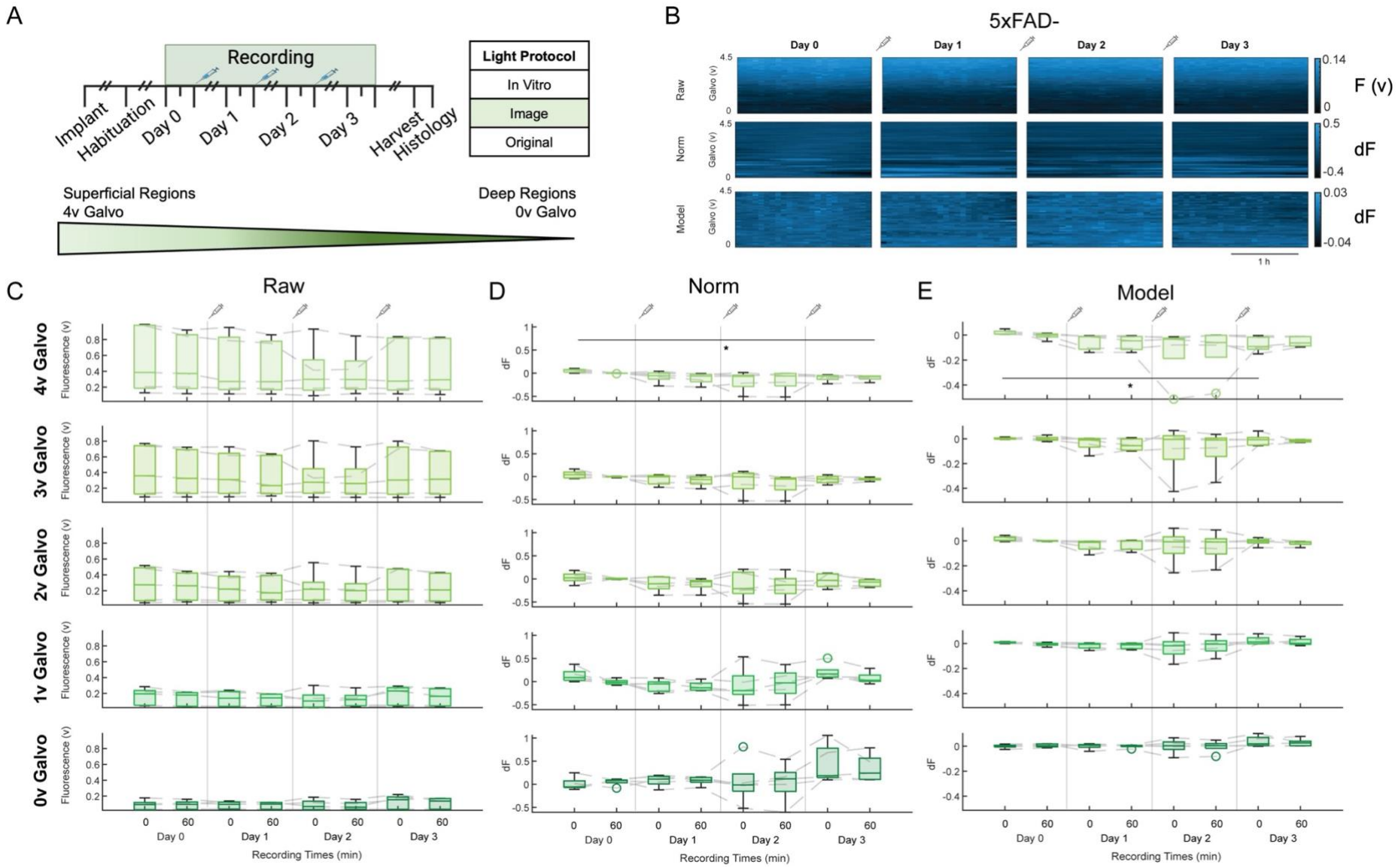
A
Recording
Implant
Habituation
Day 0
Day 1
Day 2
Day 3
Harvest
Histology
Light Protocol
In Vitro
Image
Original
Superficial Regions
4v Galvo
Deep Regions
0v Galvo
B
5xFAD-
Day 0
Day 1
Day 2
Day 3
Raw
Norm
Model
Galvo (v)
F (v)
dF
1 h
C
Raw
D
Norm
E
Model
4v Galvo
3v Galvo
2v Galvo
1v Galvo
0v Galvo
Fluorescence (v)
dF
Recording Times (min)

Figure 4.3.15. Fluorescence profile while re-dosing Methoxy-x04 in a 5xFAD- mouse using an in image-based light protocol, analysed with different approaches. (A) *Top left*, Recording paradigm. Methoxy-x04 was injected at the end of recording on days 0, 1 and 2 and recorded for 2-h across days 0, 1, 2 and 3. Each dash on the recording days represents 1-h. *Top right,* Table highlighting the light protocol: image. *Bottom,* Schematic of the TF showing that higher GVs represent superficial regions, whereas lower GVs represent deeper brain regions. Colour coding is consistent with the colour coding of the summary plots. (B) Example heatmaps of the fluorescence across depth and time, over the 4-day re-dose recording in a 5xFAD- mouse. Each vertical row represents a different data analytical approach: raw, normalised to day 0 (Norm) and modelled to day 0 (Model). Syringes represent the time of Methoxy-x04 injection. Colour map represents the fluorescence range. Scale: 1 h. Example plots come from FAD69. (C, D, E) Summary plots of the re-dose profile of Methoxy-x04 across time and depth, for raw (C), Norm (D), and Model (E) data. Plot colours get darker as the recording region on the TF gets deeper. Grey line illustrates the time of Methoxy-x04 injection. Data was statistically compared using a Kruskal-Wallis test, followed by multi-comparison tests with Bonferroni correction if $p < 0.05$, with p-values shown: $p < 0.001$ (****), $p < 0.005$ (***), $p < 0.01$ (**), $p < 0.05$ (*), ns not significant. n = 5 recordings in 4 5xFAD- mice.

Overall, we found that following repeat dosing of Methoxy-x04, an increased fluorescence was seen in 5xFAD+ mice, but not 5xFAD- mice. Injection 24-h before each recording allowed levels of fluorescence to remain relatively consistent, greater than at baseline with no Methoxy-x04. Additionally, across analytical approaches, the combination of *in vitro* light protocol and Norm data appears to show the most prominent fluorescence profile, proving to be an optimal approach for analysing TF data.

4.3.4 TF light profile may influence appropriate correlation analysis

Now we have confirmed plaque pathology can be monitored in freely behaving AD mouse models, in a real-time and depth-resolved manner, we wished to confirm that TF photometry data is representative of the plaque pathology present within the brain. To do so, histological sections from each mouse were prepared and histological quantification of plaques surrounding the TF on the contralateral hemisphere, as described in **section 4.2.3.2.2**, was completed. For comparison, the median fluorescence across hours 2-3 on day 1 of the last pharmacokinetic recording was taken across depth **(Figure 4.3.16A)**. Photometry signals from each light protocol and analytical approach were then compared with histological quantification to determine if a positive correlation between photometry and histological signals exists **(Figure 4.3.16A)**. Since Norm data, with an *in*

vitro light protocol appeared to provide optimal photometry signals, we hypothesised that this data would be the most strongly correlated with histological data.

Figure 4.3.16 shows histological correlation analysis for photometry data using the original light protocol. Histological images illustrate show the distribution of Methoxy-x04 stained plaques in the example 5xFAD+ and 5xFAD- mice **(Figure 4.3.16C)**. In the 5xFAD+ mouse, plaque load surrounding the TF increases from superficial to deeper cortical layers. Then, plaque load decreases at the white matter, before reaching the plaque-dense SUB **(Figure 4.3.16C)**. While the TF passes through similar brain regions in the 5xFAD- mouse, there are no visible plaques **(Figure 4.3.16C)**. Histological quantification mirrors this: plaque number increases as it passes from the superficial cortical areas, deeper cortical layers, and hippocampus, with a dip ~2-V galvo, matching white matter **(Figures 4.3.16D, G, J)**.

For original photometry, the raw signal is largely consistent across depths, showing no peaks in fluorescence at regions which show high plaque load, resulting in a negative correlation with histological plaque number ($r = -0.26$, $p = 0.1002$, Pearson's correlation coefficient) **(Figure 4.3.16D)**. Norm data shows variations of fluorescence along the depth of the TF, with increased signal intensity at 0-1-V galvo, corresponding with the large plaque load in the SUB. However, while a slight trend may be visible, distinctive changes between fluorescence of cortical layers is not prominent **(Figure 4.3.16G)**. Additionally, the depth resolution appears to have a shift, but despite this, there is a positive corelation between Norm data and histological plaque number ($r = 0.32$, $p = 0.0416$, Pearson's correlation coefficient). Also, Model photometry data illustrates a similar depth profile as the histological quantification, resulting in a positive correlation ($r = 0.24$, $p = 0.1380$, Pearson's correlation coefficient) **(Figure 4.3.16J)**.

Again, 5xFAD- photometry data shows a weaker fluorescence across all analytical approaches, with no clear fluorescence profile seen **(Figures 4.3.16E, H, K)**. With no plaque pathology quantified in histological sections, no correlation was seen when comparing histological quantification with raw data ($r = 0.07$, $p = 0.6594$, Pearson's correlation coefficient) **(Figure 4.3.16E)**, Norm data ($r = 0.12$, $p = 0.4472$, Pearson's correlation coefficient) **(Figure 4.3.16H)** and Model data ($r = 0.09$, $p = 0.5951$, Pearson's correlation coefficient) **(Figure 4.3.16K)**.

Summary data for raw data shows mostly negative correlation coefficients for 5xFAD+ mice **(Figure 4.3.16F)**. However, inconsistent coefficients result in no significant differences between 5xFAD+ and 5xFAD- mice for raw ($p = 0.0902$, two-sample t-test) **(Figure 4.3.16F)**, Norm ($p = 0.6481$, two-sample t-test) **(Figure 4.3.16I)** and Model data ($p = 0.9032$, two-sample t-test) **(Figure 4.3.16L)**.

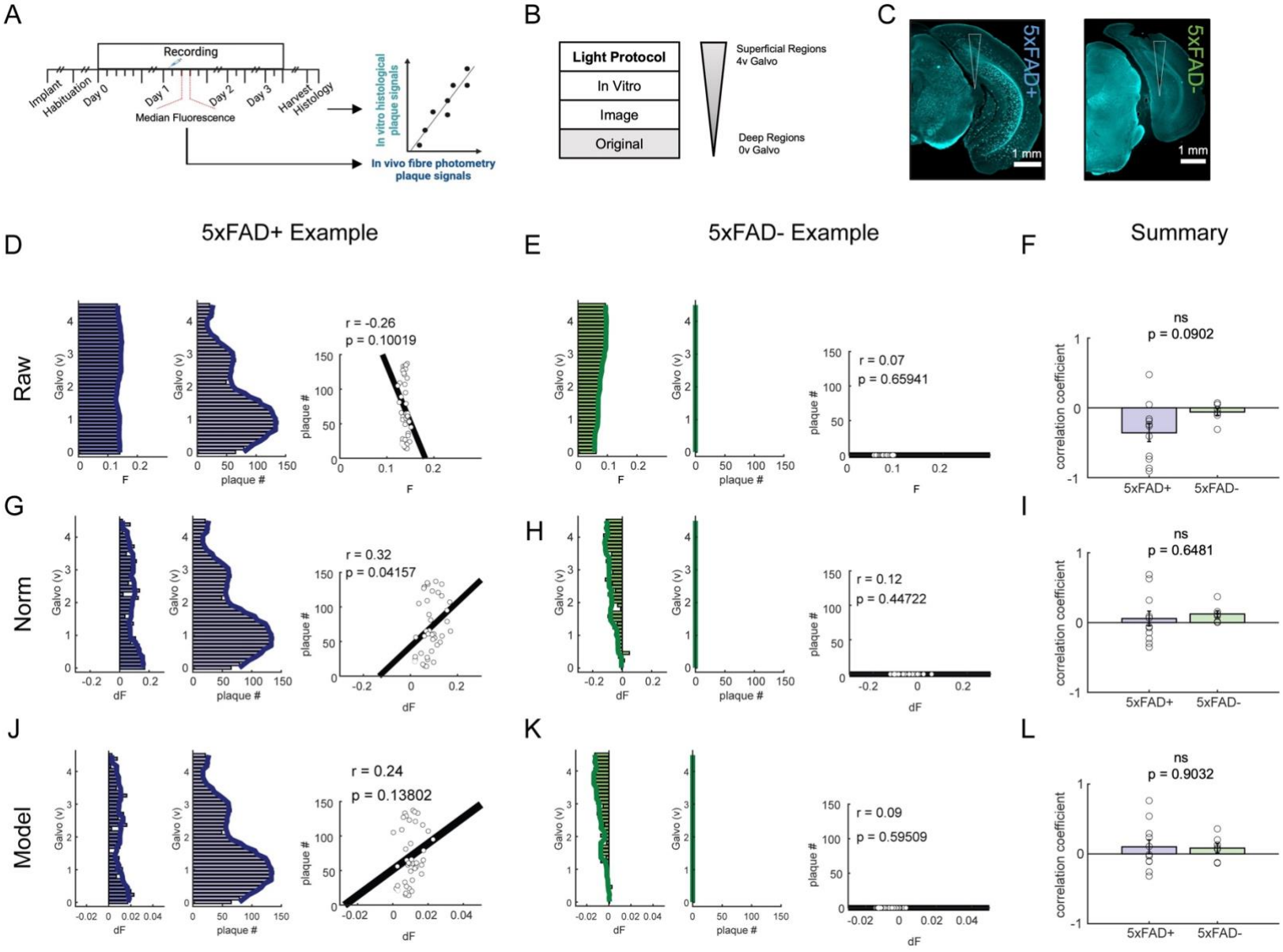
A
Recording
Implant
Habituation
Day 0
Day 1
Day 2
Day 3
Harvest
Histology
Median Fluorescence
In vitro histological plaque signals
In vivo fibre photometry plaque signals
B
Light Protocol
In Vitro
Image
Original
Superficial Regions
4v Galvo
Deep Regions
0v Galvo
C
5xFAD+
5xFAD-
1 mm
D
5xFAD+ Example
E
5xFAD- Example
F
Summary
Raw
Norm
Model
Galvo (v)
F
dF
plaque #
r = -0.26
p = 0.10019
r = 0.07
p = 0.65941
r = 0.32
p = 0.04157
r = 0.12
p = 0.44722
r = 0.24
p = 0.13802
r = 0.09
p = 0.59509
correlation coefficient
ns
p = 0.0902
p = 0.6481
p = 0.9032
5xFAD+
5xFAD-

Figure 4.3.16. Histological correlation analysis of TF photometry data using original light imaging. (A) Schematic of data collection. Median fluorescence from 2-3-h on day 1 of the last pharmacokinetic recording completed on each mouse was used and compared to histological plaque quantification using correlation analysis. (B) Light protocol being used: original. TF diagram shows a key for galvo depth. (C) Histological images of the example 5xFAD+ and 5xFAD- mice used in the following plots. White triangle shows the TF track. Scale: 1-mm. (D, G, J) *Left,* Depth profile of photometry (left) and histology (right) data. *Right,* Correlation analysis comparing histology and photometry raw (D), Norm (G) and Model (J) data for a 5xFAD+ mouse model. (E, H, K) Shows the same as D, G and J but for 5xFAD- mice. Bold lines show filtered data, calculating the moving median across depths. Each dot on the scatter plot represents a single depth. Black line shows a linear trend line. R- and p-values are shown on the plot. (F, I, L) Summary correlation coefficient analysis for raw (F), Norm (I) and Model (L) photometry data. Each data point represents a mouse. Summary data was statistically compared using two-sample t-test and p-values are shown: $p < 0.001$ (****), $p < 0.005$ (***), $p < 0.01$ (**), $p < 0.05$ (*), ns not significant. 5xFAD+ mice: $n = 11$; 5xFAD- mice: $n = 7$.

Figure 4.3.17 shows histological correlation analysis for photometry data using an *in vitro*-based light protocol. 5xFAD+ and 5xFAD- examples are the same as **Figure 4.3.16.**

5xFAD+ raw photometry data shows increased fluorescence at 0 and 1-V galvo, resulting in a strong positive correlation between raw and histological data ($r = 0.74$, $p = < 0.0001$, Pearson's correlation coefficient) **(Figure 4.3.17D)**. Notably, the varied intensity across depth seen in histology, is not reflected in raw data signals. Instead, a consistent level of fluorescence is seen from 2-4-V galvo **(Figure 4.3.17D)**. Alternatively, this trend is better represented by Norm data where increases and decreases in fluorescence occur in a similar pattern as histological data **(Figure 4.3.17G)**. While this trend appears to give a better representation of the spatial pattern of plaques within the brain, the depth resolution appears to be inconsistent with histological data, resulting in a lower, albeit positively correlation between Norm and histology data ($r = 0.13$, $p = 0.4146$, Pearson's correlation coefficient) **(Figure 4.3.17G)**. A similar pattern is seen with Model data ($r = 0.34$, $p = 0.0280$, Pearson's correlation coefficient) **(Figure 4.3.17J)**.

5xFAD- photometry data shows a weaker fluorescence across all analytical approaches, with no clear fluorescence profile seen **(Figures 4.3.17E, H, K)**. With no plaque pathology quantified in histological sections, no correlation was seen when comparing histological quantification with raw ($r = 0.02$, $p = 0.9179$, Pearson's correlation coefficient) **(Figure 4.3.17E)**, Norm ($r = -0.05$, $p = 0.7790$, Pearson's correlation coefficient) **(Figure 4.3.17H)** and Model data ($r = -0.02$, $p = 0.9190$, Pearson's correlation coefficient) **(Figure 4.3.17K)**.

While a positive correlation is seen in this 5xFAD+ example, summary data shows that this was not consistent across all mice **(Figures 4.3.17F, I, L)**. While some show a positive correlation, others show no or negative correlation, resulting in no significant difference between 5xFAD+ and 5xFAD- mice for raw ($p = 0.2974$, two-sample t-test) **(Figure 4.3.17F)**, Norm ($p = 0.9649$, two-sample t-test) **(Figure 4.3.17I)** but a significantly increased coefficient for 5xFAD+ mice compared to 5xFAD- mice for Model data ($p = 0.0127$, two sample t-test) **(Figure 4.3.17L).**

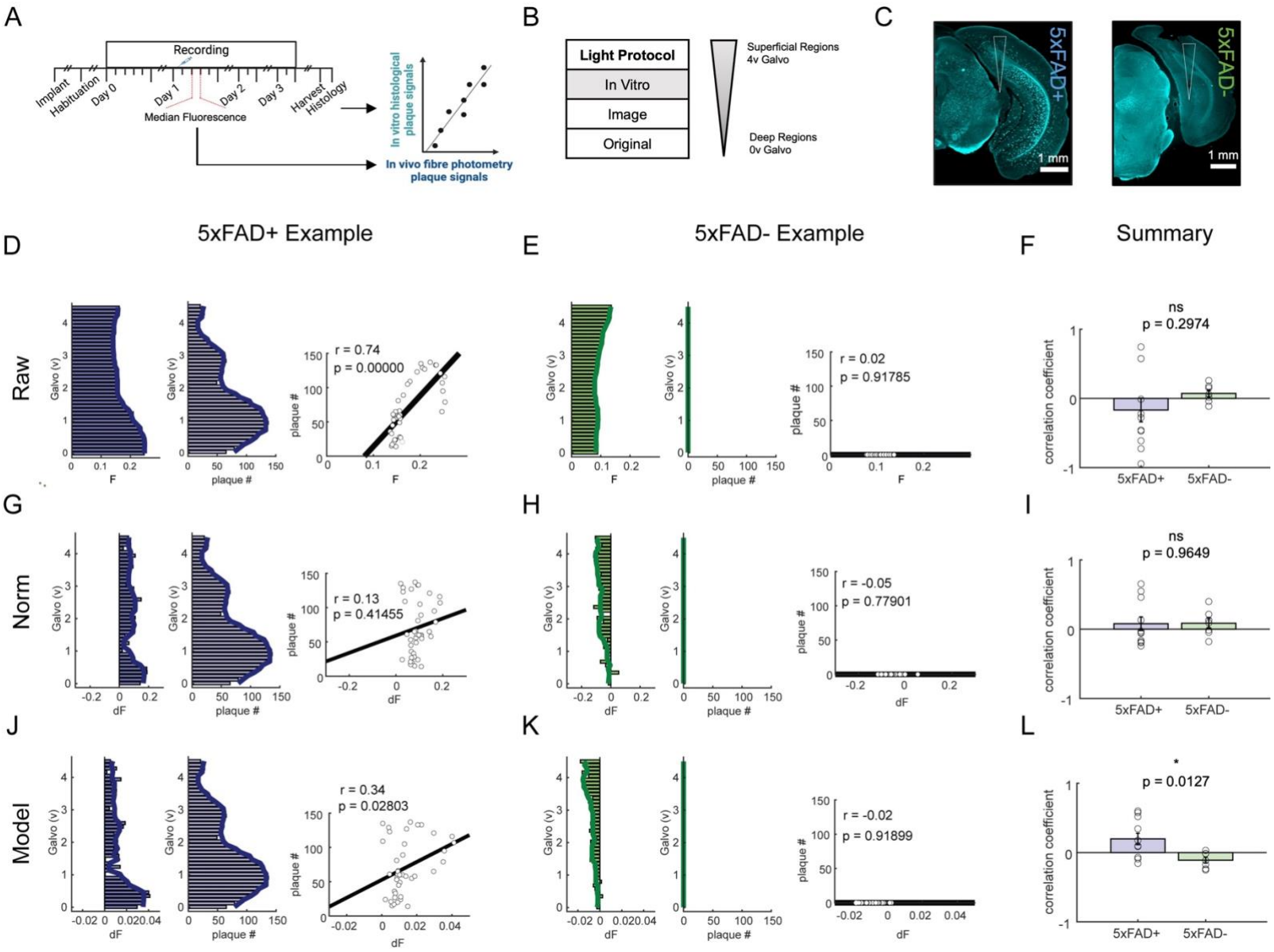
A
Recording
Implant
Habituation
Day 0
Day 1
Day 2
Day 3
Harvest
Histology
Median Fluorescence
In vitro histological plaque signals
In vivo fibre photometry plaque signals
B
Light Protocol
In Vitro
Image
Original
Superficial Regions 4v Galvo
Deep Regions 0v Galvo
C
5xFAD+
5xFAD-
1 mm
1 mm
D
5xFAD+ Example
E
5xFAD- Example
F
Summary
Raw
Norm
Model
Galvo (v)
F
dF
plaque #
r = 0.74
p = 0.00000
r = 0.02
p = 0.91785
r = 0.13
p = 0.41455
r = -0.05
p = 0.77901
r = 0.34
p = 0.02803
r = -0.02
p = 0.91899
correlation coefficient
ns
p = 0.2974
ns
p = 0.9649
*
p = 0.0127
5xFAD+
5xFAD-
G
H
I
J
K
L

Figure 4.3.17. Histological correlation analysis of TF photometry data using *in vitro*-based light imaging. (A) Schematic of data collection. Median fluorescence from 2-3-h on day 1 of the last pharmacokinetic recording completed on each mouse was used and compared to histological plaque quantification using correlation analysis. (B) Light protocol being used: *in vitro*. TF diagram shows a key for galvo depth. (C) Histological images of the example 5xFAD+ and 5xFAD- mice used in the following plots. White triangle shows the TF track. Scale: 1-mm. (D, G, J) *Left,* Depth profile of photometry (left) and histology (right) data. *Right,* Correlation analysis comparing histology and photometry raw (D), Norm (G) and Model (J) data for a 5xFAD+ mouse model. (E, H, K) Shows the same as D, G and J but for 5xFAD- mice. Bold lines show filtered data, calculating the moving median across depths. Each dot on the scatter plot represents a single depth. Black line shows a linear trend line. R- and p-values are shown on the plot. (F, I, L) Summary correlation coefficient analysis for raw (F), Norm (I) and Model (L) photometry data. Each data point represents a mouse. Summary data was statistically compared using a two-sample t-test and p-values are shown. $p < 0.001$ (****), $p < 0.005$ (***), $p < 0.01$ (**), $p < 0.05$ (*), ns not significant. 5xFAD+ mice: $n = 11$; 5xFAD- mice: $n = 7$.

Figure 4.3.18 shows histological correlation analysis for photometry data using an image-based light protocol. 5xFAD+ and 5xFAD- examples are the same as **Figure 4.3.16.**

For image-based photometry, the raw signal is highly fluorescent at higher GVs, decreasing at deeper brain regions. This is strongly negatively correlated with the histological quantification ($r = -0.88$, $p < 0.0001$, Pearson's correlation coefficient) **(Figure 4.3.18D)**. Alternatively, Norm data continues to show a photometry trend that is representative of the histological profile, despite irregular depth comparisons, resulting in a positive correlation ($r = 0.55$, $p = 0.0002$, Pearson's correlation coefficient) **(Figure 4.3.18G)**. Whereas Model data does not show maximum fluorescence at deeper brain regions, resulting in a negative correlation ($r = -0.12$, $p = 0.4675$, Pearson's correlation coefficient) **(Figure 4.3.18J)**.

Again, 5xFAD- photometry data shows a weaker fluorescence across all analytical approaches, with no clear fluorescence profile seen **(Figures 4.3.18E, H, K)**. With no plaque pathology quantified in histological sections, no correlation was seen when comparing histological quantification with raw ($r = 0.01$, $p = 0.9715$, Pearson's correlation coefficient) **(Figure 4.3.18E)**, Norm ($r = -0.22$, $p = 0.1638$, Pearson's correlation coefficient) **(Figure 4.3.18H)** and Model data ($r = -0.08$, $p = 0.6167$, Pearson's correlation coefficient) **(Figure 4.3.18K)**.

Summary data for raw data shows mostly negative correlation coefficients for 5xFAD+ mice resulting in a significantly smaller correlation coefficient in 5xFAD+ mice, compared to 5xFAD- mice ($p = 0.0139$, two-sample t-test) **(Figure 4.3.18F)**. Also, a significantly greater correlation

coefficient for 5xFAD+ mice compared to 5xFAD-, was reported for Norm data ($p = 0.0208$, two-sample t-test). However, no significant differences between 5xFAD+ and 5xFAD- mice was seen for Model data ($p = 0.8868$, two-sample t-test) **(Figure 4.3.18L)**.

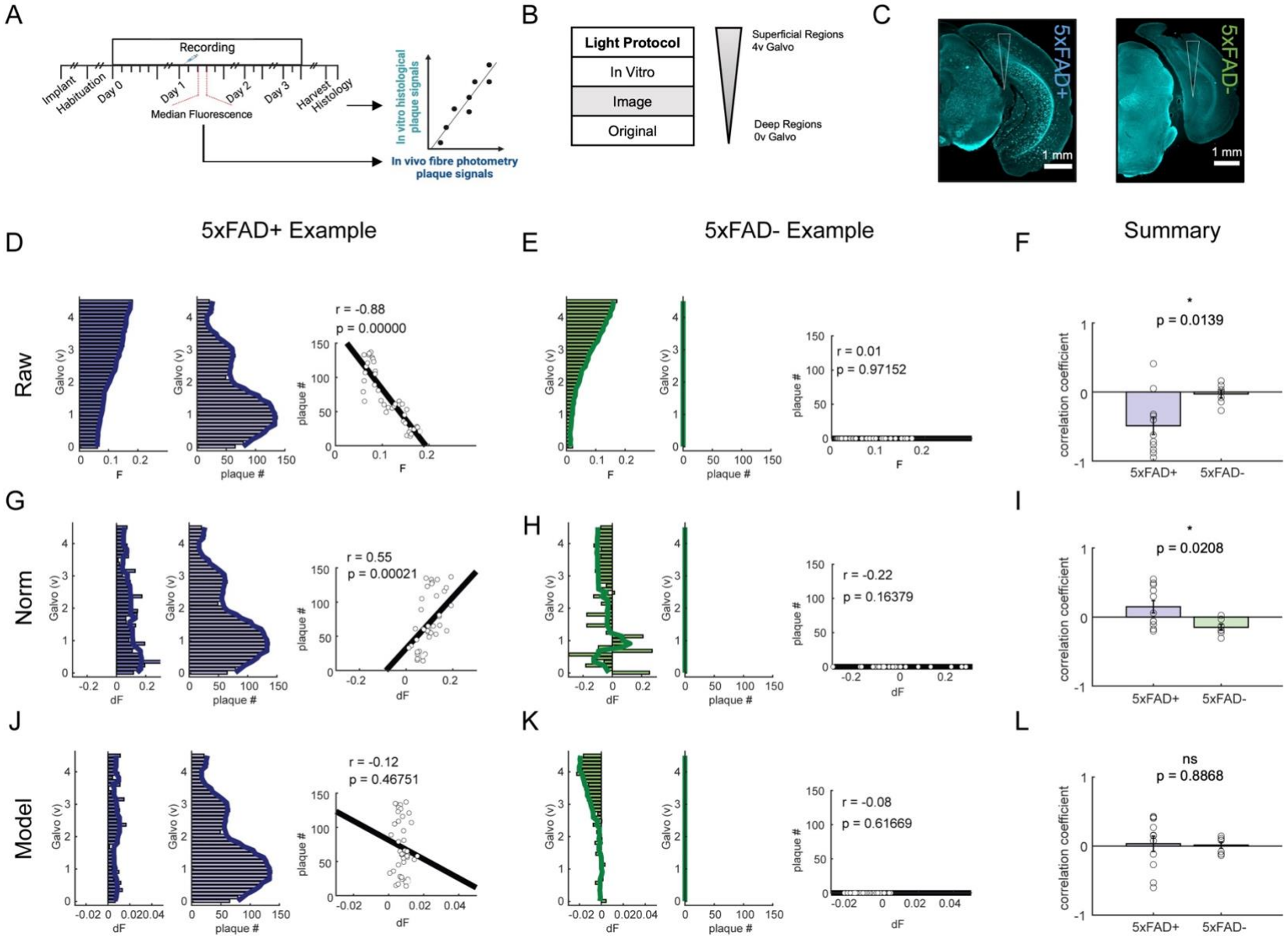
A
Recording
Implant
Habituation
Day 0
Day 1
Day 2
Day 3
Harvest
Histology
Median Fluorescence
In vitro histological plaque signals
In vivo fibre photometry plaque signals
B
Light Protocol
In Vitro
Image
Original
Superficial Regions 4v Galvo
Deep Regions 0v Galvo
C
5xFAD+
5xFAD-
1 mm
D
5xFAD+ Example
E
5xFAD- Example
F
Summary
Raw
Norm
Model
Galvo (v)
F
dF
plaque #
r = -0.88
p = 0.00000
r = 0.01
p = 0.97152
r = 0.55
p = 0.00021
r = -0.22
p = 0.16379
r = -0.12
p = 0.46751
r = -0.08
p = 0.61669
correlation coefficient
p = 0.0139
p = 0.0208
ns
p = 0.8868
5xFAD+
5xFAD-

Figure 4.3.18. Histological correlation analysis of TF photometry data using image-based light imaging. (A) Schematic of data collection. Median fluorescence from 2-3-h on day 1 of the last pharmacokinetic recording completed on each mouse was used and compared to histological plaque quantification using correlation analysis. (B) Light protocol being used: image. TF diagram shows a key for galvo depth. (C) Histological images of the example 5xFAD+ and 5xFAD- mice used in the following plots. White triangle shows the TF track. Scale: 1-mm. (D, G, J) *Left,* Depth profile of photometry (left) and histology (right) data. *Right,* Correlation analysis comparing histology and photometry raw (D), Norm (G) and Model (J) data for a 5xFAD+ mouse model. (E, H, K) Shows the same as D, G and J but for 5xFAD- mice. Bold lines show filtered data, calculating the moving median across depths. Each dot on the scatter plot represents a single depth. Black line shows a linear trend line. R- and p-values are shown on the plot. (F, I, L) Summary correlation coefficient analysis for raw (F), Norm (I) and Model (L) photometry data. Each data point represents a mouse. Summary data was statistically compared using a two-sample t-test and p-values are shown. $p < 0.001$ (****), $p < 0.005$ (***), $p < 0.01$ (**), $p < 0.05$ (*), ns not significant. 5xFAD+ mice: $n = 11$; 5xFAD- mice: $n = 7$.

We directly compared the correlation coefficients for each light protocol and analytical approach **(Figure 4.3.19)**. For 5xFAD+ mice, raw analytical approach consistently resulted in a negative correlation with histological plaque number across all analytical approaches **(Figures 4.3.19A-C)**. The correlation coefficient was slightly positively correlated for Norm and Model data when using the *in vitro* and image light protocols **(Figures 4.3.19B-C)**.

Statistical tests show no significant difference of correlation coefficients across analytical approaches for the *in vitro* light protocol ($F(2) = 2.2438$, $p = 0.1236$, one-way ANOVA), but does for image ($F(2) = 9.5621$, $p = 0.0001$, one-way AVOVA) and original ($F(2) = 5.1192$, $p = 0.0122$, one-way ANOVA) light protocols **(Figures 4.3.19A & C)**. Specifically, post-hoc tests show a significant increase in correlation coefficients for Norm ($p = 0.0009$ and $p = 0.0409$, post-hoc comparison with Bonferroni correction) and Model ($p = 0.0063$ and $p = 0.0208$, post-hoc Bonferroni tests) approaches compared to raw data for the image and original light protocols, respectively **(Figures 4.3.19A & C)**.

For 5xFAD- mice, the mean correlation coefficient was mostly centred around 0, suggesting no correlation between histology and each photometry analytical approach **(Figures 4.3.19D-F)**. Specifically, the correlation coefficient was not significantly different across analytical approaches for image ($F(2) = 3.1150$, $p = 0.0689$, one-way ANOVA) **(Figure 4.3.19F)** and original ($F(2) = 3.1123$, $p = 0.0690$, one-way ANOVA) light protocols **(Figure 4.3.19D)**. A significant difference of the correlation coefficients across analytical approaches was reported for the *in vitro* light protocol

(F(2) = 3.8098, p = 0.0411, one-way ANOVA), but no post-hoc significance was found (p > 0.0559 for all, post-hoc Bonferroni tests) **(Figure 4.3.19E)**.

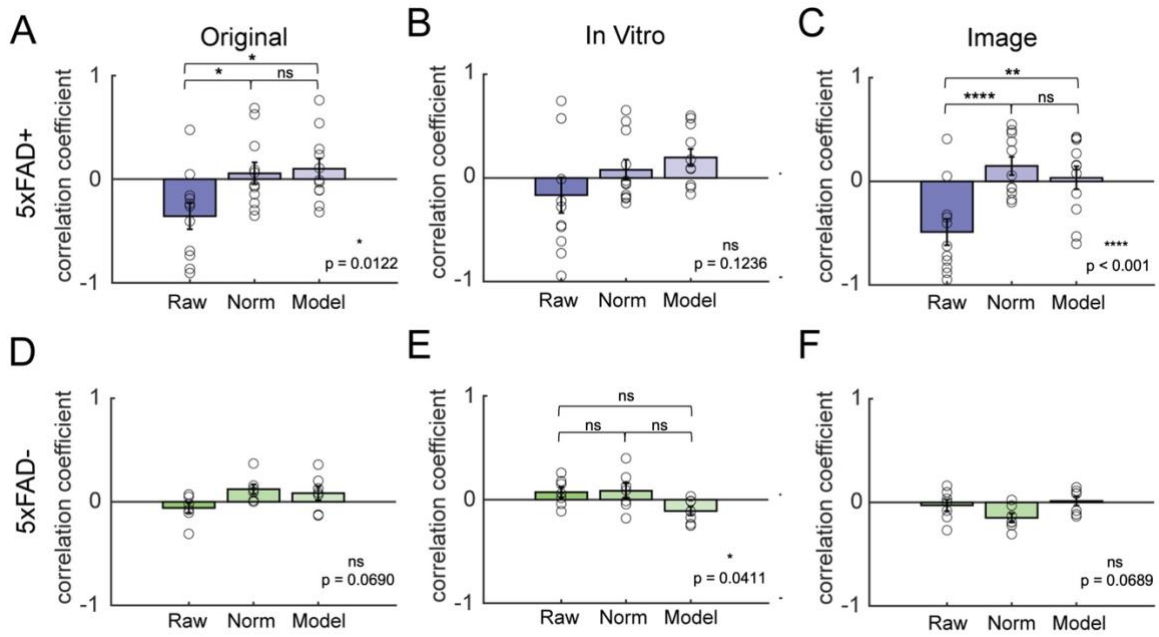

Figure 4.3.19. Correlation coefficient across light protocols and analytical approaches for 5xFAD+ and 5xFAD-. (A-C) Correlation coefficients for 5xFAD+ mice for *in vitro* (A), image (B) and original (C) light protocols. (D-F) Correlation coefficients for 5xFAD- mice for *in vitro* (D), image (E) and original (F) light protocols. One-way ANOVA was completed with post-hoc Bonferroni tests. P-value for one-way ANOVA is shown on the bottom left corner. P-values for post-hoc tests are shown. p < 0.001 (****), p < 0.005 (***), p < 0.01 (**), p < 0.05 (*), ns not significant. 5xFAD+ mice: n = 11; 5xFAD- mice: n = 7.

Overall, confirming TF photometry signals are representative of plaque load with the brain, proves challenging. Some example data show strong positive correlation, particularly with Norm and Model data. Contractively, original light protocol and raw data are unable to provide appropriate depth resolution reflective of the pathological state within the brain. Therefore, this leaves us currently unable to confirm the photometry signals are reflective of the plaque load. However, this approach for analysing the correlation of photometry and histology data has limitations and therefore, a novel method may help clarify this further, which we discuss in **section 4.4.2.2**.

4.4 Discussion

4.4.1 Discussion of findings

4.4.1.1 Main findings

As previously discussed, monitoring plaques *in vivo*, across depth and in freely behaving AD mouse models has not been established. While we showed that our novel approach combining Methoxy-x04 and conventional fibre photometry was a feasible method of monitoring plaque pathology **(Chapter 3)**, this was yet to be successfully implemented in a chronic, freely behaving condition. Therefore, by overcoming depth-resolved limitations of conventional FFs, we hypothesised that implementation of state-of-the-art TFs will allow real-time, depth-resolved plaque assessment, in freely behaving animals. To do so, we aimed to identify optimal experimental and analytical conditions for TF photometry, while using said approaches to monitor Methoxy-x04 plaque signals.

Acute pharmacokinetic recordings illustrated that AF and TF light propagation can highly influence recorded photometry signals **(Figure 4.3.2)**, emphasising the requirement of appropriate protocols for TFs measurements. Therefore, light protocols and analytical approaches were adopted and tested. Firstly, we examined the pharmacokinetic profile of Methoxy-x04 over several days, which illustrated a small and non-significant, depth-resolved increase in fluorescence within 30-minutes of Methoxy-x04 injection, with a decline seen across days **(Figures 4.3.4-6)**. Secondly, we investigated the fluorescence upon re-dose of Methoxy-x04 and found that injecting every 24-h allows maintained depth-resolved increased fluorescence compared to pre-injection **(Figures 4.3.10-12)**. For both pharmacokinetic **(Figures 4.3.7-9)** and re-dose experiments **(Figures 4.3.13-15)**, the effect was specific to 5xFAD+ mice, with 5xFAD- mice showing no significant change in fluorescence post-injection. However, while attempting to correlate TF photometry data with histological plaque load, inconsistencies were noted across all light protocols and analytical approaches **(Figures 4.3.16-19).** Notably, the *in vitro*-based light protocol and Norm analytical approach proved to provide convincing detection of plaque pathology for both pharmacokinetic **(Figures 4.3.4-6)** and re-dose **(Figures 4.3.10-12)** experiments. Overall, while we require an improved approach for histology correlation analysis, TF photometry appears to provide an increased fluorescent signal that can potentially be reflective of the plaque pathology across depth, in freely behaving mouse models.

4.4.1.2 System AF and light configuration are vital contributors to signal collection

We wished to complete acute pharmacokinetic recordings on mice under terminal anaesthetic using TFs to examine if a change in fluorescence could be recorded after injection of Methoxy-x04 **(Figure 4.3.2)**. In doing so, we seen a large increase in fluorescence, at varying degrees along the depth of the TF, in both 5xFAD+ and 5xFAD- mice, with the greatest signal increase occurring at higher GVs **(Figures 4.3.2B-C)**. As histology confirmed 5xFAD- mice had no plaques, other contributing factors were investigated. We discovered an increase in system AF at a similar time resolution as the rise seen in acute pharmacokinetic experiments **(Figure 4.3.2D)**. Additionally, light power from the TFs declines with increasing GVs **(Figure 4.3.2E)**. Therefore, we believed these two factors are likely to be contributing *in vivo* fluorescent profiles.

The substrates and epoxy within the internal cladding of the patch cable will generate substantial AF, which likely contributed to increases in acute pharmacokinetic recordings **(Figure 4.3.2)**. In addition, the short (405-nm) excitation wavelength increases absorption of light by substances within the patch cable, resulting in AF emitted within the range of emission collection. This coincides with previous studies that illustrate the influence of AF on fibre photometry signal collection (Bianco et al., 2021, Formozov et al., 2023, Schlegel et al., 2018, Simpson et al., 2023). Therefore, when considering the depth-resolved AF, it is possible that higher GVs have larger AF due to the angle of light being greater, resulting in greater interaction with the fibre patch cable. As well as this, TFs have been shown to have greater AF than FFs because of the cladding used for manufacture (Bianco et al., 2021).

Notably, while no major studies report the regeneration of AF from a patch cable, suppliers such as Thorlabs have shown the recovery of fluorescence over-time (https://www.thorlabs.com/newgrouppage9.cfm?objectgroup_id=12516), with other low-AF patch cable users suggesting that recovery is slow, occurring over days (Tang et al., 2022). Conflictingly, we illustrate a recovery of AF at a much faster scale, with an increase within 30-minutes post-bleaching. This suggests that this AF recovery may occur quicker due to an accumulation of AF from many sources: short excitation wavelength, brain tissue, patch cable and TF. This multi-factorial AF influence has been carefully considered before (Formozov et al., 2023).

As well as this, recent work has reported that different anatomical structures within brain regions can alter the volume of signal collection due to heterogenous optical properties which reflect and distort light propagation (Montinaro et al., 2021). Importantly, they mention the influence of AD plaque pathology, with the plaque's ability to modify light propagation due to their different refractive index and other light properties (Montinaro et al., 2021). In all, AF is an important

parameter to control tightly, and use of established light protocols and analytical approaches are vital for reliable Methoxy-x04 signal detection.

4.4.1.3 In vitro-based light protocol and Norm analysis approach proves optimal for analysing biological TF recordings

4.4.1.3.1 Methoxy-x04 pharmacokinetic profile can be seen within 30-minutes, with varied intensities across depth

To prove we could detect plaque signals in real-time, across depth in freely behaving mice, we monitored the pharmacokinetic profile of Methoxy-x04 in 5xFAD+ and 5xFAD- mice **(Figures 4.3.4-9)**. Across all light protocols and analytical approaches, an increase in fluorescence was recorded across depth following Methoxy-x04 injection in 5xFAD+ mice, to varying degrees **(Figures 4.3.4-6)**. For example, results showed that a change in fluorescence was most prominent with a combination of *in vitro* and Norm approaches, showing a rise in fluorescence within 30-minutes, compared to 60-minutes with raw data **(Figure 4.3.5)**. This suggests that accounting for the average baseline signal allows identification of small changes in Methoxy-x04 concentration. Also, the consistent increase in fluorescence in 5xFAD+ mice suggests that Methoxy-x04 has good affinity for plaques, with unbound Methoxy-x04 clearing from the brain quickly, consistent with previous studies (Bacskai et al., 2003, Klunk et al., 2002) . This is further confirmed with no fluorescence change detected post-injection in 5xFAD- mice **(Figures 4.3.7-9).** The lack of fluorescence increase seen in 5xFAD- mice is consistent with previous findings that state that in plaque-free brains, amyloid-binding dyes, such as PiB, have quick clearance from the brain (Bacskai et al., 2003). While the chemical nature of Methoxy-x04 differs from PiB, using i.v. injection of a radio-labelled Methoxy-x04 ligand to estimate brain entry in rats shows an injected dose in the brain of 81% at 20-minutes, falling to 50% within 30-minutes, with an estimated $t_{1/2}$ of ~45-minutes (Klunk et al., 2002). These findings represent the rapid clearance of Methoxy-x04 from non-plaque samples and suggests that Methoxy-x04 is rapidly cleared before a substantial level can accumulate and be detected by the photometry system.

Whereas, in 5xFAD+ mice, findings suggest that Methoxy-x04 reaches the bloodstream and passes the BBB rapidly, allowing almost instant binding to plaques. Despite the system detecting fluorescence within 30-minutes, it is possible that this represents an accumulation of bound Methoxy-x04 above the sensitivity threshold of the TF photometry system, where below this went undetected. In any case, this fluorescence continues to increase over several hours, reaching maximal fluorescence within 4-h **(Figures 4.3.4-6)**. However, previous findings show that after i.p. administration of Methoxy-x04, dim fluorescence is first detected at 2-h post-injection, with an

increase over 72-hours, and maximal fluorescence at 48-hours (Condello et al., 2011). Others show detection of Methoxy-x04 post-mortem, 3-h post injection (Friesen et al., 2022), while the landmark study states that optimal 2PM imaging conditions occur 24-h post i.p. injection, due to the reduction of background fluorescence (Klunk et al., 2002). However, i.p. administration of various other drugs or indicators illustrates detection within the brain from ~30-minutes, with maximal concentrations varying from ~1-8-h (Al Shoyaib et al., 2019, Chauhan and Chauhan, 2015, Griffiths et al., 2019, Hunter and Holscher, 2012, Jiang et al., 2016). Therefore, these findings suggest that the TF photometry system is very sensitive, allowing detection of very small changes in Methoxy-x04 concentration within 30-minutes, that were only seen as dim fluorescence with 2PM after 2-h (Condello et al., 2011). In addition, the maximal fluorescence being reached within 4-h suggests that the illumination protocol and intense sampling, compared to other approaches, results in a trade-off between Methoxy-x04 bleaching and Methoxy-x04 fluorescence. We believe this diminished maximal response must be due to bleaching as previous studies show that Methoxy-x04 is a stable plaque-binding dye, remaining bound to the plaque for at least 90-days, with maintained fluorescence (Condello et al., 2011, Liu et al., 2010). This finding is backed as we found no significant differences in fluorescence from 5-h on day 1 to the first measure of day 2, suggesting that the level of Methoxy-x04 within the brain remains consistent when no light is applied. Additionally, the decline in fluorescence seen on days 2 and 3 suggest that Methoxy-x04 is starting to bleach. Therefore, bleaching of Methoxy-x04 is an important factor for longitudinal recordings. To counteract this decline, a lower laser power, reduced sampling interval or shorter recording time may be used.

An important aspect of these findings is the capability of this approach to detect depth-resolved signals. We see a greater increase in fluorescence levels at lower GVs, which were consistent with plaque pathology. Whereas, at higher GVs where a lower signal change was detected, plaque pathology was sparse. Interestingly, we seen a significant decline in fluorescence from the baseline recording at day 3 at these plaque-sparse, low signal change, high GVs. Therefore, this decline in fluorescence below baseline signals suggests that when no plaques and Methoxy-x04 surround the TF, the illumination protocols can contribute to bleaching of surrounding anatomical structures, resulting in a decline in AF below baseline. Additionally, this may be shown when across *in vitro* light protocols, a decline in fluorescence was seen across depth on day 0 for raw and Norm data analytical approaches **(Figure 4.3.5B)**. Furthermore, this decline was not seen in Model Day 0 data **(Figure 4.3.5B)**, where AF has been extracted. While this confirms the Model analytical approach is successful in removing AF components from data, long-term recordings can contribute to bleaching of internal brain anatomy which is an important consideration when completing longitudinal recordings.

In summary, using *in vitro* and Norm data, we seen a depth-resolved increase in fluorescence, with a trend for increased fluorescence at deeper GVs and lower changes at superficial brain regions, corresponding to the plaque density surrounding the TF implants **(Figure 4.4.1A)**. As confirmed with our histological sections **(Figure 4.2.3)** and the landmark study on 5xFAD mouse models (Oakley et al., 2006), plaque pathology is low within superficial cortical regions, increasing in deeper cortical layers with a highly populated plaque load within the SUB. Therefore, we believe that this novel approach has the capabilities to detect varied signal intensities across depth of the brain, reflective of the pathological state.

However, we note the lack of statistical significance and believe that pooling of TF data together may contribute to this small fluorescent increase as a result of small variations in TF implant site. Accordingly, we believe that establishing an approach for aligning TF implant depths may allow stronger detection of Methoxy-x04. Despite this, using this approach and current analytical methods, we see trends for Methoxy-x04 reaching a maximum fluorescence within 4-h, which appears to return to near-baseline levels after 48-hours, thought to be due to bleaching of Methoxy-x04 **(Figure 4.4.1B**). While we were unable to confirm that bleaching of Methoxy-x04 had occurred, previous studies show that the binding properties of Methoxy-x04 remain largely stable up to 90 days (Condello et al., 2011, Liu et al., 2010) and thus, suggests that it is likely that bleaching is occurring rather than Methoxy-x04 becoming dissociated and clearing from the brain. However, we must consider other possibilities for only small increases in fluorescence occurring upon Methoxy-x04 injection. Specifically, if a Methoxy-x04 injection had previously been completed, this may contribute to the signal on the following recordings. For example, if Methoxy-x04 binds irreversibly, yet is susceptible to bleaching, we remain unclear on how this may affect further binding of Methoxy-x04 and the acquired signal. Overall, it is imperative that further research is completed on the long-term binding and bleaching characteristics of Methoxy-04.

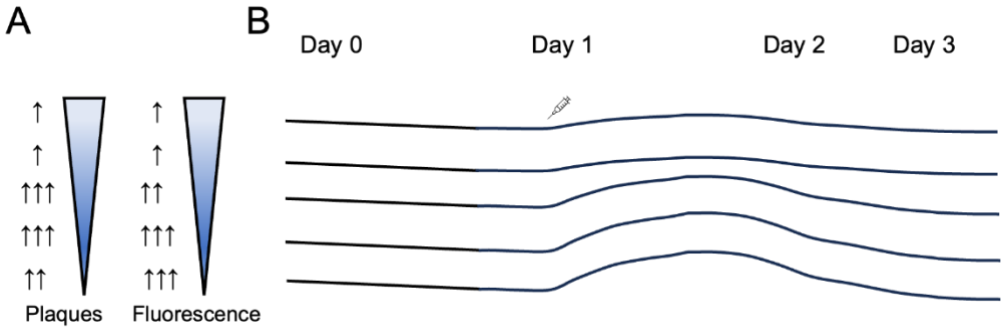

Figure 4.4.1. Suggested pharmacokinetic profile of Methoxy-x04 based on acquired data.
(A) Schematic illustrating an estimate of the plaque load and fluorescence level along the TF.
(B) Schematic showing a summary of the pharmacokinetic findings. Not to scale.

4.4.1.3.2 Redosing Methoxy-x04 at 24-h intervals allows increased fluorescence for longitudinal recording

After proving we could detect plaques in real-time, we wanted to establish a suitable re-dosing protocol for longitudinal recordings **(Figures 4.3.10-15)**. Therefore, we monitored the fluorescence signal across depth, after injecting Methoxy-x04 at 24-h intervals, consistent with previous studies (Crowe and Ellis-Davies, 2013, Hefendehl et al., 2011). *In vitro* and Norm data show a significant increase in fluorescence from baseline at days 1, 2 and 3 at low GVs, consistent with the plaque load. Whereas signals from other approaches were less pronounced. No significant differences across days 1, 2 and 3 were found, implying that fluorescence levels are maintained at a near-consistent level with this re-dosing paradigm, consistent with other studies that use this re-dosing paradigm. Consequently, once plaque pathology aggregation reaches a plateau (Bhattacharya et al., 2014), Methoxy-x04 binding sites may be minimised. Also, without the 4.5-h recording following Methoxy-x04 injection, a greater maximal fluorescence should be achieved which may be representative of the stronger significant difference seen compared to pharmacokinetic recordings.

In summary, using *in vitro* and Norm data, we seen a depth-resolved increase in fluorescence that was maintained over several days with repeat injection of Methoxy-x04, corresponding to the plaque density surrounding the TF implants **(Figure 4.4.2A)**. Fluorescence measurements suggest a small decline throughout each 2-hour recording that was boosted to a near-consistent level following Methoxy-x04 injection **(Figure 4.4.2B)**. Therefore, injecting Methoxy-x04 at 24-h intervals may be a reasonable re-dose approach for longitudinal recordings. However, it is important to note that we have not confirmed that the decline seen across days is due to bleaching. Additionally, there is a lack of knowledge surrounding the binding and bleaching properties of Methoxy-x04. Therefore, another potential possibility for the slight decline in fluorescence could be that repeat dosing of Methoxy-x04 is occupying all binding sites, with an irreversible binding property preventing further signal illumination. Alternatively, consistent illumination could cause bleaching but not dissociation of Methoxy-x04, blocking binding sites for the re-dosed molecule. Lastly, Methoxy-x04 may bind differently to different sized plaques. Overall, while we are able to detect depth-resolved changes in fluorescence that appear reflective of the plaque load within the brain, it is vital to uncover more information on the binding and bleaching characteristics of Methoxy-x04 to implement a reliable re-dosing protocol.

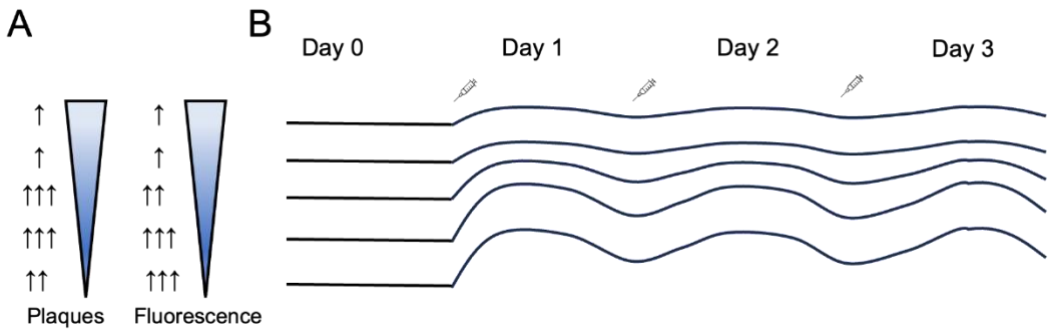

Figure 4.4.2. Suggested re-dose profile of Methoxy-x04 based on acquired data. (A) Schematic illustrating an estimate of the plaque load and fluorescence level along the TF. (B) Schematic showing a summary of the re-dose findings. Not to scale.

4.4.1.4 Correlating TF photometry data to histology proves challenging

After identifying optimal protocols for acquiring and analysing TF photometry data, while detecting plaque signals, we wished to confirm TF data was reflective of plaque pathology within the brain regions recorded **(Figures 4.3.16-19)**. Across all light protocols and analytical approaches, the i*n vitro* with Norm or Model methods showed similar patterns of fluorescence across depth to histological quantification. However, the fluorescence and histological profiles were shifted across depths, resulting in correlation analysis being poor **(Figures 4.3.16-19).** Instead of implying that photometry data is not reflective of plaque pathology, we believe these inconsistences are largely contributed to by the correlation approach. For example, the photometry data and histological quantification may be irreflective of the final recording state (see **section 4.4.2.2**). Therefore, by optimising this analytical process, we believe strong positive correlations of *in vitro*, Norm data with histological quantification will be shown.

4.4.2 Limitations

While we confirmed that this novel approach is feasible for monitoring plaque pathology, there are several limitations with the equipment and analysis that should be noted.

4.4.2.1 System limitations

Firstly, the TF system included a laser for 405-nm illumination, which proved to greatly influence system stability as they require appropriate cooling and stabilisation tools. For example, within several months, the original laser started to rapidly decline in power. After implementation of the new laser, with appropriate cooling conditions, we continued to see both low (minutes-days) and high (milliseconds) frequency instability. Therefore, each recording point had instable laser power,

as well as alterations seen across recordings. In attempt to counteract and monitor this, the laser was left on for 30-minutes before recordings, a photodetector was introduced to monitor the output of the laser and the number of repetitions of illumination protocol was increased to calculate a better median signal. Potentially, this high frequency instability is due to the way the laser is driven. Currently, the laser is driven by the NIDAQ, which may introduce instability across the voltage supply. Therefore, introducing a voltage modulator may decouple noise from the NIDAQ from noise within the laser. To minimise low frequency noise a feedback loop, could be implemented, done by Pisano and colleagues (Pisano et al., 2019), where the laser power is adjusted in real-time to keep laser output stable.

As well as the optical components functionality, their general AF proved a vital obstacle for TF recordings. The time resolution of our expected Methoxy-x04 signals matched the AF recovery, introducing difficulties determining the difference between Methoxy-x04 signals and AF **(Figure 4.3.2)**. The main source of AF recovery was the patch cable as light propagates at several angles along the cable which illuminates the internal cladding **(Figure 4.2.5)**, resulting in AF. Due to light at high GVs reflecting along the patch cable more often, AF was increased. To minimise this, a bleaching protocol was implemented, the length of patch cable was reduced to minimise internal reflectance, and baseline day 0 recordings were completed.

Finally, despite TFs being less invasive than conventional FFs (Pisanello et al., 2017, Pisano et al., 2019), implanting any foreign object into the brain will result in neuroinflammation. Hence, microglia will aggregate around the TF. Microglia and plaques are highly correlated, with microglia being involved in plaque clearance and once overwhelmed, further aggregation of plaques (Heneka et al., 2015a, Hickman et al., 2018, Malm et al., 2015, Mrak, 2012). Therefore, our plaque pathology measure may be influenced by the inflammatory condition surrounding the TF. Post-mortem histology illustrates the aggregation of microglia, but it is unclear if plaque pathology is increased around the TF. Notably, off-target TF implants have microglia accumulation around the fibre track, with minimal plaque pathology, which may suggest that microglia recruitment did not greatly influence plaque pathology at the TF track. In all, this is an important consideration when completing longitudinal recordings.

4.4.2.2 Analysis limitations

While a benefit of TFs is their minimally invasive tip (Pisanello et al., 2017, Pisano et al., 2019), this made identifying the TF track on histological images challenging. For acute experiments, we failed to identify the fibre track despite using thinner histological sections (50-µm) and imaging at X10 magnification. However, for chronic implants, counter-staining histological sections with a microglial marker allowed identification of the fibre track due to neuroinflammation surrounding the

implant. While this illustrated the fibre tip, we had to estimate the active region of the track using scale bars, with manual marking onto the aligned section. This may introduce some error when identifying the fibre track. These limitations coincide with limitations previously discussed with the alignment approach, where section warping can contribute to inaccurate fibre track estimation **(**see **section 3.4.2.2)**.

While we aimed to target the TF across the same regions in every mouse, some implants were slightly off-target **(Figure 4.3.3)**. Therefore, some TFs pass different brain regions, resulting in varied plaque density across TF depth across mice. For example, while most of the TF implants have greatest plaque density at lower GVs, a small minority do not replicate this trend **(Figure 4.3.3)**. Currently, data is analysed by combining all recordings, without considering these alignment differences. Therefore, a reduction in depth-resolution fluorescence may occur, resulting in false-negatives. For example, while pharmacokinetic **(Figures 4.3.4-6)** and re-dose **(Figures 4.3.10-12)** experiments show a trend of increased signal intensity at deeper regions, the lack of strong significance across appropriate time-points may be contributed to by this analytical approach.

On another note, AF proved to be a major influence on signal collection. Therefore, we implemented a modelling approach to extract pure Methoxy-x04 signals by estimating the AF throughout each recording **(Figure 4.2.17)**. This model assumed that the day 0 recording provides an estimate of AF from the brain tissue, patch cable and TF, with some unknown noise, not accounting for day-to-day changes. Additionally, the requirement of using the appropriate day 0 recording limits the quantity of training data for the model. While we sub-sampled this data to increase the number of training iterations, more training data is optimal to achieve a better model fit.

Finally, correlating with histological signals is vital for full confirmation of this approach. However, our histology correlation analysis showed poor correlation between photometry and histological data **(Figures 4.3.16-19)**. We believe this is highly contributed by the plaque and histological data used for analysis. Firstly, photometry data was quantified from the last pharmacokinetic recording completed on each mouse. However, most mice were kept for several weeks after their last pharmacokinetic recording. Thereby, this may not be reflective of the final plaque state. However, the final recording for each mouse varied meaning taking data from another recording would not be reflective across all mice. Secondly, light distributes from the TF in a downwards and vertical manner, with higher GVs providing a cone of light that passes over the TF shaft **(Figure 4.2.2).** With this approach, plaques are quantified from a uniform $5x10^6$-μm^3 cylinder (radius: 200-µm, height: 40.5-µm) at each depth. Therefore, some plaques may not be quantified that were likely to have been recorded by photometry. Accordingly, an approach to counteract these limitations could

be by calculating the volume of the light cone for each TF and quantifying plaques within this region.

4.4.3 Future work

Overall, this approach appears to be an exciting step towards real-time, depth-resolved plaque monitoring in freely behaving animals. Using this will help interrogate many aspects of AD. Particularly, we believe this will allow assessment of potential AD treatments, encouraging the progression of treatments to a clinical setting. For example, the use of non-invasive 40-Hz sensory stimulation, known as GENUS, has gained traction with evidence pointing towards potential plaque-modifying effects (Iaccarino et al., 2016, Martorell et al., 2019). However, a recent study contradicts these findings (Soula et al., 2023), which may be contributed to by the lack of technology for monitoring the effect on plaque pathology in real-time, across depth. Therefore, we believe that investigating novel treatments like GENUS, will help uncover potential plaque-modifying effects in regions and at time-points that have previously been missed. Consequently, this helps establish a closed-loop treatment paradigm where once an effective approach has been identified, optimal parameters can be tested to result in optimal disease treatment.

4.4.4 Summary

In conclusion, we have illustrated for the first time that TFs can allow real-time, depth-resolved plaque monitoring in freely behaving mice. We were able to optimise TF signal collection by identifying optimal light protocol and analytical approaches: *in vitro* and Norm. By doing so, we detected real-time, depth resolved Methoxy-x04 signals which uncovered important information about Methoxy-x04 for use in longitudinal recordings. This is the first technology with these capabilities, which will ultimately help gain knowledge about disease pathogenesis and treatment success on a greater scale. However, we note that further characterisation on the binding and bleaching properties of Methoxy-x04 is required, with optimisation of the correlation to histological plaque load to confidently conclude the signals are due to plaque pathology.

5. Investigation of the plaque modifying effects of GENUS on 5xFAD+ mice in real-time, across depth

5.1 Introduction

5.1.1 Background

We have confirmed, for the first time, that TF photometry and Methoxy-x04 can monitor plaques in freely behaving 5xFAD mouse models in a real-time, depth-resolved manner. Now, we wish to apply this approach to track plaque pathology while mice are exposed to a potential AD treatment. GENUS is a non-invasive sensory stimulation approach that has previously been shown to have beneficial effects at reducing plaque pathology (Adaikkan et al., 2019, Iaccarino et al., 2016, Martorell et al., 2019, Yao et al., 2020). However, recent studies contradict this finding (Soula et al., 2023), perhaps due to limitations with post-mortem plaque assessment or their singular sensory stimulus approach. Therefore, further study must be completed to understand the real-time effects of both singular and combined sensory stimulus treatments.

5.1.2 Aims and hypotheses

Within this chapter, we hypothesised that our novel approach allows monitoring of plaque pathology modifications caused by GENUS treatment. To test this hypothesis, we aimed to expose AD models to various forms of GENUS treatment to monitor changes in electrophysiological and plaque pathology. For this, we confirmed the enhanced power of gamma oscillations by monitoring electrophysiological signals in response to GENUS. Then, we investigated if plaque pathology modifications were detected using both TF photometry and histological quantification. Throughout, we investigated the potential for combined sensory treatment to have stronger effects than a singular sensory treatment.

5.1.3 Overview

Within this chapter, I will begin by discussing the methodology of the experiments completed to attain the following results **(section 5.2)**. Then, we report increased gamma power detected from electrophysiological signals **(section 5.3.2)**. Once confirmed, we investigated the potential changes in plaque pathology throughout each treatment using our novel TF photometry and Methoxy-x04 approach **(section 5.3.3)**. To confirm the findings from photometry recordings, histological analysis was completed to determine the differences of plaque load in 5xFAD mice

that underwent GENUS or not **(section 5.3.4)**. Finally, we discuss the implication of these findings, limitations of this study and future directions for this treatment and monitoring approach **(section 5.4)**.

5.2 Methods

This section provides a detailed description of the GENUS treatment and TF photometry recordings completed to test for potential disease-modifying effects **(Figure 5.2.1)**. Firstly, I introduce animals used, the chamber they were situated in for GENUS and the GENUS system set-up **(section 5.2.1)**. Then, electrophysiological recordings are introduced, with information on the surgery **(section 5.2.2.1)**, recording **(section 5.2.2.2)**, data analysis **(section 5.2.2.3)** and completed statistics **(section 5.2.2.4)**. Lastly, GENUS and TF photometry experiments are described, specifically the recording **(section 5.2.3.1)**, data analysis **(section 5.2.3.2)** and statistics **(section 5.2.3.3)**. All protocols completed across various sub-projects, such as Methoxy-x04 properties, animals and histological processing are discussed in **Chapter 2, sections 2.1.1, 2.1.2** and **2.1.3**, respectively. Information on the TF system and subsequent data analysis is discussed in **Chapter 4**, **sections 4.2.1** and **4.2.3**, respectively.

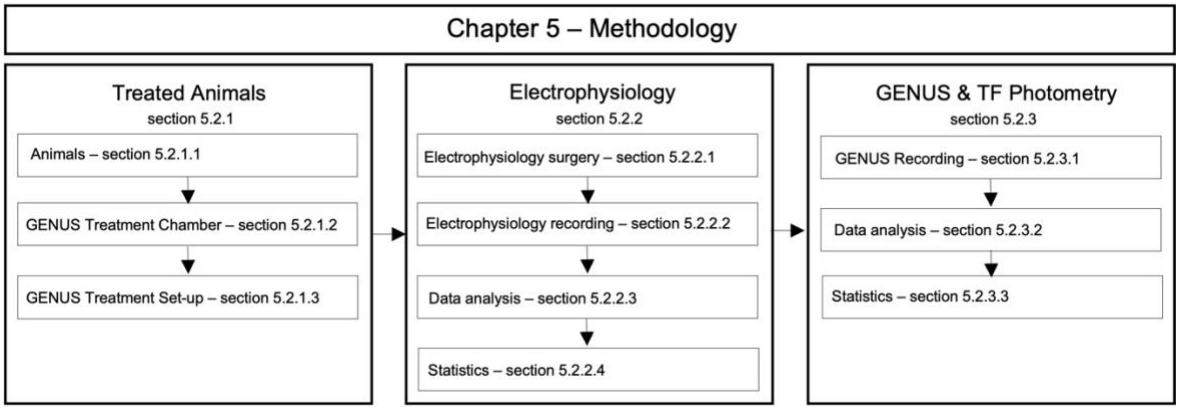

Figure 5.2.1. Roadmap of chapter 5 methodology. Animal information is covered in **section 5.2.1.** Electrophysiology procedures are described in **section 5.2.2.** GENUS & TF photometry procedures are described in **section 5.2.3.**

5.2.1 Treated Animals

Mice used for GENUS experiments had been previously used for chronic recordings described in **Chapter 4, section 4.2.2.3** and shown in **Figure 4.2.10** and **Table 4.2.1**. As before, all *in vivo* measurements were completed in dark conditions.

Mice were aged between 4-6-months consistent with previous GENUS studies which show a significant decline in plaque pathology (Iaccarino et al., 2016, Martorell et al., 2019).

As previous studies have illustrated that a chronic treatment paradigm of GENUS for 1-h per day for 7-days appears to have a more aggressive effect at modifying plaque pathology, we initially had planned to use our novel approach to investigate the real-time effects of this chronic treatment. However, time constraints meant that was not possible. Additionally, as discussed in **Chapter 4**, we require a deeper insight into the signals achieved following chronic re-dosing of Methoxy-x04. Therefore, we opted for an acute treatment paradigm of GENUS for 1-h on 1-day, which previously has been shown to reduce soluble Aβ levels (Iaccarino et al., 2016), with more recent findings illustrating a reduction of plaque size with combined audio-visual treatment (Murdock et al., 2024).

5.2.1.1 Animals

Detailed animal information can be found in **Chapter 2, section 2.1.2**. Mice used for GENUS experiments were previously used for other chronic experiments, with detailed information on the fate of each mouse shown in detail in **Table 4.2.1.** A total of 12 mice underwent GENUS treatment & TF photometry recordings **(Table 4.2.1 & Figure 4.2.10 & Figure 5.2.2)**. Out of the 12 mice, 6 were 5xFAD+ and 5xFAD-, with all 5xFAD+ mice going through all treatments. GENUS treatment for 5xFAD+ mice was either visual (V), auditory (A), audio-visual (AV) or no stimulation (NS), while 5xFAD- mice underwent AV stimulation only **(Figure 5.2.2)**. GENUS experiments involved fibre photometry recordings within a chamber before brain tissue was recovered for post-mortem analysis.

Additionally, six mice were used for electrophysiology recordings: 3 5xFAD+ and 3 5xFAD- **(Figure 5.2.2 & Table 5.2.1)**. These were different mice compared to any fibre photometry experimental mice and had cortical EEG and hippocampal (HIP) bipolar electrodes implanted to monitor neuronal signals **(**see **section 5.2.2)**.

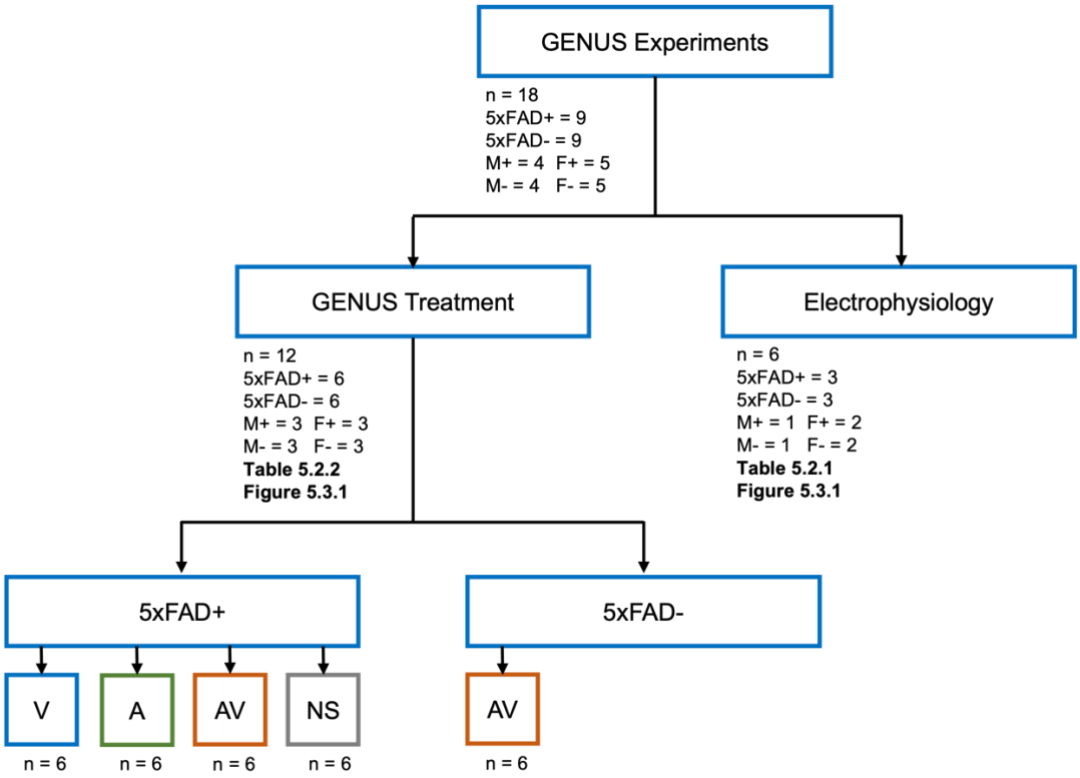

Figure 5.2.2. Flow chart illustrating the number of animals used per recording. Sex sample numbers are shown. Figure and table numbers show summary plots of animals. M+, 5xFAD+ male. F+, 5xFAD+ female. M-, 5xFAD- male. F-, 5xFAD- female.

5.2.1.2 GENUS treatment chamber

Mice were placed in a transparent recording chamber (30 x 14-cm), with all walls lined with black tape (727-1300, RS Components). This had a white LED strip (WOWLED) covered with several layers of tracing paper (to reduce and spread the light intensity) along the transparent floor, providing a visual intensity ranging from 280-450-lux, when driven at 5-V (described in **section 5.2.1.3**), confirmed with a light meter (Urceri). An electrostatic speaker (ES1, Tucker-Davis Technologies) was situated on the centre of the long chamber wall, 20-cm from the chamber floor and produced broadband noise at 70-dB SPL, by providing variable voltage signals to the speaker at 0.77-V root-mean-squared (RMS) (as described in **section 5.2.1.3**).

5.2.1.3 GENUS treatment set-up

GENUS treatment was either V stimulation with light flicker generated by LEDs (WOWLED), A stimulation generated by a speaker (ES1, Tucker-Davis Technologies) or AV stimulation with both LED and speaker activation in parallel. Both A and V stimulation was delivered with a pulse frequency of 40-Hz with a 50% duty cycle (10-kHz). For AV stimulation, both LEDs and speakers

were driven as described in parallel. A stimulation of 40-Hz at these intensities was chosen consistent with previous studies that show a frequency-specific reduction in plaque pathology at 40-Hz (Iaccarino et al., 2016, Martorell et al., 2019).

For light flicker generation, an LED strip was used (WOWLED). This was controlled by an NIDAQ (USB-6343, National Instruments), breadboard, power supply and electrical components **(Figure 5.2.3A)**. This was completed as the NIDAQ alone cannot provide enough current to the LEDs for sufficient brightness. First, a 5-V power supply (RS components) was attached to the breadboard. However, this power supply was tightly controlled using a MOSFET driver (BSS-138, RS Components), a gate resistor (1-kOhm, RS Components) and pull-down resistor (10-kOhm, RS Components). Specifically, the gate resistor is situated between the NIDAQ output and MOSFET, and prevents overcurrent from the NIDAQ, which can damage the NIDAQ or MOSFET **(Figure 5.2.3A)**. 1-kOhm was chosen to reduce the current to a safe range of a few milliamps. The pull-down resistor works as the switch to the MOSFET, where when the NIDAQ is connected, the MOSFET is on and allows current flow, turning the LEDs ON **(Figure 5.2.3B)**. However, if the NIDAQ is not connected, the MOSFET remains off and prevents current flow, with LEDs remaining OFF **(Figure 5.2.3C)**. 10-kOhm was chosen as it is sufficiently higher than the 1-kOhm gate resistor, so when the NIDAQ pin is powered, there will be sufficient voltage at the MOSFET gate pin and the MOSFET will switch on. If the pull-down resistor value is not high enough, it's possible when the NIDAQ pin is powered the MOSFET will remain off as there is insufficient voltage at the MOSFET gate (MOSFET requires that a threshold voltage is reached at the gate before switching on). Square wave pulses were created for LED stimulation at 5 V, providing a visual intensity ranging from 280-450-lux, confirmed with a light meter (Urceri). The light was controlled through NI-DAQ (USB-6343, National Instruments), using a LABVIEW program (2022 version, National Instruments).

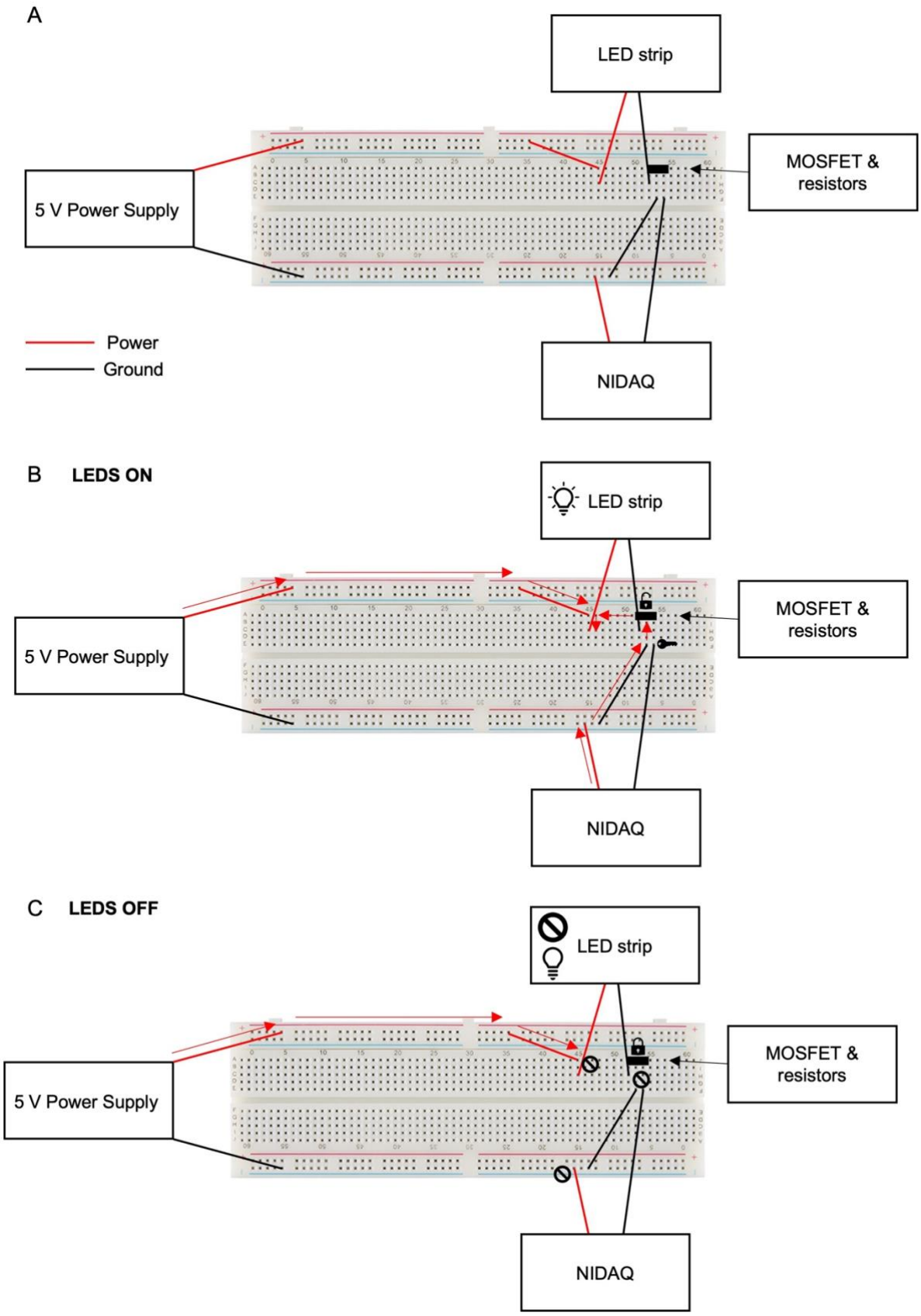

Figure 5.2.3. LED strip set-up. (A) Electrical breadboard set-up. NIDAQ connections release the resistor gate on the MOSFET to turn it on, allowing the release of 5-V power supply to turn on the LED strip. (B) For LEDs on, the NIDAQ connection acts as the key to unlock the gate on

the MOSFET. Therefore, it will allow the 5-V power supply to provide current to the LED strip. (C) For LEDS off, there is no NIDAQ connection so the MOSFET remains locked, and the 5-V power supply will not reach the LED strip. Black and red lines show wired connections on the breadboard. Arrows illustrate the direction of power flow through the breadboard.

For sound generation, the speaker was calibrated before recordings were completed using a microphone and speaker. The microphone (PS9200KIT-1/4, ACO Pacific Inc) was placed the same distance as the speaker to the recording chamber floor (20-cm). Then, broadband noise and pure tones were played at varying intensities (decibel sound pressure level (dB SPL)), driven at 1-V. The sound (broadband white noise) was generated by NIDAQ (USB-6343, National Instruments) and amplified (System 3 ED1, Tucker-Davis Technologies) before being transmitted to the speaker (ES1, Tucker-Davis Technologies), controlled using a LABVIEW program (2022 version, National Instruments). The sound was recorded by a microphone (PS9200KIT-1/4, ACO Pacific Inc), before being amplified (System 3 MA3, Tucker-Davis Technologies) and recorded by NIDAQ (USB-6343, National Instruments), controlled using a LABVIEW program (2022 version, National Instruments). This allows estimation of the V-dB SPL relationship, producing a list of voltages that represent the root-mean-squared (RMS) of a broadband noise, that would produce each sound intensity. Accordingly, this information was used to determine the driving voltage of the speaker. To produce broadband noise at 70-dB, we found that we needed to provide variable voltage signals to a speaker at 0.77-V RMS. Therefore, during A stimulation, sound (broadband white noise) was generated by NIDAQ (USB-6343, National Instruments) and amplified (System 3 ED1, Tucker-Davis Technologies) before being transmitted to the speaker (ES1, Tucker-Davis Technologies), controlled using a LABVIEW program (2022 version, National Instruments).

5.2.2 Electrophysiology

Electrophysiology recordings were completed to confirm our set-up was causing an increase in gamma power throughout GENUS treatment. For this, we used mice also being used for a sleep project being completed by Paulina Schnur, where a cortical EEG was placed above the prefrontal cortex and a bipolar electrode within the CA1. Therefore, these brain regions were different from those targeted with the TF. However, as this implant can provide a general overview of the oscillatory state within the prefrontal cortex and hippocampus, this allows us to compare to previous papers which show that when there are changes in gamma power in these areas, there appears to be a consistent increase in the appropriate sensory cortex (Adaikkan et al., 2019, Iaccarino et al., 2016, Martorell et al., 2019, Soula et al., 2023). Therefore, this suggests that if the oscillation is seen in the prefrontal cortex and hippocampus, it should be present at our TF target, the visual cortex and subiculum.

5.2.2.1 Electrophysiology head-cap surgery

For electrophysiological recordings, a head-cap surgery was completed for implantation of a bipolar electrode into the HIP, plus attachment of 2 cortical EEGs, 2 electromyography (EMG) connections and grounding wires **(Figure 5.2.4)**. This was to allow for monitoring of neuronal signals across the prefrontal cortex and hippocampal regions. Electrophysiological head-cap surgeries were completed by Paulina Schnur, with electrophysiological recordings completed by Paulina Schnur and Nicole Byron.

5.2.2.1.1 Connector fabrication

A connector was custom-made to allow for 2 EEG, 2 EMG and two grounding connections on the brain surface using three 2-row connectors (SDL-112-T-12, Semtec) **(Figure 5.2.4C)**. First, two copper wires (⌀ 0.2-mm diameter, 357-918, RS-Pro) were prepared for cortical EEG (length: 1.5-cm) and for grounding (length: 1.5 & 1-cm) by stripping them of their insulation at either end over 0.3-cm. One ground wire was being used, with one prepared as a back-up in case of a faulty connection. Next, two wires were prepared for EMG connections (2840/7, Alpha Wire) (length: 1.5-cm), before stripping them of their insulation at either end over 0.3-cm. Once completed, each wire was connected to one connector pin by soldering. Then, all connections and wires were insulated using dental cement (Simplex rapid liquid and powder mixed, Kemdent) **(Figure 5.2.4C)**. Electrical connections from the stripped end of the wire to the connector were checked using a voltmeter.

5.2.2.1.2 Electrode fabrication

A bipolar electrode involves monitoring signals from two wires, where one is slightly shorter than the other **(Figure 5.2.4C)**. Stainless steel wires (0.1-mm diameter, FE205850/2, Goodfellow) were prepared by cutting them to 1.5-cm and stripping them of their insulation by 0.3-cm on one end. The stripped ends were wrapped around one pin of two 1-row connectors (SS-132-T-2-N, Semtec) before being covered with silver conductive paint (186-3593, RS-Pro) and secured with dental cement (Simplex rapid liquid and powder mixed, Kemdent) once dry. Next, the steel wires were superglued (918-6872, RS-Pro) together in a twisted conformation, leaving the tips free. At this point, one wire was trimmed to create a 0.1-cm offset **(Figure 5.2.4C)**. After completion, impedance was measured and if within the 100-200-kOhm range, they were deemed appropriate for use.

5.2.2.1.3 Surgery

5xFAD+ and 5xFAD- littermates underwent electrophysiology head-cap surgery from 3-4 months. Mice housed together underwent surgery on the same day. After surgery, mice were housed alone. On the day before surgery, the surgeon's gowns, and tools, including the electrodes and EEG/EMG being implanted were autoclaved. On the day of surgery, surgical procedures were completed mostly as described in **Chapter 4, section 4.2.2.3.1**, bar described below.

Skull alignment between bregma and lambda was set <100 μm, before marking the bipolar electrode implant site, under a stereomicroscope (SZ51, Olympus). This was CA1 (AP: -2.00-mm, ML: 1.50-mm, DV: -1.50-mm) **(Figures 5.2.4A-B)**. Next, using surgical callipers, sites of skull screws were marked, and burr holes were completed using a surgical drill (Volvere Vmas drill, NSK). Two skull screws (418-7123, RS Components) were implanted above the prefrontal cortex on each hemisphere, for cortical EEG (AP: +1.50-mm, ML: 1:00-mm) **(Figures 5.2.4A-B)**. Two skull screws were implanted above the cerebellum on each hemisphere, as a ground (AP: -2.00-mm, ML: 2.00-mm) **(Figures 5.2.4A-B)**. The appropriate cortical EEG and ground wires from the connector were now wrapped around the cortical skull screws. At this point, connections were confirmed using a voltmeter. Then, the two EMG wires are implanted into the neck muscle. Following this, the stereotaxic holder with the bipolar electrode was mounted onto the stereotaxic frame (KOPF Instruments). The bipolar electrode was slowly lowered to the brain surface, before slowly descending to the target depth. Once reached, a small volume of Kwik-Sil (World Precision Instruments) was applied to cover the remaining exposed brain tissue using a toothpick.

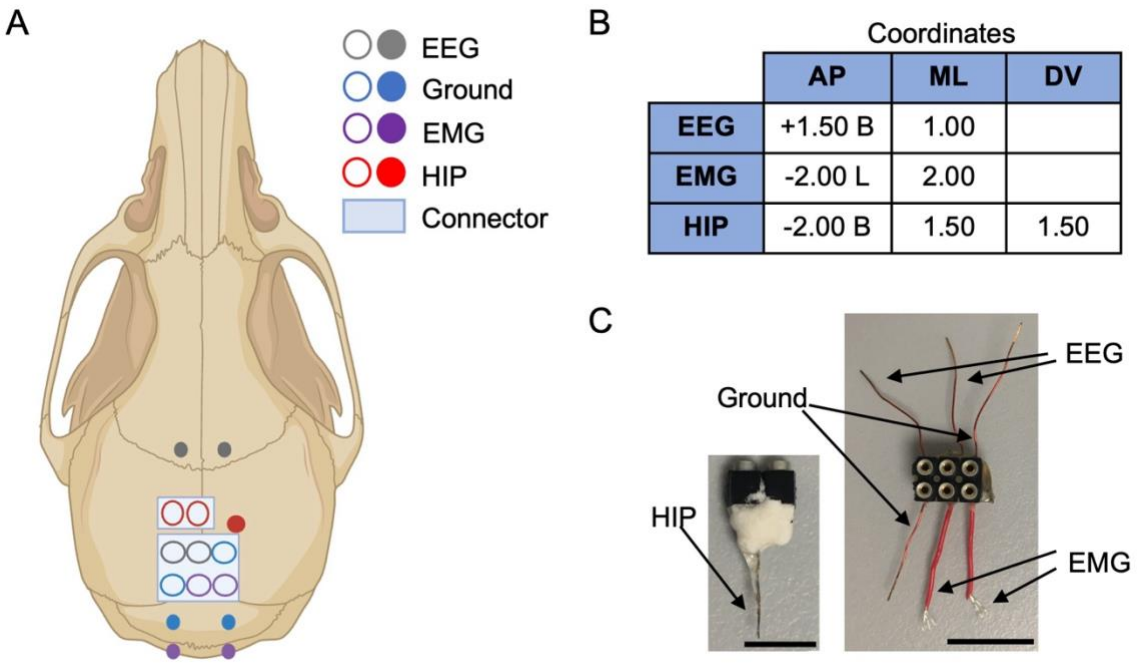

Figure 5.2.4. Implants for the head-cap surgery. (A) Schematic showing implants of the EEG, EMG, ground, and bipolar electrodes (HIP). (B) Exact coordinates for the implants in millimetres. B is from bregma, and L is from lambda. (C) Image of the bipolar electrode (HIP) (Scale: 0.5-cm) and EEG/EMG connector (Scale: 1-cm).

5.2.2.2 Electrophysiological recording

Table 5.2.1. Animals used for electrophysiological recordings.

Animals	Genotype	Sex	Age (mo)
E_1	+	F	4.6
E_2	-	F	4.6
E_3	-	M	5.4
E_4	+	M	5.4
E_5	-	F	5.4
E_6	+	F	5.4

Mixed-sex mice aged from 4-6-months were used for electrophysiological recordings **(Table 5.2.1)**. Before recordings, the mouse's head-cap was connected to a male 18-pin nano dual row connector (Omnetics), which is connected to a head-stage amplifier (HST/32V-G20, Plexon). Wires on this connector that matched appropriate channels on the head-stage amplifier were soldered to 2-row pin connectors and insulated with dental cement. A Plexon head-stage cable (ultra-fine 36 gauge, Plexon) connects the head-stage amplifier to a preamplifier (PBX3, Plexon), powered by power

supply (P38-5X, Polytron Devices). The amplified (1000 times) signals were relayed via a BNC interface board (BNC-16B, Plexon) and digitized using a NIDAQ device (USB-6211, National Instruments). Electrophysiological signals were recorded across 8 channels (2 EEG, 2 EMG, 2 HIP, A stimulation sync (speaker) and V stimulation sync (LEDs)) at 1-kHz, using the NIDAQ device (USB-6211, National Instruments), controlled by a LABVIEW program (2022 version, National Instruments). For appropriate shielding of the GENUS stimulation, the recording chamber, was placed within a grounded faraday cage (75 x 75 x 75-cm, metal mesh) **(Figure 5.2.5A)**. Additionally, mice were placed in an internal chamber (10 x 10 x 30-cm), surrounded in copper mesh, which was grounded **(Figure 5.2.5A)**. As an extra precaution real-time power density spectrum analysis was completed to ensure no noise was being detected across all recording channels.

Once the electrophysiology recording has begun, the GENUS stimulus protocol was started **(Figure 5.2.5B)**. This ran through A, V and AV stimulus in a randomised order, generated by the LABVIEW code. LEDs (WOWLED) and the speaker (ES1, Tucker-Davis Technologies) were driven at 5-V and 0.77-V respectively, providing 280-450-lux and 70-dB SPL as in GENUS treatment recordings. This was maintained by removing some layers of tracing paper from the top of the LED strip to boost light intensity and placing the electrostatic speaker within the internal chamber. Stimulus was delivered with a pulse frequency of 40-Hz, and a 50% duty cycle (10-kHz). Each block included A, V and A+V stimulation with a 30-second baseline, 60-seconds GENUS stimulus for 5 repetitions **(Figure 5.2.5B)**. Once complete, the electrophysiology recording was stopped, and mice were removed from the chamber and returned to their home cage. Stimulus information was saved in an ASCII format as an .ord file containing a list of the block number, in block stimulation number and stimulation type. Electrophysiological data was saved in a 16-bit binary format as a .dat file. Both are used for off-line analysis and data was analysed as described in **section 5.2.2.3**.

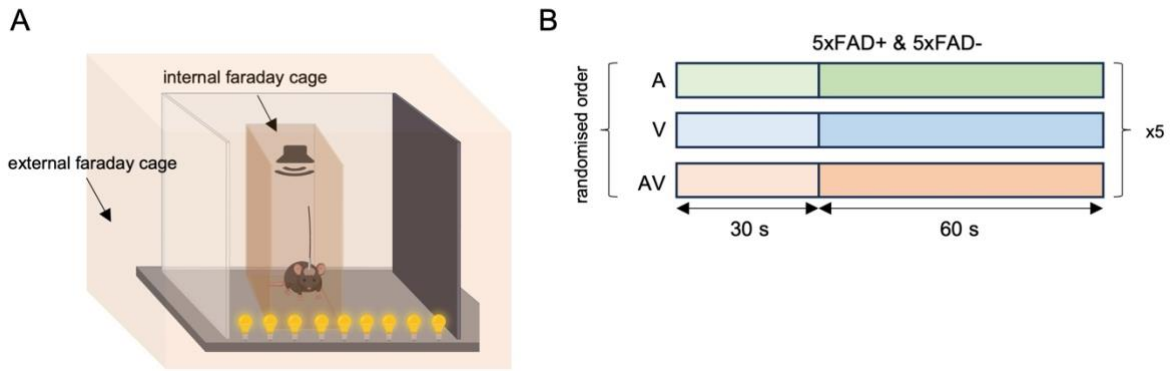

Figure 5.2.5. Electrophysiology recording paradigm. (A) Recording chamber. The GENUS treatment chamber was placed within a large external faraday cage. Mice were placed inside

the GENUS treatment chamber within an internal faraday cage. (B) GENUS stimulation paradigm throughout electrophysiological recordings.

5.2.2.3 Data analysis

5.2.2.3.1 Pre-Processing

The recording .dat file was processed using a custom MATLAB code. Firstly, the .dat file was opened, converted to int16 and the appropriate channels were extracted: two EEGs, two EMGs, hippocampal bipolar electrode and sync channels for the speaker and LED. Next, stimulation ON periods were detected when the difference between sync channels was greater than or equal to 0.5-V, as the driving voltage for both was above this threshold. These stimulation ON indexes were added to a matrix containing the stimulation information, extracted from the .ord file. Next, by determining the index on the matrix for each trial number and stimulation approach, signals were extracted from the appropriate channel from a time window of -5 to 65-seconds and sampling rate of 1000-Hz. Then, to combine data across all trials to enhance the effects seen, the mean data across trials was calculated before saving the final data matrix. Baseline data was the electrophysiological data from the appropriate channel from the start of recording until the data point before the first stimulation ON period. Lastly, data was combined into a matrix for all recordings.

5.2.2.3.2 Data analysis

Firstly, we wanted to determine the PSD change throughout each GENUS treatment. Accordingly, power spectral analysis was completed on all V, A and AV data, to determine any changes in the power of 40-Hz frequency bands, as shown in **Figures 5.3.2C-D**. First, for each mouse, power spectral analysis was completed to determine the baseline power spectral density (PSD) across a global frequency: 1-100-Hz. Then, the same was completed to determine the change in target frequency using a frequency range of 35-45-Hz. Then, we normalised the PSD with the following z-scored approach to account for variations in signal baseline:

$$Normalised\ PSD = \frac{PSD_{Target} - mean(PSD_{Global})}{std(PSD_{Global})}$$

This allowed detection of small changes in neuronal activity from the baseline signal. After, the mean and SEM of normalised PSD across all mice was calculated.

Secondly, we examined the change in PSD across several frequencies for each treatment. Accordingly, power spectral analysis was completed on all V, A, AV, and baseline data, to determine any changes in power of frequency bands, as shown in **Figures 5.3.2E-J**. First, for each

mouse, power spectral analysis was completed to determine the baseline PSD across a global frequency: 1-100-Hz. Then, the same was completed to determine the change in frequency using a frequency range of 10-60-Hz. Then, we normalised the PSD with the equation shown above to account for variations in signal baseline. After, the mean and SEM of normalised PSD across all mice, or 5xFAD+ mice and 5xFAD- mice separately, was calculated.

Thirdly, we wished to quantify the differences in 40-Hz power across GENUS treatments, for all mice, or 5xFAD+ mice and 5xFAD- mice separately, as shown in **Figures 5.3.2E-J**. Therefore, for each mouse, power spectral analysis was completed to determine the baseline PSD across a global frequency: 1-100-Hz. Then, the same was completed to determine the change in target frequency using a more specific frequency range of 39.9-40.1-Hz. Then, we normalised the PSD with the z-scored calculation shown above. After, the mean and SEM of normalised PSD across all mice, or 5xFAD+ mice and 5xFAD- mice separately, was calculated.

5.2.2.4 Statistics

All statistical analysis was completed on MATLAB. Significance was set as $\alpha = 0.05$, with p-values coded as follows: $p < 0.001$ (****), $p < 0.005$ (***), $p < 0.01$ (**), $p < 0.05$ (*), ns not significant.

Shapiro–Wilk tests was completed on 40-Hz PSD data to check the normality and therefore, was statistically tested using the One-Way ANOVA test. If $p < 0.05$, post-hoc multi-comparisons with Bonferroni corrections were completed.

5.2.3 GENUS Treatment & TF Photometry

5.2.3.1 GENUS recording

Table 5.2.2. GENUS treatment parameters. Target site is the TF implant coordinates. Number of recordings for each treatment are shown for auditory (A), visual (V), combined (AV) and no stimulation (NS), arranged in their completed order. The last treatment completed for histological comparison is shown under histology group. Parameters that varied across recordings are noted. Power is the desired laser power. Repetitions is the number of illumination protocols completed per measure. Day 0 recording was a baseline recording with no Methoxy-x04. Y is yes and N is no. Post-baseline duration is the length of recording after GENUS treatment.

Animals	Genotype	Sex	Target Site	Treatment	Age (mo)	Histology group	Power (μW)	Reps	Day 0 recording	Post-baseline duration (mins)
FAD60	-	F	2	AV	4.93	AV	60, 80, 100, 120	3	Y	30
				AV	5.95					
FAD61	-	M	2	AV	6.02	AV	60, 80, 100, 120	3	Y	30
FAD62	+	M	2	NS	4.54	AV	60, 80, 100, 120	3	Y	30
				A	4.67					
				AV	4.93					
				V	5.88					
				AV	6.02					
FAD63	+	F	2	NS	4.54	AV	60, 80, 100, 120	3	Y	30
				A	4.67					
				AV	4.93					
				V	5.88					
				AV	5.95					
FAD64	-	F	3	AV	4.70	AV	80, 100, 120, 140	5	N	60
FAD65	+	F	3	A	4.70	NS	80, 100, 120, 140	5	N	60
				AV	4.83					
				V	4.93					
				NS	5.03					
FAD66	-	M	3	AV	4.70	AV	80, 100, 120, 140	5	N	60
FAD67	+	M	3	V	4.83	AV	80, 100, 120, 140	5	N	60
				NS	4.93					
				A	5.06					
				AV	5.26					
FAD70	-	F	3	AV	5.69	AV	80, 100, 120, 140	5	N	60
FAD71	+	F	3	V	5.52	NS	80, 100, 120, 140	5	N	60
				A	5.59					
				AV	5.72					
				NS	5.79					
FAD72	+	M	3	AV	5.52	NS	80, 100, 120, 140	5	N	60
				V	5.59					
				A	5.72					
				NS	5.79					
FAD73	-	M	3	AV	5.79	AV	80, 100, 120, 140	5	N	60

After a pharmacokinetic protocol (described in **Chapter 4, section 4.2.2.3.2**) has been completed, mice were used for GENUS experiments **(Table 4.2.1)**. Treatments included V, A, AV, or NS. 4-6-month-old 5xFAD+ mice (JAX006554, The Jackson Laboratory) were exposed to all treatments in a randomised order and 5xFAD- mice were exposed to AV stimulation **(Figure 5.2.6C & Table 5.2.2)**. Recordings were blindly randomised by creating a recording schedule before any experiments began. Mice went through all stimulus options over several weeks, being immediately culled after the last session. The last session for 5xFAD- mice was AV and for 5xFAD+ mice was either AV or NS for histological comparison (described in **section 5.2.3.2.3**) **(Table 5.2.2)**.

On day 0, injection of 10-mg/kg of Methoxy-x04 (i.p.) (4920, Tocris) 24-hours before the recording protocol was completed **(Figure 5.2.6A)**. For 4 mice **(Table 5.2.2)** this injection was completed after a 2-hour TF photometry recording as a baseline with no Methoxy-x04 (Day 0). On day 1, baseline fibre photometry signals are recorded for 2-hours **(Figure 5.2.6A)**. Immediately after this recording, 10-mg/kg of Methoxy-x04 is injected (i.p.) before returning mice to their home cage. On day 2, the recording was completed throughout a treatment session. A treatment session involved a continuous TF photometry recording for a 30-minute pre-baseline, 60-minutes of treatment, with either 60- or 90-minutes of post-baseline **(Table 5.2.2) (Figure 5.2.6B)**.

Before each recording, the appropriate alignment and bleaching maintenance protocols were completed **(**see **Chapter 4, section 4.2.1.3)**. Additionally, the chamber was cleaned before and after each recording with disinfectant and 70% ethanol. Then, using the cannula holder (FCM13/M, Thorlabs), helping hand and haemostat, the mating sleeve (ADAL1-5, Thorlabs) was attached to the patch cable ferrule. Mice were head-fixed using the straw on their head-cap, for removal of the protective cap and attachment of the patch cable to the implanted TF. Then, mice were placed within the treatment recording chamber. Once the recording was complete, mice were scruffed and head-fixed, to remove the patch cable and attach the protective cap, before being returned to their home-cage. All recordings were completed in the dark, with only a red bulbed light. Throughout the recording, video monitoring via a webcam (Nulaxy), placed directly above the recording chamber was achieved. Using a custom LABVIEW code, a timelapse video was generated for each hour at 10 frames per second.

For baseline recordings, Day 0 (if completed) **(Table 5.2.2)** and Day 1 illumination protocols were as described in **Chapter 4, section 4.2.2.3.2** and shown in **Figures 4.2.16B and 5.2.2D** using the baseline LABVIEW VI. For Day 2 (the day of GENUS treatment) the illumination protocol during the pre- and post-baseline measurements **(Table 5.2.2)** were as described in **Chapter 4, section 4.2.2.3.2** and shown in **Figures 4.2.16B and 5.5.2D** using the baseline LABVIEW VI. However, for Day 2, the illumination protocol during the GENUS treatment was different **(Figure 5.2.2E)**.

Immediately after the pre-baseline measurement where the maximum duration of 30-minutes had been reached, the code automatically swapped to the treatment LABVIEW VI which starts the combined GENUS treatment and fibre photometry measure. Specifically, the treatment block involved activation of the chosen treatment approaches equipment (LEDs and/or speaker) as described in **section 5.2.1.3** for 300-seconds **(Figure 5.2.6E)**. Immediately after this 300-second treatment block, a TF photometry measure was taken which was the same illumination protocol as described in **Chapter 4, section 4.2.2.3.2** and shown in **Figure 5.2.6E** but for only one sampling iteration. After completion of this illumination protocol, the next treatment block begins, and this was repeated for 12 blocks. After the 12-block treatment series, the code automatically swaps back to the baseline LABVIEW VI, for post-baseline measurement, completed for either 30- or 60-minutes **(Table 5.2.2) (Figure 5.2.6E)**. The sampling interval for all of these recordings was 300-seconds. The baseline LABVIEW VI generated a .dat file for each photometry measure, with a text file containing time stamps of data collection. The combined treatment and photometry VI, LABVIEW generated a .dat file for each photometry measure, with a corresponding text file of the time stamp for each consecutive measure. Data was stored for offline analysis as described in **section 5.2.3.2**. Variation in recording parameters can be found in **Table 5.2.2.**

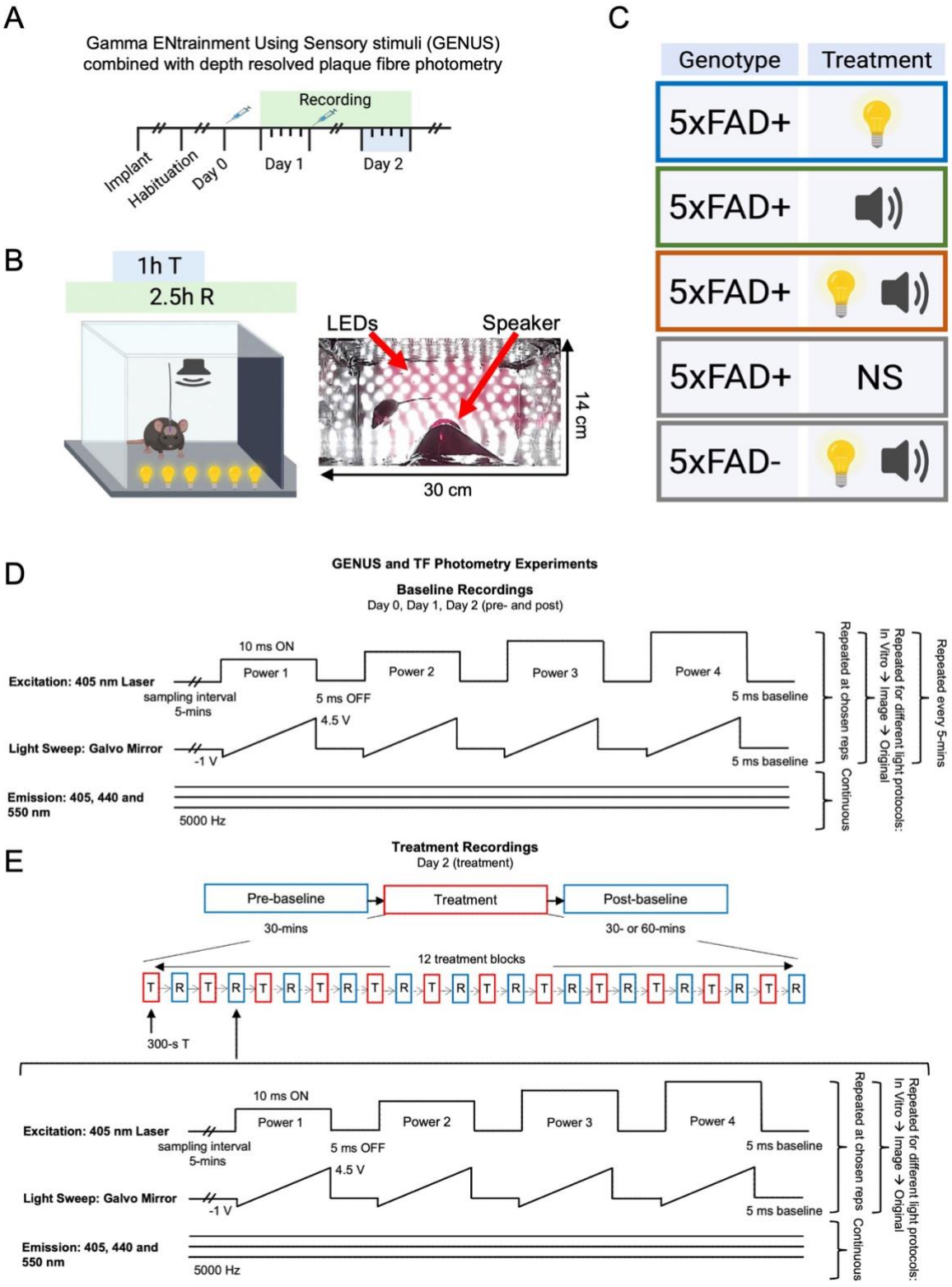

Figure 5.2.6. GENUS recording paradigm. (A) GENUS recording schedule. (B) Recording chamber and timings. (C) Treatment groups. Colours represent graph colours. Created on BioRender.com. (D) Illumination protocol for baseline recordings completed on day 0, day 1 and day 2's pre- and post-baseline measurement. (E) Recording and illumination protocol for treatment recordings completed on day 2. After a 30-minute pre-baseline recording, 12-

treatment blocks separated by a photometry measure was completed, followed by a 30- or 60-minute post-baseline recording.

5.2.3.2 Data analysis

5.2.3.2.1 Photometry analysis

Photometry data was processed as described in **Chapter 4, section 4.2.3.1.1 and 4.2.3.1.2.** For analytical approaches, data was normalised and modelled to the day 1 recording, not day 0.

For analysis, data at 120-µW and 440-nm was used, with galvo measures below 0-V removed. Additionally, as a result of **Chapter 4** findings, only *in vitro* and Norm data was presented. For summary analysis, data was extracted at time points of interest. Time points of 0, 15, 30, 45, 60, 75, 90, 105, 120, 135 and 150-minutes were taken from day 2. If data was missing at a time-point for a recording, data was NaN. Data was extracted at chosen GVs: 0, 1, 2, 3 and 4-V. Data was presented in boxplots to illustrate the distribution across recordings. Traces of the profile for each recording were presented on the same plots. A y-line at the value of the first fluorescence measure was plotted to show the change from baseline which was the fluorescence value at 0-minutes on day 2.

5.2.3.2.2 Histology correlation analysis

Image analysis was consistent with previously described methods in **Chapter 2, section 2.1.3**. Detection of the fibre track and correlative assessment was as described in **Chapter 4, section 4.2.3.2.** This data is shown in **Chapter 5, section 4.3.4**.

5.2.3.2.3 Histological Quantification

The treatment and fibre photometry paradigm for 5xFAD+ mice would end with exposure to either AV or NS to allow comparison of the difference of histological plaque load when mice had been exposed to GENUS treatment or not **(Figure 5.2.7 & Table 5.2.2)**. Therefore, only 3 5xFAD+ mice were histologically analysed for either the AV or NS group as we completed GENUS treatment experiments on a total of 6 mice. Otherwise, 5xFAD- mice would complete only AV **(Figure 5.2.7)**. After the last treatment session, mice were immediately culled by anaesthetic overdose and perfusion as described in **Chapter 4, section 4.2.2.4**, and underwent histological processing as described in **section 5.2.3.2.2** before histological quantification.

Histologically quantified plaque density using AMaSiNe was unable to be attained per brain region as we cannot estimate the volume of each brain region we have on our processed sections. Therefore, all quantification was completed using Fiji ImageJ. Two whole brain sections with the TF track were chosen for quantification for each mouse. Accordingly, the scale was set to micrometres and a region of interest (ROI) for each chosen brain region was made and the ROI area was determined using Fiji ImageJ's, 'Analyze > Measure' function. These were for the POST, pre-subiculum (PreS), SUB, lateral visual cortex (VISl), and primary visual cortex (VISp). Then, a threshold was set consistently across images before using the 'Analyze particles' function where we determined the plaque number for each ROI; excluding plaques < 10-µm. Lastly, the plaque density was determined by dividing the plaque number by ROI area. Data was presented on boxplots, with individual data points and mouse sex shown.

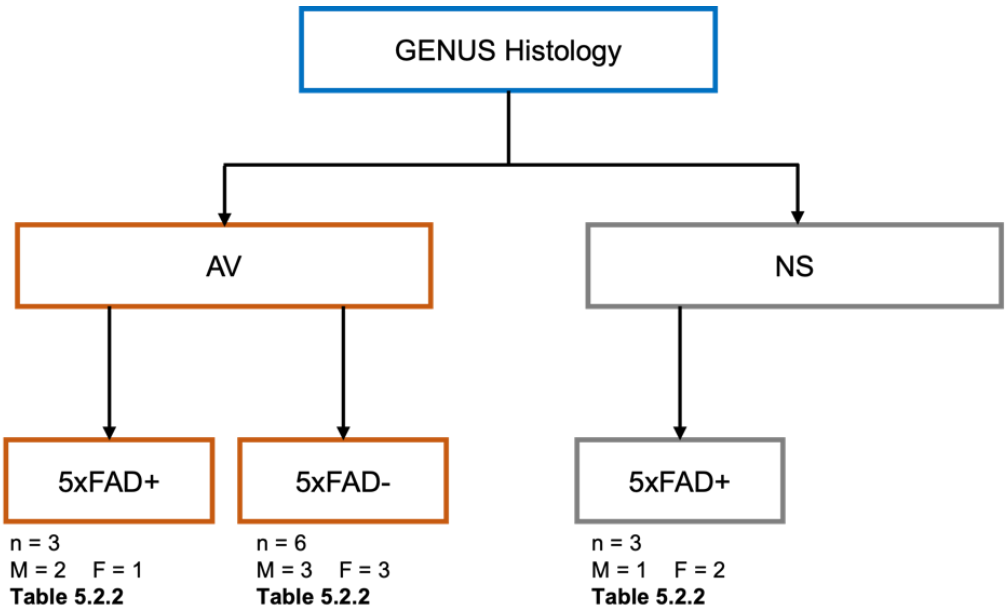

Figure 5.2.7. GENUS histology groups. 5xFAD+ mice underwent either AV or NS for their last recording before immediate perfusion. This decision was blindly randomised by creating the recording schedule before experiments were completed.

5.2.3.3 Statistics

All statistical analysis was completed on MATLAB. Significance was set as $\alpha = 0.05$, with p-values coded as follows: $p < 0.001$ (****), $p < 0.005$ (***), $p < 0.01$ (**), $p < 0.05$ (*), ns not significant.

Shapiro–Wilk tests were completed to check the normality of data. Photometry and histological quantification distribution was shown using boxplots. Photometry data was statistically tested using the non-parametric Kruskal-Wallis test. Histology quantification data was statistically tested using

the non-parametric Wilcoxon signed rank test. If $p < 0.05$, post-hoc multi-comparisons with Bonferroni corrections were completed.

5.3 Results

Therefore, we aim to use state-of-the-art TF photometry to allow *in vivo*, depth-resolved, real-time plaque monitoring in the freely behaving condition whilst mice undergo GENUS treatment. First, we began by confirming that GENUS treatment can enhance gamma power across three treatment approaches: V, A and AV sensory stimulus **(Figure 5.3.2)**. After this, we monitored plaque pathology before, during and after GENUS treatment using TF photometry **(Figure 5.3.3)**. Lastly, we confirmed findings by quantifying the histological plaque density across appropriate brain regions **(Figure 5.3.4)**.

5.3.1 Datasets and mice

Figure 5.3.1 shows animal information for TF GENUS experiments. Electrophysiological recordings were completed on an equal number of 5xFAD+ and 5xFAD- mice, aged from 4.5-5.5-months **(Figures 5.3.1A-C).** GENUS & photometry recordings were completed on mice aged from 4.5-6-months, with 6 mice used for each treatment group **(Figures 5.3.1D-F).** For histology quantification, 3 5xFAD+ mice had either AV or NS as their last treatment as described in **section 5.2.3.2.3 (Figures 5.3.1G-I)**.

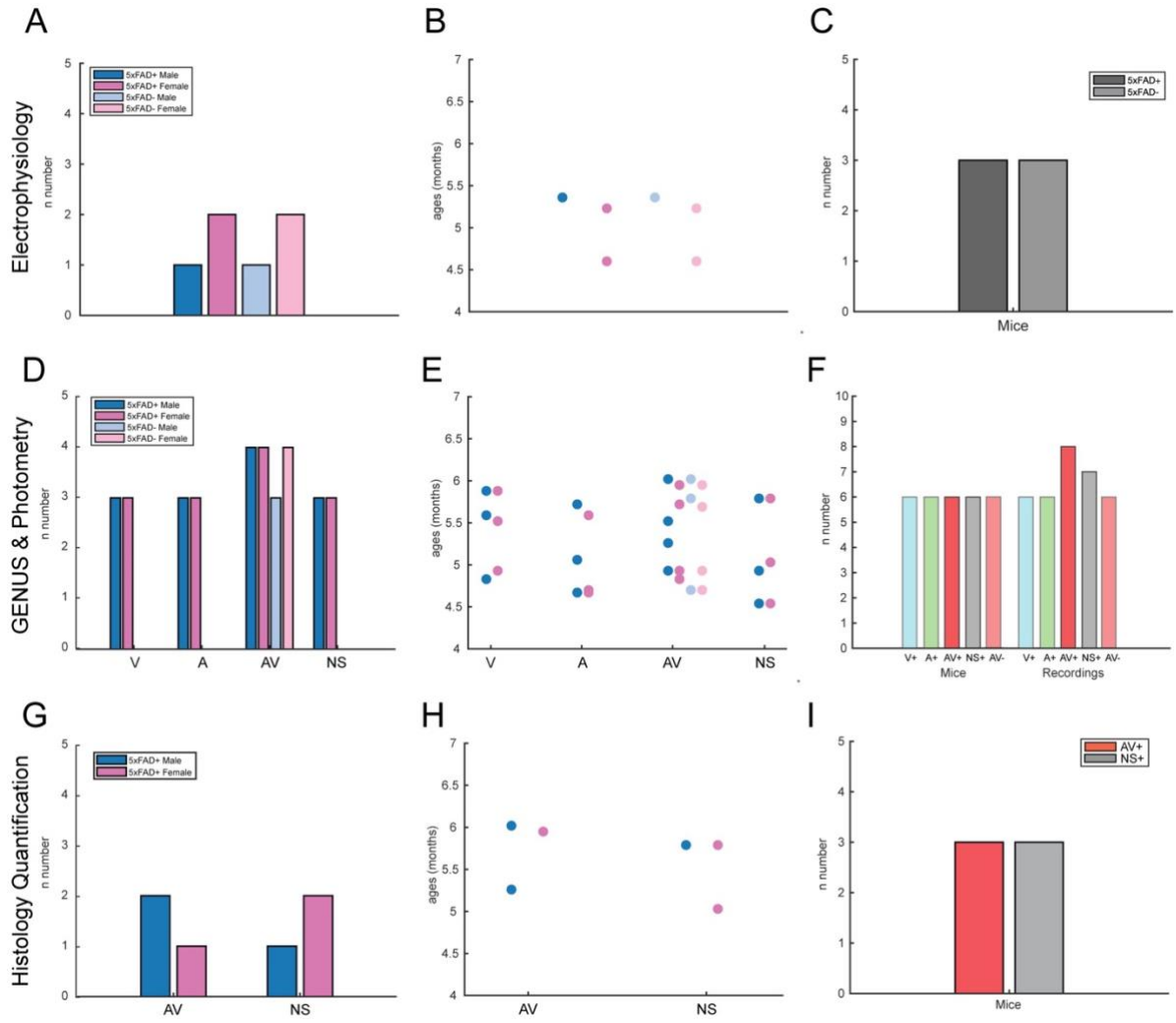

Figure 5.3.1. Sex, age, and genotype information for recordings completed and animals used for electrophysiological, GENUS & photometry and histology quantification analysis. Number of recordings and age of animals at each recording across sex and genotype for electrophysiology (A,B), GENUS & photometry (D,E) and histology quantification (G,H). Total sample number for mice or recordings for electrophysiology (C), GENUS & photometry (D) and histology quantification (I). Some mice were recorded from several times. V: visual; A: auditory; AV: auditory & visual; NS: no stimulus; +: 5xFAD+; -: 5xFAD-.

5.3.2 GENUS stimulus increases 40-Hz gamma power

To confirm if 40-Hz sensory stimulation can increase the power of gamma oscillations, we monitored electrophysiological signals from the prefrontal cortex (Cortical) and CA1 (hippocampal) by using implanted EEG screws and a bipolar electrode **(Figure 5.3.2A)**. Mice were placed within the recording chamber and two faraday cages to remove electrical noise caused by 40-Hz stimulation **(Figure 5.3.2A)**, before being exposed to all treatment options **(Figure 5.3.2B).** As seen in previous studies, we expected to see an increase in gamma power at the 40-Hz frequency

band, with a stronger response at cortical regions. Additionally, we examined if a combined stimulus approach could enhance this effect. Therefore, power spectral density analysis was completed.

Cortical electrophysiological signals show an increased power at 40-Hz for the duration of the treatment stimulus, with no increased power seen pre- or post-stimulus **(Figure 5.3.2C).** This trend is seen in hippocampal electrophysiological signals at a reduced intensity **(Figure 5.3.2D)**. Notably, the increased gamma power intensity varies across stimulus duration for both cortical and hippocampal signals **(Figures 5.3.2C-D).**

Interestingly, 40-Hz gamma power is increased during GENUS treatment, with NS resulting in no change in power at 40-Hz **(Figures 5.3.2C-J)**. Statistical tests on cortical electrophysiological signals show significant differences in 40-Hz power across treatment groups for all mice ($F(3) = 8.6362$, $p = 0.0007$, One-Way ANOVA) **(Figure 5.3.2E)** and 5xFAD+ ($F(3) = 10.7097$, $p = 0.0036$, One-Way ANOVA) **(Figure 5.3.2G)**, but not 5xFAD- ($F(3) = 3.5213$, $p = 0.0686$, One-Way ANOVA) **(Figure 5.3.2I)**. Notably, differences from post-hoc tests show a significant increase in 40-Hz gamma power for V ($p = 0.0383$ and $p = 0.0242$, post-hoc Bonferroni tests) and AV ($p = 0.0004$ and $p = 0.0040$, post-hoc Bonferroni tests) treatment, compared to NS for all mice and 5xFAD+ mice, respectively **(Figures 5.3.2E & G)**. However, no statistical differences between treatment groups were noted **(Table 5.3.1)**.

Statistical tests on hippocampal electrophysiological signals show significant differences in 40-Hz power across treatment groups for all mice ($F(3) = 3.7965$, $p = 0.0264$, One-Way ANOVA) **(Figure 5.3.2F)**, with post-hoc tests showing a significant increase in 40-Hz power for AV treatment compared to NS ($p = 0.0205$, post-hoc Bonferroni tests). Again, no statistical differences were found between treatment groups **(Table 5.3.1)**. However, no significance was found between treatment groups for 5xFAD+ ($F(3) = 3.6137$, $p = 0.0649$, One-Way ANOVA) **(Figure 5.3.2H)** and 5xFAD- mice ($F(3) = 1.4261$, $p = 0.3051$, One-Way ANOVA) **(Figure 5.3.2J)**.

Table 5.3.1. Statistical summary for GENUS electrophysiology studies, comparing the effect of each GENUS treatment for cortical and hippocampal signals. If the One-Way ANOVA test provided a p-value <0.05, post-hoc tests with Bonferroni correction were completed. Arrows indicate the direction of change. **** p < 0.001, *** p < 0.005, ** p < 0.01, * p < 0.05, ns not significant.

		Cortical			Hippocampal		
Group 1	Group 2	All Mice	5xFAD+	5xFAD-	All Mice	5xFAD+	5xFAD-
Group Comparison		****	***	ns	*	ns	ns
NS	V	0.0383 ↑	0.0242 ↑		0.3984		
	A	0.0511	0.2910		1		
	AV	0.0004 ↑	0.0040 ↑		0.0205 ↑		
V	A	1	0.8139		1		
	AV	0.3550	1		1		
A	AV	0.2750	0.0943		0.3638		

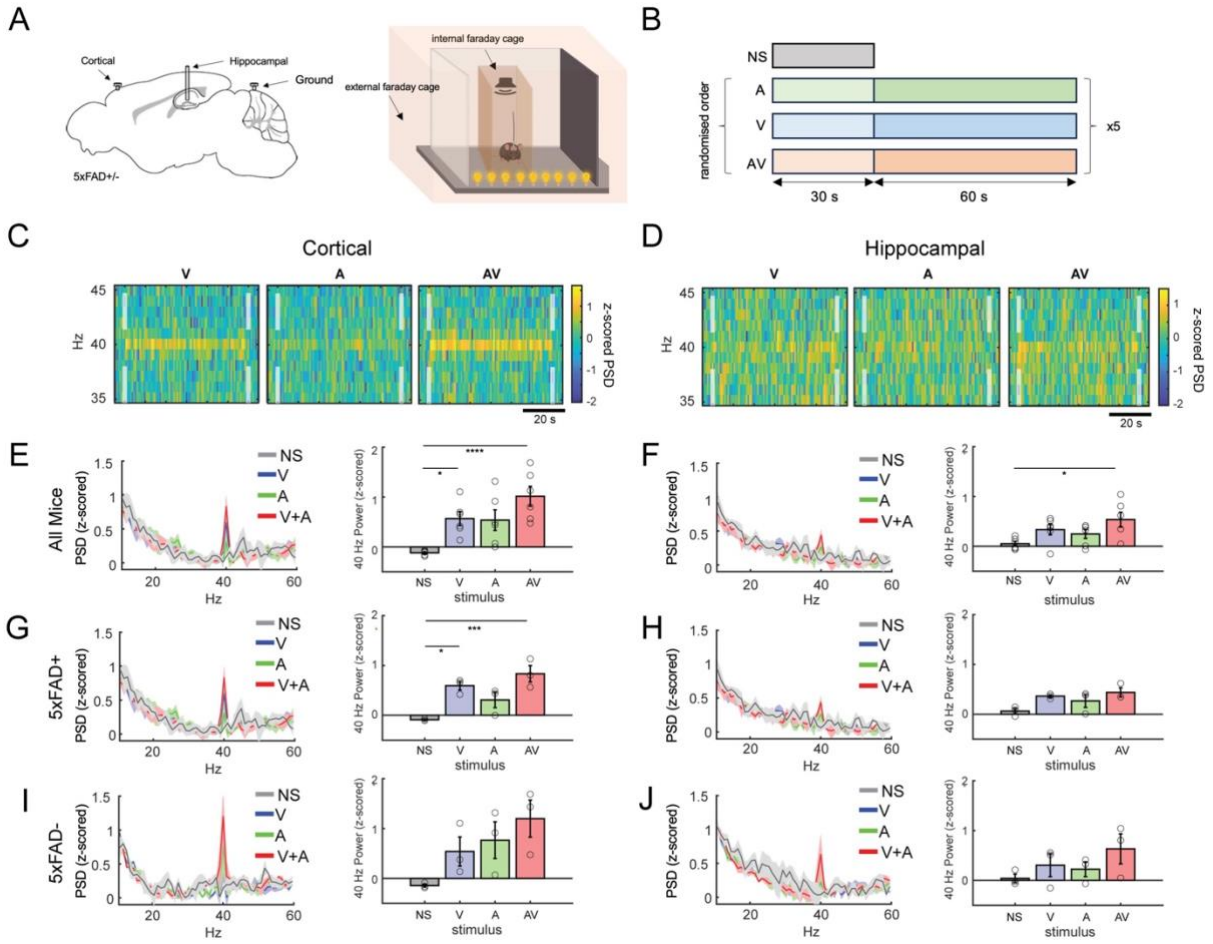

Figure 5.3.2. Cortical and hippocampal electrophysiological signals increase power at 40-Hz when 5xFAD+ and 5xFAD- mice undergo GENUS treatment. (A) Schematic showing the cortical and hippocampal implants in 5xFAD+/- mouse models. Recordings were completed in two faraday cages to remove electrical noise. (B) Recording stimulus paradigm. NS data is baseline data before any stimulation. Treatment data is averaged across 5 trials. (C,D) Heat-map showing z-scored PSD during each GENUS treatment for cortical (C) and hippocampal (D) regions. White dashed lines indicate the start and end of treatment. Scale: 20-seconds. (E,G,I) *Left,* Cortical PSD (z-scored) for all treatment groups. *Right*, Change in 40-Hz power from baseline for all treatment groups for all mice (E), 5xFAD+ (G) and 5xFAD- (I). (F,H,J) As in E, G, and I but for hippocampal signals. PSD was z-scored to the global PSD (1-100-Hz) for each mouse. Data is shown as Mean ± SEM. 40-Hz Power data was statistically compared using a One-Way ANOVA, followed by multi-comparison tests with Bonferroni correction if $p < 0.05$. $p < 0.001$ (****), $p < 0.005$ (***), $p < 0.01$ (**), $p < 0.05$ (*), ns not significant. If comparison is not shown, it was ns. 5xFAD+/- mice: n = 3.

Overall, 40-Hz GENUS increases gamma power in cortical and hippocampal regions at 40-Hz, with stronger increases seen within the cortical regions,

5.3.3 No significant modifications in 5xFAD+ plaque pathology in response to GENUS treatment were identified with our novel approach

To identify if GENUS treatment can modify plaque load in 5xFAD+ mouse models, we monitored Methoxy-x04 signals using our TF photometry system, while exposing mice to various GENUS treatments **(Figure 5.3.3).** Based off previous studies, a decline in plaque pathology was seen after only 1-hour of GENUS treatment, with samples taken 1-hour post-GENUS treatment. Therefore, mice underwent 1-hour of GENUS treatment, with a 1-hour post-baseline to identify any changes in plaque pathology during and after **(Figure 5.3.3A).** Accordingly, we expected to see a decline in Methoxy-x04 signals during and after GENUS treatment, with a greater reduction seen when undergoing AV treatment. In addition, as TFs were implanted through the visual cortex and SUB, we expected to see a greater decline at higher GVs, corresponding to the visual cortex. To illustrate this, Norm data from the *in vitro* light protocol was shown **(Figure 5.3.3A)**.

Across all treatments, while an increase or decline in fluorescence, at varied depths, from Day 1 was seen, no substantial modifications in signal intensity were seen during or post-GENUS **(Figures 5.3.3B-F)**. However, a trend of increased fluorescence is seen at higher GVs post-V treatment **(Figure 5.3.3B)**, with some declines in fluorescence seen in control groups, perhaps representing bleaching of AF **(Figures 5.3.3E-F)**.

Summary plots show for V treatment, fluorescence changes from baseline are minimal across 0-2-V galvo **(Figure 5.3.3G)**. However, for 3 and 4-V galvo, a small tendency of increased fluorescence is shown across time. This increase appears to begin at the time of treatment and continues to increase for the duration of the recording. However, individual recording traces illustrate that this trend is not consistent across mice, with some showing a decline over time or no change from baseline **(Figure 5.3.3G)**, suggesting the trend may be contributed to by the varied post-baseline durations. Interestingly, this increasing trend is replicated at 3 and 4-V galvo for A treatment, with minimal changes at other GVs **(Figure 5.3.3H)**. Additionally, no fluorescence change from baseline is seen for AV treatment across GVs **(Figure 5.3.3I)**. Therefore, no statistically significant differences in fluorescence over time was found across all GVs for V (0-V, $H(10) = 2.8074$, $p = 0.9856$; 1-V, $H(10) = 4.9291$, $p = 0.8959$; 2-V, $H(10) = 1.8208$, $p = 0.9975$; 3-V, $H(10) = 3.6968$, $p = 0.9600$; 4-V, $H(10) = 5.007$, $p = 0.8907$) **(Figure 5.3.3G)**, A (0-V, $H(10) = 0.5733$, $p = 1$; 1-V, $H(10) = 1.1719$, $p = 0.9996$; 2-V, $H(10) = 1.4566$, $p = 0.9991$; 3-V, $H(10) = 5.1590$, $p = 0.8803$; 4-V, $H(10) = 7.6123$, $p = 0.6666$, Kruskal-Wallis test) **(Figure 5.3.3H)** or AV treatment (0-V, $H(10) = 0.2088$, $p = 1$; 1-V, $H(10) = 0.7502$, $p = 1$; 2-V, $H(10) = 1.9478$, $p = 0.9967$; 3-V, $H(10) = 0.5816$, $p = 1$; 4-V, $H(10) = 0.2773$, $p = 1$, Kruskal-Wallis test) **(Figure 5.3.3I)**.

Also, statistical tests show no significant difference in fluorescence after NS in a 5xFAD+ mouse across all GVs (0-V, H(10) = 6.6596, p = 0.7571; 1-V, H(10) = 7.0759, p = 0.7183; 2V, H(10) = 10.1527, p = 0.4272; 3-V, H(10) = 6.0121, p = 0.8142; 4-V, H(10) = 3.2011, p = 0.9763, Kruskal-Wallis test) **(Figure 5.3.3J)** or AV in a 5xFAD- mouse model across all GVs (0-V, H(10) = 3.3310, p = 0.9725; 1-V, H(10) = 2.8280, p = 0.9852; 2-V, H(10) = 0.8864, p = 0.9999; 3-V, H(10) = 1.4645, p = 0.9990; 4-V, H(10) = 1.1832, p = 0.9996, Kruskal-Wallis test) **(Figure 5.3.3K)**. However, a trend for decreased fluorescence is seen across all depths, specifically 0 and 1-V galvo **(Figures 5.3.3J-K)**. Whereas, this decline is not seen for V, A, AV treatment groups **(Figures G-I)**.

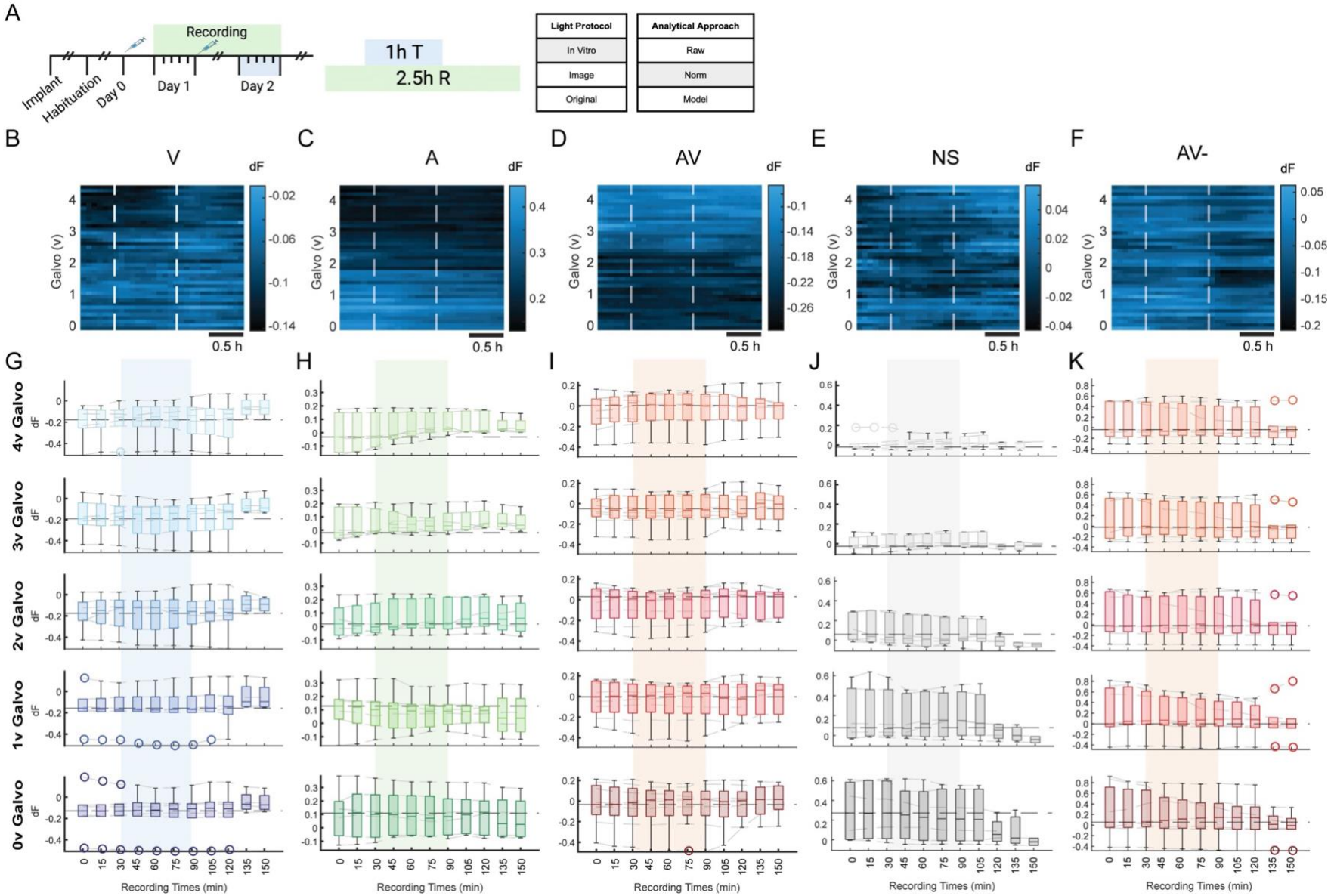
A
Recording
Implant
Habituation
Day 0
Day 1
Day 2
1h T
2.5h R
Light Protocol
In Vitro
Image
Original
Analytical Approach
Raw
Norm
Model
B
V
C
A
D
AV
E
NS
F
AV-
dF
Galvo (v)
0.5 h
G
H
I
J
K
4v Galvo
3v Galvo
2v Galvo
1v Galvo
0v Galvo
Recording Times (min)

Figure 5.3.3. Changes in 5xFAD+ plaque pathology when undergoing GENUS treatment. (A) *Left*, Recording paradigm. Methoxy-x04 was injected 24-h before a 2-h baseline recording on day 1. After, Methoxy-x04 was injected before a combined GENUS and photometry recording on day 2. Each dash on the recording days represents 1-h. *Middle,* A 2.5-h recording was completed, with 1-h of treatment after the initial 30-min baseline. *Right,* Table highlighting the light protocol and analytical approach shown: *in vitro* and Norm. (B-F) Example plots of the change of fluorescence over time when 5xFAD+ mice were exposed to visual (V) (B), auditory (A) (C), combined audio-visual (AV) (D) stimulation or no stimulation (NS) (E), and when 5xFAD- mice were exposed to AV (F). White dashed lines show the start and end of GENUS treatment. Scale: 0.5-h. V, A, AV, and NS data is from FAD72. AV- data is from FAD64. (G-K) Summary plots of Methoxy-x04 fluorescence across time and depth, when exposed to V (G), A (H), AV (I) or NS (J) in a 5xFAD+ mouse model. Data from 5xFAD- mice exposed to AV- is shown (K). Plot colours get darker as the recording region on the TF gets deeper. Shaded area represents the duration of GENUS treatment. Data was statistically compared using a Kruskal-Wallis test, followed by multi-comparison tests with Bonferroni correction if $p < 0.05$. As a note, some timepoints are missing at the end due to different post-baseline periods of recordings. V, A, NS: n = 6 5xFAD+ mice; AV: n =.8 recordings from 6 5xFAD+ mice; AV-: n = 7 recordings from 6 5xFAD- mice.

Overall, no significant changes in Methoxy-x04 signal were detected in response to any GENUS treatment. However, at this stage it remains unclear whether this is due to the system sensitivity being unable to detect such minuscule changes or due to GENUS treatment not substantially reducing plaque pathology. Therefore, histological quantification on treated mice is required to determine if a change in plaque pathology is seen with a well-established plaque assessment approach.

5.3.4 No change in histologically quantified plaque density following AV GENUS treatment

Previous studies used histological quantification of plaque pathology as a measure of GENUS success in modifying plaque load. Therefore, to confirm photometry data was reflective of the plaque pathology, plaque density was quantified from post-mortem histological sections **(Figure 5.3.4)**. To do so, mice underwent either AV or NS as their last treatment before being immediately culled. This meant the histological sections were reflective of the plaque load, 1-h post-GENUS treatment.

Histological images show the quantified brain regions **(Figure 5.3.4A).** In this example, a reduced plaque load can be seen after AV, rather than NS. For example, there is a trend for reduced plaque density after AV in VISl, VISp, SUB and POST areas **(Figure 5.3.4A).** However, statistical tests

show no significant difference between AV and NS histologically quantified plaque density for the POST ($p = 0.2188$, Wilcoxon signed rank test), PreS ($p = 0.4375$, Wilcoxon signed rank test), SUB ($p = 0.6875$, Wilcoxon signed rank test), VISl ($p = 1$, Wilcoxon signed rank test) and VISp ($p = 1$, Wilcoxon signed rank test) **(Figure 5.3.4B)**.

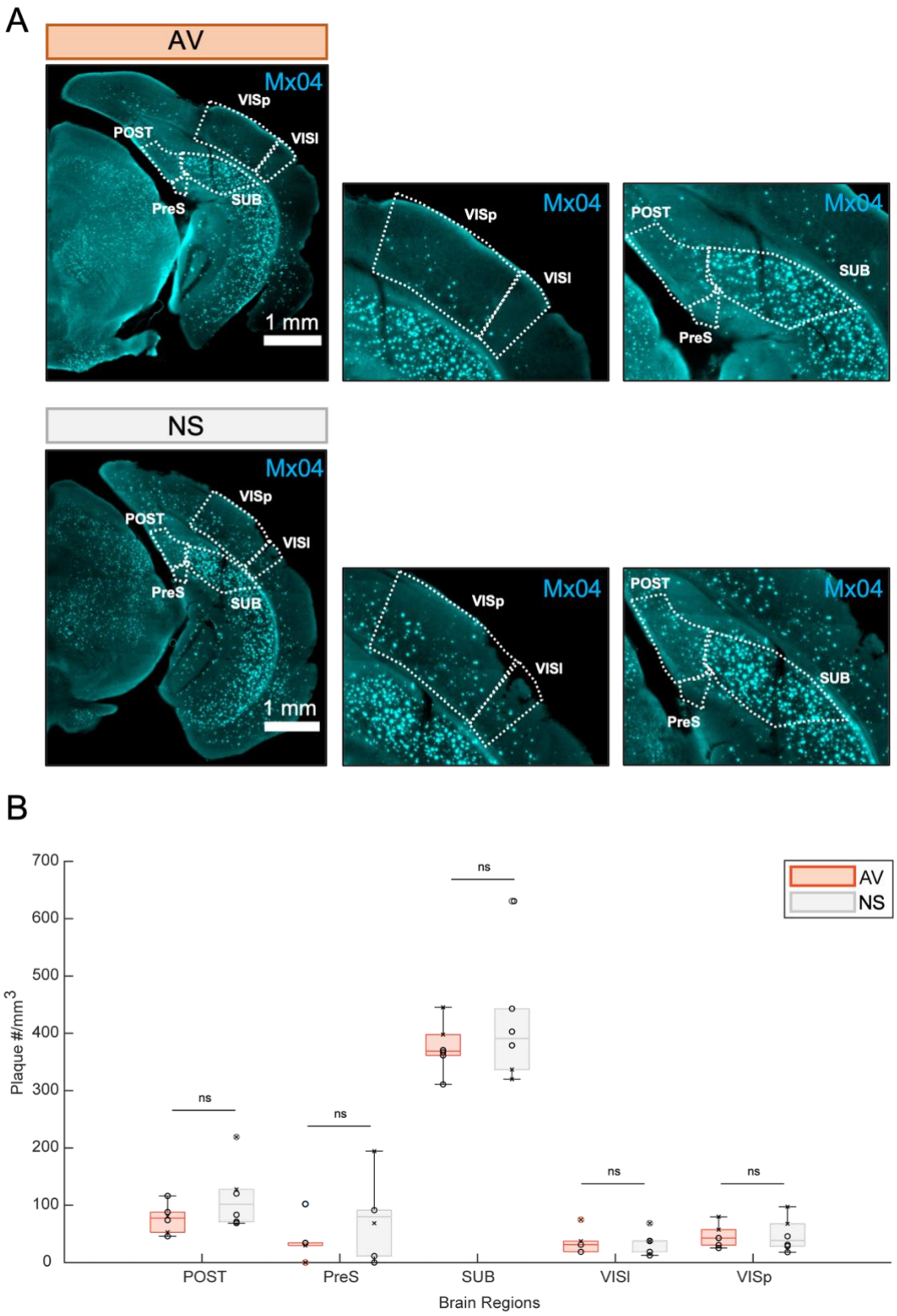

Figure 5.3.4. Plaque density across visual and hippocampal brain regions following either AV or NS GENUS treatment. (A) Histological images showing example sections from a mouse that underwent either AV (top) or NS (bottom) treatment. White dashed shapes illustrate the regions quantified. Zoomed images of the regions of interest are shown. Scale: 1-mm. (B)

Plaque density in visual and hippocampal regions. Data points show the density for each mouse. Crosses are female and circles are male. POST: post-subiculum, PreS: pre-subiculum, SUB: subiculum, VISl: lateral visual cortex, VISp: primary visual cortex. Histologically quantified plaque density was statistically compared using the Wilcoxon signed rank test and corrected for multi-comparisons. AV and NS: n = 6 measurements from 3 5xFAD+ mice.

5.4 Discussion

5.4.1 Discussion of findings

5.4.1.1 Main findings

As previously discussed, GENUS treatment has proved to reduce AD pathology, and even improve cognitive function (Adaikkan et al., 2019, Iaccarino et al., 2016, Martorell et al., 2019, Yao et al., 2020). However, conflicting findings have arisen which may be contributed to by a lack of real-time, depth-resolved feedback (Soula et al., 2023). Therefore, with use of our real-time, depth-resolved plaque assessment, in freely behaving animals, we aimed to identify if GENUS treatment can modify electrophysiological and plaque pathology in 5xFAD mice.

Electrophysiological recordings illustrated an increase in gamma power at 40-Hz **(Figure 5.3.2).** Photometry measurements during GENUS show no significant differences in plaque pathology for all treatment groups, with little change from baseline across GVs **(Figure 5.3.3).** Notably, some trends for an increase in fluorescence was seen at higher GVs across V, A and AV treatment groups, with a decline at lower GVs for AV- and NS treatment groups **(Figure 5.3.3).** In parallel with photometry analysis, histological quantification shows no significant changes in plaque density following AV treatment, across brain regions **(Figure 5.3.4).** Overall, while the set-up shows that we were able to monitor fluorescent signals while exposing freely behaving mice to a treatment, it remains to be confirmed if this novel approach could detect small changes in Methoxy-x04 concentration, representative of a plaque modifying effect of the treatment. Additionally, as previous studies have shown that GENUS may or may not modify plaque pathology, applying an alternative therapy already confirmed to reduce plaque pathology may aid the confirmation of this approach. Thus, a larger study with greater sample numbers and using the chronic treatment paradigm may help confirm the success of this treatment and the capabilities of this novel protocol for monitoring changes in real-time.

5.4.1.2 GENUS treatment enhances 40-Hz gamma power

To determine if our set-up for non-invasive GENUS treatment was able to induce changes in electrophysiological cortical and hippocampal signals at the gamma frequency, we recorded electrophysiological signals from 5xFAD mice undergoing treatment **(Figure 5.3.2).** Across all GENUS treatments – V, A & AV – an increase in 40-Hz gamma power was evident, with a stronger effect in the PFC. Whereas no change was seen for NS. While there was a trend for an increased 40-Hz gamma band in a treatment-dependent manner, as AV presented with a stronger effect, no statistical differences were found between treatment groups to confirm this. This could be contributed to by this mouse models genetic background having age-related hearing loss which prevents a greater power being reached, seen with no significant increases in 40-Hz gamma band power during A stimulation. In addition, we seen enhanced 40-Hz gamma power in the hippocampus, at a weaker strength, likely due to the neuronal activity having to pass through various brain regions and pathways causing filtering of the signal. These findings are consistent with previous studies that show that GENUS treatment can increase neuronal activity at 40-Hz within the appropriate sensory cortex (Adaikkan et al., 2019, Iaccarino et al., 2016, Martorell et al., 2019), and even increase c-Fos immunostaining after V treatment in various cortical and hippocampal regions (Adaikkan et al., 2019). However, our findings of increased 40-Hz gamma power within the hippocampus conflict with previous studies which show V stimulation does not enhance gamma power at 40-Hz within the hippocampus (Soula et al., 2023). Notably, despite Soula and colleagues describing no narrow-band local field potential response in these regions, they do observe a fraction of neurons phase-entrained to the 40-Hz stimulation in both the hippocampus and entorhinal cortex (Soula et al., 2023). Also, this paper did not test the effects of A or AV treatment, which have shown increased 40-Hz gamma power in the prefrontal cortex and hippocampus, consistent with our findings (Martorell et al., 2019).

Overall, using the 5xFAD mouse model at 4-6-months, we provide further evidence for increased gamma power due to GENUS. However, we note that these electrophysiological implants were in different brain regions to our TF implant. Also, monitoring only the LFP does not allow us to infer a strong understanding of the entrainment of gamma within these regions. Therefore, while this provides evidence for some increased power of gamma oscillations within cortical and hippocampal regions, it would be beneficial to complete single-unit electrophysiological recordings to investigate spike information across various brain regions throughout GENUS treatment. In addition, as we are monitoring the neuronal signals in the PFC and CA1, investigating the change at the sensory cortices is desirable. In summary, non-invasive GENUS treatment likely increases 40-Hz gamma power in cortical and hippocampal regions.

5.4.1.3 No modifications in plaque pathology were detected using this novel approach following GENUS treatment

To monitor the real-time, depth-resolved effects of GENUS treatment on plaque pathology in freely behaving 5xFAD mice, we used our novel approach while exposing mice to various types of GENUS treatment. Mice underwent either V, A, AV, or NS treatment, while Methoxy-x04 signals were recording for 0.5-h pre, 1-h during and 1-h post treatment. This was based on previous findings that show that non-invasive sensory stimulus at 40-Hz can have pronounced effects on reducing AD pathology (Adaikkan et al., 2019, Iaccarino et al., 2016, Martorell et al., 2019, Yao et al., 2020). However, despite seeing that GENUS treatment enhanced gamma power **(Figure 5.3.2)**, we found no significant difference in plaque load across all treatment options **(Figure 5.3.3)**. While this is conflicting with previous studies that show a decrease in soluble $A\beta_{40/42}$ after acute V treatment (Iaccarino et al., 2016), a decrease in insoluble $A\beta_{40/42}$ and plaque number was found only after a chronic treatment paradigm (Iaccarino et al., 2016, Martorell et al., 2019). Therefore, as we are quantifying Aβ fibrils, a largely insoluble form, a direct comparison with these acute findings may be misleading. Instead, a recent paper by Soula and colleagues complete an *in vivo* pre- and post-measure after acute V stimulus, using Methoxy-x04 and 2PM, and found no significant differences in plaque area, consistent with our findings (Soula et al., 2023). Overall, this suggests that this acute treatment paradigm may not provide a substantial change in plaque load that would be detectable using this monitoring approach. Instead, using a chronic treatment paradigm, like previously completed (Adaikkan et al., 2019, Iaccarino et al., 2016, Martorell et al., 2019, Yao et al., 2020), may illustrate the potential of this novel approach and treatment. However, it is important to note that at this point we cannot confirm that the lack of change in fluorescence over-time is due to GENUS not having an effect or due to the system being unable to track such small changes in plaque pathology. Accordingly, we believe further optimisation of this novel approach and a better understanding of the bleaching and binding properties of Methoxy-x04 may allow for stronger conclusions to be drawn on the effect of GENUS.

5.4.1.4 Histology shows no change in plaque density following AV GENUS treatment

To confirm findings from TF photometry recordings, histological analysis of the plaque density was completed across visual cortical and hippocampal brain regions **(Figure 5.3.4).** This presented the novel approach and GENUS treatment with four potential options:

1. Both photometry and histological data show decreased plaque pathology proving success of novel approach and treatment.

2. Photometry but not histological data show decreased plaque pathology, proving success of the treatment and novel approach emphasising its real-time benefits, but with no histological confirmation as a control.
3. Histological but not photometry data show decreased plaque pathology, showing success of the treatment, but not the novel approach.
4. Neither photometry nor histological data show decreased plaque pathology showing success of neither.

Therefore, brains were taken from mice that had either underwent AV or NS treatment, and aligned histological sections were analysed. Overall, no significant differences in plaque density was seen across brain regions, consistent with Soula and colleagues when investigating V treatment **(Figure 5.3.4)** (Soula et al., 2023). However, they discuss the possibility of such changes being contributed to by changes in plaque pathology across each mouse. Consequently, these experiments must be replicated with a greater sample number to fully conclude the success of this novel approach and GENUS treatment.

5.4.2 Limitations

One major limitation of this study was the low sample number. For example, for photometry and histology experiments, the sample number was 6 and 3 per group, respectively. Therefore, small modifications may go undetected. According to a recent pre-print investigating the appropriate sample numbers required to see a substantially significant difference in plaque number within the visual cortical and hippocampal regions following acute GENUS exposure, a sample number of 176 and 344 is required, respectively (Carstensen, 2023). This was despite the landmark paper showing significant differences in relative $A\beta_{1\text{-}40}$ and $A\beta_{1\text{-}42}$ in the visual cortex of 6, 3-month 5xFAD mice following 1-h 40-Hz visual stimulation (Iaccarino et al., 2016). However, completing an ELISA can be more sensitive that quantifying plaque density. Overall, to confirm a solid conclusion on the effects of acute GENUS on plaque pathology within the visual cortex and SUB, these experiments must be replicated. This limitation is also transferable to the electrophysiological studies. With a sample number of 3 for 5xFAD+ and 5xFAD- mice, treatment-specific differences remain unclear.

As described, previous studies that show successful results of GENUS are completed in young mouse models, with changes seen from 3-6-month-old 5xFAD mice across both acute and chronic treatment paradigms (Adaikkan et al., 2019, Iaccarino et al., 2016, Martorell et al., 2019). Our mice were on a C57 background which have previously been shown to have progressive hearing loss from ~4-months due to a mutation in the cdh23 gene (Frisina et al., 2011, Noben-Trauth et al., 2003) Consequently, we tested 4-6-month-old mice, with an A intensity of 70-dB, as mice at 6-months had been shown to have a sound intensity of ~35-dB SPL (Lyngholm and Sakata, 2019). As a result of the progressive hearing loss, mice may have differing effects to A treatment

depending on their hearing abilities. Therefore, completing these experiments on a crossbreed of C57 x CBA, which has been shown to prevent progressive hearing loss (Frisina et al., 2011, Lyngholm and Sakata, 2019) or using <4-month-old 5xFAD mice may minimise this risk. Although, it is important to note that variable genetic background can also introduce variable AD phenotypes (Neuner et al., 2019). However, another limitation with this age group is that plaque density is low, meaning that Methoxy-x04 signals are reduced. As well as this, depending on the surrounding tissue of the TF implant, plaque pathology may be very sparse, making it difficult to detect fluorescence or any fluorescence changes within that window. Consequently, while changes in plaque pathology may occur, this may be missed due to the signal intensity.

Finally, another limitation of this experiment was the acute treatment paradigm. While previous studies show a pronounced change in AD pathology after only acute treatment, they illustrate a greater and prolonged effect following chronic GENUS exposure (Adaikkan et al., 2019, Iaccarino et al., 2016, Martorell et al., 2019, Yao et al., 2020). As our novel approach will be collecting very low changes in signal intensity due to the reduced surrounding plaques at this younger age group, changes in plaque pathology may go undetected with this acute paradigm. Additionally, it is noteworthy that with a sample size of 8, the original paper seen a significant decrease in plaque number and size in the visual cortex after 40-Hz V stimulus for 1-h over 7-days in 6-month-old 5xFAD mice (Iaccarino et al., 2016), with other papers again illustrating the capabilities of reducing plaque number with chronic exposure (Martorell et al., 2019). This suggests that our novel approach may be unable to detect changes in plaque pathology as chronic exposure is required to significantly reduce plaque load, with acute exposure modifying the soluble Aβ fragments. Therefore, by completing chronic GENUS treatment, a pronounced change in plaque pathology may be notable.

5.4.3 Future work

To fully understand the effects of GENUS treatment on plaque pathology, an extensive study must be completed. This includes larger sample numbers, an optimal age group and varied parameters. With the real-time capabilities of this approach, a closed-loop system can be implemented to identify treatment parameters that result in enhanced beneficial effect. Consequently, this can be transferable to other potential treatment options. For example, therapeutic agents that work to reduce the plaque load may have a stronger effect than GENUS, making it easier to detect and confirm the success of this approach.

5.4.4 Summary

Overall, we illustrate in practice how this novel approach can be adopted for monitoring plaque pathology while exposing mice to a potential AD treatment, but at this moment cannot confirm the capability of detecting plaque modifying effects. While electrophysiological signals illustrate that this treatment successfully increased gamma power, we failed to detect significant changes in plaque pathology across both photometry and histological approaches. This implies a requirement for further study to gain solid conclusions on the real-time effects of GENUS on plaque pathology, as well as confirming the sensitivity of our novel approach for such experiments. In all, this provides a first step in implementing TF photometry technology for assessment of novel AD treatments.

6. General discussion and conclusions

6.1 Summary of findings

Overall, the aim of this project was to establish a novel technology for monitoring plaque pathology in real-time, in deep brain regions and in freely behaving AD mouse models. This involved the combination of the peripherally administrated BBB-permeable plaque marker, Methoxy-x04, and TF photometry. Then, this approach was used to assess the real-time, depth-resolved effects of a potential AD treatment. To do so, this involved three main steps:

1. Confirmation of this novel approach to monitor plaque pathology using FF photometry **(Chapter 3)**
2. Real-time, depth-resolved plaque detection using TF photometry in freely behaving conditions **(Chapter 4)**
3. Monitoring plaque pathology in response to GENUS **(Chapter 5)**

Therefore, step 1 involved correlation analysis of FF photometry and histological plaque signals across various brain regions **(Figure 3.3.7)**. Once shown to be feasible, TF photometry was implemented and investigated to achieve plaque monitoring in a real-time, depth-resolved manner. This helped establish appropriate protocols and analytical approaches for realising optimal TF photometry signals. Consequently, Methoxy-x04 properties were investigated – pharmacokinetic and re-dosing strategies **(Figures 4.3.4-15)**. Finally, this approach was applied to test the real-time plaque modifying effects of GENUS treatment **(Figure 5.3.3)**. Therefore, this study shows, for the first time, successful implementation of Methoxy-x04 and fibre photometry for real-time, depth-resolved plaque monitoring in freely behaving 5xFAD mice, while providing insights into the effects of GENUS treatment. However, we must note that further characterisation of the binding and bleaching characteristics of Methoxy-x04 is required to back this finding. Although all findings have been greatly discussed in each subsequent chapter, a summary of the main findings are described below.

Within **Chapter 3,** Methoxy-x04 signals were strongly detected at 440-nm in 5xFAD+, but not 5xFAD-, mice across various brain regions. Therefore, photometry and histological plaque signals were strongly positively correlated across brain regions, confirming the feasibility of this novel approach for monitoring plaque pathology **(Figure 3.3.7)**. However, real-time detection of Methoxy-x04 signals was challenging using FF photometry, with the pharmacokinetic profile in terminally anaesthetised mice going undetected **(Figure 3.3.9)**.

Next, in **Chapter 4**, AF and light configuration proved to be vital contributors to signal collection **(Figure 4.3.2)**, as previously found (Bianco et al., 2021, Formozov et al., 2023, Schlegel et al.,

2018, Simpson et al., 2023). Therefore, various light protocols and analytical approaches to counteract this were implemented. Following *in vivo* recordings using these approaches, the *in vitro* light protocol and Norm analytical approach provided optimal signal collection **(Figures 4.3.4-15)**. Then, using TF photometry in 5xFAD+ mice, Methoxy-x04 was detected within 30-minutes of injection, reached maximum fluorescence within 4-h, and returned to near-baseline levels after 48-h **(Figures 4.3.4-6)**, thought to be due to bleaching of Methoxy-x04 as previous studies illustrate the stability of Methoxy-x04 binding (Condello et al., 2011, Liu et al., 2010). Whereas, in 5xFAD- mice, no change in fluorescence was detected **(Figures 4.3.7-9)**, consistent with previous findings that illustrate rapid clearance from non-plaque brains (Bacskai et al., 2003, Klunk et al., 2002). Additionally, re-dosing Methoxy-x04 at 24-h intervals provided an increased fluorescence from baseline that was maintained following daily injection **(Figures 4.3.10-12)**, consistent with previous Methoxy-x04 re-dosing protocols (Crowe and Ellis-Davies, 2013, Hefendehl et al., 2011). Again, no change in fluorescence was detected in 5xFAD- mice **(Figures 4.3.13-15).** The depth-resolved capabilities of the TF photometry are shown for both pharmacokinetic and re-dose recordings **(Figures 4.3.3-18)**. For example, greater signal intensities were evident at regions where a greater plaque load surrounded the appropriate region of the TF, therefore suggesting that the varied signal intensities are reflective of the pathological state within the brain. However, attempts to correlate TF photometry and histological plaque signals were inconsistent **(Figures 4.3.16-19)**. Therefore, to fully understand and confirm that the increases in fluorescence seen were Methoxy-x04, further research must be completed to understand the binding and bleaching properties of Methoxy-x04. Additionally, work must be done to optimise the correlation analytical approach as it is vital to confirm that these TF photometry signals are reflective of the plaque load.

Lastly, in **Chapter 5**, non-invasive GENUS treatment resulted in increased 40-Hz gamma band power, consistent with previous studies (Adaikkan et al., 2019, Iaccarino et al., 2016, Martorell et al., 2019). In addition, this enhanced 40-Hz power was seen in both cortical and hippocampal regions, consistent with the original study completed with A and AV stimulation (Martorell et al., 2019) but conflicting with some conclusions drawn from silicon probe recordings investigating the firing patterns of neurons across many cortical and hippocampal brain regions (Soula et al., 2023). No significant changes in plaque pathology were detected in real-time, using TF photometry, even at 1-h post-treatment **(Figure 5.3.3)**, which is not consistent with previous findings (Iaccarino et al., 2016, Murdock et al., 2024). Coinciding with no detected changes in Methoxy-x04 signals monitored by TF photometry, no significant changes in histological plaque density were found **(Figure 5.3.4)**. Consequently, with low sample size, further studies are required before drawing any major conclusions.

Overall, for the first time, we have illustrated the capabilities of a novel technology allowing real-time, depth-resolved plaque detection in freely behaving AD mice. Consequently, this illustrated

how this approach could be implemented for optical interrogation of plaque pathology while mice undergo exposure to a potential AD therapeutic. However, further work is required to characterise the binding and bleaching properties of Methoxy-x04 before this can be fully understood. Therefore, once completed, this should provide the field with a novel tool for preclinical screening of possible treatment options for a well-rounded image of the effects on plaque pathology.

6.2 Limitations

One of the main limitations of this project, and novel approach, is the depth coverage and spatial resolution of TFs. As we have covered, TFs are the current state-of-the-art implantable optical tool due to their outstanding depth-resolved capacity (Pisanello et al., 2017, Pisano et al., 2019). However, currently the length of the active region is limited to 1.8-mm from -5 to 5V galvo, allowing 50 measures (~36-µm resolution) along the TF. While this number of measures could be increased, the length of the TF is a major limitation. While 1.8-mm is much greater than achievable with FFs, the mouse brain reaches ~6-mm in depth, leaving many brain regions unresolved. Work has shown that increasing the NA and decreasing the taper angle can increase the collection length to a maximum of 2-mm (Pisanello et al., 2017). Thus, a longer TF could be developed for light collection only and implanted in parallel with a µLED array for light illumination (Scharf et al., 2016). Also, the NA results in an illumination cone which will lose resolution if the number of measures increases.

In addition, Methoxy-x04 is the most commonly used fluorescent plaque marker that can be peripherally administered and pass the BBB (Klunk et al., 2002). With proof *in vitro* and *in vivo*, it was an undeniable choice. However, this did not come without challenges. Methoxy-x04 is largely insoluble in pre-injectable solution, effecting the maximum concentration achievable. In addition, it is susceptible to photobleaching, with rapid declines occurring within seconds. Both these factors meant that signal intensity was reduced, potentially contributing to low fluorescence seen across some recordings **(Figures 4.3.4-15)**. As well as this, Methoxy-x04 does not bind specifically to plaques, preventing the targeting of specific plaque stages, with the clearance of Methoxy-x04 from the brain remaining largely unclear (Klunk et al., 2002). Finally, Methoxy-x04 is a blue-shifted dye which means the signal will be largely susceptible to AF. In all, development of novel plaque-binding dyes is desirable, but in the meantime, use of a higher dose of Methoxy-x04 and a less intense illumination protocol would minimise bleaching of the boosted Methoxy-x04 signal.

In the future, taking into consideration such methodological hurdles, we believe we can acquire stronger, stable signals at a greater intensity over a larger depth.

6.3 Future directions

While we previously discussed the potential of this novel approach for testing other AD treatments and aiding the progression to a clinical status, this approach can be adaptable for many aspects of AD pathogenesis, as well as other neurodegenerative disorders. For example, this can be used across many scales of disease: molecular, neurotransmitter, neuroinflammation and neuronal. In addition, as disease pathogenesis spreads brain-wide, having an approach to monitor this is vital going forward. As all these directions are protocol based, this will provide several opportunities for many research questions to be broached. We believe that application of such measures will allow interrogation of the disease to uncover potential targets and decipher the effects of new therapeutics.

Firstly, the field would benefit from development of new molecular tools to monitor AD pathology: plaques, neurofibrillary tangles, or other neurodegenerative molecular hallmarks. Methoxy-x04 is mostly incompatible for combination with many other optical sensors currently established due to their overlapping emission spectra (Akerboom et al., 2012, Chen et al., 2013b, Dana et al., 2019, Jing et al., 2020, Nakai et al., 2001, Patriarchi et al., 2018, Zhang et al., 2023). Therefore, we suggest establishment of a novel plaque marker with red-shifted spectra will open possibility for many all-optical experiments. In addition, development of BBB-permeable dyes for other molecular hallmarks will allow investigation of several aspects of disease pathogenesis in unison or the study of other neurodegenerative diseases.

Secondly, using this approach for combinational measurement of molecular, inflammatory, and neuronal markers is desirable. For example, adopting an all-optical approach by expressing tools for sensing neurotransmitters (Abdelfattah et al., 2022) in mice injected with Methoxy-x04, both molecular and neurotransmitter pathogenesis can be monitored. In addition, neuroinflammation greatly contributes to AD pathogenesis, as well as being linked to the progression of molecular pathologies (Heneka et al., 2015a, Hickman et al., 2018, Malm et al., 2015, Mrak, 2012). Therefore, using optical tools targeted at microglia (Gu et al., 2023), astrocytes or oligodendrocytes, we can interrogate AD pathogenesis on another scale.

On another note, a multi-modal approach, combining this with electrophysiology, optogenetics, chemogenetics or pharmacological intervention will be invaluable. Firstly, fibre photometry has numerous benefits, but its low temporal resolution to collect neuronal information when using genetically modified calcium sensors is a drawback that emphasises the need for combination with electrophysiology. Some groups have shown success combining fibre photometry and electrophysiology by creating an ‘optrode’ (optical fibre and wire electrode) (Legaria et al., 2022, Patel et al., 2020). However, a new development that may progress this novel approach is the

addition of microelectrodes along the shaft of the TF, thereby allowing depth-resolved photometry and electrophysiological measurements (Spagnolo et al., 2022). Secondly, the group of John Rogers has developed a multi-modal device that allows optical stimulation and micro-fluidic delivery of therapeutics (Wu et al., 2022a). By building on this device though the addition sensing capabilities, this will allow region-specific pharmacological and optical intervention. In addition, this opens the possibility for simultaneous monitoring and manipulation of neuronal or non-neuronal activity. Accordingly, like previous studies that show manipulating neuronal activity can alter Aβ pathology (Bero et al., 2011, Cirrito et al., 2005, Rodriguez et al., 2020, Yamamoto et al., 2015, Yuan and Grutzendler, 2016), using optogenetics or chemogenetics to manipulate specific neuronal activity, such as astrocytic calcium signalling, may help further understand its role in Aβ pathogenesis. Not only would these devices benefit further investigation of the real-time, depth-resolved neuronal and pathological effects of GENUS treatment, it advances technology available for neuroscience research.

Finally, while this novel approach provides real-time, depth-resolution in a manner that has previously been unachievable, this is at only one implant site. As disease progresses across several brain regions, affecting brain-wide neurotransmitter pathways and the neuroinflammatory state, a measure of pathology brain-wide is vital. Many groups have worked to develop large implantable fibre bundles, and adopting new implants and optical devices, showing potential to acquire volumetric signals across the brain (Adelsberger et al., 2014, Guo et al., 2015, Guo et al., 2023, Kim et al., 2016, Sych et al., 2019). Alternatively, creating a multi-shank TF to allow for signal collection across both depth and width would be beneficial. While requirement of an intricate optical system would be required, this would provide an abundance of information.

6.4 Final conclusions

In all, for the first time, we illustrate real-time, depth-resolved plaque monitoring in freely behaving AD mouse models. Using Methoxy-x04 and fibre photometry we optically interrogated the Methoxy-x04 pharmacokinetic profile and established an appropriate re-dosing strategy. Finally, we illustrate the capability of using this novel approach for investigating the plaque modifying effects of novel treatments by monitoring plaque pathology in mice under GENUS treatment. While no plaque modifications were detected, with a greater sample size, other treatments, and characterisation of Methoxy-x04s binding and bleaching properties, a pronounced signal change should be achievable. Overall, our work establishing this novel approach will aid the testing of possible AD treatments, with the potential to be adapted for other aspects of disease pathogenesis.

7. References

ABBOTT, N. J., RONNBACK, L. & HANSSON, E. 2006. Astrocyte-endothelial interactions at the blood-brain barrier. *Nat Rev Neurosci,* 7**,** 41-53.

ABBOTT, R. D., WHITE, L. R., ROSS, G. W., MASAKI, K. H., CURB, J. D. & PETROVITCH, H. 2004. Walking and dementia in physically capable elderly men. *JAMA,* 292**,** 1447-53.

ABD-ELRAHMAN, K. S., ALBAKER, A., DE SOUZA, J. M., RIBEIRO, F. M., SCHLOSSMACHER, M. G., TIBERI, M., HAMILTON, A. & FERGUSON, S. S. G. 2020. Abeta oligomers induce pathophysiological mGluR5 signaling in Alzheimer's disease model mice in a sex-selective manner. *Sci Signal,* 13.

ABDELFATTAH, A. S., AHUJA, S., AKKIN, T., ALLU, S. R., BRAKE, J., BOAS, D. A., BUCKLEY, E. M., CAMPBELL, R. E., CHEN, A. I., CHENG, X., CIZMAR, T., COSTANTINI, I., DE VITTORIO, M., DEVOR, A., DORAN, P. R., EL KHATIB, M., EMILIANI, V., FOMIN-THUNEMANN, N., FAINMAN, Y., FERNANDEZ-ALFONSO, T., FERRI, C. G. L., GILAD, A., HAN, X., HARRIS, A., HILLMAN, E. M. C., HOCHGESCHWENDER, U., HOLT, M. G., JI, N., KILIC, K., LAKE, E. M. R., LI, L., LI, T., MACHLER, P., MILLER, E. W., MESQUITA, R. C., NADELLA, K., NAGERL, U. V., NASU, Y., NIMMERJAHN, A., ONDRACKOVA, P., PAVONE, F. S., PEREZ CAMPOS, C., PETERKA, D. S., PISANO, F., PISANELLO, F., PUPPO, F., SABATINI, B. L., SADEGH, S., SAKADZIC, S., SHOHAM, S., SHROFF, S. N., SILVER, R. A., SIMS, R. R., SMITH, S. L., SRINIVASAN, V. J., THUNEMANN, M., TIAN, L., TIAN, L., TROXLER, T., VALERA, A., VAZIRI, A., VINOGRADOV, S. A., VITALE, F., WANG, L. V., UHLIROVA, H., XU, C., YANG, C., YANG, M. H., YELLEN, G., YIZHAR, O. & ZHAO, Y. 2022. Neurophotonic tools for microscopic measurements and manipulation: status report. *Neurophotonics,* 9**,** 013001.

ABOUNIT, S., WU, J. W., DUFF, K., VICTORIA, G. S. & ZURZOLO, C. 2016. Tunneling nanotubes: A possible highway in the spreading of tau and other prion-like proteins in neurodegenerative diseases. *Prion,* 10**,** 344-351.

ABRAMOV, A. Y., CANEVARI, L. & DUCHEN, M. R. 2003. Changes in intracellular calcium and glutathione in astrocytes as the primary mechanism of amyloid neurotoxicity. *J Neurosci,* 23**,** 5088-95.

ABRAMOV, A. Y., CANEVARI, L. & DUCHEN, M. R. 2004. Beta-amyloid peptides induce mitochondrial dysfunction and oxidative stress in astrocytes and death of neurons through activation of NADPH oxidase. *J Neurosci,* 24**,** 565-75.

ADAIKKAN, C., MIDDLETON, S. J., MARCO, A., PAO, P. C., MATHYS, H., KIM, D. N., GAO, F., YOUNG, J. Z., SUK, H. J., BOYDEN, E. S., MCHUGH, T. J. & TSAI, L. H. 2019. Gamma Entrainment Binds Higher-Order Brain Regions and Offers Neuroprotection. *Neuron,* 102**,** 929-943 e8.

ADAIKKAN, C. & TSAI, L. H. 2020. Gamma Entrainment: Impact on Neurocircuits, Glia, and Therapeutic Opportunities. *Trends Neurosci,* 43**,** 24-41.

ADELSBERGER, H., GARASCHUK, O. & KONNERTH, A. 2005. Cortical calcium waves in resting newborn mice. *Nat Neurosci,* 8**,** 988-90.

ADELSBERGER, H., ZAINOS, A., ALVAREZ, M., ROMO, R. & KONNERTH, A. 2014. Local domains of motor cortical activity revealed by fiber-optic calcium recordings in behaving nonhuman primates. *Proc Natl Acad Sci U S A,* 111**,** 463-8.

AHMED, M., DAVIS, J., AUCOIN, D., SATO, T., AHUJA, S., AIMOTO, S., ELLIOTT, J. I., VAN NOSTRAND, W. E. & SMITH, S. O. 2010. Structural conversion of neurotoxic amyloid-beta(1-42) oligomers to fibrils. *Nat Struct Mol Biol,* 17**,** 561-7.

AHMED, Z., COOPER, J., MURRAY, T. K., GARN, K., MCNAUGHTON, E., CLARKE, H., PARHIZKAR, S., WARD, M. A., CAVALLINI, A., JACKSON, S., BOSE, S., CLAVAGUERA, F., TOLNAY, M., LAVENIR, I., GOEDERT, M., HUTTON, M. L. & O'NEILL, M. J. 2014. A novel in vivo model of tau propagation with rapid and progressive neurofibrillary tangle pathology: the pattern of spread is determined by connectivity, not proximity. *Acta Neuropathol,* 127**,** 667-83.

AKERBOOM, J., CHEN, T. W., WARDILL, T. J., TIAN, L., MARVIN, J. S., MUTLU, S., CALDERON, N. C., ESPOSTI, F., BORGHUIS, B. G., SUN, X. R., GORDUS, A., ORGER, M. B., PORTUGUES, R., ENGERT, F., MACKLIN, J. J., FILOSA, A., AGGARWAL, A., KERR, R. A., TAKAGI, R., KRACUN, S., SHIGETOMI, E., KHAKH, B. S., BAIER, H., LAGNADO, L., WANG, S. S., BARGMANN, C. I., KIMMEL, B. E., JAYARAMAN, V., SVOBODA, K., KIM, D. S., SCHREITER,

E. R. & LOOGER, L. L. 2012. Optimization of a GCaMP calcium indicator for neural activity imaging. *J Neurosci,* 32**,** 13819-40.
AL SHOYAIB, A., ARCHIE, S. R. & KARAMYAN, V. T. 2019. Intraperitoneal Route of Drug Administration: Should it Be Used in Experimental Animal Studies? *Pharm Res,* 37**,** 12.
ALBERDI, E., SANCHEZ-GOMEZ, M. V., CAVALIERE, F., PEREZ-SAMARTIN, A., ZUGAZA, J. L., TRULLAS, R., DOMERCQ, M. & MATUTE, C. 2010. Amyloid beta oligomers induce Ca2+ dysregulation and neuronal death through activation of ionotropic glutamate receptors. *Cell Calcium,* 47**,** 264-72.
ALEXANDER, A. G., MARFIL, V. & LI, C. 2014. Use of Caenorhabditis elegans as a model to study Alzheimer's disease and other neurodegenerative diseases. *Front Genet,* 5**,** 279.
ALLEN, N. J. 2014. Astrocyte regulation of synaptic behavior. *Annu Rev Cell Dev Biol,* 30**,** 439-63.
ALLEN, N. J. & EROGLU, C. 2017. Cell Biology of Astrocyte-Synapse Interactions. *Neuron,* 96**,** 697-708.
ALZHEIMER, A. 1907. Über eine eigenartige Erkrankung der Hirnrinde. *Allgemeine Z Psychiatrie Psychisch Gerichtliche Med.,* 64**,** 146–148.
ALZHEIMER'S ASSOCIATION REPORT 2023. 2023 Alzheimer's disease facts and figures. *Alzheimers Dement,* 19**,** 1598-1695.
ALZHEIMER'S RESEARCH UK. *Statistics about dementia* [Online]. Available: https://dementiastatistics.org/about-dementia/ [Accessed 2 Jun 2023].
AMRO, Z., YOOL, A. J. & COLLINS-PRAINO, L. E. 2021. The potential role of glial cells in driving the prion-like transcellular propagation of tau in tauopathies. *Brain Behav Immun Health,* 14**,** 100242.
ANANDATHEERTHAVARADA, H. K., BISWAS, G., ROBIN, M. A. & AVADHANI, N. G. 2003. Mitochondrial targeting and a novel transmembrane arrest of Alzheimer's amyloid precursor protein impairs mitochondrial function in neuronal cells. *J Cell Biol,* 161**,** 41-54.
ANDERSON, J. P., CHEN, Y., KIM, K. S. & ROBAKIS, N. K. 1992. An alternative secretase cleavage produces soluble Alzheimer amyloid precursor protein containing a potentially amyloidogenic sequence. *J Neurochem,* 59**,** 2328-31.
ANDERSON, J. P., ESCH, F. S., KEIM, P. S., SAMBAMURTI, K., LIEBERBURG, I. & ROBAKIS, N. K. 1991. Exact cleavage site of Alzheimer amyloid precursor in neuronal PC-12 cells. *Neurosci Lett,* 128**,** 126-8.
ANDRIEZEN, W. L. 1893. The Neuroglia Elements in the Human Brain. *Br Med J,* 2**,** 227-30.
ANGULO, M. C., LE MEUR, K., KOZLOV, A. S., CHARPAK, S. & AUDINAT, E. 2008. GABA, a forgotten gliotransmitter. *Prog Neurobiol,* 86**,** 297-303.
ANTONENKO, D., FAXEL, M., GRITTNER, U., LAVIDOR, M. & FLOEL, A. 2016. Effects of Transcranial Alternating Current Stimulation on Cognitive Functions in Healthy Young and Older Adults. *Neural Plast,* 2016**,** 4274127.
ANTZUTKIN, O. N., BALBACH, J. J., LEAPMAN, R. D., RIZZO, N. W., REED, J. & TYCKO, R. 2000. Multiple quantum solid-state NMR indicates a parallel, not antiparallel, organization of beta-sheets in Alzheimer's beta-amyloid fibrils. *Proc Natl Acad Sci U S A,* 97**,** 13045-50.
ARDID, S., WANG, X. J., GOMEZ-CABRERO, D. & COMPTE, A. 2010. Reconciling coherent oscillation with modulation of irregular spiking activity in selective attention: gamma-range synchronization between sensory and executive cortical areas. *J Neurosci,* 30**,** 2856-70.
ASAI, H., IKEZU, S., TSUNODA, S., MEDALLA, M., LUEBKE, J., HAYDAR, T., WOLOZIN, B., BUTOVSKY, O., KUGLER, S. & IKEZU, T. 2015. Depletion of microglia and inhibition of exosome synthesis halt tau propagation. *Nat Neurosci,* 18**,** 1584-93.
ATTOKAREN, M. K., JEONG, N., BLANPAIN, L., PAULSON, A. L., GARZA, K. M., BORRON, B., WALELIGN, M., WILLIE, J. & SINGER, A. C. 2023. BrainWAVE: A Flexible Method for Noninvasive Stimulation of Brain Rhythms across Species. *eNeuro,* 10.
BACKSTROM, J. R., LIM, G. P., CULLEN, M. J. & TOKES, Z. A. 1996. Matrix metalloproteinase-9 (MMP-9) is synthesized in neurons of the human hippocampus and is capable of degrading the amyloid-beta peptide (1-40). *J Neurosci,* 16**,** 7910-9.
BACSKAI, B. J., HICKEY, G. A., SKOCH, J., KAJDASZ, S. T., WANG, Y., HUANG, G. F., MATHIS, C. A., KLUNK, W. E. & HYMAN, B. T. 2003. Four-dimensional multiphoton imaging of brain entry, amyloid binding, and clearance of an amyloid-beta ligand in transgenic mice. *Proc Natl Acad Sci U S A,* 100**,** 12462-7.
BALBACH, J. J., PETKOVA, A. T., OYLER, N. A., ANTZUTKIN, O. N., GORDON, D. J., MEREDITH, S. C. & TYCKO, R. 2002. Supramolecular structure in full-length Alzheimer's beta-amyloid fibrils: evidence for a parallel beta-sheet organization from solid-state nuclear magnetic resonance. *Biophys J,* 83**,** 1205-16.

BALLATORE, C., LEE, V. M. & TROJANOWSKI, J. Q. 2007. Tau-mediated neurodegeneration in Alzheimer's disease and related disorders. *Nat Rev Neurosci,* 8**,** 663-72.
BARD, F., CANNON, C., BARBOUR, R., BURKE, R. L., GAMES, D., GRAJEDA, H., GUIDO, T., HU, K., HUANG, J., JOHNSON-WOOD, K., KHAN, K., KHOLODENKO, D., LEE, M., LIEBERBURG, I., MOTTER, R., NGUYEN, M., SORIANO, F., VASQUEZ, N., WEISS, K., WELCH, B., SEUBERT, P., SCHENK, D. & YEDNOCK, T. 2000. Peripherally administered antibodies against amyloid beta-peptide enter the central nervous system and reduce pathology in a mouse model of Alzheimer disease. *Nat Med,* 6**,** 916-9.
BARKER, A. T., JALINOUS, R. & FREESTON, I. L. 1985. Non-invasive magnetic stimulation of human motor cortex. *Lancet,* 1**,** 1106-7.
BARSOUM, M. J., YUAN, H., GERENCSER, A. A., LIOT, G., KUSHNAREVA, Y., GRABER, S., KOVACS, I., LEE, W. D., WAGGONER, J., CUI, J., WHITE, A. D., BOSSY, B., MARTINOU, J. C., YOULE, R. J., LIPTON, S. A., ELLISMAN, M. H., PERKINS, G. A. & BOSSY-WETZEL, E. 2006. Nitric oxide-induced mitochondrial fission is regulated by dynamin-related GTPases in neurons. *EMBO J,* 25**,** 3900-11.
BASAR, E., EMEK-SAVAS, D. D., GUNTEKIN, B. & YENER, G. G. 2016. Delay of cognitive gamma responses in Alzheimer's disease. *Neuroimage Clin,* 11**,** 106-115.
BASAR, E., FEMIR, B., EMEK-SAVAS, D. D., GUNTEKIN, B. & YENER, G. G. 2017. Increased long distance event-related gamma band connectivity in Alzheimer's disease. *Neuroimage Clin,* 14**,** 580-590.
BAUER, E. P., PAZ, R. & PARE, D. 2007. Gamma oscillations coordinate amygdalo-rhinal interactions during learning. *J Neurosci,* 27**,** 9369-79.
BEN HAIM, L. & ROWITCH, D. H. 2017. Functional diversity of astrocytes in neural circuit regulation. *Nat Rev Neurosci,* 18**,** 31-41.
BENUSSI, A., CANTONI, V., COTELLI, M. S., COTELLI, M., BRATTINI, C., DATTA, A., THOMAS, C., SANTARNECCHI, E., PASCUAL-LEONE, A. & BORRONI, B. 2021. Exposure to gamma tACS in Alzheimer's disease: A randomized, double-blind, sham-controlled, crossover, pilot study. *Brain Stimul,* 14**,** 531-540.
BENVENISTE, H. & DIEMER, N. H. 1987. Cellular reactions to implantation of a microdialysis tube in the rat hippocampus. *Acta Neuropathol,* 74**,** 234-8.
BENZINGER, T. L., GREGORY, D. M., BURKOTH, T. S., MILLER-AUER, H., LYNN, D. G., BOTTO, R. E. & MEREDITH, S. C. 1998. Propagating structure of Alzheimer's beta-amyloid(10-35) is parallel beta-sheet with residues in exact register. *Proc Natl Acad Sci U S A,* 95**,** 13407-12.
BENZINGER, T. L., GREGORY, D. M., BURKOTH, T. S., MILLER-AUER, H., LYNN, D. G., BOTTO, R. E. & MEREDITH, S. C. 2000. Two-dimensional structure of beta-amyloid(10-35) fibrils. *Biochemistry,* 39**,** 3491-9.
BERG, J., HUNG, Y. P. & YELLEN, G. 2009. A genetically encoded fluorescent reporter of ATP:ADP ratio. *Nat Methods,* 6**,** 161-6.
BERGER, H. 1929. Über das Elektrenkephalogramm des Menschen. *Eur. Arch. Psychiatry Clin. Neurosci.,* 87**,** 527–570.
BERKE, J. D., OKATAN, M., SKURSKI, J. & EICHENBAUM, H. B. 2004. Oscillatory entrainment of striatal neurons in freely moving rats. *Neuron,* 43**,** 883-96.
BERO, A. W., YAN, P., ROH, J. H., CIRRITO, J. R., STEWART, F. R., RAICHLE, M. E., LEE, J. M. & HOLTZMAN, D. M. 2011. Neuronal activity regulates the regional vulnerability to amyloid-beta deposition. *Nat Neurosci,* 14**,** 750-6.
BERTRAM, L. & TANZI, R. E. 2009. Genome-wide association studies in Alzheimer's disease. *Hum Mol Genet,* 18**,** R137-45.
BESHEL, J., KOPELL, N. & KAY, L. M. 2007. Olfactory bulb gamma oscillations are enhanced with task demands. *J Neurosci,* 27**,** 8358-65.
BEZZI, P., CARMIGNOTO, G., PASTI, L., VESCE, S., ROSSI, D., RIZZINI, B. L., POZZAN, T. & VOLTERRA, A. 1998. Prostaglandins stimulate calcium-dependent glutamate release in astrocytes. *Nature,* 391**,** 281-5.
BEZZI, P., GUNDERSEN, V., GALBETE, J. L., SEIFERT, G., STEINHAUSER, C., PILATI, E. & VOLTERRA, A. 2004. Astrocytes contain a vesicular compartment that is competent for regulated exocytosis of glutamate. *Nat Neurosci,* 7**,** 613-20.
BHATTACHARYA, S., HAERTEL, C., MAELICKE, A. & MONTAG, D. 2014. Galantamine slows down plaque formation and behavioral decline in the 5XFAD mouse model of Alzheimer's disease. *PLoS One,* 9**,** e89454.
BIANCO, M., BALENA, A., PISANELLO, M., PISANO, F., SILEO, L., SPAGNOLO, B., MONTINARO, C., SABATINI, B. L., VITTORIO, M. & PISANELLO, F. 2021. Comparative study of

autofluorescence in flat and tapered optical fibers towards application in depth-resolved fluorescence lifetime photometry in brain tissue. *Biomed Opt Express,* 12**,** 993-1010.
BOASSO, A. H., E.; HAJOS, M.; MALCHANO, Z. 2021. Gamma sensory stimulation in AD patients, a randomized controlled trial. *Alzheimer's & Dementia,* 17**,** e056485.
BOBOLA, M. S., CHEN, L., EZEOKEKE, C. K., OLMSTEAD, T. A., NGUYEN, C., SAHOTA, A., WILLIAMS, R. G. & MOURAD, P. D. 2020. Transcranial focused ultrasound, pulsed at 40 Hz, activates microglia acutely and reduces Abeta load chronically, as demonstrated in vivo. *Brain Stimul,* 13**,** 1014-1023.
BOLMONT, T., CLAVAGUERA, F., MEYER-LUEHMANN, M., HERZIG, M. C., RADDE, R., STAUFENBIEL, M., LEWIS, J., HUTTON, M., TOLNAY, M. & JUCKER, M. 2007. Induction of tau pathology by intracerebral infusion of amyloid-beta -containing brain extract and by amyloid-beta deposition in APP x Tau transgenic mice. *Am J Pathol,* 171**,** 2012-20.
BOLOS, M., LLORENS-MARTIN, M., JURADO-ARJONA, J., HERNANDEZ, F., RABANO, A. & AVILA, J. 2016. Direct Evidence of Internalization of Tau by Microglia In Vitro and In Vivo. *J Alzheimers Dis,* 50**,** 77-87.
BOLOS, M., LLORENS-MARTIN, M., PEREA, J. R., JURADO-ARJONA, J., RABANO, A., HERNANDEZ, F. & AVILA, J. 2017. Absence of CX3CR1 impairs the internalization of Tau by microglia. *Mol Neurodegener,* 12**,** 59.
BONS, N., MESTRE, N., RITCHIE, K., PETTER, A., PODLISNY, M. & SELKOE, D. 1994. Identification of amyloid beta protein in the brain of the small, short-lived lemurian primate Microcebus murinus. *Neurobiol Aging,* 15**,** 215-20.
BORCHELT, D. R., RATOVITSKI, T., VAN LARE, J., LEE, M. K., GONZALES, V., JENKINS, N. A., COPELAND, N. G., PRICE, D. L. & SISODIA, S. S. 1997. Accelerated amyloid deposition in the brains of transgenic mice coexpressing mutant presenilin 1 and amyloid precursor proteins. *Neuron,* 19**,** 939-45.
BORCHELT, D. R., THINAKARAN, G., ECKMAN, C. B., LEE, M. K., DAVENPORT, F., RATOVITSKY, T., PRADA, C. M., KIM, G., SEEKINS, S., YAGER, D., SLUNT, H. H., WANG, R., SEEGER, M., LEVEY, A. I., GANDY, S. E., COPELAND, N. G., JENKINS, N. A., PRICE, D. L., YOUNKIN, S. G. & SISODIA, S. S. 1996. Familial Alzheimer's disease-linked presenilin 1 variants elevate Abeta1-42/1-40 ratio in vitro and in vivo. *Neuron,* 17**,** 1005-13.
BORDJI, K., BECERRIL-ORTEGA, J., NICOLE, O. & BUISSON, A. 2010. Activation of extrasynaptic, but not synaptic, NMDA receptors modifies amyloid precursor protein expression pattern and increases amyloid-ss production. *J Neurosci,* 30**,** 15927-42.
BOTCHERBY, E. J., SMITH, C. W., KOHL, M. M., DEBARRE, D., BOOTH, M. J., JUSKAITIS, R., PAULSEN, O. & WILSON, T. 2012. Aberration-free three-dimensional multiphoton imaging of neuronal activity at kHz rates. *Proc Natl Acad Sci U S A,* 109**,** 2919-24.
BOUCHON, A., DIETRICH, J. & COLONNA, M. 2000. Cutting edge: inflammatory responses can be triggered by TREM-1, a novel receptor expressed on neutrophils and monocytes. *J Immunol,* 164**,** 4991-5.
BOURGADE, K., LE PAGE, A., BOCTI, C., WITKOWSKI, J. M., DUPUIS, G., FROST, E. H. & FULOP, T., JR. 2016. Protective Effect of Amyloid-beta Peptides Against Herpes Simplex Virus-1 Infection in a Neuronal Cell Culture Model. *J Alzheimers Dis,* 50**,** 1227-41.
BRAAK, H., ALAFUZOFF, I., ARZBERGER, T., KRETZSCHMAR, H. & DEL TREDICI, K. 2006. Staging of Alzheimer disease-associated neurofibrillary pathology using paraffin sections and immunocytochemistry. *Acta Neuropathol,* 112**,** 389-404.
BRAAK, H. & BRAAK, E. 1991. Neuropathological stageing of Alzheimer-related changes. *Acta Neuropathol,* 82**,** 239-59.
BRAAK, H. & BRAAK, E. 1997. Frequency of stages of Alzheimer-related lesions in different age categories. *Neurobiol Aging,* 18**,** 351-7.
BRAIDY, N., POLJAK, A., JAYASENA, T., MANSOUR, H., INESTROSA, N. C. & SACHDEV, P. S. 2015. Accelerating Alzheimer's research through 'natural' animal models. *Curr Opin Psychiatry,* 28**,** 155-64.
BRANNSTROM, K., OHMAN, A., NILSSON, L., PIHL, M., SANDBLAD, L. & OLOFSSON, A. 2014. The N-terminal region of amyloid beta controls the aggregation rate and fibril stability at low pH through a gain of function mechanism. *J Am Chem Soc,* 136**,** 10956-64.
BRESSLER, S. L. & FREEMAN, W. J. 1980. Frequency analysis of olfactory system EEG in cat, rabbit, and rat. *Electroencephalogr Clin Neurophysiol,* 50**,** 19-24.
BRIGGS, R., KENNELLY, S. P. & O'NEILL, D. 2016. Drug treatments in Alzheimer's disease. *Clin Med (Lond),* 16**,** 247-53.

BROWN, P., KUPSCH, A., MAGILL, P. J., SHAROTT, A., HARNACK, D. & MEISSNER, W. 2002. Oscillatory local field potentials recorded from the subthalamic nucleus of the alert rat. *Exp Neurol,* 177**,** 581-5.

BRUNEL, N. & WANG, X. J. 2003. What determines the frequency of fast network oscillations with irregular neural discharges? I. Synaptic dynamics and excitation-inhibition balance. *J Neurophysiol,* 90**,** 415-30.

BUDD HAEBERLEIN, S., AISEN, P. S., BARKHOF, F., CHALKIAS, S., CHEN, T., COHEN, S., DENT, G., HANSSON, O., HARRISON, K., VON HEHN, C., IWATSUBO, T., MALLINCKRODT, C., MUMMERY, C. J., MURALIDHARAN, K. K., NESTOROV, I., NISENBAUM, L., RAJAGOVINDAN, R., SKORDOS, L., TIAN, Y., VAN DYCK, C. H., VELLAS, B., WU, S., ZHU, Y. & SANDROCK, A. 2022. Two Randomized Phase 3 Studies of Aducanumab in Early Alzheimer's Disease. *J Prev Alzheimers Dis,* 9**,** 197-210.

BUEE, L., BUSSIERE, T., BUEE-SCHERRER, V., DELACOURTE, A. & HOF, P. R. 2000. Tau protein isoforms, phosphorylation and role in neurodegenerative disorders. *Brain Res Brain Res Rev,* 33**,** 95-130.

BUFFALO, E. A., FRIES, P., LANDMAN, R., BUSCHMAN, T. J. & DESIMONE, R. 2011. Laminar differences in gamma and alpha coherence in the ventral stream. *Proc Natl Acad Sci U S A,* 108**,** 11262-7.

BUTTON, K. S., IOANNIDIS, J. P., MOKRYSZ, C., NOSEK, B. A., FLINT, J., ROBINSON, E. S. & MUNAFO, M. R. 2013. Power failure: why small sample size undermines the reliability of neuroscience. *Nat Rev Neurosci,* 14**,** 365-76.

BUZSAKI, G. & DRAGUHN, A. 2004. Neuronal oscillations in cortical networks. *Science,* 304**,** 1926-9.

BUZSAKI, G., LEUNG, L. W. & VANDERWOLF, C. H. 1983. Cellular bases of hippocampal EEG in the behaving rat. *Brain Res,* 287**,** 139-71.

BUZSAKI, G., LOGOTHETIS, N. & SINGER, W. 2013. Scaling brain size, keeping timing: evolutionary preservation of brain rhythms. *Neuron,* 80**,** 751-64.

BUZSAKI, G. & WANG, X. J. 2012. Mechanisms of gamma oscillations. *Annu Rev Neurosci,* 35**,** 203-25.

BYRON, N. & SAKATA, S. 2024. Fiber photometry-based investigation of brain function and dysfunction. *Neurophotonics,* 11**,** S11502.

BYRON, N., SEMENOVA, A. & SAKATA, S. 2021. Mutual Interactions between Brain States and Alzheimer's Disease Pathology: A Focus on Gamma and Slow Oscillations. *Biology (Basel),* 10.

CAJAL, S. R. Y. 1913. Un nuevo proceder para la impregnación de la neuroglía.

CARDIN, J. A., CARLEN, M., MELETIS, K., KNOBLICH, U., ZHANG, F., DEISSEROTH, K., TSAI, L. H. & MOORE, C. I. 2009. Driving fast-spiking cells induces gamma rhythm and controls sensory responses. *Nature,* 459**,** 663-7.

CARLSON, M. C., HELMS, M. J., STEFFENS, D. C., BURKE, J. R., POTTER, G. G. & PLASSMAN, B. L. 2008. Midlife activity predicts risk of dementia in older male twin pairs. *Alzheimers Dement,* 4**,** 324-31.

CARMONA, S., ZAHS, K., WU, E., DAKIN, K., BRAS, J. & GUERREIRO, R. 2018. The role of TREM2 in Alzheimer's disease and other neurodegenerative disorders. *Lancet Neurol,* 17**,** 721-730.

CARSTENSEN, M. P., J. T.; CARSTENSEN, J. 2023. Unexpected contribution to the prevailing trend of positive results for 40 Hz light flicker. *BioRxiv,* 10.27.564342.

CARTER, D. B. & CHOU, K. C. 1998. A model for structure-dependent binding of Congo red to Alzheimer beta-amyloid fibrils. *Neurobiol Aging,* 19**,** 37-40.

CARULLA, N., CADDY, G. L., HALL, D. R., ZURDO, J., GAIRI, M., FELIZ, M., GIRALT, E., ROBINSON, C. V. & DOBSON, C. M. 2005. Molecular recycling within amyloid fibrils. *Nature,* 436**,** 554-8.

CASAS, C., SERGEANT, N., ITIER, J. M., BLANCHARD, V., WIRTHS, O., VAN DER KOLK, N., VINGTDEUX, V., VAN DE STEEG, E., RET, G., CANTON, T., DROBECQ, H., CLARK, A., BONICI, B., DELACOURTE, A., BENAVIDES, J., SCHMITZ, C., TREMP, G., BAYER, T. A., BENOIT, P. & PRADIER, L. 2004. Massive CA1/2 neuronal loss with intraneuronal and N-terminal truncated Abeta42 accumulation in a novel Alzheimer transgenic model. *Am J Pathol,* 165**,** 1289-300.

CASULA, E. P., PELLICCIARI, M. C., BONNI, S., BORGHI, I., MAIELLA, M., ASSOGNA, M., MINEI, M., MOTTA, C., D'ACUNTO, A., PORRAZZINI, F., PEZZOPANE, V., MENCARELLI, L., RONCAIOLI, A., ROCCHI, L., SPAMPINATO, D. A., CALTAGIRONE, C., SANTARNECCHI, E., MARTORANA, A. & KOCH, G. 2022. Decreased Frontal Gamma Activity in Alzheimer Disease Patients. *Ann Neurol,* 92**,** 464-475.

CHAMBERS, J. K., KURIBAYASHI, H., IKEDA, S. & UNE, Y. 2010. Distribution of neprilysin and deposit patterns of Abeta subtypes in the brains of aged squirrel monkeys (Saimiri sciureus). *Amyloid,* 17**,** 75-82.

CHAN, D., SUK, H. J., JACKSON, B., MILMAN, N., STARK, D., FERNANDEZ, V., KITCHENER, E., BANERJEE, A., KLERMAN, E. B., BOYDEN, E. S., BROWN, E. N., DICKERSON, B. & TSAI, L. H. 2021a. Gamma Frequency Sensory Stimulation in Probable Mild Alzheimer's Dementia Patients: Results of a Preliminary Clinical Trial. *Annals of Neurology,* 90**,** S93-S94.

CHAN, D., SUK, H. J., JACKSON, B., MILMAN, N. P., STARK, D., BEACH, S. D. & TSAI, L. H. 2021b. Induction of specific brain oscillations may restore neural circuits and be used for the treatment of Alzheimer's disease. *J Intern Med,* 290**,** 993-1009.

CHAN, D., SUK, H. J., JACKSON, B. L., MILMAN, N. P., STARK, D., KLERMAN, E. B., KITCHENER, E., FERNANDEZ AVALOS, V. S., DE WECK, G., BANERJEE, A., BEACH, S. D., BLANCHARD, J., STEARNS, C., BOES, A. D., UITERMARKT, B., GANDER, P., HOWARD, M., 3RD, STERNBERG, E. J., NIETO-CASTANON, A., ANTERAPER, S., WHITFIELD-GABRIELI, S., BROWN, E. N., BOYDEN, E. S., DICKERSON, B. C. & TSAI, L. H. 2022. Gamma frequency sensory stimulation in mild probable Alzheimer's dementia patients: Results of feasibility and pilot studies. *PLoS One,* 17**,** e0278412.

CHANG, C. H., LANE, H. Y. & LIN, C. H. 2018. Brain Stimulation in Alzheimer's Disease. *Front Psychiatry,* 9**,** 201.

CHANG, K. A. & SUH, Y. H. 2005. Pathophysiological roles of amyloidogenic carboxy-terminal fragments of the beta-amyloid precursor protein in Alzheimer's disease. *J Pharmacol Sci,* 97**,** 461-71.

CHARLES, A. C., MERRILL, J. E., DIRKSEN, E. R. & SANDERSON, M. J. 1991. Intercellular signaling in glial cells: calcium waves and oscillations in response to mechanical stimulation and glutamate. *Neuron,* 6**,** 983-92.

CHARPAK, S., PARE, D. & LLINAS, R. 1995. The entorhinal cortex entrains fast CA1 hippocampal oscillations in the anaesthetized guinea-pig: role of the monosynaptic component of the perforant path. *Eur J Neurosci,* 7**,** 1548-57.

CHAUHAN, M. B. & CHAUHAN, N. B. 2015. Brain Uptake of Neurotherapeutics after Intranasal versus Intraperitoneal Delivery in Mice. *J Neurol Neurosurg,* 2.

CHEN, C., LIANG, Z., ZHOU, B., LI, X., LUI, C., IP, N. Y. & QU, J. Y. 2018. In Vivo Near-Infrared Two-Photon Imaging of Amyloid Plaques in Deep Brain of Alzheimer's Disease Mouse Model. *ACS Chem Neurosci,* 9**,** 3128-3136.

CHEN, G. F., XU, T. H., YAN, Y., ZHOU, Y. R., JIANG, Y., MELCHER, K. & XU, H. E. 2017. Amyloid beta: structure, biology and structure-based therapeutic development. *Acta Pharmacol Sin,* 38**,** 1205-1235.

CHEN, R. J., CHANG, W. W., LIN, Y. C., CHENG, P. L. & CHEN, Y. R. 2013a. Alzheimer's amyloid-beta oligomers rescue cellular prion protein induced tau reduction via the Fyn pathway. *ACS Chem Neurosci,* 4**,** 1287-96.

CHEN, T. W., WARDILL, T. J., SUN, Y., PULVER, S. R., RENNINGER, S. L., BAOHAN, A., SCHREITER, E. R., KERR, R. A., ORGER, M. B., JAYARAMAN, V., LOOGER, L. L., SVOBODA, K. & KIM, D. S. 2013b. Ultrasensitive fluorescent proteins for imaging neuronal activity. *Nature,* 499**,** 295-300.

CHEN, W., ABUD, E. A., YEUNG, S. T., LAKATOS, A., NASSI, T., WANG, J., BLUM, D., BUEE, L., POON, W. W. & BLURTON-JONES, M. 2016. Increased tauopathy drives microglia-mediated clearance of beta-amyloid. *Acta Neuropathol Commun,* 4**,** 63.

CHENG, I. H., SCEARCE-LEVIE, K., LEGLEITER, J., PALOP, J. J., GERSTEIN, H., BIEN-LY, N., PUOLIVALI, J., LESNE, S., ASHE, K. H., MUCHOWSKI, P. J. & MUCKE, L. 2007. Accelerating amyloid-beta fibrillization reduces oligomer levels and functional deficits in Alzheimer disease mouse models. *J Biol Chem,* 282**,** 23818-28.

CHIBA, K., ARASEKI, M., NOZAWA, K., FURUKORI, K., ARAKI, Y., MATSUSHIMA, T., NAKAYA, T., HATA, S., SAITO, Y., UCHIDA, S., OKADA, Y., NAIRN, A. C., DAVIS, R. J., YAMAMOTO, T., KINJO, M., TARU, H. & SUZUKI, T. 2014. Quantitative analysis of APP axonal transport in neurons: role of JIP1 in enhanced APP anterograde transport. *Mol Biol Cell,* 25**,** 3569-80.

CHISHTI, M. A., YANG, D. S., JANUS, C., PHINNEY, A. L., HORNE, P., PEARSON, J., STROME, R., ZUKER, N., LOUKIDES, J., FRENCH, J., TURNER, S., LOZZA, G., GRILLI, M., KUNICKI, S., MORISSETTE, C., PAQUETTE, J., GERVAIS, F., BERGERON, C., FRASER, P. E., CARLSON, G. A., GEORGE-HYSLOP, P. S. & WESTAWAY, D. 2001. Early-onset amyloid deposition and cognitive deficits in transgenic mice expressing a double mutant form of amyloid precursor protein 695. *J Biol Chem,* 276**,** 21562-70.

CHROBAK, J. J. & BUZSAKI, G. 1998. Gamma oscillations in the entorhinal cortex of the freely behaving rat. *J Neurosci,* 18**,** 388-98.
CHU, L. W. 2012. Alzheimer's disease: early diagnosis and treatment. *Hong Kong Med J,* 18**,** 228-37.
CIMENSER, A., HEMPEL, E., TRAVERS, T., STROZEWSKI, N., MARTIN, K., MALCHANO, Z. & HAJOS, M. 2021. Sensory-Evoked 40-Hz Gamma Oscillation Improves Sleep and Daily Living Activities in Alzheimer's Disease Patients. *Front Syst Neurosci,* 15**,** 746859.
CIRRITO, J. R., MAY, P. C., O'DELL, M. A., TAYLOR, J. W., PARSADANIAN, M., CRAMER, J. W., AUDIA, J. E., NISSEN, J. S., BALES, K. R., PAUL, S. M., DEMATTOS, R. B. & HOLTZMAN, D. M. 2003. In vivo assessment of brain interstitial fluid with microdialysis reveals plaque-associated changes in amyloid-beta metabolism and half-life. *J Neurosci,* 23**,** 8844-53.
CIRRITO, J. R., YAMADA, K. A., FINN, M. B., SLOVITER, R. S., BALES, K. R., MAY, P. C., SCHOEPP, D. D., PAUL, S. M., MENNERICK, S. & HOLTZMAN, D. M. 2005. Synaptic activity regulates interstitial fluid amyloid-beta levels in vivo. *Neuron,* 48**,** 913-22.
CITRON, M., TEPLOW, D. B. & SELKOE, D. J. 1995. Generation of amyloid beta protein from its precursor is sequence specific. *Neuron,* 14**,** 661-70.
CITRON, M., WESTAWAY, D., XIA, W., CARLSON, G., DIEHL, T., LEVESQUE, G., JOHNSON-WOOD, K., LEE, M., SEUBERT, P., DAVIS, A., KHOLODENKO, D., MOTTER, R., SHERRINGTON, R., PERRY, B., YAO, H., STROME, R., LIEBERBURG, I., ROMMENS, J., KIM, S., SCHENK, D., FRASER, P., ST GEORGE HYSLOP, P. & SELKOE, D. J. 1997. Mutant presenilins of Alzheimer's disease increase production of 42-residue amyloid beta-protein in both transfected cells and transgenic mice. *Nat Med,* 3**,** 67-72.
CLAVAGUERA, F., AKATSU, H., FRASER, G., CROWTHER, R. A., FRANK, S., HENCH, J., PROBST, A., WINKLER, D. T., REICHWALD, J., STAUFENBIEL, M., GHETTI, B., GOEDERT, M. & TOLNAY, M. 2013. Brain homogenates from human tauopathies induce tau inclusions in mouse brain. *Proc Natl Acad Sci U S A,* 110**,** 9535-40.
CLAVAGUERA, F., BOLMONT, T., CROWTHER, R. A., ABRAMOWSKI, D., FRANK, S., PROBST, A., FRASER, G., STALDER, A. K., BEIBEL, M., STAUFENBIEL, M., JUCKER, M., GOEDERT, M. & TOLNAY, M. 2009. Transmission and spreading of tauopathy in transgenic mouse brain. *Nat Cell Biol,* 11**,** 909-13.
CLAYTON, K. A., VAN ENOO, A. A. & IKEZU, T. 2017. Alzheimer's Disease: The Role of Microglia in Brain Homeostasis and Proteopathy. *Front Neurosci,* 11**,** 680.
COGNITO THERAPEUTICS INC. 2023. *A Pivotal Study of Sensory Stimulation in Alzheimer's Disease (Hope Study, CA-0011) (Hope)* [Online]. ClinicalTrials.gov. Available: https://clinicaltrials.gov/study/NCT05637801 [Accessed 17 Jan 2024].
COHEN, M. X., AXMACHER, N., LENARTZ, D., ELGER, C. E., STURM, V. & SCHLAEPFER, T. E. 2009. Good vibrations: cross-frequency coupling in the human nucleus accumbens during reward processing. *J Cogn Neurosci,* 21**,** 875-89.
COHEN, S. I., LINSE, S., LUHESHI, L. M., HELLSTRAND, E., WHITE, D. A., RAJAH, L., OTZEN, D. E., VENDRUSCOLO, M., DOBSON, C. M. & KNOWLES, T. P. 2013. Proliferation of amyloid-beta42 aggregates occurs through a secondary nucleation mechanism. *Proc Natl Acad Sci U S A,* 110**,** 9758-63.
COLCOMBE, S. & KRAMER, A. F. 2003. Fitness effects on the cognitive function of older adults: a meta-analytic study. *Psychol Sci,* 14**,** 125-30.
COLES, M., BICKNELL, W., WATSON, A. A., FAIRLIE, D. P. & CRAIK, D. J. 1998. Solution structure of amyloid beta-peptide(1-40) in a water-micelle environment. Is the membrane-spanning domain where we think it is? *Biochemistry,* 37**,** 11064-77.
CONDELLO, C., SCHAIN, A. & GRUTZENDLER, J. 2011. Multicolor time-stamp reveals the dynamics and toxicity of amyloid deposition. *Sci Rep,* 1**,** 19.
CONDELLO, C., YUAN, P., SCHAIN, A. & GRUTZENDLER, J. 2015. Microglia constitute a barrier that prevents neurotoxic protofibrillar Abeta42 hotspots around plaques. *Nat Commun,* 6**,** 6176.
CORDER, E. H., SAUNDERS, A. M., STRITTMATTER, W. J., SCHMECHEL, D. E., GASKELL, P. C., SMALL, G. W., ROSES, A. D., HAINES, J. L. & PERICAK-VANCE, M. A. 1993. Gene dose of apolipoprotein E type 4 allele and the risk of Alzheimer's disease in late onset families. *Science,* 261**,** 921-3.
COSTA, R. O., LACOR, P. N., FERREIRA, I. L., RESENDE, R., AUBERSON, Y. P., KLEIN, W. L., OLIVEIRA, C. R., REGO, A. C. & PEREIRA, C. M. 2012. Endoplasmic reticulum stress occurs downstream of GluN2B subunit of N-methyl-d-aspartate receptor in mature hippocampal cultures treated with amyloid-beta oligomers. *Aging Cell,* 11**,** 823-33.
CRAFT, S. 2007. Insulin resistance and Alzheimer's disease pathogenesis: potential mechanisms and implications for treatment. *Curr Alzheimer Res,* 4**,** 147-52.

CROWE, S. E. & ELLIS-DAVIES, G. C. 2013. In vivo characterization of a bigenic fluorescent mouse model of Alzheimer's disease with neurodegeneration. *J Comp Neurol,* 521**,** Spc1.

CRYSTAL, A. S., GIASSON, B. I., CROWE, A., KUNG, M. P., ZHUANG, Z. P., TROJANOWSKI, J. Q. & LEE, V. M. 2003. A comparison of amyloid fibrillogenesis using the novel fluorescent compound K114. *J Neurochem,* 86**,** 1359-68.

CSICSVARI, J., JAMIESON, B., WISE, K. D. & BUZSAKI, G. 2003. Mechanisms of gamma oscillations in the hippocampus of the behaving rat. *Neuron,* 37**,** 311-22.

CUI, G., JUN, S. B., JIN, X., PHAM, M. D., VOGEL, S. S., LOVINGER, D. M. & COSTA, R. M. 2013. Concurrent activation of striatal direct and indirect pathways during action initiation. *Nature,* 494**,** 238-42.

D'ERRICO, P. & MEYER-LUEHMANN, M. 2020. Mechanisms of Pathogenic Tau and Abeta Protein Spreading in Alzheimer's Disease. *Front Aging Neurosci,* 12**,** 265.

DA, X., HEMPEL, E., OU, Y., ROWE, O. E., MALCHANO, Z., HAJOS, M., KERN, R., MEGERIAN, J. T. & CIMENSER, A. 2024. Noninvasive Gamma Sensory Stimulation May Reduce White Matter and Myelin Loss in Alzheimer's Disease. *J Alzheimers Dis,* 97**,** 359-372.

DANA, H., MOHAR, B., SUN, Y., NARAYAN, S., GORDUS, A., HASSEMAN, J. P., TSEGAYE, G., HOLT, G. T., HU, A., WALPITA, D., PATEL, R., MACKLIN, J. J., BARGMANN, C. I., AHRENS, M. B., SCHREITER, E. R., JAYARAMAN, V., LOOGER, L. L., SVOBODA, K. & KIM, D. S. 2016. Sensitive red protein calcium indicators for imaging neural activity. *Elife,* 5.

DANA, H., SUN, Y., MOHAR, B., HULSE, B. K., KERLIN, A. M., HASSEMAN, J. P., TSEGAYE, G., TSANG, A., WONG, A., PATEL, R., MACKLIN, J. J., CHEN, Y., KONNERTH, A., JAYARAMAN, V., LOOGER, L. L., SCHREITER, E. R., SVOBODA, K. & KIM, D. S. 2019. High-performance calcium sensors for imaging activity in neuronal populations and microcompartments. *Nat Methods,* 16**,** 649-657.

DAS, S., LI, Z., NOORI, A., HYMAN, B. T. & SERRANO-POZO, A. 2020. Meta-analysis of mouse transcriptomic studies supports a context-dependent astrocyte reaction in acute CNS injury versus neurodegeneration. *J Neuroinflammation,* 17**,** 227.

DAVALOS, D., GRUTZENDLER, J., YANG, G., KIM, J. V., ZUO, Y., JUNG, S., LITTMAN, D. R., DUSTIN, M. L. & GAN, W. B. 2005. ATP mediates rapid microglial response to local brain injury in vivo. *Nat Neurosci,* 8**,** 752-8.

DAVIES, P. & MALONEY, A. J. 1976. Selective loss of central cholinergic neurons in Alzheimer's disease. *Lancet,* 2**,** 1403.

DE CEGLIA, R., LEDONNE, A., LITVIN, D. G., LIND, B. L., CARRIERO, G., LATAGLIATA, E. C., BINDOCCI, E., DI CASTRO, M. A., SAVTCHOUK, I., VITALI, I., RANJAK, A., CONGIU, M., CANONICA, T., WISDEN, W., HARRIS, K., MAMELI, M., MERCURI, N., TELLEY, L. & VOLTERRA, A. 2023. Specialized astrocytes mediate glutamatergic gliotransmission in the CNS. *Nature,* 622**,** 120-129.

DE FELICE, F. G., VELASCO, P. T., LAMBERT, M. P., VIOLA, K., FERNANDEZ, S. J., FERREIRA, S. T. & KLEIN, W. L. 2007. Abeta oligomers induce neuronal oxidative stress through an N-methyl-D-aspartate receptor-dependent mechanism that is blocked by the Alzheimer drug memantine. *J Biol Chem,* 282**,** 11590-601.

DE MARIO, A., CASTELLANI, A., PEGGION, C., MASSIMINO, M. L., LIM, D., HILL, A. F., SORGATO, M. C. & BERTOLI, A. 2015. The prion protein constitutively controls neuronal store-operated Ca(2+) entry through Fyn kinase. *Front Cell Neurosci,* 9**,** 416.

DE STROOPER, B., SAFTIG, P., CRAESSAERTS, K., VANDERSTICHELE, H., GUHDE, G., ANNAERT, W., VON FIGURA, K. & VAN LEUVEN, F. 1998. Deficiency of presenilin-1 inhibits the normal cleavage of amyloid precursor protein. *Nature,* 391**,** 387-90.

DEANE, R., BELL, R. D., SAGARE, A. & ZLOKOVIC, B. V. 2009. Clearance of amyloid-beta peptide across the blood-brain barrier: implication for therapies in Alzheimer's disease. *CNS Neurol Disord Drug Targets,* 8**,** 16-30.

DEANE, R., DU YAN, S., SUBMAMARYAN, R. K., LARUE, B., JOVANOVIC, S., HOGG, E., WELCH, D., MANNESS, L., LIN, C., YU, J., ZHU, H., GHISO, J., FRANGIONE, B., STERN, A., SCHMIDT, A. M., ARMSTRONG, D. L., ARNOLD, B., LILIENSIEK, B., NAWROTH, P., HOFMAN, F., KINDY, M., STERN, D. & ZLOKOVIC, B. 2003. RAGE mediates amyloid-beta peptide transport across the blood-brain barrier and accumulation in brain. *Nat Med,* 9**,** 907-13.

DEANE, R., WU, Z., SAGARE, A., DAVIS, J., DU YAN, S., HAMM, K., XU, F., PARISI, M., LARUE, B., HU, H. W., SPIJKERS, P., GUO, H., SONG, X., LENTING, P. J., VAN NOSTRAND, W. E. & ZLOKOVIC, B. V. 2004. LRP/amyloid beta-peptide interaction mediates differential brain efflux of Abeta isoforms. *Neuron,* 43**,** 333-44.

DEARDORFF, W. J. & GROSSBERG, G. T. 2017. Targeting neuroinflammation in Alzheimer's disease: evidence for NSAIDs and novel therapeutics. *Expert Rev Neurother,* 17**,** 17-32.
DELATOUR, B., EPELBAUM, S., PETIET, A. & DHENAIN, M. 2010. In vivo imaging biomarkers in mouse models of Alzheimer's disease: are we lost in translation or breaking through? *Int J Alzheimers Dis,* 2010.
DELEKATE, A., FUCHTEMEIER, M., SCHUMACHER, T., ULBRICH, C., FODDIS, M. & PETZOLD, G. C. 2014. Metabotropic P2Y1 receptor signalling mediates astrocytic hyperactivity in vivo in an Alzheimer's disease mouse model. *Nat Commun,* 5**,** 5422.
DETURE, M. A. & DICKSON, D. W. 2019. The neuropathological diagnosis of Alzheimer's disease. *Mol Neurodegener,* 14**,** 32.
DEVI, L. & OHNO, M. 2010. Phospho-eIF2alpha level is important for determining abilities of BACE1 reduction to rescue cholinergic neurodegeneration and memory defects in 5XFAD mice. *PLoS One,* 5**,** e12974.
DEVI, L., PRABHU, B. M., GALATI, D. F., AVADHANI, N. G. & ANANDATHEERTHAVARADA, H. K. 2006. Accumulation of amyloid precursor protein in the mitochondrial import channels of human Alzheimer's disease brain is associated with mitochondrial dysfunction. *J Neurosci,* 26**,** 9057-68.
DEWITT, D. A., PERRY, G., COHEN, M., DOLLER, C. & SILVER, J. 1998. Astrocytes regulate microglial phagocytosis of senile plaque cores of Alzheimer's disease. *Exp Neurol,* 149**,** 329-40.
DISHMAN, R. K., BERTHOUD, H. R., BOOTH, F. W., COTMAN, C. W., EDGERTON, V. R., FLESHNER, M. R., GANDEVIA, S. C., GOMEZ-PINILLA, F., GREENWOOD, B. N., HILLMAN, C. H., KRAMER, A. F., LEVIN, B. E., MORAN, T. H., RUSSO-NEUSTADT, A. A., SALAMONE, J. D., VAN HOOMISSEN, J. D., WADE, C. E., YORK, D. A. & ZIGMOND, M. J. 2006. Neurobiology of exercise. *Obesity (Silver Spring),* 14**,** 345-56.
DODART, J. C., MEZIANE, H., MATHIS, C., BALES, K. R., PAUL, S. M. & UNGERER, A. 1999. Behavioral disturbances in transgenic mice overexpressing the V717F beta-amyloid precursor protein. *Behav Neurosci,* 113**,** 982-90.
DOMERT, J., RAO, S. B., AGHOLME, L., BRORSSON, A. C., MARCUSSON, J., HALLBECK, M. & NATH, S. 2014. Spreading of amyloid-beta peptides via neuritic cell-to-cell transfer is dependent on insufficient cellular clearance. *Neurobiol Dis,* 65**,** 82-92.
DONAHUE, J. E., FLAHERTY, S. L., JOHANSON, C. E., DUNCAN, J. A., 3RD, SILVERBERG, G. D., MILLER, M. C., TAVARES, R., YANG, W., WU, Q., SABO, E., HOVANESIAN, V. & STOPA, E. G. 2006. RAGE, LRP-1, and amyloid-beta protein in Alzheimer's disease. *Acta Neuropathol,* 112**,** 405-15.
DONG, J., REVILLA-SANCHEZ, R., MOSS, S. & HAYDON, P. G. 2010. Multiphoton in vivo imaging of amyloid in animal models of Alzheimer's disease. *Neuropharmacology,* 59**,** 268-75.
DONG, Y., ZHANG, G., ZHANG, B., MOIR, R. D., XIA, W., MARCANTONIO, E. R., CULLEY, D. J., CROSBY, G., TANZI, R. E. & XIE, Z. 2009. The common inhalational anesthetic sevoflurane induces apoptosis and increases beta-amyloid protein levels. *Arch Neurol,* 66**,** 620-31.
DREWES, G., LICHTENBERG-KRAAG, B., DORING, F., MANDELKOW, E. M., BIERNAT, J., GORIS, J., DOREE, M. & MANDELKOW, E. 1992. Mitogen activated protein (MAP) kinase transforms tau protein into an Alzheimer-like state. *EMBO J,* 11**,** 2131-8.
DUCKWORTH, W. C., BENNETT, R. G. & HAMEL, F. G. 1998. Insulin acts intracellularly on proteasomes through insulin-degrading enzyme. *Biochem Biophys Res Commun,* 244**,** 390-4.
DUDEFFANT, C., VANDESQUILLE, M., HERBERT, K., GARIN, C. M., ALVES, S., BLANCHARD, V., COMOY, E. E., PETIT, F. & DHENAIN, M. 2017. Contrast-enhanced MR microscopy of amyloid plaques in five mouse models of amyloidosis and in human Alzheimer's disease brains. *Sci Rep,* 7**,** 4955.
EANES, E. D. & GLENNER, G. G. 1968. X-ray diffraction studies on amyloid filaments. *J Histochem Cytochem,* 16**,** 673-7.
ECKENHOFF, R. G., JOHANSSON, J. S., WEI, H., CARNINI, A., KANG, B., WEI, W., PIDIKITI, R., KELLER, J. M. & ECKENHOFF, M. F. 2004. Inhaled anesthetic enhancement of amyloid-beta oligomerization and cytotoxicity. *Anesthesiology,* 101**,** 703-9.
ECKMAN, E. A., ADAMS, S. K., TROENDLE, F. J., STODOLA, B. A., KAHN, M. A., FAUQ, A. H., XIAO, H. D., BERNSTEIN, K. E. & ECKMAN, C. B. 2006. Regulation of steady-state beta-amyloid levels in the brain by neprilysin and endothelin-converting enzyme but not angiotensin-converting enzyme. *J Biol Chem,* 281**,** 30471-8.
ECKMAN, E. A., REED, D. K. & ECKMAN, C. B. 2001. Degradation of the Alzheimer's amyloid beta peptide by endothelin-converting enzyme. *J Biol Chem,* 276**,** 24540-8.

EDBAUER, D., WILLEM, M., LAMMICH, S., STEINER, H. & HAASS, C. 2002. Insulin-degrading enzyme rapidly removes the beta-amyloid precursor protein intracellular domain (AICD). *J Biol Chem,* 277**,** 13389-93.

EECKMAN, F. H. & FREEMAN, W. J. 1990. Correlations between unit firing and EEG in the rat olfactory system. *Brain Res,* 528**,** 238-44.

EICHHOFF, G., BUSCHE, M. A. & GARASCHUK, O. 2008. In vivo calcium imaging of the aging and diseased brain. *Eur J Nucl Med Mol Imaging,* 35 Suppl 1**,** S99-106.

EIMER, W. A. & VASSAR, R. 2013. Neuron loss in the 5XFAD mouse model of Alzheimer's disease correlates with intraneuronal Abeta42 accumulation and Caspase-3 activation. *Mol Neurodegener,* 8**,** 2.

EIMER, W. A., VIJAYA KUMAR, D. K., NAVALPUR SHANMUGAM, N. K., RODRIGUEZ, A. S., MITCHELL, T., WASHICOSKY, K. J., GYORGY, B., BREAKEFIELD, X. O., TANZI, R. E. & MOIR, R. D. 2018. Alzheimer's Disease-Associated beta-Amyloid Is Rapidly Seeded by Herpesviridae to Protect against Brain Infection. *Neuron,* 99**,** 56-63 e3.

EISELE, Y. S., BOLMONT, T., HEIKENWALDER, M., LANGER, F., JACOBSON, L. H., YAN, Z. X., ROTH, K., AGUZZI, A., STAUFENBIEL, M., WALKER, L. C. & JUCKER, M. 2009. Induction of cerebral beta-amyloidosis: intracerebral versus systemic Abeta inoculation. *Proc Natl Acad Sci U S A,* 106**,** 12926-31.

ENGELHART, M. J., GEERLINGS, M. I., RUITENBERG, A., VAN SWIETEN, J. C., HOFMAN, A., WITTEMAN, J. C. & BRETELER, M. M. 2002. Dietary intake of antioxidants and risk of Alzheimer disease. *JAMA,* 287**,** 3223-9.

ENGLER, H., FORSBERG, A., ALMKVIST, O., BLOMQUIST, G., LARSSON, E., SAVITCHEVA, I., WALL, A., RINGHEIM, A., LANGSTROM, B. & NORDBERG, A. 2006. Two-year follow-up of amyloid deposition in patients with Alzheimer's disease. *Brain,* 129**,** 2856-66.

ESCARTIN, C., GALEA, E., LAKATOS, A., O'CALLAGHAN, J. P., PETZOLD, G. C., SERRANO-POZO, A., STEINHAUSER, C., VOLTERRA, A., CARMIGNOTO, G., AGARWAL, A., ALLEN, N. J., ARAQUE, A., BARBEITO, L., BARZILAI, A., BERGLES, D. E., BONVENTO, G., BUTT, A. M., CHEN, W. T., COHEN-SALMON, M., CUNNINGHAM, C., DENEEN, B., DE STROOPER, B., DIAZ-CASTRO, B., FARINA, C., FREEMAN, M., GALLO, V., GOLDMAN, J. E., GOLDMAN, S. A., GOTZ, M., GUTIERREZ, A., HAYDON, P. G., HEILAND, D. H., HOL, E. M., HOLT, M. G., IINO, M., KASTANENKA, K. V., KETTENMANN, H., KHAKH, B. S., KOIZUMI, S., LEE, C. J., LIDDELOW, S. A., MACVICAR, B. A., MAGISTRETTI, P., MESSING, A., MISHRA, A., MOLOFSKY, A. V., MURAI, K. K., NORRIS, C. M., OKADA, S., OLIET, S. H. R., OLIVEIRA, J. F., PANATIER, A., PARPURA, V., PEKNA, M., PEKNY, M., PELLERIN, L., PEREA, G., PEREZ-NIEVAS, B. G., PFRIEGER, F. W., POSKANZER, K. E., QUINTANA, F. J., RANSOHOFF, R. M., RIQUELME-PEREZ, M., ROBEL, S., ROSE, C. R., ROTHSTEIN, J. D., ROUACH, N., ROWITCH, D. H., SEMYANOV, A., SIRKO, S., SONTHEIMER, H., SWANSON, R. A., VITORICA, J., WANNER, I. B., WOOD, L. B., WU, J., ZHENG, B., ZIMMER, E. R., ZOREC, R., SOFRONIEW, M. V. & VERKHRATSKY, A. 2021. Reactive astrocyte nomenclature, definitions, and future directions. *Nat Neurosci,* 24**,** 312-325.

ESCH, F. S., KEIM, P. S., BEATTIE, E. C., BLACHER, R. W., CULWELL, A. R., OLTERSDORF, T., MCCLURE, D. & WARD, P. J. 1990. Cleavage of amyloid beta peptide during constitutive processing of its precursor. *Science,* 248**,** 1122-4.

ETTER, G., VAN DER VELDT, S., MANSEAU, F., ZARRINKOUB, I., TRILLAUD-DOPPIA, E. & WILLIAMS, S. 2019. Optogenetic gamma stimulation rescues memory impairments in an Alzheimer's disease mouse model. *Nat Commun,* 10**,** 5322.

FANDRICH, M. 2012. Oligomeric intermediates in amyloid formation: structure determination and mechanisms of toxicity. *J Mol Biol,* 421**,** 427-40.

FARRIS, W., MANSOURIAN, S., CHANG, Y., LINDSLEY, L., ECKMAN, E. A., FROSCH, M. P., ECKMAN, C. B., TANZI, R. E., SELKOE, D. J. & GUENETTE, S. 2003. Insulin-degrading enzyme regulates the levels of insulin, amyloid beta-protein, and the beta-amyloid precursor protein intracellular domain in vivo. *Proc Natl Acad Sci U S A,* 100**,** 4162-7.

FEART, C., SAMIERI, C., RONDEAU, V., AMIEVA, H., PORTET, F., DARTIGUES, J. F., SCARMEAS, N. & BARBERGER-GATEAU, P. 2009. Adherence to a Mediterranean diet, cognitive decline, and risk of dementia. *JAMA,* 302**,** 638-48.

FELLIN, T. & CARMIGNOTO, G. 2004. Neurone-to-astrocyte signalling in the brain represents a distinct multifunctional unit. *J Physiol,* 559**,** 3-15.

FELLIN, T., PASCUAL, O., GOBBO, S., POZZAN, T., HAYDON, P. G. & CARMIGNOTO, G. 2004. Neuronal synchrony mediated by astrocytic glutamate through activation of extrasynaptic NMDA receptors. *Neuron,* 43**,** 729-43.

FELSKY, D., ROOSTAEI, T., NHO, K., RISACHER, S. L., BRADSHAW, E. M., PETYUK, V., SCHNEIDER, J. A., SAYKIN, A., BENNETT, D. A. & DE JAGER, P. L. 2019. Neuropathological correlates and genetic architecture of microglial activation in elderly human brain. *Nat Commun,* 10**,** 409.

FERNANDEZ-FUNEZ, P., DE MENA, L. & RINCON-LIMAS, D. E. 2015. Modeling the complex pathology of Alzheimer's disease in Drosophila. *Exp Neurol,* 274**,** 58-71.

FINGER, C. E., MORENO-GONZALEZ, I., GUTIERREZ, A., MORUNO-MANCHON, J. F. & MCCULLOUGH, L. D. 2022. Age-related immune alterations and cerebrovascular inflammation. *Mol Psychiatry,* 27**,** 803-818.

FLANIGAN, T. J., XUE, Y., KISHAN RAO, S., DHANUSHKODI, A. & MCDONALD, M. P. 2014. Abnormal vibrissa-related behavior and loss of barrel field inhibitory neurons in 5xFAD transgenics. *Genes Brain Behav,* 13**,** 488-500.

FLOOD, D. G., REAUME, A. G., DORFMAN, K. S., LIN, Y. G., LANG, D. M., TRUSKO, S. P., SAVAGE, M. J., ANNAERT, W. G., DE STROOPER, B., SIMAN, R. & SCOTT, R. W. 2002. FAD mutant PS-1 gene-targeted mice: increased A beta 42 and A beta deposition without APP overproduction. *Neurobiol Aging,* 23**,** 335-48.

FONTAINE, S. N., ZHENG, D., SABBAGH, J. J., MARTIN, M. D., CHAPUT, D., DARLING, A., TROTTER, J. H., STOTHERT, A. R., NORDHUES, B. A., LUSSIER, A., BAKER, J., SHELTON, L., KAHN, M., BLAIR, L. J., STEVENS, S. M., JR. & DICKEY, C. A. 2016. DnaJ/Hsc70 chaperone complexes control the extracellular release of neurodegenerative-associated proteins. *EMBO J,* 35**,** 1537-49.

FOO, L. C., ALLEN, N. J., BUSHONG, E. A., VENTURA, P. B., CHUNG, W. S., ZHOU, L., CAHOY, J. D., DANEMAN, R., ZONG, H., ELLISMAN, M. H. & BARRES, B. A. 2011. Development of a method for the purification and culture of rodent astrocytes. *Neuron,* 71**,** 799-811.

FORMOZOV, A., DIETER, A. & WIEGERT, J. S. 2023. A flexible and versatile system for multi-color fiber photometry and optogenetic manipulation. *Cell Rep Methods,* 3**,** 100418.

FRANCIS, P. T., PALMER, A. M., SNAPE, M. & WILCOCK, G. K. 1999. The cholinergic hypothesis of Alzheimer's disease: a review of progress. *J Neurol Neurosurg Psychiatry,* 66**,** 137-47.

FRATIGLIONI, L. & WANG, H. X. 2007. Brain reserve hypothesis in dementia. *J Alzheimers Dis,* 12**,** 11-22.

FRAUTSCHY, S. A., YANG, F., IRRIZARRY, M., HYMAN, B., SAIDO, T. C., HSIAO, K. & COLE, G. M. 1998. Microglial response to amyloid plaques in APPsw transgenic mice. *Am J Pathol,* 152**,** 307-17.

FREEMAN, W. J. 1975. *Mass Action in the Nervous System*, Academic Press: New York, NY, USA.

FREEMAN, W. J., ROGERS, L. J., HOLMES, M. D. & SILBERGELD, D. L. 2000. Spatial spectral analysis of human electrocorticograms including the alpha and gamma bands. *J Neurosci Methods,* 95**,** 111-21.

FRIES, P. 2015. Rhythms for Cognition: Communication through Coherence. *Neuron,* 88**,** 220-35.

FRIESEN, M., ZIEGLER-WALDKIRCH, S., EGENOLF, M., D'ERRICO, P., HELM, C., MEZO, C., DOKALIS, N., ERNY, D., KATZMARSKI, N., COELHO, R., LORETH, D., PRINZ, M. & MEYER-LUEHMANN, M. 2022. Distinct Abeta pathology in the olfactory bulb and olfactory deficits in a mouse model of Abeta and alpha-syn co-pathology. *Brain Pathol,* 32**,** e13032.

FRISINA, R. D., SINGH, A., BAK, M., BOZORG, S., SETH, R. & ZHU, X. 2011. F1 (CBAxC57) mice show superior hearing in old age relative to their parental strains: hybrid vigor or a new animal model for "golden ears"? *Neurobiol Aging,* 32**,** 1716-24.

FU, H., POSSENTI, A., FREER, R., NAKANO, Y., HERNANDEZ VILLEGAS, N. C., TANG, M., CAUHY, P. V. M., LASSUS, B. A., CHEN, S., FOWLER, S. L., FIGUEROA, H. Y., HUEY, E. D., JOHNSON, G. V. W., VENDRUSCOLO, M. & DUFF, K. E. 2019. A tau homeostasis signature is linked with the cellular and regional vulnerability of excitatory neurons to tau pathology. *Nat Neurosci,* 22**,** 47-56.

FUCHS, E. C., ZIVKOVIC, A. R., CUNNINGHAM, M. O., MIDDLETON, S., LEBEAU, F. E., BANNERMAN, D. M., ROZOV, A., WHITTINGTON, M. A., TRAUB, R. D., RAWLINS, J. N. & MONYER, H. 2007. Recruitment of parvalbumin-positive interneurons determines hippocampal function and associated behavior. *Neuron,* 53**,** 591-604.

FUENTEALBA, R. A., LIU, Q., ZHANG, J., KANEKIYO, T., HU, X., LEE, J. M., LADU, M. J. & BU, G. 2010. Low-density lipoprotein receptor-related protein 1 (LRP1) mediates neuronal Abeta42 uptake and lysosomal trafficking. *PLoS One,* 5**,** e11884.

FUJISAWA, S. & BUZSAKI, G. 2011. A 4 Hz oscillation adaptively synchronizes prefrontal, VTA, and hippocampal activities. *Neuron,* 72**,** 153-65.

GAMBLIN, T. C., CHEN, F., ZAMBRANO, A., ABRAHA, A., LAGALWAR, S., GUILLOZET, A. L., LU, M., FU, Y., GARCIA-SIERRA, F., LAPOINTE, N., MILLER, R., BERRY, R. W., BINDER, L. I. & CRYNS, V. L. 2003. Caspase cleavage of tau: linking amyloid and neurofibrillary tangles in Alzheimer's disease. *Proc Natl Acad Sci U S A,* 100**,** 10032-7.

GAMES, D., ADAMS, D., ALESSANDRINI, R., BARBOUR, R., BERTHELETTE, P., BLACKWELL, C., CARR, T., CLEMENS, J., DONALDSON, T., GILLESPIE, F. & ET AL. 1995. Alzheimer-type neuropathology in transgenic mice overexpressing V717F beta-amyloid precursor protein. *Nature,* 373**,** 523-7.

GANDY, S. 2005. The role of cerebral amyloid beta accumulation in common forms of Alzheimer disease. *J Clin Invest,* 115**,** 1121-9.

GARCIA-MARIN, V., GARCIA-LOPEZ, P. & FREIRE, M. 2007. Cajal's contributions to glia research. *Trends Neurosci,* 30**,** 479-87.

GARVER, T. D., HARRIS, K. A., LEHMAN, R. A., LEE, V. M., TROJANOWSKI, J. Q. & BILLINGSLEY, M. L. 1994. Tau phosphorylation in human, primate, and rat brain: evidence that a pool of tau is highly phosphorylated in vivo and is rapidly dephosphorylated in vitro. *J Neurochem,* 63**,** 2279-87.

GARZA, K. M., ZHANG, L., BORRON, B., WOOD, L. B. & SINGER, A. C. 2020. Gamma Visual Stimulation Induces a Neuroimmune Signaling Profile Distinct from Acute Neuroinflammation. *J Neurosci,* 40**,** 1211-1225.

GAUBERT, S., RAIMONDO, F., HOUOT, M., CORSI, M. C., NACCACHE, L., DIEGO SITT, J., HERMANN, B., OUDIETTE, D., GAGLIARDI, G., HABERT, M. O., DUBOIS, B., DE VICO FALLANI, F., BAKARDJIAN, H., EPELBAUM, S. & ALZHEIMER'S DISEASE NEUROIMAGING, I. 2019. EEG evidence of compensatory mechanisms in preclinical Alzheimer's disease. *Brain,* 142**,** 2096-2112.

GEISLER, C., BRUNEL, N. & WANG, X. J. 2005. Contributions of intrinsic membrane dynamics to fast network oscillations with irregular neuronal discharges. *J Neurophysiol,* 94**,** 4344-61.

GEULA, C., WU, C. K., SAROFF, D., LORENZO, A., YUAN, M. & YANKNER, B. A. 1998. Aging renders the brain vulnerable to amyloid beta-protein neurotoxicity. *Nat Med,* 4**,** 827-31.

GIANNAKOPOULOS, P., SILHOL, S., JALLAGEAS, V., MALLET, J., BONS, N., BOURAS, C. & DELAERE, P. 1997. Quantitative analysis of tau protein-immunoreactive accumulations and beta amyloid protein deposits in the cerebral cortex of the mouse lemur, Microcebus murinus. *Acta Neuropathol,* 94**,** 131-9.

GILLESPIE, A. K., JONES, E. A., LIN, Y. H., KARLSSON, M. P., KAY, K., YOON, S. Y., TONG, L. M., NOVA, P., CARR, J. S., FRANK, L. M. & HUANG, Y. 2016. Apolipoprotein E4 Causes Age-Dependent Disruption of Slow Gamma Oscillations during Hippocampal Sharp-Wave Ripples. *Neuron,* 90**,** 740-51.

GLENNER, G. G. 1979. Congophilic microangiopathy in the pathogenesis of Alzheimer's syndrome (presenile dementia). *Med Hypotheses,* 5**,** 1231-6.

GLENNER, G. G. 1988. Alzheimer's disease: its proteins and genes. *Cell,* 52**,** 307-8.

GLENNER, G. G. & WONG, C. W. 1984a. Alzheimer's disease and Down's syndrome: sharing of a unique cerebrovascular amyloid fibril protein. *Biochem Biophys Res Commun,* 122**,** 1131-5.

GLENNER, G. G. & WONG, C. W. 1984b. Alzheimer's disease: initial report of the purification and characterization of a novel cerebrovascular amyloid protein. *Biochem Biophys Res Commun,* 120**,** 885-90.

GOATE, A., CHARTIER-HARLIN, M. C., MULLAN, M., BROWN, J., CRAWFORD, F., FIDANI, L., GIUFFRA, L., HAYNES, A., IRVING, N., JAMES, L. & ET AL. 1991. Segregation of a missense mutation in the amyloid precursor protein gene with familial Alzheimer's disease. *Nature,* 349**,** 704-6.

GOEDERT, M. 1987. Neuronal localization of amyloid beta protein precursor mRNA in normal human brain and in Alzheimer's disease. *EMBO J,* 6**,** 3627-32.

GONZALES, M. M., GARBARINO, V. R., KAUTZ, T. F., PALAVICINI, J. P., LOPEZ-CRUZAN, M., DEHKORDI, S. K., MATHEWS, J. J., ZARE, H., XU, P., ZHANG, B., FRANKLIN, C., HABES, M., CRAFT, S., PETERSEN, R. C., TCHKONIA, T., KIRKLAND, J. L., SALARDINI, A., SESHADRI, S., MUSI, N. & ORR, M. E. 2023. Senolytic therapy in mild Alzheimer's disease: a phase 1 feasibility trial. *Nat Med,* 29**,** 2481-2488.

GONZALEZ, J. A., JENSEN, L. T., IORDANIDOU, P., STROM, M., FUGGER, L. & BURDAKOV, D. 2016. Inhibitory Interplay between Orexin Neurons and Eating. *Curr Biol,* 26**,** 2486-2491.

GONZALEZ-PRIETO, M., GUTIERREZ, I. L., GARCIA-BUENO, B., CASO, J. R., LEZA, J. C., ORTEGA-HERNANDEZ, A., GOMEZ-GARRE, D. & MADRIGAL, J. L. M. 2021. Microglial

CX3CR1 production increases in Alzheimer's disease and is regulated by noradrenaline. *Glia,* 69**,** 73-90.
GOUTAGNY, R., GU, N., CAVANAGH, C., JACKSON, J., CHABOT, J. G., QUIRION, R., KRANTIC, S. & WILLIAMS, S. 2013. Alterations in hippocampal network oscillations and theta-gamma coupling arise before Abeta overproduction in a mouse model of Alzheimer's disease. *Eur J Neurosci,* 37**,** 1896-902.
GOUWENS, L. K., ISMAIL, M. S., ROGERS, V. A., ZELLER, N. T., GARRAD, E. C., AMTASHAR, F. S., MAKONI, N. J., OSBORN, D. C. & NICHOLS, M. R. 2018. Abeta42 Protofibrils Interact with and Are Trafficked through Microglial-Derived Microvesicles. *ACS Chem Neurosci,* 9**,** 1416-1425.
GOUWENS, L. K., MAKONI, N. J., ROGERS, V. A. & NICHOLS, M. R. 2016. Amyloid-beta42 protofibrils are internalized by microglia more extensively than monomers. *Brain Res,* 1648**,** 485-495.
GRAY, D. A. & WOULFE, J. 2005. Lipofuscin and aging: a matter of toxic waste. *Sci Aging Knowledge Environ,* 2005**,** re1.
GRIFFIN, W. S., STANLEY, L. C., LING, C., WHITE, L., MACLEOD, V., PERROT, L. J., WHITE, C. L., 3RD & ARAOZ, C. 1989. Brain interleukin 1 and S-100 immunoreactivity are elevated in Down syndrome and Alzheimer disease. *Proc Natl Acad Sci U S A,* 86**,** 7611-5.
GRIFFITHS, K., BINDER, U., MCDOWELL, W., TOMMASI, R., FRIGERIO, M., DARBY, W. G., HOSKING, C. G., RENAUD, L., MACHACEK, M., LLOYD, P., SKERRA, A. & FOLEY, M. 2019. Half-life extension and non-human primate pharmacokinetic safety studies of i-body AD-114 targeting human CXCR4. *MAbs,* 11**,** 1331-1340.
GRUNING, C. S., KLINKER, S., WOLFF, M., SCHNEIDER, M., TOKSOZ, K., KLEIN, A. N., NAGEL-STEGER, L., WILLBOLD, D. & HOYER, W. 2013. The off-rate of monomers dissociating from amyloid-beta protofibrils. *J Biol Chem,* 288**,** 37104-11.
GU, X., ZHAO, Z., CHEN, X., ZHANG, L., FANG, H., ZHAO, T., JU, S., GAO, W., QIAN, X., WANG, X., ZHANG, J. & CHENG, H. 2023. Imaging microglia surveillance during sleep-wake cycles in freely behaving mice. *Elife,* 12.
GUAN, A., WANG, S., HUANG, A., QIU, C., LI, Y., LI, X., WANG, J., WANG, Q. & DENG, B. 2022. The role of gamma oscillations in central nervous system diseases: Mechanism and treatment. *Front Cell Neurosci,* 16**,** 962957.
GUERREIRO, R., WOJTAS, A., BRAS, J., CARRASQUILLO, M., ROGAEVA, E., MAJOUNIE, E., CRUCHAGA, C., SASSI, C., KAUWE, J. S., YOUNKIN, S., HAZRATI, L., COLLINGE, J., POCOCK, J., LASHLEY, T., WILLIAMS, J., LAMBERT, J. C., AMOUYEL, P., GOATE, A., RADEMAKERS, R., MORGAN, K., POWELL, J., ST GEORGE-HYSLOP, P., SINGLETON, A., HARDY, J. & ALZHEIMER GENETIC ANALYSIS, G. 2013. TREM2 variants in Alzheimer's disease. *N Engl J Med,* 368**,** 117-27.
GUNAWARDENA, S. & GOLDSTEIN, L. S. 2001. Disruption of axonal transport and neuronal viability by amyloid precursor protein mutations in Drosophila. *Neuron,* 32**,** 389-401.
GUO, J. L., NARASIMHAN, S., CHANGOLKAR, L., HE, Z., STIEBER, A., ZHANG, B., GATHAGAN, R. J., IBA, M., MCBRIDE, J. D., TROJANOWSKI, J. Q. & LEE, V. M. 2016. Unique pathological tau conformers from Alzheimer's brains transmit tau pathology in nontransgenic mice. *J Exp Med,* 213**,** 2635-2654.
GUO, L., ZHONG, M. B., ZHANG, L., ZHANG, B. & CAI, D. 2022. Sex Differences in Alzheimer's Disease: Insights From the Multiomics Landscape. *Biol Psychiatry,* 91**,** 61-71.
GUO, Q., ZHOU, J., FENG, Q., LIN, R., GONG, H., LUO, Q., ZENG, S., LUO, M. & FU, L. 2015. Multi-channel fiber photometry for population neuronal activity recording. *Biomed Opt Express,* 6**,** 3919-31.
GUO, Z., YIN, L., DIAZ, V., DAI, B., OSAKADA, T., LISCHINSKY, J. E., CHIEN, J., YAMAGUCHI, T., URTECHO, A., TONG, X., CHEN, Z. S. & LIN, D. 2023. Neural dynamics in the limbic system during male social behaviors. *Neuron*.
HAAS, L. T., KOSTYLEV, M. A. & STRITTMATTER, S. M. 2014. Therapeutic molecules and endogenous ligands regulate the interaction between brain cellular prion protein (PrPC) and metabotropic glutamate receptor 5 (mGluR5). *J Biol Chem,* 289**,** 28460-77.
HAASS, C., LEMERE, C. A., CAPELL, A., CITRON, M., SEUBERT, P., SCHENK, D., LANNFELT, L. & SELKOE, D. J. 1995. The Swedish mutation causes early-onset Alzheimer's disease by beta-secretase cleavage within the secretory pathway. *Nat Med,* 1**,** 1291-6.
HAASS, C., SCHLOSSMACHER, M. G., HUNG, A. Y., VIGO-PELFREY, C., MELLON, A., OSTASZEWSKI, B. L., LIEBERBURG, I., KOO, E. H., SCHENK, D., TEPLOW, D. B. & ET AL. 1992. Amyloid beta-peptide is produced by cultured cells during normal metabolism. *Nature,* 359**,** 322-5.

HALL, F. L., MITCHELL, J. P. & VULLIET, P. R. 1990. Phosphorylation of synapsin I at a novel site by proline-directed protein kinase. *J Biol Chem,* 265**,** 6944-8.
HAMANI, C., MCANDREWS, M. P., COHN, M., OH, M., ZUMSTEG, D., SHAPIRO, C. M., WENNBERG, R. A. & LOZANO, A. M. 2008. Memory enhancement induced by hypothalamic/fornix deep brain stimulation. *Ann Neurol,* 63**,** 119-23.
HAMM, V., HERAUD, C., BOTT, J. B., HERBEAUX, K., STRITTMATTER, C., MATHIS, C. & GOUTAGNY, R. 2017. Differential contribution of APP metabolites to early cognitive deficits in a TgCRND8 mouse model of Alzheimer's disease. *Sci Adv,* 3**,** e1601068.
HAMPEL, H., HARDY, J., BLENNOW, K., CHEN, C., PERRY, G., KIM, S. H., VILLEMAGNE, V. L., AISEN, P., VENDRUSCOLO, M., IWATSUBO, T., MASTERS, C. L., CHO, M., LANNFELT, L., CUMMINGS, J. L. & VERGALLO, A. 2021. The Amyloid-beta Pathway in Alzheimer's Disease. *Mol Psychiatry,* 26**,** 5481-5503.
HAMPEL, H., MESULAM, M. M., CUELLO, A. C., FARLOW, M. R., GIACOBINI, E., GROSSBERG, G. T., KHACHATURIAN, A. S., VERGALLO, A., CAVEDO, E., SNYDER, P. J. & KHACHATURIAN, Z. S. 2018. The cholinergic system in the pathophysiology and treatment of Alzheimer's disease. *Brain,* 141**,** 1917-1933.
HANGER, D. P., HUGHES, K., WOODGETT, J. R., BRION, J. P. & ANDERTON, B. H. 1992. Glycogen synthase kinase-3 induces Alzheimer's disease-like phosphorylation of tau: generation of paired helical filament epitopes and neuronal localisation of the kinase. *Neurosci Lett,* 147**,** 58-62.
HANSSON, O., ZETTERBERG, H., BUCHHAVE, P., ANDREASSON, U., LONDOS, E., MINTHON, L. & BLENNOW, K. 2007. Prediction of Alzheimer's disease using the CSF Abeta42/Abeta40 ratio in patients with mild cognitive impairment. *Dement Geriatr Cogn Disord,* 23**,** 316-20.
HARDY, J. 1997. Amyloid, the presenilins and Alzheimer's disease. *Trends Neurosci,* 20**,** 154-9.
HARDY, J. & SELKOE, D. J. 2002. The amyloid hypothesis of Alzheimer's disease: progress and problems on the road to therapeutics. *Science,* 297**,** 353-6.
HARDY, J. A. & HIGGINS, G. A. 1992. Alzheimer's disease: the amyloid cascade hypothesis. *Science,* 256**,** 184-5.
HARRIS, K. D., CSICSVARI, J., HIRASE, H., DRAGOI, G. & BUZSAKI, G. 2003. Organization of cell assemblies in the hippocampus. *Nature,* 424**,** 552-6.
HARRIS, K. D. & THIELE, A. 2011. Cortical state and attention. *Nat Rev Neurosci,* 12**,** 509-23.
HARTLAGE-RUBSAMEN, M., ZEITSCHEL, U., APELT, J., GARTNER, U., FRANKE, H., STAHL, T., GUNTHER, A., SCHLIEBS, R., PENKOWA, M., BIGL, V. & ROSSNER, S. 2003. Astrocytic expression of the Alzheimer's disease beta-secretase (BACE1) is stimulus-dependent. *Glia,* 41**,** 169-79.
HARTLEY, D. M., WALSH, D. M., YE, C. P., DIEHL, T., VASQUEZ, S., VASSILEV, P. M., TEPLOW, D. B. & SELKOE, D. J. 1999. Protofibrillar intermediates of amyloid beta-protein induce acute electrophysiological changes and progressive neurotoxicity in cortical neurons. *J Neurosci,* 19**,** 8876-84.
HARTMAN, R. E., IZUMI, Y., BALES, K. R., PAUL, S. M., WOZNIAK, D. F. & HOLTZMAN, D. M. 2005. Treatment with an amyloid-beta antibody ameliorates plaque load, learning deficits, and hippocampal long-term potentiation in a mouse model of Alzheimer's disease. *J Neurosci,* 25**,** 6213-20.
HASENSTAUB, A., SHU, Y., HAIDER, B., KRAUSHAAR, U., DUQUE, A. & MCCORMICK, D. A. 2005. Inhibitory postsynaptic potentials carry synchronized frequency information in active cortical networks. *Neuron,* 47**,** 423-35.
HASHIMOTO, Y., KANEKO, Y., TSUKAMOTO, E., FRANKOWSKI, H., KOUYAMA, K., KITA, Y., NIIKURA, T., AISO, S., BREDESEN, D. E., MATSUOKA, M. & NISHIMOTO, I. 2004. Molecular characterization of neurohybrid cell death induced by Alzheimer's amyloid-beta peptides via p75NTR/PLAIDD. *J Neurochem,* 90**,** 549-58.
HE, Q., COLON-MOTAS, K. M., PYBUS, A. F., PIENDEL, L., SEPPA, J. K., WALKER, M. L., MANZANARES, C. M., QIU, D., MIOCINOVIC, S., WOOD, L. B., LEVEY, A. I., LAH, J. J. & SINGER, A. C. 2021. A feasibility trial of gamma sensory flicker for patients with prodromal Alzheimer's disease. *Alzheimers Dement (N Y),* 7**,** e12178.
HEFENDEHL, J. K., LEDUE, J., KO, R. W., MAHLER, J., MURPHY, T. H. & MACVICAR, B. A. 2016. Mapping synaptic glutamate transporter dysfunction in vivo to regions surrounding Abeta plaques by iGluSnFR two-photon imaging. *Nat Commun,* 7**,** 13441.
HEFENDEHL, J. K., WEGENAST-BRAUN, B. M., LIEBIG, C., EICKE, D., MILFORD, D., CALHOUN, M. E., KOHSAKA, S., EICHNER, M. & JUCKER, M. 2011. Long-term in vivo imaging of beta-

amyloid plaque appearance and growth in a mouse model of cerebral beta-amyloidosis. *J Neurosci,* 31**,** 624-9.
HEMPEL, E. H., M.; WILLIAMS, M.; MALCHANO, Z. 2021. Study design of gamma sensory stimulation at multiple dose levels in MCI patients. *Alzheimer's & Dementia,* 17**,** e056614.
HENEKA, M. T., CARSON, M. J., EL KHOURY, J., LANDRETH, G. E., BROSSERON, F., FEINSTEIN, D. L., JACOBS, A. H., WYSS-CORAY, T., VITORICA, J., RANSOHOFF, R. M., HERRUP, K., FRAUTSCHY, S. A., FINSEN, B., BROWN, G. C., VERKHRATSKY, A., YAMANAKA, K., KOISTINAHO, J., LATZ, E., HALLE, A., PETZOLD, G. C., TOWN, T., MORGAN, D., SHINOHARA, M. L., PERRY, V. H., HOLMES, C., BAZAN, N. G., BROOKS, D. J., HUNOT, S., JOSEPH, B., DEIGENDESCH, N., GARASCHUK, O., BODDEKE, E., DINARELLO, C. A., BREITNER, J. C., COLE, G. M., GOLENBOCK, D. T. & KUMMER, M. P. 2015a. Neuroinflammation in Alzheimer's disease. *Lancet Neurol,* 14**,** 388-405.
HENEKA, M. T., GOLENBOCK, D. T. & LATZ, E. 2015b. Innate immunity in Alzheimer's disease. *Nat Immunol,* 16**,** 229-36.
HENEKA, M. T., RODRIGUEZ, J. J. & VERKHRATSKY, A. 2010. Neuroglia in neurodegeneration. *Brain Res Rev,* 63**,** 189-211.
HENEKA, M. T., SASTRE, M., DUMITRESCU-OZIMEK, L., DEWACHTER, I., WALTER, J., KLOCKGETHER, T. & VAN LEUVEN, F. 2005. Focal glial activation coincides with increased BACE1 activation and precedes amyloid plaque deposition in APP[V717I] transgenic mice. *J Neuroinflammation,* 2**,** 22.
HEPPNER, F. L., RANSOHOFF, R. M. & BECHER, B. 2015. Immune attack: the role of inflammation in Alzheimer disease. *Nat Rev Neurosci,* 16**,** 358-72.
HERNANDEZ, P., LEE, G., SJOBERG, M. & MACCIONI, R. B. 2009. Tau phosphorylation by cdk5 and Fyn in response to amyloid peptide Abeta (25-35): involvement of lipid rafts. *J Alzheimers Dis,* 16**,** 149-56.
HERRMANN, C. S. 2001. Human EEG responses to 1-100 Hz flicker: resonance phenomena in visual cortex and their potential correlation to cognitive phenomena. *Exp Brain Res,* 137**,** 346-53.
HERRUP, K. 2015. The case for rejecting the amyloid cascade hypothesis. *Nat Neurosci,* 18**,** 794-9.
HEUER, E., ROSEN, R. F., CINTRON, A. & WALKER, L. C. 2012. Nonhuman primate models of Alzheimer-like cerebral proteopathy. *Curr Pharm Des,* 18**,** 1159-69.
HICKMAN, S., IZZY, S., SEN, P., MORSETT, L. & EL KHOURY, J. 2018. Microglia in neurodegeneration. *Nat Neurosci,* 21**,** 1359-1369.
HIPPIUS, H. & NEUNDORFER, G. 2003. The discovery of Alzheimer's disease. *Dialogues Clin Neurosci,* 5**,** 101-8.
HOCK, B. J., JR. & LAMB, B. T. 2001. Transgenic mouse models of Alzheimer's disease. *Trends Genet,* 17**,** S7-12.
HOGLUND, K., HANSSON, O., BUCHHAVE, P., ZETTERBERG, H., LEWCZUK, P., LONDOS, E., BLENNOW, K., MINTHON, L. & WILTFANG, J. 2008. Prediction of Alzheimer's disease using a cerebrospinal fluid pattern of C-terminally truncated beta-amyloid peptides. *Neurodegener Dis,* 5**,** 268-76.
HOLCOMB, L., GORDON, M. N., MCGOWAN, E., YU, X., BENKOVIC, S., JANTZEN, P., WRIGHT, K., SAAD, I., MUELLER, R., MORGAN, D., SANDERS, S., ZEHR, C., O'CAMPO, K., HARDY, J., PRADA, C. M., ECKMAN, C., YOUNKIN, S., HSIAO, K. & DUFF, K. 1998. Accelerated Alzheimer-type phenotype in transgenic mice carrying both mutant amyloid precursor protein and presenilin 1 transgenes. *Nat Med,* 4**,** 97-100.
HOLTZMAN, D. M., HERZ, J. & BU, G. 2012. Apolipoprotein E and apolipoprotein E receptors: normal biology and roles in Alzheimer disease. *Cold Spring Harb Perspect Med,* 2**,** a006312.
HOWARD, M. W., RIZZUTO, D. S., CAPLAN, J. B., MADSEN, J. R., LISMAN, J., ASCHENBRENNER-SCHEIBE, R., SCHULZE-BONHAGE, A. & KAHANA, M. J. 2003. Gamma oscillations correlate with working memory load in humans. *Cereb Cortex,* 13**,** 1369-74.
HOWIE, A. J. & BREWER, D. B. 2009. Optical properties of amyloid stained by Congo red: history and mechanisms. *Micron,* 40**,** 285-301.
HSIAO, K., CHAPMAN, P., NILSEN, S., ECKMAN, C., HARIGAYA, Y., YOUNKIN, S., YANG, F. & COLE, G. 1996. Correlative memory deficits, Abeta elevation, and amyloid plaques in transgenic mice. *Science,* 274**,** 99-102.
HU, N. W., NICOLL, A. J., ZHANG, D., MABLY, A. J., O'MALLEY, T., PURRO, S. A., TERRY, C., COLLINGE, J., WALSH, D. M. & ROWAN, M. J. 2014. mGlu5 receptors and cellular prion protein mediate amyloid-beta-facilitated synaptic long-term depression in vivo. *Nat Commun,* 5**,** 3374.

HUANG, Y. R. & LIU, R. T. 2020. The Toxicity and Polymorphism of beta-Amyloid Oligomers. *Int J Mol Sci,* 21.
HUNTER, K. & HOLSCHER, C. 2012. Drugs developed to treat diabetes, liraglutide and lixisenatide, cross the blood brain barrier and enhance neurogenesis. *BMC Neurosci,* 13**,** 33.
HUTTON, M., PEREZ-TUR, J. & HARDY, J. 1998. Genetics of Alzheimer's disease. *Essays Biochem,* 33**,** 117-31.
IACCARINO, H. F., SINGER, A. C., MARTORELL, A. J., RUDENKO, A., GAO, F., GILLINGHAM, T. Z., MATHYS, H., SEO, J., KRITSKIY, O., ABDURROB, F., ADAIKKAN, C., CANTER, R. G., RUEDA, R., BROWN, E. N., BOYDEN, E. S. & TSAI, L. H. 2016. Gamma frequency entrainment attenuates amyloid load and modifies microglia. *Nature,* 540**,** 230-235.
IADECOLA, C. & NEDERGAARD, M. 2007. Glial regulation of the cerebral microvasculature. *Nat Neurosci,* 10**,** 1369-76.
IRIZARRY, M. C., MCNAMARA, M., FEDORCHAK, K., HSIAO, K. & HYMAN, B. T. 1997. APPSw transgenic mice develop age-related A beta deposits and neuropil abnormalities, but no neuronal loss in CA1. *J Neuropathol Exp Neurol,* 56**,** 965-73.
ISMAIL, R., HANSEN, A. K., PARBO, P., BRAENDGAARD, H., GOTTRUP, H., BROOKS, D. J. & BORGHAMMER, P. 2018. The Effect of 40-Hz Light Therapy on Amyloid Load in Patients with Prodromal and Clinical Alzheimer's Disease. *Int J Alzheimers Dis,* 2018**,** 6852303.
ITAGAKI, S., MCGEER, P. L., AKIYAMA, H., ZHU, S. & SELKOE, D. 1989. Relationship of microglia and astrocytes to amyloid deposits of Alzheimer disease. *J Neuroimmunol,* 24**,** 173-82.
ITTNER, L. M., KE, Y. D., DELERUE, F., BI, M., GLADBACH, A., VAN EERSEL, J., WOLFING, H., CHIENG, B. C., CHRISTIE, M. J., NAPIER, I. A., ECKERT, A., STAUFENBIEL, M., HARDEMAN, E. & GOTZ, J. 2010. Dendritic function of tau mediates amyloid-beta toxicity in Alzheimer's disease mouse models. *Cell,* 142**,** 387-97.
IU/JAX/UCI MODEL-AD CONSORTIUM. 2023. *MODEL-AD* [Online]. Available: https://www.model-ad.org/ [Accessed 1 November 2023].
JACOB, C. P., KOUTSILIERI, E., BARTL, J., NEUEN-JACOB, E., ARZBERGER, T., ZANDER, N., RAVID, R., ROGGENDORF, W., RIEDERER, P. & GRUNBLATT, E. 2007. Alterations in expression of glutamatergic transporters and receptors in sporadic Alzheimer's disease. *J Alzheimers Dis,* 11**,** 97-116.
JAQUINS-GERSTL, A. & MICHAEL, A. C. 2009. Comparison of the brain penetration injury associated with microdialysis and voltammetry. *J Neurosci Methods,* 183**,** 127-35.
JASPER, H. H. A., H. L. 1939. Brain potentials and voluntary muscle activity in man. *J. Neurophysiol,* 1**,** 87–100.
JEFFERYS, J. G., TRAUB, R. D. & WHITTINGTON, M. A. 1996. Neuronal networks for induced '40 Hz' rhythms. *Trends Neurosci,* 19**,** 202-8.
JENSEN, O., KAISER, J. & LACHAUX, J. P. 2007. Human gamma-frequency oscillations associated with attention and memory. *Trends Neurosci,* 30**,** 317-24.
JEREMIC, D., JIMENEZ-DIAZ, L. & NAVARRO-LOPEZ, J. D. 2021. Past, present and future of therapeutic strategies against amyloid-beta peptides in Alzheimer's disease: a systematic review. *Ageing Res Rev,* 72**,** 101496.
JIANG, J. & JIANG, H. 2015. Effect of the inhaled anesthetics isoflurane, sevoflurane and desflurane on the neuropathogenesis of Alzheimer's disease (review). *Mol Med Rep,* 12**,** 3-12.
JIANG, N., FRENZEL, D., SCHARTMANN, E., VAN GROEN, T., KADISH, I., SHAH, N. J., LANGEN, K. J., WILLBOLD, D. & WILLUWEIT, A. 2016. Blood-brain barrier penetration of an Abeta-targeted, arginine-rich, d-enantiomeric peptide. *Biochim Biophys Acta,* 1858**,** 2717-2724.
JIANG, T., YU, J. T., ZHU, X. C. & TAN, L. 2013. TREM2 in Alzheimer's disease. *Mol Neurobiol,* 48**,** 180-5.
JIE, C., TREYER, V., SCHIBLI, R. & MU, L. 2021. Tauvid: The First FDA-Approved PET Tracer for Imaging Tau Pathology in Alzheimer's Disease. *Pharmaceuticals (Basel),* 14.
JING, M., LI, Y., ZENG, J., HUANG, P., SKIRZEWSKI, M., KLJAKIC, O., PENG, W., QIAN, T., TAN, K., ZOU, J., TRINH, S., WU, R., ZHANG, S., PAN, S., HIRES, S. A., XU, M., LI, H., SAKSIDA, L. M., PRADO, V. F., BUSSEY, T. J., PRADO, M. A. M., CHEN, L., CHENG, H. & LI, Y. 2020. An optimized acetylcholine sensor for monitoring in vivo cholinergic activity. *Nat Methods,* 17**,** 1139-1146.
JING, M., ZHANG, P., WANG, G., FENG, J., MESIK, L., ZENG, J., JIANG, H., WANG, S., LOOBY, J. C., GUAGLIARDO, N. A., LANGMA, L. W., LU, J., ZUO, Y., TALMAGE, D. A., ROLE, L. W., BARRETT, P. Q., ZHANG, L. I., LUO, M., SONG, Y., ZHU, J. J. & LI, Y. 2018. A genetically encoded fluorescent acetylcholine indicator for in vitro and in vivo studies. *Nat Biotechnol,* 36**,** 726-737.

JO, S., YARISHKIN, O., HWANG, Y. J., CHUN, Y. E., PARK, M., WOO, D. H., BAE, J. Y., KIM, T., LEE, J., CHUN, H., PARK, H. J., LEE, D. Y., HONG, J., KIM, H. Y., OH, S. J., PARK, S. J., LEE, H., YOON, B. E., KIM, Y., JEONG, Y., SHIM, I., BAE, Y. C., CHO, J., KOWALL, N. W., RYU, H., HWANG, E., KIM, D. & LEE, C. J. 2014. GABA from reactive astrocytes impairs memory in mouse models of Alzheimer's disease. *Nat Med,* 20**,** 886-96.

JONES, D. T., KNOPMAN, D. S., GUNTER, J. L., GRAFF-RADFORD, J., VEMURI, P., BOEVE, B. F., PETERSEN, R. C., WEINER, M. W., JACK, C. R., JR. & ALZHEIMER'S DISEASE NEUROIMAGING, I. 2016. Cascading network failure across the Alzheimer's disease spectrum. *Brain,* 139**,** 547-62.

JONES, M., MCDERMOTT, B., OLIVEIRA, B. L., O'BRIEN, A., COOGAN, D., LANG, M., MORIARTY, N., DOWD, E., QUINLAN, L., MC GINLEY, B., DUNNE, E., NEWELL, D., PORTER, E., ELAHI, M. A., M, O. H. & SHAHZAD, A. 2019. Gamma Band Light Stimulation in Human Case Studies: Groundwork for Potential Alzheimer's Disease Treatment. *J Alzheimers Dis,* 70**,** 171-185.

JOURDAIN, P., BERGERSEN, L. H., BHAUKAURALLY, K., BEZZI, P., SANTELLO, M., DOMERCQ, M., MATUTE, C., TONELLO, F., GUNDERSEN, V. & VOLTERRA, A. 2007. Glutamate exocytosis from astrocytes controls synaptic strength. *Nat Neurosci,* 10**,** 331-9.

JUCKER, M. & WALKER, L. C. 2013. Self-propagation of pathogenic protein aggregates in neurodegenerative diseases. *Nature,* 501**,** 45-51.

JUN, Y. W., KIM, H. R., REO, Y. J., DAI, M. & AHN, K. H. 2017. Addressing the autofluorescence issue in deep tissue imaging by two-photon microscopy: the significance of far-red emitting dyes. *Chem Sci,* 8**,** 7696-7704.

JUNG, C. K., KEPPLER, K., STEINBACH, S., BLAZQUEZ-LLORCA, L. & HERMS, J. 2015. Fibrillar amyloid plaque formation precedes microglial activation. *PLoS One,* 10**,** e0119768.

KAGIAMPAKI, Z., ROHNER, V., KISS, C., CURRELI, S., DIETER, A., WILHELM, M., HARADA, M., DUSS, S. N., DERNIC, J., BHAT, M. A., ZHOU, X., RAVOTTO, L., ZIEBARTH, T., WASIELEWSKI, L. M., SONMEZ, L., BENKE, D., WEBER, B., BOHACEK, J., REINER, A., WIEGERT, J. S., FELLIN, T. & PATRIARCHI, T. 2023. Sensitive multicolor indicators for monitoring norepinephrine in vivo. *Nat Methods,* 20**,** 1426-1436.

KAHAN, A., GREENBAUM, A., JANG, M. J., ROBINSON, J. E., CHO, J. R., CHEN, X., KASSRAIAN, P., WAGENAAR, D. A. & GRADINARU, V. 2021. Light-guided sectioning for precise in situ localization and tissue interface analysis for brain-implanted optical fibers and GRIN lenses. *Cell Rep,* 36**,** 109744.

KAMENETZ, F., TOMITA, T., HSIEH, H., SEABROOK, G., BORCHELT, D., IWATSUBO, T., SISODIA, S. & MALINOW, R. 2003. APP processing and synaptic function. *Neuron,* 37**,** 925-37.

KAMPHUIS, W., MAMBER, C., MOETON, M., KOOIJMAN, L., SLUIJS, J. A., JANSEN, A. H., VERVEER, M., DE GROOT, L. R., SMITH, V. D., RANGARAJAN, S., RODRIGUEZ, J. J., ORRE, M. & HOL, E. M. 2012. GFAP isoforms in adult mouse brain with a focus on neurogenic astrocytes and reactive astrogliosis in mouse models of Alzheimer disease. *PLoS One,* 7**,** e42823.

KANAI, R., CHAIEB, L., ANTAL, A., WALSH, V. & PAULUS, W. 2008. Frequency-dependent electrical stimulation of the visual cortex. *Curr Biol,* 18**,** 1839-43.

KANE, M. D., LIPINSKI, W. J., CALLAHAN, M. J., BIAN, F., DURHAM, R. A., SCHWARZ, R. D., ROHER, A. E. & WALKER, L. C. 2000. Evidence for seeding of beta -amyloid by intracerebral infusion of Alzheimer brain extracts in beta -amyloid precursor protein-transgenic mice. *J Neurosci,* 20**,** 3606-11.

KANG, J., LEMAIRE, H. G., UNTERBECK, A., SALBAUM, J. M., MASTERS, C. L., GRZESCHIK, K. H., MULTHAUP, G., BEYREUTHER, K. & MULLER-HILL, B. 1987. The precursor of Alzheimer's disease amyloid A4 protein resembles a cell-surface receptor. *Nature,* 325**,** 733-6.

KARRAN, E., MERCKEN, M. & DE STROOPER, B. 2011. The amyloid cascade hypothesis for Alzheimer's disease: an appraisal for the development of therapeutics. *Nat Rev Drug Discov,* 10**,** 698-712.

KATZMARSKI, N., ZIEGLER-WALDKIRCH, S., SCHEFFLER, N., WITT, C., ABOU-AJRAM, C., NUSCHER, B., PRINZ, M., HAASS, C. & MEYER-LUEHMANN, M. 2020. Abeta oligomers trigger and accelerate Abeta seeding. *Brain Pathol,* 30**,** 36-45.

KAYED, R., SOKOLOV, Y., EDMONDS, B., MCINTIRE, T. M., MILTON, S. C., HALL, J. E. & GLABE, C. G. 2004. Permeabilization of lipid bilayers is a common conformation-dependent activity of soluble amyloid oligomers in protein misfolding diseases. *J Biol Chem,* 279**,** 46363-6.

KERRIDGE, C., KOZLOVA, D. I., NALIVAEVA, N. N. & TURNER, A. J. 2015. Hypoxia Affects Neprilysin Expression Through Caspase Activation and an APP Intracellular Domain-dependent Mechanism. *Front Neurosci,* 9**,** 426.

KESSELS, H. W., NGUYEN, L. N., NABAVI, S. & MALINOW, R. 2010. The prion protein as a receptor for amyloid-beta. *Nature,* 466**,** E3-4; discussion E4-5.
KHAKH, B. S. & SOFRONIEW, M. V. 2015. Diversity of astrocyte functions and phenotypes in neural circuits. *Nat Neurosci,* 18**,** 942-52.
KHEDR, E. M., GAMAL, N. F., EL-FETOH, N. A., KHALIFA, H., AHMED, E. M., ALI, A. M., NOAMAN, M., EL-BAKI, A. A. & KARIM, A. A. 2014. A double-blind randomized clinical trial on the efficacy of cortical direct current stimulation for the treatment of Alzheimer's disease. *Front Aging Neurosci,* 6**,** 275.
KHETERPAL, I., WETZEL, R. & COOK, K. D. 2003. Enhanced correction methods for hydrogen exchange-mass spectrometric studies of amyloid fibrils. *Protein Sci,* 12**,** 635-43.
KIDD, M. 1963. Paired helical filaments in electron microscopy of Alzheimer's disease. *Nature,* 197**,** 192-3.
KIM, C. K., YANG, S. J., PICHAMOORTHY, N., YOUNG, N. P., KAUVAR, I., JENNINGS, J. H., LERNER, T. N., BERNDT, A., LEE, S. Y., RAMAKRISHNAN, C., DAVIDSON, T. J., INOUE, M., BITO, H. & DEISSEROTH, K. 2016. Simultaneous fast measurement of circuit dynamics at multiple sites across the mammalian brain. *Nat Methods,* 13**,** 325-8.
KIM, J., CASTELLANO, J. M., JIANG, H., BASAK, J. M., PARSADANIAN, M., PHAM, V., MASON, S. M., PAUL, S. M. & HOLTZMAN, D. M. 2009. Overexpression of low-density lipoprotein receptor in the brain markedly inhibits amyloid deposition and increases extracellular A beta clearance. *Neuron,* 64**,** 632-44.
KIM, S. H., FRASER, P. E., WESTAWAY, D., ST GEORGE-HYSLOP, P. H., EHRLICH, M. E. & GANDY, S. 2010. Group II metabotropic glutamate receptor stimulation triggers production and release of Alzheimer's amyloid(beta)42 from isolated intact nerve terminals. *J Neurosci,* 30**,** 3870-5.
KLEIN, A. S., DONOSO, J. R., KEMPTER, R., SCHMITZ, D. & BEED, P. 2016. Early Cortical Changes in Gamma Oscillations in Alzheimer's Disease. *Front Syst Neurosci,* 10**,** 83.
KLUNK, W. E., BACSKAI, B. J., MATHIS, C. A., KAJDASZ, S. T., MCLELLAN, M. E., FROSCH, M. P., DEBNATH, M. L., HOLT, D. P., WANG, Y. & HYMAN, B. T. 2002. Imaging Abeta plaques in living transgenic mice with multiphoton microscopy and methoxy-X04, a systemically administered Congo red derivative. *J Neuropathol Exp Neurol,* 61**,** 797-805.
KLUNK, W. E., DEBNATH, M. L. & PETTEGREW, J. W. 1994. Development of small molecule probes for the beta-amyloid protein of Alzheimer's disease. *Neurobiol Aging,* 15**,** 691-8.
KLUNK, W. E., DEBNATH, M. L. & PETTEGREW, J. W. 1995. Chrysamine-G binding to Alzheimer and control brain: autopsy study of a new amyloid probe. *Neurobiol Aging,* 16**,** 541-8.
KLUNK, W. E., ENGLER, H., NORDBERG, A., WANG, Y., BLOMQVIST, G., HOLT, D. P., BERGSTROM, M., SAVITCHEVA, I., HUANG, G. F., ESTRADA, S., AUSEN, B., DEBNATH, M. L., BARLETTA, J., PRICE, J. C., SANDELL, J., LOPRESTI, B. J., WALL, A., KOIVISTO, P., ANTONI, G., MATHIS, C. A. & LANGSTROM, B. 2004. Imaging brain amyloid in Alzheimer's disease with Pittsburgh Compound-B. *Ann Neurol,* 55**,** 306-19.
KLUNK, W. E., PETTEGREW, J. W. & ABRAHAM, D. J. 1989. Quantitative evaluation of congo red binding to amyloid-like proteins with a beta-pleated sheet conformation. *J Histochem Cytochem,* 37**,** 1273-81.
KNOWLES, R. B., WYART, C., BULDYREV, S. V., CRUZ, L., URBANC, B., HASSELMO, M. E., STANLEY, H. E. & HYMAN, B. T. 1999. Plaque-induced neurite abnormalities: implications for disruption of neural networks in Alzheimer's disease. *Proc Natl Acad Sci U S A,* 96**,** 5274-9.
KOO, E. H., PARK, L. & SELKOE, D. J. 1993. Amyloid beta-protein as a substrate interacts with extracellular matrix to promote neurite outgrowth. *Proc Natl Acad Sci U S A,* 90**,** 4748-52.
KORONYO-HAMAOUI, M., KORONYO, Y., LJUBIMOV, A. V., MILLER, C. A., KO, M. K., BLACK, K. L., SCHWARTZ, M. & FARKAS, D. L. 2011. Identification of amyloid plaques in retinas from Alzheimer's patients and noninvasive in vivo optical imaging of retinal plaques in a mouse model. *Neuroimage,* 54 Suppl 1**,** S204-17.
KOZAI, T. D., JAQUINS-GERSTL, A. S., VAZQUEZ, A. L., MICHAEL, A. C. & CUI, X. T. 2015. Brain tissue responses to neural implants impact signal sensitivity and intervention strategies. *ACS Chem Neurosci,* 6**,** 48-67.
KOZAI, T. D., VAZQUEZ, A. L., WEAVER, C. L., KIM, S. G. & CUI, X. T. 2012. In vivo two-photon microscopy reveals immediate microglial reaction to implantation of microelectrode through extension of processes. *J Neural Eng,* 9**,** 066001.
KRAMES, E. P., P. H.; REZAI, A. 2018. *Neuromodulation: Comprehensive Textbook of Principles, Technologies, and Terapies, 2nd ed.*, Academic Press: Cambridge, MA, USA.

KUNER, P., SCHUBENEL, R. & HERTEL, C. 1998. Beta-amyloid binds to p57NTR and activates NFkappaB in human neuroblastoma cells. *J Neurosci Res,* 54**,** 798-804.
KUPFERSCHMIDT, D. A., JUCZEWSKI, K., CUI, G., JOHNSON, K. A. & LOVINGER, D. M. 2017. Parallel, but Dissociable, Processing in Discrete Corticostriatal Inputs Encodes Skill Learning. *Neuron,* 96**,** 476-489 e5.
KUROCHKIN, I. V. & GOTO, S. 1994. Alzheimer's beta-amyloid peptide specifically interacts with and is degraded by insulin degrading enzyme. *FEBS Lett,* 345**,** 33-7.
KWAN, A. C., DUFF, K., GOURAS, G. K. & WEBB, W. W. 2009. Optical visualization of Alzheimer's pathology via multiphoton-excited intrinsic fluorescence and second harmonic generation. *Opt Express,* 17**,** 3679-89.
LACHENAL, G., PERNET-GALLAY, K., CHIVET, M., HEMMING, F. J., BELLY, A., BODON, G., BLOT, B., HAASE, G., GOLDBERG, Y. & SADOUL, R. 2011. Release of exosomes from differentiated neurons and its regulation by synaptic glutamatergic activity. *Mol Cell Neurosci,* 46**,** 409-18.
LASAGNA-REEVES, C. A., CASTILLO-CARRANZA, D. L., SENGUPTA, U., GUERRERO-MUNOZ, M. J., KIRITOSHI, T., NEUGEBAUER, V., JACKSON, G. R. & KAYED, R. 2012. Alzheimer brain-derived tau oligomers propagate pathology from endogenous tau. *Sci Rep,* 2**,** 700.
LASAGNA-REEVES, C. A. & KAYED, R. 2011. Astrocytes contain amyloid-beta annular protofibrils in Alzheimer's disease brains. *FEBS Lett,* 585**,** 3052-7.
LASAGNA-REEVES, C. A., SENGUPTA, U., CASTILLO-CARRANZA, D., GERSON, J. E., GUERRERO-MUNOZ, M., TRONCOSO, J. C., JACKSON, G. R. & KAYED, R. 2014. The formation of tau pore-like structures is prevalent and cell specific: possible implications for the disease phenotypes. *Acta Neuropathol Commun,* 2**,** 56.
LAUREN, J., GIMBEL, D. A., NYGAARD, H. B., GILBERT, J. W. & STRITTMATTER, S. M. 2009. Cellular prion protein mediates impairment of synaptic plasticity by amyloid-beta oligomers. *Nature,* 457**,** 1128-32.
LAWRENCE, J. M., SCHARDIEN, K., WIGDAHL, B. & NONNEMACHER, M. R. 2023. Roles of neuropathology-associated reactive astrocytes: a systematic review. *Acta Neuropathol Commun,* 11**,** 42.
LAXTON, A. W., TANG-WAI, D. F., MCANDREWS, M. P., ZUMSTEG, D., WENNBERG, R., KEREN, R., WHERRETT, J., NAGLIE, G., HAMANI, C., SMITH, G. S. & LOZANO, A. M. 2010. A phase I trial of deep brain stimulation of memory circuits in Alzheimer's disease. *Ann Neurol,* 68**,** 521-34.
LE, L., FEIDLER, A. M., LI, H., KARA-PABANI, K., LAMANTIA, C., O'BANION, M. K. & MAJEWSKA, K. A. 2023. Noradrenergic signaling controls Alzheimer's disease pathology via activation of microglial beta2 adrenergic receptors. *bioRxiv*.
LEBLANC, A. C., CHEN, H. Y., AUTILIO-GAMBETTI, L. & GAMBETTI, P. 1991. Differential APP gene expression in rat cerebral cortex, meninges, and primary astroglial, microglial and neuronal cultures. *FEBS Lett,* 292**,** 171-8.
LEE, E. G., TULLOCH, J., CHEN, S., LEONG, L., SAXTON, A. D., KRAEMER, B., DARVAS, M., KEENE, C. D., SHUTES-DAVID, A., TODD, K., MILLARD, S. & YU, C. E. 2020. Redefining transcriptional regulation of the APOE gene and its association with Alzheimer's disease. *PLoS One,* 15**,** e0227667.
LEE, H. S., GHETTI, A., PINTO-DUARTE, A., WANG, X., DZIEWCZAPOLSKI, G., GALIMI, F., HUITRON-RESENDIZ, S., PINA-CRESPO, J. C., ROBERTS, A. J., VERMA, I. M., SEJNOWSKI, T. J. & HEINEMANN, S. F. 2014a. Astrocytes contribute to gamma oscillations and recognition memory. *Proc Natl Acad Sci U S A,* 111**,** E3343-52.
LEE, S., XU, G., JAY, T. R., BHATTA, S., KIM, K. W., JUNG, S., LANDRETH, G. E., RANSOHOFF, R. M. & LAMB, B. T. 2014b. Opposing effects of membrane-anchored CX3CL1 on amyloid and tau pathologies via the p38 MAPK pathway. *J Neurosci,* 34**,** 12538-46.
LEE, Y., MESSING, A., SU, M. & BRENNER, M. 2008. GFAP promoter elements required for region-specific and astrocyte-specific expression. *Glia,* 56**,** 481-93.
LEGARIA, A. A., MATIKAINEN-ANKNEY, B. A., YANG, B., AHANONU, B., LICHOLAI, J. A., PARKER, J. G. & KRAVITZ, A. V. 2022. Fiber photometry in striatum reflects primarily nonsomatic changes in calcium. *Nat Neurosci,* 25**,** 1124-1128.
LEI, M., XU, H., LI, Z., WANG, Z., O'MALLEY, T. T., ZHANG, D., WALSH, D. M., XU, P., SELKOE, D. J. & LI, S. 2016. Soluble Abeta oligomers impair hippocampal LTP by disrupting glutamatergic/GABAergic balance. *Neurobiol Dis,* 85**,** 111-121.
LEIBSON, C. L., ROCCA, W. A., HANSON, V. A., CHA, R., KOKMEN, E., O'BRIEN, P. C. & PALUMBO, P. J. 1997. The risk of dementia among persons with diabetes mellitus: a population-based cohort study. *Ann N Y Acad Sci,* 826**,** 422-7.

LEISSRING, M. A., FARRIS, W., CHANG, A. Y., WALSH, D. M., WU, X., SUN, X., FROSCH, M. P. & SELKOE, D. J. 2003. Enhanced proteolysis of beta-amyloid in APP transgenic mice prevents plaque formation, secondary pathology, and premature death. *Neuron,* 40**,** 1087-93.
LENG, F. & EDISON, P. 2021. Neuroinflammation and microglial activation in Alzheimer disease: where do we go from here? *Nat Rev Neurol,* 17**,** 157-172.
LESNE, S., ALI, C., GABRIEL, C., CROCI, N., MACKENZIE, E. T., GLABE, C. G., PLOTKINE, M., MARCHAND-VERRECCHIA, C., VIVIEN, D. & BUISSON, A. 2005. NMDA receptor activation inhibits alpha-secretase and promotes neuronal amyloid-beta production. *J Neurosci,* 25**,** 9367-77.
LEUBA, G., WERNLI, G., VERNAY, A., KRAFTSIK, R., MOHAJERI, M. H. & SAINI, K. D. 2005. Neuronal and nonneuronal quantitative BACE immunocytochemical expression in the entorhinohippocampal and frontal regions in Alzheimer's disease. *Dement Geriatr Cogn Disord,* 19**,** 171-83.
LEVY, E., CARMAN, M. D., FERNANDEZ-MADRID, I. J., POWER, M. D., LIEBERBURG, I., VAN DUINEN, S. G., BOTS, G. T., LUYENDIJK, W. & FRANGIONE, B. 1990. Mutation of the Alzheimer's disease amyloid gene in hereditary cerebral hemorrhage, Dutch type. *Science,* 248**,** 1124-6.
LEVY-LAHAD, E., WASCO, W., POORKAJ, P., ROMANO, D. M., OSHIMA, J., PETTINGELL, W. H., YU, C. E., JONDRO, P. D., SCHMIDT, S. D., WANG, K. & ET AL. 1995. Candidate gene for the chromosome 1 familial Alzheimer's disease locus. *Science,* 269**,** 973-7.
LEWIS, J., DICKSON, D. W., LIN, W. L., CHISHOLM, L., CORRAL, A., JONES, G., YEN, S. H., SAHARA, N., SKIPPER, L., YAGER, D., ECKMAN, C., HARDY, J., HUTTON, M. & MCGOWAN, E. 2001. Enhanced neurofibrillary degeneration in transgenic mice expressing mutant tau and APP. *Science,* 293**,** 1487-91.
LI, C. & GOTZ, J. 2018. Pyk2 is a Novel Tau Tyrosine Kinase that is Regulated by the Tyrosine Kinase Fyn. *J Alzheimers Dis,* 64**,** 205-221.
LI, H., GUO, Q., INOUE, T., POLITO, V. A., TABUCHI, K., HAMMER, R. E., PAUTLER, R. G., TAFFET, G. E. & ZHENG, H. 2014. Vascular and parenchymal amyloid pathology in an Alzheimer disease knock-in mouse model: interplay with cerebral blood flow. *Mol Neurodegener,* 9**,** 28.
LI, K., LI, J., ZHENG, J. & QIN, S. 2019. Reactive Astrocytes in Neurodegenerative Diseases. *Aging Dis,* 10**,** 664-675.
LI, S. & SELKOE, D. J. 2020. A mechanistic hypothesis for the impairment of synaptic plasticity by soluble Abeta oligomers from Alzheimer's brain. *J Neurochem,* 154**,** 583-597.
LI, Y., LIU, L., BARGER, S. W. & GRIFFIN, W. S. 2003. Interleukin-1 mediates pathological effects of microglia on tau phosphorylation and on synaptophysin synthesis in cortical neurons through a p38-MAPK pathway. *J Neurosci,* 23**,** 1605-11.
LIANG, R., OU, S., HAN, Y., XU, J. & ZHOU, S. 2020. Plasma amyloid beta level changes in aged mice with cognitive dysfunction following sevoflurane exposure. *Exp Gerontol,* 129**,** 110737.
LIDDELOW, S. A., GUTTENPLAN, K. A., CLARKE, L. E., BENNETT, F. C., BOHLEN, C. J., SCHIRMER, L., BENNETT, M. L., MUNCH, A. E., CHUNG, W. S., PETERSON, T. C., WILTON, D. K., FROUIN, A., NAPIER, B. A., PANICKER, N., KUMAR, M., BUCKWALTER, M. S., ROWITCH, D. H., DAWSON, V. L., DAWSON, T. M., STEVENS, B. & BARRES, B. A. 2017. Neurotoxic reactive astrocytes are induced by activated microglia. *Nature,* 541**,** 481-487.
LIM, H. K., NEBES, R., SNITZ, B., COHEN, A., MATHIS, C., PRICE, J., WEISSFELD, L., KLUNK, W. & AIZENSTEIN, H. J. 2014. Regional amyloid burden and intrinsic connectivity networks in cognitively normal elderly subjects. *Brain,* 137**,** 3327-38.
LINDWALL, G. & COLE, R. D. 1984. Phosphorylation affects the ability of tau protein to promote microtubule assembly. *J Biol Chem,* 259**,** 5301-5.
LIU, C. C., HU, J., ZHAO, N., WANG, J., WANG, N., CIRRITO, J. R., KANEKIYO, T., HOLTZMAN, D. M. & BU, G. 2017. Astrocytic LRP1 Mediates Brain Abeta Clearance and Impacts Amyloid Deposition. *J Neurosci,* 37**,** 4023-4031.
LIU, C. C., LIU, C. C., KANEKIYO, T., XU, H. & BU, G. 2013. Apolipoprotein E and Alzheimer disease: risk, mechanisms and therapy. *Nat Rev Neurol,* 9**,** 106-18.
LIU, L., DROUET, V., WU, J. W., WITTER, M. P., SMALL, S. A., CLELLAND, C. & DUFF, K. 2012. Trans-synaptic spread of tau pathology in vivo. *PLoS One,* 7**,** e31302.
LIU, Y. U., YING, Y., LI, Y., EYO, U. B., CHEN, T., ZHENG, J., UMPIERRE, A. D., ZHU, J., BOSCO, D. B., DONG, H. & WU, L. J. 2019. Neuronal network activity controls microglial process surveillance in awake mice via norepinephrine signaling. *Nat Neurosci,* 22**,** 1771-1781.

LIU, Z., CONDELLO, C., SCHAIN, A., HARB, R. & GRUTZENDLER, J. 2010. CX3CR1 in microglia regulates brain amyloid deposition through selective protofibrillar amyloid-beta phagocytosis. *J Neurosci,* 30**,** 17091-101.

LIVINGSTON, G., HUNTLEY, J., SOMMERLAD, A., AMES, D., BALLARD, C., BANERJEE, S., BRAYNE, C., BURNS, A., COHEN-MANSFIELD, J., COOPER, C., COSTAFREDA, S. G., DIAS, A., FOX, N., GITLIN, L. N., HOWARD, R., KALES, H. C., KIVIMAKI, M., LARSON, E. B., OGUNNIYI, A., ORGETA, V., RITCHIE, K., ROCKWOOD, K., SAMPSON, E. L., SAMUS, Q., SCHNEIDER, L. S., SELBAEK, G., TERI, L. & MUKADAM, N. 2020. Dementia prevention, intervention, and care: 2020 report of the Lancet Commission. *Lancet,* 396**,** 413-446.

LOBAS, M. A., TAO, R., NAGAI, J., KRONSCHLAGER, M. T., BORDEN, P. M., MARVIN, J. S., LOOGER, L. L. & KHAKH, B. S. 2019. A genetically encoded single-wavelength sensor for imaging cytosolic and cell surface ATP. *Nat Commun,* 10**,** 711.

LOPEZ, O. L., KULLER, L. H., MEHTA, P. D., BECKER, J. T., GACH, H. M., SWEET, R. A., CHANG, Y. F., TRACY, R. & DEKOSKY, S. T. 2008. Plasma amyloid levels and the risk of AD in normal subjects in the Cardiovascular Health Study. *Neurology,* 70**,** 1664-71.

LOZANO, A. M., FOSDICK, L., CHAKRAVARTY, M. M., LEOUTSAKOS, J. M., MUNRO, C., OH, E., DRAKE, K. E., LYMAN, C. H., ROSENBERG, P. B., ANDERSON, W. S., TANG-WAI, D. F., PENDERGRASS, J. C., SALLOWAY, S., ASAAD, W. F., PONCE, F. A., BURKE, A., SABBAGH, M., WOLK, D. A., BALTUCH, G., OKUN, M. S., FOOTE, K. D., MCANDREWS, M. P., GIACOBBE, P., TARGUM, S. D., LYKETSOS, C. G. & SMITH, G. S. 2016. A Phase II Study of Fornix Deep Brain Stimulation in Mild Alzheimer's Disease. *J Alzheimers Dis,* 54**,** 777-87.

LU, J. X., QIANG, W., YAU, W. M., SCHWIETERS, C. D., MEREDITH, S. C. & TYCKO, R. 2013. Molecular structure of beta-amyloid fibrils in Alzheimer's disease brain tissue. *Cell,* 154**,** 1257-68.

LUCHSINGER, J. A., TANG, M. X., STERN, Y., SHEA, S. & MAYEUX, R. 2001. Diabetes mellitus and risk of Alzheimer's disease and dementia with stroke in a multiethnic cohort. *Am J Epidemiol,* 154**,** 635-41.

LUI, J. K., LAWS, S. M., LI, Q. X., VILLEMAGNE, V. L., AMES, D., BROWN, B., BUSH, A. I., DE RUYCK, K., DROMEY, J., ELLIS, K. A., FAUX, N. G., FOSTER, J., FOWLER, C., GUPTA, V., HUDSON, P., LAUGHTON, K., MASTERS, C. L., PERTILE, K., REMBACH, A., RIMAJOVA, M., RODRIGUES, M., ROWE, C. C., RUMBLE, R., SZOEKE, C., TADDEI, K., TADDEI, T., TROUNSON, B., WARD, V., MARTINS, R. N. & GROUP, A. R. 2010. Plasma amyloid-beta as a biomarker in Alzheimer's disease: the AIBL study of aging. *J Alzheimers Dis,* 20**,** 1233-42.

LUO, L., CALLAWAY, E. M. & SVOBODA, K. 2008. Genetic dissection of neural circuits. *Neuron,* 57**,** 634-60.

LUO, L., CALLAWAY, E. M. & SVOBODA, K. 2018. Genetic Dissection of Neural Circuits: A Decade of Progress. *Neuron,* 98**,** 256-281.

LUSTBADER, J. W., CIRILLI, M., LIN, C., XU, H. W., TAKUMA, K., WANG, N., CASPERSEN, C., CHEN, X., POLLAK, S., CHANEY, M., TRINCHESE, F., LIU, S., GUNN-MOORE, F., LUE, L. F., WALKER, D. G., KUPPUSAMY, P., ZEWIER, Z. L., ARANCIO, O., STERN, D., YAN, S. S. & WU, H. 2004. ABAD directly links Abeta to mitochondrial toxicity in Alzheimer's disease. *Science,* 304**,** 448-52.

LUSTENBERGER, C., PATEL, Y. A., ALAGAPAN, S., PAGE, J. M., PRICE, B., BOYLE, M. R. & FROHLICH, F. 2018. High-density EEG characterization of brain responses to auditory rhythmic stimuli during wakefulness and NREM sleep. *Neuroimage,* 169**,** 57-68.

LYNGHOLM, D. & SAKATA, S. 2019. Cre-Dependent Optogenetic Transgenic Mice Without Early Age-Related Hearing Loss. *Front Aging Neurosci,* 11**,** 29.

LYTTON, W. W. & SEJNOWSKI, T. J. 1991. Simulations of cortical pyramidal neurons synchronized by inhibitory interneurons. *J Neurophysiol,* 66**,** 1059-79.

MA, C., HONG, F. & YANG, S. 2022. Amyloidosis in Alzheimer's Disease: Pathogeny, Etiology, and Related Therapeutic Directions. *Molecules,* 27.

MABLY, A. J. & COLGIN, L. L. 2018. Gamma oscillations in cognitive disorders. *Curr Opin Neurobiol,* 52**,** 182-187.

MABLY, A. J., GEREKE, B. J., JONES, D. T. & COLGIN, L. L. 2017. Impairments in spatial representations and rhythmic coordination of place cells in the 3xTg mouse model of Alzheimer's disease. *Hippocampus,* 27**,** 378-392.

MACKAY, D. F., RUSSELL, E. R., STEWART, K., MACLEAN, J. A., PELL, J. P. & STEWART, W. 2019. Neurodegenerative Disease Mortality among Former Professional Soccer Players. *N Engl J Med,* 381**,** 1801-1808.

MAEZAWA, I., HONG, H. S., LIU, R., WU, C. Y., CHENG, R. H., KUNG, M. P., KUNG, H. F., LAM, K. S., ODDO, S., LAFERLA, F. M. & JIN, L. W. 2008. Congo red and thioflavin-T analogs detect Abeta oligomers. *J Neurochem,* 104**,** 457-68.

MAHASE, E. 2021. Three FDA advisory panel members resign over approval of Alzheimer's drug. *BMJ,* 373**,** n1503.

MAKOVKIN, S., KOZINOV, E., IVANCHENKO, M. & GORDLEEVA, S. 2022. Controlling synchronization of gamma oscillations by astrocytic modulation in a model hippocampal neural network. *Sci Rep,* 12**,** 6970.

MALM, T. M., JAY, T. R. & LANDRETH, G. E. 2015. The evolving biology of microglia in Alzheimer's disease. *Neurotherapeutics,* 12**,** 81-93.

MANIPPA, V., PALMISANO, A., FILARDI, M., VILELLA, D., NITSCHE, M. A., RIVOLTA, D. & LOGROSCINO, G. 2022. An update on the use of gamma (multi)sensory stimulation for Alzheimer's disease treatment. *Front Aging Neurosci,* 14**,** 1095081.

MANN, E. O., SUCKLING, J. M., HAJOS, N., GREENFIELD, S. A. & PAULSEN, O. 2005. Perisomatic feedback inhibition underlies cholinergically induced fast network oscillations in the rat hippocampus in vitro. *Neuron,* 45**,** 105-17.

MAPHIS, N., XU, G., KOKIKO-COCHRAN, O. N., JIANG, S., CARDONA, A., RANSOHOFF, R. M., LAMB, B. T. & BHASKAR, K. 2015. Reactive microglia drive tau pathology and contribute to the spreading of pathological tau in the brain. *Brain,* 138**,** 1738-55.

MARSHALL, L., HELGADOTTIR, H., MOLLE, M. & BORN, J. 2006. Boosting slow oscillations during sleep potentiates memory. *Nature,* 444**,** 610-3.

MARTINEZ-LOSA, M., TRACY, T. E., MA, K., VERRET, L., CLEMENTE-PEREZ, A., KHAN, A. S., COBOS, I., HO, K., GAN, L., MUCKE, L., ALVAREZ-DOLADO, M. & PALOP, J. J. 2018. Nav1.1-Overexpressing Interneuron Transplants Restore Brain Rhythms and Cognition in a Mouse Model of Alzheimer's Disease. *Neuron,* 98**,** 75-89 e5.

MARTINI-STOICA, H., COLE, A. L., SWARTZLANDER, D. B., CHEN, F., WAN, Y. W., BAJAJ, L., BADER, D. A., LEE, V. M. Y., TROJANOWSKI, J. Q., LIU, Z., SARDIELLO, M. & ZHENG, H. 2018. TFEB enhances astroglial uptake of extracellular tau species and reduces tau spreading. *J Exp Med,* 215**,** 2355-2377.

MARTINS, R. N., TADDEI, K., KENDALL, C., EVIN, G., BATES, K. A. & HARVEY, A. R. 2001. Altered expression of apolipoprotein E, amyloid precursor protein and presenilin-1 is associated with chronic reactive gliosis in rat cortical tissue. *Neuroscience,* 106**,** 557-69.

MARTORELL, A. J., PAULSON, A. L., SUK, H. J., ABDURROB, F., DRUMMOND, G. T., GUAN, W., YOUNG, J. Z., KIM, D. N., KRITSKIY, O., BARKER, S. J., MANGENA, V., PRINCE, S. M., BROWN, E. N., CHUNG, K., BOYDEN, E. S., SINGER, A. C. & TSAI, L. H. 2019. Multi-sensory Gamma Stimulation Ameliorates Alzheimer's-Associated Pathology and Improves Cognition. *Cell,* 177**,** 256-271 e22.

MARVIN, J. S., SHIMODA, Y., MAGLOIRE, V., LEITE, M., KAWASHIMA, T., JENSEN, T. P., KOLB, I., KNOTT, E. L., NOVAK, O., PODGORSKI, K., LEIDENHEIMER, N. J., RUSAKOV, D. A., AHRENS, M. B., KULLMANN, D. M. & LOOGER, L. L. 2019. A genetically encoded fluorescent sensor for in vivo imaging of GABA. *Nat Methods,* 16**,** 763-770.

MASAKI, K. H., LOSONCZY, K. G., IZMIRLIAN, G., FOLEY, D. J., ROSS, G. W., PETROVITCH, H., HAVLIK, R. & WHITE, L. R. 2000. Association of vitamin E and C supplement use with cognitive function and dementia in elderly men. *Neurology,* 54**,** 1265-72.

MASTERS, C. L., SIMMS, G., WEINMAN, N. A., MULTHAUP, G., MCDONALD, B. L. & BEYREUTHER, K. 1985. Amyloid plaque core protein in Alzheimer disease and Down syndrome. *Proc Natl Acad Sci U S A,* 82**,** 4245-9.

MASUDA, A., KOBAYASHI, Y., KOGO, N., SAITO, T., SAIDO, T. C. & ITOHARA, S. 2016. Cognitive deficits in single App knock-in mouse models. *Neurobiol Learn Mem,* 135**,** 73-82.

MATOS, M., AUGUSTO, E., OLIVEIRA, C. R. & AGOSTINHO, P. 2008. Amyloid-beta peptide decreases glutamate uptake in cultured astrocytes: involvement of oxidative stress and mitogen-activated protein kinase cascades. *Neuroscience,* 156**,** 898-910.

MATSUMURA, S., SHINODA, K., YAMADA, M., YOKOJIMA, S., INOUE, M., OHNISHI, T., SHIMADA, T., KIKUCHI, K., MASUI, D., HASHIMOTO, S., SATO, M., ITO, A., AKIOKA, M., TAKAGI, S., NAKAMURA, Y., NEMOTO, K., HASEGAWA, Y., TAKAMOTO, H., INOUE, H., NAKAMURA, S., NABESHIMA, Y., TEPLOW, D. B., KINJO, M. & HOSHI, M. 2011. Two distinct amyloid beta-protein (Abeta) assembly pathways leading to oligomers and fibrils identified by combined fluorescence correlation spectroscopy, morphology, and toxicity analyses. *J Biol Chem,* 286**,** 11555-62.

MATSUO, E. S., SHIN, R. W., BILLINGSLEY, M. L., VAN DEVOORDE, A., O'CONNOR, M., TROJANOWSKI, J. Q. & LEE, V. M. 1994. Biopsy-derived adult human brain tau is phosphorylated at many of the same sites as Alzheimer's disease paired helical filament tau. *Neuron,* 13**,** 989-1002.

MCDERMOTT, B., PORTER, E., HUGHES, D., MCGINLEY, B., LANG, M., O'HALLORAN, M. & JONES, M. 2018. Gamma Band Neural Stimulation in Humans and the Promise of a New Modality to Prevent and Treat Alzheimer's Disease. *J Alzheimers Dis,* 65**,** 363-392.

MCDERMOTT, J. R. & GIBSON, A. M. 1996. Degradation of Alzheimer's beta-amyloid protein by human cathepsin D. *Neuroreport,* 7**,** 2163-6.

MCGEER, P. L. & MCGEER, E. G. 1995. The inflammatory response system of brain: implications for therapy of Alzheimer and other neurodegenerative diseases. *Brain Res Brain Res Rev,* 21**,** 195-218.

MCKEAN, N. E., HANDLEY, R. R. & SNELL, R. G. 2021. A Review of the Current Mammalian Models of Alzheimer's Disease and Challenges That Need to Be Overcome. *Int J Mol Sci,* 22.

MCNETT, S. D., VYSHEDSKIY, A., SAVCHENKO, A., DURAKOVIC, D., HEREDIA, G., CAHN, R. & KOGAN, M. 2023. A Feasibility Study of AlzLife 40 Hz Sensory Therapy in Patients with MCI and Early AD. *Healthcare (Basel),* 11.

MEHTA, P. D., PIRTTILA, T., MEHTA, S. P., SERSEN, E. A., AISEN, P. S. & WISNIEWSKI, H. M. 2000. Plasma and cerebrospinal fluid levels of amyloid beta proteins 1-40 and 1-42 in Alzheimer disease. *Arch Neurol,* 57**,** 100-5.

MENDIOLA-PRECOMA, J., BERUMEN, L. C., PADILLA, K. & GARCIA-ALCOCER, G. 2016. Therapies for Prevention and Treatment of Alzheimer's Disease. *Biomed Res Int,* 2016**,** 2589276.

MEREZHKO, M., BRUNELLO, C. A., YAN, X., VIHINEN, H., JOKITALO, E., URONEN, R. L. & HUTTUNEN, H. J. 2018. Secretion of Tau via an Unconventional Non-vesicular Mechanism. *Cell Rep,* 25**,** 2027-2035 e4.

MERTON, P. A. & MORTON, H. B. 1980. Stimulation of the cerebral cortex in the intact human subject. *Nature,* 285**,** 227.

MEYER-LUEHMANN, M., COOMARASWAMY, J., BOLMONT, T., KAESER, S., SCHAEFER, C., KILGER, E., NEUENSCHWANDER, A., ABRAMOWSKI, D., FREY, P., JATON, A. L., VIGOURET, J. M., PAGANETTI, P., WALSH, D. M., MATHEWS, P. M., GHISO, J., STAUFENBIEL, M., WALKER, L. C. & JUCKER, M. 2006. Exogenous induction of cerebral beta-amyloidogenesis is governed by agent and host. *Science,* 313**,** 1781-4.

MEYER-LUEHMANN, M., SPIRES-JONES, T. L., PRADA, C., GARCIA-ALLOZA, M., DE CALIGNON, A., ROZKALNE, A., KOENIGSKNECHT-TALBOO, J., HOLTZMAN, D. M., BACSKAI, B. J. & HYMAN, B. T. 2008. Rapid appearance and local toxicity of amyloid-beta plaques in a mouse model of Alzheimer's disease. *Nature,* 451**,** 720-4.

MEZ, J., DANESHVAR, D. H., KIERNAN, P. T., ABDOLMOHAMMADI, B., ALVAREZ, V. E., HUBER, B. R., ALOSCO, M. L., SOLOMON, T. M., NOWINSKI, C. J., MCHALE, L., CORMIER, K. A., KUBILUS, C. A., MARTIN, B. M., MURPHY, L., BAUGH, C. M., MONTENIGRO, P. H., CHAISSON, C. E., TRIPODIS, Y., KOWALL, N. W., WEUVE, J., MCCLEAN, M. D., CANTU, R. C., GOLDSTEIN, L. E., KATZ, D. I., STERN, R. A., STEIN, T. D. & MCKEE, A. C. 2017. Clinicopathological Evaluation of Chronic Traumatic Encephalopathy in Players of American Football. *JAMA,* 318**,** 360-370.

MICHAELS, T. C. T., SARIC, A., CURK, S., BERNFUR, K., AROSIO, P., MEISL, G., DEAR, A. J., COHEN, S. I. A., DOBSON, C. M., VENDRUSCOLO, M., LINSE, S. & KNOWLES, T. P. J. 2020. Dynamics of oligomer populations formed during the aggregation of Alzheimer's Abeta42 peptide. *Nat Chem,* 12**,** 445-451.

MILLER, E. C., TERAVSKIS, P. J., DUMMER, B. W., ZHAO, X., HUGANIR, R. L. & LIAO, D. 2014. Tau phosphorylation and tau mislocalization mediate soluble Abeta oligomer-induced AMPA glutamate receptor signaling deficits. *Eur J Neurosci,* 39**,** 1214-24.

MILLS, J. & REINER, P. B. 1999. Regulation of amyloid precursor protein cleavage. *J Neurochem,* 72**,** 443-60.

MINLEBAEV, M., COLONNESE, M., TSINTSADZE, T., SIROTA, A. & KHAZIPOV, R. 2011. Early gamma oscillations synchronize developing thalamus and cortex. *Science,* 334**,** 226-9.

MONTEREY, M. D., WEI, H., WU, X. & WU, J. Q. 2021. The Many Faces of Astrocytes in Alzheimer's Disease. *Front Neurol,* 12**,** 619626.

MONTINARO, C., PISANELLO, M., BIANCO, M., SPAGNOLO, B., PISANO, F., BALENA, A., DE NUCCIO, F., LOFRUMENTO, D. D., VERRI, T., DE VITTORIO, M. & PISANELLO, F. 2021. Influence of the anatomical features of different brain regions on the spatial localization of fiber photometry signals. *Biomed Opt Express,* 12**,** 6081-6094.

MONTOLIU-GAYA, L., MULDER, S. D., VEERHUIS, R. & VILLEGAS, S. 2017. Effects of an Abeta-antibody fragment on Abeta aggregation and astrocytic uptake are modulated by apolipoprotein E and J mimetic peptides. *PLoS One,* 12**,** e0188191.
MORALES, I., JIMENEZ, J. M., MANCILLA, M. & MACCIONI, R. B. 2013. Tau oligomers and fibrils induce activation of microglial cells. *J Alzheimers Dis,* 37**,** 849-56.
MORMINO, E. C., SMILJIC, A., HAYENGA, A. O., ONAMI, S. H., GREICIUS, M. D., RABINOVICI, G. D., JANABI, M., BAKER, S. L., YEN, I. V., MADISON, C. M., MILLER, B. L. & JAGUST, W. J. 2011. Relationships between beta-amyloid and functional connectivity in different components of the default mode network in aging. *Cereb Cortex,* 21**,** 2399-407.
MORRIS, M. C., EVANS, D. A., BIENIAS, J. L., TANGNEY, C. C., BENNETT, D. A., AGGARWAL, N., WILSON, R. S. & SCHERR, P. A. 2002. Dietary intake of antioxidant nutrients and the risk of incident Alzheimer disease in a biracial community study. *JAMA,* 287**,** 3230-7.
MORRISON, L. E. 2008. Basic principles of fluorescence and energy transfer. *Methods Mol Biol,* 429**,** 3-19.
MRAK, R. E. 2012. Microglia in Alzheimer brain: a neuropathological perspective. *Int J Alzheimers Dis,* 2012**,** 165021.
MUCKE, L., MASLIAH, E., YU, G. Q., MALLORY, M., ROCKENSTEIN, E. M., TATSUNO, G., HU, K., KHOLODENKO, D., JOHNSON-WOOD, K. & MCCONLOGUE, L. 2000. High-level neuronal expression of abeta 1-42 in wild-type human amyloid protein precursor transgenic mice: synaptotoxicity without plaque formation. *J Neurosci,* 20**,** 4050-8.
MULLIGAN, S. J. & MACVICAR, B. A. 2004. Calcium transients in astrocyte endfeet cause cerebrovascular constrictions. *Nature,* 431**,** 195-9.
MURDOCK, M. H., YANG, C. Y., SUN, N., PAO, P. C., BLANCO-DUQUE, C., KAHN, M. C., KIM, T., LAVOIE, N. S., VICTOR, M. B., ISLAM, M. R., GALIANA, F., LEARY, N., WANG, S., BUBNYS, A., MA, E., AKAY, L. A., SNEVE, M., QIAN, Y., LAI, C., MCCARTHY, M. M., KOPELL, N., KELLIS, M., PIATKEVICH, K. D., BOYDEN, E. S. & TSAI, L. H. 2024. Multisensory gamma stimulation promotes glymphatic clearance of amyloid. *Nature,* 627**,** 149-156.
MURPHY, M. P. & LEVINE, H., 3RD 2010. Alzheimer's disease and the amyloid-beta peptide. *J Alzheimers Dis,* 19**,** 311-23.
MUSIEK, E. S. & HOLTZMAN, D. M. 2015. Three dimensions of the amyloid hypothesis: time, space and 'wingmen'. *Nat Neurosci,* 18**,** 800-6.
NAGELE, R. G., D'ANDREA, M. R., ANDERSON, W. J. & WANG, H. Y. 2002. Intracellular accumulation of beta-amyloid(1-42) in neurons is facilitated by the alpha 7 nicotinic acetylcholine receptor in Alzheimer's disease. *Neuroscience,* 110**,** 199-211.
NAGELE, R. G., D'ANDREA, M. R., LEE, H., VENKATARAMAN, V. & WANG, H. Y. 2003. Astrocytes accumulate A beta 42 and give rise to astrocytic amyloid plaques in Alzheimer disease brains. *Brain Res,* 971**,** 197-209.
NAGELE, R. G., WEGIEL, J., VENKATARAMAN, V., IMAKI, H., WANG, K. C. & WEGIEL, J. 2004. Contribution of glial cells to the development of amyloid plaques in Alzheimer's disease. *Neurobiol Aging,* 25**,** 663-74.
NAIR, J., KLAASSEN, A. L., ARATO, J., VYSSOTSKI, A. L., HARVEY, M. & RAINER, G. 2018. Basal forebrain contributes to default mode network regulation. *Proc Natl Acad Sci U S A,* 115**,** 1352-1357.
NAKAI, J., OHKURA, M. & IMOTO, K. 2001. A high signal-to-noise Ca(2+) probe composed of a single green fluorescent protein. *Nat Biotechnol,* 19**,** 137-41.
NAKAZONO, T., LAM, T. N., PATEL, A. Y., KITAZAWA, M., SAITO, T., SAIDO, T. C. & IGARASHI, K. M. 2017. Impaired In Vivo Gamma Oscillations in the Medial Entorhinal Cortex of Knock-in Alzheimer Model. *Front Syst Neurosci,* 11**,** 48.
NARASIMHAN, S., GUO, J. L., CHANGOLKAR, L., STIEBER, A., MCBRIDE, J. D., SILVA, L. V., HE, Z., ZHANG, B., GATHAGAN, R. J., TROJANOWSKI, J. Q. & LEE, V. M. Y. 2017. Pathological Tau Strains from Human Brains Recapitulate the Diversity of Tauopathies in Nontransgenic Mouse Brain. *J Neurosci,* 37**,** 11406-11423.
NARITA, M., HOLTZMAN, D. M., SCHWARTZ, A. L. & BU, G. 1997. Alpha2-macroglobulin complexes with and mediates the endocytosis of beta-amyloid peptide via cell surface low-density lipoprotein receptor-related protein. *J Neurochem,* 69**,** 1904-11.
NATSUBORI, A., TSUTSUI-KIMURA, I., NISHIDA, H., BOUCHEKIOUA, Y., SEKIYA, H., UCHIGASHIMA, M., WATANABE, M., DE KERCHOVE D'EXAERDE, A., MIMURA, M., TAKATA, N. & TANAKA, K. F. 2017. Ventrolateral Striatal Medium Spiny Neurons Positively Regulate Food-Incentive, Goal-Directed Behavior Independently of D1 and D2 Selectivity. *J Neurosci,* 37**,** 2723-2733.

NAVARRETE, M. & ARAQUE, A. 2014. The Cajal school and the physiological role of astrocytes: a way of thinking. *Front Neuroanat,* 8**,** 33.
NEUNER, S. M., HEUER, S. E., HUENTELMAN, M. J., O'CONNELL, K. M. S. & KACZOROWSKI, C. C. 2019. Harnessing Genetic Complexity to Enhance Translatability of Alzheimer's Disease Mouse Models: A Path toward Precision Medicine. *Neuron,* 101**,** 399-411 e5.
NHAN, H. S., CHIANG, K. & KOO, E. H. 2015. The multifaceted nature of amyloid precursor protein and its proteolytic fragments: friends and foes. *Acta Neuropathol,* 129**,** 1-19.
NI, R., CHEN, Z., DEAN-BEN, X. L., VOIGT, F. F., KIRSCHENBAUM, D., SHI, G., VILLOIS, A., ZHOU, Q., CRIMI, A., AROSIO, P., NITSCH, R. M., NILSSON, K. P. R., AGUZZI, A., HELMCHEN, F., KLOHS, J. & RAZANSKY, D. 2022. Multiscale optical and optoacoustic imaging of amyloid-beta deposits in mice. *Nat Biomed Eng,* 6**,** 1031-1044.
NICHOLS, M. R., MOSS, M. A., REED, D. K., LIN, W. L., MUKHOPADHYAY, R., HOH, J. H. & ROSENBERRY, T. L. 2002. Growth of beta-amyloid(1-40) protofibrils by monomer elongation and lateral association. Characterization of distinct products by light scattering and atomic force microscopy. *Biochemistry,* 41**,** 6115-27.
NICOLAS, M. & HASSAN, B. A. 2014. Amyloid precursor protein and neural development. *Development,* 141**,** 2543-8.
NITSCHE, M. A. & PAULUS, W. 2000. Excitability changes induced in the human motor cortex by weak transcranial direct current stimulation. *J Physiol,* 527 Pt 3**,** 633-9.
NITSCHE, M. A., SEEBER, A., FROMMANN, K., KLEIN, C. C., ROCHFORD, C., NITSCHE, M. S., FRICKE, K., LIEBETANZ, D., LANG, N., ANTAL, A., PAULUS, W. & TERGAU, F. 2005. Modulating parameters of excitability during and after transcranial direct current stimulation of the human motor cortex. *J Physiol,* 568**,** 291-303.
NOBEN-TRAUTH, K., ZHENG, Q. Y. & JOHNSON, K. R. 2003. Association of cadherin 23 with polygenic inheritance and genetic modification of sensorineural hearing loss. *Nat Genet,* 35**,** 21-3.
O'LEARY, T. P., MANTOLINO, H. M., STOVER, K. R. & BROWN, R. E. 2020. Age-related deterioration of motor function in male and female 5xFAD mice from 3 to 16 months of age. *Genes Brain Behav,* 19**,** e12538.
O'LEARY, T. P., ROBERTSON, A., CHIPMAN, P. H., RAFUSE, V. F. & BROWN, R. E. 2018. Motor function deficits in the 12 month-old female 5xFAD mouse model of Alzheimer's disease. *Behav Brain Res,* 337**,** 256-263.
OAKLEY, H., COLE, S. L., LOGAN, S., MAUS, E., SHAO, P., CRAFT, J., GUILLOZET-BONGAARTS, A., OHNO, M., DISTERHOFT, J., VAN ELDIK, L., BERRY, R. & VASSAR, R. 2006. Intraneuronal beta-amyloid aggregates, neurodegeneration, and neuron loss in transgenic mice with five familial Alzheimer's disease mutations: potential factors in amyloid plaque formation. *J Neurosci,* 26**,** 10129-40.
OBLAK, A. L., FORNER, S., TERRITO, P. R., SASNER, M., CARTER, G. W., HOWELL, G. R., SUKOFF-RIZZO, S. J., LOGSDON, B. A., MANGRAVITE, L. M., MORTAZAVI, A., BAGLIETTO-VARGAS, D., GREEN, K. N., MACGREGOR, G. R., WOOD, M. A., TENNER, A. J., LAFERLA, F. M., LAMB, B. T., AND THE, M.-A. & CONSORTIUM 2020. Model organism development and evaluation for late-onset Alzheimer's disease: MODEL-AD. *Alzheimers Dement (N Y),* 6**,** e12110.
OBLAK, A. L., LIN, P. B., KOTREDES, K. P., PANDEY, R. S., GARCEAU, D., WILLIAMS, H. M., UYAR, A., O'ROURKE, R., O'ROURKE, S., INGRAHAM, C., BEDNARCZYK, D., BELANGER, M., COPE, Z. A., LITTLE, G. J., WILLIAMS, S. G., ASH, C., BLECKERT, A., RAGAN, T., LOGSDON, B. A., MANGRAVITE, L. M., SUKOFF RIZZO, S. J., TERRITO, P. R., CARTER, G. W., HOWELL, G. R., SASNER, M. & LAMB, B. T. 2021. Comprehensive Evaluation of the 5XFAD Mouse Model for Preclinical Testing Applications: A MODEL-AD Study. *Front Aging Neurosci,* 13**,** 713726.
ODDO, S., CACCAMO, A., SHEPHERD, J. D., MURPHY, M. P., GOLDE, T. E., KAYED, R., METHERATE, R., MATTSON, M. P., AKBARI, Y. & LAFERLA, F. M. 2003. Triple-transgenic model of Alzheimer's disease with plaques and tangles: intracellular Abeta and synaptic dysfunction. *Neuron,* 39**,** 409-21.
OKADA, Y., HOSOI, N., MATSUZAKI, Y., FUKAI, Y., HIRAGA, A., NAKAI, J., NITTA, K., SHINOHARA, Y., KONNO, A. & HIRAI, H. 2022. Development of microglia-targeting adeno-associated viral vectors as tools to study microglial behavior in vivo. *Commun Biol,* 5**,** 1224.
OLABARRIA, M., NORISTANI, H. N., VERKHRATSKY, A. & RODRIGUEZ, J. J. 2010. Concomitant astroglial atrophy and astrogliosis in a triple transgenic animal model of Alzheimer's disease. *Glia,* 58**,** 831-8.

OLIVEIRA, J. F. & ARAQUE, A. 2022. Astrocyte regulation of neural circuit activity and network states. *Glia,* 70**,** 1455-1466.
OPEN SCIENCE COLLABORATION 2015. PSYCHOLOGY. Estimating the reproducibility of psychological science. *Science,* 349**,** aac4716.
OSIPOVA, D., PEKKONEN, E. & AHVENINEN, J. 2006a. Enhanced magnetic auditory steady-state response in early Alzheimer's disease. *Clin Neurophysiol,* 117**,** 1990-5.
OSIPOVA, D., TAKASHIMA, A., OOSTENVELD, R., FERNANDEZ, G., MARIS, E. & JENSEN, O. 2006b. Theta and gamma oscillations predict encoding and retrieval of declarative memory. *J Neurosci,* 26**,** 7523-31.
OTT, A., STOLK, R. P., VAN HARSKAMP, F., POLS, H. A., HOFMAN, A. & BRETELER, M. M. 1999. Diabetes mellitus and the risk of dementia: The Rotterdam Study. *Neurology,* 53**,** 1937-42.
PAGANETTI, P. A., LIS, M., KLAFKI, H. W. & STAUFENBIEL, M. 1996. Amyloid precursor protein truncated at any of the gamma-secretase sites is not cleaved to beta-amyloid. *J Neurosci Res,* 46**,** 283-93.
PALOP, J. J., CHIN, J., ROBERSON, E. D., WANG, J., THWIN, M. T., BIEN-LY, N., YOO, J., HO, K. O., YU, G. Q., KREITZER, A., FINKBEINER, S., NOEBELS, J. L. & MUCKE, L. 2007. Aberrant excitatory neuronal activity and compensatory remodeling of inhibitory hippocampal circuits in mouse models of Alzheimer's disease. *Neuron,* 55**,** 697-711.
PALOP, J. J. & MUCKE, L. 2016. Network abnormalities and interneuron dysfunction in Alzheimer disease. *Nat Rev Neurosci,* 17**,** 777-792.
PAQUET, D., BHAT, R., SYDOW, A., MANDELKOW, E. M., BERG, S., HELLBERG, S., FALTING, J., DISTEL, M., KOSTER, R. W., SCHMID, B. & HAASS, C. 2009. A zebrafish model of tauopathy allows in vivo imaging of neuronal cell death and drug evaluation. *J Clin Invest,* 119**,** 1382-95.
PARAVASTU, A. K., LEAPMAN, R. D., YAU, W. M. & TYCKO, R. 2008. Molecular structural basis for polymorphism in Alzheimer's beta-amyloid fibrils. *Proc Natl Acad Sci U S A,* 105**,** 18349-54.
PARDOSSI-PIQUARD, R., PETIT, A., KAWARAI, T., SUNYACH, C., ALVES DA COSTA, C., VINCENT, B., RING, S., D'ADAMIO, L., SHEN, J., MULLER, U., ST GEORGE HYSLOP, P. & CHECLER, F. 2005. Presenilin-dependent transcriptional control of the Abeta-degrading enzyme neprilysin by intracellular domains of betaAPP and APLP. *Neuron,* 46**,** 541-54.
PARK, I., DIAZ, J., MATSUMOTO, S., IWAYAMA, K., NABEKURA, Y., OGATA, H., KAYABA, M., AOYAGI, A., YAJIMA, K., SATOH, M., TOKUYAMA, K. & VOGT, K. E. 2021. Exercise improves the quality of slow-wave sleep by increasing slow-wave stability. *Sci Rep,* 11**,** 4410.
PARK, K., KOHL, M. M. & KWAG, J. 2024. Memory encoding and retrieval by retrosplenial parvalbumin interneurons are impaired in Alzheimer's disease model mice. *Curr Biol,* 34**,** 434-443 e4.
PARK, K., LEE, J., JANG, H. J., RICHARDS, B. A., KOHL, M. M. & KWAG, J. 2020. Optogenetic activation of parvalbumin and somatostatin interneurons selectively restores theta-nested gamma oscillations and oscillation-induced spike timing-dependent long-term potentiation impaired by amyloid beta oligomers. *BMC Biol,* 18**,** 7.
PASTOR, M. A., ARTIEDA, J., ARBIZU, J., MARTI-CLIMENT, J. M., PENUELAS, I. & MASDEU, J. C. 2002. Activation of human cerebral and cerebellar cortex by auditory stimulation at 40 Hz. *J Neurosci,* 22**,** 10501-6.
PASTOR, M. A., ARTIEDA, J., ARBIZU, J., VALENCIA, M. & MASDEU, J. C. 2003. Human cerebral activation during steady-state visual-evoked responses. *J Neurosci,* 23**,** 11621-7.
PATEL, A. A., MCALINDEN, N., MATHIESON, K. & SAKATA, S. 2020. Simultaneous Electrophysiology and Fiber Photometry in Freely Behaving Mice. *Front Neurosci,* 14**,** 148.
PATEL, N., RAMACHANDRAN, S., AZIMOV, R., KAGAN, B. L. & LAL, R. 2015. Ion Channel Formation by Tau Protein: Implications for Alzheimer's Disease and Tauopathies. *Biochemistry,* 54**,** 7320-5.
PATRIARCHI, T., CHO, J. R., MERTEN, K., HOWE, M. W., MARLEY, A., XIONG, W. H., FOLK, R. W., BROUSSARD, G. J., LIANG, R., JANG, M. J., ZHONG, H., DOMBECK, D., VON ZASTROW, M., NIMMERJAHN, A., GRADINARU, V., WILLIAMS, J. T. & TIAN, L. 2018. Ultrafast neuronal imaging of dopamine dynamics with designed genetically encoded sensors. *Science,* 360.
PATRIARCHI, T., MOHEBI, A., SUN, J., MARLEY, A., LIANG, R., DONG, C., PUHGER, K., MIZUNO, G. O., DAVIS, C. M., WILTGEN, B., VON ZASTROW, M., BERKE, J. D. & TIAN, L. 2020. An expanded palette of dopamine sensors for multiplex imaging in vivo. *Nat Methods,* 17**,** 1147-1155.
PEKNY, M. & NILSSON, M. 2005. Astrocyte activation and reactive gliosis. *Glia,* 50**,** 427-434.
PEREA, J. R., LOPEZ, E., DIEZ-BALLESTEROS, J. C., AVILA, J., HERNANDEZ, F. & BOLOS, M. 2019. Extracellular Monomeric Tau Is Internalized by Astrocytes. *Front Neurosci,* 13**,** 442.

PEREZ, S. E., RAGHANTI, M. A., HOF, P. R., KRAMER, L., IKONOMOVIC, M. D., LACOR, P. N., ERWIN, J. M., SHERWOOD, C. C. & MUFSON, E. J. 2013. Alzheimer's disease pathology in the neocortex and hippocampus of the western lowland gorilla (Gorilla gorilla gorilla). *J Comp Neurol,* 521**,** 4318-38.

PEREZ, S. E., SHERWOOD, C. C., CRANFIELD, M. R., ERWIN, J. M., MUDAKIKWA, A., HOF, P. R. & MUFSON, E. J. 2016. Early Alzheimer's disease-type pathology in the frontal cortex of wild mountain gorillas (Gorilla beringei beringei). *Neurobiol Aging,* 39**,** 195-201.

PERINI, G., DELLA-BIANCA, V., POLITI, V., DELLA VALLE, G., DAL-PRA, I., ROSSI, F. & ARMATO, U. 2002. Role of p75 neurotrophin receptor in the neurotoxicity by beta-amyloid peptides and synergistic effect of inflammatory cytokines. *J Exp Med,* 195**,** 907-18.

PETKOVA, A. T., LEAPMAN, R. D., GUO, Z., YAU, W. M., MATTSON, M. P. & TYCKO, R. 2005. Self-propagating, molecular-level polymorphism in Alzheimer's beta-amyloid fibrils. *Science,* 307**,** 262-5.

PIACENTINI, R., LI PUMA, D. D., MAINARDI, M., LAZZARINO, G., TAVAZZI, B., ARANCIO, O. & GRASSI, C. 2017. Reduced gliotransmitter release from astrocytes mediates tau-induced synaptic dysfunction in cultured hippocampal neurons. *Glia,* 65**,** 1302-1316.

PICQ, J. L., AUJARD, F., VOLK, A. & DHENAIN, M. 2012. Age-related cerebral atrophy in nonhuman primates predicts cognitive impairments. *Neurobiol Aging,* 33**,** 1096-109.

PISANELLO, F., MANDELBAUM, G., PISANELLO, M., OLDENBURG, I. A., SILEO, L., MARKOWITZ, J. E., PETERSON, R. E., DELLA PATRIA, A., HAYNES, T. M., EMARA, M. S., SPAGNOLO, B., DATTA, S. R., DE VITTORIO, M. & SABATINI, B. L. 2017. Dynamic illumination of spatially restricted or large brain volumes via a single tapered optical fiber. *Nat Neurosci,* 20**,** 1180-1188.

PISANELLO, F., SILEO, L., OLDENBURG, I. A., PISANELLO, M., MARTIRADONNA, L., ASSAD, J. A., SABATINI, B. L. & DE VITTORIO, M. 2014. Multipoint-emitting optical fibers for spatially addressable in vivo optogenetics. *Neuron,* 82**,** 1245-54.

PISANELLO, M., PISANO, F., HYUN, M., MAGLIE, E., BALENA, A., DE VITTORIO, M., SABATINI, B. L. & PISANELLO, F. 2019. The Three-Dimensional Signal Collection Field for Fiber Photometry in Brain Tissue. *Front Neurosci,* 13**,** 82.

PISANO, F., PISANELLO, M., LEE, S. J., LEE, J., MAGLIE, E., BALENA, A., SILEO, L., SPAGNOLO, B., BIANCO, M., HYUN, M., DE VITTORIO, M., SABATINI, B. L. & PISANELLO, F. 2019. Depth-resolved fiber photometry with a single tapered optical fiber implant. *Nat Methods,* 16**,** 1185-1192.

PLOUFFE, V., MOHAMED, N. V., RIVEST-MCGRAW, J., BERTRAND, J., LAUZON, M. & LECLERC, N. 2012. Hyperphosphorylation and cleavage at D421 enhance tau secretion. *PLoS One,* 7**,** e36873.

POLANIA, R., NITSCHE, M. A. & RUFF, C. C. 2018. Studying and modifying brain function with non-invasive brain stimulation. *Nat Neurosci,* 21**,** 174-187.

POOLER, A. M., PHILLIPS, E. C., LAU, D. H., NOBLE, W. & HANGER, D. P. 2013. Physiological release of endogenous tau is stimulated by neuronal activity. *EMBO Rep,* 14**,** 389-94.

POOLER, A. M., USARDI, A., EVANS, C. J., PHILPOTT, K. L., NOBLE, W. & HANGER, D. P. 2012. Dynamic association of tau with neuronal membranes is regulated by phosphorylation. *Neurobiol Aging,* 33**,** 431 e27-38.

POPESCU, A. T., POPA, D. & PARE, D. 2009. Coherent gamma oscillations couple the amygdala and striatum during learning. *Nat Neurosci,* 12**,** 801-7.

PRICHARD, A., GARZA, K. M., SHRIDHAR, A., HE, C., BITARAFAN, S., PYBUS, A., WANG, Y., SNYDER, E., GOODSON, M. C., FRANKLIN, T. C., JAEGER, D., WOOD, L. B. & SINGER, A. C. 2023. Brain rhythms control microglial response and cytokine expression via NF-kappaB signaling. *Sci Adv,* 9**,** eadf5672.

QUILICHINI, P., SIROTA, A. & BUZSAKI, G. 2010. Intrinsic circuit organization and theta-gamma oscillation dynamics in the entorhinal cortex of the rat. *J Neurosci,* 30**,** 11128-42.

RADDE, R., BOLMONT, T., KAESER, S. A., COOMARASWAMY, J., LINDAU, D., STOLTZE, L., CALHOUN, M. E., JAGGI, F., WOLBURG, H., GENGLER, S., HAASS, C., GHETTI, B., CZECH, C., HOLSCHER, C., MATHEWS, P. M. & JUCKER, M. 2006. Abeta42-driven cerebral amyloidosis in transgenic mice reveals early and robust pathology. *EMBO Rep,* 7**,** 940-6.

RADMAN, T., RAMOS, R. L., BRUMBERG, J. C. & BIKSON, M. 2009. Role of cortical cell type and morphology in subthreshold and suprathreshold uniform electric field stimulation in vitro. *Brain Stimul,* 2**,** 215-28, 228 e1-3.

RAFF, M. C., MILLER, R. H. & NOBLE, M. 1983. A glial progenitor cell that develops in vitro into an astrocyte or an oligodendrocyte depending on culture medium. *Nature,* 303**,** 390-396.

RAGER, G. & SINGER, W. 1998. The response of cat visual cortex to flicker stimuli of variable frequency. *Eur J Neurosci,* 10**,** 1856-77.
RAHMAN, A., JACKSON, H., HRISTOV, H., ISAACSON, R. S., SAIF, N., SHETTY, T., ETINGIN, O., HENCHCLIFFE, C., BRINTON, R. D. & MOSCONI, L. 2019. Sex and Gender Driven Modifiers of Alzheimer's: The Role for Estrogenic Control Across Age, Race, Medical, and Lifestyle Risks. *Front Aging Neurosci,* 11**,** 315.
RAHMAN, A., REATO, D., ARLOTTI, M., GASCA, F., DATTA, A., PARRA, L. C. & BIKSON, M. 2013. Cellular effects of acute direct current stimulation: somatic and synaptic terminal effects. *J Physiol,* 591**,** 2563-78.
RAJENDRAN, L., HONSHO, M., ZAHN, T. R., KELLER, P., GEIGER, K. D., VERKADE, P. & SIMONS, K. 2006. Alzheimer's disease beta-amyloid peptides are released in association with exosomes. *Proc Natl Acad Sci U S A,* 103**,** 11172-7.
REINHART, R. M. G. & NGUYEN, J. A. 2019. Working memory revived in older adults by synchronizing rhythmic brain circuits. *Nat Neurosci,* 22**,** 820-827.
REINKE, A. A. & GESTWICKI, J. E. 2011. Insight into amyloid structure using chemical probes. *Chem Biol Drug Des,* 77**,** 399-411.
REITZ, C., BRAYNE, C. & MAYEUX, R. 2011. Epidemiology of Alzheimer disease. *Nat Rev Neurol,* 7**,** 137-52.
REVETT, T. J., BAKER, G. B., JHAMANDAS, J. & KAR, S. 2013. Glutamate system, amyloid ss peptides and tau protein: functional interrelationships and relevance to Alzheimer disease pathology. *J Psychiatry Neurosci,* 38**,** 6-23.
RIBARY, U., IOANNIDES, A. A., SINGH, K. D., HASSON, R., BOLTON, J. P., LADO, F., MOGILNER, A. & LLINAS, R. 1991. Magnetic field tomography of coherent thalamocortical 40-Hz oscillations in humans. *Proc Natl Acad Sci U S A,* 88**,** 11037-41.
RICHARD, B. C., KURDAKOVA, A., BACHES, S., BAYER, T. A., WEGGEN, S. & WIRTHS, O. 2015. Gene Dosage Dependent Aggravation of the Neurological Phenotype in the 5XFAD Mouse Model of Alzheimer's Disease. *J Alzheimers Dis,* 45**,** 1223-36.
RICHETIN, K., STEULLET, P., PACHOUD, M., PERBET, R., PARIETTI, E., MAHESWARAN, M., EDDARKAOUI, S., BEGARD, S., PYTHOUD, C., REY, M., CAILLIEREZ, R., K, Q. D., HALLIEZ, S., BEZZI, P., BUEE, L., LEUBA, G., COLIN, M., TONI, N. & DEGLON, N. 2020. Tau accumulation in astrocytes of the dentate gyrus induces neuronal dysfunction and memory deficits in Alzheimer's disease. *Nat Neurosci,* 23**,** 1567-1579.
ROBERSON, E. D., HALABISKY, B., YOO, J. W., YAO, J., CHIN, J., YAN, F., WU, T., HAMTO, P., DEVIDZE, N., YU, G. Q., PALOP, J. J., NOEBELS, J. L. & MUCKE, L. 2011. Amyloid-beta/Fyn-induced synaptic, network, and cognitive impairments depend on tau levels in multiple mouse models of Alzheimer's disease. *J Neurosci,* 31**,** 700-11.
ROBERSON, E. D., SCEARCE-LEVIE, K., PALOP, J. J., YAN, F., CHENG, I. H., WU, T., GERSTEIN, H., YU, G. Q. & MUCKE, L. 2007. Reducing endogenous tau ameliorates amyloid beta-induced deficits in an Alzheimer's disease mouse model. *Science,* 316**,** 750-4.
RODRIGUEZ, G. A., BARRETT, G. M., DUFF, K. E. & HUSSAINI, S. A. 2020. Chemogenetic attenuation of neuronal activity in the entorhinal cortex reduces Abeta and tau pathology in the hippocampus. *PLoS Biol,* 18**,** e3000851.
RODRIGUEZ-GIRALDO, M., GONZALEZ-REYES, R. E., RAMIREZ-GUERRERO, S., BONILLA-TRILLERAS, C. E., GUARDO-MAYA, S. & NAVA-MESA, M. O. 2022. Astrocytes as a Therapeutic Target in Alzheimer's Disease-Comprehensive Review and Recent Developments. *Int J Mol Sci,* 23.
ROMBOUTS, S. A., BARKHOF, F., VELTMAN, D. J., MACHIELSEN, W. C., WITTER, M. P., BIERLAAGH, M. A., LAZERON, R. H., VALK, J. & SCHELTENS, P. 2000. Functional MR imaging in Alzheimer's disease during memory encoding. *AJNR Am J Neuroradiol,* 21**,** 1869-75.
RONICKE, R., MIKHAYLOVA, M., RONICKE, S., MEINHARDT, J., SCHRODER, U. H., FANDRICH, M., REISER, G., KREUTZ, M. R. & REYMANN, K. G. 2011. Early neuronal dysfunction by amyloid beta oligomers depends on activation of NR2B-containing NMDA receptors. *Neurobiol Aging,* 32**,** 2219-28.
RONNBACK, A., SAGELIUS, H., BERGSTEDT, K. D., NASLUND, J., WESTERMARK, G. T., WINBLAD, B. & GRAFF, C. 2012. Amyloid neuropathology in the single Arctic APP transgenic model affects interconnected brain regions. *Neurobiol Aging,* 33**,** 831 e11-9.
ROSEN, R. F., FARBERG, A. S., GEARING, M., DOOYEMA, J., LONG, P. M., ANDERSON, D. C., DAVIS-TURAK, J., COPPOLA, G., GESCHWIND, D. H., PARE, J. F., DUONG, T. Q.,

HOPKINS, W. D., PREUSS, T. M. & WALKER, L. C. 2008. Tauopathy with paired helical filaments in an aged chimpanzee. *J Comp Neurol,* 509**,** 259-70.
ROSSINI, P. M., DEL PERCIO, C., PASQUALETTI, P., CASSETTA, E., BINETTI, G., DAL FORNO, G., FERRERI, F., FRISONI, G., CHIOVENDA, P., MINIUSSI, C., PARISI, L., TOMBINI, M., VECCHIO, F. & BABILONI, C. 2006. Conversion from mild cognitive impairment to Alzheimer's disease is predicted by sources and coherence of brain electroencephalography rhythms. *Neuroscience,* 143**,** 793-803.
ROSSNER, S., APELT, J., SCHLIEBS, R., PEREZ-POLO, J. R. & BIGL, V. 2001. Neuronal and glial beta-secretase (BACE) protein expression in transgenic Tg2576 mice with amyloid plaque pathology. *J Neurosci Res,* 64**,** 437-46.
ROSSNER, S., LANGE-DOHNA, C., ZEITSCHEL, U. & PEREZ-POLO, J. R. 2005. Alzheimer's disease beta-secretase BACE1 is not a neuron-specific enzyme. *J Neurochem,* 92**,** 226-34.
RUSSELL, E. R., MACKAY, D. F., LYALL, D., STEWART, K., MACLEAN, J. A., ROBSON, J., PELL, J. P. & STEWART, W. 2022. Neurodegenerative disease risk among former international rugby union players. *J Neurol Neurosurg Psychiatry,* 93**,** 1262-1268.
RUSSELL, E. R., STEWART, K., MACKAY, D. F., MACLEAN, J., PELL, J. P. & STEWART, W. 2019. Football's InfluencE on Lifelong health and Dementia risk (FIELD): protocol for a retrospective cohort study of former professional footballers. *BMJ Open,* 9**,** e028654.
SAGARE, A., DEANE, R., BELL, R. D., JOHNSON, B., HAMM, K., PENDU, R., MARKY, A., LENTING, P. J., WU, Z., ZARCONE, T., GOATE, A., MAYO, K., PERLMUTTER, D., COMA, M., ZHONG, Z. & ZLOKOVIC, B. V. 2007. Clearance of amyloid-beta by circulating lipoprotein receptors. *Nat Med,* 13**,** 1029-31.
SAITO, T., MATSUBA, Y., MIHIRA, N., TAKANO, J., NILSSON, P., ITOHARA, S., IWATA, N. & SAIDO, T. C. 2014. Single App knock-in mouse models of Alzheimer's disease. *Nat Neurosci,* 17**,** 661-3.
SAMAN, S., KIM, W., RAYA, M., VISNICK, Y., MIRO, S., SAMAN, S., JACKSON, B., MCKEE, A. C., ALVAREZ, V. E., LEE, N. C. & HALL, G. F. 2012. Exosome-associated tau is secreted in tauopathy models and is selectively phosphorylated in cerebrospinal fluid in early Alzheimer disease. *J Biol Chem,* 287**,** 3842-9.
SANCHES, C., STENGEL, C., GODARD, J., MERTZ, J., TEICHMANN, M., MIGLIACCIO, R. & VALERO-CABRE, A. 2020. Past, Present, and Future of Non-invasive Brain Stimulation Approaches to Treat Cognitive Impairment in Neurodegenerative Diseases: Time for a Comprehensive Critical Review. *Front Aging Neurosci,* 12**,** 578339.
SANCHEZ, L., MADURGA, S., PUKALA, T., VILASECA, M., LOPEZ-IGLESIAS, C., ROBINSON, C. V., GIRALT, E. & CARULLA, N. 2011. Abeta40 and Abeta42 amyloid fibrils exhibit distinct molecular recycling properties. *J Am Chem Soc,* 133**,** 6505-8.
SANCHEZ-VARO, R., MEJIAS-ORTEGA, M., FERNANDEZ-VALENZUELA, J. J., NUNEZ-DIAZ, C., CACERES-PALOMO, L., VEGAS-GOMEZ, L., SANCHEZ-MEJIAS, E., TRUJILLO-ESTRADA, L., GARCIA-LEON, J. A., MORENO-GONZALEZ, I., VIZUETE, M., VITORICA, J., BAGLIETTO-VARGAS, D. & GUTIERREZ, A. 2022. Transgenic Mouse Models of Alzheimer's Disease: An Integrative Analysis. *Int J Mol Sci,* 23.
SANKAR, T., CHAKRAVARTY, M. M., BESCOS, A., LARA, M., OBUCHI, T., LAXTON, A. W., MCANDREWS, M. P., TANG-WAI, D. F., WORKMAN, C. I., SMITH, G. S. & LOZANO, A. M. 2015. Deep Brain Stimulation Influences Brain Structure in Alzheimer's Disease. *Brain Stimul,* 8**,** 645-54.
SANTACRUZ, K., LEWIS, J., SPIRES, T., PAULSON, J., KOTILINEK, L., INGELSSON, M., GUIMARAES, A., DETURE, M., RAMSDEN, M., MCGOWAN, E., FORSTER, C., YUE, M., ORNE, J., JANUS, C., MARIASH, A., KUSKOWSKI, M., HYMAN, B., HUTTON, M. & ASHE, K. H. 2005. Tau suppression in a neurodegenerative mouse model improves memory function. *Science,* 309**,** 476-81.
SARLUS, H. & HENEKA, M. T. 2017. Microglia in Alzheimer's disease. *J Clin Invest,* 127**,** 3240-3249.
SASAGURI, H., NILSSON, P., HASHIMOTO, S., NAGATA, K., SAITO, T., DE STROOPER, B., HARDY, J., VASSAR, R., WINBLAD, B. & SAIDO, T. C. 2017. APP mouse models for Alzheimer's disease preclinical studies. *EMBO J,* 36**,** 2473-2487.
SATO, K., WATAMURA, N., FUJIOKA, R., MIHIRA, N., SEKIGUCHI, M., NAGATA, K., OHSHIMA, T., SAITO, T., SAIDO, T. C. & SASAGURI, H. 2021. A third-generation mouse model of Alzheimer's disease shows early and increased cored plaque pathology composed of wild-type human amyloid beta peptide. *J Biol Chem,* 297**,** 101004.
SCARMEAS, N., STERN, Y., MAYEUX, R. & LUCHSINGER, J. A. 2006a. Mediterranean diet, Alzheimer disease, and vascular mediation. *Arch Neurol,* 63**,** 1709-17.

SCARMEAS, N., STERN, Y., TANG, M. X., MAYEUX, R. & LUCHSINGER, J. A. 2006b. Mediterranean diet and risk for Alzheimer's disease. *Ann Neurol,* 59**,** 912-21.
SCHARF, R., TSUNEMATSU, T., MCALINDEN, N., DAWSON, M. D., SAKATA, S. & MATHIESON, K. 2016. Depth-specific optogenetic control in vivo with a scalable, high-density muLED neural probe. *Sci Rep,* 6**,** 28381.
SCHENK, D., BARBOUR, R., DUNN, W., GORDON, G., GRAJEDA, H., GUIDO, T., HU, K., HUANG, J., JOHNSON-WOOD, K., KHAN, K., KHOLODENKO, D., LEE, M., LIAO, Z., LIEBERBURG, I., MOTTER, R., MUTTER, L., SORIANO, F., SHOPP, G., VASQUEZ, N., VANDEVERT, C., WALKER, S., WOGULIS, M., YEDNOCK, T., GAMES, D. & SEUBERT, P. 1999. Immunization with amyloid-beta attenuates Alzheimer-disease-like pathology in the PDAPP mouse. *Nature,* 400**,** 173-7.
SCHLEGEL, F., SYCH, Y., SCHROETER, A., STOBART, J., WEBER, B., HELMCHEN, F. & RUDIN, M. 2018. Fiber-optic implant for simultaneous fluorescence-based calcium recordings and BOLD fMRI in mice. *Nat Protoc,* 13**,** 840-855.
SCHMAND, B., HUIZENGA, H. M. & VAN GOOL, W. A. 2010. Meta-analysis of CSF and MRI biomarkers for detecting preclinical Alzheimer's disease. *Psychol Med,* 40**,** 135-45.
SCHMID, C. D., SAUTKULIS, L. N., DANIELSON, P. E., COOPER, J., HASEL, K. W., HILBUSH, B. S., SUTCLIFFE, J. G. & CARSON, M. J. 2002. Heterogeneous expression of the triggering receptor expressed on myeloid cells-2 on adult murine microglia. *J Neurochem,* 83**,** 1309-20.
SCHMIDT, F., BOLTZE, J., JAGER, C., HOFMANN, S., WILLEMS, N., SEEGER, J., HARTIG, W. & STOLZING, A. 2015. Detection and Quantification of beta-Amyloid, Pyroglutamyl Abeta, and Tau in Aged Canines. *J Neuropathol Exp Neurol,* 74**,** 912-23.
SCHMITZ, C., RUTTEN, B. P., PIELEN, A., SCHAFER, S., WIRTHS, O., TREMP, G., CZECH, C., BLANCHARD, V., MULTHAUP, G., REZAIE, P., KORR, H., STEINBUSCH, H. W., PRADIER, L. & BAYER, T. A. 2004. Hippocampal neuron loss exceeds amyloid plaque load in a transgenic mouse model of Alzheimer's disease. *Am J Pathol,* 164**,** 1495-502.
SCHNEIDER, L. 2020. A resurrection of aducanumab for Alzheimer's disease. *Lancet Neurol,* 19**,** 111-112.
SCHUTT, T., HELBOE, L., PEDERSEN, L. O., WALDEMAR, G., BERENDT, M. & PEDERSEN, J. T. 2016. Dogs with Cognitive Dysfunction as a Spontaneous Model for Early Alzheimer's Disease: A Translational Study of Neuropathological and Inflammatory Markers. *J Alzheimers Dis,* 52**,** 433-49.
SEKIYA, M., WANG, M., FUJISAKI, N., SAKAKIBARA, Y., QUAN, X., EHRLICH, M. E., DE JAGER, P. L., BENNETT, D. A., SCHADT, E. E., GANDY, S., ANDO, K., ZHANG, B. & IIJIMA, K. M. 2018. Integrated biology approach reveals molecular and pathological interactions among Alzheimer's Abeta42, Tau, TREM2, and TYROBP in Drosophila models. *Genome Med,* 10**,** 26.
SELKOE, D. J. 2001. Clearing the brain's amyloid cobwebs. *Neuron,* 32**,** 177-80.
SELKOE, D. J. 2021. Treatments for Alzheimer's disease emerge. *Science,* 373**,** 624-626.
SERNEELS, L., VAN BIERVLIET, J., CRAESSAERTS, K., DEJAEGERE, T., HORRE, K., VAN HOUTVIN, T., ESSELMANN, H., PAUL, S., SCHAFER, M. K., BEREZOVSKA, O., HYMAN, B. T., SPRANGERS, B., SCIOT, R., MOONS, L., JUCKER, M., YANG, Z., MAY, P. C., KARRAN, E., WILTFANG, J., D'HOOGE, R. & DE STROOPER, B. 2009. gamma-Secretase heterogeneity in the Aph1 subunit: relevance for Alzheimer's disease. *Science,* 324**,** 639-42.
SERRANO-POZO, A., FROSCH, M. P., MASLIAH, E. & HYMAN, B. T. 2011. Neuropathological Alterations in Alzheimer Disease. *Cold Spring Harbor Perspectives in Medicine,* 1.
SEUBERT, P., OLTERSDORF, T., LEE, M. G., BARBOUR, R., BLOMQUIST, C., DAVIS, D. L., BRYANT, K., FRITZ, L. C., GALASKO, D., THAL, L. J. & ET AL. 1993. Secretion of beta-amyloid precursor protein cleaved at the amino terminus of the beta-amyloid peptide. *Nature,* 361**,** 260-3.
SEUBERT, P., VIGO-PELFREY, C., ESCH, F., LEE, M., DOVEY, H., DAVIS, D., SINHA, S., SCHLOSSMACHER, M., WHALEY, J., SWINDLEHURST, C. & ET AL. 1992. Isolation and quantification of soluble Alzheimer's beta-peptide from biological fluids. *Nature,* 359**,** 325-7.
SEVIGNY, J., CHIAO, P., BUSSIERE, T., WEINREB, P. H., WILLIAMS, L., MAIER, M., DUNSTAN, R., SALLOWAY, S., CHEN, T., LING, Y., O'GORMAN, J., QIAN, F., ARASTU, M., LI, M., CHOLLATE, S., BRENNAN, M. S., QUINTERO-MONZON, O., SCANNEVIN, R. H., ARNOLD, H. M., ENGBER, T., RHODES, K., FERRERO, J., HANG, Y., MIKULSKIS, A., GRIMM, J., HOCK, C., NITSCH, R. M. & SANDROCK, A. 2016. The antibody aducanumab reduces Abeta plaques in Alzheimer's disease. *Nature,* 537**,** 50-6.

SGOURAKIS, N. G., YAN, Y., MCCALLUM, S. A., WANG, C. & GARCIA, A. E. 2007. The Alzheimer's peptides Abeta40 and 42 adopt distinct conformations in water: a combined MD / NMR study. *J Mol Biol,* 368**,** 1448-57.

SHAMASH, P., CARANDINI, M., HARRIS, K. & STEINMETZ, N. 2018. A tool for analyzing electrode tracks from slice histology. *BioRxiv*.

SHANKAR, G. M., BLOODGOOD, B. L., TOWNSEND, M., WALSH, D. M., SELKOE, D. J. & SABATINI, B. L. 2007. Natural oligomers of the Alzheimer amyloid-beta protein induce reversible synapse loss by modulating an NMDA-type glutamate receptor-dependent signaling pathway. *J Neurosci,* 27**,** 2866-75.

SHARPLES, R. A., VELLA, L. J., NISBET, R. M., NAYLOR, R., PEREZ, K., BARNHAM, K. J., MASTERS, C. L. & HILL, A. F. 2008. Inhibition of gamma-secretase causes increased secretion of amyloid precursor protein C-terminal fragments in association with exosomes. *FASEB J,* 22**,** 1469-78.

SHERRINGTON, R., ROGAEV, E. I., LIANG, Y., ROGAEVA, E. A., LEVESQUE, G., IKEDA, M., CHI, H., LIN, C., LI, G., HOLMAN, K., TSUDA, T., MAR, L., FONCIN, J. F., BRUNI, A. C., MONTESI, M. P., SORBI, S., RAINERO, I., PINESSI, L., NEE, L., CHUMAKOV, I., POLLEN, D., BROOKES, A., SANSEAU, P., POLINSKY, R. J., WASCO, W., DA SILVA, H. A., HAINES, J. L., PERKICAK-VANCE, M. A., TANZI, R. E., ROSES, A. D., FRASER, P. E., ROMMENS, J. M. & ST GEORGE-HYSLOP, P. H. 1995. Cloning of a gene bearing missense mutations in early-onset familial Alzheimer's disease. *Nature,* 375**,** 754-60.

SHI, A., PETRACHE, A. L., SHI, J. & ALI, A. B. 2020. Preserved Calretinin Interneurons in an App Model of Alzheimer's Disease Disrupt Hippocampal Inhibition via Upregulated P2Y1 Purinoreceptors. *Cereb Cortex,* 30**,** 1272-1290.

SHIBATA, M., YAMADA, S., KUMAR, S. R., CALERO, M., BADING, J., FRANGIONE, B., HOLTZMAN, D. M., MILLER, C. A., STRICKLAND, D. K., GHISO, J. & ZLOKOVIC, B. V. 2000. Clearance of Alzheimer's amyloid-ss(1-40) peptide from brain by LDL receptor-related protein-1 at the blood-brain barrier. *J Clin Invest,* 106**,** 1489-99.

SHIROTANI, K., TSUBUKI, S., IWATA, N., TAKAKI, Y., HARIGAYA, W., MARUYAMA, K., KIRYU-SEO, S., KIYAMA, H., IWATA, H., TOMITA, T., IWATSUBO, T. & SAIDO, T. C. 2001. Neprilysin degrades both amyloid beta peptides 1-40 and 1-42 most rapidly and efficiently among thiorphan- and phosphoramidon-sensitive endopeptidases. *J Biol Chem,* 276**,** 21895-901.

SHIVANGE, A. V., BORDEN, P. M., MUTHUSAMY, A. K., NICHOLS, A. L., BERA, K., BAO, H., BISHARA, I., JEON, J., MULCAHY, M. J., COHEN, B., O'RIORDAN, S. L., KIM, C., DOUGHERTY, D. A., CHAPMAN, E. R., MARVIN, J. S., LOOGER, L. L. & LESTER, H. A. 2019. Determining the pharmacokinetics of nicotinic drugs in the endoplasmic reticulum using biosensors. *J Gen Physiol,* 151**,** 738-757.

SHUMKOVA, V., SITDIKOVA, V., RECHAPOV, I., LEUKHIN, A. & MINLEBAEV, M. 2021. Effects of urethane and isoflurane on the sensory evoked response and local blood flow in the early postnatal rat somatosensory cortex. *Sci Rep,* 11**,** 9567.

SILVERMAN, D. H., SMALL, G. W., CHANG, C. Y., LU, C. S., KUNG DE ABURTO, M. A., CHEN, W., CZERNIN, J., RAPOPORT, S. I., PIETRINI, P., ALEXANDER, G. E., SCHAPIRO, M. B., JAGUST, W. J., HOFFMAN, J. M., WELSH-BOHMER, K. A., ALAVI, A., CLARK, C. M., SALMON, E., DE LEON, M. J., MIELKE, R., CUMMINGS, J. L., KOWELL, A. P., GAMBHIR, S. S., HOH, C. K. & PHELPS, M. E. 2001. Positron emission tomography in evaluation of dementia: Regional brain metabolism and long-term outcome. *JAMA,* 286**,** 2120-7.

SIMARD, M. & NEDERGAARD, M. 2004. The neurobiology of glia in the context of water and ion homeostasis. *Neuroscience,* 129**,** 877-96.

SIMON, D., GARCIA-GARCIA, E., GOMEZ-RAMOS, A., FALCON-PEREZ, J. M., DIAZ-HERNANDEZ, M., HERNANDEZ, F. & AVILA, J. 2012. Tau overexpression results in its secretion via membrane vesicles. *Neurodegener Dis,* 10**,** 73-5.

SIMPSON, E. H., AKAM, T., PATRIARCHI, T., BLANCO-POZO, M., BURGENO, L. M., MOHEBI, A., CRAGG, S. J. & WALTON, M. E. 2023. Lights, fiber, action! A primer on in vivo fiber photometry. *Neuron*.

SIMS, J. R., ZIMMER, J. A., EVANS, C. D., LU, M., ARDAYFIO, P., SPARKS, J., WESSELS, A. M., SHCHERBININ, S., WANG, H., MONKUL NERY, E. S., COLLINS, E. C., SOLOMON, P., SALLOWAY, S., APOSTOLOVA, L. G., HANSSON, O., RITCHIE, C., BROOKS, D. A., MINTUN, M., SKOVRONSKY, D. M. & INVESTIGATORS, T.-A. 2023. Donanemab in Early Symptomatic Alzheimer Disease: The TRAILBLAZER-ALZ 2 Randomized Clinical Trial. *JAMA,* 330**,** 512-527.

SINGER, W. & GRAY, C. M. 1995. Visual feature integration and the temporal correlation hypothesis. *Annu Rev Neurosci,* 18**,** 555-86.
SJOGREN, M. J., HELLSTROM, P. T., JONSSON, M. A., RUNNERSTAM, M., SILANDER, H. C. & BEN-MENACHEM, E. 2002. Cognition-enhancing effect of vagus nerve stimulation in patients with Alzheimer's disease: a pilot study. *J Clin Psychiatry,* 63**,** 972-80.
SKOVRONSKY, D. M., ZHANG, B., KUNG, M. P., KUNG, H. F., TROJANOWSKI, J. Q. & LEE, V. M. 2000. In vivo detection of amyloid plaques in a mouse model of Alzheimer's disease. *Proc Natl Acad Sci U S A,* 97**,** 7609-14.
SMALL, G. W., BOOKHEIMER, S. Y., THOMPSON, P. M., COLE, G. M., HUANG, S. C., KEPE, V. & BARRIO, J. R. 2008. Current and future uses of neuroimaging for cognitively impaired patients. *Lancet Neurol,* 7**,** 161-72.
SMOLEK, T., MADARI, A., FARBAKOVA, J., KANDRAC, O., JADHAV, S., CENTE, M., BREZOVAKOVA, V., NOVAK, M. & ZILKA, N. 2016. Tau hyperphosphorylation in synaptosomes and neuroinflammation are associated with canine cognitive impairment. *J Comp Neurol,* 524**,** 874-95.
SNYDER, E. M., NONG, Y., ALMEIDA, C. G., PAUL, S., MORAN, T., CHOI, E. Y., NAIRN, A. C., SALTER, M. W., LOMBROSO, P. J., GOURAS, G. K. & GREENGARD, P. 2005. Regulation of NMDA receptor trafficking by amyloid-beta. *Nat Neurosci,* 8**,** 1051-8.
SOFRONIEW, M. V. 2020. Astrocyte Reactivity: Subtypes, States, and Functions in CNS Innate Immunity. *Trends Immunol,* 41**,** 758-770.
SOFRONIEW, M. V. & VINTERS, H. V. 2010. Astrocytes: biology and pathology. *Acta Neuropathol,* 119**,** 7-35.
SOHAL, V. S., ZHANG, F., YIZHAR, O. & DEISSEROTH, K. 2009. Parvalbumin neurons and gamma rhythms enhance cortical circuit performance. *Nature,* 459**,** 698-702.
SONG, J. H., CHOI, W., SONG, Y. H., KIM, J. H., JEONG, D., LEE, S. H. & PAIK, S. B. 2020. Precise Mapping of Single Neurons by Calibrated 3D Reconstruction of Brain Slices Reveals Topographic Projection in Mouse Visual Cortex. *Cell Rep,* 31**,** 107682.
SOULA, M., MARTIN-AVILA, A., ZHANG, Y., DHINGRA, A., NITZAN, N., SADOWSKI, M. J., GAN, W. B. & BUZSAKI, G. 2023. Forty-hertz light stimulation does not entrain native gamma oscillations in Alzheimer's disease model mice. *Nat Neurosci,* 26**,** 570-578.
SPAGNOLO, B., BALENA, A., PEIXOTO, R. T., PISANELLO, M., SILEO, L., BIANCO, M., RIZZO, A., PISANO, F., QUALTIERI, A., LOFRUMENTO, D. D., DE NUCCIO, F., ASSAD, J. A., SABATINI, B. L., DE VITTORIO, M. & PISANELLO, F. 2022. Tapered fibertrodes for optoelectrical neural interfacing in small brain volumes with reduced artefacts. *Nat Mater,* 21**,** 826-835.
SPIRES, T. L. & HYMAN, B. T. 2005. Transgenic models of Alzheimer's disease: learning from animals. *NeuroRx,* 2**,** 423-37.
SPRUGNOLI, G., MUNSCH, F., CAPPON, D., PACIOREK, R., MACONE, J., CONNOR, A., EL FAKHRI, G., SALVADOR, R., RUFFINI, G., DONOHOE, K., SHAFI, M. M., PRESS, D., ALSOP, D. C., PASCUAL LEONE, A. & SANTARNECCHI, E. 2021. Impact of multisession 40Hz tACS on hippocampal perfusion in patients with Alzheimer's disease. *Alzheimers Res Ther,* 13**,** 203.
STAM, C. J., VAN CAPPELLEN VAN WALSUM, A. M., PIJNENBURG, Y. A., BERENDSE, H. W., DE MUNCK, J. C., SCHELTENS, P. & VAN DIJK, B. W. 2002. Generalized synchronization of MEG recordings in Alzheimer's Disease: evidence for involvement of the gamma band. *J Clin Neurophysiol,* 19**,** 562-74.
STERIADE, M. 2001. Impact of network activities on neuronal properties in corticothalamic systems. *J Neurophysiol,* 86**,** 1-39.
STEWART, W., BUCKLAND, M. E., ABDOLMOHAMMADI, B., AFFLECK, A. J., ALVAREZ, V. E., GILCHRIST, S., HUBER, B. R., LEE, E. B., LYALL, D. M., NOWINSKI, C. J., RUSSELL, E. R., STEIN, T. D., SUTER, C. M. & MCKEE, A. C. 2023. Risk of chronic traumatic encephalopathy in rugby union is associated with length of playing career. *Acta Neuropathol,* 146**,** 829-832.
STRITTMATTER, W. J., SAUNDERS, A. M., SCHMECHEL, D., PERICAK-VANCE, M., ENGHILD, J., SALVESEN, G. S. & ROSES, A. D. 1993. Apolipoprotein E: high-avidity binding to beta-amyloid and increased frequency of type 4 allele in late-onset familial Alzheimer disease. *Proc Natl Acad Sci U S A,* 90**,** 1977-81.
STURCHLER-PIERRAT, C., ABRAMOWSKI, D., DUKE, M., WIEDERHOLD, K. H., MISTL, C., ROTHACHER, S., LEDERMANN, B., BURKI, K., FREY, P., PAGANETTI, P. A., WARIDEL, C., CALHOUN, M. E., JUCKER, M., PROBST, A., STAUFENBIEL, M. & SOMMER, B. 1997. Two amyloid precursor protein transgenic mouse models with Alzheimer disease-like pathology. *Proc Natl Acad Sci U S A,* 94**,** 13287-92.

STYREN, S. D., HAMILTON, R. L., STYREN, G. C. & KLUNK, W. E. 2000. X-34, a fluorescent derivative of Congo red: a novel histochemical stain for Alzheimer's disease pathology. *J Histochem Cytochem,* 48**,** 1223-32.

SUK, H. J., BUIE, N., XU, G., BANERJEE, A., BOYDEN, E. S. & TSAI, L. H. 2023. Vibrotactile stimulation at gamma frequency mitigates pathology related to neurodegeneration and improves motor function. *Front Aging Neurosci,* 15**,** 1129510.

SUK, H. J. C., D.; JACKSON, B.; FERNANDEZ, V.; STARK, D.; MILMAN, N.; BEACH, S.; UITERMARKT, B.; GANDER, P.; BOES, A. D..; BROWN, E.; BOYDEN, E.; TSAI, L. 2020. Sensory gamma frequency stimulation in cognitively healthy and AD individuals safely induces highly coordinated 40 hz neural oscillation: A preliminary study of non-invasive sensory stimulation for treating Alzheimer's disease. *Alzheimer's & Dementia,* 16**,** e041146.

SUN, F., ZENG, J., JING, M., ZHOU, J., FENG, J., OWEN, S. F., LUO, Y., LI, F., WANG, H., YAMAGUCHI, T., YONG, Z., GAO, Y., PENG, W., WANG, L., ZHANG, S., DU, J., LIN, D., XU, M., KREITZER, A. C., CUI, G. & LI, Y. 2018. A Genetically Encoded Fluorescent Sensor Enables Rapid and Specific Detection of Dopamine in Flies, Fish, and Mice. *Cell,* 174**,** 481-496 e19.

SUNDARAM, G. S., GARAI, K., RATH, N. P., YAN, P., CIRRITO, J. R., CAIRNS, N. J., LEE, J. M. & SHARMA, V. 2014. Characterization of a brain permeant fluorescent molecule and visualization of Abeta parenchymal plaques, using real-time multiphoton imaging in transgenic mice. *Org Lett,* 16**,** 3640-3.

SWANSON, C. J., ZHANG, Y., DHADDA, S., WANG, J., KAPLOW, J., LAI, R. Y. K., LANNFELT, L., BRADLEY, H., RABE, M., KOYAMA, A., REYDERMAN, L., BERRY, D. A., BERRY, S., GORDON, R., KRAMER, L. D. & CUMMINGS, J. L. 2021. A randomized, double-blind, phase 2b proof-of-concept clinical trial in early Alzheimer's disease with lecanemab, an anti-Abeta protofibril antibody. *Alzheimers Res Ther,* 13**,** 80.

SYCH, Y., CHERNYSHEVA, M., SUMANOVSKI, L. T. & HELMCHEN, F. 2019. High-density multi-fiber photometry for studying large-scale brain circuit dynamics. *Nat Methods,* 16**,** 553-560.

TAKAHASHI, H., KLEIN, Z. A., BHAGAT, S. M., KAUFMAN, A. C., KOSTYLEV, M. A., IKEZU, T., STRITTMATTER, S. M. & ALZHEIMER'S DISEASE NEUROIMAGING, I. 2017. Opposing effects of progranulin deficiency on amyloid and tau pathologies via microglial TYROBP network. *Acta Neuropathol,* 133**,** 785-807.

TAKANO, T., TIAN, G. F., PENG, W., LOU, N., LIBIONKA, W., HAN, X. & NEDERGAARD, M. 2006. Astrocyte-mediated control of cerebral blood flow. *Nat Neurosci,* 9**,** 260-7.

TALLINI, Y. N., OHKURA, M., CHOI, B. R., JI, G., IMOTO, K., DORAN, R., LEE, J., PLAN, P., WILSON, J., XIN, H. B., SANBE, A., GULICK, J., MATHAI, J., ROBBINS, J., SALAMA, G., NAKAI, J. & KOTLIKOFF, M. I. 2006. Imaging cellular signals in the heart in vivo: Cardiac expression of the high-signal Ca2+ indicator GCaMP2. *Proc Natl Acad Sci U S A,* 103**,** 4753-8.

TANG, Y., BENUSIGLIO, D., LEFEVRE, A., KUPPERS, S., LAPIES, O., KERSPERN, D., CHARLET, A. & GRINEVICH, V. 2022. Viral vectors for opto-electrode recording and photometry-based imaging of oxytocin neurons in anesthetized and socially interacting rats. *STAR Protoc,* 3**,** 101032.

TANTAMA, M., MARTINEZ-FRANCOIS, J. R., MONGEON, R. & YELLEN, G. 2013. Imaging energy status in live cells with a fluorescent biosensor of the intracellular ATP-to-ADP ratio. *Nat Commun,* 4**,** 2550.

TANZI, R. E. 2012. The genetics of Alzheimer disease. *Cold Spring Harb Perspect Med,* 2.

TANZI, R. E. & BERTRAM, L. 2005. Twenty years of the Alzheimer's disease amyloid hypothesis: a genetic perspective. *Cell,* 120**,** 545-55.

TANZI, R. E., GUSELLA, J. F., WATKINS, P. C., BRUNS, G. A., ST GEORGE-HYSLOP, P., VAN KEUREN, M. L., PATTERSON, D., PAGAN, S., KURNIT, D. M. & NEVE, R. L. 1987. Amyloid beta protein gene: cDNA, mRNA distribution, and genetic linkage near the Alzheimer locus. *Science,* 235**,** 880-4.

TARDIVEL, M., BEGARD, S., BOUSSET, L., DUJARDIN, S., COENS, A., MELKI, R., BUEE, L. & COLIN, M. 2016. Tunneling nanotube (TNT)-mediated neuron-to neuron transfer of pathological Tau protein assemblies. *Acta Neuropathol Commun,* 4**,** 117.

TECUAPETLA, F., MATIAS, S., DUGUE, G. P., MAINEN, Z. F. & COSTA, R. M. 2014. Balanced activity in basal ganglia projection pathways is critical for contraversive movements. *Nat Commun,* 5**,** 4315.

TEIPEL, S. J., SCHAPIRO, M. B., ALEXANDER, G. E., KRASUSKI, J. S., HORWITZ, B., HOEHNE, C., MOLLER, H. J., RAPOPORT, S. I. & HAMPEL, H. 2003. Relation of corpus callosum and

hippocampal size to age in nondemented adults with Down's syndrome. *Am J Psychiatry,* 160**,** 1870-8.
TERRY, R. D. 1963. The Fine Structure of Neurofibrillary Tangles in Alzheimer's Disease. *J Neuropathol Exp Neurol,* 22**,** 629-42.
TERWEL, D., MUYLLAERT, D., DEWACHTER, I., BORGHGRAEF, P., CROES, S., DEVIJVER, H. & VAN LEUVEN, F. 2008. Amyloid activates GSK-3beta to aggravate neuronal tauopathy in bigenic mice. *Am J Pathol,* 172**,** 786-98.
TEXIDO, L., MARTIN-SATUE, M., ALBERDI, E., SOLSONA, C. & MATUTE, C. 2011. Amyloid beta peptide oligomers directly activate NMDA receptors. *Cell Calcium,* 49**,** 184-90.
TEZUKA, T., UMEMORI, H., AKIYAMA, T., NAKANISHI, S. & YAMAMOTO, T. 1999. PSD-95 promotes Fyn-mediated tyrosine phosphorylation of the N-methyl-D-aspartate receptor subunit NR2A. *Proc Natl Acad Sci U S A,* 96**,** 435-40.
THAL, D. R., RUB, U., ORANTES, M. & BRAAK, H. 2002. Phases of A beta-deposition in the human brain and its relevance for the development of AD. *Neurology,* 58**,** 1791-800.
TIAN, L., HIRES, S. A., MAO, T., HUBER, D., CHIAPPE, M. E., CHALASANI, S. H., PETREANU, L., AKERBOOM, J., MCKINNEY, S. A., SCHREITER, E. R., BARGMANN, C. I., JAYARAMAN, V., SVOBODA, K. & LOOGER, L. L. 2009. Imaging neural activity in worms, flies and mice with improved GCaMP calcium indicators. *Nat Methods,* 6**,** 875-81.
TIESINGA, P. & SEJNOWSKI, T. J. 2009. Cortical enlightenment: are attentional gamma oscillations driven by ING or PING? *Neuron,* 63**,** 727-32.
TORT, A. B., KRAMER, M. A., THORN, C., GIBSON, D. J., KUBOTA, Y., GRAYBIEL, A. M. & KOPELL, N. J. 2008. Dynamic cross-frequency couplings of local field potential oscillations in rat striatum and hippocampus during performance of a T-maze task. *Proc Natl Acad Sci U S A,* 105**,** 20517-22.
TRAUB, R. D., WHITTINGTON, M. A., COLLING, S. B., BUZSAKI, G. & JEFFERYS, J. G. 1996a. Analysis of gamma rhythms in the rat hippocampus in vitro and in vivo. *J Physiol,* 493 (Pt 2)**,** 471-84.
TRAUB, R. D., WHITTINGTON, M. A., STANFORD, I. M. & JEFFERYS, J. G. 1996b. A mechanism for generation of long-range synchronous fast oscillations in the cortex. *Nature,* 383**,** 621-4.
TUCKER, H. M., KIHIKO, M., CALDWELL, J. N., WRIGHT, S., KAWARABAYASHI, T., PRICE, D., WALKER, D., SCHEFF, S., MCGILLIS, J. P., RYDEL, R. E. & ESTUS, S. 2000. The plasmin system is induced by and degrades amyloid-beta aggregates. *J Neurosci,* 20**,** 3937-46.
TURNBULL, I. M., MCGEER, P. L., BEATTIE, L., CALNE, D. & PATE, B. 1985. Stimulation of the basal nucleus of Meynert in senile dementia of Alzheimer's type. A preliminary report. *Appl Neurophysiol,* 48**,** 216-21.
ULRICH, J. D. & HOLTZMAN, D. M. 2016. TREM2 Function in Alzheimer's Disease and Neurodegeneration. *ACS Chem Neurosci,* 7**,** 420-7.
ULRICH, J. D., ULLAND, T. K., COLONNA, M. & HOLTZMAN, D. M. 2017. Elucidating the Role of TREM2 in Alzheimer's Disease. *Neuron,* 94**,** 237-248.
UM, J. W., KAUFMAN, A. C., KOSTYLEV, M., HEISS, J. K., STAGI, M., TAKAHASHI, H., KERRISK, M. E., VORTMEYER, A., WISNIEWSKI, T., KOLESKE, A. J., GUNTHER, E. C., NYGAARD, H. B. & STRITTMATTER, S. M. 2013. Metabotropic glutamate receptor 5 is a coreceptor for Alzheimer abeta oligomer bound to cellular prion protein. *Neuron,* 79**,** 887-902.
UM, J. W., NYGAARD, H. B., HEISS, J. K., KOSTYLEV, M. A., STAGI, M., VORTMEYER, A., WISNIEWSKI, T., GUNTHER, E. C. & STRITTMATTER, S. M. 2012. Alzheimer amyloid-beta oligomer bound to postsynaptic prion protein activates Fyn to impair neurons. *Nat Neurosci,* 15**,** 1227-35.
UNGER, E. K., KELLER, J. P., ALTERMATT, M., LIANG, R., MATSUI, A., DONG, C., HON, O. J., YAO, Z., SUN, J., BANALA, S., FLANIGAN, M. E., JAFFE, D. A., HARTANTO, S., CARLEN, J., MIZUNO, G. O., BORDEN, P. M., SHIVANGE, A. V., CAMERON, L. P., SINNING, S., UNDERHILL, S. M., OLSON, D. E., AMARA, S. G., TEMPLE LANG, D., RUDNICK, G., MARVIN, J. S., LAVIS, L. D., LESTER, H. A., ALVAREZ, V. A., FISHER, A. J., PRESCHER, J. A., KASH, T. L., YAROV-YAROVOY, V., GRADINARU, V., LOOGER, L. L. & TIAN, L. 2020. Directed Evolution of a Selective and Sensitive Serotonin Sensor via Machine Learning. *Cell,* 183**,** 1986-2002 e26.
VAN DEURSEN, J. A., VUURMAN, E. F., VAN KRANEN-MASTENBROEK, V. H., VERHEY, F. R. & RIEDEL, W. J. 2011. 40-Hz steady state response in Alzheimer's disease and mild cognitive impairment. *Neurobiol Aging,* 32**,** 24-30.

VAN DEURSEN, J. A., VUURMAN, E. F., VERHEY, F. R., VAN KRANEN-MASTENBROEK, V. H. & RIEDEL, W. J. 2008. Increased EEG gamma band activity in Alzheimer's disease and mild cognitive impairment. *J Neural Transm (Vienna),* 115**,** 1301-11.

VAN DYCK, C. H., SWANSON, C. J., AISEN, P., BATEMAN, R. J., CHEN, C., GEE, M., KANEKIYO, M., LI, D., REYDERMAN, L., COHEN, S., FROELICH, L., KATAYAMA, S., SABBAGH, M., VELLAS, B., WATSON, D., DHADDA, S., IRIZARRY, M., KRAMER, L. D. & IWATSUBO, T. 2023. Lecanemab in Early Alzheimer's Disease. *N Engl J Med,* 388**,** 9-21.

VAN ELDIK, L. J., CARRILLO, M. C., COLE, P. E., FEUERBACH, D., GREENBERG, B. D., HENDRIX, J. A., KENNEDY, M., KOZAUER, N., MARGOLIN, R. A., MOLINUEVO, J. L., MUELLER, R., RANSOHOFF, R. M., WILCOCK, D. M., BAIN, L. & BALES, K. 2016. The roles of inflammation and immune mechanisms in Alzheimer's disease. *Alzheimers Dement (N Y),* 2**,** 99-109.

VAN OIJEN, M., HOFMAN, A., SOARES, H. D., KOUDSTAAL, P. J. & BRETELER, M. M. 2006. Plasma Abeta(1-40) and Abeta(1-42) and the risk of dementia: a prospective case-cohort study. *Lancet Neurol,* 5**,** 655-60.

VANNOSTRAND, W. E. R., A. J. M.; CHUNG, R.; COTMAN, C. W.; SAPORITOIRWIN, S. M. 1994. Amyloid beta-protein precursor in cultured leptomeningeal smooth-muscle cells. *Amyloid-Int J Exp Clin Invest,* 1**,** 1-7.

VENEGAS, C., KUMAR, S., FRANKLIN, B. S., DIERKES, T., BRINKSCHULTE, R., TEJERA, D., VIEIRA-SAECKER, A., SCHWARTZ, S., SANTARELLI, F., KUMMER, M. P., GRIEP, A., GELPI, E., BEILHARZ, M., RIEDEL, D., GOLENBOCK, D. T., GEYER, M., WALTER, J., LATZ, E. & HENEKA, M. T. 2017. Microglia-derived ASC specks cross-seed amyloid-beta in Alzheimer's disease. *Nature,* 552**,** 355-361.

VERKHRATSKY, A., OLABARRIA, M., NORISTANI, H. N., YEH, C. Y. & RODRIGUEZ, J. J. 2010. Astrocytes in Alzheimer's disease. *Neurotherapeutics,* 7**,** 399-412.

VERRET, L., MANN, E. O., HANG, G. B., BARTH, A. M., COBOS, I., HO, K., DEVIDZE, N., MASLIAH, E., KREITZER, A. C., MODY, I., MUCKE, L. & PALOP, J. J. 2012. Inhibitory interneuron deficit links altered network activity and cognitive dysfunction in Alzheimer model. *Cell,* 149**,** 708-21.

VOLTERRA, A. & MELDOLESI, J. 2005. Astrocytes, from brain glue to communication elements: the revolution continues. *Nat Rev Neurosci,* 6**,** 626-40.

VULLIET, R., HALLORAN, S. M., BRAUN, R. K., SMITH, A. J. & LEE, G. 1992. Proline-directed phosphorylation of human Tau protein. *J Biol Chem,* 267**,** 22570-4.

WALKER, L. C., CALLAHAN, M. J., BIAN, F., DURHAM, R. A., ROHER, A. E. & LIPINSKI, W. J. 2002. Exogenous induction of cerebral beta-amyloidosis in betaAPP-transgenic mice. *Peptides,* 23**,** 1241-7.

WALKER, L. C., KITT, C. A., SCHWAM, E., BUCKWALD, B., GARCIA, F., SEPINWALL, J. & PRICE, D. L. 1987. Senile plaques in aged squirrel monkeys. *Neurobiol Aging,* 8**,** 291-6.

WALKER, L. C., MASTERS, C., BEYREUTHER, K. & PRICE, D. L. 1990. Amyloid in the brains of aged squirrel monkeys. *Acta Neuropathol,* 80**,** 381-7.

WALSH, D. M., LOMAKIN, A., BENEDEK, G. B., CONDRON, M. M. & TEPLOW, D. B. 1997. Amyloid beta-protein fibrillogenesis. Detection of a protofibrillar intermediate. *J Biol Chem,* 272**,** 22364-72.

WALSH, D. M. & SELKOE, D. J. 2004. Deciphering the molecular basis of memory failure in Alzheimer's disease. *Neuron,* 44**,** 181-93.

WANG, C., FAN, L., KHAWAJA, R. R., LIU, B., ZHAN, L., KODAMA, L., CHIN, M., LI, Y., LE, D., ZHOU, Y., CONDELLO, C., GRINBERG, L. T., SEELEY, W. W., MILLER, B. L., MOK, S. A., GESTWICKI, J. E., CUERVO, A. M., LUO, W. & GAN, L. 2022. Microglial NF-kappaB drives tau spreading and toxicity in a mouse model of tauopathy. *Nat Commun,* 13**,** 1969.

WANG, D., FU, Q., ZHOU, Y., XU, B., SHI, Q., IGWE, B., MATT, L., HELL, J. W., WISELY, E. V., ODDO, S. & XIANG, Y. K. 2013. beta2 adrenergic receptor, protein kinase A (PKA) and c-Jun N-terminal kinase (JNK) signaling pathways mediate tau pathology in Alzheimer disease models. *J Biol Chem,* 288**,** 10298-307.

WANG, D., GOVINDAIAH, G., LIU, R., DE ARCANGELIS, V., COX, C. L. & XIANG, Y. K. 2010. Binding of amyloid beta peptide to beta2 adrenergic receptor induces PKA-dependent AMPA receptor hyperactivity. *FASEB J,* 24**,** 3511-21.

WANG, H. Y., LEE, D. H., D'ANDREA, M. R., PETERSON, P. A., SHANK, R. P. & REITZ, A. B. 2000. beta-Amyloid(1-42) binds to alpha7 nicotinic acetylcholine receptor with high affinity. Implications for Alzheimer's disease pathology. *J Biol Chem,* 275**,** 5626-32.

WANG, H. Y., LI, W., BENEDETTI, N. J. & LEE, D. H. 2003. Alpha 7 nicotinic acetylcholine receptors mediate beta-amyloid peptide-induced tau protein phosphorylation. *J Biol Chem,* 278**,** 31547-53.

WANG, J., FANG, Y., WANG, X., YANG, H., YU, X. & WANG, H. 2017. Enhanced Gamma Activity and Cross-Frequency Interaction of Resting-State Electroencephalographic Oscillations in Patients with Alzheimer's Disease. *Front Aging Neurosci,* 9**,** 243.

WANG, R., MESCHIA, J. F., COTTER, R. J. & SISODIA, S. S. 1991. Secretion of the beta/A4 amyloid precursor protein. Identification of a cleavage site in cultured mammalian cells. *J Biol Chem,* 266**,** 16960-4.

WANG, X. J. & BUZSAKI, G. 1996. Gamma oscillation by synaptic inhibition in a hippocampal interneuronal network model. *J Neurosci,* 16**,** 6402-13.

WATAMURA, N., SATO, K. & SAIDO, T. C. 2022a. Mouse models of Alzheimer's disease for preclinical research. *Neurochem Int,* 158**,** 105361.

WATAMURA, N., SATO, K., SHIIHASHI, G., IWASAKI, A., KAMANO, N., TAKAHASHI, M., SEKIGUCHI, M., MIHIRA, N., FUJIOKA, R., NAGATA, K., HASHIMOTO, S., SAITO, T., OHSHIMA, T., SAIDO, T. C. & SASAGURI, H. 2022b. An isogenic panel of App knock-in mouse models: Profiling beta-secretase inhibition and endosomal abnormalities. *Sci Adv,* 8**,** eabm6155.

WEIDEMANN, A., KONIG, G., BUNKE, D., FISCHER, P., SALBAUM, J. M., MASTERS, C. L. & BEYREUTHER, K. 1989. Identification, biogenesis, and localization of precursors of Alzheimer's disease A4 amyloid protein. *Cell,* 57**,** 115-26.

WEINGARTEN, M. D., LOCKWOOD, A. H., HWO, S. Y. & KIRSCHNER, M. W. 1975. A protein factor essential for microtubule assembly. *Proc Natl Acad Sci U S A,* 72**,** 1858-62.

WELLER, J. & BUDSON, A. 2018. Current understanding of Alzheimer's disease diagnosis and treatment. *F1000Res,* 7.

WES, P. D., EASTON, A., CORRADI, J., BARTEN, D. M., DEVIDZE, N., DECARR, L. B., TRUONG, A., HE, A., BARREZUETA, N. X., POLSON, C., BOURIN, C., FLYNN, M. E., KEENAN, S., LIDGE, R., MEREDITH, J., NATALE, J., SANKARANARAYANAN, S., CADELINA, G. W., ALBRIGHT, C. F. & CACACE, A. M. 2014. Tau overexpression impacts a neuroinflammation gene expression network perturbed in Alzheimer's disease. *PLoS One,* 9**,** e106050.

WHITSON, J. S., SELKOE, D. J. & COTMAN, C. W. 1989. Amyloid beta protein enhances the survival of hippocampal neurons in vitro. *Science,* 243**,** 1488-90.

WHITTINGTON, M. A., TRAUB, R. D. & JEFFERYS, J. G. 1995. Synchronized oscillations in interneuron networks driven by metabotropic glutamate receptor activation. *Nature,* 373**,** 612-5.

WHITTINGTON, M. A., TRAUB, R. D., KOPELL, N., ERMENTROUT, B. & BUHL, E. H. 2000. Inhibition-based rhythms: experimental and mathematical observations on network dynamics. *Int J Psychophysiol,* 38**,** 315-36.

WILLIAMS, M. C., A.; HEMPEL, E.; COTTER, C.; SHUKLA, M.; JIANG, K.; ZHANG, A.; MROZAK, H.; KONISKY, A.; KWAN, K.; HAJOS, M.; MALCHANO, Z. 2021. Safety, feasibility, and adherence of a daily, in-home gamma sensory stimulation therapy with the Cognito Sensory Stimulation System in Alzheimer's subjects. *Alzheimer's & Dementia,* 17**,** e056480.

WILSON, C. A., FOUDA, S. & SAKATA, S. 2020. Effects of optogenetic stimulation of basal forebrain parvalbumin neurons on Alzheimer's disease pathology. *Sci Rep,* 10**,** 15456.

WOODROOFE, M. N., SARNA, G. S., WADHWA, M., HAYES, G. M., LOUGHLIN, A. J., TINKER, A. & CUZNER, M. L. 1991. Detection of interleukin-1 and interleukin-6 in adult rat brain, following mechanical injury, by in vivo microdialysis: evidence of a role for microglia in cytokine production. *J Neuroimmunol,* 33**,** 227-36.

WRIGHT, A. L., ZINN, R., HOHENSINN, B., KONEN, L. M., BEYNON, S. B., TAN, R. P., CLARK, I. A., ABDIPRANOTO, A. & VISSEL, B. 2013. Neuroinflammation and neuronal loss precede Abeta plaque deposition in the hAPP-J20 mouse model of Alzheimer's disease. *PLoS One,* 8**,** e59586.

WU, C., WANG, Z., LEI, H., ZHANG, W. & DUAN, Y. 2007. Dual binding modes of Congo red to amyloid protofibril surface observed in molecular dynamics simulations. *J Am Chem Soc,* 129**,** 1225-32.

WU, T., DEJANOVIC, B., GANDHAM, V. D., GOGINENI, A., EDMONDS, R., SCHAUER, S., SRINIVASAN, K., HUNTLEY, M. A., WANG, Y., WANG, T. M., HEDEHUS, M., BARCK, K. H., STARK, M., NGU, H., FOREMAN, O., MEILANDT, W. J., ELSTROTT, J., CHANG, M. C., HANSEN, D. V., CARANO, R. A. D., SHENG, M. & HANSON, J. E. 2019. Complement C3 Is Activated in Human AD Brain and Is Required for Neurodegeneration in Mouse Models of Amyloidosis and Tauopathy. *Cell Rep,* 28**,** 2111-2123 e6.

WU, Y., WU, M., VAZQUEZ-GUARDADO, A., KIM, J., ZHANG, X., AVILA, R., KIM, J. T., DENG, Y., YU, Y., MELZER, S., BAI, Y., YOON, H., MENG, L., ZHANG, Y., GUO, H., HONG, L., KANATZIDIS, E. E., HANEY, C. R., WATERS, E. A., BANKS, A. R., HU, Z., LIE, F.,

CHAMORRO, L. P., SABATINI, B. L., HUANG, Y., KOZOROVITSKIY, Y. & ROGERS, J. A. 2022a. Wireless multi-lateral optofluidic microsystems for real-time programmable optogenetics and photopharmacology. *Nat Commun,* 13**,** 5571.

WU, Z., LIN, D. & LI, Y. 2022b. Pushing the frontiers: tools for monitoring neurotransmitters and neuromodulators. *Nat Rev Neurosci,* 23**,** 257-274.

WULFF, P., PONOMARENKO, A. A., BARTOS, M., KOROTKOVA, T. M., FUCHS, E. C., BAHNER, F., BOTH, M., TORT, A. B., KOPELL, N. J., WISDEN, W. & MONYER, H. 2009. Hippocampal theta rhythm and its coupling with gamma oscillations require fast inhibition onto parvalbumin-positive interneurons. *Proc Natl Acad Sci U S A,* 106**,** 3561-6.

WYSS-CORAY, T., LOIKE, J. D., BRIONNE, T. C., LU, E., ANANKOV, R., YAN, F., SILVERSTEIN, S. C. & HUSEMANN, J. 2003. Adult mouse astrocytes degrade amyloid-beta in vitro and in situ. *Nat Med,* 9**,** 453-7.

XIAO, N. A., ZHANG, J., ZHOU, M., WEI, Z., WU, X. L., DAI, X. M., ZHU, Y. G. & CHEN, X. C. 2015. Reduction of Glucose Metabolism in Olfactory Bulb is an Earlier Alzheimer's Disease-related Biomarker in 5XFAD Mice. *Chin Med J (Engl),* 128**,** 2220-7.

XIE, L., KANG, H., XU, Q., CHEN, M. J., LIAO, Y., THIYAGARAJAN, M., O'DONNELL, J., CHRISTENSEN, D. J., NICHOLSON, C., ILIFF, J. J., TAKANO, T., DEANE, R. & NEDERGAARD, M. 2013. Sleep drives metabolite clearance from the adult brain. *Science,* 342**,** 373-7.

XIE, Z., CULLEY, D. J., DONG, Y., ZHANG, G., ZHANG, B., MOIR, R. D., FROSCH, M. P., CROSBY, G. & TANZI, R. E. 2008. The common inhalation anesthetic isoflurane induces caspase activation and increases amyloid beta-protein level in vivo. *Ann Neurol,* 64**,** 618-27.

XIE, Z., DONG, Y., MAEDA, U., ALFILLE, P., CULLEY, D. J., CROSBY, G. & TANZI, R. E. 2006. The common inhalation anesthetic isoflurane induces apoptosis and increases amyloid beta protein levels. *Anesthesiology,* 104**,** 988-94.

XU, Z., DONG, Y., WU, X., ZHANG, J., MCAULIFFE, S., PAN, C., ZHANG, Y., ICHINOSE, F., YUE, Y. & XIE, Z. 2011. The potential dual effects of anesthetic isoflurane on Abeta-induced apoptosis. *Curr Alzheimer Res,* 8**,** 741-52.

YAAR, M., ZHAI, S., PILCH, P. F., DOYLE, S. M., EISENHAUER, P. B., FINE, R. E. & GILCHREST, B. A. 1997. Binding of beta-amyloid to the p75 neurotrophin receptor induces apoptosis. A possible mechanism for Alzheimer's disease. *J Clin Invest,* 100**,** 2333-40.

YAGUE, J. G., TSUNEMATSU, T. & SAKATA, S. 2017. Distinct Temporal Coordination of Spontaneous Population Activity between Basal Forebrain and Auditory Cortex. *Front Neural Circuits,* 11**,** 64.

YAMADA, K., HASHIMOTO, T., YABUKI, C., NAGAE, Y., TACHIKAWA, M., STRICKLAND, D. K., LIU, Q., BU, G., BASAK, J. M., HOLTZMAN, D. M., OHTSUKI, S., TERASAKI, T. & IWATSUBO, T. 2008. The low density lipoprotein receptor-related protein 1 mediates uptake of amyloid beta peptides in an in vitro model of the blood-brain barrier cells. *J Biol Chem,* 283**,** 34554-62.

YAMADA, K., HOLTH, J. K., LIAO, F., STEWART, F. R., MAHAN, T. E., JIANG, H., CIRRITO, J. R., PATEL, T. K., HOCHGRAFE, K., MANDELKOW, E. M. & HOLTZMAN, D. M. 2014. Neuronal activity regulates extracellular tau in vivo. *J Exp Med,* 211**,** 387-93.

YAMAGISHI, S., NAKAMURA, K., INOUE, H., KIKUCHI, S. & TAKEUCHI, M. 2005. Serum or cerebrospinal fluid levels of glyceraldehyde-derived advanced glycation end products (AGEs) may be a promising biomarker for early detection of Alzheimer's disease. *Med Hypotheses,* 64**,** 1205-7.

YAMAMOTO, K., TANEI, Z. I., HASHIMOTO, T., WAKABAYASHI, T., OKUNO, H., NAKA, Y., YIZHAR, O., FENNO, L. E., FUKAYAMA, M., BITO, H., CIRRITO, J. R., HOLTZMAN, D. M., DEISSEROTH, K. & IWATSUBO, T. 2015. Chronic optogenetic activation augments abeta pathology in a mouse model of Alzheimer disease. *Cell Rep,* 11**,** 859-865.

YAN, S. D., CHEN, X., FU, J., CHEN, M., ZHU, H., ROHER, A., SLATTERY, T., ZHAO, L., NAGASHIMA, M., MORSER, J., MIGHELI, A., NAWROTH, P., STERN, D. & SCHMIDT, A. M. 1996. RAGE and amyloid-beta peptide neurotoxicity in Alzheimer's disease. *Nature,* 382**,** 685-91.

YANG, H. D., KIM, D. H., LEE, S. B. & YOUNG, L. D. 2016. History of Alzheimer's Disease. *Dement Neurocogn Disord,* 15**,** 115-121.

YANG, J., DING, W., ZHU, B., ZHEN, S., KUANG, S., ZHANG, C., WANG, P., YANG, F., YANG, L., YIN, W., TANZI, R E, SHEN, S., RAN, C. 2021. Reporting amyloid beta levels via bioluminescence imaging with amyloid reservoirs in Alzheimer's disease models. *BioRxiv*.

YANG, M. & TEPLOW, D. B. 2008. Amyloid beta-protein monomer folding: free-energy surfaces reveal alloform-specific differences. *J Mol Biol,* 384**,** 450-64.

YAO, Y., YING, Y., DENG, Q., ZHANG, W., ZHU, H., LIN, Z., ZHANG, S., MA, J. & ZHAO, Y. 2020. Non-invasive 40-Hz Light Flicker Ameliorates Alzheimer's-Associated Rhythm Disorder via Regulating Central Circadian Clock in Mice. *Front Physiol,* 11**,** 294.

YEH, F. L., HANSEN, D. V. & SHENG, M. 2017. TREM2, Microglia, and Neurodegenerative Diseases. *Trends Mol Med,* 23**,** 512-533.

YIN, K. J., CIRRITO, J. R., YAN, P., HU, X., XIAO, Q., PAN, X., BATEMAN, R., SONG, H., HSU, F. F., TURK, J., XU, J., HSU, C. Y., MILLS, J. C., HOLTZMAN, D. M. & LEE, J. M. 2006. Matrix metalloproteinases expressed by astrocytes mediate extracellular amyloid-beta peptide catabolism. *J Neurosci,* 26**,** 10939-48.

YOKOYAMA, M., KOBAYASHI, H., TATSUMI, L. & TOMITA, T. 2022. Mouse Models of Alzheimer's Disease. *Front Mol Neurosci,* 15**,** 912995.

YOON, S. S. & JO, S. A. 2012. Mechanisms of Amyloid-beta Peptide Clearance: Potential Therapeutic Targets for Alzheimer's Disease. *Biomol Ther (Seoul),* 20**,** 245-55.

YOSHIYAMA, Y., HIGUCHI, M., ZHANG, B., HUANG, S. M., IWATA, N., SAIDO, T. C., MAEDA, J., SUHARA, T., TROJANOWSKI, J. Q. & LEE, V. M. 2007. Synapse loss and microglial activation precede tangles in a P301S tauopathy mouse model. *Neuron,* 53**,** 337-51.

YU, L., EDALJI, R., HARLAN, J. E., HOLZMAN, T. F., LOPEZ, A. P., LABKOVSKY, B., HILLEN, H., BARGHORN, S., EBERT, U., RICHARDSON, P. L., MIESBAUER, L., SOLOMON, L., BARTLEY, D., WALTER, K., JOHNSON, R. W., HAJDUK, P. J. & OLEJNICZAK, E. T. 2009. Structural characterization of a soluble amyloid beta-peptide oligomer. *Biochemistry,* 48**,** 1870-7.

YUAN, P. & GRUTZENDLER, J. 2016. Attenuation of beta-Amyloid Deposition and Neurotoxicity by Chemogenetic Modulation of Neural Activity. *J Neurosci,* 36**,** 632-41.

YUEDE, C. M., LEE, H., RESTIVO, J. L., DAVIS, T. A., HETTINGER, J. C., WALLACE, C. E., YOUNG, K. L., HAYNE, M. R., BU, G., LI, C. Z. & CIRRITO, J. R. 2016. Rapid in vivo measurement of beta-amyloid reveals biphasic clearance kinetics in an Alzheimer's mouse model. *J Exp Med,* 213**,** 677-85.

ZEMPEL, H., THIES, E., MANDELKOW, E. & MANDELKOW, E. M. 2010. Abeta oligomers cause localized Ca(2+) elevation, missorting of endogenous Tau into dendrites, Tau phosphorylation, and destruction of microtubules and spines. *J Neurosci,* 30**,** 11938-50.

ZHANG, C., WANG, Y., WANG, D., ZHANG, J. & ZHANG, F. 2018a. NSAID Exposure and Risk of Alzheimer's Disease: An Updated Meta-Analysis From Cohort Studies. *Front Aging Neurosci,* 10**,** 83.

ZHANG, F., GANNON, M., CHEN, Y., YAN, S., ZHANG, S., FENG, W., TAO, J., SHA, B., LIU, Z., SAITO, T., SAIDO, T., KEENE, C. D., JIAO, K., ROBERSON, E. D., XU, H. & WANG, Q. 2020. beta-amyloid redirects norepinephrine signaling to activate the pathogenic GSK3beta/tau cascade. *Sci Transl Med,* 12.

ZHANG, H., WEI, W., ZHAO, M., MA, L., JIANG, X., PEI, H., CAO, Y. & LI, H. 2021. Interaction between Abeta and Tau in the Pathogenesis of Alzheimer's Disease. *Int J Biol Sci,* 17**,** 2181-2192.

ZHANG, J., YAROWSKY, P., GORDON, M. N., DI CARLO, G., MUNIREDDY, S., VAN ZIJL, P. C. & MORI, S. 2004. Detection of amyloid plaques in mouse models of Alzheimer's disease by magnetic resonance imaging. *Magn Reson Med,* 51**,** 452-7.

ZHANG, S., IWATA, K., LACHENMANN, M. J., PENG, J. W., LI, S., STIMSON, E. R., LU, Y., FELIX, A. M., MAGGIO, J. E. & LEE, J. P. 2000. The Alzheimer's peptide a beta adopts a collapsed coil structure in water. *J Struct Biol,* 130**,** 130-41.

ZHANG, Y., GUO, O., HUO, Y., WANG, G. & MAN, H. Y. 2018b. Amyloid-beta Induces AMPA Receptor Ubiquitination and Degradation in Primary Neurons and Human Brains of Alzheimer's Disease. *J Alzheimers Dis,* 62**,** 1789-1801.

ZHANG, Y., ROZSA, M., LIANG, Y., BUSHEY, D., WEI, Z., ZHENG, J., REEP, D., BROUSSARD, G. J., TSANG, A., TSEGAYE, G., NARAYAN, S., OBARA, C. J., LIM, J. X., PATEL, R., ZHANG, R., AHRENS, M. B., TURNER, G. C., WANG, S. S., KORFF, W. L., SCHREITER, E. R., SVOBODA, K., HASSEMAN, J. P., KOLB, I. & LOOGER, L. L. 2023. Fast and sensitive GCaMP calcium indicators for imaging neural populations. *Nature,* 615**,** 884-891.

ZHAO, J., LI, Z., CONG, Y., ZHANG, J., TAN, M., ZHANG, H., GENG, N., LI, M., YU, W. & SHAN, P. 2017. Repetitive transcranial magnetic stimulation improves cognitive function of Alzheimer's disease patients. *Oncotarget,* 8**,** 33864-33871.

ZHOU, C., WU, Q., WANG, Z., WANG, Q., LIANG, Y. & LIU, S. 2020. The Effect of Hormone Replacement Therapy on Cognitive Function in Female Patients With Alzheimer's Disease: A Meta-Analysis. *Am J Alzheimers Dis Other Demen,* 35**,** 1533317520938585.

ZLOKOVIC, B. V., DEANE, R., SALLSTROM, J., CHOW, N. & MIANO, J. M. 2005. Neurovascular pathways and Alzheimer amyloid beta-peptide. *Brain Pathol,* 15**,** 78-83.